Structure-Property Correlations in the $BiFeO_3$-$NaNbO_3$ Solid Solution

Kevin J. W. Etherdo-Sibley

A thesis presented for the degree of

Doctor of Philosophy

School of Physical Sciences

University of Kent

August 2020

This thesis is dedicated to the memory of my father

Christopher Etherdo-Sibley

Abstract

Multiferroic materials are those which possess two or more ferroic orders, where '*ferroic*' relates to the spontaneous ordering of a property on application of a stimulus. For example, a ferromagnet shows spontaneous ordering of magnetic moments on the application of a magnetic field. Multiferroic materials have garnered high interest due to the possibility that they could be used to create faster memory, especially random access memory (RAM), which would be non-destructive and more energy efficient compared to ferroelectric RAM. Bismuth ferrite (BFO) is currently one of the most researched multiferroic materials as it is multiferroic at room temperature possessing both ferroelectric and antiferromagnetic order. However, applications are limited by a complicated magnetic structure (spin cycloid) which leaves the net magnetic moment close to zero as well as high conductivities and leakage currents.

Doping BFO, by adding another interesting compound to form a solid solution, is currently seen as a potential way to solve these issues and improve the properties. It is hoped that a morphotropic phase boundary, similar to that seen in lead zirconate titananate between the polar rhombohedral and tetragonal phases, can be realised which leads to enhanced dielectric and piezoelectric properties of BFO based materials.

In this research ferroelectric sodium niobate (NNO) was added to multiferroic BFO to form a solid solution to determine whether enhanced properties could be found. The BFO-NNO solid solution has received little attention within the literature and only a limited number of papers have covered the possible phase transitions present with fewer still investigating the change in magnetic and/or electrical properties. Compositions from $x = 0.05$ to 0.95 in $Bi_{1-x}Na_xFe_{1-x}Nb_xO_3$ in 5% increments were synthesised and analysed using X-Ray and neutron diffraction. Potassium niobate doped materials were prepared at $x = 0.1$ and 0.5 to enable comparison between the material behaviours. The data clearly shows a series of complex phase transitions occurring (*R*3*c* to *P*4*mm* to $P2_1ma$) with increasing NNO content (*chapter 5*). This included diffuse scattering seen throughout the neutron diffraction data of the *P*4*mm* region which can be related to short range NNO order (*chapters 4 and 5*). Improved magnetic behaviour was observed in the $Bi_{0.9}Na_{0.1}Fe_{0.9}Nb_{0.1}O_3$ composition with the spin cycloid lengthened as a result of chemical strain arising through a reduction of the size of domains resulting in switchable magnetic hysteresis (*chapter 3*). The work presented in this thesis clearly demonstrates the complex nature of materials formed within the BFO-NNO solid solution with these materials showing promise for next generation applications.

Acknowledgements

I want to say a big thank you to my supervisor Dr Donna Arnold for her continuous help, support and guidance throughout my PhD project. I would also like to thank my second supervisor Dr Emma McCabe and previous postdoctoral researcher Dr Laura Vera Stimpson for their help. My sincere thanks goes to Dr Gavin Stenning, Dr Dominic Fortes, Dr Alexandra Gibbs, and Dr Pascal Manuel of ISIS for their help in experiments at the materials characterisation laboratory, HRPD and WISH beamlines at ISIS. I would like to thank Dr Karen Johnston for her solid state NMR collaboration. I would also like to thank Dr Mark Price for his help with the SEM and Dr Tim Kinnear for his help in processing Raman data.

Thank you to my fellow research students Sally Pang, Richard Dixey, and Dash Bequiri for their help and support. I would also like to mention my friends Chris Simpson, Jacob Harman and Josh How for their years of support.

Lastly, I would like to thank my mum, aunt, uncle and sister for always being there when I need them.

Table of Contents

Table of Contents

Table of Contents

Summary of Figure Captions

Summary of Figure Captions

Summary of Figure Captions

Summary of Figure Captions

Summary of Figure Captions

Summary of Figure Captions

Summary of Figure Captions

Summary of Figure Captions

Summary of Figure Captions

Summary of Figure Captions

Summary of Figure Captions

Summary of Table Captions

Chapter One: Introduction

1.1 Introduction into the Perovskite Structure

Society, as it develops, is becoming ever more reliant on new powerful technology to progress driving the exponential growth in the discovery of new materials to improve the current generation of devices. One of the most important areas for new materials research is currently in the energy sector with extensive effort looking at new materials for battery technologies, fuel cells and photovoltaics etc.[1]. For example, a new approach to increase efficiency in photovoltaics has seen devices prepared which incorporate quantum dot nanostructures made using gallium arsenide derivatives[2]. In battery advancements, a recent study by Li *et al*[3] has suggested that calcium may be a viable replacement for lithium due to improvements in compatible electrolytes which could lead to the development of lower cost and potentially safer batteries. Likewise, an unconventional approach to materials design can be seen in the work by Tizno *et al*[4] who produced electronic devices by transposing layers of indium arsenide and aluminium antimonide with a gallium antimonide base which led to a memory device that was non-volatile and low power.

Before discussing materials properties in detail, it is first important to describe the perovskite structure since these systems form the cornerstone of the work presented in this thesis. Perovskites are one of the most studied structural types due to their ease of synthesis and compositional flexibility. Perovskite is a general name given to a material with the basic structure ABX_3 (where *A* is a large cation such as Ca^{2+}, *B* is typically a transition metal such as Mn^{4+} and *X* is an anion typically O^{2-}) named after the mineral Perovskite, $CaTiO_3$. The perfect perovskite structure adopts cubic $Pm\bar{3}m$ symmetry where the *A* site cations are located at the corners of the unit cell with the *B* site cations sited at the centre of the cube and surrounded by six face centred anions in an octahedral arrangement. This structure is adopted by the material $SrTiO_3$ at room temperature and is shown in *figure 1.1*.

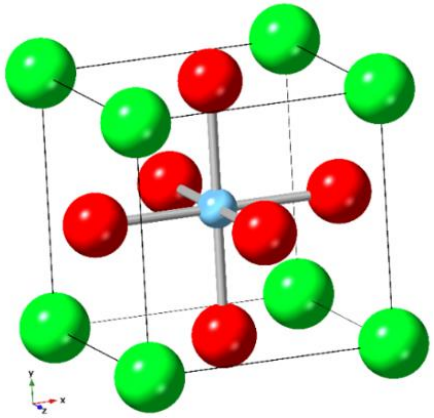

Figure 1.1: *Schematic representation of the unit cell of $SrTiO_3$ with cubic $Pm\bar{3}m$ symmetry. Green atoms are strontium, the blue atom is titanium and red atoms are oxygen.*

One of the most important aspects of perovskite materials is the versatility of the structure in that the *A* and *B* sites can greatly vary in size allowing a wide range of compositions and symmetries, and thus properties, to be realised. The Goldschmidt tolerance factor (shown in *equation 1.1*) is used to determine the difference in size between the *A* and *B* sites something which directly affects the symmetry of the perovskite structure[5]:

$$t = \frac{r_A + r_X}{\sqrt{2}\,(r_B + r_X)} \tag{1.1}$$

Where *t* is the tolerance factor, r_A is the radius of the *A*-cation, r_B is the radius of the *B*-cation and r_x is the radius of the anion. When *t* is close to 1 the material is most likely to adopt a cubic structure as the *A* and *B* cations are of ideal size.

In materials outside of the '*perfect cubic*' structure, i.e. with tolerance factors which are not equal to 1, we see tilting of the oxygen octahedra. Tilts are mostly found as the size of the *A*-site cation is too small, which leads to changes in the oxygen positions to reduce the *A*-site-oxygen bond length, leading to rotations of the octahedra[6]. Perovskites with *t* between 0.9 and 1.0 are likely to be cubic. When *t* is smaller than 0.9 but greater than 0.8 the perovskite is likely to crystallise with orthorhombic or rhombohedral symmetry but tetragonal symmetry can also be found to due to tilting. Below 0.8 the material will not crystallise with a perovskite structure[7]. In contrast if *t* is between 1.0 and ~1.08 then the perovskite is likely to adopt a tetragonal or hexagonal structure[6]. Above a tolerance factor of ~1.08 alternative structures are realised. Tilts are identified using Glazer notations where *a*, *b* and *c* are used to indicate the three directional axes of the octahedra[8,9]. Superscript notation is added to the given axis to designate the phase with a ($^+$) or ($^-$) indicating in phase and out of phase tilts respectively or with an (^{0}) to indicate that no tilts are present[8,9]. Phase transitions are often linked to changes in tilts in perovskites. For example, increasing the temperature of $CaTiO_3$ leads to a series of phase transitions from orthorhombic *Pbnm* to tetragonal *I*4/*mcm* to cubic $Pm\overline{3}m$[10,11]. In this series of transitions the tilts start at $a^-a^-c^+$ then become $a^0a^0c^-$ and once cubic $a^0b^0c^0$, effectively straightening the tilts as the temperature increases.

Double perovskites are a modification of the normal perovskite structure with the formula $A_2B_2X_6$. Materials can be found with the $A_2B'B''X_6$ structure as shown by the Sr_2YTaO_6 and Sr_2YNbO_6 double perovskites which crystallise in the monoclinic $P2_1/n$ structure with *B*-site cation order[12]. It is also possible to find materials with the $A'A''B'B''X_6$ configuration where it is then possible to find both *A* and *B* site order as seen in $NaLaMgWO_6$[13]. $NaLaMgWO_6$ was originally thought to crystallise in the *C*2/*m* space group[13], however, additional work using selected area electron diffraction and neutron

diffraction found the presence of a tilt modulation which led to a lowering of the symmetry and a revised trigonal structure which is elongated along the [100] direction[14]. This is not true of all *A*'*A*''*B*'*B*''X_6 double perovskites as shown by $BaLaMgTaO_6$ which is found in the cubic structure $Fm\overline{3}m$ with *B*-site order but without *A*-site order[15].

1.2 Dielectric Properties

If we now consider the properties of materials. Electrical materials are usually divided into three different categories depending on their properties. The first type of materials are known as conductors which allow an electrical current, electrons, to pass freely through the material when a voltage is applied. The second type, semi-conductors, also allow an electrical current to pass but to a much lesser degree. The third type are insulators which do not allow electrical current to pass through the material.

This insulating property is found in dielectrics due to the fact that electrons in the outer electron shells are unable to move throughout a structure[16]. An electric dipole is found when the electron cloud is distorted resulting in an uneven distribution of charge. This leads to an area with high electron density, negative charge and an area with low electron density, positive charge. This is known as the electric polarizability and this can be calculated from the total of all dipole moments present in the material. The dielectric constant (ε) is used to describe the polarizability of a material, the magnitude of induced electric dipoles. The dielectric constant can be calculated using the following equation[6].

$$\varepsilon = \varepsilon_0 C \frac{A}{t} \tag{1.2}$$

Where ε_0 is the constant, permittivity of free space, *C* is the capacitance, *A* is the area of the material, and *t* is the thickness of the material. The capacitance in this equation is used to detail the amount of electrical charge present for a given applied voltage (+ or -) on the surface of the material. Capacitance is calculated using the equation[6].

$$C = \frac{Q}{V} \tag{1.3}$$

Where *Q* is the total charge, and *V* is the potential difference.

Piezoelectrics describe a category of dielectric materials which develop an electrical charge on the application of mechanical stress in the absence of an electric field. For a dielectric material to be a piezoelectric it must have a structure that is non-centrosymmetric, i.e. it does not possess a centre of symmetry or an inversion centre. The crystal structure of a piezoelectric will dictate the direction of the applied stress necessary to drive the charge[6]. Within the piezoelectric class of materials there

are additional groups of materials. The first are known as pyroelectrics and the second, which shares the properties of both piezoelectrics and pyroelectrics, are called ferroelectrics. For a material to be a pyroelectric or ferroelectric it must adopt a symmetry with a polar point group. Piezoelectrics display a spontaneous displacement from applied pressure, pyroelectrics display a spontaneous displacement from change in temperature and ferroelectrics display a reversible spontaneous displacement[6].

The main differences between pyroelectrics and piezoelectrics are that pyroelectrics possess a permanent dipole which is dependent on temperature without requiring a mechanical stress. The change in polarisation for a pyroelectric can be calculated using the equation[17].

$$\Delta P = \pi \Delta T \tag{1.4}$$

Where P is the polarisation, T is the temperature and π is the pyroelectric coefficient, which is dependent on the material. The change of polarisation occurs as the structure of the pyroelectric alters due to thermal expansion arising as a result of the change in temperature.

Ferroelectrics possess the properties found in piezoelectrics and pyroelectrics, however, the permanent dipole of a ferroelectric can be switched in an applied electric field. The main feature of a ferroelectric is the polarisation-electric field (PE) hysteresis loop obtained when measuring voltage or electric field against polarisation. These measurements lead to a characteristic loop which will saturate at a high positive field known as the coercive field (E_c) and at the saturation polarisation (P_s) as shown in figure 1.2. On reversing the electric field the dipoles will reorientate so that they are reversed. At zero field some of the dipoles will remain orientated in the original way. This is known as the remnant polarisation (P_r)[18] as shown in figure 1.2. Despite this reasonably simple definition there are at least six mechanisms for ferroelectricity to occur: lone pair displacement, d^0 transition metal perovskites, charge-order, geometrically frustrated materials, and compounds with permanent dipole moments and through hydrogen bonding[19].

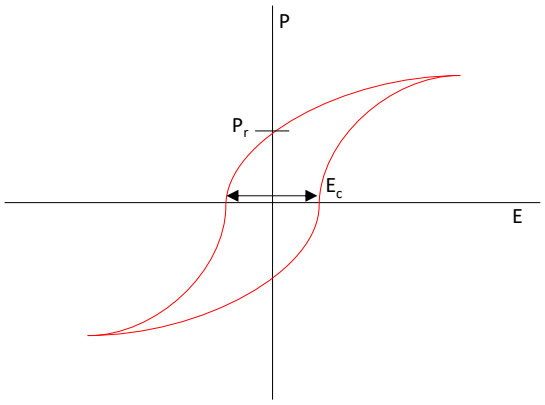

Figure 1.2: *Schematic representation of a ferroelectric polarisation (P) – electric field (E) hysteresis loop where P_r is remnant polarization and E_c is the coercive field.*

Since all ferroelectrics are pyroelectric there is a temperature dependence of the polarisation. Above a given temperature, known as the Curie temperature (T_c), the material will display paraelectric properties such that the material will not display a permanent dipole but will retain a dielectric constant and this can be calculated using the Curie-Weiss law[6].

$$\varepsilon = \frac{C}{(T - \theta)} \tag{1.5}$$

Where ε is the dielectric constant, *C* is the Curie constant, *T* is the temperature and θ is the Curie-Weiss temperature. The ferroelectric to paraelectric transition will also involve a structural transition of the material from a non-centrosymmetric symmetry to a centrosymmetric symmetry as the non-centrosymmetric distortions are lost.

Antiferroelectrics are related to ferroelectric materials. However, the dipole moments align antiparallel. This results in a net polarisation of zero as the dipole moments effectively cancel each other out. On application of high enough applied electric fields it is possible to convert an antiferroelectric to a ferroelectric. This transition results in what is known as a double hysteresis loop, when measuring the voltage or electric field against polarisation, with a separate hysteresis loop seen at both positive and negative electric fields. A variation of antiferroelectrics which possess a small net polarisation are ferrielectrics. Ferrielectric dipole moments are tilted away from each other leading to a V like shape so they do not fully cancel out.

1.3 Ferroelectric Perovskites

There are many examples of ferroelectric materials within the literature. The most recognised of the d^0 transition metal perovskite ferroelectrics is barium titanate, $BaTiO_3$[20]. At room temperature it is shown to have a tetragonal *P*4*mm* structure with the Ti^{4+} on the *B* site sitting off centre leading to a non-centrosymmetric structure[21]. It is energetically more favourable to form a stronger bond with a single oxygen than two weaker bonds leading to the displacement of the Ti^{4+} giving rise to switchable polarisation leading to ferroelectric properties[19]. As the temperature is lowered the *P*4*mm* ($a^0a^0c^0_+$) structure further distorts to an orthorhombic *Amm*2 ($a^0_+a^0_+c^0$) structure at around 278 K and then at around 183 K it adopts the rhombohedral *R*3*m* ($a^0_+a^0_+a^0_+$) structure[22-24]. The change in the direction of the polar displacement leads to the changes in structure from [001] in *P*4*mm* to [011] in *Amm*2 and [111] in *R*3*m* as shown in figure 1.3. This is primarily due to the displacement of the *B*-site increasing with decreasing temperature which leads to an increase of the unit cell changing the symmetry. As the temperature is increased $BaTiO_3$ adopts paraelectric cubic $Pm\bar{3}m$ symmetry, the structure adopted by the prototypical perovskite $SrTiO_3$ (figure 1.3)[22,25].

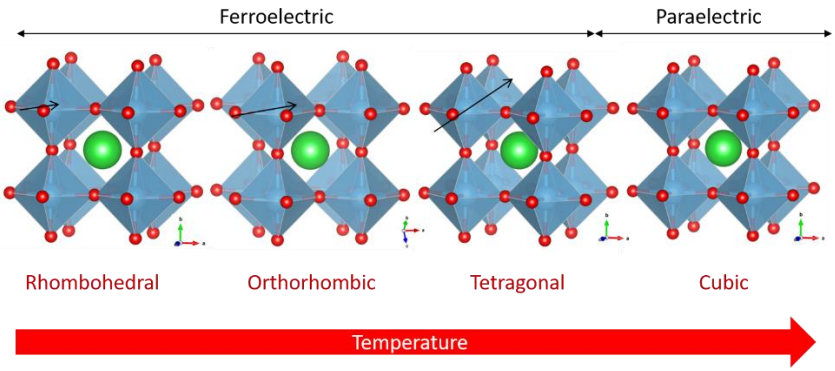

Figure 1.3: *Structural phase transitions of barium titanate as temperature is increased. Reproduced with permission of Dr Arnold.*

Lead zirconate titanate (PZT) is the solid solution between lead zirconate ($PbZrO_3$) and lead titanate ($PbTiO_3$) typically found commercially as the ferroelectric composition $PbZr_{0.52}Ti_{0.48}O_3$, which occurs at the so called morphotropic phase boundary (MPB)[26]. The MPB is formed as a result of two competing polar phases coexisting on both sides of the boundary. At a composition of 52% $PbZrO_3$ and 48% $PbTiO_3$ there is a phase boundary between polar rhombohedral *R*3*m* and tetragonal *P*4*mm* phases resulting in a MPB, this can be seen in *figure 1.4*[27,28]. This MPB is important as enhanced properties are found at this composition which lead to an increased dielectric constant and piezoelectric properties. Despite mass use in late 20th century electronics, such as in ferroelectric memory devices, EU regulations introduced in 2002 and 2011 have restricted the use of Pb in electronics by weight percentage due to the toxic nature of lead. However, PZT currently has an exemption for use in piezoelectrics due to the lack of a commercially competitive lead-free alternative[29,30]. However, due to the expectation that PZT will be banned completely in the near future current research into piezoelectrics has focused on non-toxic alternatives.

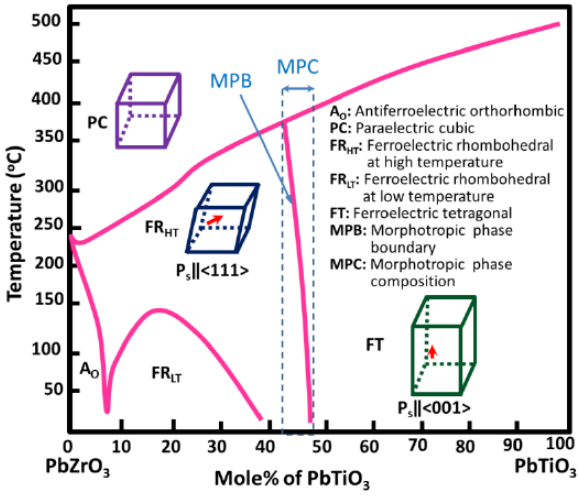

Figure 1.4: *Phase diagram of the lead zirconate and lead titanate solid solution where $PbZr_{0.52}Ti_{0.48}O_3$ is found at the morphotropic phase boundary between the tetragonal P4mm and rhombohedral R3m phases. Produced from Pramanik et al*[31,32].

Two of the current Pb-free PZT replacements studied are potassium niobate, $KNbO_3$ (KNO) and sodium niobate, $NaNbO_3$ (NNO). KNO is a d^0 ferroelectric compound that crystallises in the *Amm*2 space group at room temperature[33]. At high temperature two structural phase transitions occur, the first to a tetragonal, *P*4*mm* phase at around 498 K and a second to a cubic, $Pm\bar{3}m$ phase at around at 708 K[33,34]. This set of transitions mirrors those seen in $BaTiO_3$ with a low temperature (around 263 K) rhombohedral *R*3*m* transition also present[34]. KNO has been found to possess a dielectric constant of around 500 and a spontaneous polarization of 0.41 Cm^{-2} at room temperature[35,36]. There have been attempts as shown by Kakimoto *et al*[37] to improve the properties of KNO through the doping of rare earths such as $LaFeO_3$. However, the properties did not show an improvement with a decrease in the Curie temperature. However, the authors noted that the addition of the rare earths increased the density of the ceramics[37].

In contrast, NNO is a polymorphic compound that can be found in both ferroelectric and anti-ferroelectric phases with impressive electrical properties[38]. At room temperature NNO can be found in the antipolar orthorhombic space group *Pbcm* and, as reported by Johnston *et al*[39], the polar orthorhombic space group $P2_1ma$ at a smaller percentage. Further work by Johnston *et al*[40] found that the compositions of the polymorphs could be controlled by the procedure used to prepare the sodium niobate sample. It was found that the $P2_1ma$ phase could be made the major contribution in the sample by changing the synthesis procedure from solid state to a sol-gel reaction. When looking at the phase diagram of sodium niobate at lower temperatures it is found to be rhombohedral, *R*3*c,* at 12 K as the temperature increases the orthorhombic phase can be seen growing in[41,42]. At 280 K only the orthorhombic phase is seen until 633 K where a new orthorhombic *Pbnm* phase is observed and then at 810 K another orthorhombic, *Cmcm,* phase is found[43]. NNO then turns tetragonal, *P4/mbm*, at 865 K before finally becoming cubic ($Pm\bar{3}m$) at 950 K as reported by Darlington *et al*[41] and Mishra *et al*[43]. In terms of electrical properties sodium niobate has low leakage currents and a dielectric constant of around 200[44].

The solid solution, $K_xNa_{1-x}NbO_3$, has also attracted extensive research attention investigating phase transitions and space groups associated with these materials and probing the possibility of MPB behaviour. One of the earliest papers by Ahtee *et al*[45] proposed a series of complex transitions across a large temperature range. At room temperature it was found that the sodium rich end adopted a *Pm* structure with a change in the magnitude of the tilts described as potassium content was increased. The *Pm* phase then changes to an unidentified orthorhombic phase at around 50:50 Na:K ratio[45,46]. Further work by Baker *et al*[47] led to an improved understanding with the unidentified orthorhombic phase identified as *Amm*2 and a variable temperature study which simplified the previous series of complex temperature dependent phase transitions. Unfortunately despite major

interest no clear evidence of a PZT-like MPB has been found despite constant speculation with Baker *et al*[47] unable to conclude it was present[48]. It was found that the transition from *Pm* to *Amm*2 was a first order transition, without a bridging phase and with only a small structural change which led to the conclusion it did not behave similarly to PZT[47].

Unlike the niobate derivative, sodium tantalate, $NaTaO_3$, (NTO) is not a ferroelectric perovskite found in the non-polar orthorhombic structure, *Pcmn*/*Pbnm*[49-51] at room temperature. However, it is referred to as an incipient ferroelectric where a transition to a polar structure is inhibited by quantum fluctuations[52]. A series of phase transitions can be seen with increasing temperature at ~720 K to an orthorhombic *Cmcm* phase and to a tetragonal *P*4/*mbm* phase at around 835 K and finally to the cubic $Pm\bar{3}m$ phase at around 890 K[50,51,53]. The main area of interest for NTO in the literature is in the application of photocatalysts in the splitting of water[54-56]. It has been suggested by Hu *et al*[56] that NTO may be a room temperature polymorph similar to NNO. When synthesised using a sol gel technique they found that the X-ray diffraction (XRD) pattern slightly differed to that synthesised via solid state synthesis and that it could be indexed to the monoclinic *P*2/*m* phase[56].

Unlike the niobate derivative potassium tantalate $KTaO_3$ (KTO) is found in the cubic space group $Pm\bar{3}m$ at room temperature and is thus paraelectric similar to $SrTiO_3$[57]. As a result there is little literature on the high temperature behaviour of KTO. Since, KTO is non-polar at room temperature, the literature focuses on ways of modifying the material to improve its properties such as producing ferroelectric order through doping of niobium on to the *B*-site[58]. There is also an unusual paper that claims to produce superconductivity through the use of an ionic liquid below 1 K[59]. The authors found immersing a KTO single crystal in an electrolyte at 50 mK and applying a high electric field induced superconducting behaviour through electrostatic carrier doping[59].

1.4 Magnetic Properties

Magnetism is also an important material property. It is found due to the spin and orbital angular momentum of an electron, which can produce a magnetic field. Where the spin angular momentum of the electron originates from its spin or intrinsic angular momentum and the orbital angular momentum originates from the electron's movement around the nucleus. Essentially, it is dependent on how electrons move around the nucleus in an atom and is described as the magnetic dipole moment. These magnetic dipole moments are found in materials that possess unpaired electrons and they interact with magnetic fields and/or other dipole moments to produce different magnetic behaviours.

A magnetic field is produced by the motion of an electric charge seen by electrons. The magnetic field describes a magnetic force produced over an area with an energy gradient, as the force becomes weaker further from the point of origin[60]. This area of force can be described further as a series of lines and the density of these lines is called the magnetic flux density[6]. The magnetic flux density is dependent on the type of magnetic material placed inside of the field. Paramagnetic materials lead to an increase in the density when placed inside the field but diamagnetic materials lead to a decrease.

The magnetic field and magnetic flux density are related by the following equation[61]:

$$B = \mu_0 H \tag{1.6}$$

Where *B* is the magnetic flux density, *H* is the magnetic field and μ_0 is the permeability of free space. When a material is placed into the field, paramagnetic or diamagnetic, the equation changes to[61]:

$$B = \mu_0 \, (H + M) \tag{1.7}$$

Where *M* is the magnetic moment per unit mass or magnetisation of the sample. The magnetisation can then be described in terms of magnetic susceptibility χ, which is the magnetisation as a function of magnetic field strength[6].

$$\chi = \frac{M}{H} \tag{1.8}$$

The magnetic moment of a single atom (μ) can be calculated using the following equation[61]:

$$\mu = g\sqrt{J(J+1)} \tag{1.9}$$

Where *g* is the gyromagnetic ratio and *J* is the total angular momentum; the sum of the spin and orbital momentum. The problem with this equation is that it only takes into account a single atom.

All materials (bar H^+) can be defined as diamagnets, this is because it is related to the orbital momentum of electrons in a full electron shell. The magnetic moment of diamagnets is equal to zero as the electrons cancel out[62]. This is due to the electrons being present in a full shell and so the spins are oppositely orientated. However, diamagnets possess an extremely small and negative magnetic susceptibility.

Paramagnetic materials are those that have unpaired electrons and when under an applied magnetic field possess a magnetic moment that will align with the direction of the field to a certain degree. However, without an applied field this moment will be equal to zero as the electrons will randomly orient, effectively cancelling each other out. The magnetic susceptibility for a paramagnet is dependent on the temperature by the Curie law relationship[63]:

$$\chi = \frac{C}{T} \tag{1.10}$$

Where *C* is the Curie constant related to the magnetic moment and *T* is the temperature. This inverse relationship shows that as the temperature is increased the magnetic susceptibility of the paramagnet decreases. If the inverse of the magnetic susceptibility ($\frac{1}{\chi}$) is plotted against temperature then a straight line is obtained with an intercept at 0 K[63].

The Curie law can be modified to the following equation[63]:

$$\chi = \frac{C}{T - \theta} \tag{1.11}$$

Where θ is the Weiss constant, which indicates the average strength of the magnetic coupling in the system. This is known as the Curie-Weiss law and is used for magnetic systems with coupling between the magnetic spins. Using the Curie-Weiss law, when the inverse of the magnetic susceptibility ($\frac{1}{\chi}$) is plotted against temperature then θ may be positive or negative. If a positive value for θ is obtained then the transition temperature is described as the Curie temperature, T_C, and the material is said to be ferromagnetic. Ferromagnetic order describes when the electron spins align parallel in a single direction leading to a net magnetic moment in that direction. However, if the value for θ is negative then the transition temperature is described as the Néel temperature, T_N, and antiferromagnetic behaviour is shown. Antiferromagnetic order describes how the electron spins align anti-parallel to each other which leads to a net magnetic moment of near zero. A third type of magnetic order is ferrimagnetism, which is a mixture of ferromagnetism and antiferromagnetism. Here unequal spins are arranged anti-parallel. One set of spins in a single direction are dominant resulting in a small net magnetic moment in that direction. This type of order is usually found in compounds with two magnetic ions with the most well-known ferrimagnet being magnetite (Fe_3O_4), a mixture of Fe^{2+} and Fe^{3+} [64].

For ordered magnetic behaviour, coupling of the electron spins must occur. In oxides such as perovskites this coupling is realised by a mechanism known as superexchange. The distance between the magnetic ions is too large for strong direct exchange, where the orbitals between the magnetic ions overlap, and thus coupling instead occurs through the nonmagnetic neighbour anions such as oxygen. In superexchange interactions, electrons are shared partially covalently between the magnetic cation and nonmagnetic anion with the bond angle between the two cations determining the magnetic order present[6]. Using an iron based perovskite ($AFeO_3$) as example, bond angles close to 180° favour antiferromagnetic order via the superexchange pathway shown in *figure 1.5 (a)*, the Fe^{3+} $3d_{x2-y2}$ orbitals overlap with the O^{2-} $2p_x$ orbital. Due to the Pauli Exclusion Principle both the spins must align antiparallel with the electrons in the O^{2-} orbital resulting in the spins on

each of the Fe^{3+} orbitals ordering antiparallel to each other and thus antiferromagnetic character. In contrast, bond angles close to 90° favour ferromagnetic order as shown in *figure 1.5 (b)*, where the magnetic cations interact with the nonmagnetic anion $2p_x$ and $2p_y$ orbitals. The $3d_{x2-y2}$ orbital of one of the magnetic cations interacts with the $2p_x$ orbital of the O^{2-} anion and the $3d_{x2-y2}$ orbital of the other metal cation with the $2p_y$ orbital. The orbitals are again filled according to Pauli Exclusion Principle which results in the electron spins aligning in the same direction in the metal orbitals and thus ferromagnetic character is observed.

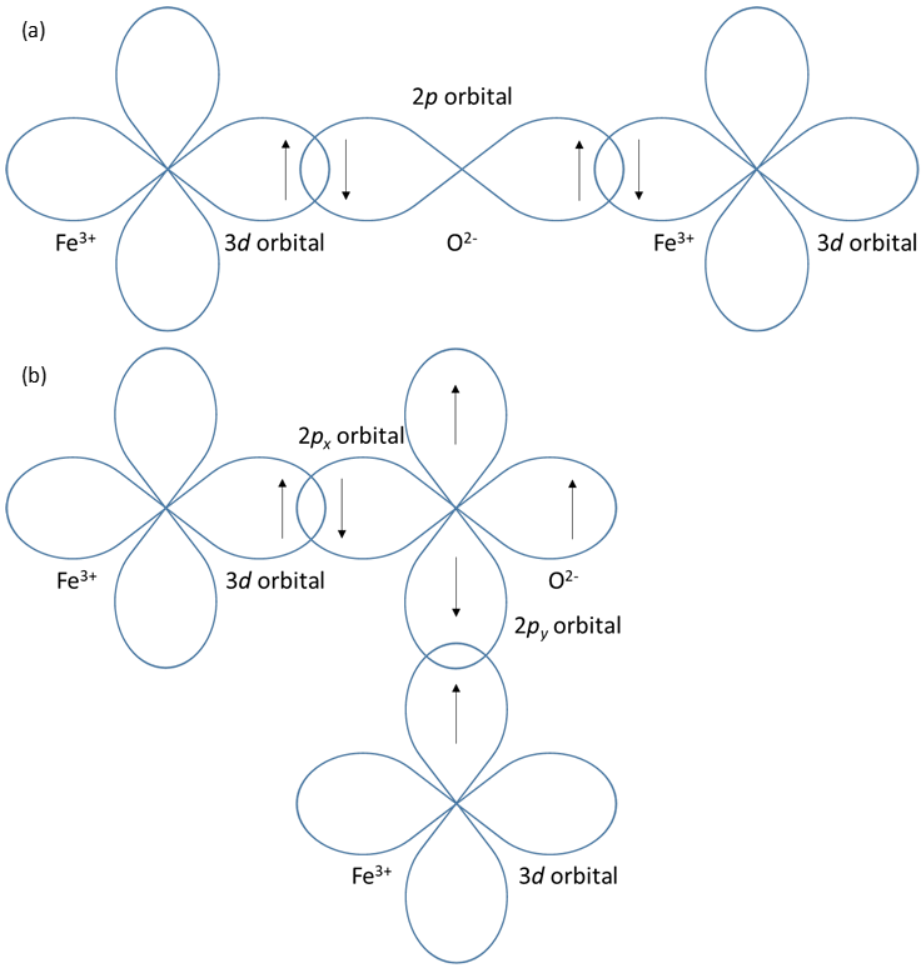

Figure 1.5: *(a) Antiferromagnetic superexchange coupling of Fe^{3+} $3d_{x2-y2}$ orbital electrons with O^{2-} $2p_z$ orbital electrons when Fe-O-Fe bond angle close to 180°. (b) Ferromagnetic superexchange coupling of Fe^{3+} $3d_{x2-y2}$ orbital electrons with O^{2-} $2p_z$ and $2p_x$ orbital electrons when Fe-O-Fe bond angle close to 90°.*

Disordered magnetic systems which possess no long-range order can also be formed with the two most common known as spin glass and spin ice systems. Spin glass systems are a complex magnetic system which is composed of a random combination of ferromagnetic and antiferromagnetic behaviour. This behaviour is not ordered, it must be disordered in terms of both the magnetic ion position and the position of this behaviour and thus may be described as random[65] Spin ices are modelled after Pauling's model of water ice to describe frustrated antiferromagnetic order typically seen in pyrochlore systems[66].

1.5 Multiferroics

Multiferroic materials are those which possess two or more ferroic orders, those which show spontaneous ordering of a property on application of a stimulus. For example, a ferromagnet shows spontaneous ordering of magnetic moments on the application of a magnetic field. These ferroic orders are able to show coupling which means one property can be spontaneously ordered with another's stimulus. For example, the use of a magnetic field to spontaneously order electric dipoles known as magnetoelectric coupling and shown in figure 1.6. Coupling of ferroelectricity with magnetism is of particular interest. Currently, both ferroelectric and magnetic materials are used in memory devices. For example, PZT is used in ferroelectric RAM (FRAM) which unlike conventional RAM is non-volatile ensuring data is not lost on shutdown/removal of electrical power. Multiferroics could be used in the manufacture of a new type of faster memory called multiferroic random access memory (MFRAM) which would be non-destructive when compared to FRAM[67]. The advantage of MFRAM over FRAM is that magnetic properties are used to read data rather than electrical properties. By using electrical properties to read data FRAM has a shorter lifespan as it reads and deletes and rewrites the same data through switching the polarization of the material used in the memory. This is considered destructive as over time the response will degrade. Using magnetic properties to read data is considered to be non-destructive, similar to how hard disk drives (HDDs) work. However, generating a magnetic field uses more energy than an electric field. This is where the magnetoelectric coupling would be useful as it could allow manipulation of the magnetization through the strain produced when an electric field is passed through a ferroelectric material[68]. The MFRAM should then require less energy and potentially be more efficient than current devices. One limitation in the search for multiferroics, however, is that it is rare to have a material show both ferroelectricity and ferromagnetism due to the opposing conditions required for both[69]. For a material to be ferroelectric it typically must have all electrons paired (no unpaired electrons) whereas ferromagnetism requires unpaired electrons to be present. Furthermore, materials which exhibit magnetoelectric coupling are even rarer still as shown in figure 1.7.

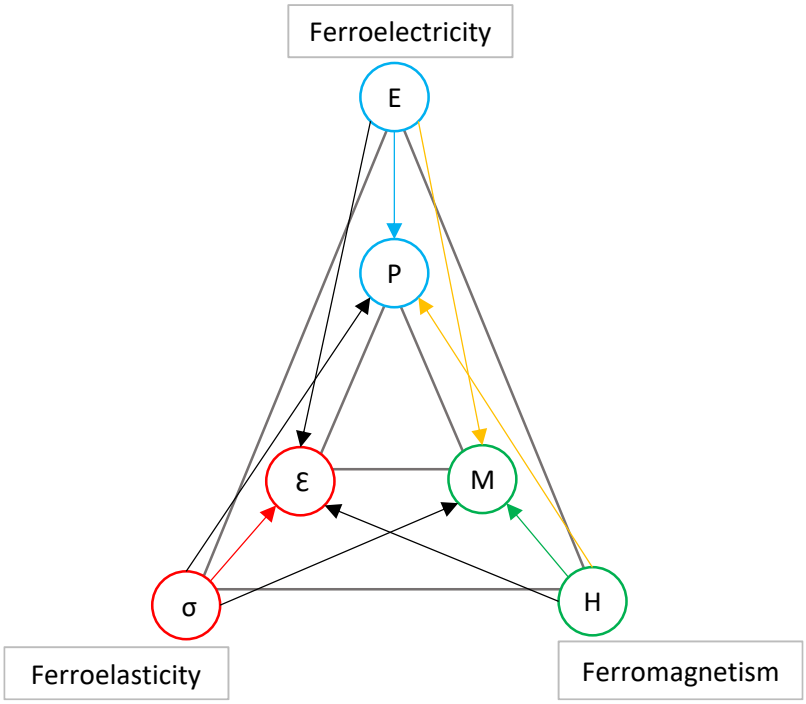

Figure 1.6: *Schematic representation of the ferroic order parameters and their coupling paths in multiferroic materials, reproduced from Spaldin et al*[68]*.*

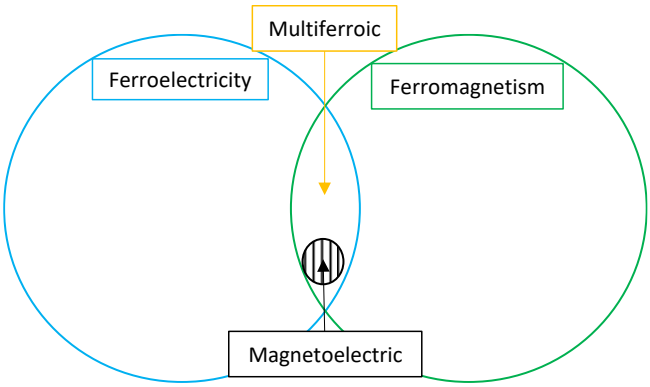

Figure 1.7: *Diagram showing that despite large numbers of ferroelectric and magnetic materials the number of expected multiferroics are limited with the number of those exhibiting magnetoelectric coupling smaller still. Reproduced from Khomskii and Eerenstein et al*[70,71]*.*

Materials exhibiting multiferroic behaviour are categorised into two types depending on the properties of the material[70]. Type I multiferroics are those that have ferroic properties which are independent of each other and thus the transition temperatures are different. Examples of type I multiferroics include bismuth ferrite ($BiFeO_3$) and yttrium manganite $YMnO_3$. $YMnO_3$ is unusual in that it is expected to be a type II multiferroic due to improper ferroelectric behaviour[72]. However, it was found that this character is wholly structurally dependent and separate from the magnetic transition. Type II multiferroics are different in that the ferroic orders are dependent on each other and so the transition temperatures are the same. This occurs due to the onset of a break in the inversion symmetry caused by the alignment of magnetic spins, which leads to a non-centrosymmetric structure. It can essentially be described as magnetism induced improper

ferroelectricity[73]. Examples of a type II multiferroic are the terbium manganites $TbMnO_3$ and $TbMn_2O_5$[74,75]. $TbMnO_3$ is found in the orthorhombic *Pbnm* structure at room temperature with a magnetic transition at 28 K, which leads to antiferromagnetic and ferroelectric behaviour[74]. Similarly $TbMn_2O_5$ is found in the orthorhombic *Pbam* structure at room temperature with a magnetic transition at 38 K which also leads to antiferromagnetic and ferroelectric behaviour[75].

1.6 Bismuth Ferrite, $BiFeO_3$

Bismuth ferrite, $BiFeO_3$, (BFO) is currently one of the most researched multiferroic materials. At room temperature it is found in the rhombohedral *R*3*c* structure (Glazer notation $a^-a^-a^-$) as shown in figure 1.8. BFO is special as it is multiferroic at room temperature showing ferroelectric (Curie temperature ≈ 1100 K) and antiferromagnetic (Néel temperature ≈ 635 K) behaviour[76]. However, currently, its commercial use is limited since the antiferromagnet ordering exhibits a complex incommensurate spin cycloid magnetic structure with an approximate length of 64 nm which leaves the net magnetic moment close to zero (figure 1.8) as well as high conductivities and dielectric loss[77]. Ferroelectric behaviour is seen in BFO due to displacement in the structure of bismuth atoms due to the Bi^{3+} lone pair resulting in a large dipole. Additionally, the iron sits slightly off centre in the FeO_6 octahedra generating a small dipole and contribution to the overall polarisation.

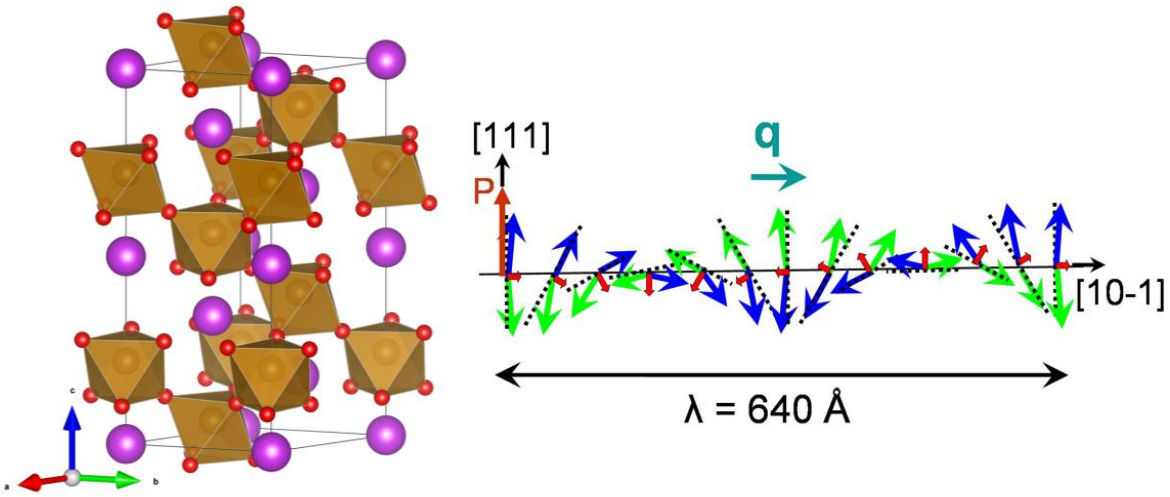

Figure 1.8: *(a) Room temperature R3c structure of bismuth ferrite. Purple atoms are bismuth, orange atoms are iron and red atoms are oxygen and (b) Schematic representation of the spin cycloid magnetic structure of bismuth ferrite. Reproduced from Lebeugle et al*[78].

The high conductivities and high leakage currents are caused by the '*lossy*' behaviour of BFO which is linked to oxygen vacancies in the structure and leads to the reduction of Fe^{3+} to Fe^{2+} due to charge balancing. Oxygen vacancies can be formed from heating BFO samples to high temperatures and then cooling rapidly (quenching) though it has been found that this process is reversible through oxygen treatment by heating to a lower temperature and allowing slow cooling to room

temperature[79]. It has also been found to be difficult to prepare samples that are phase pure due to the presence of other bismuth iron oxide impurities such as $Bi_2Fe_4O_9$ and $Bi_{24}Fe_2O_{39}$[80]. This issue arises from the narrow window in which BFO can be synthesised from Bi_2O_3 and Fe_2O_3. Thus being off stoichiometry by only a small amount and considering Bi_2O_3 is volatile when heating this can easily lead to formation of other phases[81].

On heating BFO from room temperature new phases are found that have different structures and properties. The phase found at room temperature is the α-phase which is the rhombohedral *R*3*c* phase. The second phase known as the β-phase is found around 1098 K and was reported to have an orthorhombic structure, with *P*2*mm* symmetry, by Palai *et al*[81] though the more accepted structure is that reported by Arnold *et al*[82] as *Pbnm*. This leads to a change in properties from ferroelectric to paraelectric [81,82]. At 1206 K a third phase is found called the γ-phase which has been suggested to be a cubic $Pm\overline{3}m$ *phase* though this was again disputed by Arnold *et al*[83] who identified the structure as orthorhombic (possibly *Pbnm*) which was similar to the beta phase but with different lattice parameters. However, the authors noted it was difficult to distinguish between *Pbnm* and *Imma* symmetries[81,83].

1.7 Doped Bismuth Ferrite Materials

Doping BFO is currently seen as a potential way to solve the problems described above. It is hoped that a similar solid solution to PZT with a MPB, between two polar phases may lead to enhanced dielectric and piezoelectric properties.

A-site doping of BFO is a strategy used to reduce the amount of bismuth in the structure. Substituting calcium on to the *A*-site of BFO has been found to improve both the magnetic and ferroelectric properties[84,85]. A study by Chen *et al*[84] found that adding Ca^{2+} to BFO led to improved magnetic properties changing it from the complex spin cycloid to a canted antiferromagnetic structure. This behaviour was seen at a composition of $Bi_{0.9}Ca_{0.1}FeO_3$. Electrical properties were found to be similar to unmodified BFO showing leaky dielectric behaviour with an increase in the conductivity. This leaky behaviour is likely a result of charge balancing of the Ca^{2+} ion resulting in oxygen vacancies in the structure. To investigate this Masó *et al*[85] varied the oxygen content via sintering Ca doped BFO samples in different atmospheres. It was consistently found that samples sintered in nitrogen compared to air and oxygen were more insulating with the latter two environments producing conductive samples. This was seen as the Fe^{3+} was oxidised to Fe^{4+} which led to an increase in oxygen contents[85].

Rare earth doping of BFO has attracted extensive attention as it is seen as being promising to replace the bismuth on the *A*-site with other +3 ions without compromising the properties and with the end result stabilising the structure[86]. The phase diagram between BFO and the rare earths with the composition $Bi_{1-x}RE_xFeO_3$ is complicated and the best summary in the literature can be found from Arnold[86]. From Lanthanum to Europium an *R*3*c* to *Pbam* phase transition can be seen at around $x = 0.1$ on lowering the ionic radii of the rare earth. This is interesting as *Pbam* is an anti-polar phase which could potentially lead to antiferroelectric properties[86-89]. These phases then change to a non-polar *Pnma* phase with increased RE content, which is consistent across all REs[86]. La on the other hand behaves slightly differently and exhibits an incommensurate modulation in the *Imma* structure as reported by Karpinsky *et al*[87] which does not seem to be present in any of the other RE phases. From gadolinium to thulium a possible monoclinic *Cc* phase may be present, with increasing values of *x* above 0.1, between the *R*3*c* and *Pnma* phases[86]. The *Cc* phase was first suggested by Lennox *et al*[90] in the study of the phase transitions of dysprosium doped BFO.

Alternatively, *B*-site doping has been used in BFO to replace iron and to truncate the spin modulation changing the magnetic order and improving the magnetic properties. *B*-site doping with manganese was found to lead to an improvement in the dielectric and magnetic properties as presented by Sahu *et al*[91]. In the composition $BiFe_{0.7}Mn_{0.3}O_3$ a magnetic hysteresis loop can be found at 10 K. The same composition was also found to have a much higher dielectric constant than the unmodified BFO. However, a decrease in the ferroelectric T_C to approximately 933 K was observed in thermal data[91]. Further work by Gibbs *et al*[92] confirmed that the structure changed at around 963 K to a non-polar orthorhombic *Pnma* phase using neutron diffraction. Furthermore, increasing the temperature to 1153 K led to another change in symmetry, the γ-phase, which was metrically cubic making it difficult to assign a symmetry. The symmetry $R\bar{3}c$ was assigned after the authors felt it gave the most sensible fit[92].

A paper by Jun *et al*[93] focused on doping BFO with niobium on the *B*-site to determine how the magnetic and electrical properties changed. The authors do not report any phase transitions over the small dopant levels (1% to 3%) investigated. In terms of the electrical properties it was found that the conductivity was reduced on addition of niobium and that the dielectric constant increased[93]. When attempting to produce a ferroelectric hysteresis loop, however, it was found that the PE loop was only partially reversed, this could be due to high leakage currents. Weak ferromagnetic behaviour is also reported. Magnetoelectric coupling was also reported in these samples with changes in the dielectric constant observed on the application of a magnetic field.

KNO doping has been shown to produce enhanced properties in BFO. The radius of the potassium ion compared to that of bismuth ion is much larger (1.64 Å compared to 1.36 Å respectively)[94,95] so it would be expected that there would be an increase in the Goldschmidt tolerance factor. This could, potentially, lead to a tolerance factor value over one leading to a structural change similar to what can be found in PZT, since the tolerance factor increases in PZT with increasing $PbTiO_3$ content[94].

A possible phase diagram for the $Bi_{1-x}K_xFe_{1-x}Nb_xO_3$ solid solution was proposed by Teslenko *et al*[96]. It consisted of a rhombohedral *R*3*c* phase from $x = 0.0$ to 0.25, an orthorhombic *Pbnm* phase from $x = 0.3$ to 0.4, a tetragonal *P*4*mm* phase from $x = 0.45$ to 0.70 and an orthorhombic *Amm*2 phase from $x = 0.75$ to 1.0[96]. Dash *et al*[97] explored the properties of KNO doping focusing on the $x = 0.4$ KNO composition. The authors found that a hexagonal symmetry was present through the use of a Rietveld refinement of XRD data[97]. The material showed ferroelectric behaviour with a polarisation-electric field (PE) hysteresis loop with an increase in polarization as the applied field was increased. Weak ferromagnetic behaviour was also reported[97].

A further paper by Dash *et al*[98] explored the properties of KNO focusing on $x = 0.0$, 0.1, 0.2 and 0.3 KNO doped BFO compositions. The authors suggest that on increasing KNO content from $x = 0.0$ to 0.3 a phase transition from the rhombohedral phase to a tetragonal phase is observed due to changes in the XRD pattern peaks[98]. No space group is assigned to the tetragonal phase making it hard to compare to the work of Teslenko *et al*[96]. When examining the electrical properties of the samples it was found that compared to pure BFO, doped samples showed improvements in leakage currents as the amount of KNO was increased with the dielectric constant also found to increase. Magnetic studies showed a weak hysteresis loop which implies weak ferromagnetism but with no saturation and low coercive fields.

The most recent paper by Lennox *et al*[99] synthesised a series of samples from $x = 0.0$ to 1.0 KNO doped BFO and attempted to determine the phase diagram for this solid solution. The method used was a typical solid state reaction with excesses of both bismuth oxide and potassium oxide used to compensate for the volatility of the reagents and avoid the formation of iron based impurities. Analysis of samples was performed using a variety of methods including XRD, XRF, SQUID magnetometry, Raman, impedance spectroscopy, neutron diffraction and synchrotron diffraction (HRPD and I11 respectively). The inclusion of neutron diffraction which complements the use of XRD was useful in determining structural information such as octahedral tilts which can be linked to the ferroelectric properties. The authors reported that synchrotron diffraction data could not easily be refined, possibly due to inhomogeneous samples caused by the synthesis method[99]. It was,

however, found that refinement of neutron diffraction data was possible, leading to a hypothesised phase diagram which showed a change from BFOs rhombohedral space group (*R*3*c)* at around *x* = 0.1 KNO to a mixture of *R*3*c* and tetragonal phases (space group *P*4*mm*). At around *x* = 0.3 a full change to *P*4*mm* was observed which then formed a mixed phase region with an orthorhombic phase with the space group *Amm*2 at *x* = 0.6. Finally the system adopts a single *Amm*2 phase at around *x* = 0.7. Measurement of the magnetic and electrical properties did not seem to show any improvements on increasing KNO content.

1.8 $Bi_{1-x}Na_xFe_{1-x}Nb_xO_3$ Solid Solution

The $Bi_{1-x}Na_xFe_{1-x}Nb_xO_3$ solid solution has also attracted attention. A study by Raevski *et al*[100] found that a phase transition was present from the BFO rhombohedral phase to an orthorhombic symmetry on the addition of a small amount of NNO which then becomes cubic at *x* > 0.25. An unusual step the authors took was to use sodium niobate which was described as *'previously synthesised'*[100]. However, no information is provided on how it was synthesised or where it was purchased from. A Mössbauer spectroscopy study performed by the same group suggested that iron remained as Fe^{3+} even with increased NNO doping[101]. Ma *et al*[102] reported that when BFO was doped with sodium niobate at *x* = 0.1, 0.3 and 0.5, that the electrical properties showed improvements such as a reduction in the leakage current and dielectric loss leading to an improved ferroelectric hysteresis loop. Interestingly on addition of *x* = 0.1 sodium niobate, ferromagnetic behaviour is suggested on the basis of magnetic hysteresis. However, impurities are noted in the XRD data and as such their contribution to the magnetic behaviour observed cannot be ruled out. A phase change is reported with the *x* = 0.3 and 0.5 sodium niobate compositions suggested to exhibit either cubic or pseudo-cubic symmetry[102].

In contrast, Dash *et al*[103] found differing results to these works[100-102]. In their work the authors proposed a phase transition from the BFO rhombohedral phase to a tetragonal phase at around *x* = 0.2[103]. This assertion was based on peak changes present in the XRD patterns and no tetragonal space group was suggested. When examining the electrical properties of the compounds the authors found that the leakage current is reduced with increasing amounts of NNO and that the remnant polarisation is found to increase[103]. Magnetoelectric coupling is observed on application of a magnetic field producing an induced voltage. A follow up paper by Dash *et al*[104] focused singularly on the *x* = 0.5 composition. In contrast to their previous work they now propose that *x* = 0.5 is orthorhombic[104]. The same team also looked at doping with *x* = 0.5 lithium niobate $LiNbO_3$. A transition to a tetragonal structure was seen with the material suggested to exhibit ferroelectric behaviour[105]. Ummer *et al*[106] synthesised four samples with compositions *x* = 0.0, 0.1, 0.5 and 0.7.

The authors note a phase change from the rhombohedral structure to an orthorhombic phase described as an NNO phase which potentially could either mean *Pbcm* or $P2_1ma$[106]. Magnetic data for the x = 0.1 material showed antiferromagnetic behaviour with a magnetic hysteresis loop which lacks saturation and coercive field behaviour. It was also found that with increasing levels of NNO that the dielectric constant increases which was linked to the decreasing of particle sizes[106]. Recent papers by De *et al*[107-109] found results similar to Raevski *et al*[100] where a cubic phase was found on addition of x = 0.3 NNO. Saad *et al*[110] detailed a complete phase diagram for the BFO-NNO solid solution. The phase diagram was created using six samples with the compositions x = 0.15, 0.25, 0.5, 0.75, 0.85 and 1.0[110]. They found that from x = 0.15 NNO to around x = 0.5 the rhombohedral *R*3*c* model could be fit to the data through Rietveld refinement. The x = 0.5 sample was found to be a mixture of *R*3*c* and the orthorhombic structure of NNO, $P2_1ma$. From x = 0.5 onwards the sample was refined to the $P2_1ma$ model.

By far the most detailed BFO-NNO phase diagram to date has been reported by Teslenko *et al*[111]. The phase diagram proposed that the symmetry starts as rhombohedral *R*3*c* which then becomes, on addition of x = 0.5 NNO, orthorhombic *Pbnm*. Further addition of NNO results in a transition to a tetragonal *P*4/*mbm* phase at x = 0.65 NNO. Finally, with addition of x = 0.9 NNO an orthorhombic *Pbcm* phase is observed which is a room temperature space group reported for the parent $NaNbO_3$ material[111].

A different approach was taken by Qi *et al*[112] who investigated the solid solution between BFO, NNO and barium titanate, with the formula $(BiFeO_3)_{0.67-x}(BaTiO_3)_{0.33}(NaNbO_3)_x$ where x = 0.0 to 0.15. Selected area diffraction and PXRD were used to characterise the x = 0.10 sample. Interestingly it was found that both techniques led to different answers about the structure. Selected area diffraction suggested the local structure was the BFO parent rhombohedral structure, *R*3*c*, but Rietveld refinement of the PXRD data suggested it was cubic $Pm\bar{3}m$[112]. This suggests that the local structure differs from that of the average structure obtained through PXRD. The authors suggest that increasing NNO content leads to polar nanoregions where the ferroelectric domains become smaller compared to the x = 0.0 sample. Clearly there remains extensive contradiction within the literature surrounding the phase behaviour of the BFO-NNO solid solution. This is summarised in figure 1.9.

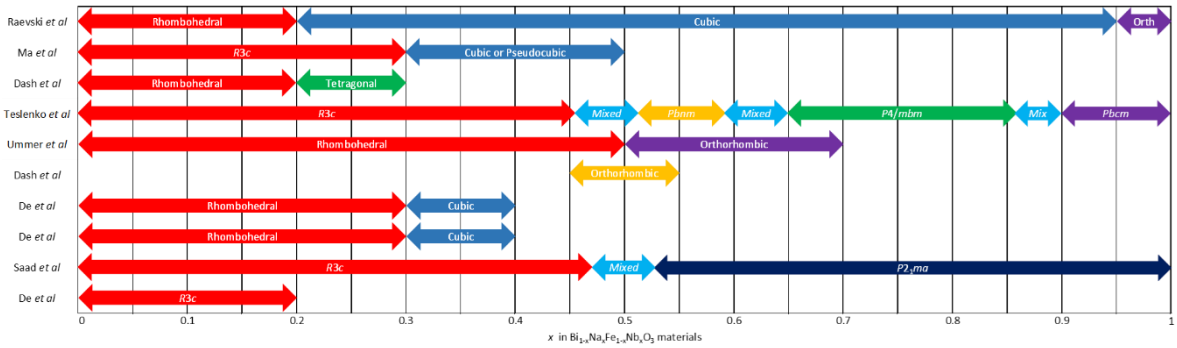

Figure 1.9: *$Bi_{1-x}Na_xFe_{1-x}Nb_xO_3$ phase diagram composed from current literature[100,102-104,106-111]. Crystal system reported where space group was not given in the paper.*

Compared to BFO-NNO, the $Bi_{1-x}Na_xFe_{1-x}Ta_xO_3$ solid solution has received very little attention in the literature. This could possibly be due to the expectation that the properties found in the BFO-NTO solid solution would mirror those seen in the BFO-NNO solid solution due to the similarities in size between Nb^{5+} (0.64 Å) and Ta^{5+} (0.64 Å)[94]. Despite this some difference could be expected due to the small differences in electronegativity (Nb = 1.6, Ta = 1.5) and the presence of *f* electrons in Ta. Mohanty *et al*[113] described the synthesis and analysis of $x = 0.1$, 0.2 and 0.3 NTO samples. According to the paper, XRD analysis performed suggested single phase materials were synthesised with a hexagonal unit cell[113]. This was further expanded on by Mohanty *et al*[114] in a following publication on the $x = 0.5$ structure. Like BFO-NTO, very little attention has also been focussed on the $Bi_{1-x}K_xFe_{1-x}Ta_xO_3$ solid solution in the literature. Mohanty *et al*[113,115] examined the $x = 0.1$, 0.2 and 0.3 KTO materials and found a transition to a hexagonal unit cell similar to the BFO-NTO system reported by the same authors.

For all of the solid solutions reviewed: BFO-KNO, BFO-NNO, BFO-NTO and BFO-KTO, it can be seen that there are still questions on the true room temperature structures and thus properties of these materials.

1.9 Thesis Aim

To improve the properties of BFO doping seems to currently be the favoured approach. When doped with a polar ferroelectric material it may be possible to form a MPB between the two competing (polar) phases which could lead to enhanced electrical properties. There is also the possibility of disrupting the modulation of the magnetism leading to enhanced magnetic ordering such as canted antiferromagnetism or even the Holy Grail, ferromagnetism. Sodium and potassium niobate provide ideal dopants due to their room temperature ferroelectric properties and potential as Pb-free replacements for PZT. However, currently there is a lack of a clear understanding of the structure and properties of these solid solutions in the literature.

This thesis reports a detailed study of the BFO-NNO phase diagram from 12 K to room temperature. XRD was performed at low temperature (12 K – 298 K) and room temperature (300 K) to establish a phase diagram with increasing NNO contribution. Two potential morphotropic phase boundaries were found between x = 0.1 and 0.175 and x = 0.65 and 0.675. The first recorded neutron experiments on these materials found diffuse scattering throughout a large composition range suggesting more complex structural behaviour which is not seen in the XRD experiments. Improved magnetic behaviour was also observed in some samples and the magnetic structure responsible for this change was resolved. Further comparisons of these data were drawn with specific compositions in the KNO-BFO, KTO-BFO and NTO-BFO solid solutions to begin to elucidate size related effects.

1.10 References

1 T. Matsui, T. Yamamoto, T. Nishihara, R. Morisawa, T. Yokoyama, T. Sekiguchi and T. Negami, *Adv Mater,* 2019, **31**, 1806823 (DOI:10.1002/adma.201806823).

2 R. E. Welser, S. J. Polly, M. Kacharia, A. Fedorenko, A. K. Sood and S. M. Hubbard, *Sci. Rep.,* 2019, **9**, 13955 (DOI:10.1038/s41598-019-50321-x).

3 Z. Li, O. Fuhr, M. Fichtner and Z. Zhao-Karger, *Energy Environ. Sci.,* 2019, **12**, 3496-3501 (DOI:10.1039/C9EE01699F).

4 O. Tizno, A. R. J. Marshall, N. Fernandez-Delgado, M. Herrera, S. Molina I. and M. Hayne, *Sci. Rep.,* 2019, **9**, 8950 (DOI:10.1038/s41598-019-45370-1).

5 V. M. Goldschmidt, *Naturwissenschaften,* 1926, **14**, 477-485 (DOI:10.1007/BF01507527).

6 A. R. West, in *Solid State Chemistry and its Applications, 2nd Edition, Student Edition*, ed. West, John Wiley & Sons Ltd, UK, Chichester, 2014, p. 1-81, 229-269, 298-301,359-444.

7 W. Travis, E. N. K. Glover, H. Bronstein, D. O. Scanlon and R. G. Palgrave, *Chem. Sci.,* 2016, **7**, 4548-4556 (DOI:10.1039/C5SC04845A).

8 A. M. Glazer, *Acta Cryst. A,* 1972, **28**, 3384-3392 (DOI:10.1107/S0567740872007976).

9 A. M. Glazer, *Acta Cryst. A,* 1975, **31**, 756-762 (DOI:10.1107/S0567739475001635).

10 H. F. Kay and P. C. Bailey, *Acta Crystallogr.,* 1957, **10**, 219-226 (DOI:10.1107/S0365110X57000675).

11 R. Ali and M. Yashima, *J. Solid State Chem.,* 2005, **178**, 2867-2872 (DOI:https://doi.org/10.1016/j.jssc.2005.06.027).

12 C. J. Howard, P. W. Barnes, B. J. Kennedy and P. M. Woodward, *Acta Cryst.,* 2005, **61**, 258-262 (DOI:10.1107/S0108768105012395).

13 M. C. Knapp and P. M. Woodward, *J. Solid State Chem.,* 2006, **179**, 1076-1085 (DOI:https://doi.org/10.1016/j.jssc.2006.01.005).

14 G. King, S. Garcia-Martin and P. M. Woodward, *Acta Cryst.,* 2009, **65**, 676-683 (DOI:10.1107/S0108768109032728).

15 Y. Kim and P. M. Woodward, *J. Solid State Chem.,* 2007, **180**, 2798-2807 (DOI:https://doi.org/10.1016/j.jssc.2007.08.003).

16 R. J. D. Tilley, in *Understanding solids the science of materials*, ed. R. J. D. Tilley, Wiley-Blackwell, Hoboken, N.J., 2013, p. 327-360.

17 R. Resta and D. Vanderbilt, in *Physics of ferroelectrics: a modern perspective*, ed. K. M. Rabe, C. H. Ahn and J. Triscone, Springer, Berlin, 2007, p. 31-68.

18 A. K. Bain and P. Chand, in *Ferroelectrics: Principles and Applications*, ed. A. K. Bain and P. Chand, Wiley-VCH, Weinheim, Germany, 2017, p. 37-78, 79-194.

19 D. I. Khomskii, in *Transition Metal Compounds*, ed. D. I. Khomskii, Cambridge University Press, Cambridge, 2014, p. 269-309.

20 G. Haertling, *J Am Ceram Soc,* 1999, **82**, 797-818 (DOI:10.1111/j.1151-2916.1999.tb01840.x).

21 P. S. Halasyamani and K. R. Poeppelmeier, *Chem. Mater.,* 1998, **10**, 2753-2769 (DOI:10.1021/cm980140w).

22 G. H. Kwei, A. C. Lawson, S. J. L. Billinge and S. W. Cheong, *J. Phys. Chem.,* 1993, **97**, 2368-2377 (DOI:10.1021/j100112a043).

23 C. N. W. Darlington, W. I. F. David and K. S. Knight, *Phase Transit.,* 1994, **48**, 217-236 (DOI:10.1080/01411599408213215).

24 H. T. Stokes, E. H. Kisi, D. M. Hatch and C. J. Howard, *Acta Cryst. B,* 2002, **58**, 934-938 (DOI:10.1107/S0108768102015756).

25 M. H. Frey and D. A. Payne, *Phys. Rev. B,* 1996, **54**, 3158-3168 (DOI:10.1103/PhysRevB.54.3158).

26 S. A. Mabud, *J. Appl. Cryst.,* 1980, **13**, 211-216 (DOI:10.1107/S0021889880011958).

27 B. Jaffe, W. R. Cook Jr. and H. Jaffe, *Piezoelectric Ceramics*, Academic Press, London, UK, 1971.

28 C. A. Randall, N. Kim, J. Kucera, W. Cao and T. R. Shrout, *J Am Ceram Soc,* 1998, **81**, 677-688 (DOI:10.1111/j.1151-2916.1998.tb02389.x).

29 Council of the European Union, *OJ L,* 2011, **174**, 88–110 (DOI:10.3000/17252555.L_2011.174.eng).

30 A. J. Bell and O. Deubzer, *MRS Bull,* 2018, **43**, 581-587 (DOI:10.1557/mrs.2018.154).

31 S. Pramanik, B. Pingguan-Murphy and N. A. Abu Osman, *Int. J. Electrochem. Sci.,* 2013, **8**, 8863-8892.

32 E. Sawaguchi, *J. Phys. Soc. Jpn.,* 1953, **8**, 615-629 (DOI:10.1143/JPSJ.8.615).

33 A. Hewat, *J. Phys. C: Solid State Phys.,* 2001, **6**, 2559 (DOI:10.1088/0022-3719/6/16/010).

34 G. Shirane, H. Danner, A. Pavlovic and R. Pepinsky, *Phys. Rev.,* 1954, **93**, 672-673 (DOI:10.1103/PhysRev.93.672).

35 B. T. Matthias and J. P. Remeika, *Phys. Rev.,* 1951, **82**, 727-729 (DOI:10.1103/PhysRev.82.727).

36 P. Günter, *J. Appl. Phys.,* 1977, **48**, 3475-3477 (DOI:10.1063/1.324196).

37 K. Kakimoto, I. Masuda and H. Ohsato, *Jpn. J. Appl. Phys. Part 1 - Regul. Pap. Short Notes Rev. Pap.,* 2003, **42**, 6102-6105 (DOI:10.1143/JJAP.42.6102).

38 M. Tyunina, A. Dejneka, D. Rytz, I. Gregora, F. Borodavka, M. Vondracek and J. Honolka, *Journal of Physics: Condensed Matter,* 2014, **26**, 125901 (DOI:10.1088/0953-8984/26/12/125901).

39 K. E. Johnston, C. C. Tang, J. E. Parker, K. S. Knight, P. Lightfoot and S. E. Ashbrook, *J. Am. Chem. Soc.,* 2010, **132**, 8732-8746 (DOI:10.1021/ja101860r).

40 K. E. Johnston, J. M. Griffin, R. I. Walton, D. M. Dawson, P. Lightfoot and S. E. Ashbrook, *Phys. Chem. Chem. Phys.,* 2011, **13**, 7565-7576 (DOI:10.1039/C1CP20258H).

41 C. N. W. Darlington and K. S. Knight, *Physica B Condens. Matter,* 1999, **266**, 368-372 (DOI:https://doi.org/10.1016/S0921-4526(99)00043-5).

42 S. K. Mishra, N. Choudhury, S. L. Chaplot, P. S. R. Krishna and R. Mittal, *Phys. Rev. B,* 2007, **76**, 024110 (DOI:10.1103/PhysRevB.76.024110).

43 S. K. Mishra, R. Mittal, V. Y. Pomjakushin and S. L. Chaplot, *Phys. Rev. B,* 2011, **83**, 134105 (DOI:10.1103/PhysRevB.83.134105).

44 L. A. Reznitchenko, A. V. Turik, E. M. Kuznetsova and V. P. Sakhnenko, *J. Phys. Condens,* 2001, **13**, 3875-3881 (DOI:10.1088/0953-8984/13/17/308).

45 M. Ahtee and A. M. Glazer, *Acta Cryst. A,* 1976, **32**, 434-446 (DOI:10.1107/S0567739476000983).

46 M. Ahtee and A. W. Hewat, *Acta Cryst. A,* 1978, **34**, 309-317.

47 D. W. Baker, P. A. Thomas, N. Zhang and A. M. Glazer, *Appl. Phys. Lett.,* 2009, **95**, 091903 (DOI:10.1063/1.3212861).

48 J. Tellier, B. Malic, B. Dkhil, D. Jenko, J. Cilensek and M. Kosec, *Solid State Sciences,* 2009, **11**, 320-324 (DOI:https://doi.org/10.1016/j.solidstatesciences.2008.07.011).

49 M. Ahtee and L. Unonius, *Acta Crystallogr. Sect. A,* 1977, **33**, 150-154 (DOI:10.1107/S056773947700031X).

50 M. Ahtee and C. N. W. Darlington, *Acta Crystallogr. Sect. B-Struct. Commun.,* 1980, **36**, 1007-1014 (DOI:10.1107/S0567740880005183).

51 B. J. Kennedy, A. K. Prodjosantoso and C. J. Howard, *J. Phys. : Condens. Matter,* 1999, **11**, 6319-6327 (DOI:10.1088/0953-8984/11/33/302).

52 S. Kamba, V. Goian, V. Bovtun, D. Nuzhnyy, M. Kempa, M. Spreitzer, J. König and D. Suvorov, *Ferroelectrics,* 2012, **426**, 206-214 (DOI:10.1080/00150193.2012.671741).

53 C. Darlington and K. Knight, *Acta Crystallogr. Sect. B-Struct. Sci.,* 1999, **55**, 24-30 (DOI:10.1107/S010876819800963X).

54 H. Kato and A. Kudo, *J. Phys. Chem. B,* 2001, **105**, 4285-4292 (DOI:10.1021/jp004386b).

55 H. Kato, K. Asakura and A. Kudo, *J. Am. Chem. Soc.,* 2003, **125**, 3082-3089 (DOI:10.1021/ja027751g).

56 C. Hu and H. Teng, *Appl. Catal. A-Gen.,* 2007, **331**, 44-50 (DOI:10.1016/j.apcata.2007.07.024).

57 P. Vousden, *Acta Cryst.,* 1951, **4**, 373-376 (DOI:https://doi.org/10.1107/S0365110X5100115X).

58 P. DiAntonio, B. Vugmeister, J. Toulouse and L. Boatner, *Phys. Rev. B,* 1993, **47**, 5629-5637 (DOI:10.1103/PhysRevB.47.5629).

59 K. Ueno, S. Nakamura, H. Shimotani, H. T. Yuan, N. Kimura, T. Nojima, H. Aoki, Y. Iwasa and M. Kawasaki, *Nat. Nanotechnol.,* 2011, **6**, 408-412 (DOI:10.1038/NNANO.2011.78).

60 D. Jiles, in *Introduction to magnetism and magnetic materials*, ed. D. Jiles, Chapman and Hall, London, 1991, p. 1-26.

61 E. A. Moore and L. E. Smart, in *Solid State Chemistry: An Introduction, Fourth Edition*, ed. E. A. Moore and L. E. Smart, Taylor & Francis CRC Press, Boca Raton, Florida, 2012, p. 124-128, 137-138.

62 B. D. Cullity and C. D. Graham, in *Introduction to magnetic materials*, ed. B. D. Cullity and C. D. Graham, John Wiley & Sons, Hoboken, New Jersey, 2009, p. 87-114.

63 A. F. Orchard, *Magnetochemistry*, Oxford University Press, UK, Oxford. USA, New York, 2007.

64 J. M. D. Coey, in *Magnetism and magnetic materials*, ed. J. M. D. Coey, Cambridge University Press, UK, Cambridge, 2010, p. 195-230.

65 J. A. Mydosh, in *Spin glasses : an experimental introduction*, ed. J. A. Mydosh, Taylor & Francis, London, 1993, p. 1-19.

66 S. T. Bramwell, M. J. P. Gingras and P. C. W. Holdsworth, in *Frustrated spin systems*, ed. H. T. Diep, World Scientific Publishing Co., Singapore ; Hackensack, N.J., 2013, p. 383–474.

67 M. M. Vopson, *Critical Reviews in Solid State and Materials Sciences,* 2015, **40**, 223-250 (DOI:10.1080/10408436.2014.992584).

68 N. A. Spaldin and M. Fiebig, *Science,* 2005, **309**, 391-392 (DOI:10.1126/science.1113357).

69 N. A. Hill, *J. Phys. Chem. B,* 2000, **104**, 6694-6709 (DOI:10.1021/jp000114x).

70 D. Khomskii, *Physics,* 2009, **2**, 20 (DOI:10.1103/Physics.2.20).

71 W. Eerenstein, N. D. Mathur and J. F. Scott, *Nature,* 2006, **442**, 759-765 (DOI:10.1038/nature05023).

72 B. B. Van Aken, T. T. M. Palstra, A. Filippetti and N. A. Spaldin, *Nature Materials,* 2004, **3**, 164-170 (DOI:10.1038/nmat1080).

73 A. J. C. Buurma, G. Blake, T. Palstra and U. Adem, in *Reference Module in Materials Science and Materials Engineering*, ed. A. J. C. Buurma, G. Blake, T. Palstra and U. Adem, Elsevier, Amsterdam, 2016.

74 T. Kimura, T. Goto, H. Shintani, K. Ishizaka, T. Arima and Y. Tokura, *Nature,* 2003, **426**, 55-58 (DOI:10.1038/nature02018).

75 N. Hur, S. Park, P. A. Sharma, J. S. Ahn, S. Guha and S. Cheong, *Nature,* 2004, **429**, 392-395 (DOI:10.1038/nature02572).

76 G. Catalan and J. F. Scott, *Adv Mater,* 2009, **21**, 2463-2485 (DOI:10.1002/adma.200802849).

77 I. Sosnowska, T. P. Neumaier and E. Steichele, *Journal of Physics C: Solid State Physics,* 1982, **15**, 4835-4846 (DOI:10.1088/0022-3719/15/23/020).

78 D. Lebeugle, D. Colson, A. Forget, M. Viret, A. M. Bataille and A. Gukasov, *Phys. Rev. Lett.,* 2008, **100**, 227602 (DOI:10.1103/PhysRevLett.100.227602).

79 K. Min, F. Huang, Y. Jin, X. Lu, H. Wu and J. Zhu, *J. Phys. D,* 2015, **48**, 445301 (DOI:10.1088/0022-3727/48/44/445301).

80 K. Feng, L. Wang, J. Lu, Y. Wu and B. Shen, *CrystEngComm; CrystEngComm,* 2013, **15**, 4900-4904 (DOI:10.1039/c3ce40473k).

81 R. Palai, R. S. Katiyar, H. Schmid, P. Tissot, S. J. Clark, J. Robertson, S. A. T. Redfern, G. Catalan and J. F. Scott, *Phys. Rev. B,* 2008, **77**, 014110 (DOI:10.1103/PhysRevB.77.014110).

82 D. C. Arnold, K. S. Knight, F. Morrison and P. Lightfoot, *Phys. Rev. Lett.,* 2009, **102**, 027602 (DOI:10.1103/PhysRevLett.102.027602).

83 D. C. Arnold, K. S. Knight, G. Catalan, S. Redfern, J. Scott, P. Lightfoot and F. Morrison, *Adv. Funct. Mater.,* 2010, **20**, 2116-2123 (DOI:10.1002/adfm.201000118).

84 W. Chen, A. J. Williams, L. Ortega-San-Martin, M. Li, D. C. Sinclair, W. Zhou and J. P. Attfield, *Chem. Mater.,* 2009, **21**, 2085-2093 (DOI:10.1021/cm8031048).

85 N. Maso and A. R. West, *Chem. Mater.,* 2012, **24**, 2127-2132 (DOI:10.1021/cm300683e).

86 D. C. Arnold, *IEEE Trans. Ultrason. Ferroelectr. Freq. Control,* 2015, **62**, 62-82 (DOI:10.1109/TUFFC.2014.006668).

87 D. V. Karpinsky, I. O. Troyanchuk, O. S. Mantytskaya, V. A. Khomchenko and A. L. Kholkin, *Solid State Commun.,* 2011, **151**, 1686-1689 (DOI:https://doi.org/10.1016/j.ssc.2011.08.002).

88 S. Karimi, I. M. Reaney, Y. Han, J. Pokorny and I. Sterianou, *J. Mater. Sci.,* 2009, **44**, 5102-5112 (DOI:10.1007/s10853-009-3545-1).

89 I. Levin, S. Karimi, V. Provenzano, C. L. Dennis, H. Wu, T. P. Comyn, T. J. Stevenson, R. I. Smith and I. M. Reaney, *Phys. Rev. B,* 2010, **81**, 020103 (DOI:10.1103/PhysRevB.81.020103).

90 R. C. Lennox, M. C. Price, W. Jamieson, M. Jura, A. Daoud-Aladine, C. A. Murray, C. Tang and D. C. Arnold, *J. Mater. Chem. C,* 2014, **2**, 3345-3360 (DOI:10.1039/c3tc32345e).

91 J. R. Sahu and C. N. R. Rao, *Solid State Sci.,* 2007, **9**, 950-954 (DOI:https://doi.org/10.1016/j.solidstatesciences.2007.06.006).

92 A. S. Gibbs, D. C. Arnold, K. S. Knight and P. Lightfoot, *Phys. Rev. B,* 2013, **87**, 224109 (DOI:10.1103/PhysRevB.87.224109).

93 Y. Jun, W. Moon, C. Chang, H. Kim, H. S. Ryu, J. W. Kim, K. H. Kim and S. Hong, *Solid State Commun.,* 2005, **135**, 133-137 (DOI:https://doi.org/10.1016/j.ssc.2005.03.038).

94 R. D. Shannon, *Acta Cryst. A,* 1976, **32**, 751-767 (DOI:10.1107/S0567739476001551).

95 D. Kan, L. Pálová, V. Anbusathaiah, C. J. Cheng, S. Fujino, V. Nagarajan, K. M. Rabe and I. Takeuchi, *Adv. Funct. Mater.,* 2010, **20**, 1108-1115 (DOI:10.1002/adfm.200902017).

96 P. Y. Teslenko, A. G. Razumnaya, V. O. Ponomarenko, A. G. Rudskaya, A. V. Nazarenko, A. S. Anokhin, M. V. Avramenko, D. I. Levshov, M. F. Kupriyanov and Y. I. Yuzyuk, *Physics of the Solid State,* 2014, **56**, 1866-1871 (DOI:10.1134/S1063783414090285).

97 S. Dash, R. N. P. Choudhary and A. Kumar, *J. Phys. Chem. Solids,* 2014, **75**, 1376-1382 (DOI:https://doi.org/10.1016/j.jpcs.2014.07.018).

98 S. Dash, R. N. P. Choudhary, P. R. Das and A. Kumar, *Applied Physics A,* 2015, **118**, 1023-1031 (DOI:10.1007/s00339-014-8862-9).

99 R. C. Lennox, D. D. Taylor, L. J. Vera Stimpson, G. B. G. Stenning, M. Jura, M. C. Price, E. E. Rodriguez and D. C. Arnold, *Dalton Trans.,* 2015, **44**, 10608-10613 (DOI:10.1039/c5dt00140d).

100 I. P. Raevski, S. P. Kubrin, J. -. Dellis, S. I. Raevskaya, D. A. Sarychev, V. G. Smotrakov, V. V. Eremkin and M. A. Seredkina, *Ferroelectrics,* 2008, **371**, 113-118 (DOI:10.1080/00150190802397767).

101 I. P. Raevski, S. P. Kubrin, S. I. Raevskaya, V. V. Stashenko, D. A. Sarychev, M. A. Malitskaya, I. N. Zakharchenko, V. G. Smotrakov and V. V. Eremkin, *Ferroelectrics,* 2008, **373**, 121-126 (DOI:10.1080/00150190802408945).

102 Y. Ma and X. Chen, *J. Appl. Phys.,* 2009, **105**, 054107 (DOI:10.1063/1.3081648).

103 S. Dash, R. Padhee, P. Das and R. Choudhary, *J Mater Sci: Mater Electron,* 2013, **24**, 3315-3323 (DOI:10.1007/s10854-013-1249-4).

104 S. Dash and R. N. P. Choudhary, *IEEE Trans. Dielectr. Electr. Insul.,* 2016, **23**, 3652-3658 (DOI:10.1109/TDEI.2016.005755).

105 S. Dash, R. Padhee, P. R. Das and R. N. P. Choudhary, *Phase Transit.,* 2014, **87**, 223-235 (DOI:10.1080/01411594.2013.812214).

106 R. P. Ummer, P. Sreekanth, B. Raneesh, R. Philip, D. Rouxel, S. Thomas and N. Kalarikkal, *RSC Adv.,* 2015, **5**, 67157-67164 (DOI:10.1039/c5ra10422j).

107 M. De, S. P. Patel and H. S. Tewari, *J. Mater. Sci. : Mater. Electron.,* 2017, **28**, 6928-6935 (DOI:10.1007/s10854-017-6393-9).

108 M. De and H. S. Tewari, *Ferroelectrics,* 2017, **519**, 43-48 (DOI:10.1080/00150193.2017.1362284).

109 M. De, S. Hajra, R. Tiwari, S. Sahoo, R. N. P. Choudhary and H. S. Tewari, *Ceram. Int.,* 2018, **44**, 11792-11797 (DOI:https://doi.org/10.1016/j.ceramint.2018.03.263).

110 Y. Saad, I. Álvarez-Serrano, M. L. López and M. Hidouri, *Ceram. Int.,* 2018, **44**, 18560-18570 (DOI:https://doi.org/10.1016/j.ceramint.2018.07.078).

111 P. Teslenko, A. Razumnaya, V. Ponomarenko, A. Rudskaya, A. Nazarenko, A. Anokhin, M. Avramenko, D. Levshov, M. Kupriyanov and Y. Yuzyuk, *Phys. Solid State,* 2014, **56**, 1866-1871 (DOI:10.1134/S1063783414090285).

112 H. Qi, A. Xie, A. Tian and R. Zuo, *Adv. Energy Mater.,* 2020, **10**, 1903338 (DOI:10.1002/aenm.201903338).

113 S. Mohanty, R. N. P. Choudhary, R. Padhee and B. N. Parida, *Ceram. Int.,* 2014, **40**, 9017-9025 (DOI:10.1016/j.ceramint.2014.01.114).

114 S. Mohanty, R. N. P. Choudhary, B. N. Parida and R. Padhee, *Appl. Phys. A-Mater. Sci. Process.,* 2014, **116**, 1833-1840 (DOI:10.1007/s00339-014-8337-z).

115 S. Mohanty and R. N. P. Choudhary, *J. Mater. Sci. -Mater. Electron.,* 2014, **25**, 1180-1187 (DOI:10.1007/s10854-014-1706-8).

Chapter Two: Experimental Techniques

2.1 Introduction

A variety of techniques were used to understand the structural and multiferroic properties of the $Bi_{1-x}Na_xFe_{1-x}Nb_xO_3$ ($0 \leq x \leq 1$) series, and related materials. A modified solid state synthesis procedure was used, based on work by Levin *et al*[1], in the attempt to synthesise single phase homogenous samples. Structural analysis was performed using powder x-ray diffraction (PXRD), powder neutron diffraction (PND) and Raman spectroscopy. The multiferroic properties were probed through SQUID magnetometry and Polarisation vs Electric field (PE) loops to determine the magnetic and electric properties respectively. Complementary techniques such as solid state nuclear magnetic resonance (NMR), scanning electron microscopy (SEM), energy-dispersive X-ray spectroscopy (EDX) and simultaneous thermal analysis (TGA/DSC) were used to provide additional information. Full experimental/instrumental conditions and technical background are given in more detail in this chapter.

2.2 Synthesis Methods

A single synthesis method was used to synthesise all materials in the $Bi_{1-x}Na_xFe_{1-x}Nb_xO_3$ series and related, $Bi_{0.9}K_{0.1}Fe_{0.9}Nb_{0.1}O_3$, $Bi_{0.5}K_{0.5}Fe_{0.5}Nb_{0.5}O_3$, $Bi_{0.5}Na_{0.25}K_{0.25}Fe_{0.5}Nb_{0.5}O_3$, $Bi_{0.9}Na_{0.1}Fe_{0.9}Ta_{0.1}O_3$, $Bi_{0.5}Na_{0.5}Fe_{0.5}Ta_{0.5}O_3$, $Bi_{0.9}K_{0.1}Fe_{0.9}Ta_{0.1}O_3$, and $Bi_{0.5}K_{0.5}Fe_{0.5}Ta_{0.5}O_3$, materials as described in this section.

2.2.1 Solid State Synthesis

Solid state synthesis is a widely used technique to prepare inorganic compounds. The technique involves mixing powders at stoichiometric ratios and heating to a required high temperature for several hours so that the reactants form a desired product. This reaction can be enhanced by first ensuring that the reactants are homogenously mixed with small particle sizes through grinding of the sample. High temperatures are often required for this method as enough energy is needed so that the cations present can move, through diffusion, to a different site in a unit cell. This requires the input energy to exceed that of the lattice[2]. Unfortunately, there are drawbacks to this method, such as the presence of second phases as it is difficult to control the diffusion of cations. This can result in areas of phase inhomogeneity. Additionally, it is important to ensure that the reactants and desired product(s) are stable at the processing temperature since more volatile cations can be

problematic. However, the effect of these can be minimised by the careful control of the synthetic parameters.

2.2.1.1 Synthesis of $Bi_{1-x}Na_xFe_{1-x}Nb_xO_3$ series

Twenty three samples from the $Bi_{1-x}Na_xFe_{1-x}Nb_xO_3$ series were synthesised from x = 0.05 to 0.95 mostly in increments of 0.05 using a solid state reaction method. Before synthesis, sodium carbonate (Sigma Aldrich, 99%) and niobium oxide (Sigma Aldrich, 99.9%) were dried to remove water by heating at 873 K for two hours. Once dried Bi_2O_3 (Sigma Aldrich, ≥98.0%), Fe_2O_3 (Sigma Aldrich, 99%), Na_2CO_3 and Nb_2O_5 were weighed and added together stoichiometrically into a mortar, with 6 mol% extra bismuth oxide and sodium carbonate used due to the volatility of bismuth and sodium upon heating. The powders were mixed together using a pestle and mortar under a few millilitres of acetone and ground until dry. The resulting mixture was then heated to 1123 K with a heating rate of 10 K/min and maintained at temperature for six hours[1,3]. The material was removed from the furnace and the resulting powder was reground using the pestle and mortar under acetone. The powder was then returned to the furnace for a total of two hundred hours, in two sixty five hour and one seventy hour interval, at 1193 K with a heating rate of 10 K/min with intermittent grinding[1].

The samples between x = 0.05 and 0.55 were leached. This was performed using 2.5 M nitric acid which was added to a sample with a magnetic stirrer in a beaker and stirred for two hours at room temperature[3]. The solution was then filtered and washed using dd H_2O. The sample was subsequently dried in a furnace at 673 K for one hour with a heating rate of 10 K/min[3].

Dense pellets were prepared from powder samples to enable further characterisation. A 10 mm die was used to press pellets with a uniaxial press. A method similar to the one presented by Mandal *et al*[4] was used to prepare samples for electrical measurements where 2% polyvinyl butyral (PVB) (Sigma Aldrich) and 0.2% MnO_2 (Sigma Aldrich, 99%) were ground with the sample and the pellet sintered at 1193 K for six hours (heating rate of 10 K/min). This was later modified by replacing MnO_2 with TiO_2 (Sigma Aldrich, 99%) in an attempt to increase the densities of pellets to over 90%.

2.2.1.2 Synthesis of Related Materials

Additional samples were synthesised using the same method described above. Samples with the formula $Bi_{1-x}A_xFe_{1-x}B_xO_3$ (A = Na, K) (B = Nb, Ta). For potassium and tantalum containing solid solutions K_2CO_3 (Sigma Aldrich, 99%) and Ta_2O_5 (Sigma Aldrich, 99%) were used respectively.

2.3 Characterisation Methods: Diffraction

2.3.1 History of Diffraction

Before speaking of diffraction as a technique it would be wise to mention the German scientist Wilhelm Conrad Röntgen who discovered and named X-rays. These were found when he observed fluorescence from a barium platinocyanide tube when under an electrical discharge inside a vacuum[5]. In 1912 Max von Laue hypothesised the possibility of X-ray diffraction in crystals and conducted an experiment using a single crystal of copper sulphate as a diffraction grating[6]. This experiment led to an array of spots on a photographic plate where the X-rays interacted with the crystal. It was determined from this experiment that the X-rays acted as waves with a small enough wavelength to diffract from the crystal with the spots formed when the waves combined constructively. The array of spots was termed a diffraction pattern which represented the crystal structure formed from the repeating arrangement of atoms[7].

From this experiment Laue conceived a set of three equations to describe diffraction from a 3-dimensional crystal. These equations must be satisfied concurrently for diffraction to be observed.

$$a_1 sin\phi_1 = n\lambda \quad (2.1)$$

$$a_2 sin\phi_2 = n\lambda \quad (2.2)$$

$$a_3 sin\phi_3 = n\lambda \quad (2.3)$$

Where λ is the wavelength of the X-rays, a is the separation between the atoms, ϕ is the diffraction angle, and n is an integer equating to the directions of the three crystallographic axes which can be replaced with *h*, *k* and *l*[8]. The main problem with the Laue equations, which limited their use, is the complexity of using multiple equations simultaneously to obtain the *h*, *k*, *l* values.

A more intuitive approach was determined by the Father and Son team, William Henry Bragg and William Lawrence Bragg. Through studies of rock salt (sodium chloride) Bragg proposed a new equation for determining diffraction[9].

$$n\lambda = 2dsin\theta \quad (2.4)$$

Where n is an integer usually equal to 1, λ is the wavelength of the X-rays, d is the interplanar spacing between atoms and ϑ is the Bragg angle of incidence. Bragg proposed that a crystal could be equated to a semi-transparent mirror where each plane present in the crystal could reflect or transmit an X-ray. These planes are separated by a distance known as the d-spacing. For Bragg's equation to be satisfied for X-rays reflected from different planes the extra reflected path length (*x-y-z* shown in Figure 2.1) needs to be equivalent to a whole number integer of the wavelength so that the X-rays will be in phase and constructively interfere. However, if the X-ray path length (*x-y-*

z) differs from a whole number integer of the wavelength then the X-rays would destructively interfere and cancel out.

In *figure 2.1* this idea can be seen schematically. In this figure two incident X-rays labelled 1 and 2 are shown interacting with a series of parallel planes separated by a distance, *d*. X-ray 1 reflects from plane A (1') with incident and reflected angles, θ. Likewise, X-ray 2 is transmitted through plane A and reflects from plane B (2'). For Bragg's law to be satisfied the reflected beams 1' and 2' must be in phase. However, beam 2' has to travel further than the original beam (1') as it is reflected from a lower plane. The distances *x-y-z* must be equal to a whole number otherwise the beams will be out of phase.

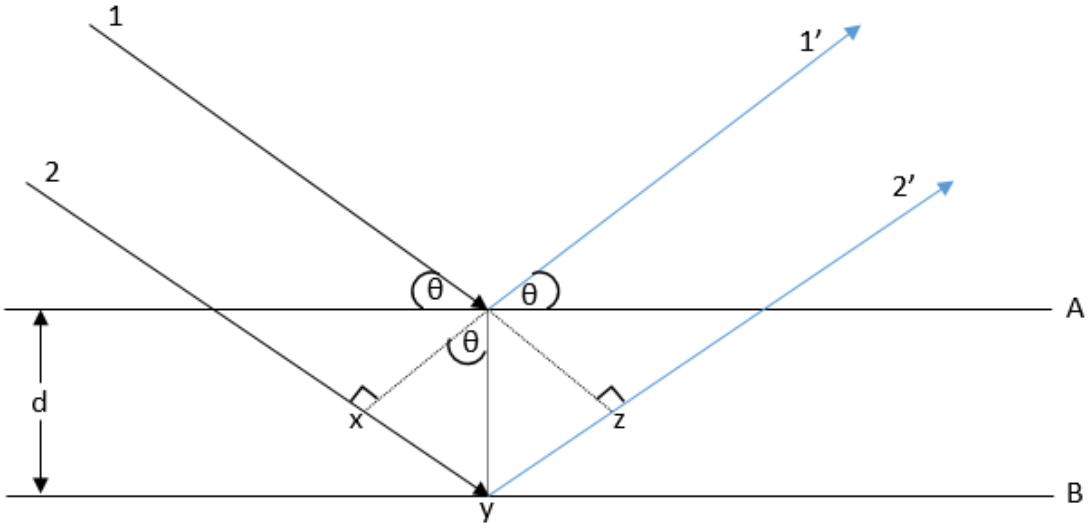

Figure 2.1: *Schematic representation of Bragg's law where the crystal is represented by a series of parallel planes separated by a distance, d. For Bragg's law to be satisfied x-ray 2 must diffract from plane B with the value of the extra distance travelled, x-y-z a whole number of wavelengths to remain in phase with the X-ray (1') reflected from plane A. Reproduced from West*[8].

2.3.2 Crystal Structures

For a material to be defined as a crystal it must show long range order in terms of the arrangement of atoms. If a material does not show this long range arrangement then it is known as amorphous (not covered here).

The long range order of atoms in a crystal can usually be broken down into a simple repeating block of atoms which represents the crystal's symmetry as a whole[10]. This three-dimensional block is known as a unit cell.

Crystals can be divided into seven different systems where the shape of the unit cell depends on the symmetry of the atoms arranged within it. The unit cell can also be defined by the three-dimensional lengths (*a*, *b*, *c*) and the angles between these axes (*α*, *β*, *γ*). This can be seen in *figure 2.2* which shows the cubic unit cell where *a* = *b* = *c* and *α*, *β*, *γ* = *90°* (*figure 2.2(a))* and a triclinic unit cell where *a* ≠ *b* ≠ *c* and *α*, *β*, *γ* ≠ *90° (figure 2.2(b))*.

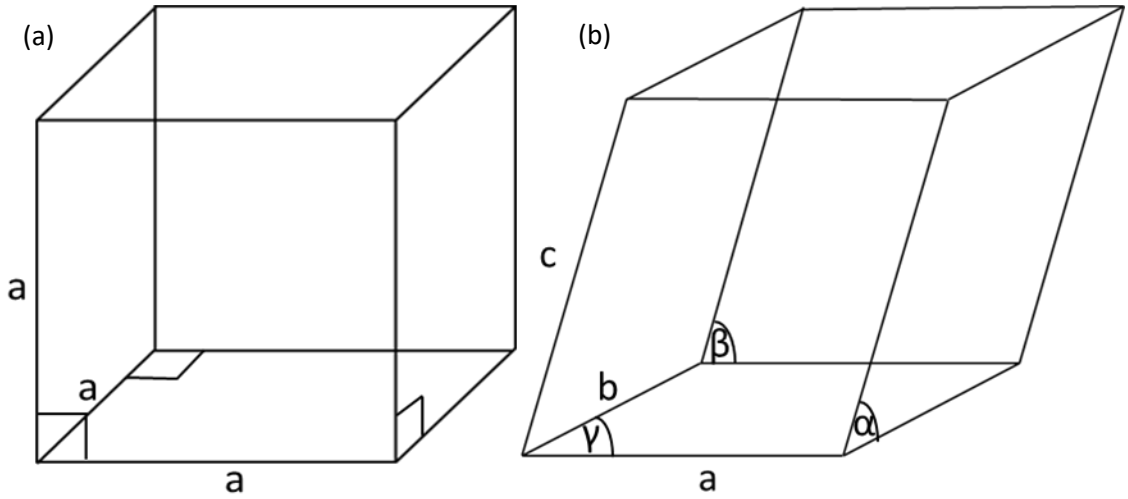

Figure 2.2: *Schematic representation of two of the seven crystal unit cells, (a) Cubic unit cell where a = b = c and α, β, γ = 90° and (b) Triclinic unit cell where a ≠ b ≠ c and α, β, γ ≠ 90°. Reproduced from West*[10].

The seven crystal systems can be seen in *table 2.1* below listed from the crystal system with the lowest symmetry, triclinic, shown in *figure 2.2(b)* to the cubic system with the highest symmetry shown in *figure 2.2(a)*. For each crystal system it possesses at least a single Bravais lattice, a lattice being points representing the symmetry of the system. There are five basic different lattice types primitive (P) which have points solely on all four corners of the unit cell, body centred (I) which has an extra point present, when compared to the primitive cell, at the centre of the lattice. Face centred (F), side centred (A, B or C) and rhombohedral centred (R) cells have extra points present, when compared with a primitive cell, on the faces of the cell. Face centred lattices (F) have extra points on all six faces of the cell. The A, B and C side centred lattices have extra points solely in faces which lie in the *a*, *b* and *c* directions respectively. Rhombohedral centred (R) cells have two extra points at the co-ordinates $(\frac{2}{3},\frac{1}{3},\frac{1}{3})$ and $(\frac{1}{3},\frac{2}{3},\frac{2}{3})$ within the hexagonal lattice.

***Table 2.1**: Unit cell dimensions and available Bravais lattices for the seven crystal systems. The letters represent the Bravais lattices where (P) denotes a primitive lattice, (A, B or C) a side centred lattice, (R) a rhombohedral centred lattice, (F) a face centred lattice, and (I) a body centred lattice. Reproduced from West[8].*

Crystal System	Unit Cell Dimensions	Bravais Lattices
Triclinic	$a \neq b \neq c$, $\alpha \neq \beta \neq \gamma \neq 90^o$	P
Monoclinic	$a \neq b \neq c$, $\alpha = \gamma = 90^o$, $\beta \neq 90^o$	P, C
Trigonal (a) Trigonal (b)	$a = b \neq c$, $\alpha = \beta = 90^o$, $\gamma = 120^o$ $a = b = c$, $\alpha = \beta = \gamma \neq 90^o$	P R
Hexagonal	$a = b \neq c$, $\alpha = \beta = 90^o$, $\gamma = 120^o$	P
Orthorhombic	$a \neq b \neq c$, $\alpha = \beta = \gamma = 90^o$	P, F, I, A (B or C)
Tetragonal	$a = b \neq c$, $\alpha = \beta = \gamma = 90^o$	P, I
Cubic	$a = b = c$, $\alpha = \beta = \gamma = 90^o$	P, F, I

Earlier in *section 2.3.1* we discussed that Bragg used the idea of planes to describe how diffraction occurs in a crystal. This idea was expanded with the concept of Miller Indices which describe the direction of planes that bisect through the unit cell. This simply means that the planes show the layers of atoms found in the unit cell, though a Miller plane does not require atoms to be present upon it. If there is zero electron density present upon a Miller plane then a peak would not be present on an XRD pattern. The directions *x*, *y* and *z* (or *a*, *b* and *c*) are labelled *h*, *k* and *l* respectively. The *hkl* integers will increase depending on the number of planes present in the unit cell. Examples of simple *hkl* planes in unit cells can be seen in *figure 2.3*.

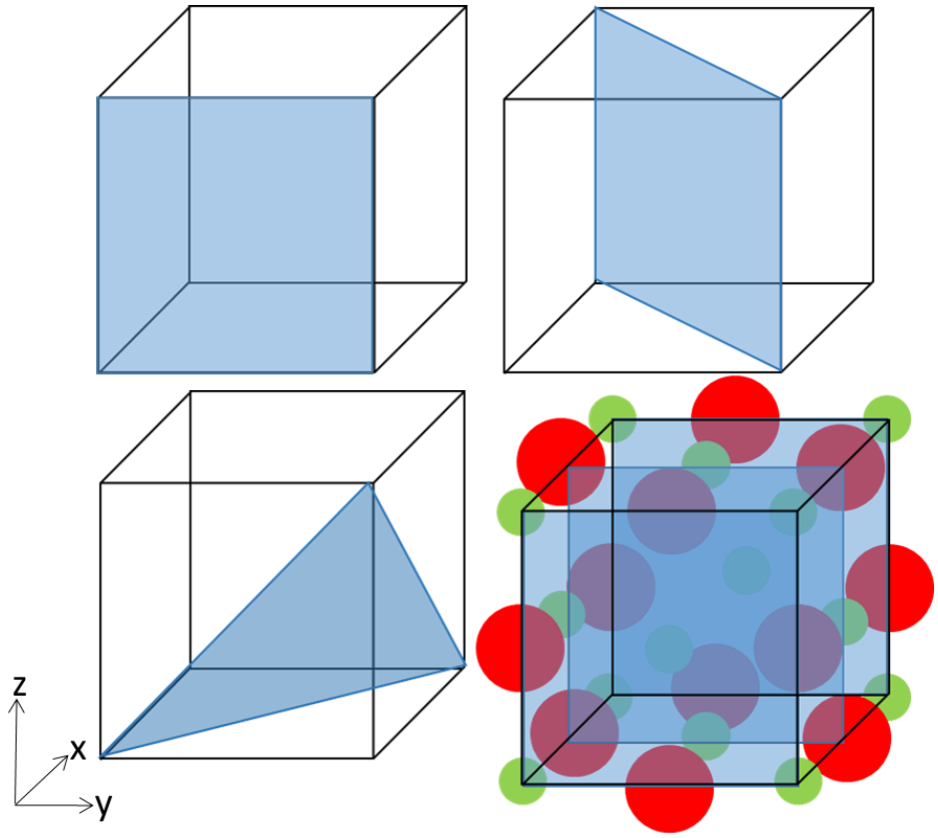

***Figure 2.3:** Examples of Miller Indices showing (a) (100) plane, (b) (110) plane, (c) (111) plane and (d) Sodium chloride unit cell showing the (200) planes. Reproduced from Ropp[11].*

These *hkl* values are directly related to peaks found in diffraction patterns due to the Bragg relationship with *d*-spacing. This can be seen in a modified version of Bragg's law[7].

$$n\lambda = 2d_{hkl}sin\theta_{hkl} \tag{2.5}$$

Table 2.2 shows the relationships between unit cell dimensions, *d*-spacing and *hkl*. It is clear that as symmetry decreases these relationships become more complex.

Table 2.2: *The seven crystal systems d-spacing relationship to hkl. Reproduced from Ropp*[11].

Crystal System	d-spacing relationship to hkl
Triclinic	$\frac{1}{d^2} = \frac{1}{V^2}[h^2b^2c^2\,sin^2\,\alpha + k^2a^2c^2\,sin^2\,\beta + l^2a^2b^2\,sin^2\,\gamma + 2hkabc^2(\cos\alpha\cos\beta - \cos\gamma) + 2kla^2bc(\cos\beta\cos\gamma - \cos\alpha) + 2hlab^2c(\cos\alpha\cos\gamma - \cos\beta)]$
Monoclinic	$\frac{1}{d^2} = \frac{1}{sin^2\beta}\left(\frac{h^2}{a^2} + \frac{k^2sin^2\beta}{b^2} + \frac{l^2}{c^2} - \frac{2hl\,cos\beta}{ac}\right)$
Rhombohedral	$\frac{1}{d^2} = \frac{(h^2+k^2+l^2)sin^2a + 2(hk+kl+hl)(cos^2\alpha cos\alpha)}{a^2(1-3cos^2\alpha+2cos^3\alpha)}$
Hexagonal	$\frac{1}{d^2} = \frac{4}{3}\left(\frac{h^2+hk+k^2}{a^2}\right) + \frac{l^2}{c^2}$
Orthorhombic	$\frac{1}{d^2} = \left(\frac{h^2}{a^2}\right) + \left(\frac{k^2}{b^2}\right) + \left(\frac{l^2}{c^2}\right)$
Tetragonal	$\frac{1}{d^2} = \frac{h^2+k^2}{a^2} + \frac{l^2}{c^2}$
Cubic	$\frac{1}{d^2} = \frac{h^2+k^2+l^2}{a^2}$

To calculate the intensity of the peaks found in a diffraction pattern an additional step is necessary, the calculation of the structure factor. The structure factor is the sum of the scattering from all the atoms in a unit cell for a given *hkl* reflection[12]. The structure factor can be written in the following form[8]:

$$F_{hkl} = \sum_j f_j\left(\cos\delta_j + i\sin\delta_j\right) \tag{2.6}$$

Where F_{hkl} is the structure factor, *j* represents atoms in the unit cell, f_j the diffracted wave of amplitude δ_j (a sine wave). The structure factor is proportionally related to the intensity by a modulus squared relationship[13].

Knowing the set of *hkl* values and structure factors for a given pattern should provide enough data to begin to narrow down the possible structure type. This is where Rietveld refinements are used to determine whether a model of the assumed structure is correct. Various parameters are refined such as the unit cell size, atomic positions, and Gaussian/Lorentzian terms for peak shape. The

refinements are based on a least squares method and compare a model to the experimental data and output statistics mathematically and graphically to determine the degree of fit as discussed in further detail in the following section.

2.3.3 Rietveld

Hugo Rietveld originally proposed the idea for a calculation method in 1969 to be used for fitting nuclear and magnetic structures to powder data[14]. This refinement method used the least squares method to calculate the best fit of the calculated model against the data observed in the experimental diffraction pattern. The calculation is continued until the best fit is obtained against all of the data points observed[15]. The residual, S_y, is used to describe the least squared method as shown in the following equation[16]:

$$S_y = \sum_i w_i (y_{io} - y_{ic})^2 \tag{2.7}$$

Where y_{io} is the intensity observed at *i*th step, y_{ic} is the intensity calculated at *i*th step and w_i is the Gaussian statistic calculated using $w_i = \frac{1}{y_{io}}$[16].

To determine the calculated intensity y_{ic}, another equation is necessary to take into account factors such as the Miller planes present, the structure factor and other crystallographic effects such as preferred orientation. Preferred orientation is found when crystallites in a polycrystalline powder show a preference towards a specific Miller plane leading to an unexpected increase in intensity for peaks associated with that planes *hkl* value. Calculated peaks must take into account the observed peak height, width and tailing with the integrated area being proportional to the Bragg intensity $I_{K(hkl)}$ which is also proportional to the square of the structure factor[15].

$$y_{ic} = s \sum_K L_K \, |F_K|^2 \, \emptyset \, (2\theta_i - 2\theta_K) \, P_K \, A + y_{ib} \tag{2.8}$$

Where y_{ib} is the intensity of the background at *i*th step, s is the scale factor, *K* are the Miller planes, L_K are the polarization, Lorentz, and multiplicity factors, $\emptyset$ is the reflection profile function, P_K represents preferred orientation, A is the absorption factor, and F_K is the structure factor for *K*[15].

During refinements a measure of fit is used to determine the probability that a model is in agreement with the experimentally observed data. The three most common goodness-of-fit parameters are the *R* factor (R_p), the weighted *R* factor (R_{wp}) and the goodness-of-fit indicator, S, or the more commonly used form, χ^2 (which is S squared)[16]. These are calculated using the following formulae[16]:

$$R_p = \frac{\sum |y_{io} - y_{ic}|}{\sum y_{io}} \quad (2.9)$$

$$R_{wp} = \left\{ \frac{\sum w_i (y_{io} - y_{ic})^2}{\sum w_i (y_{io})^2} \right\} \quad (2.10)$$

$$S = \frac{R_{wp}}{R_e} \quad \chi^2 = \left(\frac{R_{wp}}{R_e} \right)^2 \quad (2.11)$$

$$R_e = \left[\frac{(N - P)}{\sum w_i \, y_{io}} \right]^{\frac{1}{2}} \quad (2.12)$$

Where R_e is the expected *R* factor, which is calculated using *N* (the number of data points) and *P* (the number of refined parameters).

Despite the usefulness of these goodness-of-fit parameters a low value for any of these factors may not necessarily indicate a good fit of the model to the data. Another consideration that must be made is to the quality of the data used itself; lower quality data with an incorrect model may lead to lower values for the goodness-of-fit parameters than higher quality data with a sensible model[17]. This could be due to noise or lower resolution data hiding structural information which would lead to differences between the calculated and observed data.

The Le Bail method is used in refinements to test an experimental structural model against observed data without taking into account factors such as atomic positions and preferred orientation. It calculates the intensities solely from the symmetry found in the inputted model. This can be used to calculate the likely lattice parameters for the unit cell and profile parameters for the observed peaks.

When dealing with magnetic materials extra magnetic Bragg peaks can be observed (when using neutrons). This makes refining these structures more difficult and in an ideal situation a pattern would be obtained above the materials magnetic transition temperature to obtain the pure nuclear structure. From this the nuclear structural reflections can be subtracted from data collected below the magnetic transition temperature and the magnetic *k* vector can be calculated from the remaining peaks and the propagation vector ascertained.

Refinement of powder diffraction data in this thesis was performed using the General Structure Analysis System (GSAS) software suite[18,19]. The refinement of the background was performed with the shifted Chebyschev function with 12 background terms. A pseudo-Voight function comprising of Gaussian and Lorentzian terms was used to model the peak shape. Peak shape was fitted for neutron data using the type 3 profile in GSAS which uses a pseudo-Voight function and two back-to-back exponentials[20]. Refinement of magnetic neutron powder diffraction data was performed

using the FullProf software suite[21]. VESTA was used to model 3D structures from refinement data[22]. Full details of the refinements are provided in the relevant chapters.

2.3.4 Lab Based X-Ray Diffraction

2.3.4.1 Powder XRD and Experimental Details

The essential components of an X-ray diffractometer consist of an X-ray source, monochromator (if present), divergent slit, anti-scatter slit and an X-ray detector. X-rays are produced by first producing electrons through thermionic emission by heating a tungsten filament. These electrons are then accelerated using high voltages at a '*target*' or anode made of a metal such as copper. X-rays are produced as the electrons collide with the electron shells of the atoms in the anode and the wavelength of the x-rays produced is characteristic of the material used for the target due to the varying K_α wavelengths, for example copper has a K_α wavelength of 1.5406 Å.

X-rays are produced because the initial electron displaces another electron present in the electron shell of the target material. This leads to an electron located in a higher orbital replacing the displaced electron with a '*characteristic*' X-ray released as a result of the change in energy of the moving electron. Depending on the electronic transition different wavelengths of X-rays are produced. The higher wavelength X-rays K_α are produced through an electron moving from a 2*p* orbital to a 1*s* orbital and the lower wavelength X-ray, K_β, is produced through a 3*p* to 1*s* orbital transition. K_α X-rays can be further separated into two different wavelengths $K_{\alpha1}$ and $K_{\alpha2}$. $K_{\alpha1}$ X-rays have a lower wavelength and are of higher energy when compared to $K_{\alpha2}$ X-rays as the moving 2*p* electron is present in a higher energy level in a $K_{\alpha1}$ emission than in a $K_{\alpha2}$ emission. Other radiation known as Bremsstrahlung is produced as electrons decelerate due to interacting with the electron cloud. The kinetic energy difference is converted to X-rays with a spread of wavelengths.

The monochromator is used to filter X-rays by wavelength. This allows monochromatic radiation to pass through to the sample. It can be used to filter out Bremsstrahlung, K_β X-rays and also $K_{\alpha2}$ X-rays. If radiation is not monochromatic then extra intensity/peaks may be observed in the diffraction pattern which can lead to peak broadening.

The divergence slit controls the size of the x-ray beam and thus the amount of sample exposed to the beam. X-rays that do not diffract are filtered by the anti-scatter slit to stop the creation of any false detections[23]. One of the most important pieces of equipment in the diffractometer is the X-ray detector which creates an electrical current by converting the X-rays into an electrical signal and allows for the generation of a diffraction pattern.

Phase identification of powdered samples at room temperature were performed using a Malvern Panalytical Empyrean X-ray diffractometer operating at 40 kV and 40 mA and using the reflection/transmission sample spinner stage with a X'Celerator linear detector. The instrument used a Cu anode and graphite monochromator, resulting in a X-ray beam with $K_{\alpha 1}$ radiation of λ = 1.5406 Å. Data were collected over a two theta range of $10 \leq 2\theta \leq 90$ degrees with a step size of 0.0167° and a time per step of 1900 seconds. Two types of sample holder were used: a bulk sample holder and a zero background sample holder where in the latter the sample was secured with Vaseline (petroleum jelly). In measurements with both sample holders, the samples were rotated during collection to increase the probability of sampling a randomly orientated arrangement of crystallites, which can be useful in reducing preferred orientation.

Phase identification of powdered samples at low temperature (12 K to 298 K) were performed using the Malvern Panalytical Empyrean used for ambient temperature measurements with a Phenix cryostat sample chamber. Data were collected over two theta ranges of $10 \leq 2\theta \leq 90$ degrees at 12 K with a time per step of 1898 seconds, and $20 \leq 2\theta \leq 70$ degrees from 30 K to 298 K with a time per step of 201 seconds. A five minute equilibration time was used between temperatures. A zero background holder was used with the sample secured with Vaseline (petroleum jelly).

2.3.5 Neutron Based Diffraction

Neutron diffraction is a complementary experiment to XRD. The biggest difference is how neutrons and X-rays interact with the sample which results in opposing scattering cross sections. XRD is dependent on the number of electrons present, as X-rays interact with the electron cloud, so heavier elements diffract well but lighter elements may not[24]. Neutrons do not possess a charge and thus do not have this type of dependency and scatter well with lighter and heavier elements as the neutron primarily interacts with the element's nucleus rather than the electrons[25,2627]. Additionally, neutrons are able to interact with electrons in a different way since neutrons possess a magnetic moment. This means if unpaired electrons are present, neutrons should interact with the magnetic moment[28]. There are however, weaknesses for this technique such as low flux and weak scattering of neutrons which requires large amounts of sample compared to XRD (though this is improving)[28].

There are two different types of neutron sources currently in use[29]. The first type are known as reactor sources and utilise nuclear fission. An example of a reactor source is the Institut Laue–Langevin (ILL) in France. Nuclear fission of highly enriched Uranium 235 leads to the production of

a highly continuous flux of neutrons. Neutron guides, composed of supermirrors, are used to transport neutrons to the 45 ILL instruments inside guide halls away from the nuclear reactor[30].

The other type of neutron facilities are spallation sources, such as the ISIS Neutron and Muon Facility in the UK. Neutrons are generated by a particle accelerator firing a pulse of protons at high speeds at a target (tantalum coated tungsten at ISIS) leading to the ejection of neutrons. ISIS first uses a linear accelerator or LINAC to accelerate an H^- beam into the synchrotron, where the electrons of the beam are stripped on entry by an aluminium oxide foil[31]. The proton beam is then sent to two target stations where 35 neutron and muon instruments are located.

2.3.5.1 High Resolution Powder Diffractometer HRPD at ISIS, UK

Powder neutron diffraction was performed using HRPD at ISIS. HRPD has the highest resolution of a powder diffractometer of the suite of instruments at ISIS with a resolution of $\Delta d/d \sim 5\times10^{-4}$ on the backscatter detector[32,33]. Despite HRPD having one of the highest resolution of a powder diffractometer in the world, SuperHRPD at JPARC has a resolution which is equivalent but also over a wider d-spacing.

HRPD was used due to its high resolution which would allow the identification of the detailed nuclear structure of the samples in this thesis. Magnetic structural information can be gained on HRPD, however, resolution is limited at extended *d*-spacing ranges and a different instrument was used to focus specifically on samples that had a potentially interesting magnetic structure. The main antiferromagnetic peak in $BiFeO_3$ is found outside HRPD's highest resolution bank which covers the *d*-spacing range from 0.65 to 2.60 Å.

Data were collected at room temperature and temperatures between 10 K and 1093 K. At room temperature all samples were placed into a vanadium can and run for around 80 μAh. For the variable temperature experiment, samples which were only cooled were placed in an aluminium slab can and samples which were heated and cooled were placed in a vanadium can, with a cadmium mask used to hide the signal from the cryostat/furnace.

2.3.5.2 WISH at ISIS, UK

Room temperature powder neutron diffraction was performed by Xpress access using the WISH beamline at ISIS. WISH compared to HRPD has a lower peak resolution however, the resolution drop

off in WISH's resolution at higher d-spacing is not as severe resulting in higher resolutions at *d*-spacing in the medium to high region (0.7 to 17Å), makes it distinct from HRPD[34].

Data were collected with the samples loaded into vanadium cans and data collection times of approximately 40 μAh.

2.4 Characterisation Methods: Magnetism

2.4.1 SQUID and Experimental Details

A superconducting quantum interference device, SQUID, magnetometer is used to measure magnetic flux for magnetic samples. Measurement of magnetic flux can be related to magnetic field magnitude and gradient, and magnetic susceptibility[35].

The most common type of SQUID uses two y-shaped superconductors set parallel to each other with the space between the two contact points filled with a thin insulating layer. The two insulating layers are described as Josephson Junctions. The Josephson junction acts as a tunnel for Cooper pairs (paired electrons) between the superconductors[36]. This allows current transport, without a voltage, between the two superconductors, known as a supercurrent.

There are two types of SQUID in use currently. AC or RF SQUIDs use only a single Josephson junction and DC SQUIDs, the type described earlier, use two Josephson junctions. RF SQUIDs work using a radiofrequency flux bias, which is alternating, and the single Josephson junction is used to interrupt the flow of current within the superconductor[35]. In contrast, DC SQUIDs use a constant current bias.

The rest of the SQUID consists of a niobium tube, primary coil and secondary coil[37]. The sample is placed into an astatic coil within the secondary coil that when a current is applied does not produce a magnetic field. The primary coil is used to apply an external magnetic field to the secondary coil. The external magnetic field can then produce a magnetic response from the sample that leads to a change in current to the Josephson junction. This change in current will lead to a measurable change in magnetic flux which will be recorded as a change in voltage[37].

A Quantum design MPMS-7 DC SQUID was used to collect field dependent hysteresis loops between 5 T to -5 T at temperatures between 2 K and 300 K. Magnetic susceptibility data were collected under zero field cooled (ZFC) and field cooled (FC) environments at 0.1 T from 2K to 380 K.

High temperature SQUID measurements were performed using a Quantum Design MPMS 3 Vibrating Sample Squid Magnetometer. The sample was mixed with zicar cement and attached to

an oven sample stick with copper foil wrapped around it. Magnetic susceptibility data were collected at an applied field of 0.1 T from 400 K to 900 K and then back to 400 K.

2.5 Characterisation Methods: Electrical Measurements

2.5.1 PE Loop Analyzer and Experimental Details

The role of hysteresis in determining ferroelectric behaviour has been discussed in chapter 1. Measurement of materials for possible ferroelectric behaviour were required to determine multiferroic character. An Aixacct Easy Check 300 coupled with a Trek 610E high voltage amplifier were used to collect polarisation-electric field (PE) hysteresis loops at room temperature. The voltage and frequency were measured in the ranges 0-10 kV and 0-200 Hz with the current range set to auto. Pellets were coated with silver paste and annealed at ~400 K for 30 minutes to form electrodes.

2.6 Other Characterisation Methods

2.6.1 TGA/DSC and Experimental Details

This technique consists of the combination of two different instruments, thermal gravimetric analysis (TGA) and differential scanning calorimetry (DSC). TGA measures the change in mass of a sample as a function of temperature and time[38]. This can be useful to determine a sample's volatility, the release of components such as water and oxygen, or decomposition which results in the release or uptake of gas depending on the measurement environment. These changes should lead to an obvious change in mass that can be recorded and traced to a possible explanation.

DSC measures the change in energy of a sample as it is heated over time[39]. This works by comparing the sample to a reference and comparing the energy differences between the two as both are heated simultaneously. DSC can be used to detect phase transitions in materials as the change in structure should lead to a change in the physical properties such as the specific heat capacity. Thus, this change will lead to a change in the behaviour of this property, which will be represented in the DSC data. However, there are limitations with TGA/DSC such as it is dependent on the external conditions such as outside temperature and humidity.

A combined TGA/DSC instrument is usually composed of a thermobalance which has a DSC plate attached[40]. The thermobalance is used to record the mass change for the TGA component. The DSC

plate is usually a heat flux type DSC, which has two temperature sensors or thermocouples one attached to the sample chamber and another to the reference chamber[41]. The set-up works by measuring the temperature difference between the two chambers. This can lead to three outcomes. If the sample is warmer than the reference then the sample is reacting in an exothermic way by releasing heat energy. If the sample is cooler than the reference then the sample is reacting in an endothermic way by absorbing heat energy. These are displayed in the DSC pattern as peaks and troughs respectively. Lastly both systems can be equal in temperature due to equal heat flow which results in no change in the DSC pattern.

Combined TGA/DSC experiments were carried out using a Netzsch STA 409 PC Luxx. Samples were heated at 10 K a minute to 1273 K in nitrogen using alumina crucibles.

2.6.2 Raman and Experimental Details

Raman spectroscopy is named after the scientist Chandrasekhara Venkata Raman who experimentally observed the inelastic scattering of light[42]. The Raman Effect, which Raman spectroscopy is dependent on, is when inelastic scattering occurs between a photon of light and the nucleus of an atom. In Raman scattering an energy transfer will take place resulting in a change of energy for both the photon and atom so that the scattered photon will have a different energy level to the incident photon as shown in figure 2.4. This Raman effect is very weak in comparison with Rayleigh (elastic) scattering due to the photon of light only interacting with the electron cloud of an atom and so the scattered photon has the same energy as the incident photon resulting in no change of energy level (figure 2.4).

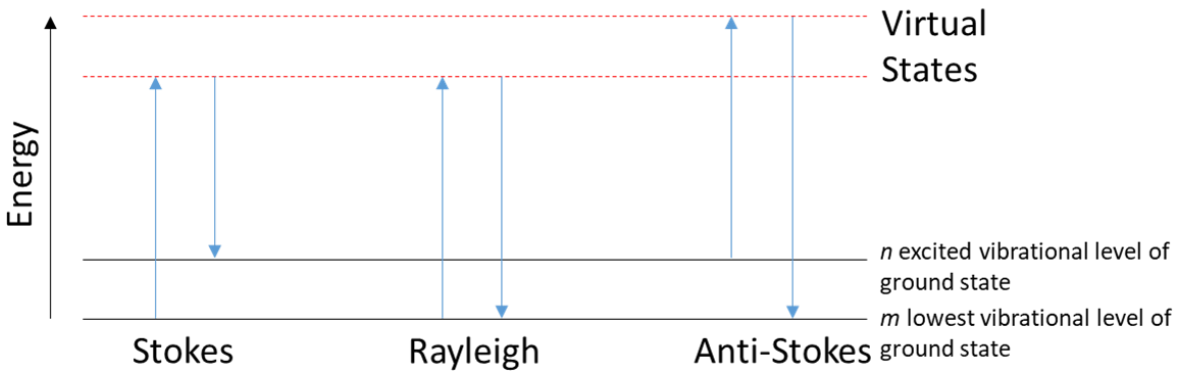

Figure 2.4: *Diagram showing Rayleigh (elastic) scattering where there is no energy change of the photon and Raman (inelastic) scattering where the photon loses energy (Stokes) or gains energy (Anti-Stokes). Reproduced from Smith et al*[43].

As a result the Raman Effect is divided into two types of scattering depending on the energy change of the photon. The first type is known as Stokes scattering, this is the process where the scattered

photon losses energy due to scattering and thus has a lower energy level compared to the incident photon. In contrast the molecule originally in the ground state gains energy and enters an excited state. The second type known as anti-Stokes scattering is the opposite, where the scattered photon gains energy compared to the incident photon, and the molecule originally in an excited state reduces down to the ground state[44].

At room temperature it is expected that most of the inelastic photon scattering is Stokes scattering as anti-stokes scattering requires the molecule to be in an excited state. A calculation can be made using the Boltzmann equation to calculate the ratio between the molecules in the excited and ground vibrational levels[43].

$$\frac{N_n}{N_m} = \frac{g_n}{g_m} exp\left[\frac{-(E_n - E_m)}{kT}\right] \tag{2.13}$$

Where N_n is the number of molecules in the excited state, N_m is the number of molecules in the ground state, g is the degeneracy levels, $(E_n - E_m)$ is the energy difference between the vibrational levels, k is the Boltzmann constant and T is the temperature.

A Raman spectrometer usually consists of a high-powered laser, microscope, objective and focusing lenses, monochromator/Rayleigh filter, and detector. The problem with Raman spectroscopy is that inelastic scattering is a weak effect; only a single photon scatters inelastically out of every 10^6-10^8 photons scattered in total[43]. A high-powered laser is employed as the source of photons due to high flux and high intensity of photons, which compensates for the weak scattering. There are, however, issues using lasers this powerful to take into consideration such as sample degradation, if the material is heat sensitive or photosensitive, and fluorescence, also a stronger effect than Raman scattering.

Optics systems are used to focus light from the laser onto the sample and focus the scattered photons from the sample towards the detector. Two types of optics systems are used that describe the angle the incident light hits the sample. A 90° system uses two focusing lens to direct the light onto the sample, which is collected at a 90° angle. The 180° system used in more modern systems uses an additional focusing lens, when compared to the 90° system, to direct the light onto the sample, which is collected at an 180° angle.

To reduce the intensity from Rayleigh scattering two types of filters can be used. The first type are monochromators which are used to separate the light by wavelength and so can be used to allow through the wavelengths of light expected from Stokes and anti-Stokes scattering. The problem with using monochromators is that it requires two or more monochromators to filter the high amount of Rayleigh scattering produced increasing the size and cost of the instrument. A simpler

and possibly more efficient solution is alternative types of Rayleigh filters, known as edge and notch filters. Edge filters absorb all light from a specific set frequency and are used to focus on Stokes scattering[43]. This unfortunately means it is not possible to record anti-Stokes scattering, however, these provide a cheap filter. Notch filters work differently by absorbing the frequency of light from the laser source with a tolerance either side, which varies in amount depending on the filter used. In contrast to the edge filter, the notch filter can be used to measure both the Stokes and anti-Stokes scattering. However, Notch filters have much shorted lifetimes when compared with Edge filters.

The two most common detectors used are either a charge coupled device (CCDs) or photodiode arrays[44]. The detectors are used to count the incoming photons and convert them into an electrical signal so the data can be extracted into a usable form.

A Horiba Yvon Jobin LabRAM HR spectrometer equipped with a red (633 nm) laser was used to collect room temperature Raman maps. Raman spectra were collected using a long working distance x50 objective and an 1800 lines per mm grating over an area of 50 µm by 50 µm (50 x 50 = 2500 spectra). Each spectrum is collected over a Raman shift range of 80 cm^{-1} and 1280 cm^{-1} with a two second acquisition time and data integrated over 10 measurements. Data were processed using MatLAB and Horiba Labspec 6 software.

2.6.3 SEM/EDX and Experimental Details

Scanning electron microscopy is used to examine specimens with a beam of electrons that allows higher magnifications to be visualised when compared to traditional optical microscopes.

Scanning electron microscopes are composed of four main components: an electron gun, condenser lenses, objective lens and detectors.

The electron gun produces electrons in a similar way to the X-ray tubes found in XRD instruments described earlier in *section 2.3.4.1*. Electrons are produced through thermionic emission by heating a tungsten filament and then using a high voltage to accelerate the electrons towards the next stage. The next stage consists of three electron lenses: two condenser lenses and a single objective lens. These lenses are used to project a demagnetised image of the electron source onto the sample's surface essentially focussing the electron beam[45].

When the electron beam interacts with the examined sample, the emission of different types of waves of varying energies are observed. These are secondary electrons (SE), backscattered

electrons (BSE), auger electrons, photons and X-rays[46]. Each of these can give compositional or topographical information of the sample.

Once electrons are emitted or deflected from the sample, detector(s) are used to examine the information and convert it to a visual image. In most detectors a scintillator is used to produce light when an electron comes into contact with it. This light is proportional to the electron's energy. A photomultiplier can then convert this light to an electric signal. The most commonly used detector for secondary electrons (SE) is the Everhart-Thornley type. This uses a voltage biased mesh to control the types of electron attracted to it. A positive voltage is used to attract only SEs to it but a negative voltage can be used to attract only backscattered electrons (BSE)[45]. However, a separate detector is usually used for BSEs due to the difference in angle required to capture SEs and BSEs.

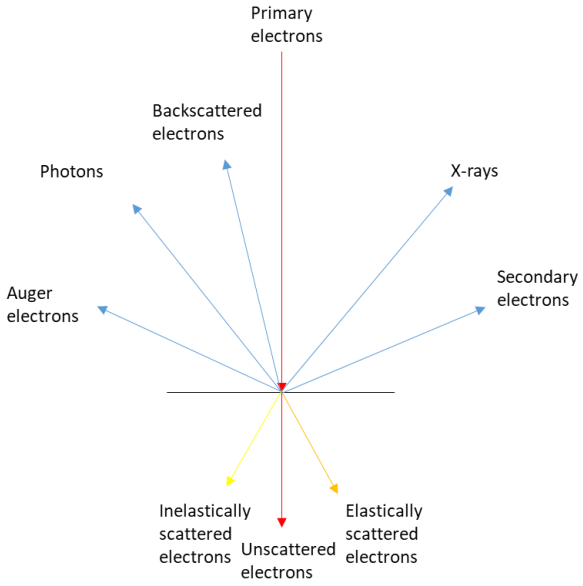

Figure 2.5: *Schematic representation of the different waves observed from an electron beam interacting with a sample. Reproduced from Krinsley et al*[46]*.*

For SEM analysis two types of emission shown in *figure 2.5* which are of interest, SEs and BSEs. SEs are produced from primary electrons which have been inelastically scattered from the sample. Inelastic scattering describes how the electron interacts with the atom which leads to a change in energy of the electron. This interaction leads to electrons which are weakly bound in the sample's electron cloud to be ejected due to the imparted energy and these electrons are thus called SEs[47]. SEs are typically used for topographical imaging.

BSEs are produced due to elastic scattering of the primary electrons. Elastic scattering occurs when an electron interacts with an atom but deflects off the atom without any energy transfer taking place. Some of these elastically scattered electrons will be deflected out of the sample as BSEs and the rest will be absorbed by the sample. BSE imaging can be used to determine differences in

composition between areas of the surface of the sample. This is because the number of BSEs scattered is proportional to the atomic number of the atoms the electron interacts with. Thus elements with a higher atomic number (*Z*) will scatter more electrons and so will produce a brighter SEM image. In contrast an element with a lower *Z* will scatter with less electrons and lead to more electrons being absorbed producing a darker image.

The amount of BSEs produced can be quantified using the following equation[46,47]:

$$\eta = \frac{N_{BSE}}{N_B} \tag{2.14}$$

Where η is the BSE coefficient, N_{BSE} is the number of BSEs and N_B is the number of primary or incident electrons. Through experimental data a relationship between η and *Z* has been found (equation 2.15), for values of *Z* above 10[46].

$$\eta = \left(\frac{ln\, Z}{6}\right) - 0.25 \tag{2.15}$$

Energy-dispersive X-ray spectroscopy (EDX) uses the X-rays emitted (shown in *figure 2.5*) for elemental analysis. EDX detects '*characteristic*' X-rays emitted from electron shells as these X-rays are unique to the emitting atom. The production of characteristic X-rays was described in *section 2.3.4.1*. However, unlike XRD, EDX measures the wavelengths of the X-rays produced from other shells, for elements with higher *Z*. These are labelled *K*, *L* and *M* where *K* is the lowest energy shell and *M* is the highest energy shell[45]. The energy difference between an electron moving from a higher energy shell to either the *K*, *L* or *M* shells is proportional to the X-ray released and this energy difference is unique for each element. This leads to the production of spectra, which are a function of the energy released and show the elements present.

A Hitachi S-3400N SEM fitted with an Oxford instruments EDX was used to image the materials described in this thesis with an accelerating voltage of the electron beam set to 20 kV. Secondary electron imaging was used to obtain topographical images of samples and backscattering electron imaging and EDX were used to obtain elemental maps and thus determine the compositional homogeneity of samples.

2.6.4 Solid State NMR and Experimental Details

Solid state nuclear magnetic resonance (NMR) spectroscopy or as its sometimes referred to magic angle spinning (MAS) NMR is used to determine the structure of solid compounds by the nuclear magnetic spin of atoms. NMR is most known for its use in the determination of organic molecular

structures through typically ^{1}H and ^{12}C NMR. NMR was originally not possible for solids as the sample was not in solution. This meant that there was no molecular motion present to compensate for anisotropic effects and dipolar interactions resulting in broad spectra that were extremely difficult to interpret[2]. However, a new method was developed to reduce broadening and enable the view of fine structure. This technique was termed magic angle spinning as the sample is spun at a '*magic angle*' of 54.74^{o} at high speed under an applied magnetic field[8].

Solid state NMR was performed by Dr Karen Johnston at the University of Durham (UK). A Bruker Avance III spectrometer was used to examine two samples from the $Bi_{1-x}Na_xFe_{1-x}Nb_xO_3$ series, $Bi_{0.1}Na_{0.9}Fe_{0.1}Nb_{0.9}O_3$ and $Bi_{0.05}Na_{0.95}Fe_{0.05}Nb_{0.95}O_3$. An 11.7 T magnet was set to the Larmor frequencies 132.3 MHz for ^{23}Na NMR and 122.4 MHz for ^{93}Nb.

2.7 References

1 I. Levin, M. G. Tucker, H. Wu, V. Provenzano, C. L. Dennis, S. Karimi, T. Comyn, T. Stevenson, R. I. Smith and I. M. Reaney, *Chem. Mater.,* 2011, **23**, 2166-2175 (DOI:10.1021/cm1036925).

2 E. A. Moore and L. E. Smart, in *Solid State Chemistry: An Introduction, Fourth Edition*, ed. E. A. Moore and L. E. Smart, Taylor & Francis CRC Press, Boca Raton, Florida, 2012, p. 124-128, 137-138.

3 R. C. Lennox, D. D. Taylor, L. J. Vera Stimpson, G. B. G. Stenning, M. Jura, M. C. Price, E. E. Rodriguez and D. C. Arnold, *Dalton Trans.,* 2015, **44**, 10608-10613 (DOI:10.1039/c5dt00140d).

4 P. Mandal, M. J. Pitcher, J. Alaria, H. Niu, P. Borisov, P. Stamenov, J. B. Claridge and M. J. Rosseinsky, *Nature,* 2015, **525**, 363-366 (DOI:10.1038/nature14881).

5 W. C. Röntgen, *Nature,* 1896, **53**, 274–277.

6 P. Ewald, in *Fifty Years of X-Ray Diffraction*, ed. Ewald, N.V.A. Oosthoek, IUCr, Netherlands, Utrecht, 1962, p. 31–56.

7 S. K. Chatterjee, in *Crystallography and the World of Symmetry*, ed. Hull, Parisi, J. Osgood and Warlimont, Springer-Verlag Berlin Heidelberg, Germany, Berlin, 2008, p. 44.

8 A. R. West, in *Solid State Chemistry and its Applications, 2nd Edition, Student Edition*, ed. West, John Wiley & Sons Ltd, UK, Chichester, 2014, p. 1-81, 229-269, 298-301,359-444.

9 W. H. Bragg and W. L. Bragg, *Proceedings of the Royal Society of London. Series A, Containing Papers of a Mathematical and Physical Character,* 1913, **88**, 428-438 (DOI:10.1098/rspa.1913.0040).

10 A. R. West, in *Basic Solid State Chemistry*, ed. West, John Wiley and Sons Ltd, UK, Chichester, 1999, p. 1.

11 R. Ropp, in *Solid State Chemistry*, ed. Ropp, Elsevier Science, Amsterdam, Netherlands, 2003, p. 36.

12 M. M. Woolfson, in *An Introduction to X-ray Crystallography*, ed. nonymous , Cambridge University Press, Cambridge, 1997, p. 50-75.

13 M. De Graef and M. E. McHenry, in *Structure of Materials: An Introduction to Crystallography, Diffraction and Symmetry*, ed. nonymous , Cambridge University Press, Cambridge, 2012, p. 291-319.

14 H. M. Rietveld, *J. Appl. Cryst.,* 1969, **2**, 65-71 (DOI:doi.org/10.1107/S0021889869006558).

15 R. A. Young, in *The Rietveld Method*, ed. Young, Oxford University Press, UK, Oxford, 1995, p. 1-38.

16 A. Clearfield and N. Bhuvanesh, in *Applications of Physical Methods to Inorganic and Bioinorganic Chemistry*, ed. R. A. Scott and C. M. Lukehart, John Wiley & Sons Ltd, UK, Chichester, 2007, p. 529-560.

17 B. H. Toby, *Powder Diffr.,* 2006, **21**, 67-70 (DOI:10.1154/1.2179804).

18 A. C. Larson and R. B. Von Dreele, *General Structure Analysis System (GSAS)*, Los Alamos National Laboratory Report LAUR 86-748, 2000.

19 B. H. Toby, *J. Appl. Crystallogr.,* 2001, **34**, 210-213 (DOI:10.1107/S0021889801002242).

20 Refinement of time-of-flight Profile Parameters in GSAS, https://www.isis.stfc.ac.uk/Pages/refinement-of-profile-parameters-with-polaris-data.pdf, (2020).

21 J. Rodríguez-Carvajal, *Physica B Condens. Matter,* 1993, **192**, 55-69 (DOI:doi.org/10.1016/0921-4526(93)90108-I).

22 K. Momma and F. Izumi, *J. Appl. Crystallogr.,* 2011, **44**, 1272-1276 (DOI:doi.org/10.1107/S0021889811038970).

23 V. K. Pecharsky, in *Fundamentals of powder diffraction and structural characterization of materials*, ed. P. Y. Zavalij, Springer, New York, 2009, p. 301-346.

24 A. F. Williams, in *A Theoretical Approach to Inorganic Chemistry*, ed. A. F. Williams, Springer, Berlin; Heidelberg, 1979, p. 282-300.

25 S. F. Parker and P. Collier, *Johnson Matthey Technol. Rev.,* 2016, **60**, 132 (DOI:doi:10.1595/205651316x691230).

26 G. E. Bacon, in *X-ray and neutron diffraction*, ed. G. E. Bacon, Pergamon, Oxford, 1966, p. 64-74.

27 F. Fernandez-Alonso and D. Price, in *Neutron Scattering, Volume 44: Experimental methods in the physical sciences*, ed. F. Fernandez-Alonso and D. Price, Elsevier, USA, California, 2013, p. 1-320.

28 C. Giacovazzo, H. L. Monaco, G. Artioli, D. Viterbo, M. Milaneso, G. Ferraris, G. Gilli, P. Gilli, G. Zanotti and M. Catti., in *Fundamentals of Crystallography*, ed. C. Giacovazzo, Oxford University Press, UK, Oxford, 2011, p. 301-406.

29 C. C. Wilson, in *Single crystal neutron diffraction from molecular materials*, ed. C. C. Wilson, World Scientific, Singapore ; London, 2000, p. 53–85.

30 ILL Brochure, https://www.ill.eu/fileadmin/user_upload/ILL/1_About_ILL/Documentation/ILL-General-brochure/Brochure-ILL-GB.pdf, (accessed June 2020).

31 How ISIS works - in depth, https://www.isis.stfc.ac.uk/Pages/How-ISIS-works--in-depth.aspx, (accessed June 2020).

32 HRPD User Manual, https://www.isis.stfc.ac.uk/Pages/hrpd-manual.pdf, (accessed March 2020).

33 R. M. Ibberson, *Nucl. Instr. Methods A,* 2009, **600**, 47-49 (DOI:doi.org/10.1016/j.nima.2008.11.066).

34 L. C. Chapon, P. Manuel, P. G. Radaelli, C. Benson, L. Perrott, S. Ansell, N. J. Rhodes, D. Raspino, D. Duxbury, E. Spill and J. Norris, *Neutron News,* 2011, **22**, 22-25 (DOI:10.1080/10448632.2011.569650).

35 J. Clarke, in *The New Superconducting Electronics*, ed. H. Weinstock and R. W. Ralston, Kluwer Academic publishers, UK, London. USA, Waterville Valley, N.H., 1993, p. 123-180.

36 J. Clarke, A. I. Braginski, B. Chesca, R. Kleiner and D. Koelle, in *The SQUID Handbook: Volume I Fundamentals and Technology of SQUIDs and SQUID Systems.*, ed. J. Clarke and A. I. Braginski, Wile-VCH, Weinheim ; Cambridge, 2004, p. 1-28, 29-92.

37 C. Enss and S. Hunklinger, in *Low-temperature physics*, ed. S. Hunklinger and C. Enss, Springer, Berlin ; New York, 2005, p. 343-446, 505-541.

38 M. E. Brown, in *Introduction to Thermal Analysis: Techniques and Applications*, ed. M. E. Brown, Springer, Netherlands, Dordrecht, 2001, p. 19-54.

39 P. J. Haines, in *Thermal Methods of Analysis: Principles, Applications and Problems*, ed. P. J. Haines, Springer, Netherlands, Dordrecht, 1995, p. 63-122, 161-205.

40 P. J. Haines and G. R. Heal, in *Principles of thermal analysis and calorimetry*, ed. S. B. Warrington, Royal Society of Chemistry, UK, Cambridge, 2002, p. 166-189.

41 E. L. Charsley and S. B. Warrington, in *Thermal analysis: techniques and applications*, ed. E. L. Charsley and S. B. Warrington, Royal Society of Chemistry, UK, Cambridge, 1992, p. 1-296.

42 J. R. Ferraro, K. Nakamoto and C. W. Brown, in *Introductory Raman spectroscopy*, ed. J. R. Ferraro, K. Nakamoto and C. W. Brown, Academic Press, USA, Boston; UK, London, 2003, p. 1-94.

43 E. Smith and G. Dent, in *Modern Raman spectroscopy : a practical approach*, ed. E. Smith and G. Dent, John Wiley, UK, Chichester, 2019, p. 1-20, 21-76, 77-100.

44 P. Larkin, in *Infrared and Raman Spectroscopy : Principles and Spectral Interpretation*, ed. P. Larkin, Elsevier, Netherlands, Amsterdam, 2018, p. 7-28, 29-61.

45 S. J. B. Reed, in *Electron Microprobe Analysis and Scanning Electron Microscopy in Geology*, ed. S. J. B. Reed, Cambridge University Press, Cambridge, 2005, p. 7-20, 21-40.

46 D. H. Krinsley, K. Pye, J. Boggs Sam and N. K. Tovey, in *Backscattered Scanning Electron Microscopy and Image Analysis of Sediments and Sedimentary Rocks*, ed. D. H. Krinsley, K. Pye, J. Boggs Sam and N. K. Tovey, Cambridge University Press, Cambridge, 1998, p. 4-24.

47 J. I. Goldstein, D. E. Newbury, J. R. Michael, N. W. M. Ritchie, J. H. J. Scott and D. C. Joy, in *Scanning electron microscopy and X-ray microanalysis*, ed. J. I. Goldstein, D. E. Newbury, J. R. Michael, N. W. M. Ritchie, J. H. J. Scott and D. C. Joy, Springer, USA, New York, 2018, p. 29-37.

Chapter Three: Investigation of $Bi_{0.9}Na_{0.1}Fe_{0.9}Nb_{0.1}O_3$ material

3.1 Introduction

As discussed in Chapter One, the aim of this research is to produce multiferroic materials with enhanced magnetic ordering over pure $BiFeO_3$ (BFO). Literature suggested that $Bi_{0.9}Na_{0.1}Fe_{0.9}Nb_{0.1}O_3$ crystallises in the *R*3*c* space group suggesting that the material is still likely ferroelectric[1-4]. In addition, Ma *et al*[1] reported weak ferromagnetism, not seen in undoped BFO, but it is unknown whether second phase material present in the sample could have contributed to this. Work undertaken in this chapter shows that $Bi_{0.9}Na_{0.1}Fe_{0.9}Nb_{0.1}O_3$ does retain the BFO parent *R*3*c* symmetry and shows enhanced magnetism over undoped BFO. The origins of this magnetic behaviour is discussed.

3.2 Room Temperature X-Ray Diffraction Characterisation

High resolution X-ray powder diffraction patterns were collected for the $x = 0.1$ sample in the $Bi_{1-x}Na_xFe_{1-x}Nb_xO_3$ solid solution using a Malvern Panalytical Empyrean diffractometer. Full refinement parameters can be found in appendix *table A1.1*.

The XRD pattern for the sample $Bi_{0.9}Na_{0.1}Fe_{0.9}Nb_{0.1}O_3$ referred to as NNO10% can be seen in *figure 3.1*. Shown in this figure is the Rietveld refinement fit using an *R*3*c* crystallographic model to the XRD data. The fit of the model shows a good degree of fit. However the fit of the peak present at 39.45° 2θ equating to the 202 *hkl* plane shows a deficiency in the fit of the intensity. This can likely be associated with a small amount of preferred orientation in this plane. The pattern itself appears to be single phase with sharp peaks suggesting high crystallinity and a homogenous distribution of cations. This confirms that the synthesis method, modelled after Levin *et al*[5], has led to better quality samples in terms of purity and homogeneity.

The *R*3*c* model used was a modified BFO with Na and Nb added at 0.1 occupancy. Shown in *table 3.1* are the cell parameters and fitting statistics for this model. An interesting point is the change seen in the lattice parameters and cell volume between pure BFO (from Arnold *et al*[6]) and NNO10%. An almost negligible increase is seen in the *a* and *b* lattice parameters (5.582 Å to 5.58341(12) Å) with a larger decrease seen, in comparison, in the *c* lattice parameter (13.88 Å to 13.8171(4) Å) leading to an overall reduction in the cell volume (374.5 $Å^3$ to 373.033(22) $Å^3$)[6]. Considering that the ionic sizes of Bi^{3+} (1.40 Å) and Na^+ (1.39 Å) in the 12 coordinate *A*-site and Fe^{3+} (0.645 Å HS) and Nb^{5+} (0.64) Å) in the octahedral site *B*-site are similar, the contraction of the cell volume is likely attributed to the reduction of Bi^{3+} and the effect of its stereochemical lone pair. It can be inferred

from this result that the substitution of 10% BFO cations for 10% NNO cations does not lead to an obvious symmetry change suggesting that functional properties, such as the magnetic and electrical properties, may not change drastically and thus these materials may remain multiferroic. However, it is hoped that the disruption of magnetic Fe^{3+} interactions and the addition of Nb^{5+} and Na^{+} may improve these properties. Previous literature for the NNO10% composition agrees with this assignment of rhombohedral *R*3*c* symmetry[1,7-9]. In all cases the data presented is consistent with the data presented here.

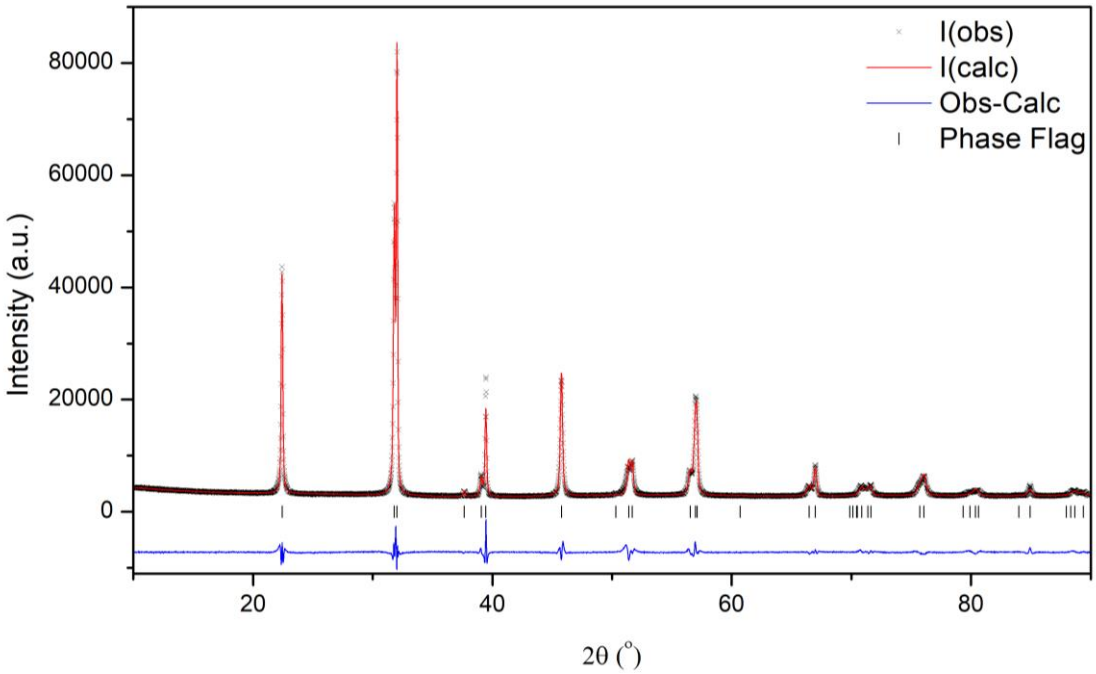

Figure 3.1: *Rietveld refinement of room temperature PXRD data collected for $Bi_{0.9}Na_{0.1}Fe_{0.9}Nb_{0.1}O_3$; χ^2 = 8.179, R_{wp} = 4.59% and R_p = 2.98; the black crosses represent the observed intensity, the red line represents the calculated intensity from the model, the blue line represents the difference between the observed pattern and calculated pattern and the black tick marker represents the R3c model.*

Table 3.1: *Cell parameters and model fit statistics extracted from the Rietveld refinement of PXRD data collected for $Bi_{0.9}Na_{0.1}Fe_{0.9}Nb_{0.1}O_3$ fitted using the R3c model.*

Space Group	X^2	wRp	Rp	a (Å)	b (Å)	c (Å)	α (°)	β (°)	γ (°)	Cell Volume (Å^3)
*R*3*c*	8.179	4.59	2.98	5.58341(12)	5.58341(12)	13.8171(4)	90	90	120	373.033(15)

Table 3.2: *Atomic coordinates extracted from the Rietveld refinement of PXRD data collected for $Bi_{0.9}Na_{0.1}Fe_{0.9}Nb_{0.1}O_3$ fitted using the R3c model. Oxygen U_{ISO}*100 fixed at 1.00.*

Bi/Na 1	x	0.0	Fe/Nb 1	x	0.0	O1	x	0.4403(25)
	y	0.0		y	0.0		y	0.0068(24)
	z	0.0		z	0.22591(23)		z	0.9632(9)
	U_{ISO}*100	2.25(4)		U_{ISO}*100	0.26(7)		U_{ISO}*100	1.00*

For comparative purposes $Bi_{0.9}K_{0.1}Fe_{0.9}Nb_{0.1}O_3$ referred to as KNO10% was also prepared using the same synthetic method as that used to prepare NNO10%. The XRD pattern for the KNO10% material is shown in *figure 3.2*. The Rietveld refinement was performed with both *R*3*c* and *P*4*mm* crystallographic models. Full refinement parameters can be found in appendix *table A1.1*. Despite the use of two models to describe this pattern the fit is lacking in intensity on the peaks at 22.36° 2θ and 45.66° 2θ which could be from preferred orientation. The decision to fit the data with two models was made as contributions could be found from both models. For example, a weak reflection at 37.56° 2θ can be attributed to the *R*3*c* model despite the pattern not displaying the characteristic splitting seen in pure BFO patterns. The phase percentages for the two models was found to be 91% *P*4*mm* and 9% *R*3*c*. Attempts were made to fit the pattern to a single model, but this proved unsuccessful. This would suggest that the KNO10% sample is mixed phase and sits within the boundary between two different phases. This result is in contrast with that previously observed from the Arnold group, with only an *R*3*c* model used to fit the data at this composition[10]. The synchrotron diffraction data in the supplementary information of Lennox *et al*[10] fits the *R*3*c* model well but there seems to be a small amount of second phase present. The modified synthesis method (reported here) involves heating these materials for extended time periods and using excess Bi_2O_3 and K_2CO_3 to mitigate the loss of volatiles. This route results in materials which exhibit improved crystallinity and cation distribution allowing their further analysis. In the previous work this composition was right at the phase boundary between *R*3*c* and *P*4*mm* symmetries with a large region of phase coexistence reported. Difficulties in absolutely controlling the phase composition and distribution is most likely the origins of these differences which results in a perceived shift of the phase boundary in the BFO-KNO solid solution phase diagram[10].

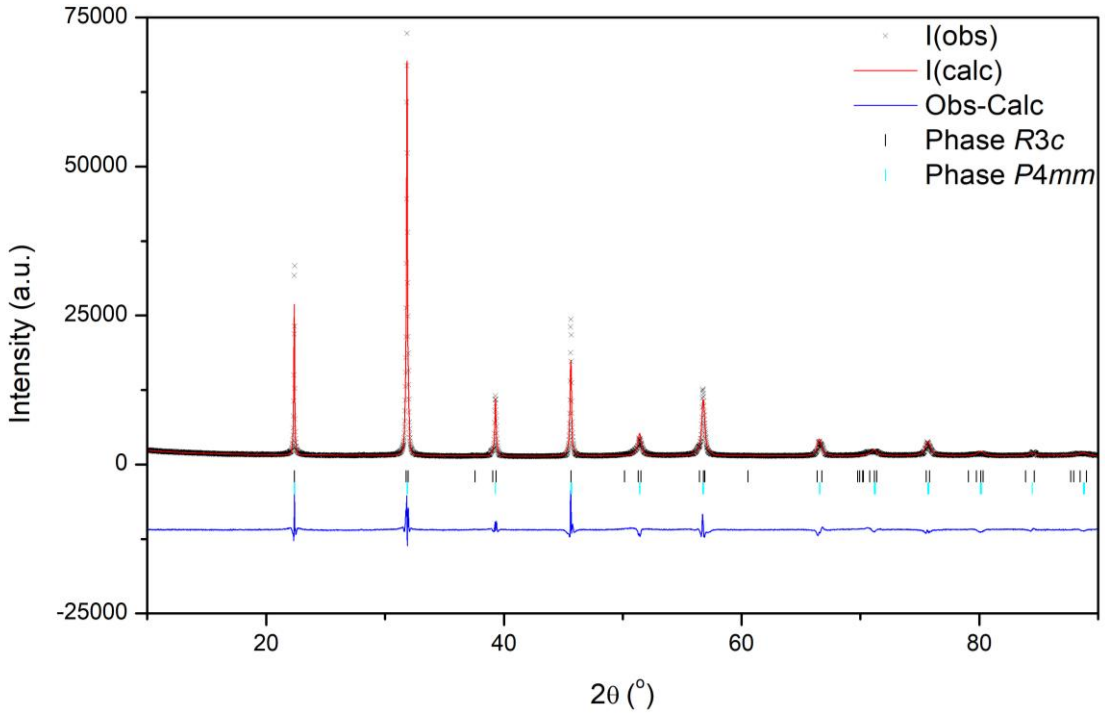

Figure 3.2: *Rietveld refinement of room temperature PXRD data collected for $Bi_{0.9}K_{0.1}Fe_{0.9}Nb_{0.1}O_3$; χ^2 = 11.95, R_{wp} = 7.82% and R_p = 5.43; the black crosses represent the observed intensity, the red line represents the calculated intensity from the model, the blue line represents the difference between the observed pattern and calculated pattern, the black tick marker represents the R3c model and the cyan tick marker represents the P4mm model.*

Since it was found that the KNO10% material was mixed phase a new composition was synthesised, $Bi_{0.925}K_{0.075}Fe_{0.925}Nb_{0.075}O_3$ referred to as KNO7.5%, to enable a KNO doped with *R*3*c* symmetry to be directly compared to the property measurements for NNO10%. *Figure 3.3* shows the Rietveld refinement profile of KNO7.5% from XRD data showing a good fit to the *R*3*c* model similar to that observed for NNO10%. Full refinement parameters can be found in appendix *table A1.1*. The XRD pattern seems to show all peaks are predicted by the model which suggests the sample is single phase with no impurity phase present. Again, there are some peaks where the intensity is not quite modelled most likely arising as a result of preferred orientation.

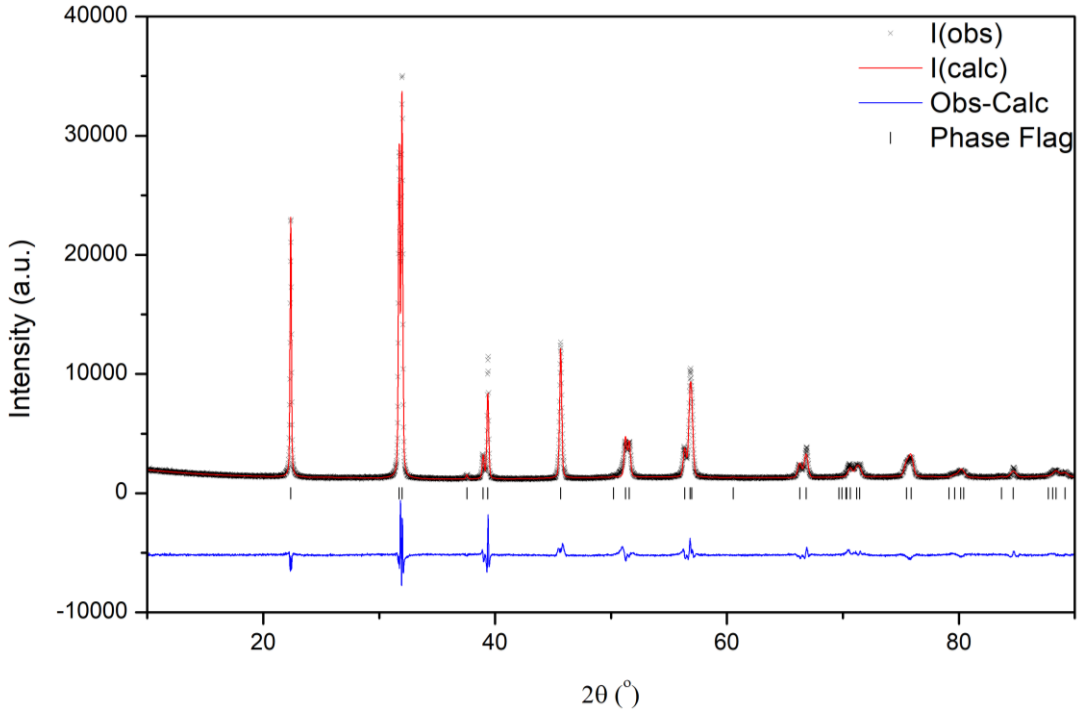

Figure 3.3: *Rietveld refinement obtained of room temperature PXRD data collected for $Bi_{0.925}K_{0.075}Fe_{0.925}Nb_{0.075}O_3$; χ^2 = 7.739, R_{wp} = 6.61% and R_p = 4.48; the black crosses represent the observed intensity, the red line represents the calculated intensity from the model, the blue line represents the difference between the observed pattern and calculated pattern and the black tick marker represents the R3c model.*

3.3 Magnetic Characterisation

The expected field dependent behaviour for undoped BFO can be seen in *figure 3.4 (a)*. The behaviour typifies pure antiferromagnetic behaviour with a closed loop with no coercive field present. To determine whether a change in the magnetism was seen with the addition of NNO compared to undoped BFO, magnetic measurements were performed using a Quantum Design MPMS-7 SQUID magnetometer from 2 K to a maximum of 380 K. The SQUID results for NNO10% can be seen in *figure 3.4 (c)* which shows magnetic hysteresis loops collected at 2 K and 300 K and zero field cooled (ZFC), field cooled (FC) data collected at 0.1 T. The hysteresis loops show a coercive field larger than undoped BFO. A small difference can be seen between the hysteresis loops collected at the two temperatures with the 2 K loop showing a better shape suggesting better saturation as expected at lower temperatures. This result is similar to the findings of Ma *et al*[1]. In this paper a similar magnetic hysteresis loop was obtained which the authors suggested was indicative of weak ferromagnetic order[1]. However, iron oxide (α-Fe_2O_3) impurities were observed in their XRD data which makes it difficult to be confident of the origins of the hysteresis loop reported in this work due to the sensitivity of SQUID magnetometers[1,11].

The ZFC, FC data shown in *figure 3.4 (c)* suggests the Néel temperature is above room temperature and outside the temperature range of the equipment used. The measurement is noisy particularly

in the temperature ranges 12 K to 60 K in both the ZFC and FC data which is most likely due to the small magnetisation values and limitations of the instrument used. From the data presented here there is clear hysteric behaviour of the magnetic structure. This may indicate a magnetic transition possibly to a canted antiferromagnetic arrangement to allow the increased coercive field.

Two extra samples were synthesised in an attempt to optimise the magnetic behviour seen in NNO10%, $Bi_{0.925}Na_{0.075}Fe_{0.925}Nb_{0.075}O_3$ and $Bi_{0.875}Na_{0.125}Fe_{0.875}Nb_{0.125}O_3$. $Bi_{0.925}Na_{0.075}Fe_{0.925}Nb_{0.075}O_3$ was found to crystallise with *R*3*c* symmetry and $Bi_{0.875}Na_{0.125}Fe_{0.875}Nb_{0.125}O_3$ was found to be mixed phase (discussed in further detail in chapter 5). The magnetic hysteresis loops at 2 K and 300 K for $Bi_{0.925}Na_{0.075}Fe_{0.925}Nb_{0.075}O_3$ and $Bi_{0.875}Na_{0.125}Fe_{0.875}Nb_{0.125}O_3$ are shown in *figure 3.4 (b) and (d)* respectively. $Bi_{0.925}Na_{0.075}Fe_{0.925}Nb_{0.075}O_3$ shows similar magnetic behaviour to NNO10% with a similar hysteresis loop but with a lower saturation magnetization and narrower hysteresis. In contrast, $Bi_{0.875}Na_{0.125}Fe_{0.875}Nb_{0.125}O_3$ behaves more like a typical antiferromagnet with a very small coercive field suggestive of glassy-like behaviour. The results from these two new samples indicate that the magnetic behaviour observed in NNO10% is optimal in the $Bi_{1-x}Na_xFe_{1-x}Nb_xO_3$ solid solution.

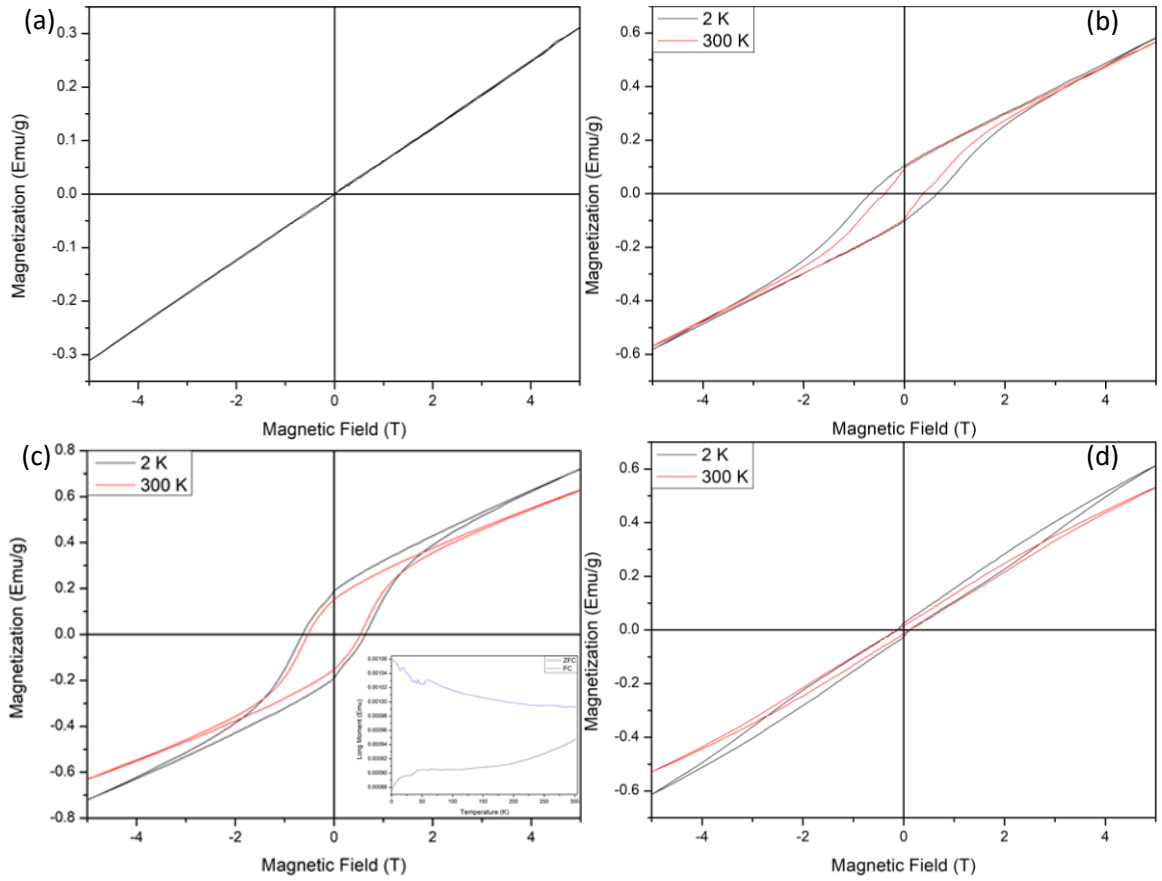

Figure 3.4: *Field dependent magnetic hysteresis loops from SQUID magnetometry measurements at temperatures of 2 K to 300 K and fields from -5 T to 5 T for (a) $BiFeO_3$, Produced from data provided by Dr Arnold. (b) $Bi_{0.925}Na_{0.075}Fe_{0.925}Nb_{0.075}O_3$, (c) $Bi_{0.9}Na_{0.1}Fe_{0.9}Nb_{0.1}O_3$, inset: variable temperature Zero field cooled and Field cooled data at 0.1 T and (d) $Bi_{0.875}Na_{0.125}Fe_{0.875}Nb_{0.125}O_3$.*

In contrast the magnetism for KNO10% seems to be more aligned with undoped BFO as shown in *figure 3.5 (a)*. The hysteresis loops at both temperatures (2 K and 300 K) displays antiferromagnetic behaviour though a small amount of coercive field can be seen.

The magnetic behaviour of KNO7.5%, in *figure 3.5 (b)*, is noticeably different from KNO10%, with a higher coercive field and (saturation) magnetization at 5 T. However, it lacks the shape of the hysteresis loops shown by NNO10% and $Bi_{0.925}Na_{0.075}Fe_{0.925}Nb_{0.075}O_3$ suggestive of glassy-like behaviour.

The magnetic results for KNO10% also differ from the previously observed results from the Arnold group in Lennox *et al*[10]. The results presented in the paper share more of a similarity with those discussed for KNO7.5% with a similar coercive field present in both. This is to be expected since the KNO10% materials studied exhibits predominantly *P*4*mm* symmetry whilst KNO7.5% is more comparable with *R*3*c* symmetry.

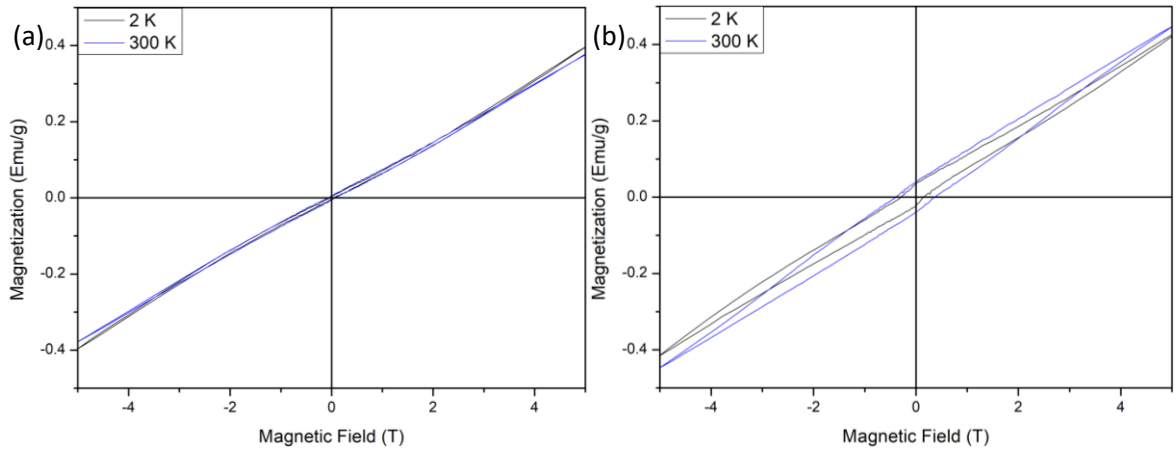

Figure 3.5: *Magnetic Hysteresis loops from SQUID at 2 K to 300 K at fields from -5 T to 5 T for (a) $Bi_{0.9}K_{0.1}Fe_{0.9}Nb_{0.1}O_3$, (b) $Bi_{0.925}K_{0.075}Fe_{0.925}Nb_{0.075}O_3$.*

These data indicate that removing Bi^{3+} and $Fe^{3+}$and replacing them with either Na^+ or K^+ and Nb^{5+} has a large effect on the magnetic properties observed. Interestingly, adding $NaNbO_3$ results in materials which exhibit switchable magnetic behaviour. This gives rise to the questions what differentiates Na^+ and K^+ based materials and secondly what is the mechanism which allows for switchable magnetic behaviour? The first question could be answered by the difference in size but the second is more complicated. The off centring of Bi^{3+} is responsible for the ferroelectric properties which can directly be related to the origin of the spin cycloid. By reducing the amount of Bi^{3+} by adding Na^+ (which have similar ionic radii) the lone pair effects are reduced potentially suppressing spin cycloid[12]. Replacing Bi^{3+} with K^+ also reduces the displacement which should also be expected to suppress the spin cycloid, however, the larger ionic radius of K^+ relative to Bi^{3+} applying chemical pressure and changing the magnetic exchange pathways changing the origins of

the magnetic behaviour. This, of course, ignores the replacement of Fe^{3+} with Nb^{5+} which would also contribute to the magnetic behaviour observed. Given the similar sizes of Nb^{5+} and Fe^{3+} and the small doping levels discussed here it is unlikely that the addition of Nb^{5+} has a large effect on magnetic percolation. However, Nb^{5+} is in a diamagnetic state which most likely contributes to the lack of saturation seen in the field dependent studies for these materials.

Due to the Néel temperature of the NNO10% being above the range of the SQUID at the University of Kent, the sample was sent to the materials characterisation lab at ISIS to collect high temperature SQUID magnetometry data. This measurement is shown in *figure 3.6* which displays the magnetization on heating, to 900 K, and subsequently cooling back to room temperature. For these measurements the sample is mixed with a ceramic/resin to affix it to the heating probe. This inevitably contributes to the measurement and results in some discrepancy between the data collected on heating and cooling. There is a clear sample response in the data in the form of deviation seen in the range 573 K to 598 K. This would suggest a Néel temperature (T_N) of approximately 585 K which suggests T_N has decreased when compared to undoped BFO. This most likely arises as a result of subtle structural changes including in the FeO_6 octahedral tilts as a result of doping which leads to changes in the *B*-O-*B* bond angles effecting the magnetic exchange pathways.

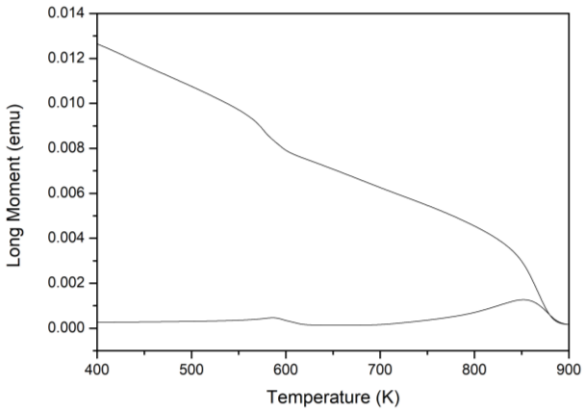

Figure 3.6: *Magnetic data from High Temperature SQUID magnetometry for $Bi_{0.9}Na_{0.1}Fe_{0.9}Nb_{0.1}O_3$. (Quoted in emu rather χ due to sample environment)*

3.4 Room Temperature Neutron Diffraction Characterisation

To try and understand the nuclear and magnetic structures seen in the PXRD and SQUID data, room temperature PND was performed at the WISH beamline at ISIS on the NNO10% sample. Shown in *figure 3.7* is the Rietveld refinement fit of an *R*3*c* crystallographic model to the PND pattern from WISH. The pattern itself seems to show a flat background with all peaks fit by the *R*3*c*

crystallographic model suggesting a single phase material with no second phase impurities mirroring the observations seen in the XRD data. This refinement was performed using the Fullprof suite of programs by Dr Arnold[13]. Initial refinements were performed using the undoped BFO nuclear and incommensurate spin cycloid models, *R*3*c* and $R\overline{1}$ with a propagation vector of δ, δ, 0, where $\delta \approx 0.0042$ respectively. A good fit was observed for the nuclear phase (as shown in *figure A1.1* in appendix 1). However, as is shown in *figure 3.7*, there are a loss of magnetic Bragg peaks in the NNO10% pattern when compared to undoped BFO which indicates that the magnetic structure may have changed

The incommensurate propagation vectors (δ) were then allowed to refine. This refinement gave an improved fit to the magnetic phase (magnetic R factor = 9.001). Full refinement parameters and the fit can be found in appendix *table A1.2 and figure A1.2*. It was found that the *k* vector was smaller than that seen in undoped BFO with a refined value for $\delta \approx 0.0011$ about a quarter of that seen for undoped BFO. The magnetic moment for Fe^{3+} was found to be around 3.5 μ_B, which is reasonably consistent with $BiFeO_3$ and $Bi_{0.9}Sm_{0.1}FeO_3$[14,15]. Reducing the δ value leads to the loss of the '*magnetic satellites*' seen in BFO. Close observation of the magnetic Bragg peaks at around 4.6 Å shows that there is peak shape over fit which indicates the fit is not ideal. The closeness of δ towards zero leads the incommensurate satellite peaks moving closer towards the central peak and ultimately leads to a lengthening of the spin cycloid as has been reported for $Bi_{0.9}Sm_{0.1}FeO_3$[15].

However, since the δ value is so close to zero a second refinement with a *k* vector of (0,0,0) was performed so that a comparison could be made. Full refinement parameters and the fit can be found in appendix *table A1.2 and figure A1.3*. As with the other refinements the nuclear structure fits well. However, whilst this *k* vector predicts peaks in the correct position the magnetic structure was found to give a slightly diminished fit with a magnetic R factor of 10.04. The same issue seen in the incommensurate model is observed in this model where the peak at 4.6 Å is over fit. However, it appears that the peak shape in this fit is marginally worse than that seen in the incommensurate model. The magnetic moment from this refinement was found to be much lower at around 1.725 μ_B.

When the SQUID data is considered from *section 3.2* it was suggested that the magnetic hysteresis was not solely from the disruption of the spin cycloid because of the addition of niobium to the magnetic sites and thus the possibility of spin canting of Fe^{3+} was suggested. When the spins were allowed to cant in this refinement this led to an improvement in the magnetic R factor (9.290). However, the magnetic moment was still found to be comparable with the initial refinement with

a low value of 1.751 μ_B. The fit can be found in appendix *figure A1.4* and magnetic model is shown in *figure 3.9 (a)* which displays an antiferromagnetic with a small degree of spin canting.

With this information further methods were considered to improve the fits to the data. Alternative commensurate *k* vectors were considered but none were found which could model the data. However, alternative incommensurate vectors were not considered, and *k*-search was not performed. Closer examination of the fit to the nuclear phase found that whilst the profile of some peaks were fit well other peaks were fit less convincingly. This issue was also found in the variable temperature HRPD data discussed later in *section 3.5*. These peak effects have been seen previously in undoped BFO under small pressure loads using the PEARL instrument at ISIS[16]. This was found to occur as a result of domain wall reorientation which led to the formation of small domains and resulted in (*hkl*) dependent peak broadening due to strain in the structure. Addition of Na and Nb to BFO results in a small amount of chemical pressure being added to the system which seems to replicate the effects seen in undoped BFO under pressure. The formation of small domains were confirmed using Raman spectroscopy and are discussed later in *section 3.6*. Considering these effects in the nuclear structure it is also, therefore, possible that this same effect is present in the magnetic phase.

With this knowledge extra variables were added to the refinements such as strain and size parameters to mitigate against this effect. Unfortunately, there is a high degree of correlation between the added terms, while the incommensurate nature of the magnetic model added additional complications. Attempts to refine strain parameters with a *k* vector of (0,0,0) led to unstable refinements. Refinements with the spin cycloid, shown in *figure 3.7*, led to an improvement in fit in both the nuclear and magnetic (R = 8.603) phases with $\delta \approx 0.0007953$ and a magnetic moment of 3.274 μ_B. Full refinement parameters be found in appendix *table A1.2*. The magnetic model shows G-type antiferromagnetic order on the local scale and is shown in *figure 3.9 (b)*. The spin moments calculated for this model also seem to show an uneven distribution of magnetic moment which may be due to the complications in refining these data or may further contribute to the origins of magnetic hysteresis. Further attempts to refine the nuclear or magnetic structure without strain terms did not yield an improvement in the fit. The most likely conclusion is that NNO10% adopts a very long spin cycloid of around 370 nm, nearly six times longer than that seen in undoped BFO. The origin of the magnetic hysteresis seen earlier in *section 3.2* arises from a combination of small domains coupled with local strain due to cation distribution leading to complex magnetic order. However, the magnetic refinements presented here are not ideal due to the complexity of these refinements and require further work as the possibility of a *k* vector of (0,0,0) with spin canting cannot be ruled out.

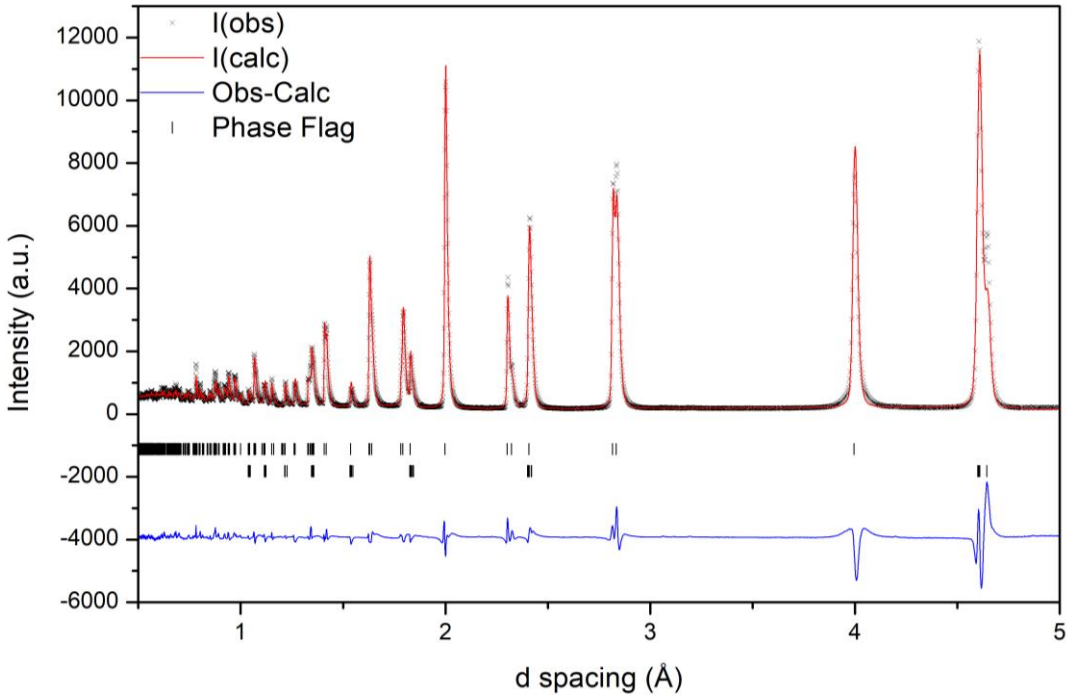

Figure 3.7: *Rietveld refinement obtained of room temperature PND data collected for $Bi_{0.9}Na_{0.1}Fe_{0.9}Nb_{0.1}O_3$ on WISH; R_{wp} = 11.7% and R_p = 13.6; the black crosses represent the observed intensity, the red line represents the calculated intensity from the model, the blue line represents the difference between the observed pattern and calculated pattern and the black tick marker represents the R3c model and incommensurate magnetic model.*

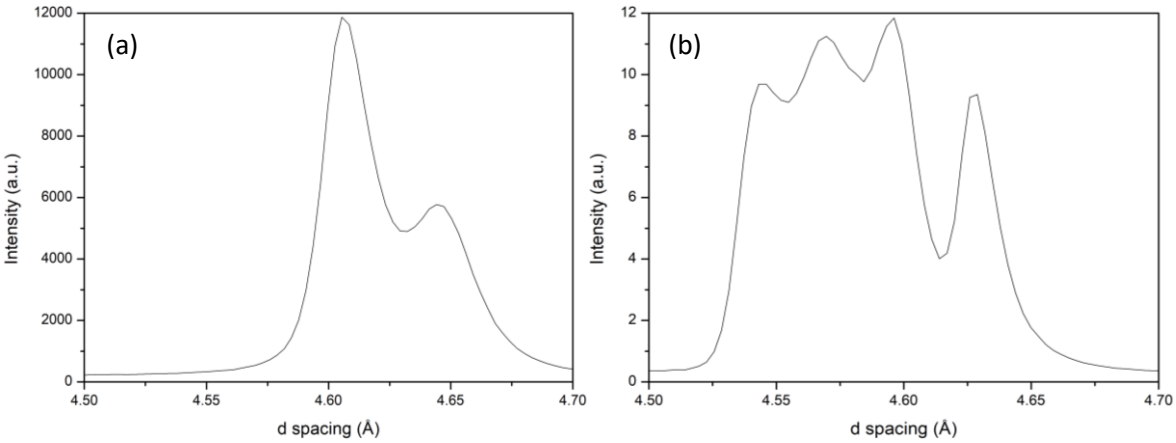

Figure 3.8: *Comparison of WISH PND data for (a) $Bi_{0.9}Na_{0.1}Fe_{0.9}Nb_{0.1}O_3$ and (b) $BiFeO_3$ focusing on Antiferromagnetic Peak at approximately ~4.60 Å showing the satellite peaks present from the spin cycloid in $BiFeO_3$. The $BiFeO_3$ plot was reproduced from data provided by Dr Arnold.*

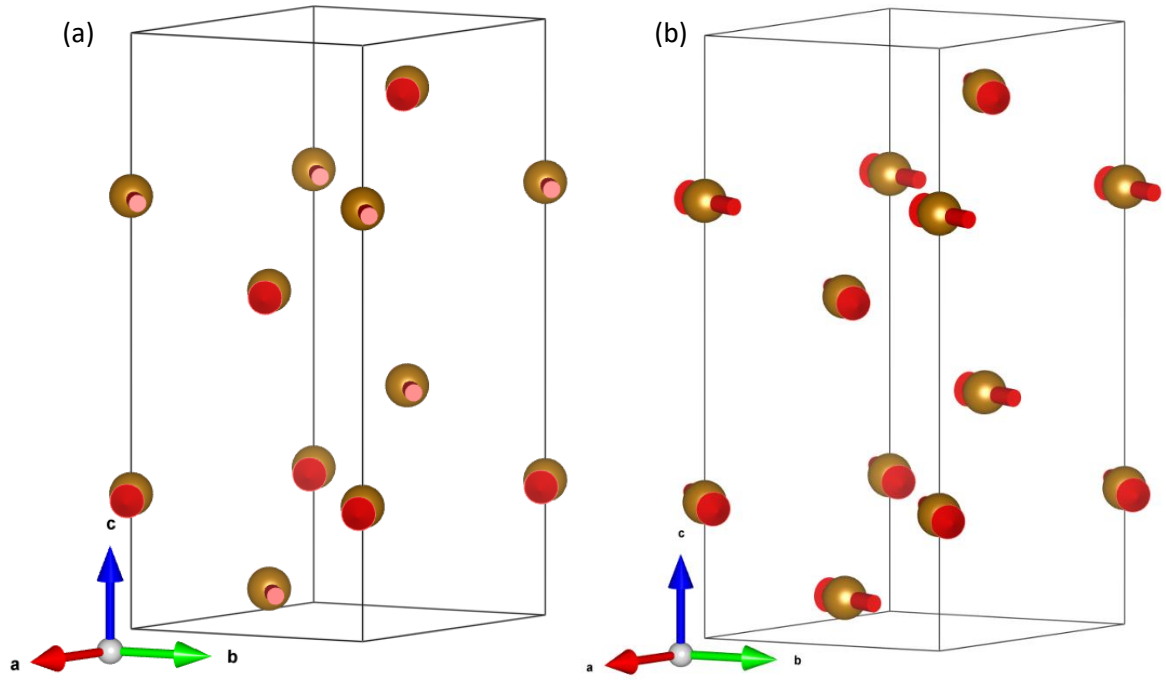

Figure 3.9: *Magnetic models for $Bi_{0.9}Na_{0.1}Fe_{0.9}Nb_{0.1}O_3$ from Rietveld refinement to R3c (a) spin canting model with k vector of (0,0,0), and (b) spin cycloid model with extra strain parameters.*

3.5 Low Temperature Characterisation

Low temperature XRD was performed using a Phenix on the Empyrean XRD to determine whether there were any phase transitions at low temperature. The result for NNO10% at 12 K can be seen in *figure 3.10*. The Rietveld refinement shows a good fit to the *R*3*c* model similar to the fit observed at room temperature. This seems to indicate that a phase change has not occurred. *Table 3.3* gives the lattice parameters and cell volume extracted from the Rietveld refinement which show an expected decrease from the room temperature values. Full refinement parameters for the 12 K refinement are given in *table A1.3 in appendix 1.* A collection of patterns across the temperature range from 12 K to 298 K can be seen in *figure 3.11*. Except for the shifting of peaks as the temperature decreases there does not seem to be any changes to peak shape which would suggest a change in the symmetry of the structure. In the lattice parameter and cell volume plots, *figure 3.12*, there appears to be a bump in the data at 90 K and 110 K which could be indicative of a subtle change of the structure or an anomaly in the data. Full refinement data and fits for the temperature range 30 K to 298 K can be found in appendix *table A1.3 and figure A1.7*.

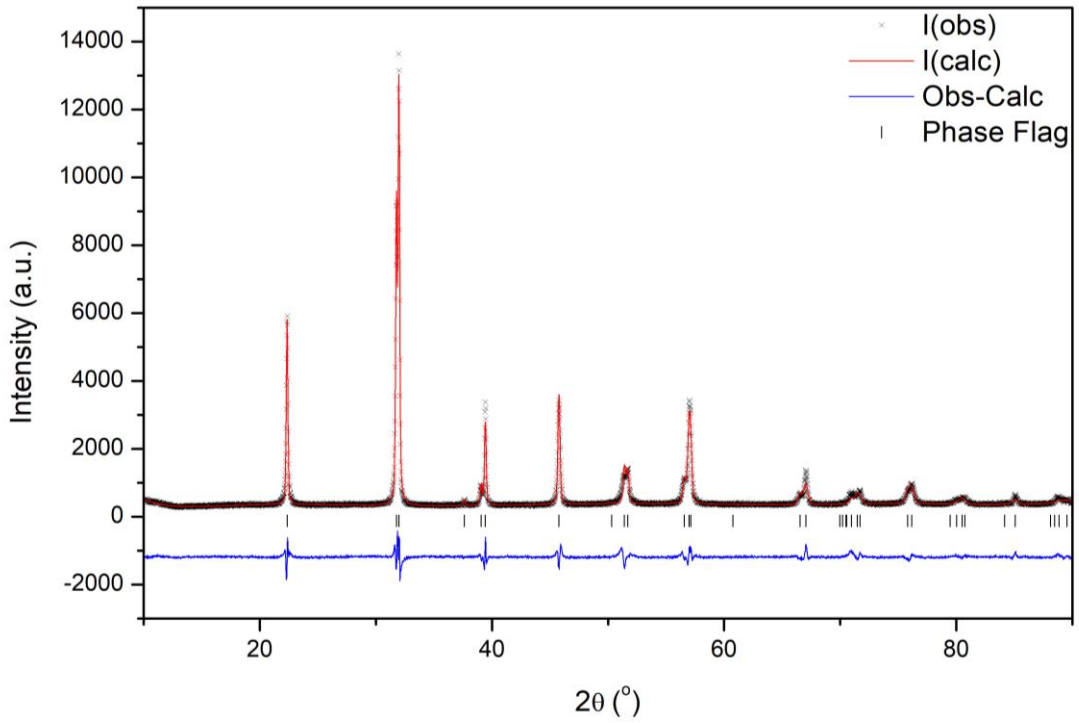

Figure 3.10: *Rietveld refinement of 12 K PXRD data collected for $Bi_{0.9}Na_{0.1}Fe_{0.9}Nb_{0.1}O_3$; $\chi^2 = 3.459$, $R_{wp} = 8.28\%$ and $R_p = 6.16$; the black crosses represent the observed intensity, the red line represents the calculated intensity from the model, the blue line represents the difference between the observed pattern and calculated pattern and the black tick marker represents the R3c model.*

Table 3.3: *Cell parameters and model fit statistics extracted from the Rietveld refinement of 12 K XRD data collected for $Bi_{0.9}Na_{0.1}Fe_{0.9}Nb_{0.1}O_3$ and fitted using the R3c model.*

Space Group	X^2	wRp	Rp	a (Å)	b (Å)	c (Å)	α (°)	β (°)	γ (°)	Cell Volume (Å^3)
R3c	3.459	8.28	6.16	5.56912(18)	5.58341(12)	13.7760(6)	90	90	120	370.020(23)

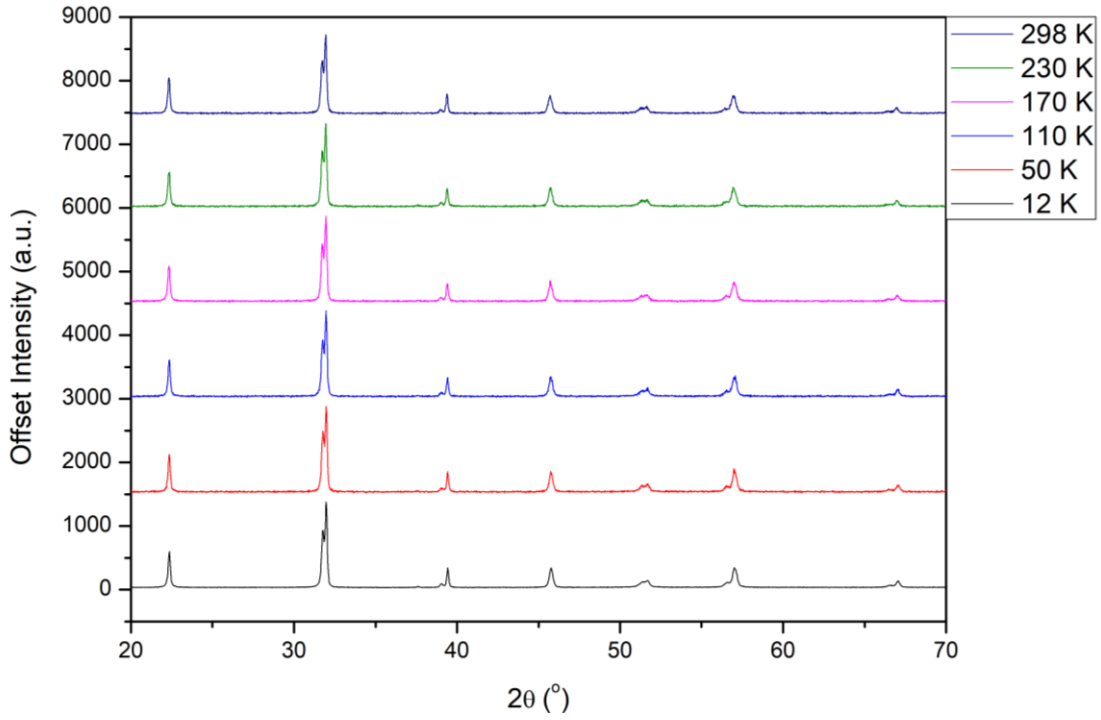

Figure 3.11: *Selection of patterns from LT PXRD collected $Bi_{0.9}Na_{0.1}Fe_{0.9}Nb_{0.1}O_3$. 12K pattern intensity has been scaled down to match the intensities of the other temperature points that were taken with shorter scan times. Data shifted for clarity.*

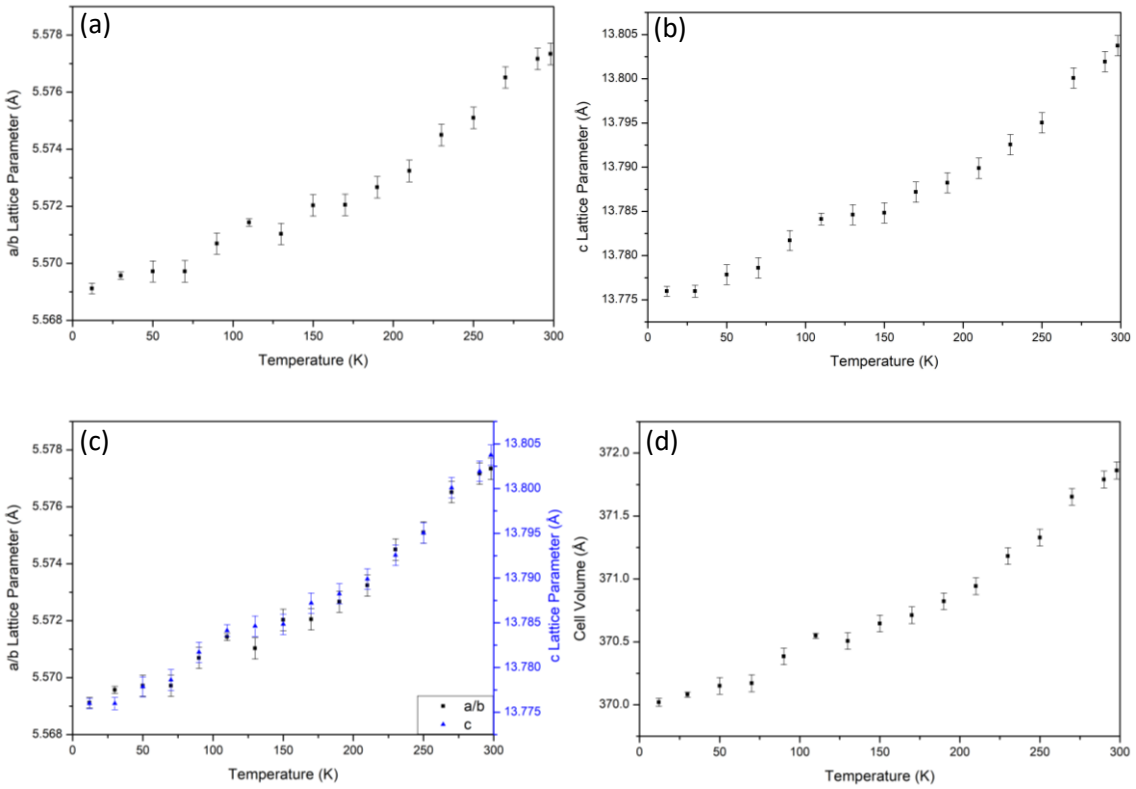

Figure 3.12: *Cell parameters extracted from the Rietveld refinement of LTXRD data collected for $Bi_{0.9}Na_{0.1}Fe_{0.9}Nb_{0.1}O_3$ (a) Lattice parameter a/b plot for temperatures between 12 K and 298 K, (b) Lattice parameter c plot for temperatures between 12 K and 298 K, (c) Lattice parameter a/b and c plot for temperatures between 12 K and 298 K, (d) Cell volume plot for temperatures between 12 K and 298 K.*

Data was also collected for the NNO10% sample at HRPD at 10 K to determine whether the model identified in the LTXRD was consistent with neutron data. The results shown in *figure 3.13* indicate that the nuclear structure is consistent with the previous diffraction findings. Full refinement parameters can be found in appendix *table A1.4*. The figure itself shows a Rietveld refinement fit to HRPD bank 1 data using an *R*3*c* model. The fit of the nuclear structure is missing peak intensity consistent with antiferromagnetic order in $BiFeO_3$, as supported by the SQUID data and room temperature WISH data discussed previously.

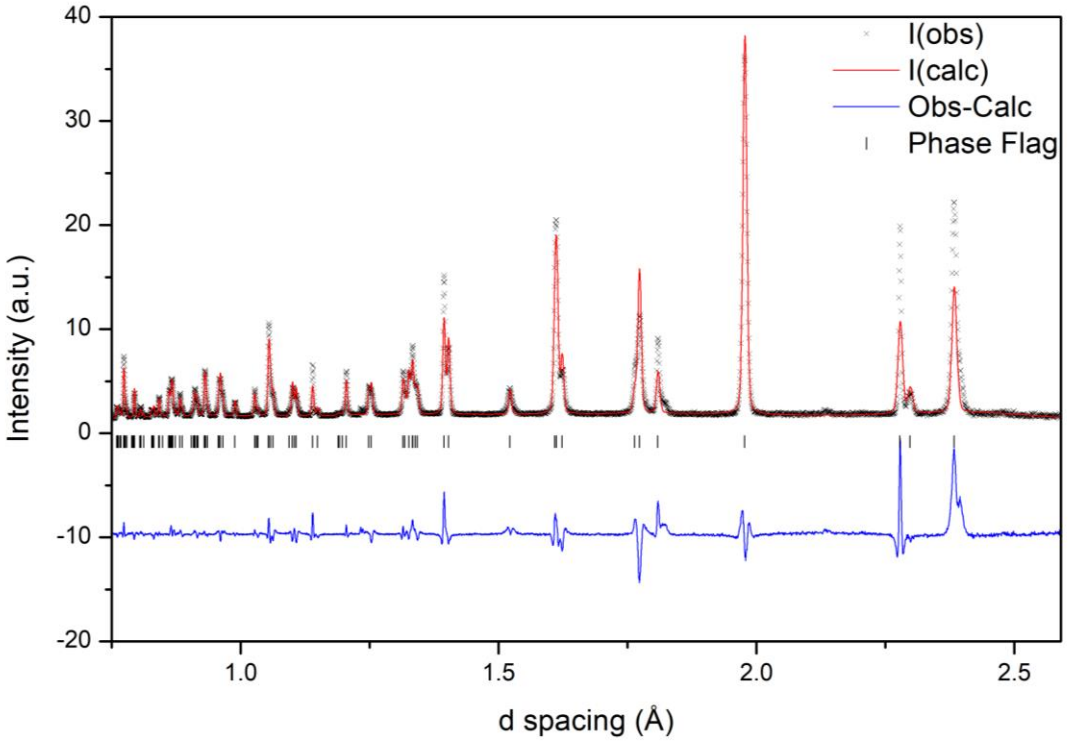

Figure 3.13: *Rietveld refinement of 10 K PND data collected for $Bi_{0.9}Na_{0.1}Fe_{0.9}Nb_{0.1}O_3$; χ^2 = 19.83, R_{wp} = 10.27% and R_p = 9.91; the black crosses represent the observed intensity, the red line represents the calculated intensity from the model, the blue line represents the difference between the observed pattern and calculated pattern and the black tick marker represents the R3c model.*

3.6 High Temperature Characterisation

Further work on HRPD was performed at high temperatures up to 1093 K to determine changes to the magnetic and nuclear structures. Shown in *figure 3.14* is the combined HRPD bank 3 PND from 4.45 Å to 4.7 Å of the NNO10% sample from 10 K to 623 K. This peak, as mentioned earlier, is a Bragg peak tied to the magnetic structure and as the temperature increases it gradually weakens as expected. Around 573 K the peak seems to be almost indistinguishable when compared to the background and at 598 K and above it cannot be distinguished from the background. This is consistent with the high temperature SQUID data and puts the Néel temperature between 573 K

and 598 K and is likely close to 580 K, 50 K less than undoped BFO[17]. Full refinement parameters and fits for the temperature range 293 K to 1093 K can be found in appendix *table A1.4 and figure A1.10*.

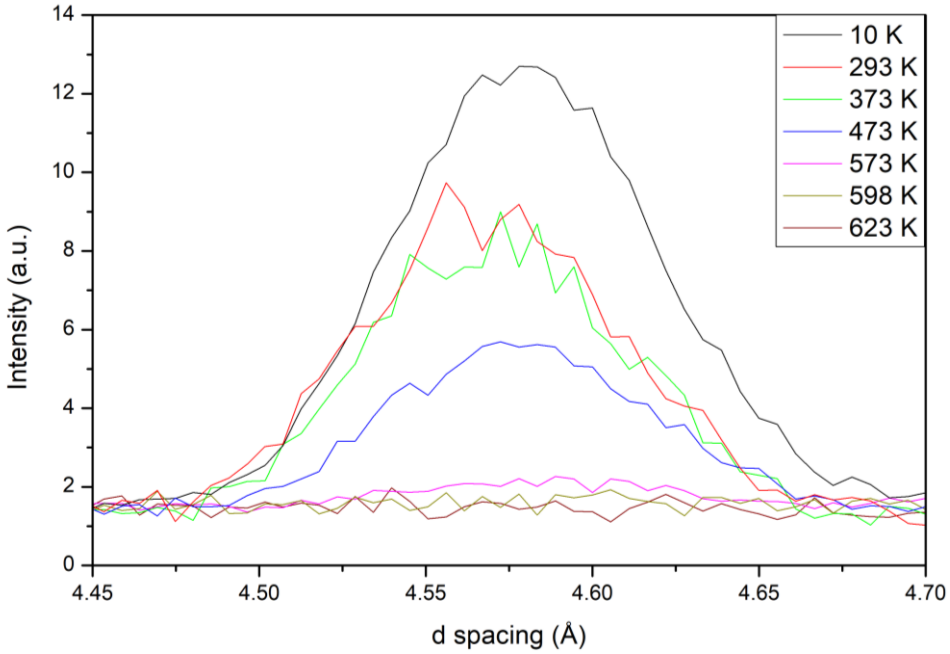

Figure 3.14: *VT HRPD Bank 3 PND data collected $Bi_{0.9}Na_{0.1}Fe_{0.9}Nb_{0.1}O_3$ focusing on the antiferromagnetic Peak in the d-spacing range 4.45 Å and 4.70 Å over a temperature range from 10 K to 623 K showing the gradual loss of the magnetic Bragg peak.*

The changes in the neutron diffraction pattern as the temperature is increased can be seen in *figure 3.15*. The structure does not appear to change until around 1023 K. *Figure 3.16* shows the Rietveld refinement of data collected at 873 K which shows a good fit to *R*3*c* symmetry. This is similar to the room temperature structure but without extra magnetic Bragg peaks. However to obtain this fit a broadening profile had to be used in GSAS (profile 4) with the S400, S004, S202 and eta terms applied which improved the fit significantly[18-22]. This behaviour is similar to that observed in undoped BFO under low pressure loadings from pressure dependent neutron diffraction data (PEARL, ISIS) and Raman mapping (using a diamond anvil cell) suggesting that NNO10% is chemically strained[16].

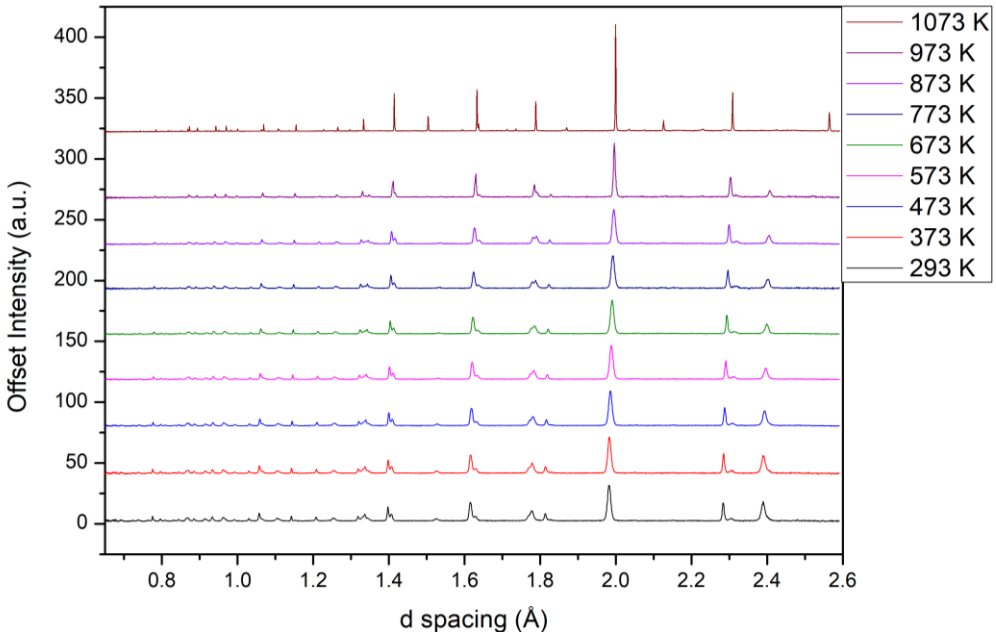

Figure 3.15: *Selection of patterns for the HT HRPD bank 1 PND data collected for $Bi_{0.9}Na_{0.1}Fe_{0.9}Nb_{0.1}O_3$ from 293 K to 1073 K. Data shifted for clarity.*

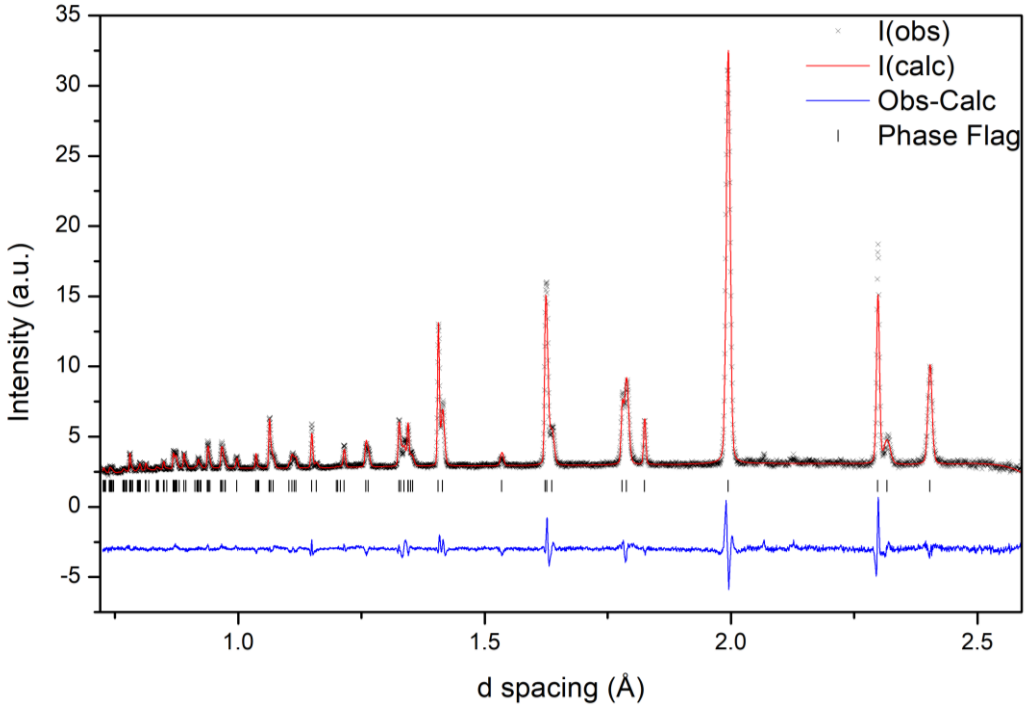

Figure 3.16: *Rietveld refinement of 873 K PND data collected for $Bi_{0.9}Na_{0.1}Fe_{0.9}Nb_{0.1}O_3$; $\chi^2 = 4.154$, $R_{wp} = 4.19\%$ and $R_p = 3.76$; the black crosses represent the observed intensity, the red line represents the calculated intensity from the model, the blue line represents the difference between the observed pattern and calculated pattern and the black tick marker represents the R3c model.*

From 1023 K a phase transition occurs which does not seem to match the published structure for undoped BFO above its ferroelectric curie temperature, the paraelectric orthorhombic *Pbnm* phase[6]. The change can especially be seen in the lattice parameter and cell volume plots in appendix *figure A1.11*. In the lattice parameter plots in appendix *figure A1.11 (a) and (b)* the *c* parameter decreased at 973 K and the *a/b* parameter increased at 1023 K, which may suggest 973 K is an

intermediate phase. This potentially indicates that the Curie temperature for NNO10% is approximately 60 K less than undoped BFO consistent with the decrease in the Néel temperature. For the pattern at 1073 K, which was a run as a long scan, the Rietveld fits to the *R*3*c* and *Pbnm* models can be seen in *figures 3.17 and 3.18* respectively. Neither of the models fit the data well with multiple peaks missed by the models. Unfortunately, it may be possible that at this temperature a mixed phase is present making it difficult to determine the new phase(s).

It seems unlikely that the sample has decomposed as the synthesis temperature was 1193 K. Though it cannot be ruled out that a combination of the phase change and the conditions in the neutron beam could have led to decomposition. In an attempt to determine the possibility of decomposition a comparison was made between the patterns taken at 1023 K and 1093 K as shown in *figure 3.19*. It can be observed that some of the new peaks that grow in with the new phase at 1.50 Å, 2.12 Å, and 2.56 Å *d*-spacing increase in intensity with increasing temperature. Additionally, the main perovskite peak observed at a *d*-spacing of ~1.99 Å seems to be weakening in intensity suggesting decomposition is occurring.

With the knowledge that some peaks present in the long scan data at 1073 K could be second phase impurity, the shorter scan data at 1023 K was also used to identify the new phase (as it appeared largely free from secondary phases). A variety of models were attempted and were found to not fit the data well, as shown in the appendix *figure A1.12*. The models include *Imma*, $P2_1ma$, *Pbam*, *Pbnm*, $R\bar{3}c$ and *P*4/*mbm*, all models suggested for doped BiFeO3 analogues and $NaNbO_3$[6,23-28]. The *Imma* model was one of the phases suspected to be the BFO γ-phase in the literature so was a possibility as the β-phase *Pbnm* did not fit[6,23]. Furthermore the *Pbam* model was based on a high temperature phase seen in rare earth doping of BFO as the model produced peaks not seen in the model[24]. The $R\bar{3}c$ model was based on a high temperature phase when doping BFO with manganese, however, this model would not fit as it was unstable and would not converge[25]. The $P2_1ma$ model was selected due to the possibility of observing a similar phase transition to that seen in NNO at low temperature from *R*3*c*[26,27]. Finally *P*4/*mbm* was selected for a similar reason as it is a high temperature transition seen in NNO but this model produced peaks not seen in the model[28].

The best Rietveld fit was observed for the tetragonal *P*4*mm* model or in the nonpolar *P*4/*mmm* structure as shown in *figure 3.20*. Despite the good fit to the data, there appears to be extra unfit peaks which may be satellite peaks suggesting a lowering of symmetry and formation of a superstructure (attempts to solve this have proved unsuccessful). Alternatively, we cannot rule out that these are second phase impurity peaks or that the material is mixed phase. To determine this new phase, a new high temperature HRPD experiment is required where a smaller incremental

increase in temperature can be made to monitor the phase progression and higher statistic data can be collected at the right temperatures to help determine the new phase.

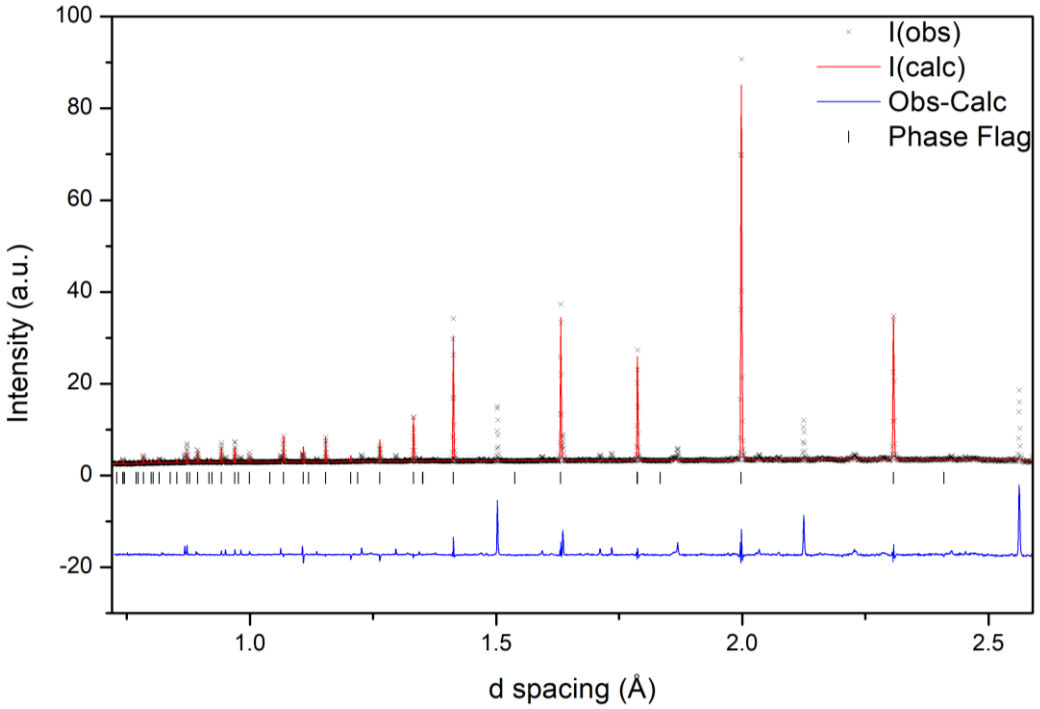

Figure 3.17: *Rietveld of 1073 K PND data collected for $Bi_{0.9}Na_{0.1}Fe_{0.9}Nb_{0.1}O_3$; χ^2 = 18.37, R_{wp} = 8.77% and R_p = 5.49; the black crosses represent the observed intensity, the red line represents the calculated intensity from the model, the blue line represents the difference between the observed pattern and calculated pattern and the black tick marker represents the R3c model.*

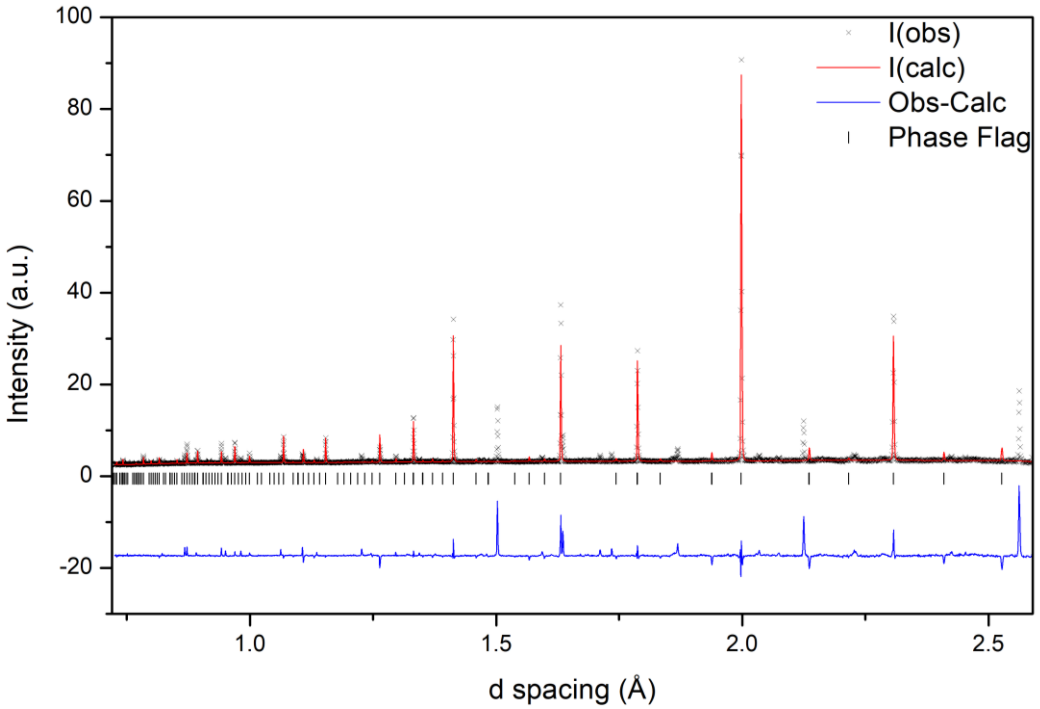

Figure 3.18: *Rietveld refinement of 1073 K PND data collected for $Bi_{0.9}Na_{0.1}Fe_{0.9}Nb_{0.1}O_3$; χ^2 = 21.17, R_{wp} = 9.42% and R_p = 6.18; the black crosses represent the observed intensity, the red line represents the calculated intensity from the model, the blue line represents the difference between the observed pattern and calculated pattern and the black tick marker represents the Pbnm model.*

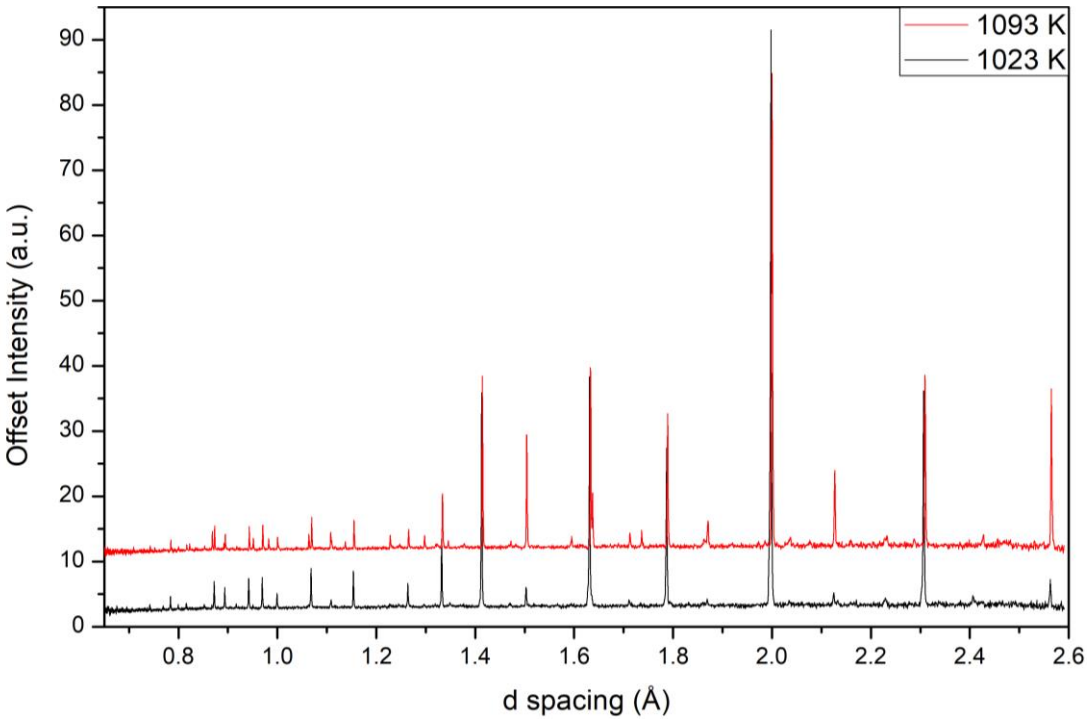

Figure 3.19: *Comparison of 1023 K and 1093 K HT HRPD bank 1 PND data collected for $Bi_{0.9}Na_{0.1}Fe_{0.9}Nb_{0.1}O_3$. Data offset for clarity.*

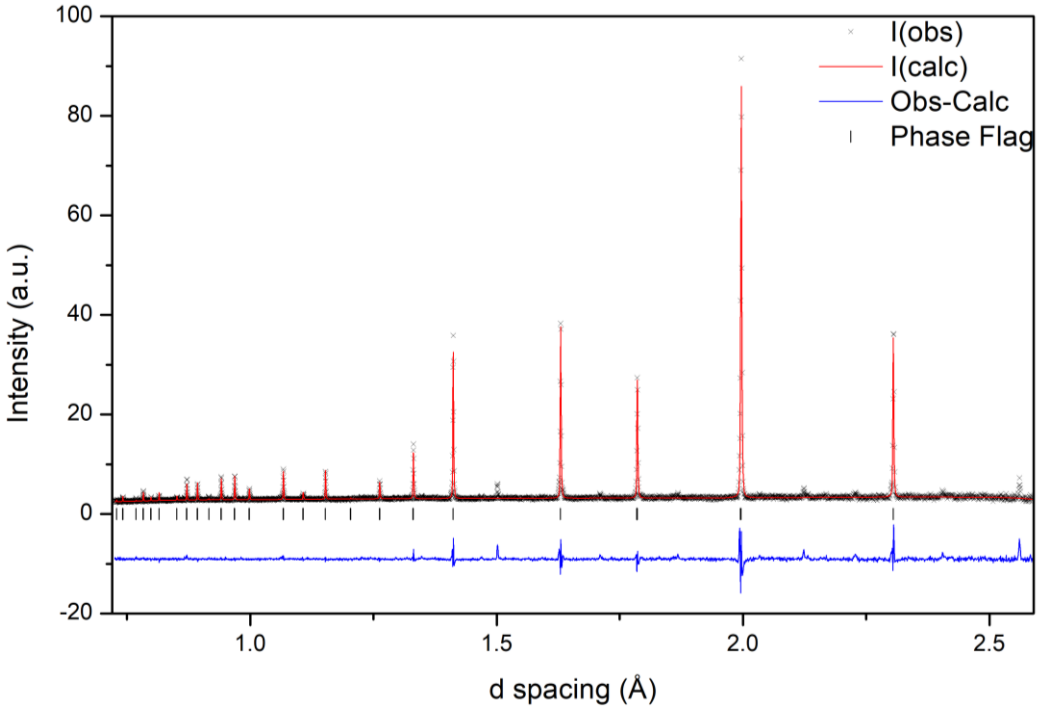

Figure 3.20: *Rietveld refinement of 1023 K PND data collected for $Bi_{0.9}Na_{0.1}Fe_{0.9}Nb_{0.1}O_3$; χ^2 = 2.441, R_{wp} = 6.38% and R_p = 5.83; the black crosses represent the observed intensity, the red line represents the calculated intensity from the model, the blue line represents the difference between the observed pattern and calculated pattern and the black tick marker represents the P4/mmm model.*

Thermogravimetric analysis (TGA) and differential scanning calorimetry (DSC) were used to determine whether it was possible to predict the Curie transition for the ferroelectric properties.

The measurements were performed using a nitrogen atmosphere with a 10 K ramp rate from 298 K to 1270 K.

The TGA/DSC results for NNO10% can be seen in *figure 3.21*. F*igure 3.21 (a)* shows the change in mass and energy required to increase the temperature of the sample. The mass does not seem to change to an obvious degree which would indicate that no intrinsic change to the sample is occurring. When using the derivative of the DSC as shown in *figure 3.21 (b)* a few noticeable peaks can be seen which could be indicative of changes in the sample. Whilst DSC can be subjective as it can be difficult to reliably pull out information, it would be reasonable to suggest there are 4 peaks at approximately 1113 K, 1158 K, 1203 K and 1253 K. $BiFeO_3$ has been shown to show 3 endotherms at approximately 1093 K, 1173 K and 1203 K[29]. The first of these is associated with the ferroelectric (*R*3*c*) to paraelectric phase transition (*Pbnm*). The second of these is linked to a combination of the β-γ phase transition and peritectic decomposition of BiFeO3 (into $Bi_2Fe_4O_9$ and Bi_2O_3) with Perejón *et al*[29] demonstrating that these two transitions overlap and are kinetically controlled. The final transition around 1203 K is the peritectic decomposition of $Bi_2Fe_4O_9$ into Fe_2O_3 and Bi_2O_3. Considering the data collected for NNO10% it can be suggested that the transitions at 1203 K and 1253 K respectively can be associated with the decomposition of NNO10% and $Bi_2Fe_4O_9$ or related phases respectively. This could be confirmed by collecting PXRD data from the TGA/DSC residue. The other two transitions are more difficult to analyse. Both peaks could be suggestive of phase transitions in the material (the first of which is at a similar temperature to that seen in the PND data), although it is impossible to say which of these, if any, can be associated with the ferroelectric – paraelectric transition. However, the first peak is very small and could easily be associated with noise. In this case this would suggest that the peak at 1158 K could be the ferroelectric-paraelectric phase transition which would suggest the structural phase transition discussed above must be associated with a ferroelectric-ferroelectric phase transition. Though it cannot be ruled out that this peak at 1158 K could be decomposition of the sample as it takes place at a similar temperature to the suspected decomposition seen in the powder neutron data. However, further work is required to confirm these suggestions.

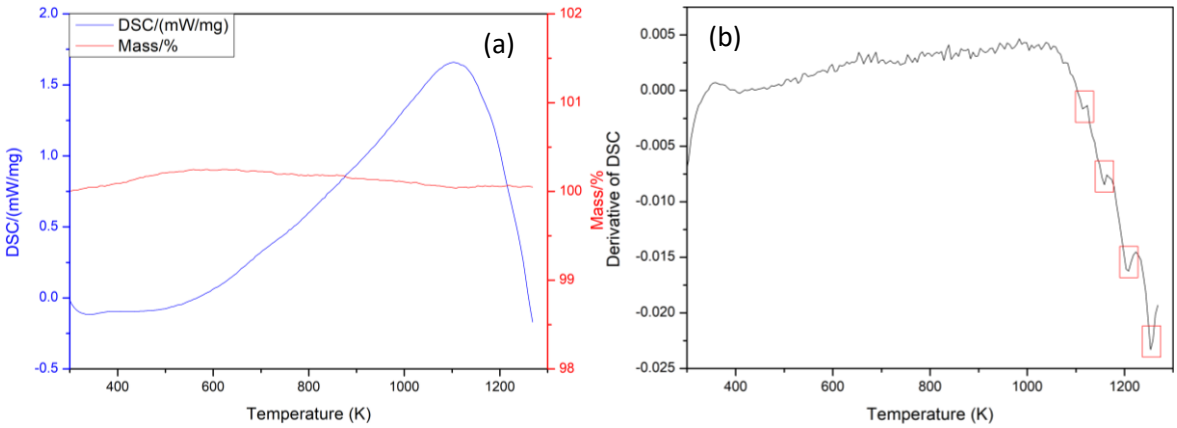

Figure 3.21: *TGA/DSC data for $Bi_{0.9}Na_{0.1}Fe_{0.9}Nb_{0.1}O_3$ (a) Full TGA/DSC plot from 298 K to 1270 K and (b) Derivative of DSC against temperature from 298 K to 1270 K.*

3.7 Room Temperature Raman Spectroscopy Analysis

Raman analysis of *R*3*c* materials can be used to provide information about polarisation direction and thus domain orientation[30]. In $BiFeO_3$ peaks at wavenumbers of approximately 120 cm^{-1} (assigned as a A_1 transverse optic mode) and 170 cm^{-1} (assigned as a A_1 longitudinal optic mode) are typically observed with the ratio between these two peaks indicative of the orientation of the polarisation[30,31]. Two different orientation and thus peak ratios are shown in *figure 3.22*. Raman mapping allows for the polarisation orientation/domains to be determined over a large area providing detailed domain mapping by plotting the peak ratio behaviour. A Raman map for undoped BFO can be seen in *figure 3.22 (c)* where the areas showing red or green correspond to spectra shown in *figure 3.22 (a) and (b)*. Here it can be seen that the grains are large and that each grain have large single domains. Additionally, characteristic striped domains are also present.

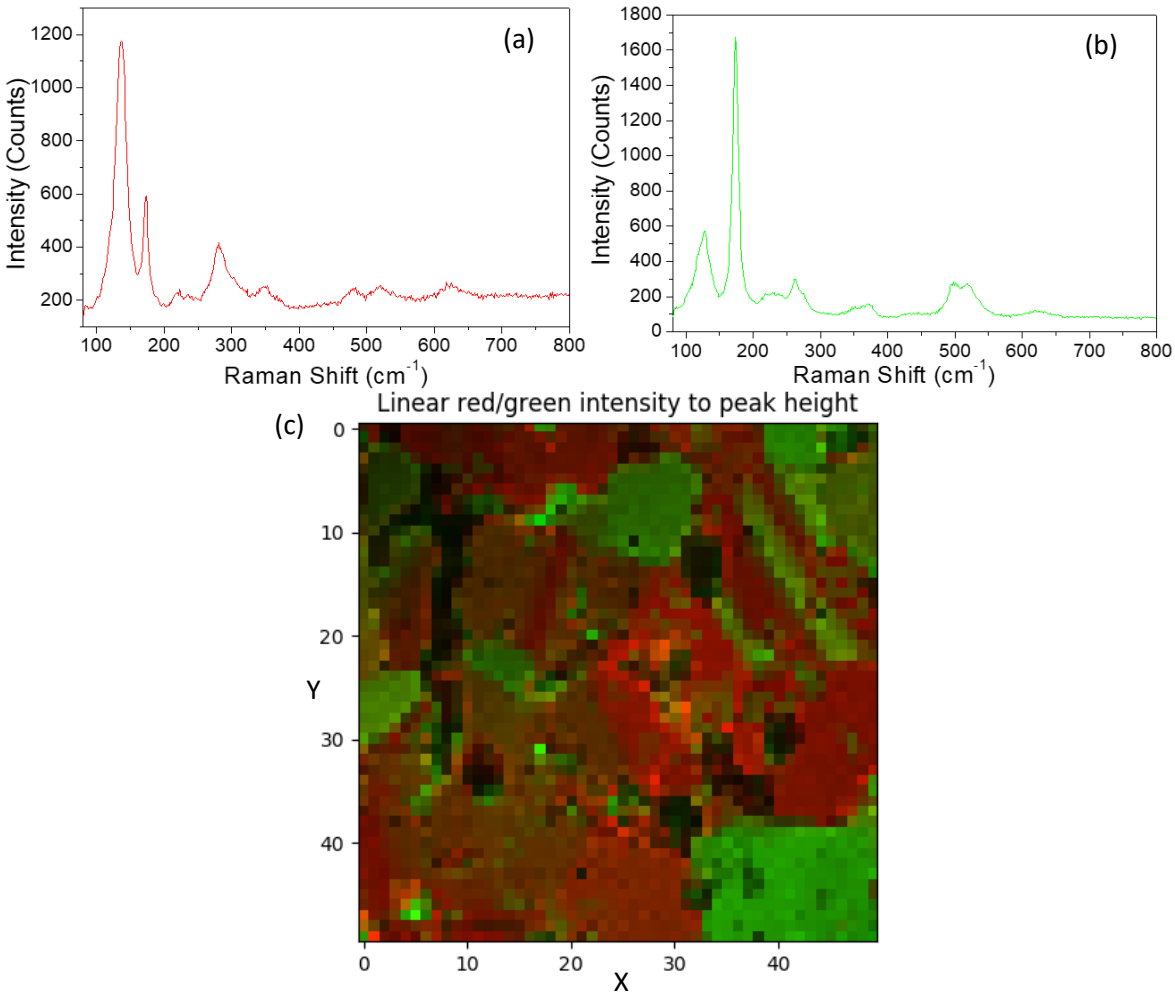

Figure 3.22: *(a) Raman spectrum of $BiFeO_3$ showing 'red' peak arrangement, (b) Raman spectrum of $BiFeO_3$ showing 'green' peak arrangement, (c) Raman map of $BiFeO_3$ showing the distribution of domains based on the orientation of the polarisation shown in parts (a) and (b). Data reproduced with permission of Dr Arnold.*

Raman mapping was performed for the NNO10% material. The intensity ratios were extracted from the collected data using MATLAB by Dr Tim Kinnear. A scaled intensity Raman map, of the ratio of red to green Raman spectra, for NNO10% can be seen in *figure 3.23*. It is clear from these data that the grains/domains appear to be much smaller in size (of the order of nm) compared to undoped BFO. This is not unexpected as doping with NNO has been found to decrease particle size and domains in the literature[9,32]. The Raman map in *figure 3.23 (b)* shows a R^2 distribution of the spread of domain structures. The histogram in appendix *figure A1.13* shows that there are a clear distribution of peak intensity ratios, making it difficult to model the data. A selection of spectra from the Raman map can be seen in appendix *figure A1.14*. The broad peaks in these spectra are indicative of doped BFO due to the mixed cations on the *A* and *B* sites. The small and uniform size of grains/domains coupled with the long spin cycloid means the cycloid is likely to be truncated by a domain wall/grain boundary before spatially averaging to zero. This would result in the observation of a net magnetic moment potentially leading to the magnetic hysteresis observed in SQUID magnetometry data.

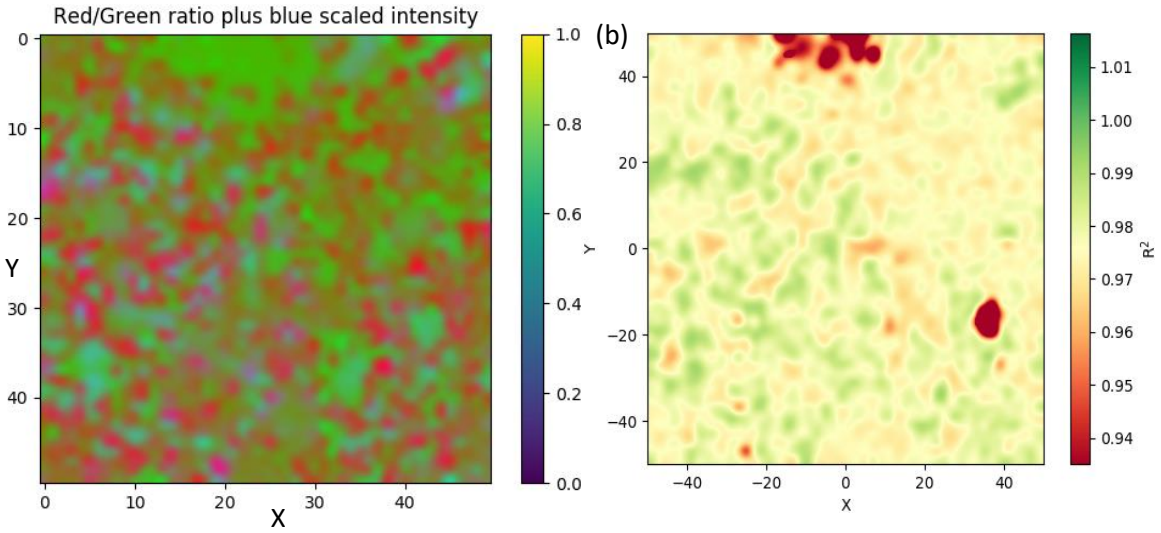

Figure 3.23: *Raman maps collected and processed for $Bi_{0.9}Na_{0.1}Fe_{0.9}Nb_{0.1}O_3$. (a) Scaled 'red' and 'green' peak intensity and (b) R^2 distribution of 'red' and 'green' peak.*

3.8 Scanning Electron Microscopy – Electron Dispersive X-Ray Analysis

Scanning electron microscopy (SEM) and electron dispersive X-Ray analysis (EDX) was used to examine the grain sizes and homogeneity of the surface of NNO10%. The surface of the NNO10% can be seen in *figure 3.24 (a)* at x10000 magnification under secondary electron imaging. It can be seen in a hole of the pellet, in the top left, that the grains appear small agreeing with the results found from the Raman mapping data. Mapping of the full image area using EDX (*figure 3.24 (b)*) demonstrated a largely homogenous distribution of Bi, Fe and Nb ions (Na and O were not included as they cannot reliably be detected due to their low atomic weight). However, there is some evidence of clustering of Fe and Nb present in areas although it cannot be ruled out that this arises as a result of surface disruption caused by the mechanical polishing of the pellet for analysis. Mapping over larger areas would be required to understand the role of clustering.

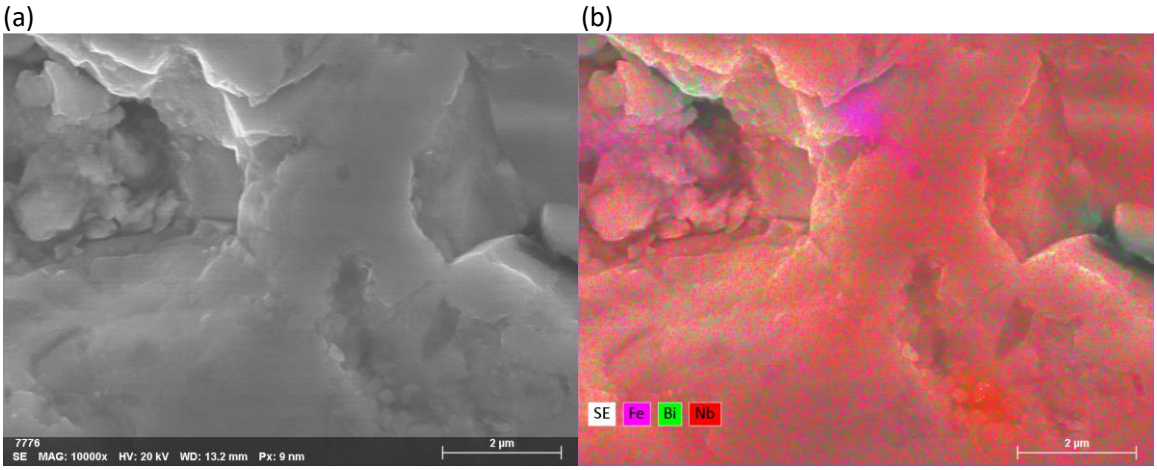

Figure 3.24: *Scanning Electron microscopy images collected for a polished $Bi_{0.9}Na_{0.1}Fe_{0.9}Nb_{0.1}O_3$ pellet. (a) Secondary electron image and (b) Electron Dispersive X-Ray Analysis map.*

3.9 Electrical Characterisation

As it seemed likely that the NNO10% sample was ferroelectric the electric characteristics of the sample were measured using a PE setup consisting of an aixacct easycheck 300 and Trek 610E voltage amplifier. Measurements were performed at room temperature using silver conductive paint as the electrode with varying amplitude and frequency.

The result for NNO10% can be seen in *figure 3.25*. The PE loop was obtained by synthesising a pellet with the addition of a binder PVB and TiO_2 inspired by Mandal *et al*[33]. The pellet was then pressed using a uniaxial press and sintered at 1193 K. The pellet was hand polished and coated with silver conductive paint. The result seems to indicate that the material is a '*lossy*' dielectric, a behaviour also seen for undoped BFO. This typically arises as a result of defects in the structure such as oxygen vacancies stemming from bismuth volatility. Unfortunately the hysteresis loop does not fully saturate but it does possess enough shape to avoid the '*banana*' label[34] suggesting that the material may be ferroelectric. The density of the pellet used here was found to be over 90%, with a calculated density of 91%, so density may not be a root cause of the behaviour observed. The measurements were made using silver paste as electrodes. Is it is not uncommon to get 'lossy' behaviour as a result of interfacial effects between the electrode and the pellet. Using a sputtered electrode such as gold or platinum may lead to improved loop characteristics.

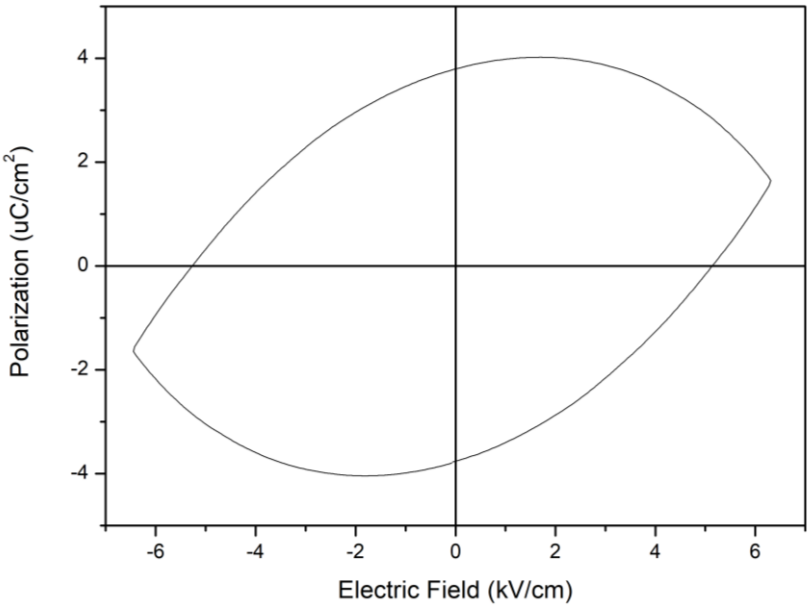

Figure 3.25: *PE loop data collected for $Bi_{0.9}Na_{0.1}Fe_{0.9}Nb_{0.1}O_3$, material modified with 2% PVB binder and 0.2% TiO_2 Frequency: 10 Hz and Amplitude: 800 V.*

3.10 Replacing Niobium with Tantalum on the *B*-Site

Two additional samples were synthesised using the same synthesis procedure, $Bi_{0.9}Na_{0.1}Fe_{0.9}Ta_{0.1}O_3$ and $Bi_{0.9}K_{0.1}Fe_{0.9}Ta_{0.1}O_3$, to assess if these materials would have similar properties to the niobium counterparts as there is very limited literature in this area. The sample $Bi_{0.9}Na_{0.1}Fe_{0.9}Ta_{0.1}O_3$ (referred to as NTO10%) was found to exhibit *R*3*c* symmetry as shown by *figure 3.26*. The Rietveld refinement of the XRD pattern to an *R*3*c* model shows good agreement. Full refinement parameters can be found in appendix *table A1.1*. Interestingly, the lattice parameters and cell volume of NTO10% show a small decrease compared to NNO10% which indicates that Ta^{5+} is leading to contraction of the unit cell. Unfortunately, despite the successful synthesis of single phase NNO10% it seems a small amount of secondary phase can be found in this sample that could not be removed through leaching. Despite this secondary phase the peaks appear sharp consistent with the NNO10% sample.

The $Bi_{0.9}K_{0.1}Fe_{0.9}Ta_{0.1}O_3$ (referred to as KTO10%) was also found to adopt *R*3*c* symmetry. However, as can be seen in *figure 3.27*, the secondary phase is found to be present to a much larger degree. The Rietveld fit to *R*3*c* seems to indicate a good degree of agreement despite this. Full refinement parameters can be found in appendix *table A1.1*. Similarly to NTO10%, KTO10% shows a decrease in the lattice parameters and cell volume when compared to the *R*3*c* phase of KNO10%, which seems to suggest that replacing Nb^{5+} with Ta^{5+} on the *B*-site leads to a contraction in the unit cell

size. The large amount of impurity seems to indicate that there is a problem with the synthesis of this sample and thus phase identification may not be accurate.

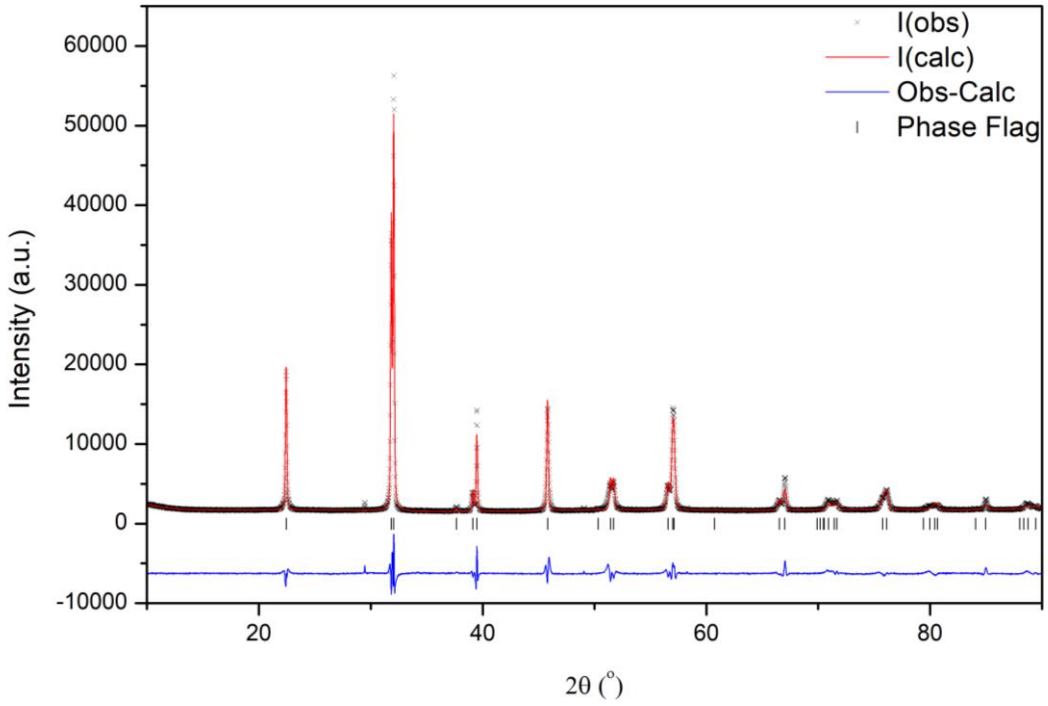

Figure 3.26: *Rietveld refinement of room temperature PXRD data collected for $Bi_{0.9}Na_{0.1}Fe_{0.9}Ta_{0.1}O_3$; χ^2 = 10.66, R_{wp} = 6.97% and R_p = 4.57; the black crosses represent the observed intensity, the red line represents the calculated intensity from the model, the blue line represents the difference between the observed pattern and calculated pattern and the black tick marker represents the R3c model.*

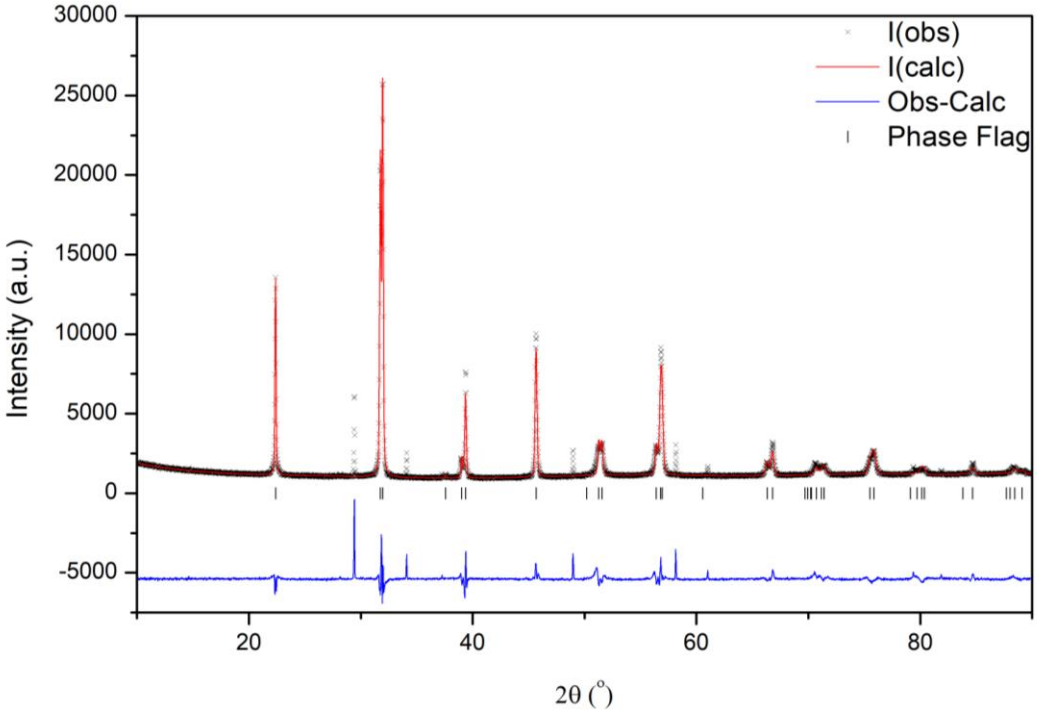

Figure 3.27: *Rietveld refinement of room temperature PXRD data collected for $Bi_{0.9}K_{0.1}Fe_{0.9}Ta_{0.1}O_3$; χ^2 = 10.60, R_{wp} = 8.59% and R_p = 4.91; the black crosses represent the observed intensity, the red line represents the calculated intensity from the model, the blue line represents the difference between the observed pattern and calculated pattern and the black tick marker represents the R3c model.*

One of the most interesting aspects of NNO10% was its improved magnetic properties compared with undoped BFO. NTO10% and KTO10% were both run on the SQUID to determine whether the same improvements could be seen. In *figure 3.28 (a)* are the magnetic hysteresis loops for NTO10% at 2 K and 300 K. They show similar behaviour to that seen in the NNO10% with increased coercive field. The biggest difference, however, is the presence of '*pinching*' in the centre of the loop that is indicative of an antiferromagnetic impurity which lines up with the PXRD data. It can be suggested that without the impurity this sample, NTO10%, would display similar magnetic behaviour to that seen in NNO10% and as a result it may have a similar magnetic structure.

The KTO10% sample shows similar behaviour to the KNO10%. As can be seen in *figure 3.28 (b)*, the hysteresis loops for KTO10%, at 2 K and 300 K, do not have the same shape as seen previously for NNO10% and NTO10%. A '*pinching*' effect can also be seen in the 2 K loop due to antiferromagnetic impurity present. The 300 K loop does display a small coercive field without this '*pinching*'. However, due to the amount of impurity present and the sensitivity of the SQUID it may not be representative of the bulk sample. Additionally multiple contributions from materials with different transition temperatures further complicate the comparison of data. It would usually be expected that the 2 K loop would have a larger coercive field, however, if this behaviour is impurity related it could be due to α-Fe_2O_3. Below 273 K α-Fe_2O_3 transitions from a canted antiferromagnet to a pure antiferromagnet, this is called the Morin transition[11,35]. This may explain the change in magnetism for KTO10%.

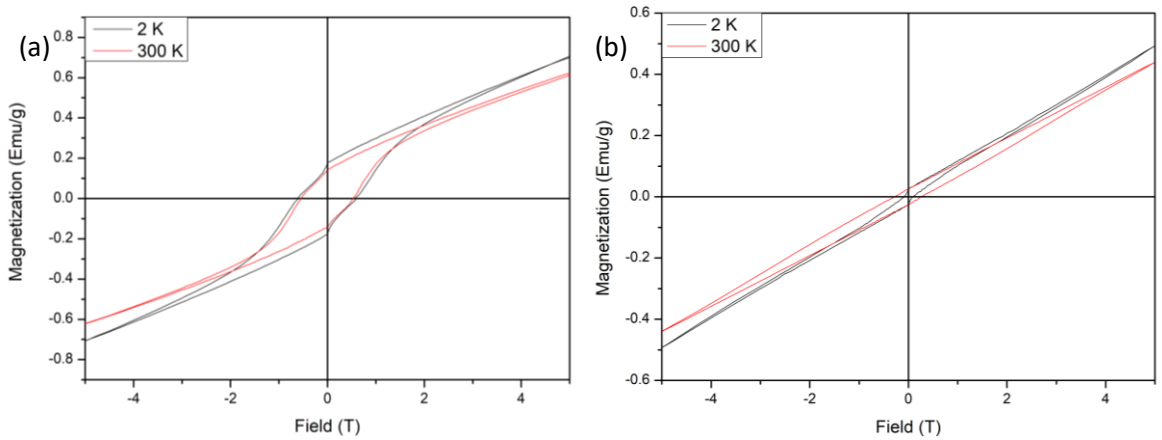

Figure 3.28: *Magnetic Hysteresis loops from SQUID data collected at temperatures of 2 K to 300 K and at fields from -5 T to 5 T for (a) $Bi_{0.9}Na_{0.1}Fe_{0.9}Ta_{0.1}O_3$ and (b) $Bi_{0.9}K_{0.1}Fe_{0.9}Ta_{0.1}O_3$.*

3.11 Conclusions

This chapter reports that it was possible to successfully synthesis BFO doped with NNO and KNO at *x* =0.1. The NNO10% material was found to crystallise in the BFO parent space group *R*3*c* through the use of X-ray and neutron diffraction techniques. Low temperature diffraction found no changes to the nuclear structure at low temperatures but a phase transition was observed above 1023 K. The observed phase transition seems to be different from the transition seen in undoped BFO and despite multiple attempts the symmetry of the high temperature phase remains unknown. TGA-DSC analysis showed a possible series of high temperature changes which suggest more than one phase change may be present explaining the complexity of the high temperature neutron data. KNO10%, however, was found to be in a mixed phase of mostly *P*4*mm* with a small amount of *R*3*c*, a different result to what was previously reported.

In terms of property measurements NNO10% was found to have improved magnetic properties when compared to undoped BFO (switchable magnetic character) with a reduction of the Néel temperature observed. Room temperature neutron analysis using WISH found that the magnetic structure deviated from undoped BFO. Further probing of the data found that it was likely that the magnetism was close to a *k* vector of (0,0,0) with a δ = 0.0007953 though a refined model of the BFO spin cycloid fit better. We were unable to rule out the possibility that a spin canting model with a *k* vector of (0,0,0). However, it was noted that a more sensible magnetic moment (3.274 μ_B for Fe^{3+}) was observed for the fit using the spin cycloid. An issue which plagued neutron refinements was the possible presence of strain which was supported by the fact that Raman and SEM analysis showed small grains and domains. It can therefore be suggested that the spin cycloid is truncated within the small domains resulting in switchable magnetic behaviour. It was found to be difficult to measure the possible ferroelectric properties due to conductive and '*lossy*' dielectric behaviour. Despite the improvements seen in NNO10%, KNO10% did not show the same results. The magnetism for KNO10% was more in line with undoped BFO. This suggests that the interplay between the Na and Bi on the *A*-site is the origin of the magnetic behaviour seen here.

Two other samples were synthesised during this investigation NTO10% and KTO10%, to determine whether similar behaviour would be seen to the niobium counterparts. Unfortunately, both samples suffered from impurity issues to different degrees which indicates an altered synthesis may be required to specifically prepare these materials. The results obtained for NTO10% seem to indicate it may have similar properties to the niobium NNO10% derivative. It was also found to crystallise in the BFO parent *R*3*c* space group using room temperature PXRD. In addition it was also found to display similar magnetic behaviour to the NNO10% sample which may indicate a similar

magnetic structure. Unfortunately, the results for KTO10% are less clear due to the large amount of impurity present which leads to ambiguous magnetic data. The PXRD data seems to indicate a change has occurred due to changes in lattice parameter but the presence of impurity suggests that a full reaction has not occurred.

3.12 References

1 Y. Ma and X. Chen, *J. Appl. Phys.,* 2009, **105**, 054107 (DOI:10.1063/1.3081648).

2 P. Teslenko, A. Razumnaya, V. Ponomarenko, A. Rudskaya, A. Nazarenko, A. Anokhin, M. Avramenko, D. Levshov, M. Kupriyanov and Y. Yuzyuk, *Phys. Solid State,* 2014, **56**, 1866-1871 (DOI:10.1134/S1063783414090285).

3 Y. Saad, I. Álvarez-Serrano, M. L. López and M. Hidouri, *Ceram. Int.,* 2018, **44**, 18560-18570 (DOI:https://doi.org/10.1016/j.ceramint.2018.07.078).

4 M. De, S. Hajra, R. Tiwari, S. Sahoo, R. N. P. Choudhary and H. S. Tewari, *Ceram. Int.,* 2018, **44**, 11792-11797 (DOI:https://doi.org/10.1016/j.ceramint.2018.03.263).

5 I. Levin, M. G. Tucker, H. Wu, V. Provenzano, C. L. Dennis, S. Karimi, T. Comyn, T. Stevenson, R. I. Smith and I. M. Reaney, *Chem. Mater.,* 2011, **23**, 2166-2175 (DOI:10.1021/cm1036925).

6 D. C. Arnold, K. S. Knight, F. Morrison and P. Lightfoot, *Phys. Rev. Lett.,* 2009, **102**, 027602 (DOI:10.1103/PhysRevLett.102.027602).

7 I. P. Raevski, S. P. Kubrin, J. -. Dellis, S. I. Raevskaya, D. A. Sarychev, V. G. Smotrakov, V. V. Eremkin and M. A. Seredkina, *Ferroelectrics,* 2008, **371**, 113-118 (DOI:10.1080/00150190802397767).

8 S. Dash, R. Padhee, P. Das and R. Choudhary, *J Mater Sci: Mater Electron,* 2013, **24**, 3315-3323 (DOI:10.1007/s10854-013-1249-4).

9 R. P. Ummer, P. Sreekanth, B. Raneesh, R. Philip, D. Rouxel, S. Thomas and N. Kalarikkal, *RSC Adv.,* 2015, **5**, 67157-67164 (DOI:10.1039/c5ra10422j).

10 R. C. Lennox, D. D. Taylor, L. J. Vera Stimpson, G. B. G. Stenning, M. Jura, M. C. Price, E. E. Rodriguez and D. C. Arnold, *Dalton Trans.,* 2015, **44**, 10608-10613 (DOI:10.1039/c5dt00140d).

11 F. J. Morin, *Phys. Rev.,* 1950, **78**, 819-820 (DOI:10.1103/PhysRev.78.819.2).

12 G. Catalan and J. F. Scott, *Adv Mater,* 2009, **21**, 2463-2485 (DOI:10.1002/adma.200802849).

13 J. Rodríguez-Carvajal, *Physica B Condens. Matter,* 1993, **192**, 55-69 (DOI:doi.org/10.1016/0921-4526(93)90108-I).

14 I. Sosnowska, W. Schäfer, W. Kockelmann, K. H. Andersen and I. O. Troyanchuk, *Appl. Phys. A,* 2002, **74**, s1040-s1042 (DOI:10.1007/s003390201604).

15 R. D. Johnson, P. A. McClarty, D. D. Khalyavin, P. Manuel, P. Svedlindh and C. S. Knee, *Phys. Rev. B,* 2017, **95**, 054420 (DOI:10.1103/PhysRevB.95.054420).

16 D. C. Arnold, T. Kinnear, C. J. Ridley and C. L. Bull, *Unpublished Data,* 2020, .

17 G. A. Smolenskii and V. M. Yudin, *Sov. Phys. Sol. St.,* 1965, **6**, 2936-2942.

18 C. J. Howard, *J. Appl. Crystallogr.,* 1982, **15**, 615-620 (DOI:10.1107/S0021889882012783).

19 B. van Laar and W. B. Yelon, *J. Appl. Crystallogr.,* 1984, **17**, 47-54 (DOI:10.1107/S0021889884011006).

20 P. Thompson, D. E. Cox and J. B. Hastings, *J. Appl. Crystallogr.,* 1987, **20**, 79-83 (DOI:10.1107/S0021889887087090).

21 L. W. Finger, D. E. Cox and A. P. Jephcoat, *J. Appl. Crystallogr.,* 1994, **27**, 892-900 (DOI:10.1107/S0021889894004218).

22 P. W. Stephens, *J. Appl. Crystallogr.,* 1999, **32**, 281-289 (DOI:10.1107/S0021889898006001).

23 D. C. Arnold, K. S. Knight, G. Catalan, S. Redfern, J. Scott, P. Lightfoot and F. Morrison, *Adv. Funct. Mater.,* 2010, **20**, 2116-2123 (DOI:10.1002/adfm.201000118).

24 I. O. Troyanchuk, D. V. Karpinsky, M. V. Bushinsky, V. A. Khomchenko, G. N. Kakazei, J. P. Araujo, M. Tovar, V. Sikolenko, V. Efimov and A. L. Kholkin, *Phys. Rev. B,* 2011, **83**, 054109 (DOI:10.1103/PhysRevB.83.054109).

25 A. S. Gibbs, D. C. Arnold, K. S. Knight and P. Lightfoot, *Phys. Rev. B,* 2013, **87**, 224109 (DOI:10.1103/PhysRevB.87.224109).

26 S. K. Mishra, N. Choudhury, S. L. Chaplot, P. S. R. Krishna and R. Mittal, *Phys. Rev. B,* 2007, **76**, 024110 (DOI:10.1103/PhysRevB.76.024110).

27 K. E. Johnston, C. C. Tang, J. E. Parker, K. S. Knight, P. Lightfoot and S. E. Ashbrook, *J. Am. Chem. Soc.,* 2010, **132**, 8732-8746 (DOI:10.1021/ja101860r).

28 S. K. Mishra, R. Mittal, V. Y. Pomjakushin and S. L. Chaplot, *Phys. Rev. B,* 2011, **83**, 134105 (DOI:10.1103/PhysRevB.83.134105).

29 A. Perejón, P. E. Sánchez-Jiménez, J. M. Criado and L. A. Pérez-Maqueda, *J. Phys. Chem. C,* 2014, **118**, 26387-26395 (DOI:10.1021/jp507831j).

30 J. Hlinka, J. Pokorny, S. Karimi and I. M. Reaney, *Phys. Rev. B,* 2011, **83**, 020101 (DOI:10.1103/PhysRevB.83.020101).

31 R. C. Lennox, M. C. Price, W. Jamieson, M. Jura, A. Daoud-Aladine, C. A. Murray, C. Tang and D. C. Arnold, *J. Mater. Chem. C,* 2014, **2**, 3345-3360 (DOI:10.1039/c3tc32345e).

32 H. Qi, A. Xie, A. Tian and R. Zuo, *Adv. Energy Mater.,* 2020, **10**, 1903338 (DOI:10.1002/aenm.201903338).

33 P. Mandal, M. J. Pitcher, J. Alaria, H. Niu, P. Borisov, P. Stamenov, J. B. Claridge and M. J. Rosseinsky, *Nature,* 2015, **525**, 363-366 (DOI:10.1038/nature14881).

34 J. Scott, *J. Phys. Condens. Matter,* 2007, **20**, 021001 (DOI:10.1088/0953-8984/20/02/021001).

35 C. G. Shull, W. A. Strauser and E. O. Wollan, *Phys. Rev.,* 1951, **83**, 333-345 (DOI:10.1103/PhysRev.83.333).

Chapter Four: Investigation of Bi*A*FeNbO$_6$ (*A* = Na, K) materials

4.1 Introduction

Due to its theoretical composition $Bi_{0.5}Na_{0.5}Fe_{0.5}Nb_{0.5}O_3$, with an equal number of cations on the *A*- and *B*-sites which exhibit similar atomic radii, was seen as a possible candidate for cation ordering. In this chapter the structure and properties of $BiNaFeNbO_6$, $BiKFeNbO_6$ and $BiNa_{0.5}K_{0.5}FeNbO_6$ are discussed. In particular, it is shown that $Bi_{0.5}Na_{0.5}Fe_{0.5}Nb_{0.5}O_3$ exhibits diffuse scattering in neutron powder diffraction, which is not seen in X-ray powder diffraction. Previously, the doubly ordered perovskite, $NaLaMgWO_6$, has been shown to exhibit satellite peaks in neutron powder diffraction which were not clearly evident in X-ray powder diffraction[1]. These, arose as a result of an incommensurate octahedral tilt modulation present due to cation order. However, in contrast, the diffuse scattering in $BiNaFeNbO_6$ was found to more likely be a consequence of short-range order of NNO rich regions rather than cation ordering.

4.2 Room Temperature Structural Characterisation

In this chapter $Bi_{0.5}Na_{0.5}Fe_{0.5}Nb_{0.5}O_3$ referred to as NNO50%, $Bi_{0.5}K_{0.5}Fe_{0.5}Nb_{0.5}O_3$ referred to as KNO50% and $Bi_{0.5}Na_{0.25}K_{0.25}Fe_{0.5}Nb_{0.5}O_3$ referred to as NKNO were prepared using a modified synthesis procedure (as described in Chapter Three). The results led to samples which were cleaner and seemingly more homogenous than the KNO samples previously reported by the Arnold group[2]. This chapter documents the structural, magnetic and electrical properties of the materials synthesised.

High resolution X-ray powder diffraction patterns were collected for these samples using a Malvern Panalytical Empyrean diffractometer. The refinement of the data was performed using the GSAS suite of programs[3,4].

A synthetic pathway consisting of solid state synthesis followed by a leaching process using nitric acid (as described in Chapter Two) led to phase pure materials as shown in *figure 4.1*. It can be seen in the powder patterns that the backgrounds are flat with no obvious impurity peaks present. The patterns themselves showed sharp peaks suggesting high crystallinity and a homogenous distribution of cations with the patterns consistent across all three materials suggesting no change in symmetry on doping. Furthermore, there is a peak shift from $Bi_{0.5}Na_{0.5}Fe_{0.5}Nb_{0.5}O_3$ to $Bi_{0.5}Na_{0.25}K_{0.25}Fe_{0.5}Nb_{0.5}O_3$ to $Bi_{0.5}K_{0.5}Fe_{0.5}Nb_{0.5}O_3$ consistent with increasing cation size. It is clear from comparison with the previous work by Lennox *et al*[2] that these data are consistent albeit with sharper peaks. However, the previous work on the bismuth ferrite – potassium niobate phase

diagram was plagued with homogeneity issues resulting in materials comprised of multiple phases (with similar lattice parameters) resulting in broadening of the diffraction peaks. This suggests the new synthesis method has led to a higher quality materials[2,5].

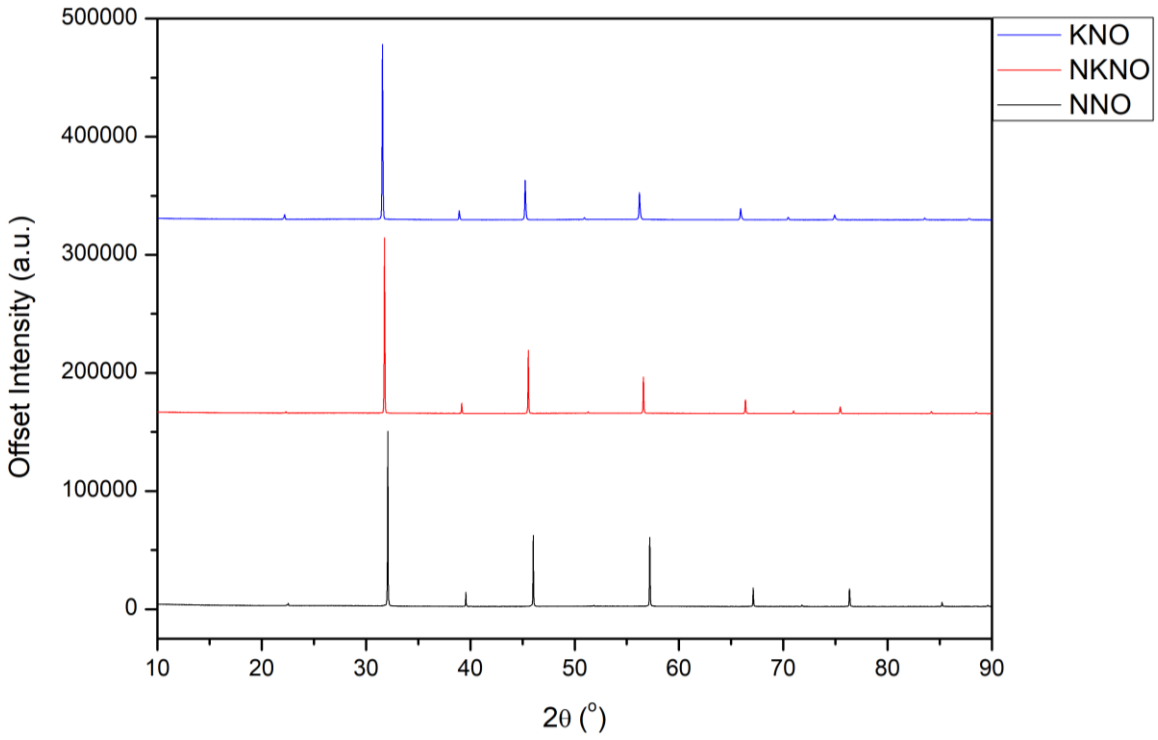

Figure 4.1: *Comparison plot of PXRD patterns of $Bi_{0.5}Na_{0.5}Fe_{0.5}Nb_{0.5}O_3$, $Bi_{0.5}K_{0.5}Fe_{0.5}Nb_{0.5}O_3$ and $Bi_{0.5}Na_{0.25}K_{0.25}Fe_{0.5}Nb_{0.5}O_3$.*

The Rietveld refinement for the NNO50% data was initially performed in the tetragonal *P*4*mm* space group (based on the previous work by Lennox *et al*[2] on $Bi_{0.5}K_{0.5}Fe_{0.5}Nb_{0.5}O_3$ and comparison of these data). A good agreement was found between the pattern and the model as shown in *figure 4.2*. *Tables 4.1* and *4.2* below give the structural parameters for the refinement. $Bi_{0.5}Na_{0.5}Fe_{0.5}Nb_{0.5}O_3$ has been previously described as cubic or pseudo-cubic in papers by Raevski *et al*[6] and Ma *et al*[7]. Unfortunately no space group is reported for these crystal systems and only Ma *et al*[7] showed the XRD pattern, which appears to be similar to those reported here. In contrast, Teslenko *et al*[8] reported an orthorhombic *Pbnm* structure, however, the XRD pattern was not included so a direct comparison could not be made with the data presented here. An orthorhombic structure was also reported by Dash *et al*[9] but no space group was reported. Instead a comparison was made to the BFO parent structure where it was identified that peak splitting seen in the *R*3*c* structure is lost on increasing BFO contents. The XRD data reported is consistent to the data shown here. Finally Saad *et al*[10] reported the NNO50% composition as a mixture between *R*3*c* and the NNO polar phase orthorhombic $P2_1ma$. A Rietveld refinement was used to reach this conclusion though the refinement itself was not presented in the paper or supplementary material, with only the fitting statistics given. The pattern presented does show differences to the work discussed here. It

can be seen that in the majority of cases the XRD patterns are similar despite the vast range of symmetries predicted but it is noted that only a single paper showed evidence of using Rietveld refinements to reach the conclusion presented but that the fit was then missing from the paper. When considering the data collected here the *Pbnm*, *R*3*c* and *P*2$_1$*ma* models can be ruled out since we are missing peaks which relate to these symmetries.

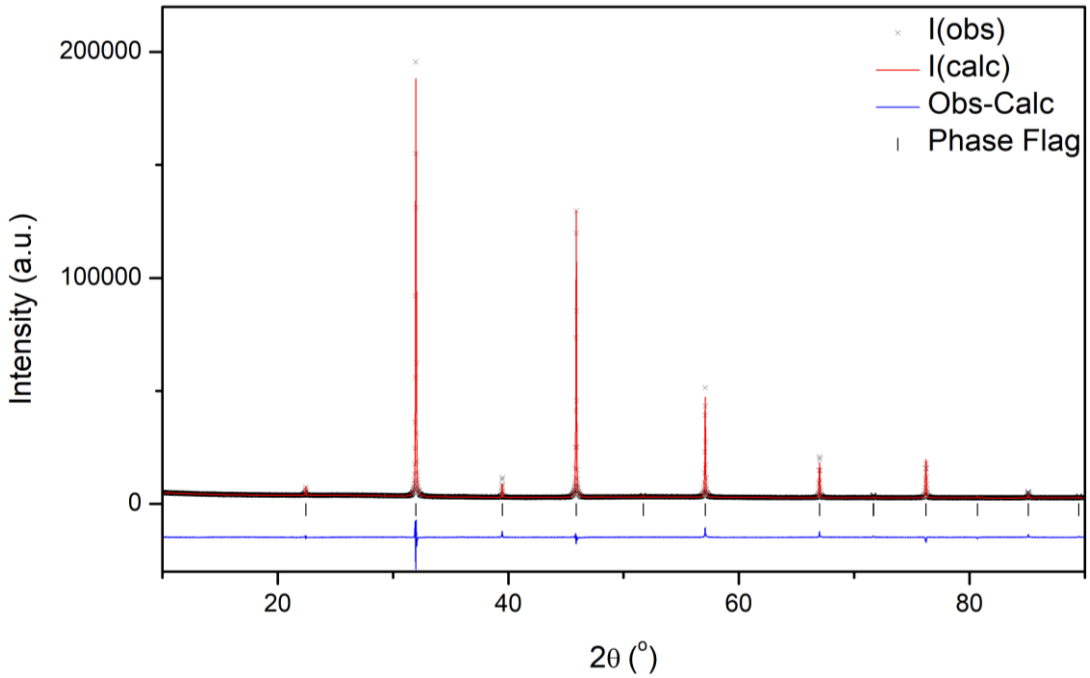

Figure 4.2: *Rietveld refinement of room temperature PXRD data collected for $Bi_{0.5}Na_{0.5}Fe_{0.5}Nb_{0.5}O_3$; χ^2 = 3.415, R_{wp} = 4.14% and R_p = 2.69; the black crosses represent the observed intensity, the red line represents the calculated intensity from the model, the blue line represents the difference between the observed pattern and calculated pattern and the black tick marker represents the P4mm model.*

Table 4.1: *Cell parameters and model fit statistics extracted from the Rietveld refinement of PXRD data collected for $Bi_{0.5}Na_{0.5}Fe_{0.5}Nb_{0.5}O_3$ fitted to the P4mm model.*

Space Group	X^2	wRp	Rp	a (Å)	b (Å)	c (Å)	α (°)	β (°)	γ (°)	Cell Volume (Å^3)
P4mm	3.415	4.14	2.69	3.941397(31)	3.941397(31)	3.94221(8)	90	90	90	61.2407(15)

Table 4.2: *Atomic coordinates extracted from the Rietveld refinement of PXRD data collected for $Bi_{0.5}Na_{0.5}Fe_{0.5}Nb_{0.5}O_3$ fitted to the P4mm model. Oxygen U_{ISO}*100 fixed at 1.00.*

Bi/Na 1	x	0	Fe/Nb 1	x	0.5	O 1	x	0.5	O 2	x	0.5
	y	0		y	0.5		y	0.5		y	0
	z	0		z	0.5421(16)		z	0.054(20)		z	0.553(10)
	U_{ISO}*100	5.26(19)		U_{ISO}*100	0.96(12)		U_{ISO}*100	1.00*		U_{ISO}*100	1.00*

As can be seen in *table 4.1* the lattice parameters for the model fitted to the pattern are near cubic. As a result the possibility that the NNO50% material crystallises with cubic $Pm\bar{3}m$ symmetry has been investigated. The results of this refinement can be seen in *figure 4.3* with the refinement

details given in *tables 4.3 and 4.4*. The fitting statistics suggest that the data is fit better with the *P*4*mm* model as indicated by the lower goodness-of-fit parameters. However, the difference does not seem significant enough which would suggest that *Pm*$\bar{3}$*m* may be a more sensible solution as it has less degrees-of-freedom than the tetragonal model. That said the fit to some of the smaller intensity peaks is superior in the fit using the *P*4*mm* model (e.g. at ~22° 2θ). This coupled with the similarities between this study and the work performed by Lennox *et al*[2] for $Bi_{0.5}K_{0.5}Fe_{0.5}Nb_{0.5}O_3$ where the symmetry assignment was based on PND it is concluded that the material adopts *P*4*mm* symmetry (as discussed further below).

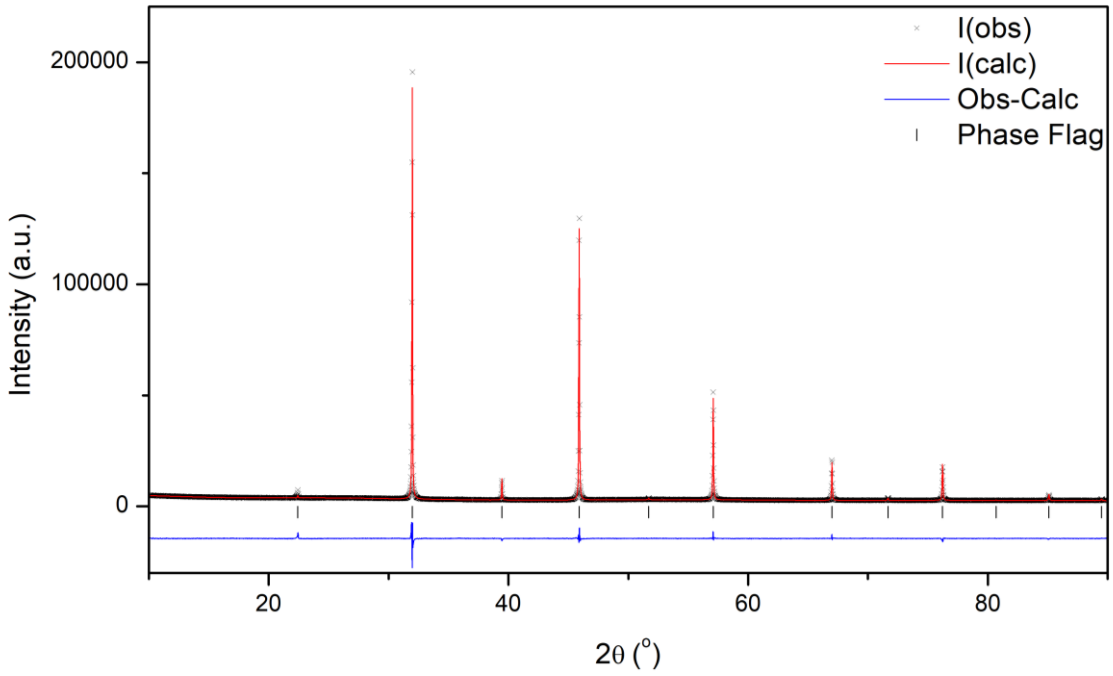

Figure 4.3: *Rietveld refinement of room temperature PXRD data collected for $Bi_{0.5}Na_{0.5}Fe_{0.5}Nb_{0.5}O_3$; χ^2 = 3.588, R_{wp} = 4.25% and R_p = 2.72; the black crosses represent the observed intensity, the red line represents the calculated intensity from the model, the blue line represents the difference between the observed pattern and calculated pattern and the black tick marker represents the Pm*$\bar{3}$*m model.*

Table 4.3: *Cell parameters and model fit statistics extracted from the Rietveld refinement of PXRD data collected for $Bi_{0.5}Na_{0.5}Fe_{0.5}Nb_{0.5}O_3$ fitted to the Pm*$\bar{3}$*m model.*

Space Group	X^2	wRp	Rp	a (Å)	b (Å)	c (Å)	α (°)	β (°)	γ (°)	Cell Volume (Å^3)
Pm$\bar{3}$*m*	3.588	4.25	2.72	3.941460(17)	3.941460(17)	3.941460(17)	90	90	90	61.2310(5)

Table 4.4: *Atomic coordinates extracted from the Rietveld refinement of PXRD data collected for $Bi_{0.5}Na_{0.5}Fe_{0.5}Nb_{0.5}O_3$ fitted to the Pm*$\bar{3}$*m model. Oxygen U_{ISO}*100 fixed at 1.00.*

Bi/Na 1	x	0.0	Fe/Nb 1	x	0.5	O1	x	0.5
	y	0.0		y	0.5		y	0.5
	z	0.0		z	0.5		z	0.0
	U_{ISO}*100	7.30(6)		U_{ISO}*100	1.40(5)		U_{ISO}*100	1.00*

As can be seen in the Rietveld refinement of KNO50% shown in *figure 4.4* (the refinement details are given in *tables 4.5 and 4.6*) the *P4mm* model fit to the pattern agrees well although there is a small shortfall in intensity associated with the peak at ~32° 2θ likely due to preferred orientation. The previously reported sample was synthesised differently and exhibits broader peaks as well as extra impurity peaks supporting the improved sample preparation used here[2]. The Rietveld fit for the previously reported sample (reproduced in Appendix *figure A2.1*) does not seem much different from that shown in *figure 4.4* suggesting that the original conclusion that the sample crystallised as *P4mm* is correct[2].

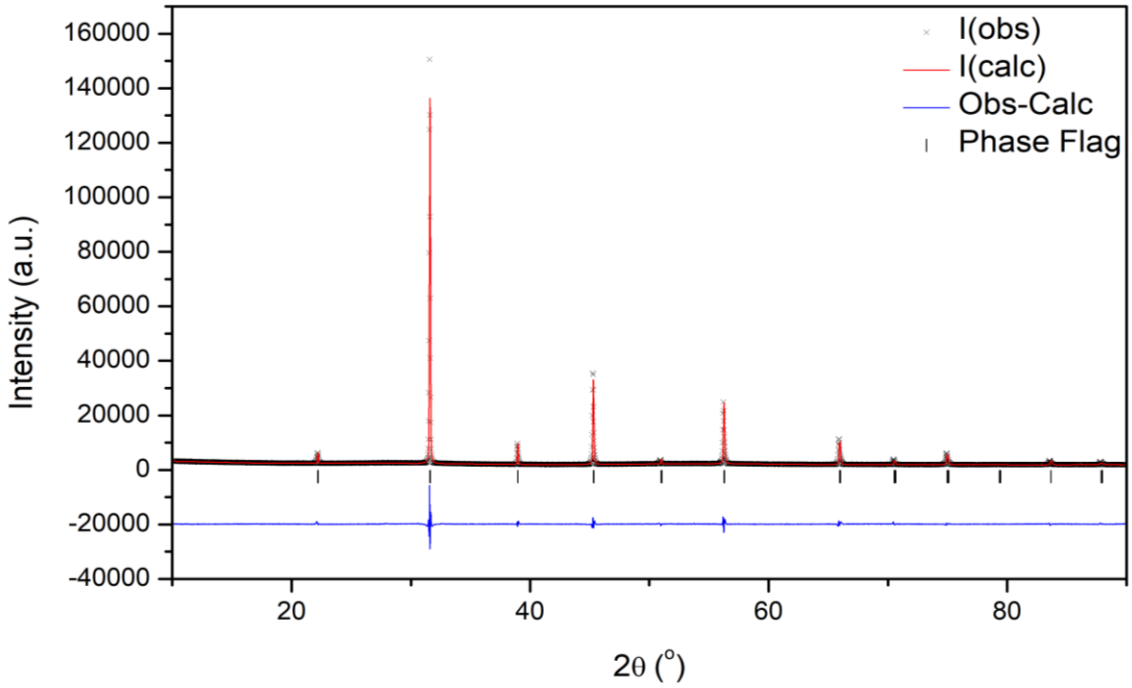

Figure 4.4: *Rietveld refinement of room temperature PXRD data collected for $Bi_{0.5}K_{0.5}Fe_{0.5}Nb_{0.5}O_3$; χ^2 = 7.334, R_{wp} = 5.37% and R_p = 3.47; the black crosses represent the observed intensity, the red line represents the calculated intensity from the model, the blue line represents the difference between the observed pattern and calculated pattern and the black tick marker represents the P4mm model.*

Table 4.5: *Cell parameters and model fit statistics extracted from the Rietveld refinement of PXRD data collected for $Bi_{0.5}K_{0.5}Fe_{0.5}Nb_{0.5}O_3$ fitted to the P4mm model.*

Space Group	X^2	wRp	Rp	a (Å)	b (Å)	c (Å)	α (°)	β (°)	γ (°)	Cell Volume (Å^3)
P4mm	7.334	5.37	3.47	4.00560(6)	4.00560(6)	4.00029(12)	90	90	90	64.1840(23)

Table 4.6*: Atomic coordinates extracted from the Rietveld refinement of PXRD data collected for $Bi_{0.5}K_{0.5}Fe_{0.5}Nb_{0.5}O_3$ fitted to the P4mm model. Oxygen U_{ISO}*100 fixed at 1.00.*

Bi/K 1	x	0	Fe/Nb 1	X	0.5	O 1	x	0.5	O 2	x	0.5
	y	0		Y	0.5		y	0.5		y	0
	z	0		Z	0.5735(21)		z	0.086(9)		z	0.564(4)
	U_{ISO}*100	8.92(6)		U_{ISO}*100	1.52(6)		U_{ISO}*100	1.00*		U_{ISO}*100	1.00*

The KNO50% material has a tolerance factor of t = 1.001 which indicates that the structure should be close to being cubic. In contrast the NNO50% material has a tolerance factor of t = 0.958 due to the similarity in sizes between Bi and Na and, Fe and Nb, which leads to a very small change in the tolerance factor. Interestingly, it can be seen from the data presented above that there is less deviation between the *a* and *c* lattice parameters in NNO50% than in KNO50%. Since the tolerance factor for PZT at the morphotropic phase boundary is t = 0.987 it is potentially interesting to tune t between KNO50% and NNO50% by preparing $Bi_{0.5}K_{0.25}Na_{0.25}Fe_{0.5}Nb_{0.5}O_3$. NKNO, has a tolerance factor of t = 0.980 putting it in between the two previous materials.

The Rietveld refinement for NKNO using the *P*4*mm* model can be seen in *figure 4.5*. It shows a good fit against the *P*4*mm* model similar to those observed for the NNO50% and KNO50% samples. The lattice parameters for NKNO, seen in *table 4.7*, are as expected in between the values observed for NNO50% and KNO50% (*tables 4.1 and 4.5*) which can be seen *figure 4.6*. It is noted that the relationship is not perfectly linear most likely arising from an imbalance in the Na^+/K^+ ratio due to the possibility that sodium is more volatile than potassium when heating during synthesis.

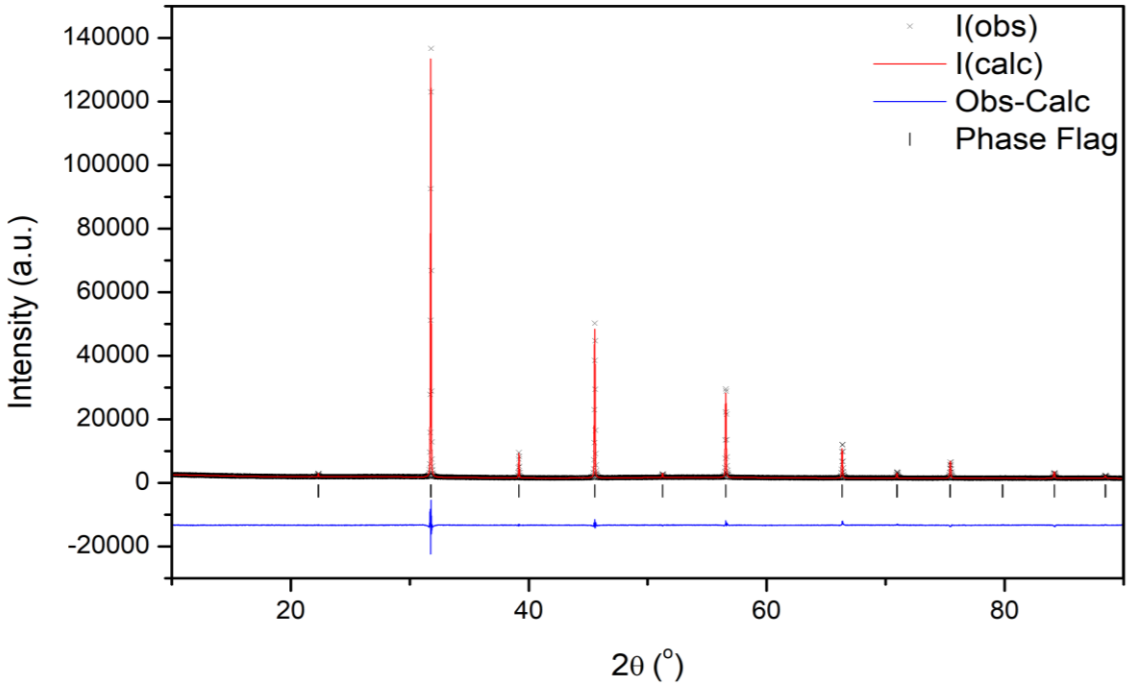

Figure 4.5: *Rietveld refinement of room temperature PXRD data collected for $Bi_{0.5}Na_{0.25}K_{0.25}Fe_{0.5}Nb_{0.5}O_3$; χ^2 = 3.580, R_{wp} = 4.27% and R_p = 2.91; the black crosses represent the observed intensity, the red line represents the calculated intensity from the model, the blue line represents the difference between the observed pattern and calculated pattern and the black tick marker represents the P4mm model.*

Table 4.7: *Cell parameters and model fit statistics extracted from the Rietveld refinement of PXRD data collected for $Bi_{0.5}K_{0.25}Na_{0.25}Fe_{0.5}Nb_{0.5}O_3$ fitted to the P4mm model.*

Space Group	X^2	wRp	Rp	a (Å)	b (Å)	c (Å)	α (°)	β (°)	γ (°)	Cell Volume (Å^3)
P4mm	3.580	4.27	2.91	3.98050(6)	3.98050(6)	3.98190(9)	90	90	90	63.0908(19)

Table 4.8: *Atomic coordinates extracted from the Rietveld refinement of PXRD data collected for $Bi_{0.5}K_{0.25}Na_{0.25}Fe_{0.5}Nb_{0.5}O_3$ fitted to the P4mm model. Oxygen U_{ISO}*100 fixed at 1.00.*

Bi/K/Na 1	x	0	Fe/Nb 1	x	0.5	O 1	x	0.5	O 2	x	0.5
	y	0		y	0.5		y	0.5		y	0
	z	0		z	0.4901(27)		z	0.000(16)		z	0.482(7)
	U_{ISO}*100	10.74(4)		U_{ISO}*100	1.761(30)		U_{ISO}*100	1.00*		U_{ISO}*100	1.00*

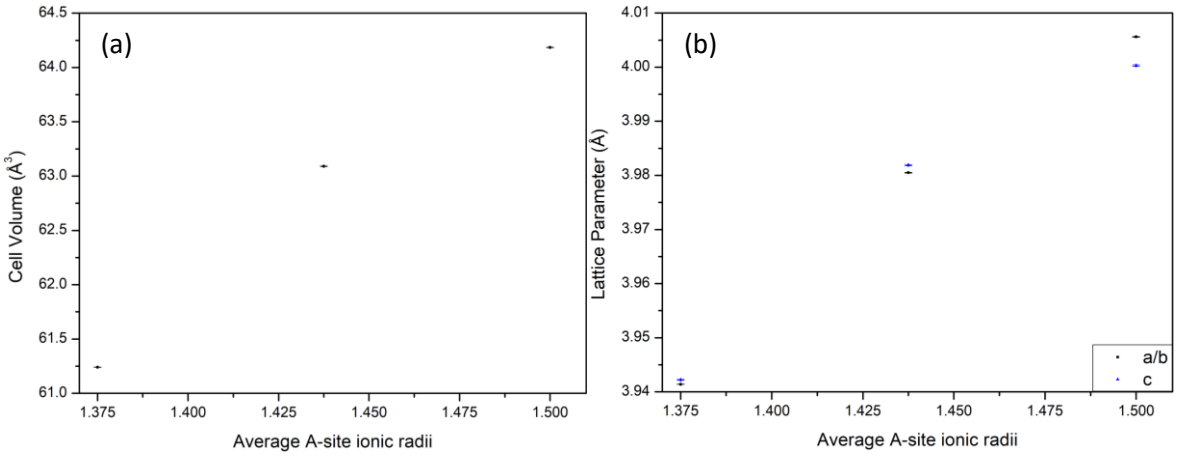

Figure 4.6: *Average A-site ionic radii against (a) lattice parameter and (b) cell volume. Average A-site ionic radii of $Bi_{0.5}Na_{0.5}Fe_{0.5}Nb_{0.5}O_3$ = 1.375, $Bi_{0.5}K_{0.25}Na_{0.25}Fe_{0.5}Nb_{0.5}O_3$ = 1.4375 and $Bi_{0.5}K_{0.5}Fe_{0.5}Nb_{0.5}O_3$ = 1.50.*

To confirm the structure of these materials between the tetragonal and cubic symmetries, the samples were run on the HRPD neutron beamline at ISIS. The results for the NNO50% material revealed that the structure is more complex than the XRD data suggested. In *figure 4.7* the Rietveld refinement can be seen showing the *P*4*mm* fit to the powder neutron data. The model appears to show a reasonable fit to the model. However, on closer inspection of the background, periodic diffuse scattering can be seen which suggests the possibility that some form of short-range order may be present. This diffuse scattering can be observed with greater ease when the logarithm of the intensity is plotted, as shown in *figure 4.8*. To get the fit shown in *figure 4.7* the thermal parameter for the oxygen were set to be anisotropic as the isotropic model was unable to fit the intensity. Due to the presence of this diffuse scattering it made it difficult to determine whether the pattern showed a better fit to the *P*4*mm* or $Pm\bar{3}m$ models. The most likely origin of the diffuse scattering, when it is taken into consideration that it does not appear in the XRD data, is to suggest it is related to oxygen ions for example a tilt driven modulation or possibly related to second order Jahn-Teller distortions through Bi^{3+} on the *A* site and Nb^{5+} on the *B* site. This is concluded since the difference in electron density between the Bi^{3+} and Na^{+} on the *A* site and Fe^{3+} and Nb^{5+} on the *B* site should be enough to be seen through XRD. Thus, it is likely that ordering of the *A* and/or *B* site

cations would lead to extra superstructure peaks in the XRD pattern. The idea of oxygen tilt modulations in perovskites is not uncommon. For example, in the doubly ordered perovskite NaLaMgWO$_6$, King *et al*[1] found satellite peaks in NPD that were extremely weak in XRD data. This was found to be an oxygen modulation as the octahedral tilts experienced one dimensional twinning[1].

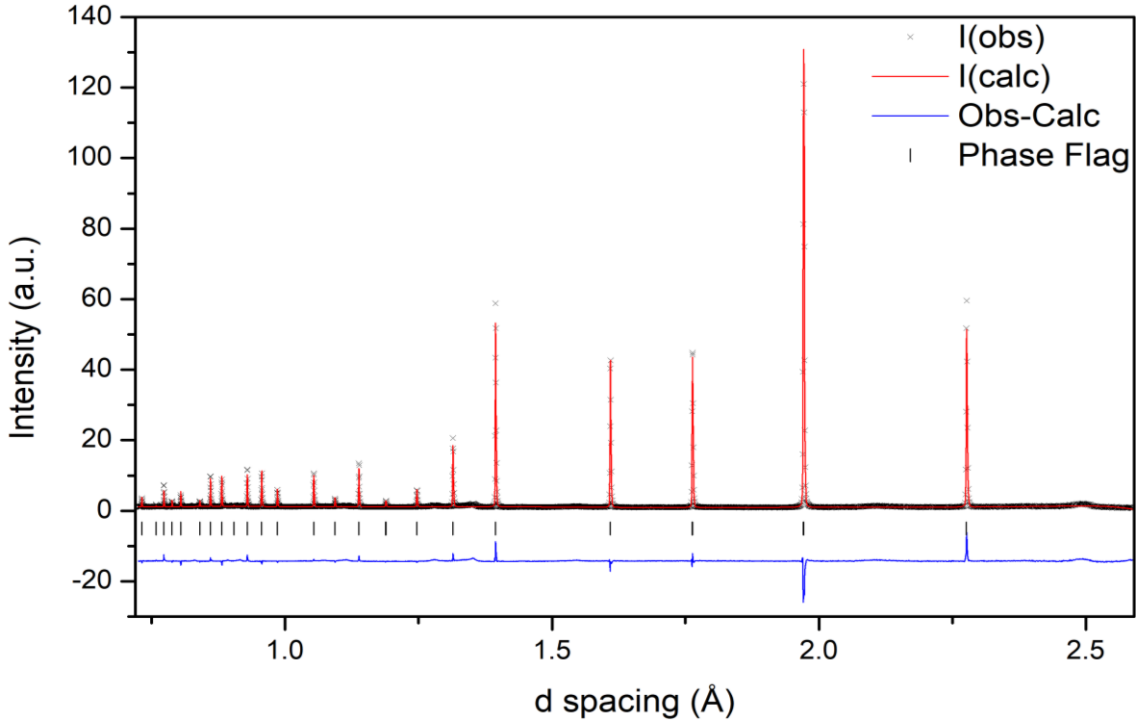

Figure 4.7: *Rietveld refinement of room temperature PND data collected for $Bi_{0.5}Na_{0.5}Fe_{0.5}Nb_{0.5}O_3$; χ^2 = 13.47, R_{wp} = 9.67% and R_p = 8.19; the black crosses represent the observed intensity, the red line represents the calculated intensity from the model, the blue line represents the difference between the observed pattern and calculated pattern and the black tick marker represents the P4mm model.*

Table 4.9: *Cell parameters and model fit statistics extracted from the Rietveld refinement of PND data collected for $Bi_{0.5}Na_{0.5}Fe_{0.5}Nb_{0.5}O_3$ fitted to the P4mm model.*

Space Group	X^2	wRp	Rp	a (Å)	b (Å)	c (Å)	α (º)	β (º)	γ (º)	Cell Volume (Å^3)
P4mm	13.47	9.67	8.19	3.94282(6)	3.94282(6)	3.94174(10)	90	90	90	61.2777(20)

Table 4.10: *Atomic coordinates extracted from the Rietveld refinement of PND data collected for $Bi_{0.5}Na_{0.5}Fe_{0.5}Nb_{0.5}O_3$ fitted to the P4mm model.*

Bi/Na 1	x	0	Fe/Nb 1	x	0.5	O 1	x	0.5	O 2	x	0.5
	y	0		y	0.5		y	0.5		y	0
	z	0		z	0.524(5)		z	0.041(5)		z	0.563(6)
	U_{ISO}*100	6.62(20)		U_{ISO}*100	1.248(30)		U111 *100	10.0(12)		U111 *100	10.4(14)
							U222 *100	10.00(119)		U222 *100	0.89(25)
							U333 *100	-0.4(4)		U333 *100	8.6(9)

Figure 4.9 shows the structure of $Bi_{0.5}Na_{0.5}Fe_{0.5}Nb_{0.5}O_3$ fitted using the *P*4*mm* model with anisotropic oxygen parameters plotted into the graphics software VESTA[11]. This figure shows that the equatorial oxygen is unusually shaped due to the unusual anisotropic displacement. This most likely arises due to a lack of degrees-of-freedom present in the *P*4*mm* structure and is likely linked to the diffuse scattering seen in the pattern. Considering this these data could possibly suggest two things (i) that the modulation suggests a lowering of symmetry and (ii) that tilt modulation may largely lie in the lattice *a*/*b* direction due to the distortion shown on the oxygens in this direction. Considering this if the *a* and *b* parameters are quadrupled in the *P*4*mm* model, shown in a Le Bail fit in appendix *figure A2.14*, it is evident that the new nuclear peaks which arise overlap with the diffuse peaks in the refinement, however, it is not possible to match the intensity of the model to the data.

It may be possible that the Na^+ on the *A*-site may be driving the structure towards order. Changing the *P*4*mm* symmetry ($a^0a^0c^0_+$) to allow tilting of the structure leads to the tilt system $a^-a^-c^{+12}$. This tilt system is the primary tilt arrangement for the $P2_1$ space group seen in doubly ordered perovskites[13]. The results of this refinement can be found in appendix *figure A2.15*. The fit is similar to the *P*4*mm* fit seen in *figure 4.7* however the $P2_1$ refinement is unstable. The $P2_1$ model does try to fit the position of the diffuse peaks but the intensities of the calculated peaks does not match the intensities of the observed data. Considering the unstable fit and the lack of improvement in fitting the data when the symmetry has been reduced from tetragonal to orthorhombic, this ordered model seems unlikely. The reason ordering is not observed may be due to the lack of *B*-site rock salt order as a size difference on the *B*-site is not present such as that seen in doubly ordered perovskites such as $NaLaMgWO_6$ and $NaLaMnWO_6$[13]. A possible solution to promote ordering and confirm this hypothesis would be to replace Fe^{3+} for Sc^{3+} or Nb^{5+} for Mo^{5+}.

An alternative theory to cation ordering is that there are localised areas of NNO rich areas resulting in deviations to the tilt pattern and leading to the diffuse scattering. To test this, the data was refined to the NNO $P2_1ma$ model from the literature[14,15]. The refinement can be found in appendix *figure A2.16*. The $P2_1ma$ fit (χ^2 = 11.63, R_{wp} = 8.99% and R_p = 7.51) is better than the *P*4*mm* (χ^2 = 13.47, R_{wp} = 9.67% and R_p = 8.19) and $P2_1$ fits seen in *figure 4.7* appendix *figure A2.15* but is also unstable similar to the $P2_1$ refinement. This may suggest a potential lowering of the symmetry due to octahedral tilts. However, the fit to the observed diffuse scattering is much better than the $P2_1$ model. When taking into account that the superstructure peaks are not sharp but diffuse and weak, it can be concluded that this structure could be representative of the local structure rather than the average structure. We can therefore conclude that on average the structure is *P*4*mm* but locally it is $P2_1ma$. This behaviour has been seen previously with BFO-NNO materials where $BaTiO_3$ was

also added resulting in what looked like *R*3*c* symmetry on the local structure through selected area electron diffraction but a $Pm\bar{3}m$ model fit their XRD data better[16]. This may suggest that Na and Bi is attempting to order but rather than drive ordering of the *B*-site, it drives a clustering effect instead. As presented later in chapter five, there is no phase segregation in these materials between the *P*4*mm* and *P*2$_1$*ma* regions of the phase diagram in contrast to the BFO-KNO phase diagram reported previously[2]. This suggests that this behaviour is intrinsic and complex in nature and requires further work for definitive understanding.

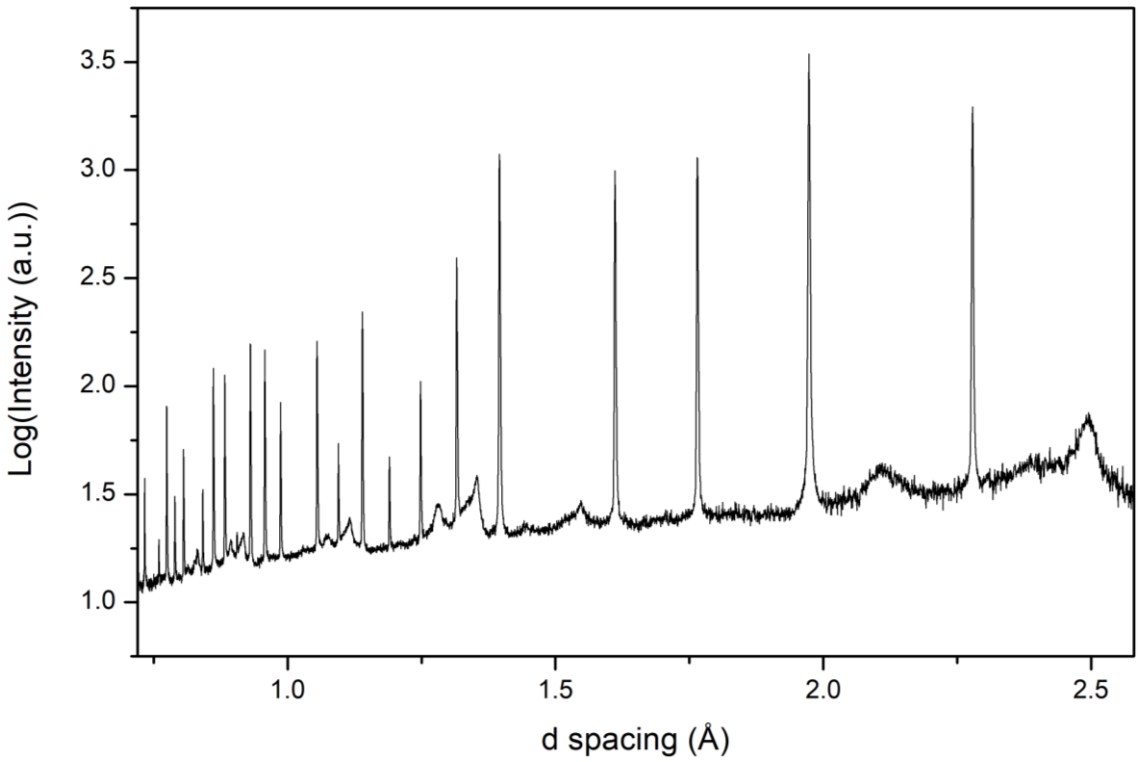

Figure 4.8: *PND pattern for $Bi_{0.5}Na_{0.5}Fe_{0.5}Nb_{0.5}O_3$ from bank 1 on HRPD plotted using a logarithm of the intensity on the y axis to more clearly show the diffuse peaks observed.*

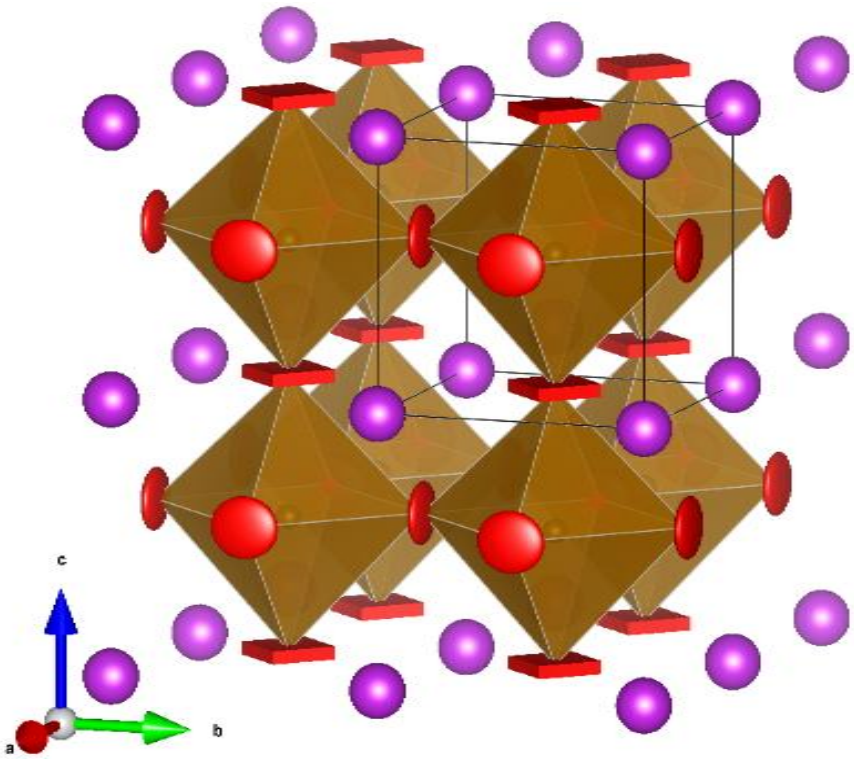

Figure 4.9: *Structure model from the Rietveld refinement of PND data collected for $Bi_{0.5}Na_{0.5}Fe_{0.5}Nb_{0.5}O_3$ using the P4mm model and fitted with anisotropic displacement parameters for oxygen. This figure shows the unusual shape exhibited by the equatorial oxygen suggesting that the diffuse scattering may arise as a result of tilt behaviour in the a/b directions. Bismuth/sodium atoms are shown in purple, iron/niobium atoms/octahedra are shown in brown and oxygen atoms shown in red.*

This behaviour was not seen in the neutron pattern reported previously for $Bi_{0.5}K_{0.5}Fe_{0.5}Nb_{0.5}O_3$[2]. To determine whether this was due to the alternative synthesis procedure used here or whether this was brought about as a consequence of specifically placing sodium on the *A*-site, KNO50% and NKNO samples were also run on HRPD.

Neither the KNO50% nor NKNO patterns, *figures 4.10 and 4.11*, show the same diffuse scattering behaviour as the NNO50% pattern shown in *figure 4.7*. The *P*4*mm* model fits both sets of data well. No additional reflections are seen in the pattern to suggest a tetragonal phase to a cubic phase, however additional peak broadening is fit better in the *P*4*mm* tetragonal model which indicates overlapping reflections not seen in the cubic model. Full refinement parameters can be found in appendix *table A2.5*. This suggests that the presence of the diffuse scattering must be related to the addition of Na^+ with the addition of K^+ suppressing this behaviour. An explanation for the behaviour observed could be suggested based on changes in both the tetragonality and tolerance factor. It can be seen in *figure 4.12* that NNO50% has the lowest tolerance factor but the lowest degree of tetragonality. In contrast, KNO50% shows the opposite behaviour (with a higher tolerance factor and a higher tetragonality) with the NKNO sample in the middle. It could be expected from these data that these materials should perhaps be cubic. However, competition between

octahedral tilting, *A*-site variance and bismuth ion off centring leads to the materials adopting *P*4*mm* symmetry. *A*-site variance defines the distribution of different sized cations on the *A*-site[17]. It can be calculated using the equation[17]:

$$\sigma^2 = \sum_i y_i {r_i}^2 - \left(\sum_i y_i r_i\right)^2 \quad (4.1)$$

Where σ^2 is the statistical *A*-site variance, y_i are the proportions of the cations present and r_i are the atomic radii of the cations present. The *A*-site variance drops to almost zero in the NNO50% (σ^2 = 0.000025) material when compared to KNO50% (σ^2 = 0.0144) or NKNO (σ^2 = 0.0111). This may suggest that the similar sizes of the Na^+ and Bi^{3+} coupled with the differences in cation location as a result of the Bi^{3+} lone pair is the driving force for local atom arrangements and the origin of the modulation for NNO50%. In contrast with larger σ^2 values the structure is less distorted and favours disorder. This can also be seen in the polyhedral distortion index calculated by VESTA which is calculated for NNO50% = 0.01170, NKNO = 0.01109 and KNO50% = 0.00741[11]. This suggests that the NNO50% has a higher degree of tilting which leads to a higher degree of disorder possibly due to the differences between the Na^+ and Bi^{3+} in terms of the displacement resulting from the stereochemical electron lone pair.

The Rietveld refinement of the KNO50% material (*P*4*mm* model), shown in *figure 4.10*, additionally misses a peak present at 2.41 Å *d*-spacing. This peak is not diffuse and careful inspection of the data collected in other HRPD banks shows weak peaks characteristic of magnetic Bragg peaks which is possibly not unsurprising given that the *B*-O2-*B* bond angle ≈180^o (appendix *table A2.5*). The magnetism is consistent with antiferromagnetic behaviour and is likely found due to the formation of a percolation pathway for Fe^{3+} ions (Nb^{5+} is diamagnetic with a d^0 arrangement)[18]. Additionally, adding K^+ to the structure straightens the *B* site to oxygen bond angles, improving superexchange pathways for magnetic behaviour. This straightening of the KNO50% unit cell when compared to the NNO50% and NKNO samples could also be predicted by the tolerance factors, which is very close to 1.00 in KNO50%.

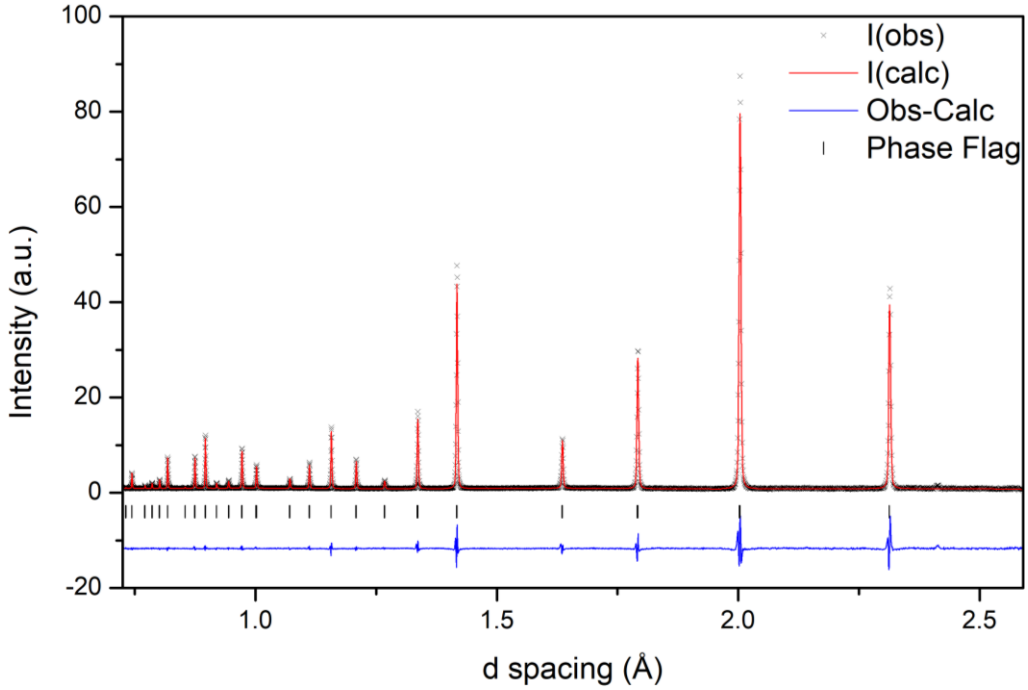

***Figure 4.10**: Rietveld refinement of room temperature PND data collected for $Bi_{0.5}K_{0.5}Fe_{0.5}Nb_{0.5}O_3$; χ^2 = 3.621, R_{wp} = 7.98% and R_p = 7.78; the black crosses represent the observed intensity, the red line represents the calculated intensity from the model, the blue line represents the difference between the observed pattern and calculated pattern and the black tick marker represents the P4mm model.*

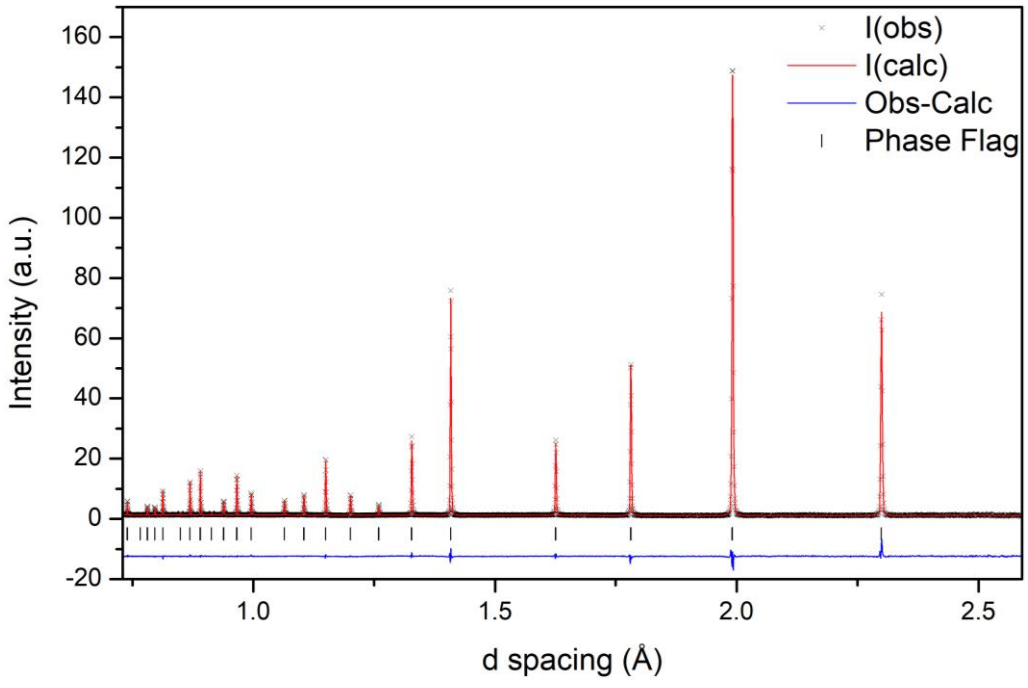

***Figure 4.11:** Rietveld refinement of room temperature PND data collected for $Bi_{0.5}Na_{0.25}K_{0.25}Fe_{0.5}Nb_{0.5}O_3$; χ^2 = 1.859, R_{wp} = 5.10% and R_p = 4.85; the black crosses represent the observed intensity, the red line represents the calculated intensity from the model, the blue line represents the difference between the observed pattern and calculated pattern and the black tick marker represents the P4mm model.*

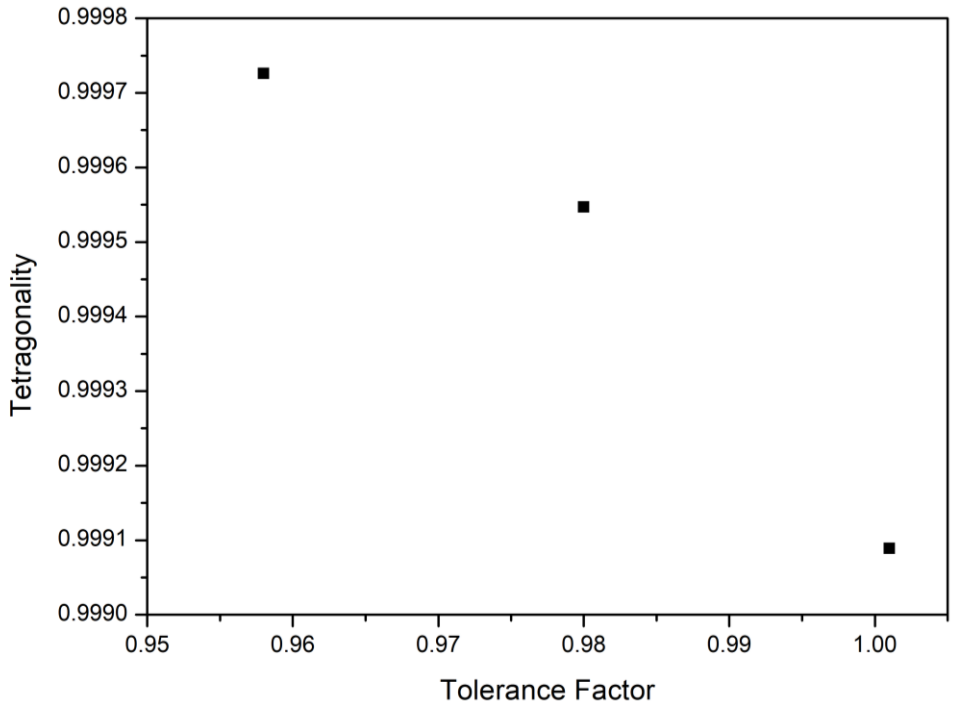

Figure 4.12: *Plot of tolerance factor against tetragonality for $Bi_{0.5}Na_{0.5}Fe_{0.5}Nb_{0.5}O_3$, $Bi_{0.5}K_{0.5}Fe_{0.5}Nb_{0.5}O_3$, and $Bi_{0.5}Na_{0.25}K_{0.25}Fe_{0.5}Nb_{0.5}O_3$ respectively.*

4.3 Variable Temperature Structural Characterisation

For characterisation at low temperature a PheniX was added to the Empyrean XRD, allowing powder diffraction data to be collected down to 12 K. The diffraction pattern for the NNO50% sample at 12 K can be seen in *figure 4.13*. It can be seen in the Rietveld refinement that there is a good fit to the *P*4*mm* model. Shown in *figure 4.14* is a collection of powder patterns from 12 K to 298 K in 20 K increments. This figure shows that the pattern does not deviate between room temperature and 12 K so it is unlikely that a phase transition occurs as a function of temperature in this range. Full refinement parameters and fits for the temperature range 30 K to 298 K can be found in appendix *table A2.2* and *figure A2.3*.

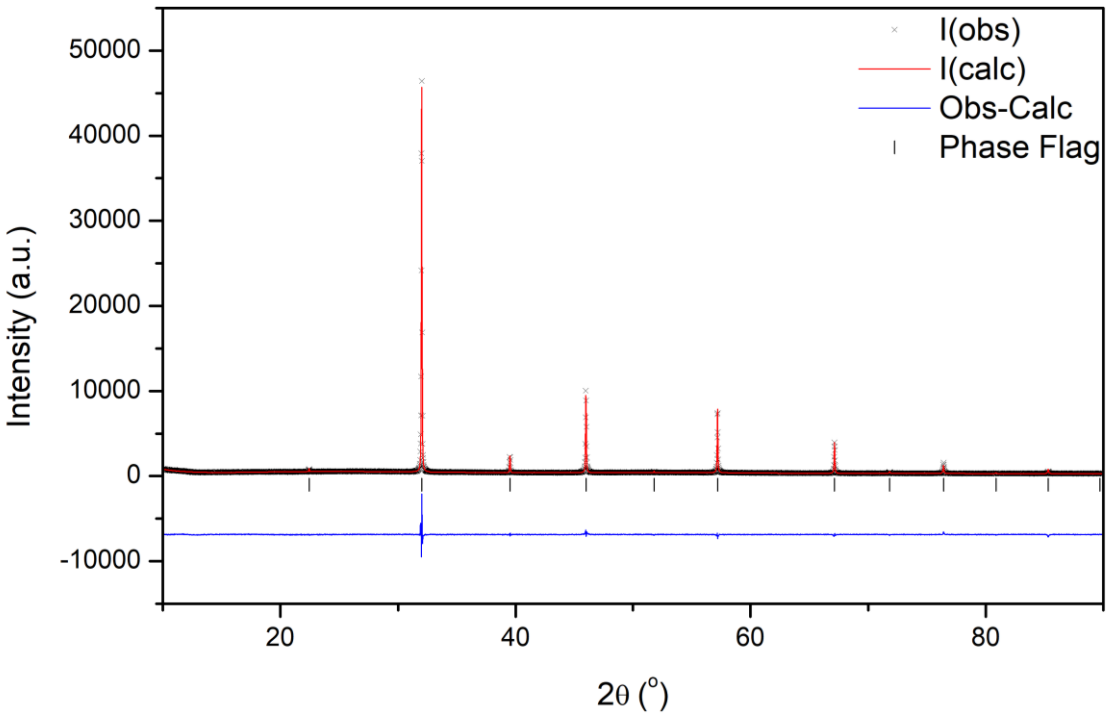

Figure 4.13: *Rietveld refinement of 12 K PXRD collected for $Bi_{0.5}Na_{0.5}Fe_{0.5}Nb_{0.5}O_3$; χ^2 = 2.201, R_{wp} = 6.76% and R_p = 4.96; the black crosses represent the observed intensity, the red line represents the calculated intensity from the model, the blue line represents the difference between the observed pattern and calculated pattern and the black tick marker represents the P4mm model.*

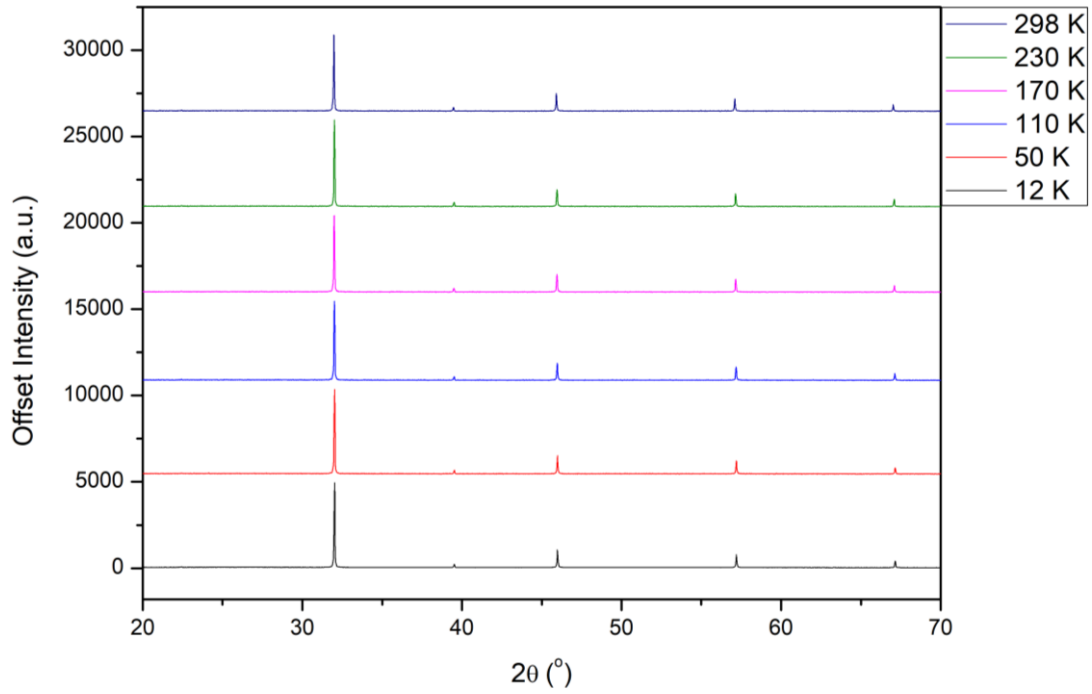

Figure 4.14: *Selection of patterns for the LT PXRD data collected for $Bi_{0.5}Na_{0.5}Fe_{0.5}Nb_{0.5}O_3$. 12 K pattern intensity has been scaled down to match the intensities of the other temperature points that were taken with shorter scan times. Data has been shifted for clarity.*

The lattice parameter and cell volume plots are shown in *figure 4.15* for the NNO50% sample. It can be seen that they follow the expected trend with a decrease in both the *a* and *c* parameters as well as cell volume with decreasing temperature. There does, however, appear to be an anomaly in both

sets of data at approximately 230 K with a spike in the values. The data points after follow the original trend and it is unlikely that this signals a phase change. It is more likely that this anomaly (which was seen in multiple data sets) links to ongoing issues with the Phenix system.

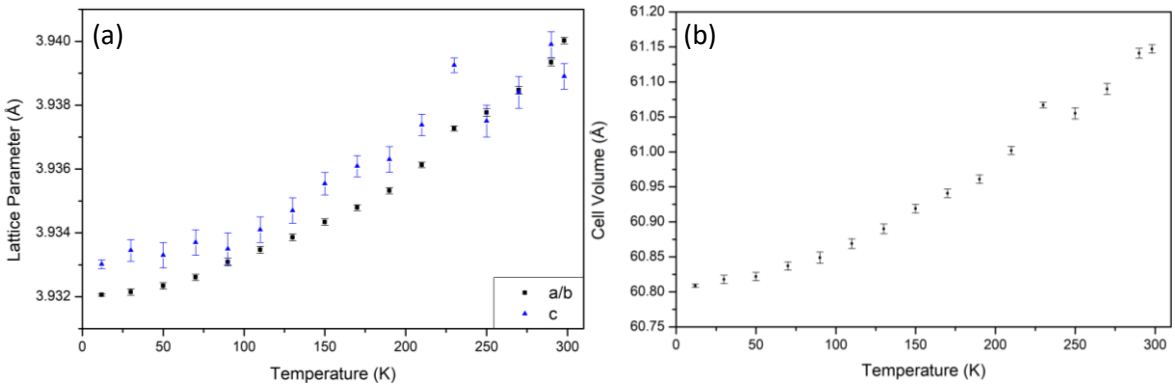

Figure 4.15: *(a) Lattice parameter plot for temperatures between 12 K and 298 K, (b) Cell volume plot for temperatures between 12 K and 298 K extracted from the Rietveld refinement of the LT XRD data collected for $Bi_{0.5}Na_{0.5}Fe_{0.5}Nb_{0.5}O_3$.*

The diffraction pattern for the KNO50% sample at 12 K can be seen in *figure 4.16*. It can be seen from the Rietveld refinement that there is a good fit to the *P4mm* model. Shown in *figure 4.17* is a selection of powder patterns collected from 12 K to 298 K in 20 K increments. This figure shows that the pattern does not deviate from that collected at room temperature so it is unlikely that a phase transition occurs as a function of temperature in this range. Full refinement parameters and fits for the temperature range 30 K to 298 K can be found in appendix *table A2.3* and *figure A2.5.*

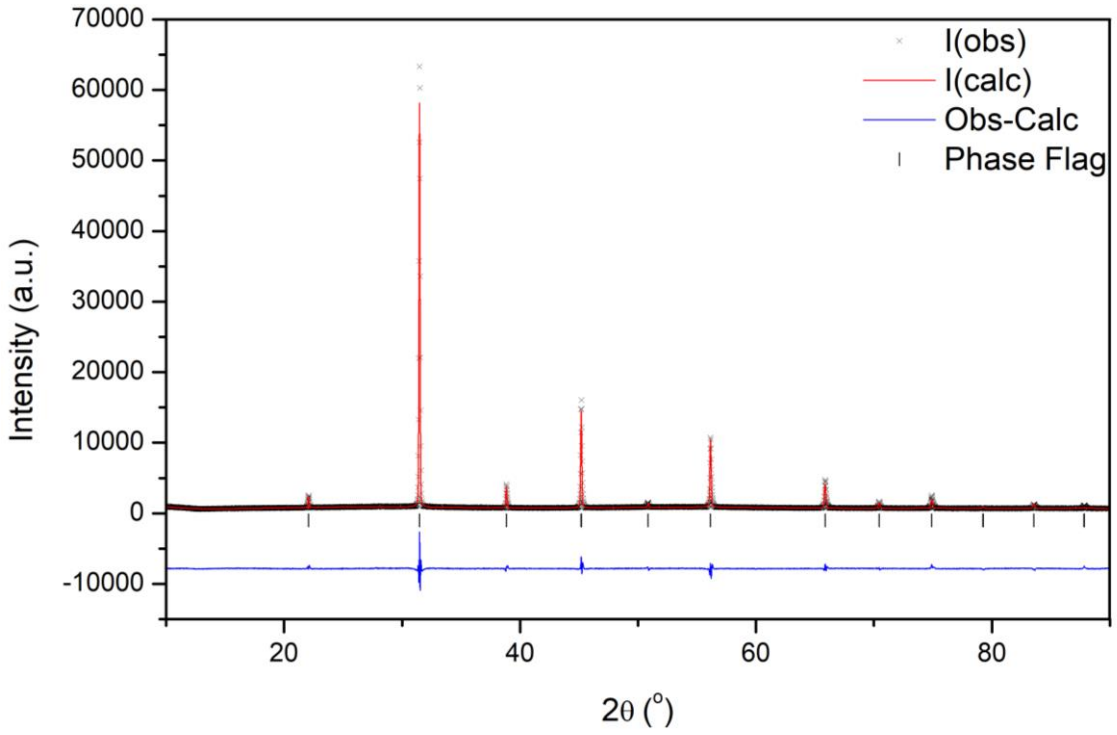

Figure 4.16: *Rietveld refinement of 12 K PXRD data collected for $Bi_{0.5}K_{0.5}Fe_{0.5}Nb_{0.5}O_3$; χ^2 = 3.976, R_{wp} = 6.53% and R_p = 4.79; the black crosses represent the observed intensity, the red line represents the calculated intensity from the model, the blue line represents the difference between the observed pattern and calculated pattern and the black tick marker represents the P4mm model.*

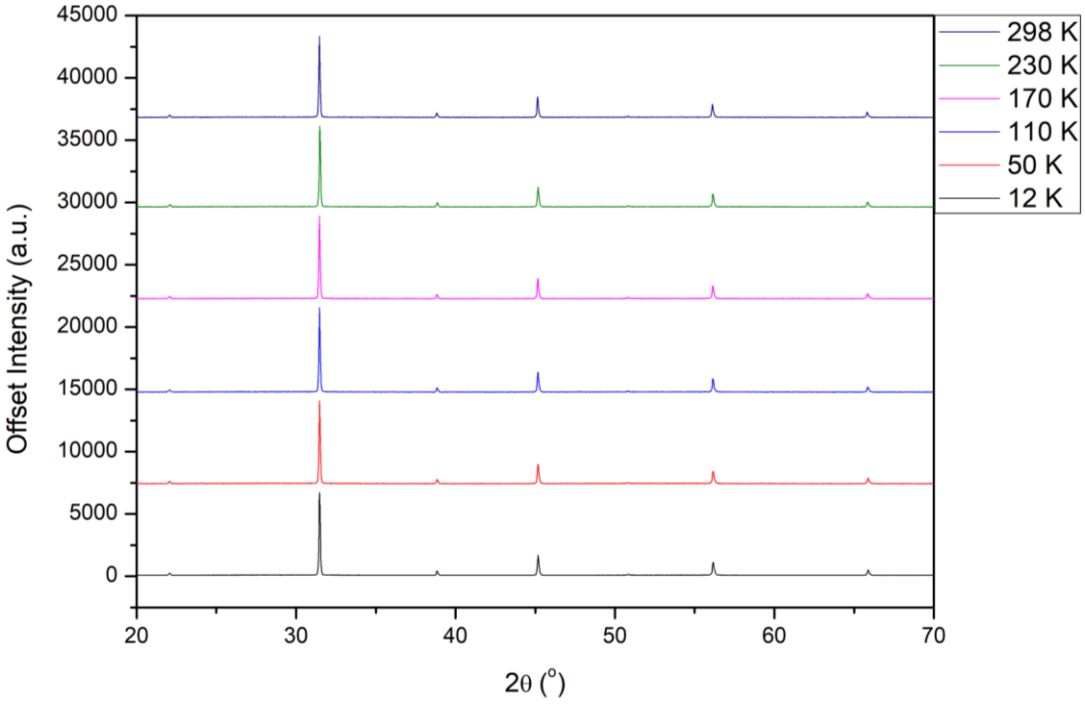

Figure 4.17: *Selection of patterns for the LT PXRD data collected for $Bi_{0.5}K_{0.5}Fe_{0.5}Nb_{0.5}O_3$. 12 K pattern intensity has been scaled down to match the intensities of the other temperature points that were taken with shorter scan times. Data has been offset for clarity.*

The lattice parameter and cell volume plots are shown in *figure 4.18* for the KNO50% sample and follow the expected trend with a decrease in all parameters with decreasing temperature. The same anomaly is observed at around 230 K as discussed above.

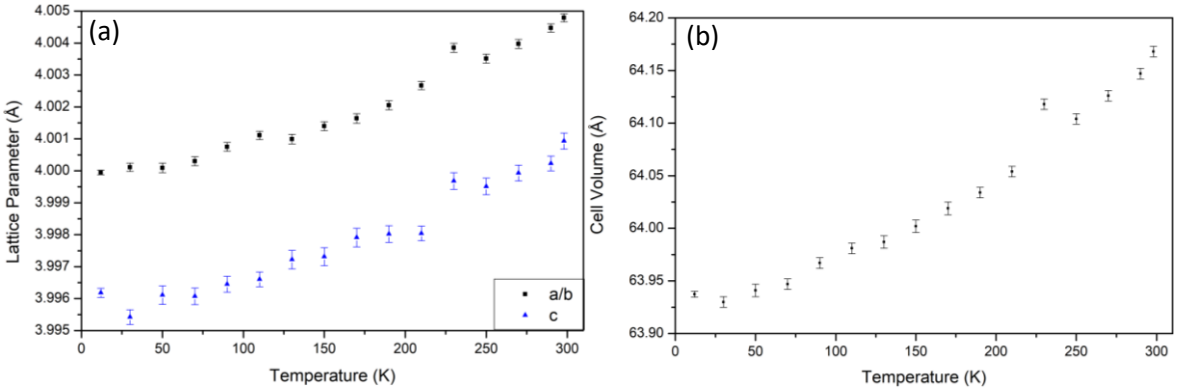

Figure 4.18: *(a) Lattice parameter plot for temperatures between 12 K and 298 K, (b) Cell volume plot for temperatures between 12 K and 298 K extracted from the Rietveld refinement of LT XRD data collected for $Bi_{0.5}K_{0.5}Fe_{0.5}Nb_{0.5}O_3$*

The diffraction pattern for the NKNO sample at 12 K can be seen in *figure 4.19*. Again, it can be seen in the Rietveld refinement that there is a good fit to the *P*4*mm* model. Shown in *figure 4.20* is a collection of powder patterns from 12 K to 298 K in 20 K increments. This figure shows that, like the KNO50% and NNO50% materials, the pattern does not deviate from that observed at room temperature. Full refinement parameters and fits for the temperature range 30 K to 298 K can be found in appendix *table A2.4* and *figure A2.7.*

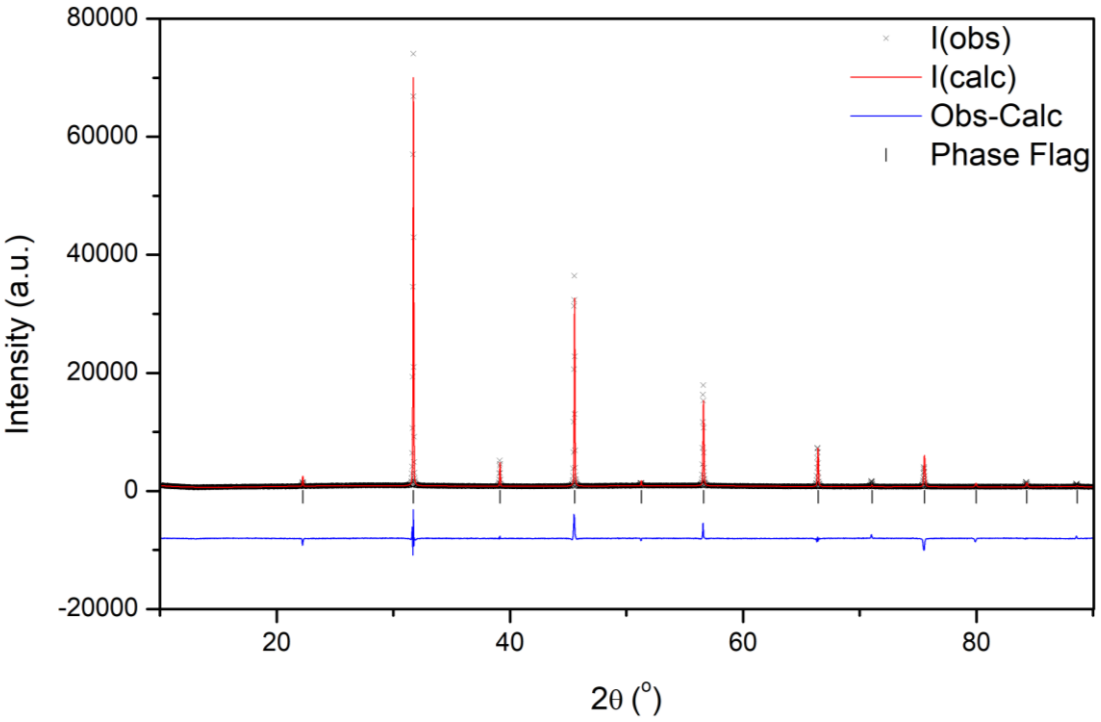

Figure 4.19: *Rietveld refinement of 12 K LT PXRD data collected for $Bi_{0.5}Na_{0.25}K_{0.25}Fe_{0.5}Nb_{0.5}O_3$; χ^2 = 7.682, R_{wp} = 8.96% and R_p = 5.33; the black crosses represent the observed intensity, the red line represents the calculated intensity from the model, the blue line represents the difference between the observed pattern and calculated pattern and the black tick marker represents the P4mm model.*

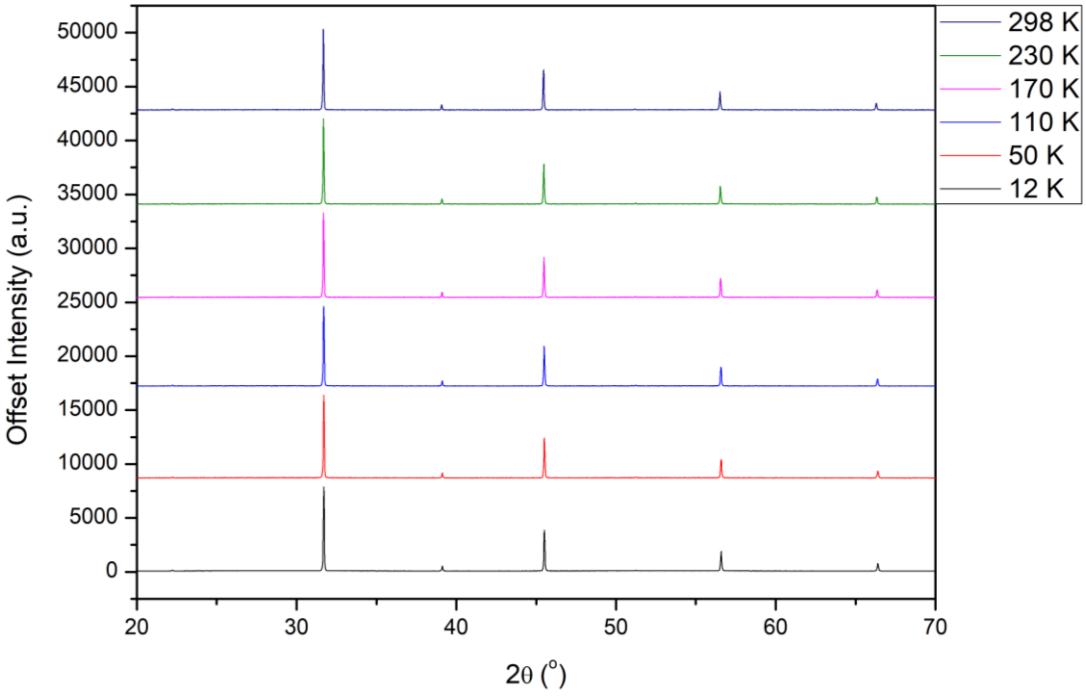

Figure 4.20: *Selection of patterns for the LT PXRD data collected for $Bi_{0.5}Na_{0.25}K_{0.25}Fe_{0.5}Nb_{0.5}O_3$. 12 K pattern intensity has been scaled down to match the intensities of the other temperature points that were taken with shorter scan times. Data is offset for clarity.*

The lattice parameter and cell volume plots are shown in *figure 4.21* for the NKNO sample and show the same trends observed previously. Unfortunately, a clear trend in the tetragonality with

temperature cannot be seen in the LT XRD for NNO, KNO and NKNO as shown in appendix *tables A2.2-A2.4*. This would likely require a low temperature powder neutron experiment to reach a conclusion.

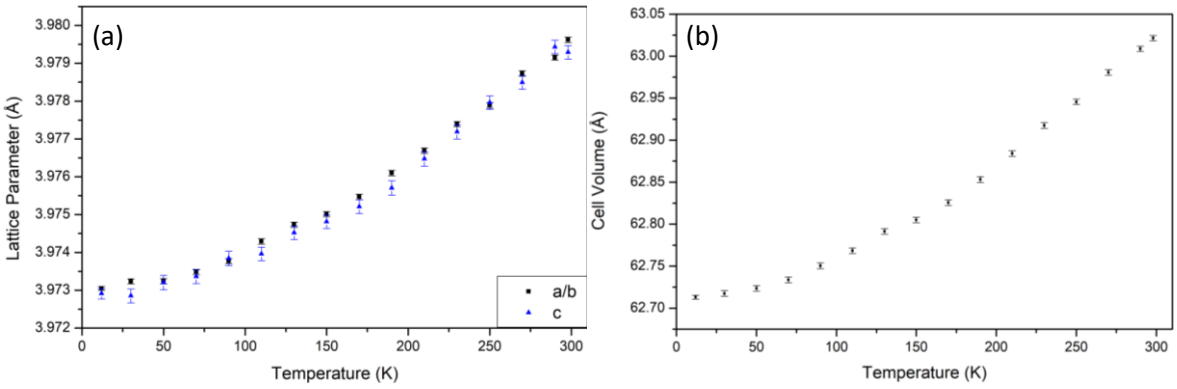

Figure 4.21: *(a) Lattice parameter plot for temperatures between 12 K and 298 K, (b) Cell volume plot for temperatures between 12 K and 298 K extracted from the Rietveld refinement of LT XRD data collected for $Bi_{0.5}Na_{0.25}K_{0.25}Fe_{0.5}Nb_{0.5}O_3$.*

To determine whether the structure suggested by the LT XRD is correct and determine the temperature dependence of both the structure and diffuse scattering data were collected for the NNO50% sample at 10 K and between 300 K and 1073 K (in 50 K increments) on HRPD. The pattern collected at 10 K, shown in *figure 4.22*, is more complicated than the pattern at room temperature. The most obvious change is the addition of sharp peaks which interestingly are in similar positions to the additional peaks found in the KNO50% room temperature neutron diffraction pattern. As such these peaks can be attributed to magnetic Bragg peaks suggesting there is a magnetic phase transition occurring at a temperature between 300 K and 12 K (discussed later). There does not seem to be any change to the diffuse scattering which can still be seen in the background. These refinements confirm that a structural change does not occur between 10 K and 300 K consistent with the LT XRD data.

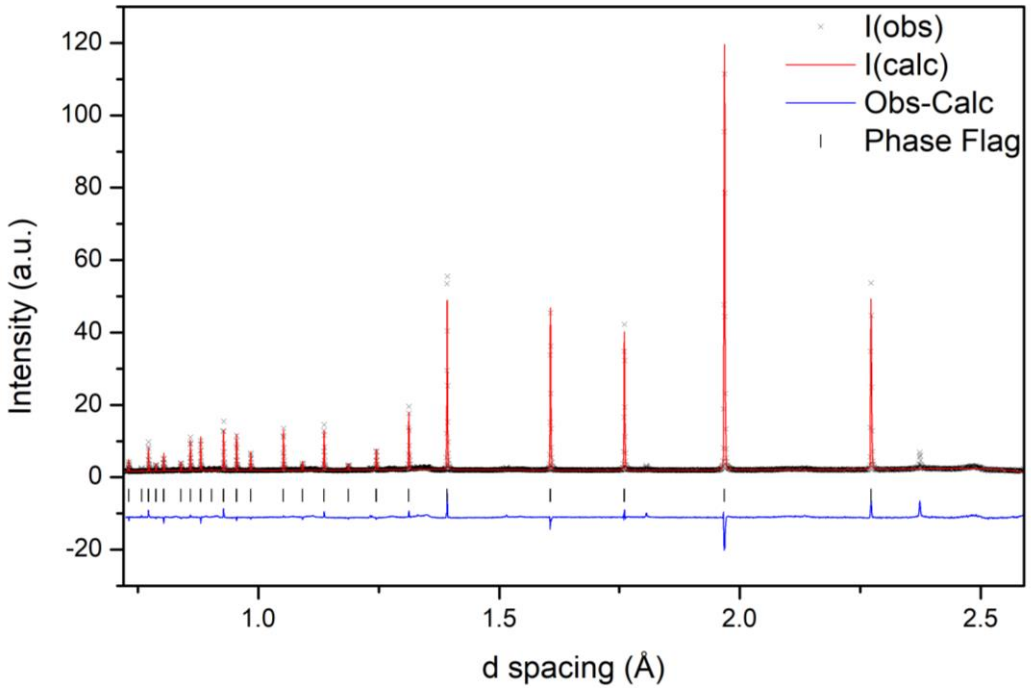

Figure 4.22: *Rietveld refinement of 10 K PND data collected for $Bi_{0.5}Na_{0.5}Fe_{0.5}Nb_{0.5}O_3$; χ^2 = 10.23, R_{wp} = 7.58% and R_p = 6.21; the black crosses represent the observed intensity, the red line represents the calculated intensity from the model, the blue line represents the difference between the observed pattern and calculated pattern and the black tick marker represents the P4mm model.*

Shown in *figure 4.23* is the Rietveld refinement fit of the *P*4*mm* model to the powder pattern collected at 1073 K (the highest temperature data was collected) which shows a good fit to the model. The diffuse scattering is no longer present in the pattern suggesting some temperature dependence of the tilt behaviour. However, this may also arise because the background has higher noise compared to the RT and LT data. In *figure 4.24* a comparison between all the neutron patterns collected across the range of temperatures is shown. Apart from characteristic shifting due to the increase in lattice parameters, expansion of the unit cell, as a function of temperature there is no obvious change in the structure. The lattice parameters and cell volume, from the *P*4*mm* model, are shown in *figure 4.25.* There is no unexpected deviation in the data to indicate a large change in structure. However, at 973 K the lattice parameters for *a*/*b* and *c* converge to a single value as seen in *figure 4.25 (a) and (c)* suggesting a transition to a cubic phase has occurred. Full refinement parameters and fits for the temperature range 293 K to 1093 K can be found in appendix *table A2.6* and *figure A2.19*.

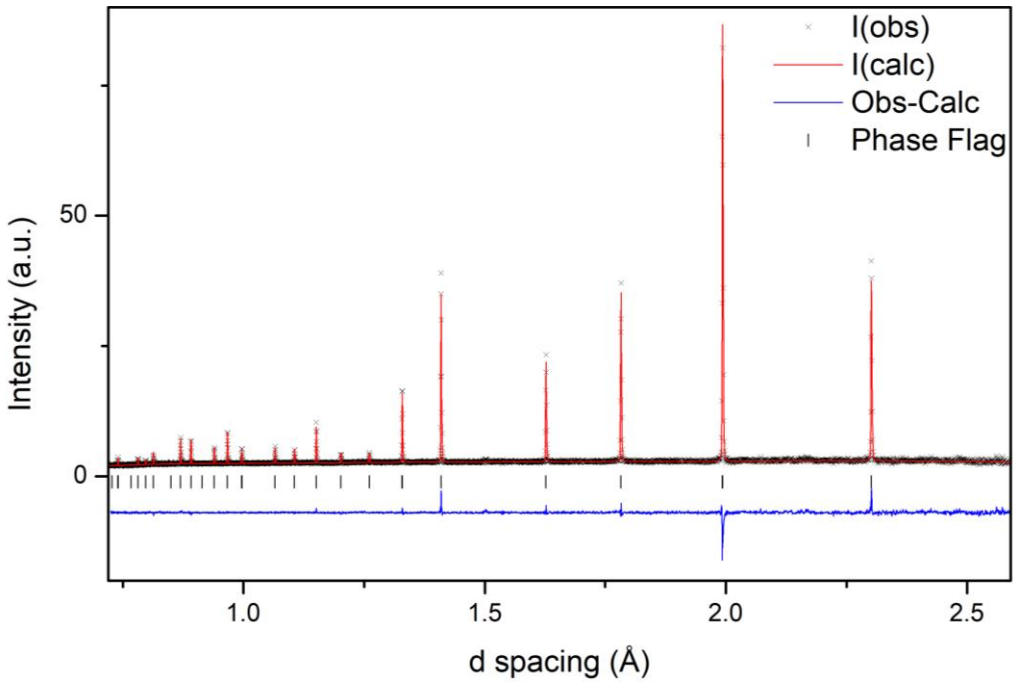

Figure 4.23: *Rietveld refinement of 1073 K PND data collected for $Bi_{0.5}Na_{0.5}Fe_{0.5}Nb_{0.5}O_3$ at 1073 K; χ^2 = 1.244*, R_{wp} = 4.59%* and R_p = 4.60*; the black crosses represent the observed intensity, the red line represents the calculated intensity from the model, the blue line represents the difference between the observed pattern and calculated pattern and the black tick marker represents the P4mm model.*Unstable refinement and was not able to converge.*

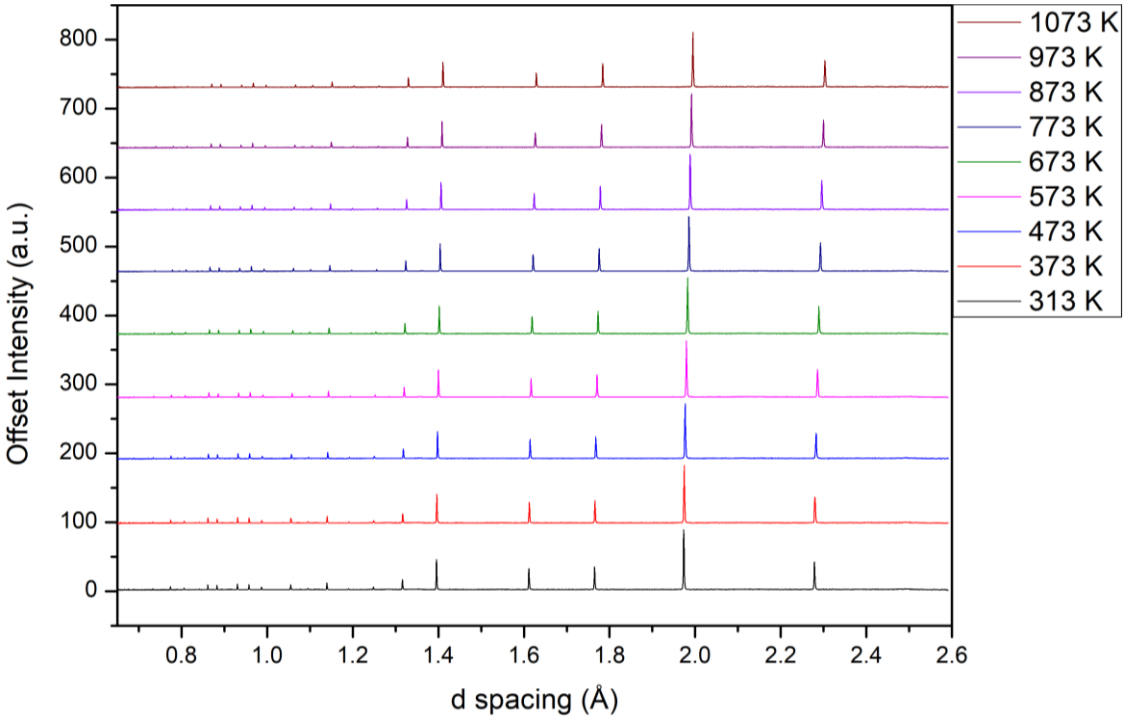

Figure 4.24: *A selection of variable temperature PND patterns collected for $Bi_{0.5}Na_{0.5}Fe_{0.5}Nb_{0.5}O_3$. Data shifted for clarity.*

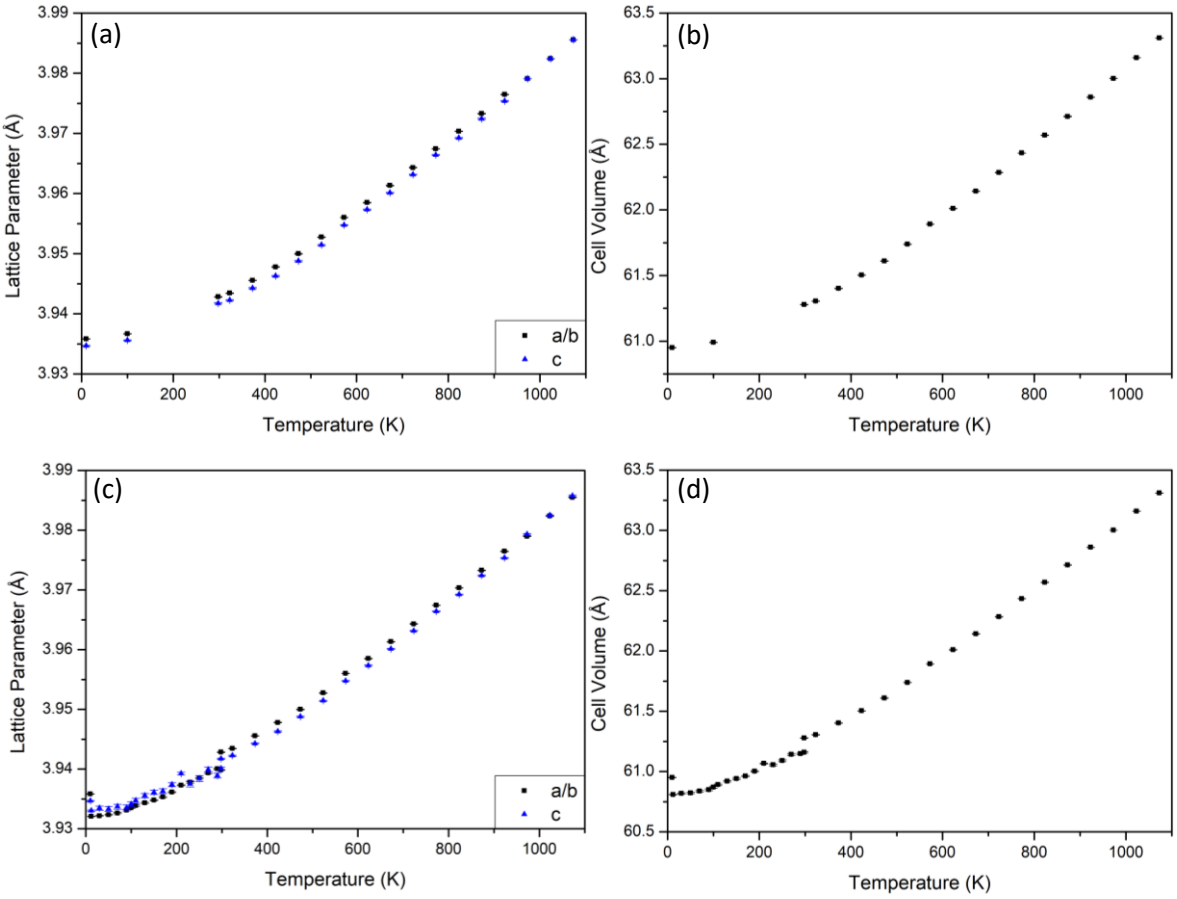

Figure 4.25: *(a) Lattice parameter plot for temperatures between 10 K and 1073 K from ND data, (b) Cell volume plot for temperatures between 10 K and 1073 K from ND data, (c) Lattice parameter plot for temperatures between 10 K and 1073 K from ND and LTXRD data, (d) Cell volume plot for temperatures between 10 K and 1073 K from ND and LTXRD data extracted from the Rietveld refinement of diffraction data collected for* $Bi_{0.5}Na_{0.5}Fe_{0.5}Nb_{0.5}O_3$

For a structure to remain polar the structure needs to remain non-centrosymmetric, i.e. that there is an element of distortion present through the *A* and *B* crystallographic sites. Shown in *figure 4.26* are the measure of displacement found on the *A* and *B* sites (based on U_{iso} and bond length values). In general, it can be seen that the change in temperature leads to a change in this displacement. In *figure 4.26 (a)* there seems to be a general increase in the U_{iso} with temperature until 920 K. At 920 K a drop is seen which then stabilises which may suggest a phase transition, consistent with the trend seen in the lattice parameters. This also seems to be reflected in the bond length data shown in *figure 4.26 (b)* which shows that the octahedral displacement distance between the *B*-site and apical oxygens reduces with an increase in temperature until at 973 K where the *B*-site cation is now equidistant between the oxygens. This would suggest that a centrosymmetric structure is present which is incompatible with the *P*4*mm* setting used to refine this data. It is sensible to suggest from these data that a subtle phase transition has occurred from the polar *P*4*mm* space group to a non-polar space group likely tetragonal *P*4/*mmm* or cubic $Pm\bar{3}m$ at around 900 K.

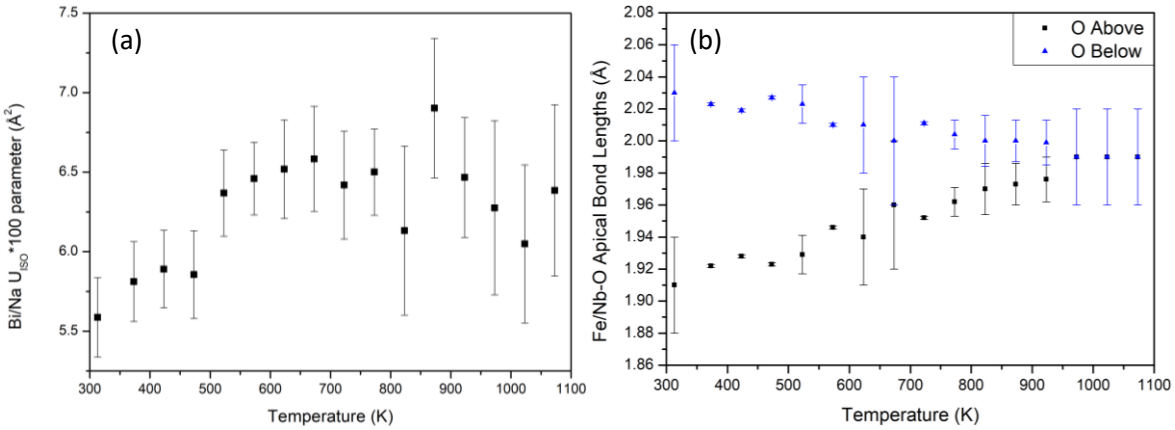

Figure 4.26: *(a) Bismuth/sodium U_{ISO} parameter as a function of temperature and (b) the distance of iron/niobium inside the octahedral cage from the oxygen atoms directly above and below as a function of temperature extracted from the Rietveld refinement of PND data collected for $Bi_{0.5}Na_{0.5}Fe_{0.5}Nb_{0.5}O_3$.*

To try and determine whether it is possible to distinguish between the two non-polar structures and determine the new phase, refinements were performed for the data from 973 K to 1073 K using the *P*4/*mmm* and *Pm*$\bar{3}$*m* models. The results of the refinements at 1073 K can be seen in *figure 4.27*. The refinement shown in *figure 4.27 (a)* displays the fit when using a cubic *Pm*$\bar{3}$*m* model (χ^2 = 1.344, R_{wp} = 4.77% and R_p = 4.81%) and *figure 4.27 (b)* displays the fit when using a tetragonal *P*4/*mmm* model (χ^2 = 1.330, R_{wp} = 4.75% and R_p = 4.76%). Both models have the oxygen set to fit the thermal parameters anisotropically. From observation it can be seen that a good degree of fit is achieved for both models. However, the *P*4/*mmm* model fits the intensities of the peaks better. The fitting statistics suggests that there is a very small difference between the two models which could be interpreted as statistically insignificant. Altogether with the consideration that the lattice parameters for the previous *P*4*mm* model were near cubic at this temperature and the data here it is likely a transition to a cubic *Pm*$\bar{3}$*m* phase has occurred. This cubic transition is further supported when investigating the change in tetragonality with temperature in the *P*4*mm* model, shown in *figure 4.28* which shows a trend towards 1.00 at 973 K. This interestingly mirrors the high temperature phase transition seen in the perovskite $BaTiO_3$[19-21]. The refinement parameters for the *Pm*$\bar{3}$*m* model to the data between 973 K and 1073 K can be found in appendix *table A2.6*.

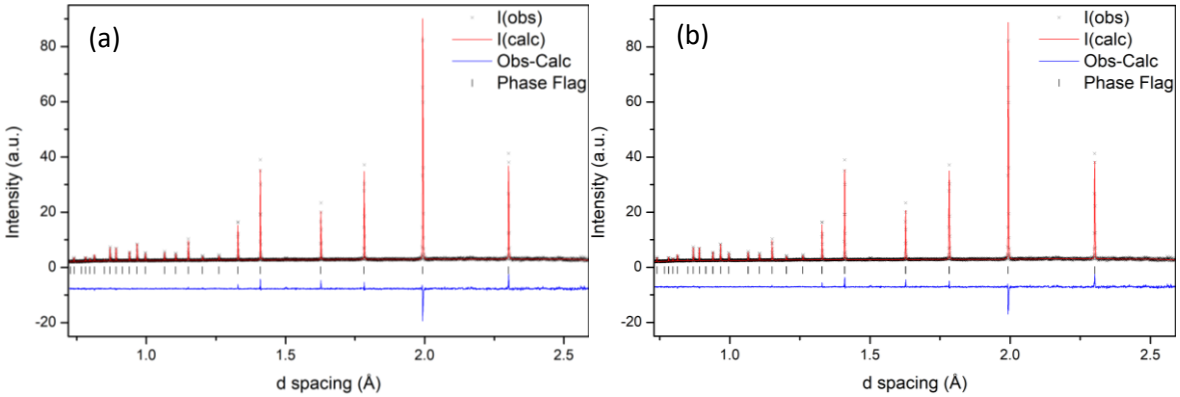

Figure 4.27: *Rietveld refinements of 1073 K PND data collected for $Bi_{0.5}Na_{0.5}Fe_{0.5}Nb_{0.5}O_3$. (a) $Pm\bar{3}m$ model, $\chi^2 = 1.344$, $R_{wp} = 4.77\%$ and $R_p = 4.81$, (b) P4/mmm model $\chi^2 = 1.330$, $R_{wp} = 4.75\%$ and $R_p = 4.76$. The black crosses represent the observed intensity, the red line represents the calculated intensity from the model, the blue line represents the difference between the observed pattern and calculated pattern and the black tick marker represents the model.*

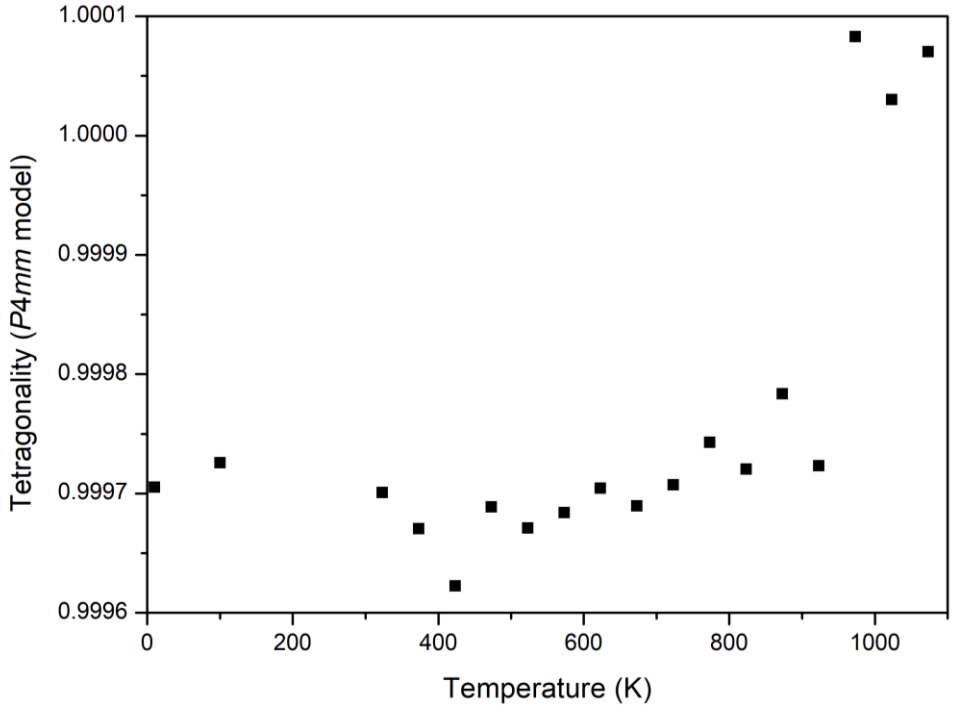

Figure 4.28: *Change in tetragonality as a function of temperature in the P4mm model extracted from Rietveld refinement of HT PND data collected for $Bi_{0.5}Na_{0.5}Fe_{0.5}Nb_{0.5}O_3$.*

4.4 Thermal Characterisation

Thermogravimetric analysis (TGA) and differential scanning calorimetry (DSC) were used to try and predict potential phase transitions of NNO50% at high temperature. The measurements were performed using a nitrogen atmosphere with a 10 K/min ramp rate from 298 K to 1170 K.

The TGA/DSC results for the NNO50% sample can be seen in *figure 4.29*. These data do not seem to indicate anything of interest as the temperature increases. The TGA plot in *figure 4.29 (a)* shows

a small decrease in mass which may be water evaporated from the sample (or crucible) and then a small 1% increase in mass likely arising as a result of fluctuations in the gas flow. The DSC plot shows a constant increase as the temperature increases with no deviation present. *Figure 4.29 (b)* shows the derivative of the DSC data, to visualise small changes. Careful analysis of these data shows weak exothermic peaks at around 920 K and ~1100K. The latter is likely to represent decomposition of the material. In contrast the peak at 920 K is consistent with the phase transition seen to occur in the PND data. This could suggest that this transition is consistent with a ferroelectric – paraelectric phase transition.

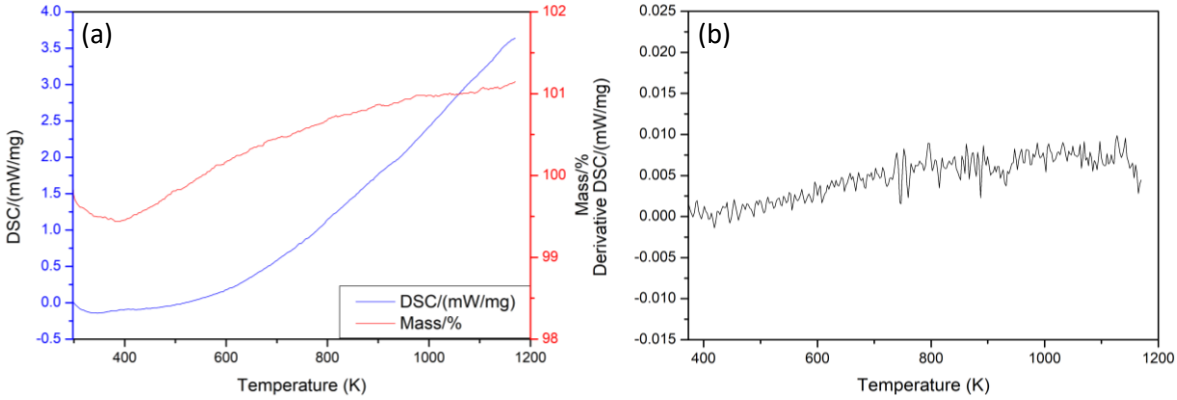

Figure 4.29: *TGA/DSC results for $Bi_{0.5}Na_{0.5}Fe_{0.5}Nb_{0.5}O_3$ showing (a) Full TGA/DSC plot from 298 K to 1170 K and (b) Derivative of DSC against temperature from 373 K to 1170 K.*

4.5 Magnetic Characterisation

Magnetic measurements were performed using a Quantum Design MPMS-7 SQUID from 12 K to a maximum of 380 K. The SQUID results for the NNO50% material can be seen in *figure 4.30*. The results in *figure 4.30 (a)* show a series of magnetic hysteresis loops collected at temperatures from 2 K to 150 K. The hysteresis loop at 2 K shows that the material shows weak hysteresis with a small coercive field suggestive of either canted antiferromagnetic or glassy-like behaviour is present. Upon increasing the temperature to 50 K the material shows no magnetic hysteresis which indicates antiferromagnetic behaviour. By 150 K the antiferromagnetic behaviour seems to be weakening further towards a paramagnetic state. This seems to be supported by the field cooled (FC) and zero field cooled (ZFC) data shown in *figure 4.30 (b)*. The FC and ZFC graph shows a kink in the data consistent with a Néel temperature of approximately 172 K consistent with the long range magnetic order seen in the PND data. At low temperature (~25 K) there is a glass-like transition which most likely arises as a result of site disorder between magnetic Fe^{3+} and non-magnetic Nb^{5+} cations.

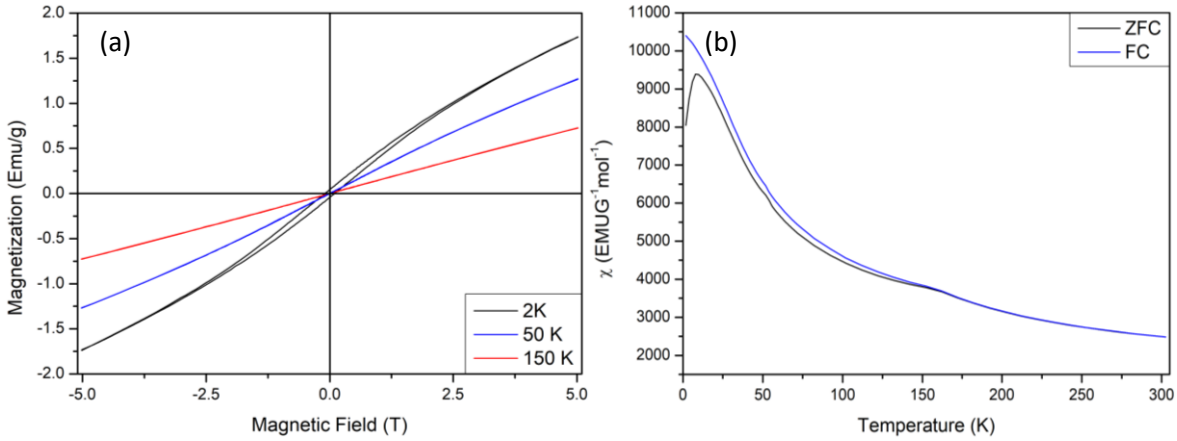

Figure 4.30: *Magnetic data collected using SQUID magnetometry for $Bi_{0.5}Na_{0.5}Fe_{0.5}Nb_{0.5}O_3$, (a) Hysteresis loops from 2 K to 150 K at fields from -5 T to 5 T and (b) Variable temperature Zero field cooled and Field cooled data at 0.1 T.*

The SQUID results for the KNO50% sample can be seen in *figure 4.31*. The results in *figure 4.31 (a)* show a magnetic hysteresis loop collected at 2 K. The hysteresis loop at 2 K shows a small coercive field similar to that seen for NNO50% and suggestive of disorder as discussed above. The field cooled (FC) and zero field cooled (ZFC) data shown in *figure 4.31 (b)* shows no evidence for a Néel transition in the temperature range studied with only a glassy-like transition observed at ~20 K consistent with NNO50%. This is consistent with the PND data collected for KNO50% which suggests the magnetic transition is above room temperature. This confirms that the placing of potassium on the *A*-site has directly led to an increase of the magnetic ordering temperature. This is confirmed by the increase in the *B*-O-*B* bond angles which are near 180° in $Bi_{0.5}K_{0.5}Fe_{0.5}Nb_{0.5}O_3$ improving the superexchange pathways and increasing the Néel temperature.

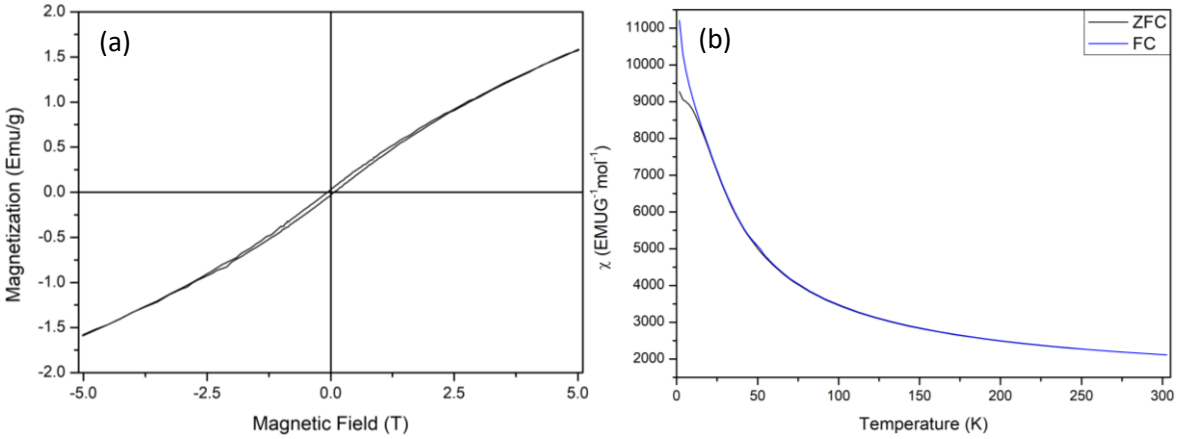

Figure 4.31: *Magnetic data collected using SQUID magnetometry for $Bi_{0.5}K_{0.5}Fe_{0.5}Nb_{0.5}O_3$, (a) Hysteresis loops at 2 K at fields from -5 T to 5 T and (b) Variable temperature Zero field cooled and Field cooled data at 0.1 T.*

The SQUID results for the NKNO sample can be seen in *figure 4.32*. These results are similar to those seen for both KNO50% and NNO50% as discussed above. Weak hysteresis is observed at 2 K which is consistent with the glassy-like transition observed at ~20 K in field cooled (FC) and zero field cooled (ZFC) data consistent with site disorder. As with NNO50% the FC and ZFC data shows a

characteristic antiferromagnetic transition with a T_N of approximately 172 K consistent with NNO50% and the bond angle data extracted for these materials from the Rietveld refinement of room temperature PND data which demonstrates the superexchange pathways are weakened on the addition of Na.

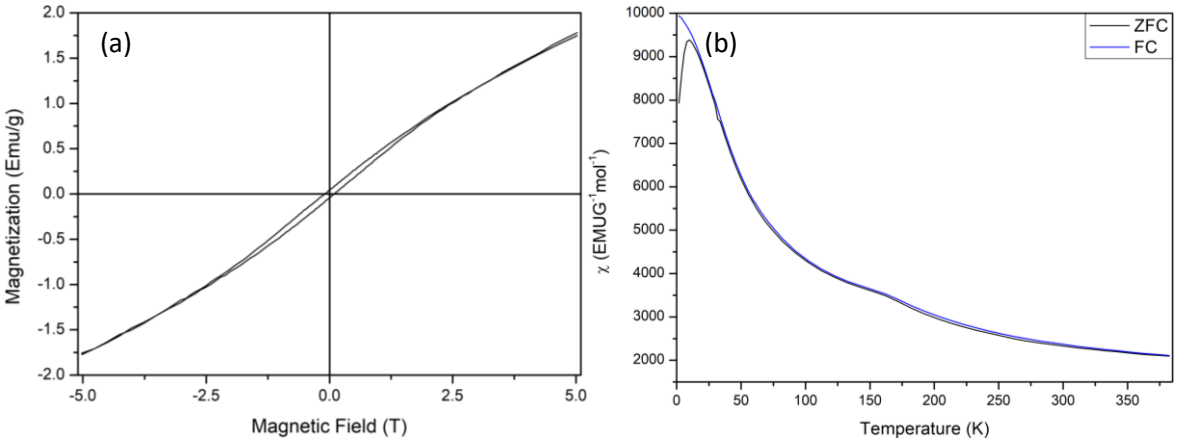

Figure 4.32: *Magnetic data collected using SQUID magnetometry for $Bi_{0.5}Na_{0.25}K_{0.25}Fe_{0.5}Nb_{0.5}O_3$, (a) Hysteresis loops at 2 K at fields from -5 T to 5 T and (b) Variable temperature Zero field cooled and Field cooled data at 0.1 T.*

4.6 Electrical Characterisation

To determine the electrical characteristics of $Bi_{0.5}Na_{0.5}Fe_{0.5}Nb_{0.5}O_3$ a setup consisting of an aixACCT easycheck 300 and a Trek 610E high voltage amplifier was used. The measurements were performed at room temperature using silver conductive paint as electrodes and by varying the amplitude and frequency.

The results for the NNO50% sample can be seen in *figure 4.33* where two pellets (with different densities and preparation routes) were measured. The first pellet to be measured was made using no sintering aids and pressed with a uniaxial press and sintered at 1193 K. The pellet was then polished by hand and coated with silver conductive paint. The result for this pellet can be seen in *figure 4.33 (a)*, the electric hysteresis loop does not fully saturate but it does seem to have a certain degree of shape to it characteristic of a '*lossy*' dielectric such that oxygen/bismuth vacancies in the structure lead to conductive behaviour[22]. Alternatively, this could also arise as result of poor pellet density as this was found to be less than 90% dense.

A modification to the pellet synthetic procedure was used based on the work by Mandal *et al*[23] which used a binder and MnO_2 to increase the density. The result from this new pellet can be seen in *figure 4.33 (b)*. Unfortunately, route did not lead to an increase in the density of the pellet and thus the hysteresis loop has a similar shape to initial pellet. It may be possible that the sintering

process in air is leading to increased oxygen vacancies and that a change to an oxygen rich environment during the sintering process may improve the pellet quality. Additionally, the use of silver paint can lead to poor connections between the electrode and the pellet which can also contribute to the '*lossy*' effects observed. Using sputter coated electrodes may improve these contacts. It is therefore, not possible to confirm or dismiss ferroelectric behaviour from these data.

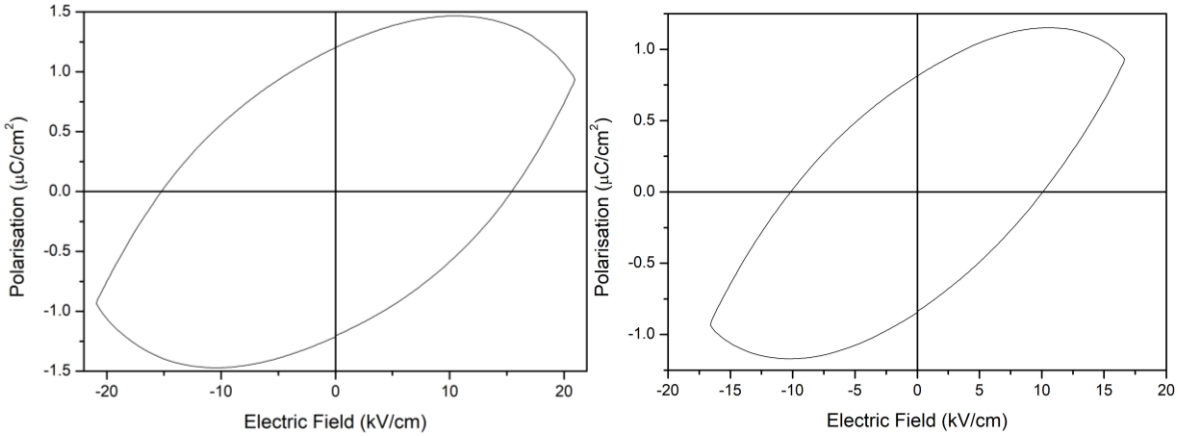

Figure 4.33: *PE loop data collected for $Bi_{0.5}Na_{0.5}Fe_{0.5}Nb_{0.5}O_3$, (a) Hysteresis loop for pure sample Frequency: 20 Hz and Amplitude: 3000 V and (b) Hysteresis loop for sample modified with 2% PVB binder and 0.2% MnO_2 Frequency: 10 Hz and Amplitude: 2000 V.*

4.7 Replacing Niobium with Tantalum on the *B*-Site

Two additional samples were synthesised using the same synthesis procedure discussed above, $Bi_{0.5}Na_{0.5}Fe_{0.5}Ta_{0.5}O_3$ and $Bi_{0.5}K_{0.5}Fe_{0.5}Ta_{0.5}O_3$, in order to potentially further investigate the role of Na and K in these materials. The sample $Bi_{0.5}Na_{0.5}Fe_{0.5}Ta_{0.5}O_3$ referred to as NTO50% was found to exhibit *P*4*mm* symmetry similar to the niobium series. The Rietveld fit to the *P*4*mm* model can be seen in *figure 4.34*. The data shows good agreement with the model with sharp peaks and low background. Full refinement parameters can be found in appendix *table A2.7*. In contrast with the $Bi_{0.9}Na_{0.1}Fe_{0.9}Ta_{0.1}FeO_3$ (NTO10%) material reported in chapter 3 this sample appears to be single phase with no second phase peaks present. It is unknown why this composition appears to be more structurally favourable than the NTO10% composition which could not be made single phase despite multiple attempts and this requires further investigation. It would be interesting for future work to determine whether this material shows similar tilt behaviour to the NNO50% sample when run on neutron diffraction instruments.

$Bi_{0.5}K_{0.5}Fe_{0.5}Ta_{0.5}O_3$, referred to as KTO50%, was also found to adopt *P*4*mm* symmetry. The Rietveld fit shown in *figure 4.35* shows good agreement with the *P*4*mm* model, however, there seems to be a very small amount of second phase present as indicated by a small peak seen at around 29° 2θ.

Unfortunately, this peak is too small to identify. Full refinement parameters can be found in appendix *table A2.7*. Similar to the NTO50% sample, the level of impurity seen in this sample is still less than that observed in the $Bi_{0.9}K_{0.1}Fe_{0.9}Ta_{0.1}FeO_3$ (KTO10%) materials discussed in chapter three which again seems to indicate this composition is more structurally stable than the KTO10% sample.

Both samples, NTO50% and KTO50%, show a contraction in the lattice parameters and unit cell volume compared to the niobium equivalents (a/b = 3.93839(5) Å, c = 3.93528(8) Å to a/b = 3.941397(31) Å, c = 3.94221(8) Å) (a/b = 3.99822(5) Å, c = 3.99884(11) Å to a/b = 4.00560(6) Å, c = 4.00029(12) Å), NNO50% and KNO50% which was also seen in chapter three. This is unexpected as Nb and Ta share the same ionic radii (0.64)[24]. In terms of tetragonality, when comparing the values obtained from the XRD lattice parameters, NTO has a slightly higher value than NNO (0.99921 to 1.00021). KTO however has a slightly lower tetragonality than KNO (1.00016 to 0.99867). The shift in the XRD patterns between NNO50%, NTO50%, KNO50% and KTO50% can be seen in *figure 4.36*. The NTO50% sample seems to have longer *B*-site to oxygen bond lengths than NNO50% but KTO50% has shorter *B*-site to oxygen bond lengths than KNO50%. Further investigation with neutron diffraction is required to determine whether this is accurate or due to XRDs limitation with detecting oxygen reliably.

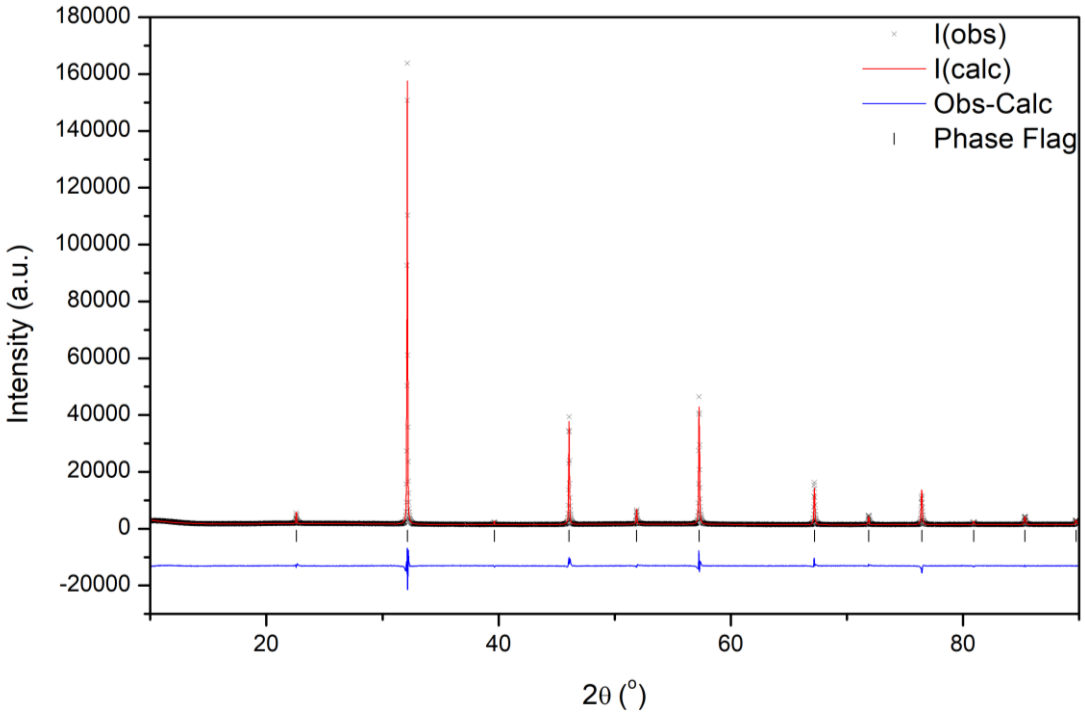

Figure 4.34: *Rietveld refinement of room temperature of PXRD data collected for $Bi_{0.5}Na_{0.5}Fe_{0.5}Ta_{0.5}O_3$; χ^2 = 7.956, R_{wp} = 6.33% and R_p = 3.94; the black crosses represent the observed intensity, the red line represents the calculated intensity from the model, the blue line represents the difference between the observed pattern and calculated pattern and the black tick marker represents the P4mm model.*

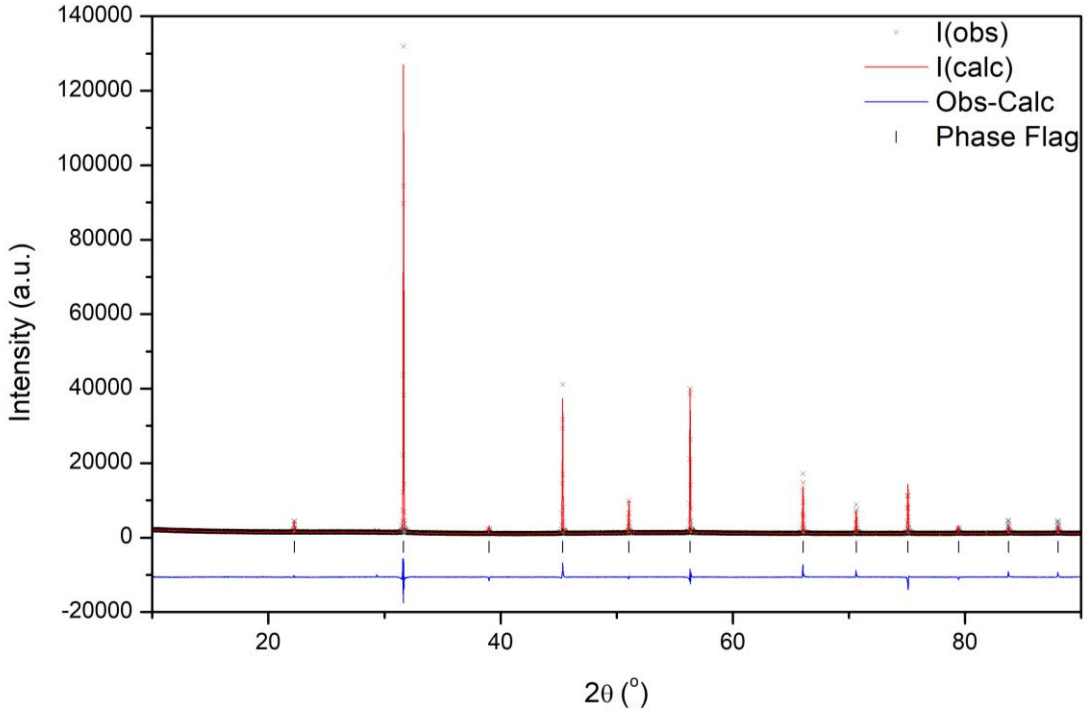

Figure 4.35: *Rietveld refinement of room temperature PXRD data collected for $Bi_{0.5}K_{0.5}Fe_{0.5}Ta_{0.5}O_3$; χ^2 = 5.773, R_{wp} = 6.19% and R_p = 3.81; the black crosses represent the observed intensity, the red line represents the calculated intensity from the model, the blue line represents the difference between the observed pattern and calculated pattern and the black tick marker represents the P4mm model.*

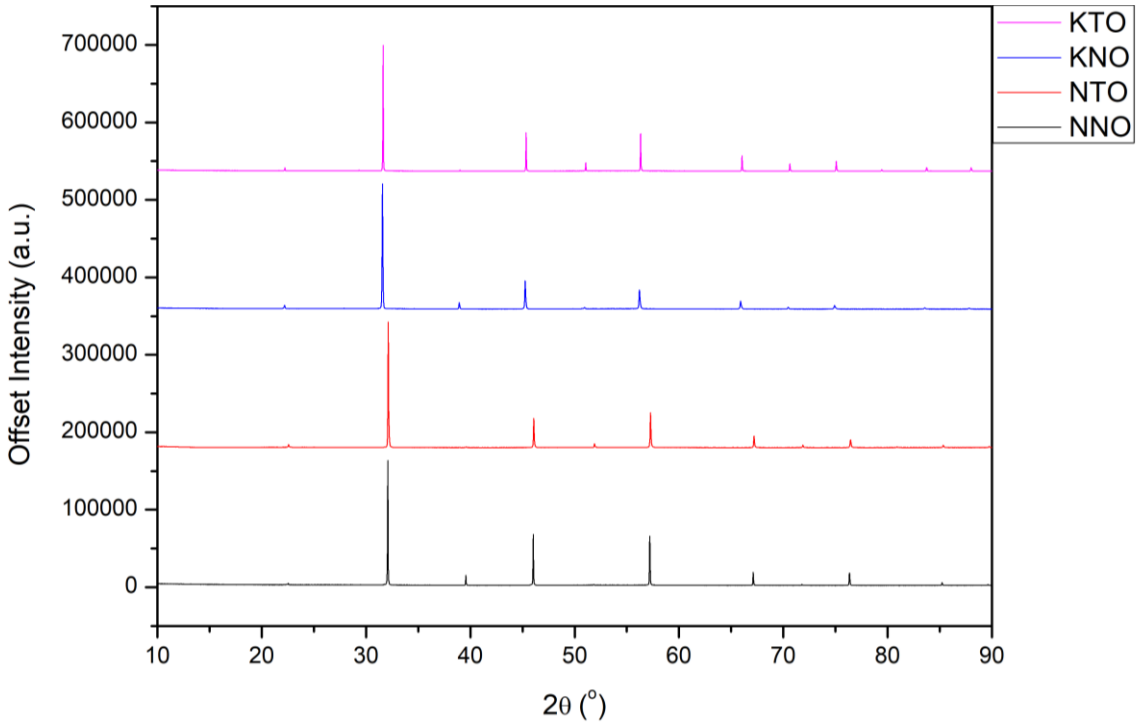

Figure 4.36: *Comparison plot of room temperature PXRD patterns collected for $Bi_{0.5}Na_{0.5}Fe_{0.5}Nb_{0.5}O_3$, $Bi_{0.5}K_{0.5}Fe_{0.5}Nb_{0.5}O_3$, $Bi_{0.5}Na_{0.5}Fe_{0.5}Ta_{0.5}O_3$ and $Bi_{0.5}K_{0.5}Fe_{0.5}Ta_{0.5}O_3$. Data shifted for clarity.*

4.8 Conclusions

This chapter reports the successful synthesis of BFO doped with NNO and KNO at x = 0.5. The samples were prepared using a modified synthesis procedure (from that used previously by Lennox *et al*[2]) which led to samples which were single phase with sharp diffraction peaks suggesting homogeneity. Low temperature and room temperature PXRD suggests that the all samples are found with polar tetragonal *P*4*mm* symmetry with no apparent phase changes observed in the temperature range of 12 K to 298 K. High temperature PND data collected for the NNO50% material suggests that there may be a subtle phase transition from the polar *P*4*mm* space group to a non-polar space group possibly either cubic $Pm\bar{3}m$ or tetragonal *P*4/*mmm*. The cubic structure was selected as the most appropriate model due to the near cubic lattice parameters seen when refining the data to the *P4mm* model and the parallels seen in the $BaTiO_3$ high temperature phase diagram.

Room temperature PND showed that the structure of NNO50% was more complicated than that found through PXRD. Extra diffuse peaks were observed that were not fit via the *P*4*mm* model which was used to fit the PXRD data. The origin of these diffuse peaks was theorised to be related to octahedral tilting as this behaviour was not observed in the PXRD data, ruling out full cation order. This led to two possible explanations for the diffuse scattering, localised *A*-site order or short-range order of NNO rich regions. Refinements with a $P2_1ma$ model indicates that short range order from NNO rich regions is the most likely explanation. However, further work is required for a definitive answer. This behaviour seems to be Na driven, as this behaviour was not found to be present in the KNO50% material.

The magnetic data suggests that NNO50% and NKNO samples at room temperature are paramagnetic with low Néel temperatures. However, KNO50% was found to be antiferromagnetic at room temperature. It was found that KNO50% had the highest T_N above room temperature which was supported by magnetic Bragg peaks in the room temperature PND. The NNO and NKNO materials saw a decrease in the T_N to around 172 K. This can only lead to the conclusion that adding K leads to an improvement of magnetic order by changing the structure so that *B*-O-*B* bond angles were around 180° improving the superexchange pathways

Attempts were made to collect polarisation hysteresis data for the NNO50% material. However, the electrical data is inconclusive due to '*lossy*' dielectric behaviour possibly due to poor pellet density, electrode-material interface effects and/or oxygen vacancies.

It is clear that these materials show interesting and complex structure-property correlations and further work is necessary to fully interpret these behaviours.

4.9 References

1 G. King, S. Garcia-Martin and P. M. Woodward, *Acta Cryst.,* 2009, **65**, 676-683 (DOI:10.1107/S0108768109032728).

2 R. C. Lennox, D. D. Taylor, L. J. Vera Stimpson, G. B. G. Stenning, M. Jura, M. C. Price, E. E. Rodriguez and D. C. Arnold, *Dalton Trans.,* 2015, **44**, 10608-10613 (DOI:10.1039/c5dt00140d).

3 A. C. Larson and R. B. Von Dreele, *General Structure Analysis System (GSAS)*, Los Alamos National Laboratory Report LAUR 86-748, 2000.

4 B. H. Toby, *J. Appl. Crystallogr.,* 2001, **34**, 210-213 (DOI:10.1107/S0021889801002242).

5 I. Levin, M. G. Tucker, H. Wu, V. Provenzano, C. L. Dennis, S. Karimi, T. Comyn, T. Stevenson, R. I. Smith and I. M. Reaney, *Chem. Mater.,* 2011, **23**, 2166-2175 (DOI:10.1021/cm1036925).

6 I. P. Raevski, S. P. Kubrin, J. -. Dellis, S. I. Raevskaya, D. A. Sarychev, V. G. Smotrakov, V. V. Eremkin and M. A. Seredkina, *Ferroelectrics,* 2008, **371**, 113-118 (DOI:10.1080/00150190802397767).

7 Y. Ma and X. Chen, *J. Appl. Phys.,* 2009, **105**, 054107 (DOI:10.1063/1.3081648).

8 P. Teslenko, A. Razumnaya, V. Ponomarenko, A. Rudskaya, A. Nazarenko, A. Anokhin, M. Avramenko, D. Levshov, M. Kupriyanov and Y. Yuzyuk, *Phys. Solid State,* 2014, **56**, 1866-1871 (DOI:10.1134/S1063783414090285).

9 S. Dash and R. N. P. Choudhary, *IEEE Trans. Dielectr. Electr. Insul.,* 2016, **23**, 3652-3658 (DOI:10.1109/TDEI.2016.005755).

10 Y. Saad, I. Álvarez-Serrano, M. L. López and M. Hidouri, *Ceram. Int.,* 2018, **44**, 18560-18570 (DOI:https://doi.org/10.1016/j.ceramint.2018.07.078).

11 K. Momma and F. Izumi, *J. Appl. Crystallogr.,* 2011, **44**, 1272-1276 (DOI:doi.org/10.1107/S0021889811038970).

12 C. J. Howard and H. T. Stokes, *Acta Cryst. B,* 2004, **60**, 674-684 (DOI:10.1107/S0108768104019901).

13 G. King and P. M. Woodward, *J. Mater. Chem.,* 2010, **20**, 5785-5796 (DOI:10.1039/B926757C).

14 K. E. Johnston, C. C. Tang, J. E. Parker, K. S. Knight, P. Lightfoot and S. E. Ashbrook, *J. Am. Chem. Soc.,* 2010, **132**, 8732-8746 (DOI:10.1021/ja101860r).

15 K. E. Johnston, J. M. Griffin, R. I. Walton, D. M. Dawson, P. Lightfoot and S. E. Ashbrook, *Phys. Chem. Chem. Phys.,* 2011, **13**, 7565-7576 (DOI:10.1039/C1CP20258H).

16 H. Qi, A. Xie, A. Tian and R. Zuo, *Adv. Energy Mater.,* 2020, **10**, 1903338 (DOI:10.1002/aenm.201903338).

17 J. P. Attfield, *Chem. Mater.,* 1998, **10**, 3239-3248 (DOI:10.1021/cm980221s).

18 P. Mandal, M. J. Pitcher, J. Alaria, H. Niu, P. Borisov, P. Stamenov, J. B. Claridge and M. J. Rosseinsky, *Nature,* 2015, **525**, 363-+ (DOI:10.1038/nature14881).

19 C. N. W. Darlington, W. I. F. David and K. S. Knight, *Phase Transit.,* 1994, **48**, 217-236 (DOI:10.1080/01411599408213215).

20 M. H. Frey and D. A. Payne, *Phys. Rev. B,* 1996, **54**, 3158-3168 (DOI:10.1103/PhysRevB.54.3158).

21 G. H. Kwei, A. C. Lawson, S. J. L. Billinge and S. W. Cheong, *J. Phys. Chem.,* 1993, **97**, 2368-2377 (DOI:10.1021/j100112a043).

22 J. Scott, *J. Phys. Condens. Matter,* 2007, **20**, 021001 (DOI:10.1088/0953-8984/20/02/021001).

23 P. Mandal, M. J. Pitcher, J. Alaria, H. Niu, P. Borisov, P. Stamenov, J. B. Claridge and M. J. Rosseinsky, *Nature,* 2015, **525**, 363-366 (DOI:10.1038/nature14881).

24 R. D. Shannon, *Acta Cryst. A,* 1976, **32**, 751-767 (DOI:10.1107/S0567739476001551).

Chapter Five: Investigation of the $BiFeO_3$-$NaNbO_3$ Phase Diagram

5.1 Introduction

As discussed in Chapter One, the literature on the $BiFeO_3$-$NaNbO_3$ solid solution is unclear and inconsistent particularly with respect to the phase transitions which occur across the series. It is suggested that in the BFO rich region that *R*3*c* symmetry is expected followed by a cubic/pseudocubic region and then finally an orthorhombic symmetry related to sodium niobate at the NNO rich region[1-9]. In this chapter we revisit the $BiFeO_3$-$NaNbO_3$ phase diagram discussing the structure-property correlations throughout the solid-solution. Powder neutron and x-ray diffraction allows us to demonstrate an *R*3*c* to *P*4*mm* to $P2_1ma$ series of phase transitions which are similar to the transitions seen in previous work on the $BiFeO_3$-$KNbO_3$ solid solution[10].

5.2 Room Temperature Structural Characterisation

To determine the phase diagram for the $BiFeO_3$-$NaNbO_3$ solid solution with the general formulae, $Bi_{1-x}Na_xFe_{1-x}Nb_xO_3$, 23 samples were synthesised from x = 0.05 to x = 0.95. *Figure 5.1* shows a selection of RT PXRD patterns across the phase diagram from x = 0.10 to x = 0.90 in 0.10 increments. From the patterns shown, it can be seen that there are at least two distinct phase transitions occurring across the composition range and these will be discussed further throughout this chapter.

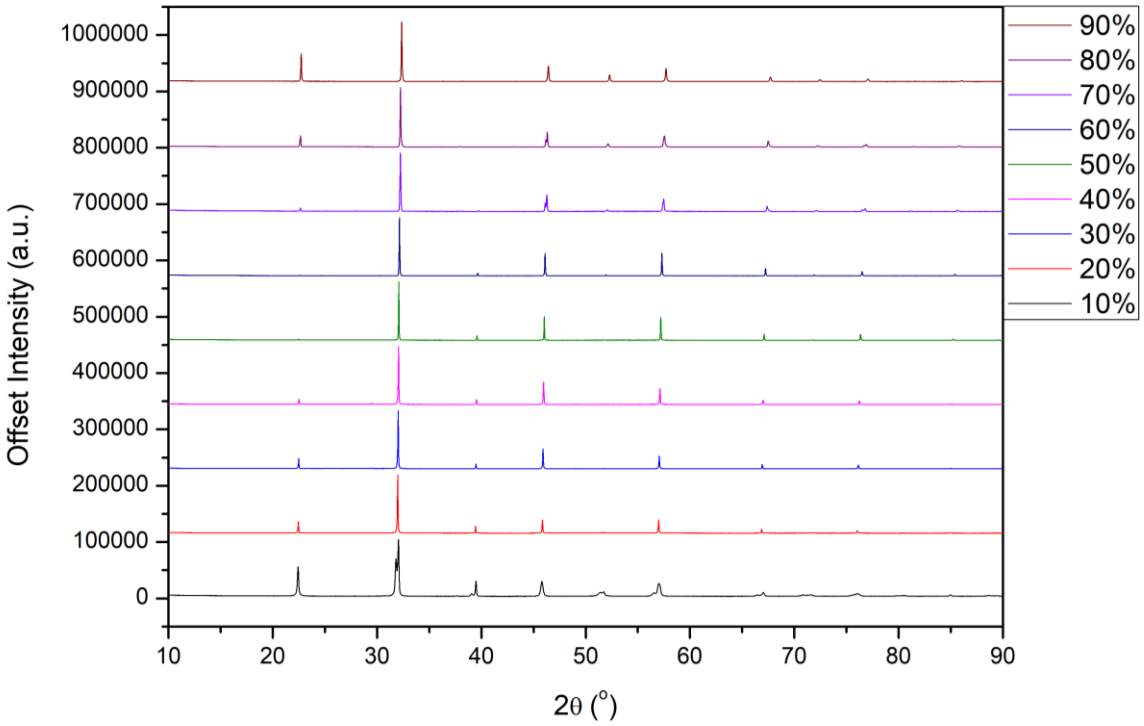

Figure 5.1: *Selection of room temperature PXRD patterns from $Bi_{0.9}Na_{0.1}Fe_{0.9}Nb_{0.1}O_3$ to $Bi_{0.1}Na_{0.9}Fe_{0.1}Nb_{0.9}O_3$. Patterns were scaled to match intensity and offset for clarity.*

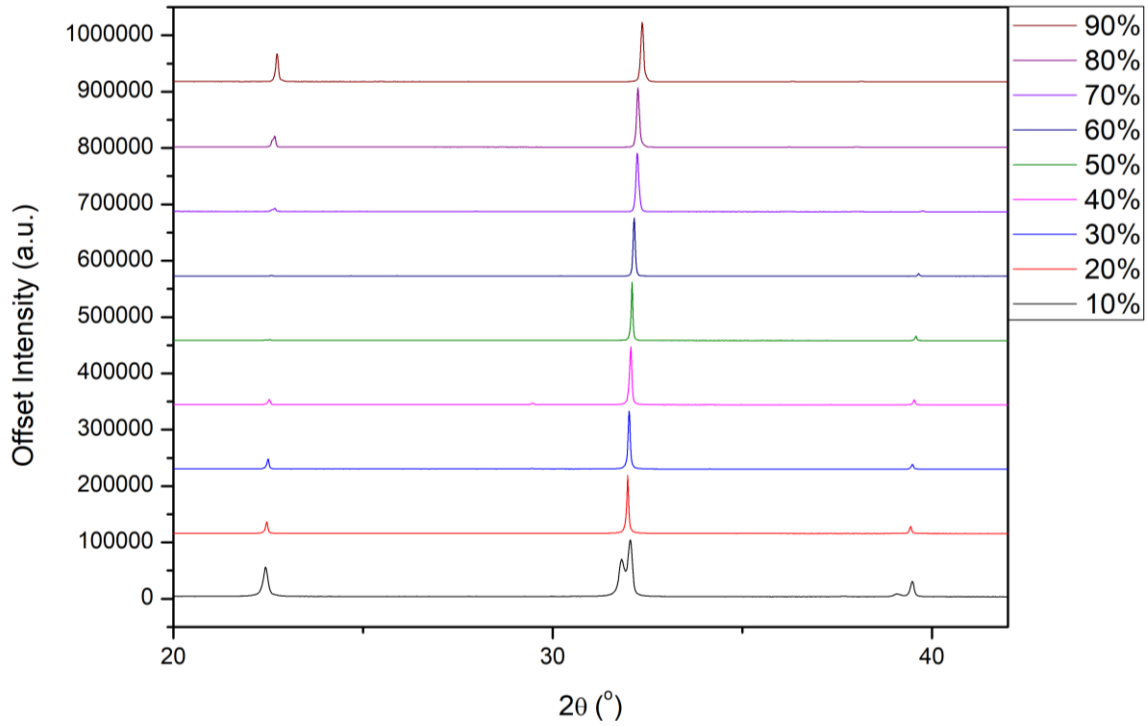

Figure 5.2: *Selection of room temperature PXRD patterns from $Bi_{0.9}Na_{0.1}Fe_{0.9}Nb_{0.1}O_3$ to $Bi_{0.1}Na_{0.9}Fe_{0.1}Nb_{0.9}O_3$, focusing on region 2ϑ = 20-42.Patterns were scaled to match intensity and offset for clarity.*

The first phase region is found from $x = 0.05$ to $x = 0.10$. The RT PXRD patterns can be seen in *figure 5.*3. The patterns show that all three samples consist of the same phase as shown by the similarities in peak structure. However, as the amount of $NaNbO_3$ (NNO) increases it can be seen that there are changes to the peak shapes. This is most obviously seen in the $x = 0.10$ material where the split peaks have begun to merge due to the change in the size of the unit cell. It can be seen from the Rietveld refinement data (discussed in more detail below) shown in Appendix *Table A3.1* that the *c* direction in the unit cell contracts greatly across this composition range. From this information it is likely that the phase is the BFO parent *R*3*c* phase consistent with the discussion presented in chapter 3 for $Bi_{0.9}Na_{0.1}Fe_{0.9}Nb_{0.1}O_3$.

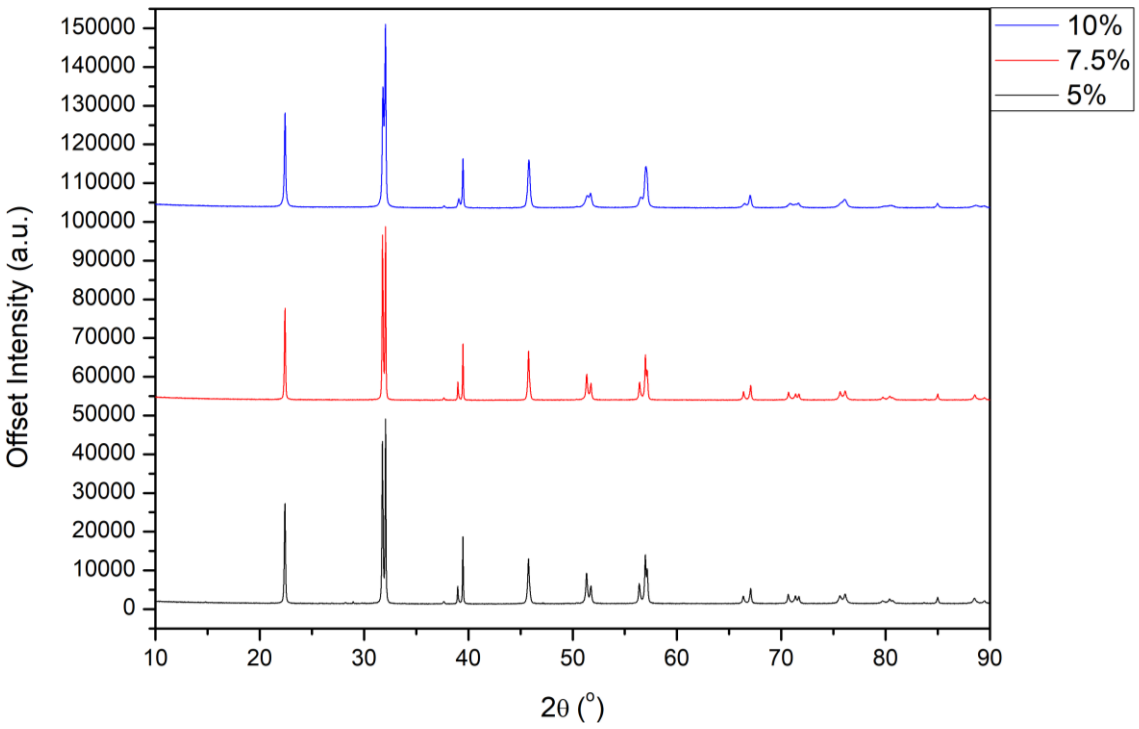

Figure 5.3: *Room temperature PXRD patterns from $Bi_{0.95}Na_{0.05}Fe_{0.95}Nb_{0.05}O_3$ to $Bi_{0.9}Na_{0.1}Fe_{0.9}Nb_{0.1}O_3$. Patterns were scaled to match intensity and offset for clarity.*

To confirm the phase present was in fact *R*3*c*, Rietveld refinements were carried out on the remaining two samples $x = 0.05$ and 0.075 as the results for the $x = 0.10$ sample have been reported in Chapter 3. The Rietveld refinement profiles for the $x = 0.05$ and $x = 0.075$ materials can be found in *figures 5.4 and 5.5* respectively. Both refinements show a good fit to the expected *R*3*c* symmetry. Unfortunately, a small amount of second phase is present in the $x = 0.05$ material (*figure 5.4*) which can be identified as excess bismuth oxide, used in synthesis, which was not removed through leaching. It can be observed in both patterns that there is an intensity deficit on a number of peaks which indicates that there are small changes occurring to the structure even with the addition of a small amount of NNO. Alternatively, this could also be attributed to preferred orientation suggesting possible changes in the microstructure. Full refinement parameters can be found in appendix *table A3.1*. As the amount of NNO increases the unit cell parameters change with the *a/b* parameters increasing and the *c* parameter decreasing. This variation in the *a, b and c* parameters leads to the cell volume varying by only a small amount as the increase in the *a/b* parameters is cancelled out by the decrease in the *c* parameter.

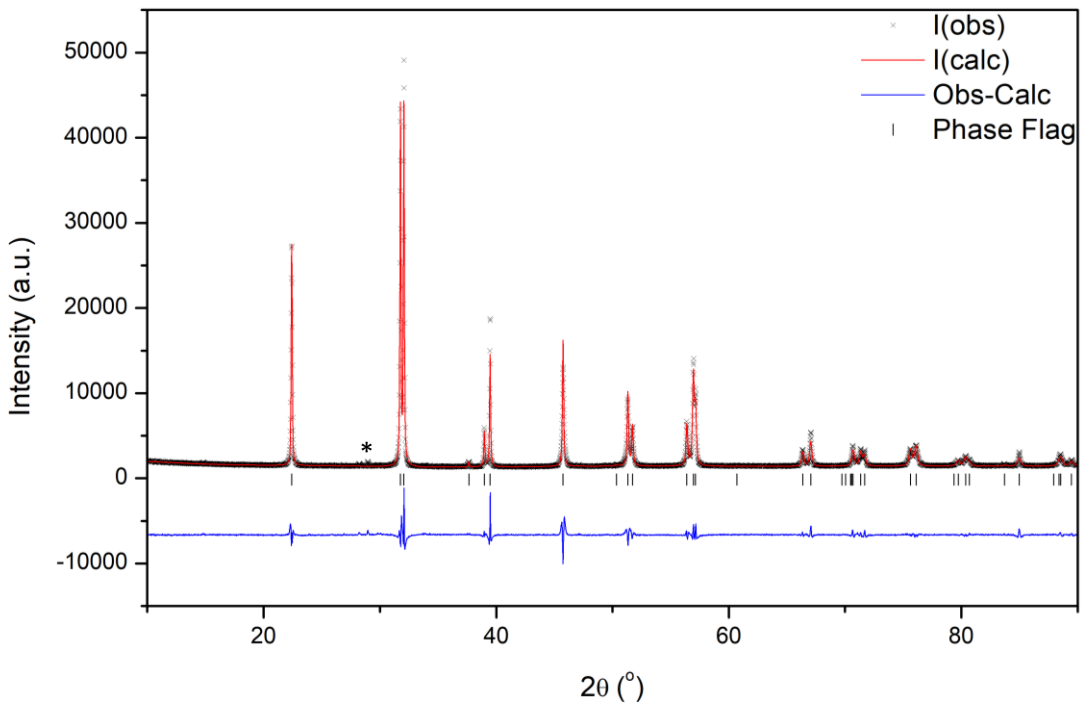

Figure 5.4: *Rietveld refinement of room temperature PXRD data collected for $Bi_{0.95}Na_{0.05}Fe_{0.95}Nb_{0.05}O_3$; $\chi^2 = 8.705$, $R_{wp} = 6.69\%$ and $R_p = 4.28$; the black crosses represent the observed intensity, the red line represents the calculated intensity from the model, the blue line represents the difference between the observed pattern and calculated pattern and the black tick marker represents the R3c model.*

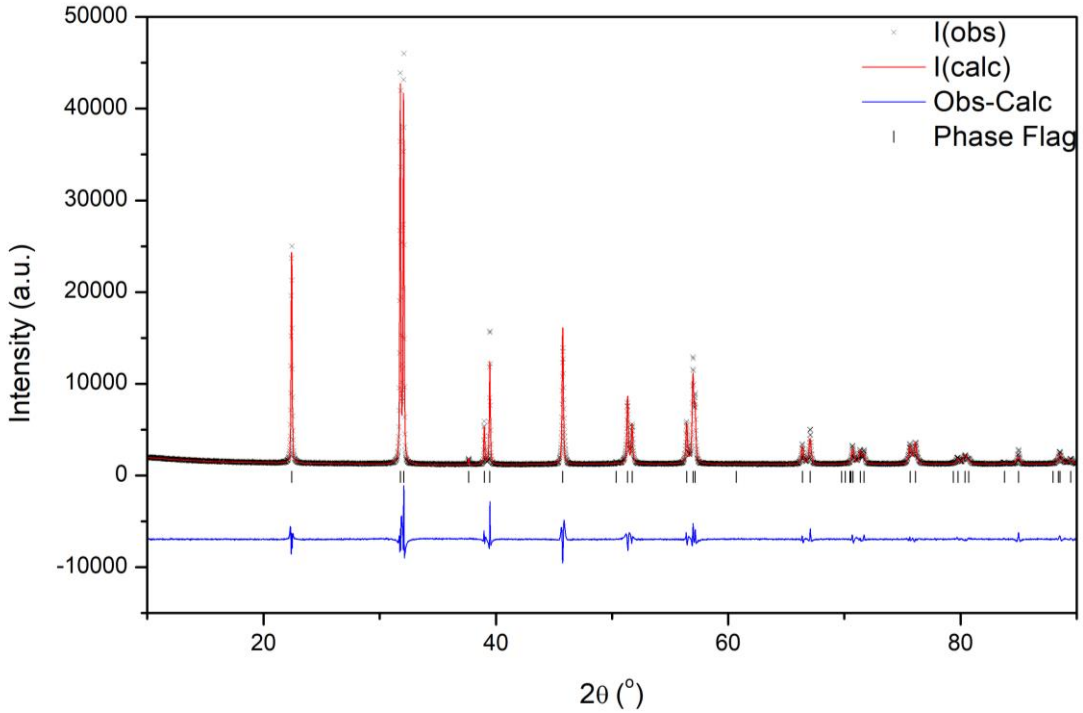

Figure 5.5: *Rietveld refinement of room temperature PXRD data collected for $Bi_{0.925}Na_{0.075}Fe_{0.925}Nb_{0.075}O_3$; $\chi^2 = 9.395$, $R_{wp} = 7.38\%$ and $R_p = 4.68$; the black crosses represent the observed intensity, the red line represents the calculated intensity from the model, the blue line represents the difference between the observed pattern and calculated pattern and the black tick marker represents the R3c model.*

The following region from the phase diagram is the *P4mm* region found between *x* = 0.175 and *x* = 0.65, the majority of the phase diagram. Shown below in *figure 5.6* are a selection of patterns across this region.

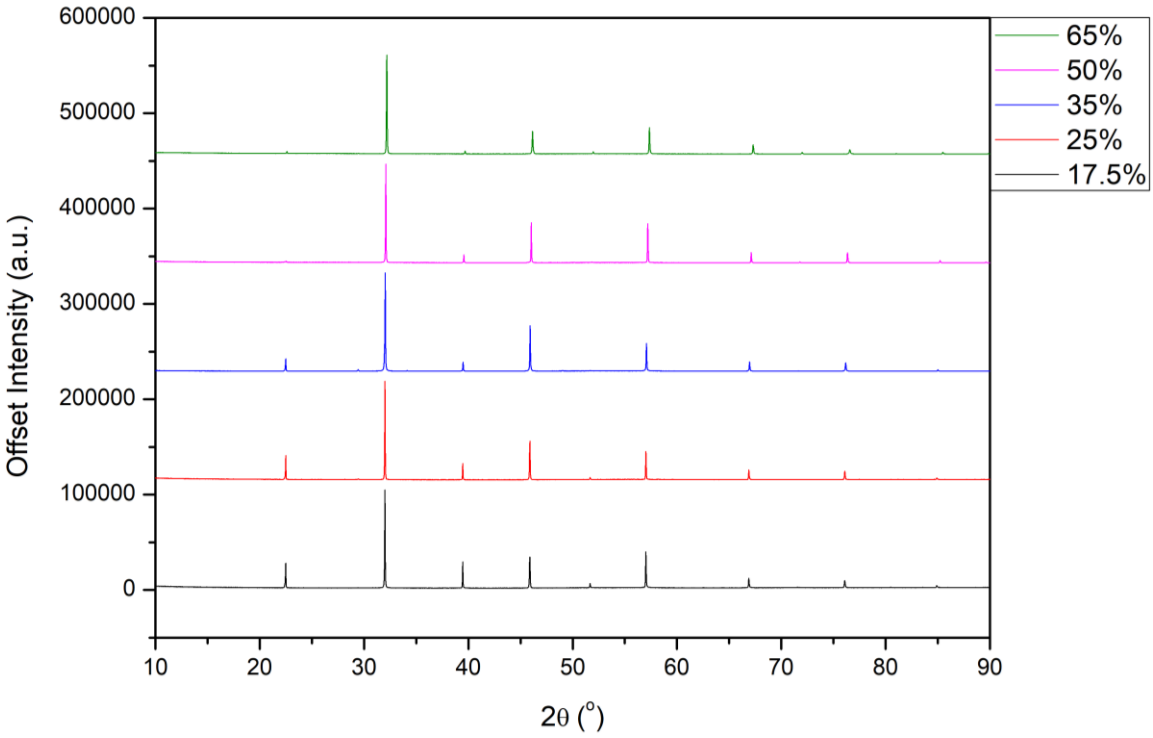

Figure 5.6: *Room temperature PXRD patterns collected for materials in the $Bi_{0.825}Na_{0.175}Fe_{0.825}Nb_{0.175}O_3$ to $Bi_{0.35}Na_{0.65}Fe_{0.35}Nb_{0.65}O_3$ range. Patterns were scaled to match intensity and offset for clarity.*

Displayed below in *figures 5.7 and 5.8* are Rietveld refinements of the samples *x* = 0.25, and 0.6 to a *P4mm* model. In all patterns peaks are sharp and the model used appears to fit the data well. Unfortunately, a small amount of second phase can be seen in the *x* = 0.25 and 0.4 patterns, which is possibly due to a small amount of either $Bi_2Fe_4O_9$ or $Bi_{24}Fe_2O_{39}$ or a bismuth iron niobium based pyrochlore impurity[11,12]. Full refinement parameters can be found in appendix *table A3.1*. All materials refined to the *P4mm* model (not included in the main body of the thesis) can be found in the appendix from *figure A3.2 to figure A3.7*.

Neutron analysis was performed on a selection of samples in this region as shown in *figure 5.9*. It was found that all samples contained the same diffuse scattering seen in the *x* = 0.5 sample discussed in chapter 4. In chapter 4 the possibility that the structure may be attempting to order on the *A* + *B* sites in this symmetry was discussed with the diffuse scattering signifying that this only occurs at short range. It was noted that long range order may not be observed since there is not a big enough size difference between Fe^{3+} and Nb^{5+} on the *B* site to promote rock salt ordering[13]. Alternatively, this behaviour could also be attributed to competing $NaNbO_3$ and $BiFeO_3$ rich regions which effect the tilts of the system locally giving rise to the diffuse scattering. The intensity of the

diffuse scattering changes across the materials within this composition range with the *x* = 0.175 noticeably displaying the weakest intensity for these peaks with the *x* = 0.25, 0.4, 0.5 and 0.6 samples displaying the highest intensities of these peaks. This is not a definitive observation as it is hard to make a comparison between the patterns due to different sample volumes with the *x* = 0.5 sample run at a different time. This observation suggests that the degree of short-range order is increasing as *x* increases. This suggests that as the content of $NaNbO_3$ increases we will eventually reach a composition where $NaNbO_3$ dominates the local tilt pattern and thus the average structure (see later discussion). Interestingly, this structural behaviour is largely tied to the symmetry change (from *R*3*c* to *P*4*mm*) as this behaviour is not (obviously) present in the earlier materials.

Rietveld refinements of the *x* = 0.25 and 0.6 samples are shown in *figures 5.10 and 5.11*. Full refinement parameters can be found in appendix *table A3.2*. The Rietveld refinements for *x* = 0.175 and 0.4 can be found in appendix *figures A3.8 and A3.9*. It can be seen that the *P*4*mm* model fits the main peaks present, however, there are problems with the fit to intensity (particularly for *x* = 0.25). Additionally, there are extra peaks seen in the *x* = 0.25 materials which are not indexed to the *P*4*mm* model. Given the quality of the fit to the PXRD data and that no extra peaks were present in these data this suggests that the extra peaks in the PND data are magnetic Bragg peaks indicative of room temperature magnetic order. These additional peaks are seen in a number of materials including the *x* = 0.175 and 0.4 materials in appendix *figures A3.8 and A3.9* and seem to weaken in intensity as the amount of NNO is increased as would be expected as the Fe^{3+} content decreases. As the NNO content is increased in the structure both the lattice parameters and cell volume contracts.

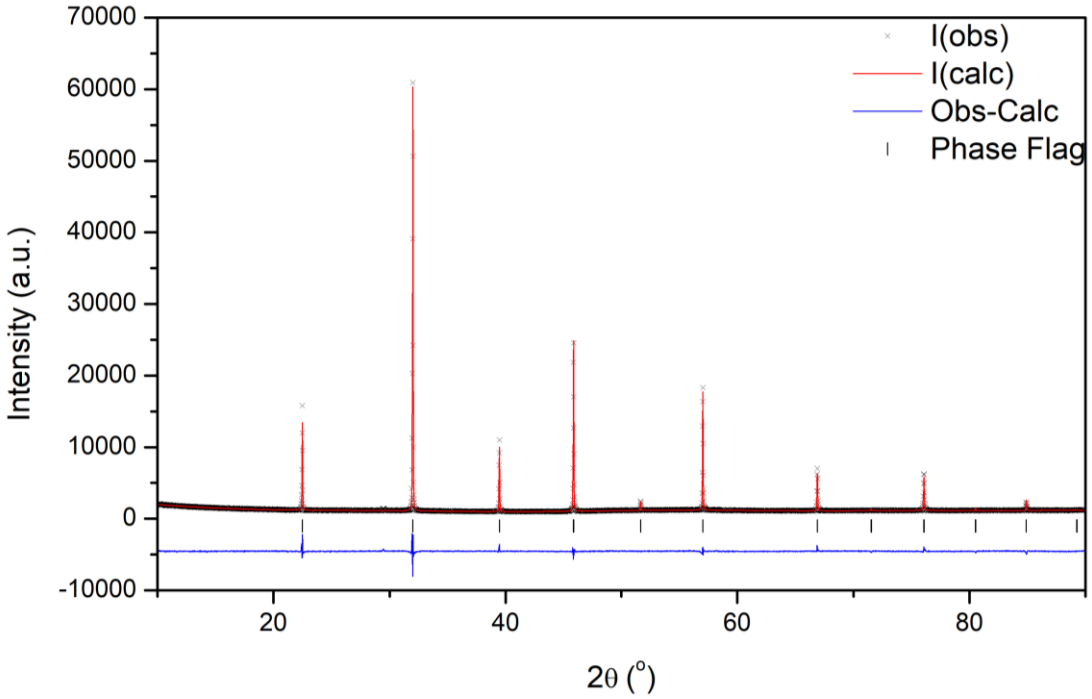

Figure 5.7: *Rietveld refinement of room temperature PXRD data collected for $Bi_{0.75}Na_{0.25}Fe_{0.75}Nb_{0.25}O_3$; $\chi^2 = 2.741$, $R_{wp} = 4.57\%$ and $R_p = 3.21$; the black crosses represent the observed intensity, the red line represents the calculated intensity from the model, the blue line represents the difference between the observed pattern and calculated pattern and the black tick marker represents the P4mm model.*

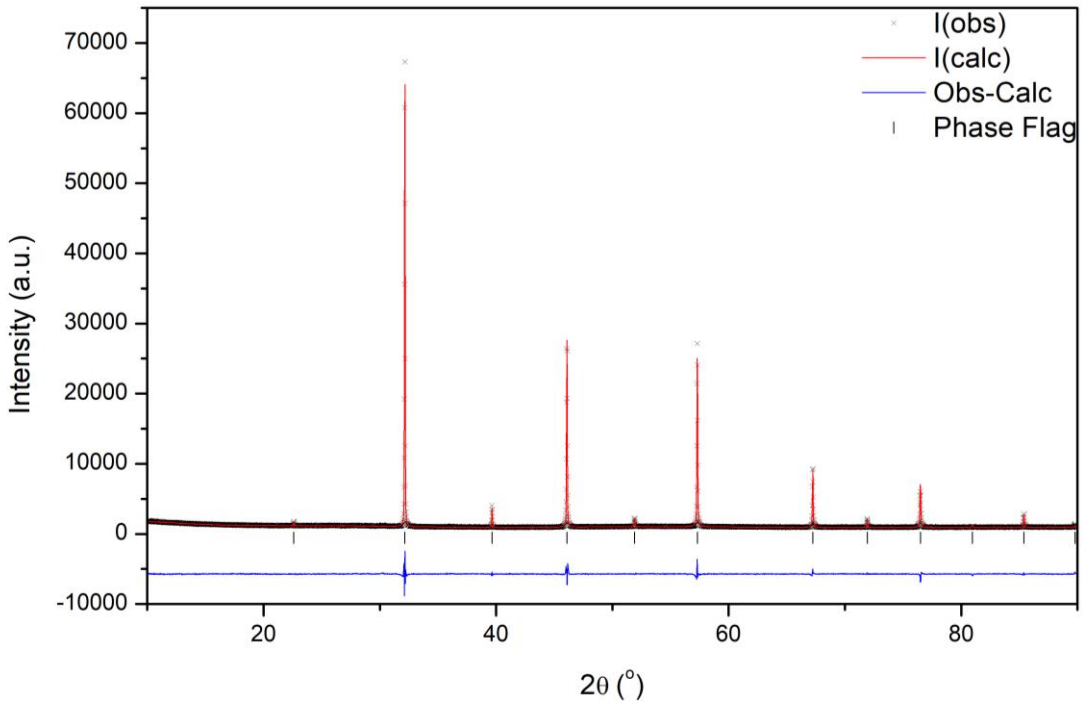

Figure 5.8: *Rietveld refinement of the room temperature PXRD data collected for $Bi_{0.4}Na_{0.6}Fe_{0.4}Nb_{0.6}O_3$; $\chi^2 = 2.974$, $R_{wp} = 4.93\%$ and $R_p = 3.44$; the black crosses represent the observed intensity, the red line represents the calculated intensity from the model, the blue line represents the difference between the observed pattern and calculated pattern and the black tick marker represents the P4mm model.*

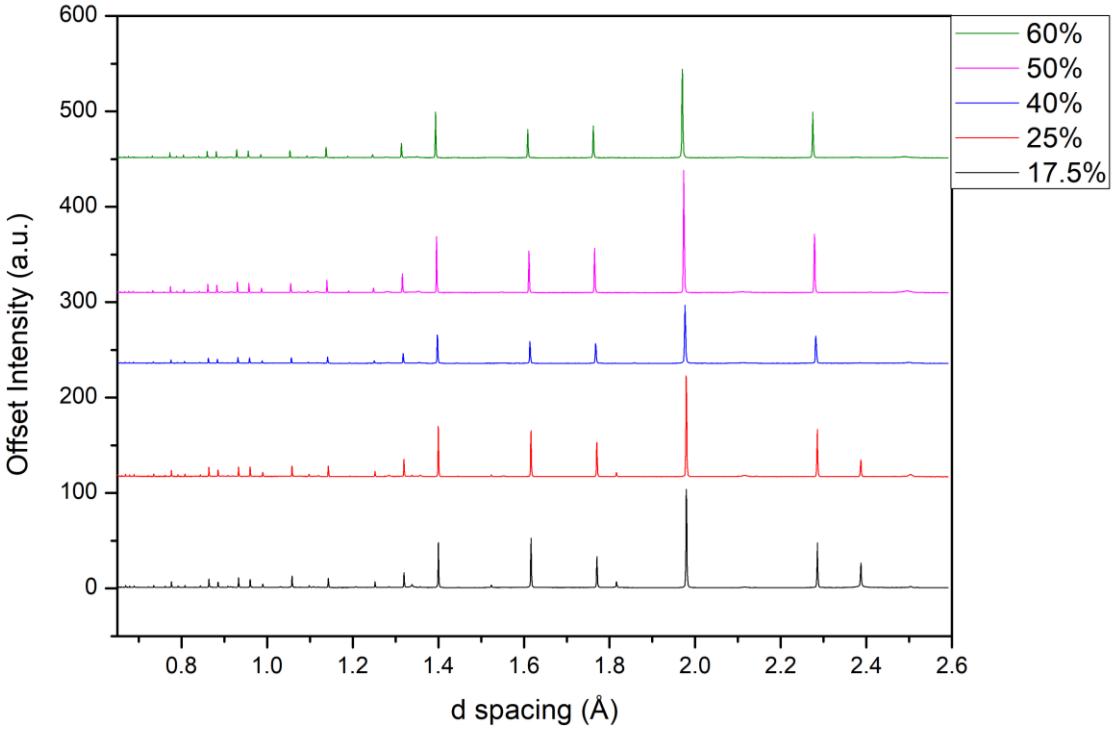

Figure 5.9: *Room temperature PND patterns collected on the HRPD beamline for compositions between $Bi_{0.825}Na_{0.175}Fe_{0.825}Nb_{0.175}O_3$ to $Bi_{0.4}Na_{0.6}Fe_{0.4}Nb_{0.6}O_3$. Note patterns are shifted for clarity.*

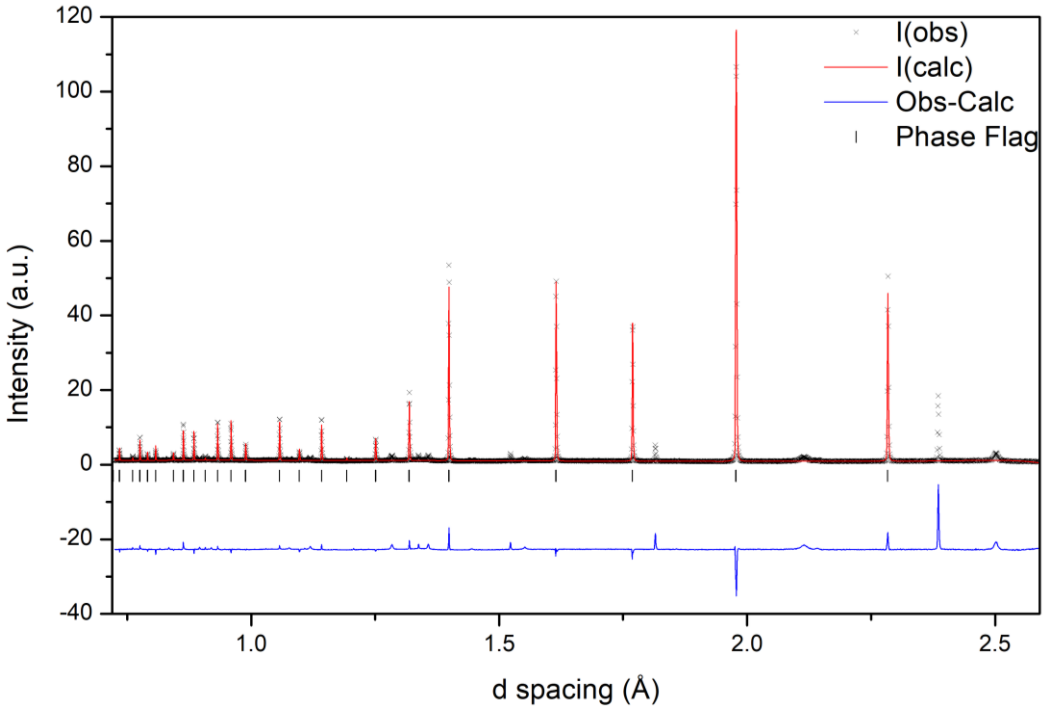

Figure 5.10: *Rietveld refinement of room temperature PND data collected for $Bi_{0.75}Na_{0.25}Fe_{0.75}Nb_{0.25}O_3$; $\chi^2 = 24.64$, $R_{wp} = 12.72\%$ and $R_p = 10.80$; the black crosses represent the observed intensity, the red line represents the calculated intensity from the model, the blue line represents the difference between the observed pattern and calculated pattern and the black tick marker represents the P4mm model.*

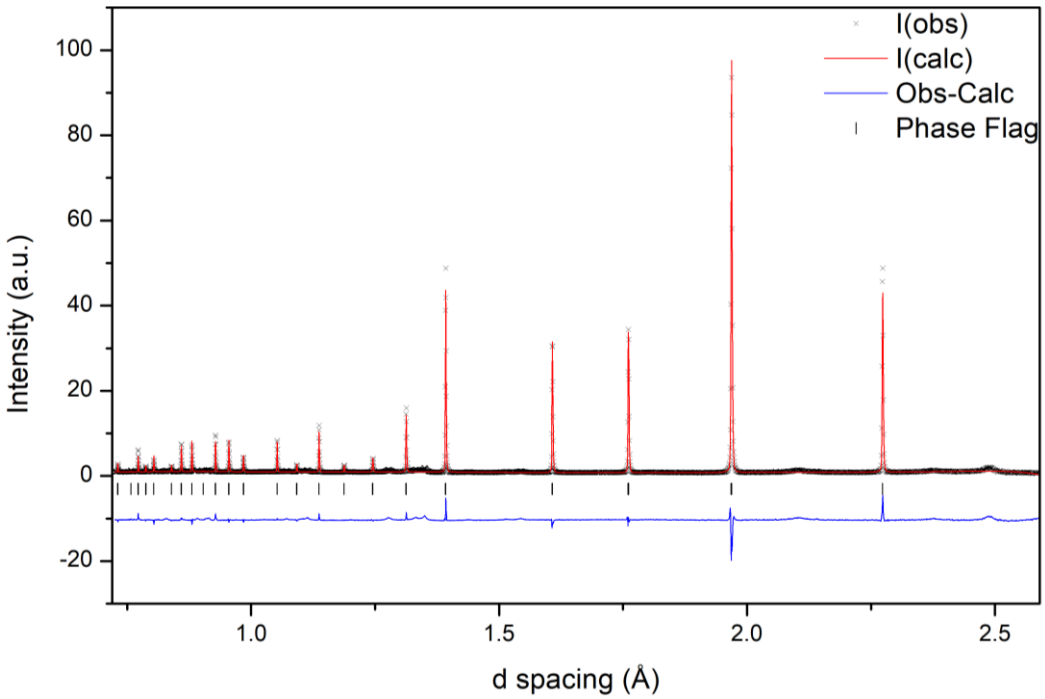

Figure 5.11: *Rietveld refinement of room temperature PND data collected for $Bi_{0.4}Na_{0.6}Fe_{0.4}Nb_{0.6}O_3$; χ^2 = 17.41, R_{wp} = 11.56% and R_p = 9.24; the black crosses represent the observed intensity, the red line represents the calculated intensity from the model, the blue line represents the difference between the observed pattern and calculated pattern and the black tick marker represents the P4mm model.*

At compositions between *x* = 0.1 and *x* = 0.175 contributions from both the *R*3*c* and *P*4*mm* phases is observed. Shown in *figure 5.12* is a comparison between the *x* = 0.1, 0.125, 0.15 and 0.175 materials showing the changes seen in these patterns as the amount of NNO is increased. It can be seen that the peak splitting in the *x* = 0.1 sample, most obvious in the peak at 32° 2θ, disappears from *x* = 0.125. The peaks are seen to be broader in the *x* = 0.125 and 0.15 samples until at *x* = 0.175 the peaks become noticeably sharper.

Furthermore, Rietveld refinements of the *x* = 0.125 and 0.15 (shown in *figures 5.13 and 5.14*) confirms this with good fits to a dual refinement with contributions from both models. Full refinement parameters can be found in appendix *table A3.1*. The simplicity of the patterns observed would seem to be more akin to the pseudocubic *P*4*mm* cell. However, the small peak at 37.7° 2θ suggests a contribution from *R*3*c* is still present. An attempt was made to determine whether this region contained a single-phase material. However, it was not possible to find a model that acceptably fit the data and as such the mixed model was used.

Room temperature neutron diffraction on the *x* = 0.15 also found the material was multi-phase. However, efforts to refine the data to *R*3*c* and *P*4*mm* models was found to be difficult as the added magnetism from both phases made it difficult to obtain a sensible refinement (χ^2 = 30.04, R_{wp} = 13.33% and R_p = 12.64). The refinement can be found in appendix *figure A3.15 (a)*. A refinement was also made against the monoclinic *Cc* phase in appendix *figure A3.15 (b)* to determine whether

a PZT transition occurred, however, the model did not fit well (χ^2 = 24.04, R_{wp} = 11.91% and R_p = 10.88). Despite the *Cc* model presenting better fitting statistics, when compared to the mixed phase model, it was found to add an unseen shoulder to the peak at 2.28 Å not seen in the observed data.

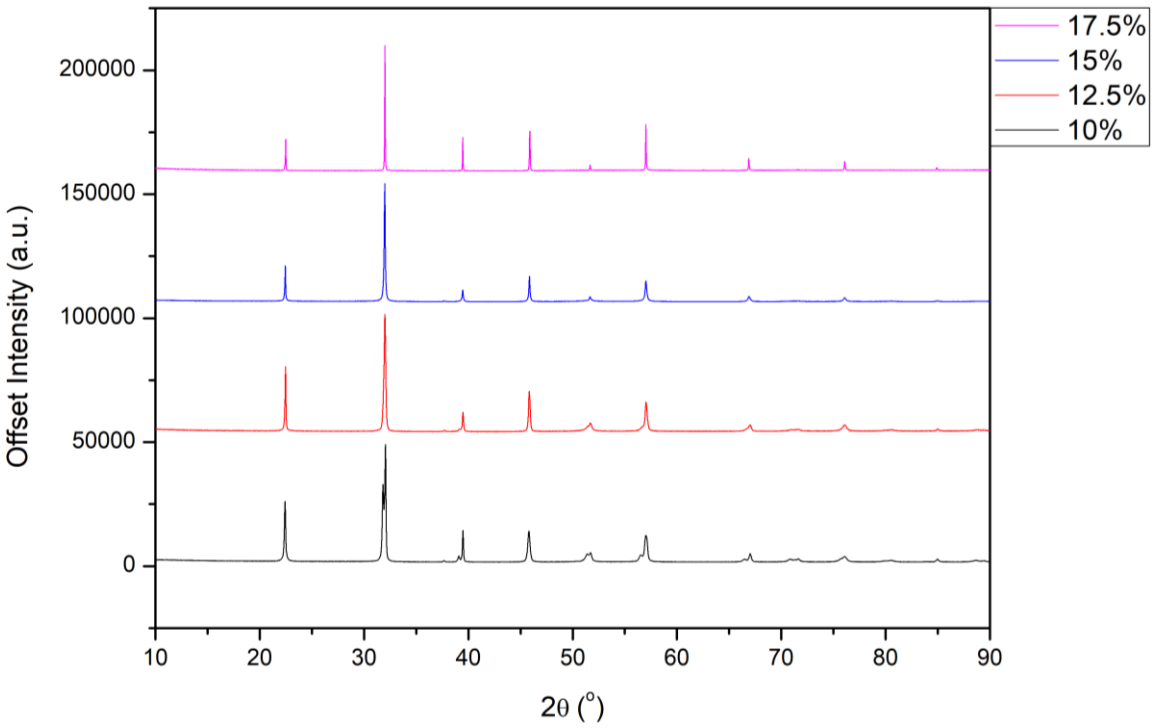

Figure 5.12: *Room temperature PXRD patterns for compositions between $Bi_{0.9}Na_{0.1}Fe_{0.9}Nb_{0.1}O_3$ and $Bi_{0.825}Na_{0.175}Fe_{0.825}Nb_{0.175}O_3$. Patterns were scaled to match intensity and shifted for clarity.*

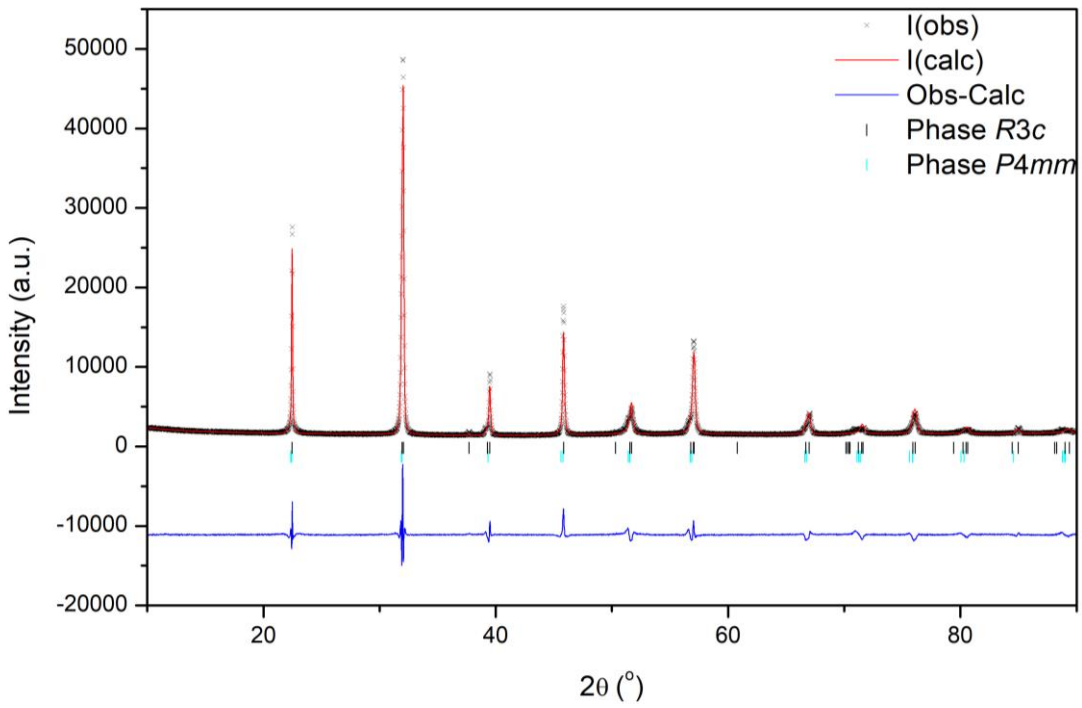

Figure 5.13: *Rietveld refinement of room temperature PXRD data collected for $Bi_{0.875}Na_{0.125}Fe_{0.875}Nb_{0.125}O_3$; χ^2 = 9.009, R_{wp} = 6.68% and R_p = 4.58; the black crosses represent the observed intensity, the red line represents the calculated intensity from the model, the blue line represents the difference between the observed pattern and calculated pattern, the black tick marker represents the R3c model and the cyan tick marker represents the P4mm model.*

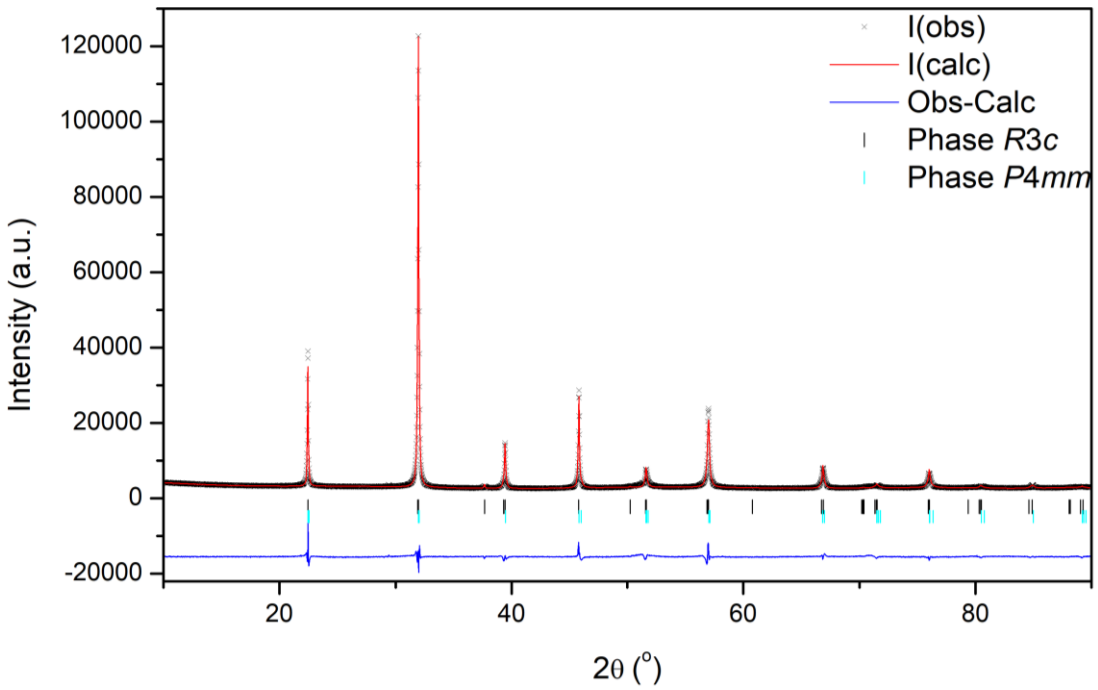

Figure 5.14: *Rietveld refinement of room temperature PXRD data collected for $Bi_{0.85}Na_{0.15}Fe_{0.85}Nb_{0.15}O_3$; χ^2 = 13.19, R_{wp} = 6.10% and R_p = 3.74; the black crosses represent the observed intensity, the red line represents the calculated intensity from the model, the blue line represents the difference between the observed pattern and calculated pattern, the black tick marker represents the R3c model and the cyan tick marker represents the P4mm model.*

The last area in the phase diagram is the $P2_1ma$ region which is the polar phase that NNO is known to crystallise in[14,15]. Shown in *figure 5.15* below are the PXRD patterns from the samples prepared at compositions between x = 0.675 and 0.95. It can be seen that as the NNO content increases certain peaks, such as the peak at 22.6° 2θ, increase in intensity. The patterns are similar to those found in the previous *P4mm* region, however, new smaller peaks are now evident (particularly between 32° 2θ and 40° 2θ) which indicate a change in symmetry occurs.

The Rietveld refinements shown in *figures 5.16* and *5.18* are of the x = 0.7 and 0.75 samples refined to an orthorhombic $P2_1ma$ model. Full refinement parameters can be found in appendix *table A3.1*. The Rietveld refinements for x = 0.675 and 0.8 can be found in appendix *figures A3.10 and A3.11*. It can be seen that in both patterns there is a good fit to the peaks present. Since, NNO is polymorphic at room temperature the second common structure, orthorhombic *Pbcm*, was also tested to determine which structure fits best[15]. It was found that the $P2_1ma$ model resulted in a better fit as the *Pbcm model* exhibits extra peaks that were not present in the patterns. The fit of the *Pbcm model* to the x = 0.7 can be found in appendix *figure A3.14*. Another possibility was the *Pm* model proposed by Baker *et al*[16] which resulted in a similar fit to the $P2_1ma$ model. However, the refinement was unstable when attempting to refine the atom positions. Neutron diffraction may help to identify which of the two models may be more sensible.

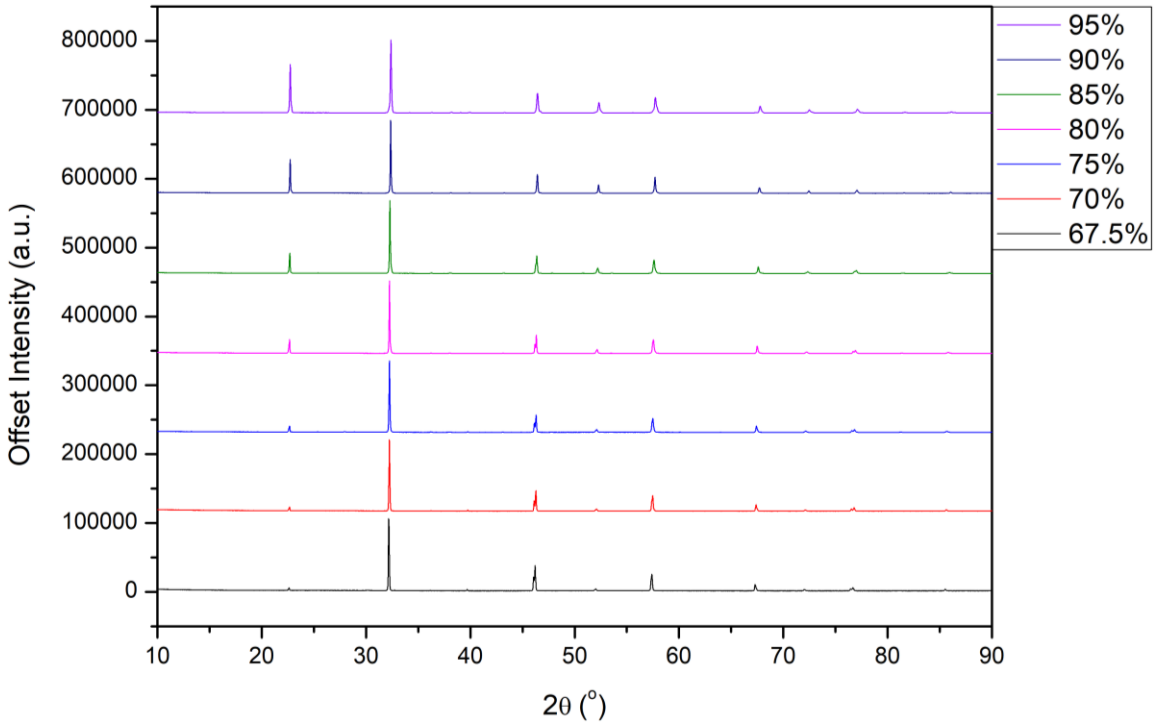

Figure 5.15: *Room temperature PXRD patterns collected at compositions between $Bi_{0.325}Na_{0.675}Fe_{0.325}Nb_{0.675}O_3$ and $Bi_{0.05}Na_{0.95}Fe_{0.05}Nb_{0.95}O_3$. Patterns were scaled to match intensity and offset for clarity.*

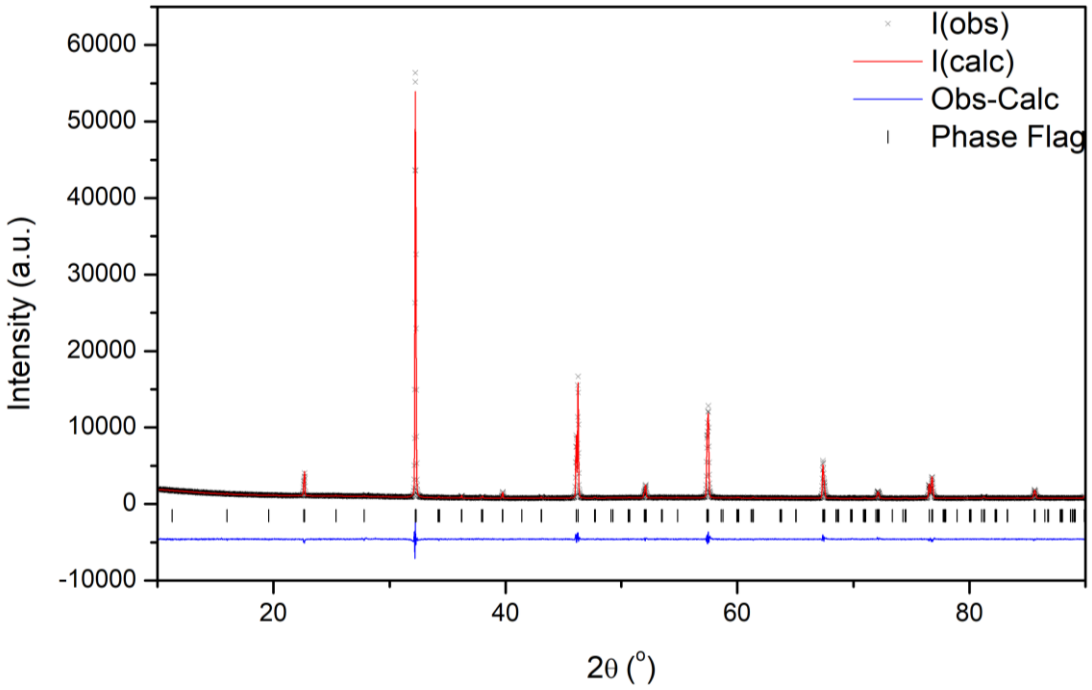

Figure 5.16: *Rietveld refinement of room temperature PXRD data collected for $Bi_{0.3}Na_{0.7}Fe_{0.3}Nb_{0.7}O_3$; $\chi^2 = 2.216$, $R_{wp} = 4.53\%$ and $R_p = 3.40$; the black crosses represent the observed intensity, the red line represents the calculated intensity from the model, the blue line represents the difference between the observed pattern and calculated pattern and the black tick marker represents the $P2_1ma$ model.*

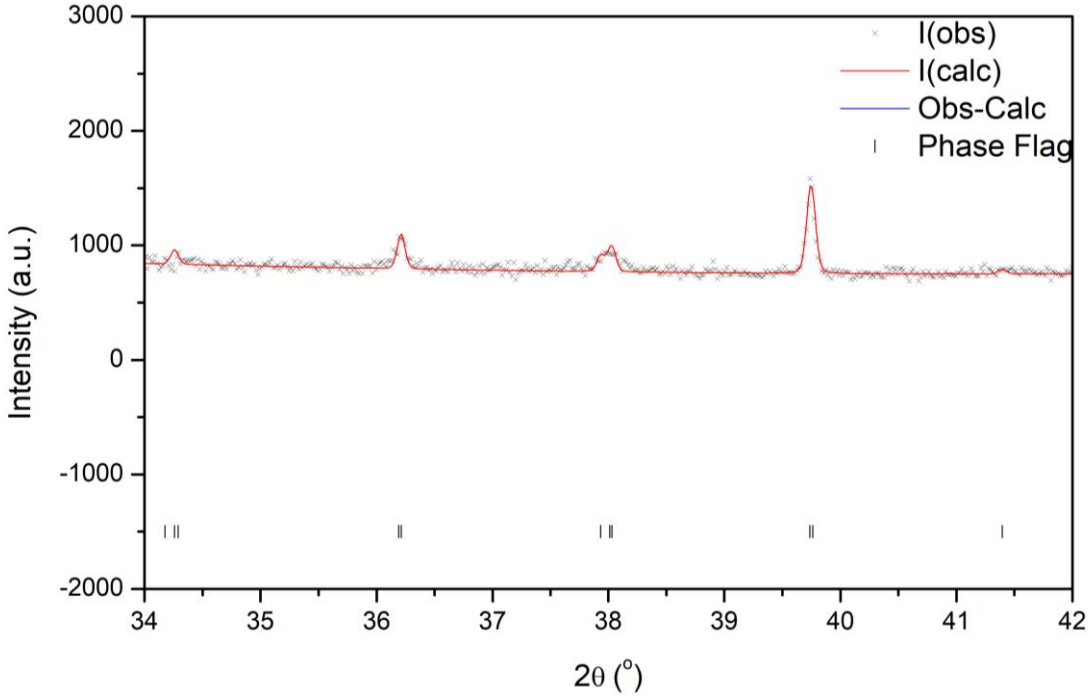

Figure 5.17: *Rietveld refinement of room temperature PXRD data collected for $Bi_{0.3}Na_{0.7}Fe_{0.3}Nb_{0.7}O_3$, focusing on region 2ϑ = 34-42.*

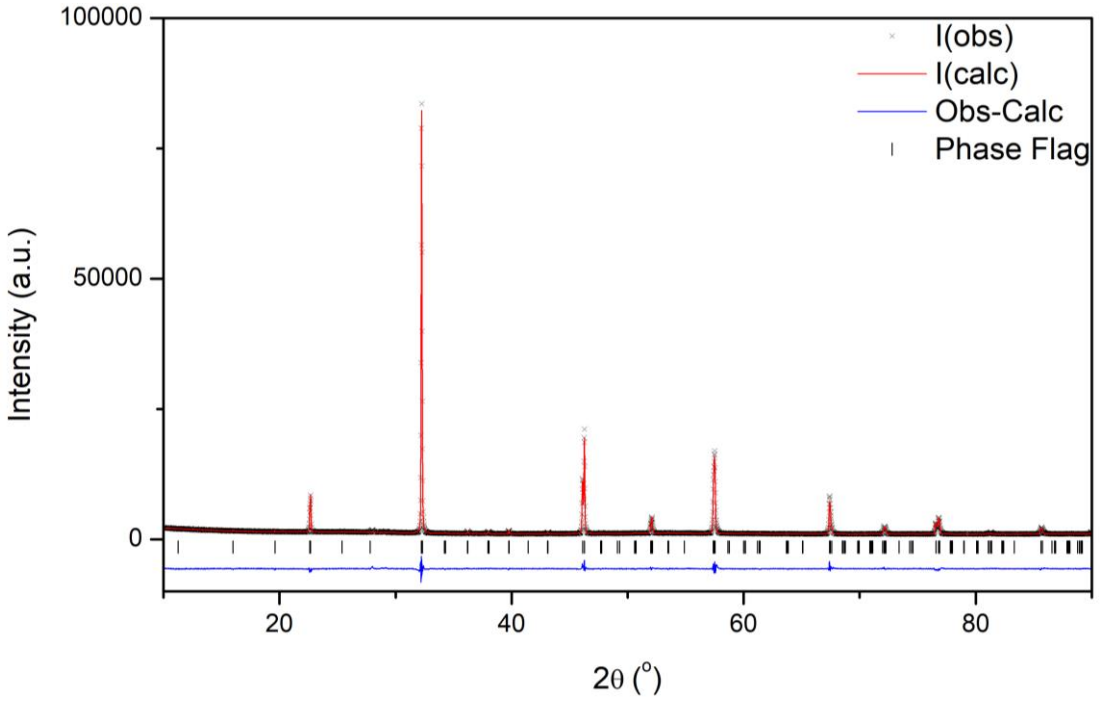

Figure 5.18: *Rietveld refinement of room temperature PXRD data collected for $Bi_{0.25}Na_{0.75}Fe_{0.25}Nb_{0.75}O_3$; χ^2 = 3.219, R_{wp} = 4.71% and R_p = 3.36; the black crosses represent the observed intensity, the red line represents the calculated intensity from the model, the blue line represents the difference between the observed pattern and calculated pattern and the black tick marker represents the $P2_1ma$ model.*

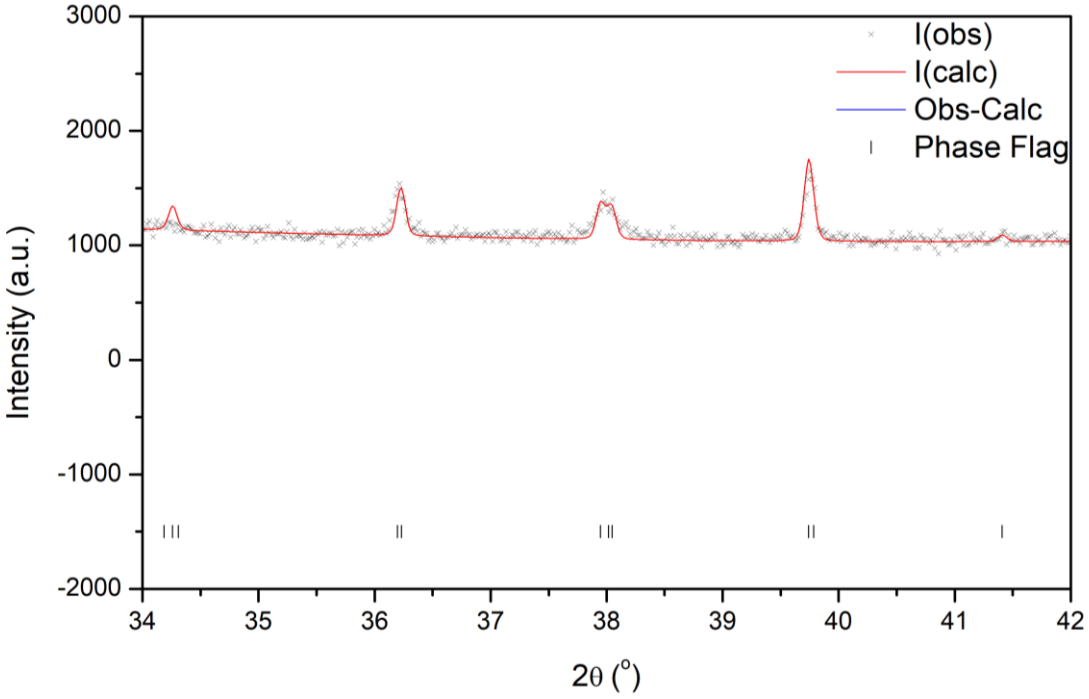

Figure 5.19: *Rietveld refinement of room temperature PXRD data collected for $Bi_{0.25}Na_{0.75}Fe_{0.25}Nb_{0.75}O_3$, focusing on region 2ϑ = 34-42.*

The Rietveld refinements of XRD data collected for the *x* = 0.85 and 0.9 samples, shown in *figures 5.20* and *5.21*, are different in that a second anti-polar *Pbcm* model is added to the refinement. Full refinement parameters can be found in appendix *table A3.1*. The Rietveld refinements for *x* = 0.95 appendix *figure A3.12*. This space group is the second phase that pure NNO can be found in due to its polymorphic nature and is typically the dominant phase for NNO synthesised via solid state synthesis[14]. This would suggest that the addition of BFO in to the NNO system is creating a bias towards the formation of the polar NNO phase. This is supported by the appearance of the *Pbcm* phase as the amount of BFO is reduced.

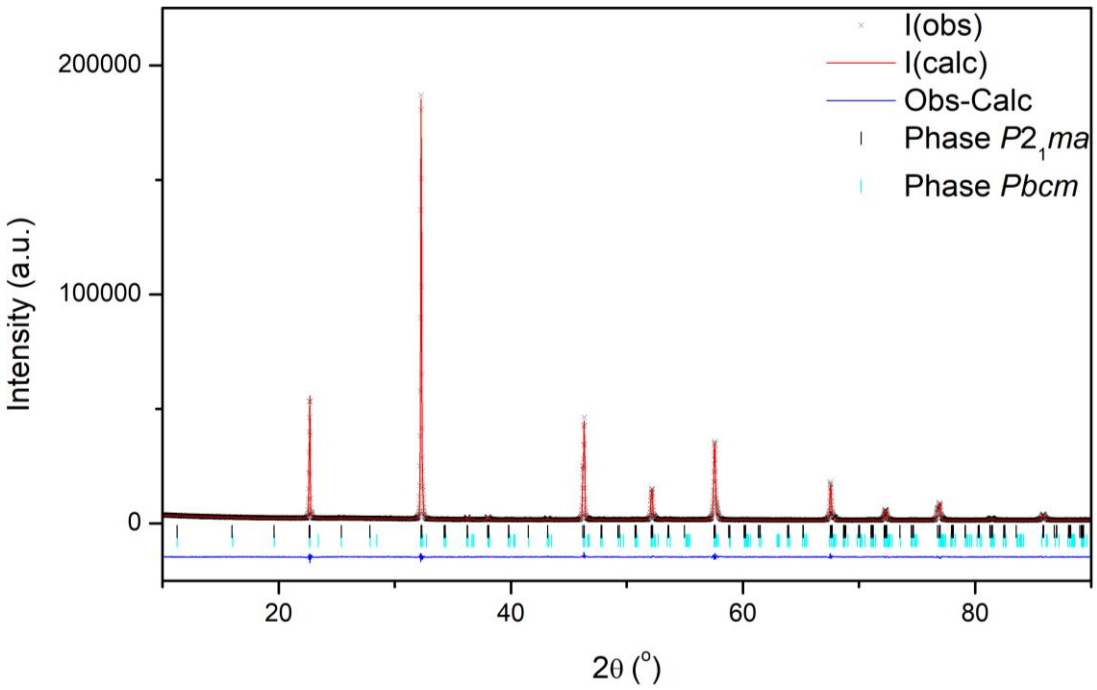

Figure 5.20: *Rietveld refinement of room temperature PXRD data collected for $Bi_{0.15}Na_{0.85}Fe_{0.15}Nb_{0.85}O_3$; χ^2 = 2.884, R_{wp} = 3.34% and R_p = 2.49; the black crosses represent the observed intensity, the red line represents the calculated intensity from the model, the blue line represents the difference between the observed pattern and calculated pattern, the black tick marker represents the $P2_1ma$ model and the cyan tick marker represents the Pbcm model.*

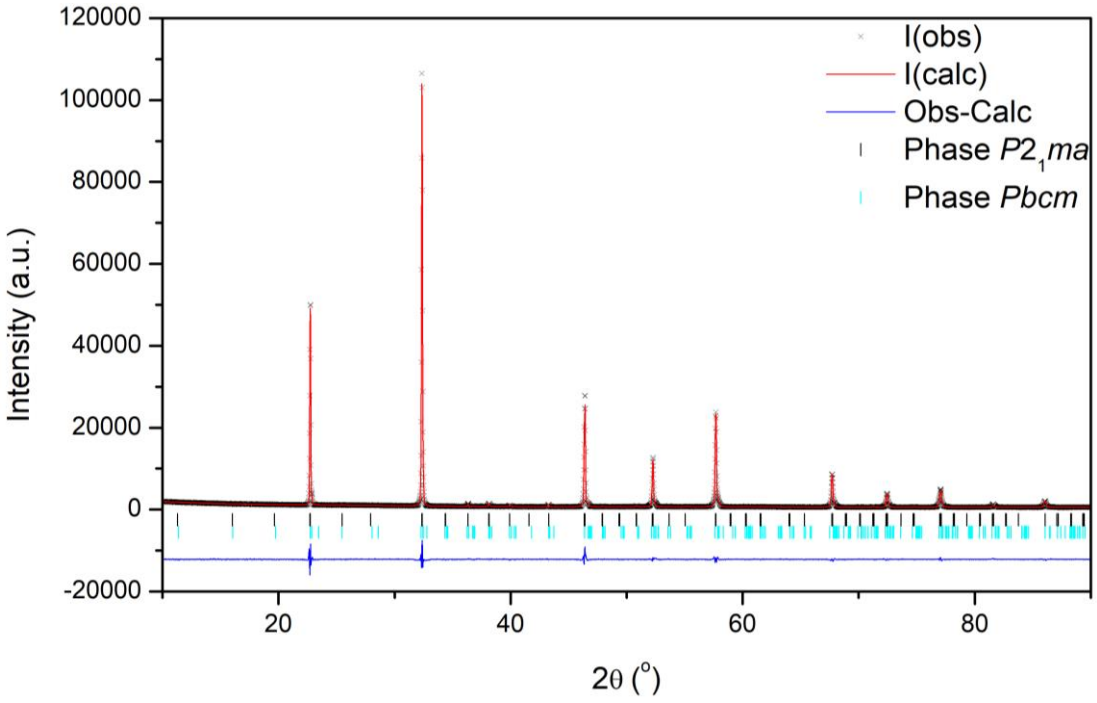

Figure 5.21: *Rietveld refinement of room temperature PXRD data collected for $Bi_{0.1}Na_{0.9}Fe_{0.1}Nb_{0.9}O_3$; χ^2 = 4.054, R_{wp} = 5.80% and R_p = 4.18; the black crosses represent the observed intensity, the red line represents the calculated intensity from the model, the blue line represents the difference between the observed pattern and calculated pattern, the black tick marker represents the $P2_1ma$ model and the cyan tick marker represents the Pbcm model.*

To confirm the structures in this region room temperature neutron diffraction was performed on HRPD at ISIS. The patterns from this composition range can be seen in *figure 5.22*. The results suggest that all of the materials are the same phase at first view. Full refinement parameters can be found in appendix *table A3.2*. The Rietveld refinements for x = 0.7 and 0.85 can be found in appendix *figures A3.13 and A3.16*.

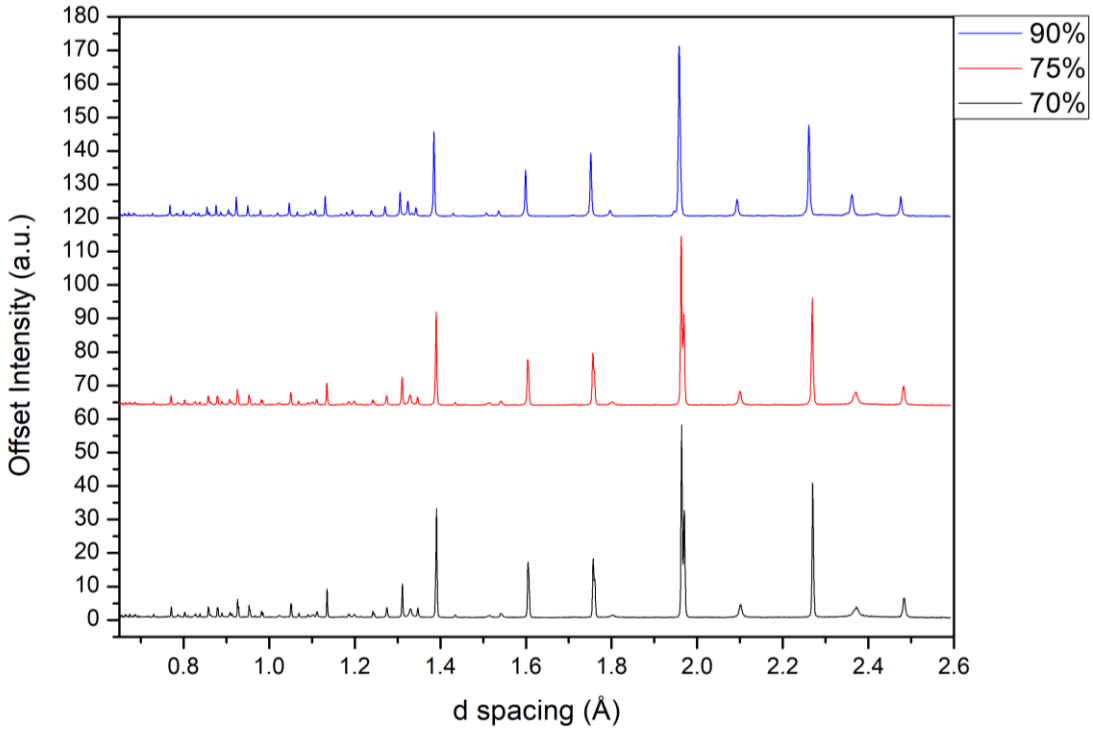

Figure 5.22: *Room temperature PND patterns collected on the HRPD beamline over a composition range from $Bi_{0.3}Na_{0.7}Fe_{0.3}Nb_{0.7}O_3$ to $Bi_{0.1}Na_{0.9}Fe_{0.1}Nb_{0.9}O_3$. Note patterns are offset for clarity.*

However, problems were found upon refining the data to the $P2_1ma$ model at higher values of x as can be seen in *figures 5.23 and 5.25.* The first figure, *figure 5.23*, shows the Rietveld refinement of the x = 0.75 sample and despite the model encompassing all peaks suggesting that the lattice parameters are correct, the intensity are again not modelled well. This is surprising given the quality of the PXRD fits achieved with the $P2_1ma$ model. Close inspection of the data shows that whilst some peaks are sharp others are broader than expected, such as the peaks at 2.1 Å and 2.37 Å d-spacing. This may suggest that similarly to the $P4mm$ region previously discussed that there is an additional affect (most likely related to oxygen/tilt behaviour) not being accounted for by the model which is evident in neutron diffraction but not PXRD. Interestingly, the peaks which appear broader are the same peaks which are associated with the local tilt behaviour observed in the $P4mm$ phase. This can be seen in a direct comparison between x = 0.6 and 0.7 in *figure 5.24*. The diffuse peaks in the x = 0.6 pattern seem to correlate with the broad badly fit peaks in the x = 0.7 refinement in *figure 5.23*. This further supports the suggestion that there are $NaNbO_3$ and $BiFeO_3$ rich areas and that as the amount of NNO content increases the average structure is closer to $P2_1ma$. Broadening

of these peaks is consistent with there still being some disorder or domains present on the local scale which is unsurprising given that the sample still contains a significant amount of BFO.

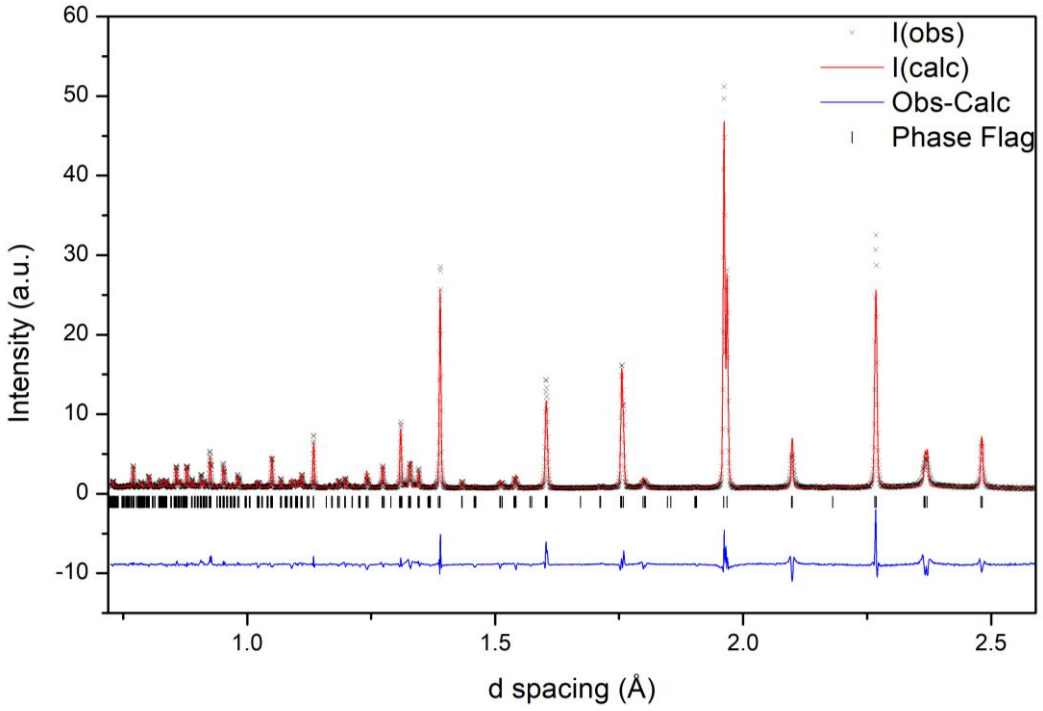

Figure 5.23: *Rietveld refinement of room temperature PND data collected for $Bi_{0.25}Na_{0.75}Fe_{0.25}Nb_{0.75}O_3$; $\chi^2 = 14.18$, $R_{wp} = 10.37\%$ and $R_p = 8.76$; the black crosses represent the observed intensity, the red line represents the calculated intensity from the model, the blue line represents the difference between the observed pattern and calculated pattern and the black tick marker represents the $P2_1ma$ model.*

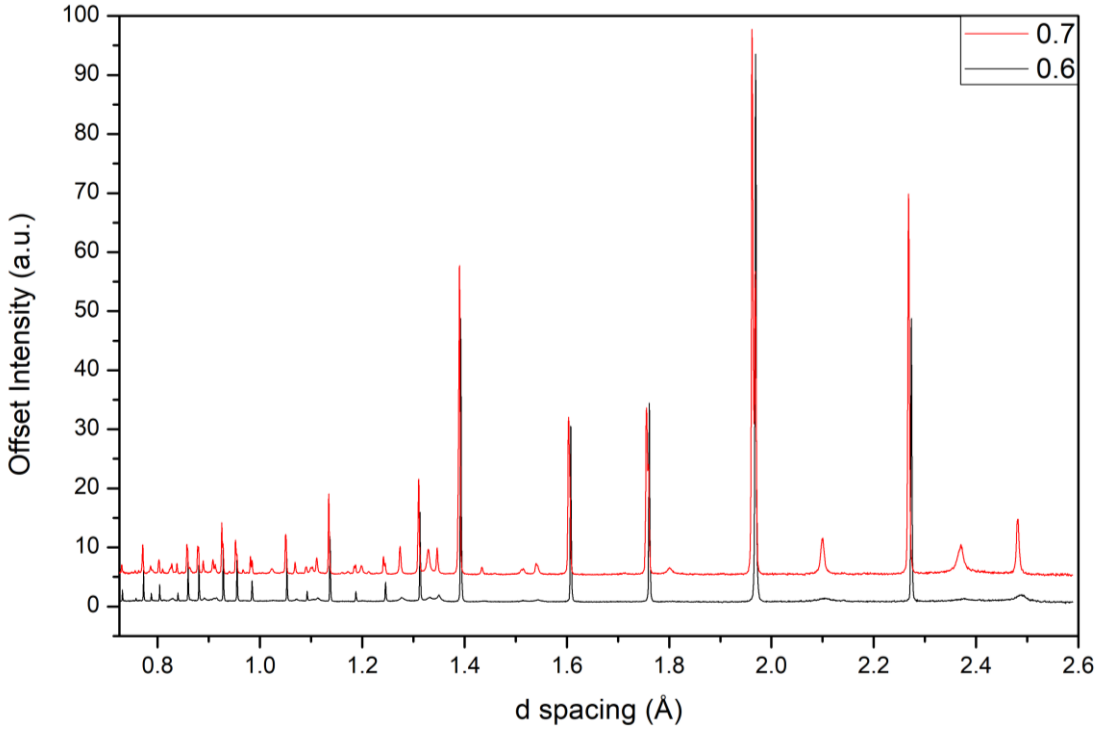

Figure 5.24: *Comparison of the room temperature PND data collected for $Bi_{0.4}Na_{0.6}Fe_{0.4}Nb_{0.6}O_3$ and $Bi_{0.3}Na_{0.7}Fe_{0.3}Nb_{0.7}O_3$.*

The second figure, *figure 5.25*, shows the Rietveld refinement of the *x* = 0.9 sample which suffers from similar issues to the *x* = 0.75 material. This refinement, however, is more complex in that it confirms that this sample is mixed phase as suggested by the XRD refinement. This can clearly be seen by the addition of a shoulder to the main peak found at 1.94 Å *d*-spacing. This peak growth can be observed in more depth in *figure 5.*26 which shows a comparison between *x* = 0.75, 0.85 and 0.9. The $P2_1ma$ model fits similarly to the *x* = 0.75 sample, however, the secondary phase does not seem to perfectly fit the *Pbcm* model with a new peak at 2.42 Å *d*-spacing left unfit. This may suggest that either the lattice parameters are not correct for the *Pbcm* model or the secondary phase is of another structure type.

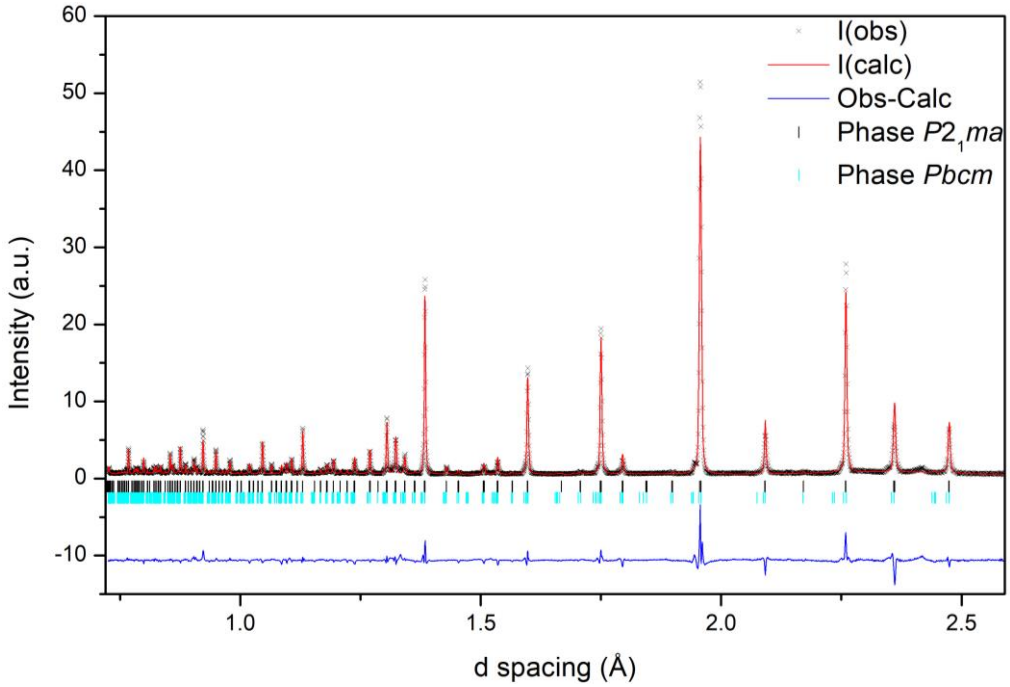

Figure 5.25: *Rietveld refinement of room temperature PND data collected for $Bi_{0.1}Na_{0.9}Fe_{0.1}Nb_{0.9}O_3$; χ^2 = 14.67, R_{wp} = 11.27% and R_p = 9.45; the black crosses represent the observed intensity, the red line represents the calculated intensity from the model, the blue line represents the difference between the observed pattern and calculated pattern, the black tick marker represents the $P2_1ma$ model and the cyan tick marker represents the Pbcm model.*

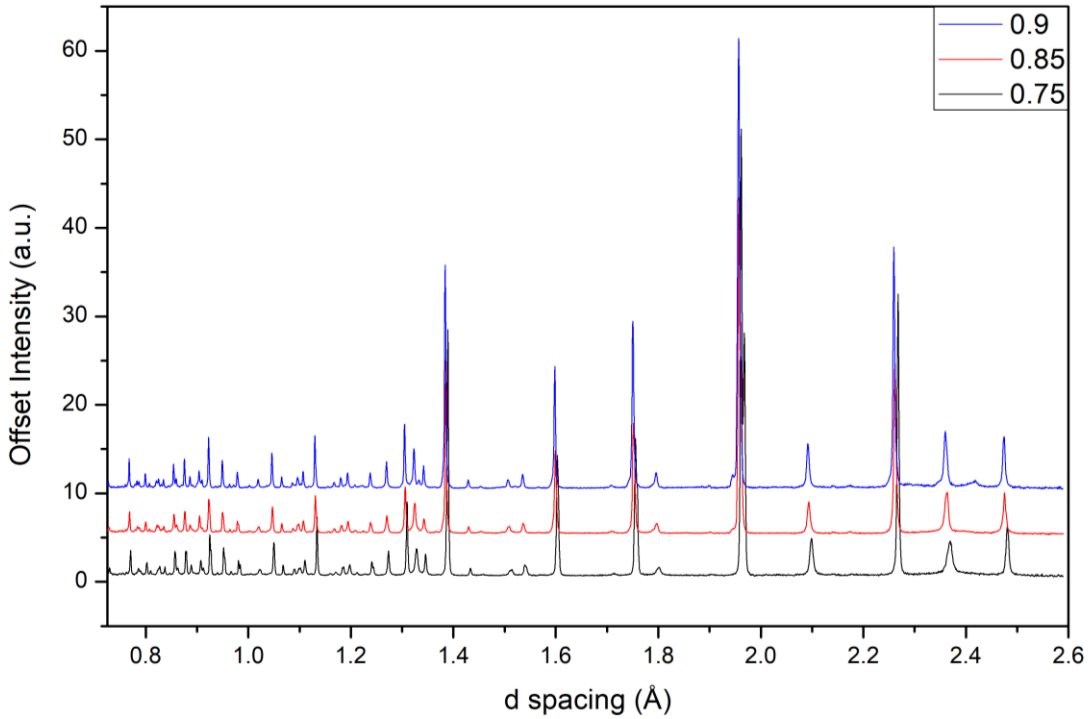

Figure 5.26: *Comparison of the room temperature PND data collected for $Bi_{0.25}Na_{0.75}Fe_{0.25}Nb_{0.75}O_3$ and $Bi_{0.15}Na_{0.85}Fe_{0.15}Nb_{0.85}O_3$ and $Bi_{0.1}Na_{0.9}Fe_{0.1}Nb_{0.9}O_3$.*

Shown below in *figure 5.27* is the proposed phase diagram for the $Bi_{1-x}Na_xFe_{1-x}Nb_xO_3$ solid solution at room temperature. It has been constructed from the PXRD and PND data described in this chapter and further in the appendices. It is ultimately similar in construction to that of the $Bi_{1-x}K_xFe_{1-x}Nb_xO_3$ (BFO-KNO) solid solution phase diagram though the PND data shows a complexity that betrays this simple looking series of transitions[10]. The BFO-KNO solid solution was found to display a series of phase transitions from rhombohedral *R*3*c* to tetragonal *P*4*mm* and finally orthorhombic *Amm*2[10]. This series of transitions also experienced areas of phase coexistence between the *R*3*c* and *P*4*mm* regions, as well as between the *P*4*mm* and *Amm*2 regions[10].

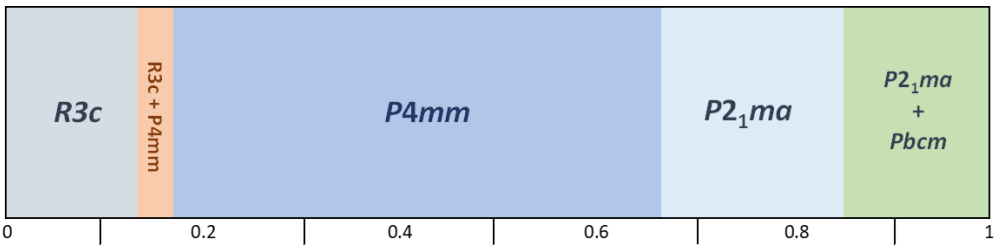

Figure 5.27: *Proposed Bi_{1-x} $Na_xFe_{1-x}Nb_xO_3$ solid solution phase diagram determined from the Rietveld refinement of both powder X-ray and neutron data.*

Unfortunately, there does not seem to be an area of the phase diagram shown in *figure 5.27* that appears to show a PZT-like morphotropic phase boundary i.e. a place where two polar phases are in competition. In theory if the space groups shown are correct and found in the polar types suggested then the two areas between *R*3*c* and *P*4*mm* and *P*4*mm* and *P*2_1*ma* should be MPB

candidates. However, the first region as discussed earlier forms a mixed phase boundary region consisting of two separate phases and not a single phase though there is the small possibility there may be an exact composition (not studied here) which leads to the formation of a single phase material. The other phase boundary does not seem to share the phase coexistence seen beforehand with the x = 0.65 and 0.675 samples identified as *P*4*mm* and $P2_1ma$ respectively. However, as discussed above there seems to be a local and gradual competition between the *P*4*mm* and $P2_1ma$ phases over a large composition range rather than a sharper transition that may be expected at an MBP. However, this phase competition could produce enhanced electrical properties if both phases are polar.

The phase diagram for the $Bi_{1-x}Na_xFe_{1-x}Nb_xO_3$ solid solution derived here shows some similarities with the phases reported in the literature, a comparison to which can be seen in *figure 5.28*. Similarly, to the conclusions drawn here the BFO rich end of the phase diagram was found to be rhombohedral, *R*3*c*. However, the remainder of the phase diagram has been the subject of much dispute[1-4,6-9,17]. The literature in this region ranged from *R*3*c*, *Pbnm,* unspecified pseudocubic, cubic, tetragonal or orthorhombic symmetries[1-4,6-8,17,18]. This is somewhat understandable given the almost cubic lattice parameters observed when looking at these materials using XRD. The *P*4*mm* space group assigned in this work could be categorised as a pseudocubic symmetry and is the tetragonal symmetry as found by Dash *et al*[2,3]. In the NNO rich end of the phase diagram not as much work has been reported, however, it has been found to agree with the results discussed here[8]. None of the previous work in the literature was found to have used neutron diffraction for determining the structures in this solid solution. What is clear from this work is the importance of PND for phase identification.

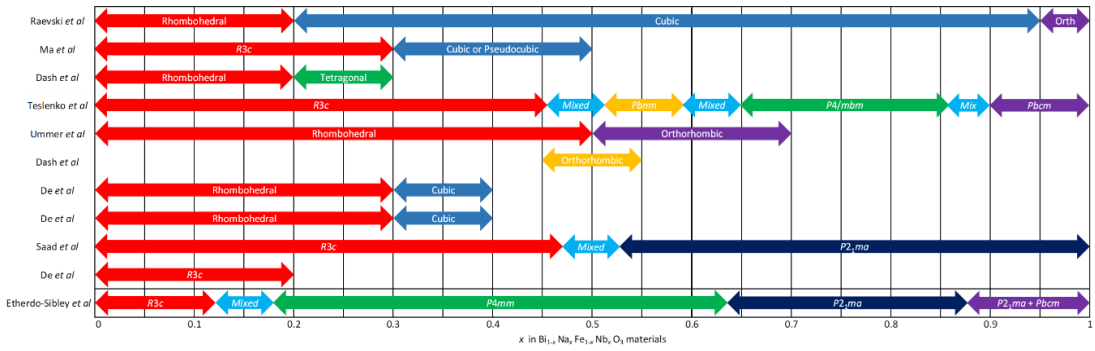

Figure 5.28: *$Bi_{1-x}Na_xFe_{1-x}Nb_xO_3$ phase diagram composed from current literature and thesis findings[1-4,6-9,17,18]. Crystal system reported where space group was not given in the paper.*

Vegards law dictates that the lattice parameters and cell volume should be found to be equal to the mean of the two components at any point in a two-component solid solution. For two materials with different lattice parameters when plotting the pseudo-cubic lattice parameters a trend should

be seen where the lattice parameters will gradually change from the first materials to the second as *x* is increased in the phase diagram. Pseudocubic lattice parameters are obtained by converting the lattice parameters of a perovskite cell to its most simple cell through a structural relationship dependent rule. The relationship to calculate this for *R*3*c* is complicated as the model used was in the hexagonal setting which must first be converted to the rhombohedral setting using the relationship; $\frac{1}{3} \times \sqrt{(3a^2 + c^2)}$, the *R*3*c* rhombohedral setting is then related to the cubic setting by $\frac{a}{\sqrt{2}}$. The relationship for $P2_1ma$ is simpler with the *a*, *b* and *c* lattice parameters related through $\frac{a}{\sqrt{2}}, \frac{b}{2}, \frac{c}{\sqrt{2}}$. This general trend can be seen in *figure 5.29* when the pseudo-cubic lattice parameters and cell volume are plotted from the room temperature XRD and ND data. It would be expected in this solid-solution that the BFO rich region will have the higher lattice parameters/cell volume and that these should then decrease as the amount of NNO is increased as BFO has higher lattice parameters/cell volume than NNO. (Ionic radii Bi^{3+} = 1.36, Fe^{3+} = 0.645, Na^{+} = 1.39, Nb^{5+} = 0.64, O^{2-} = 1.42). This is generally observed however the *x* = 0.175 material in both the XRD and neutron diffraction data seems to not fit the trend completely. It may be possible that this material is not 100% single phase.

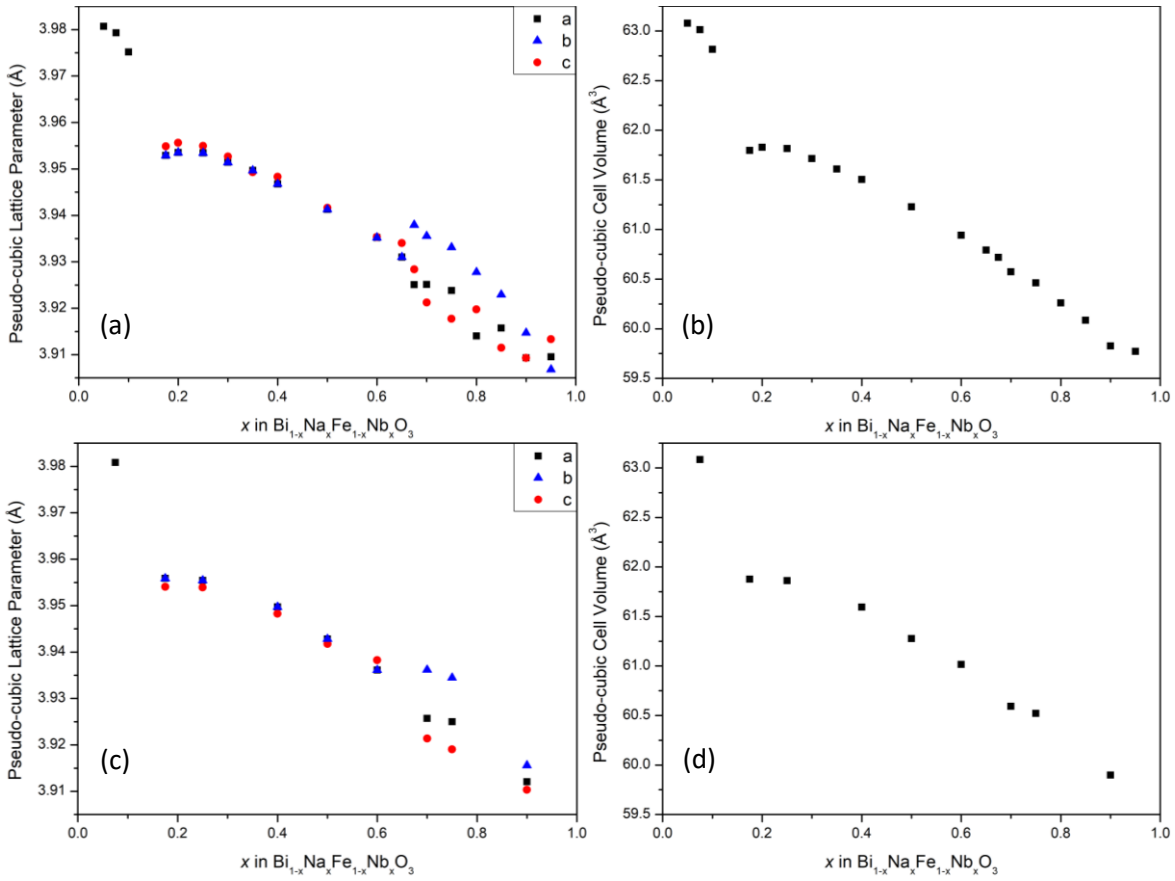

Figure 5.29: *Room temperature lattice parameter and cell volume plots as a function of x in $Bi_{1-x}Na_xFe_{1-x}Nb_xO_3$ (a) XRD lattice parameter plot, (b) XRD cell volume plot, (c) ND lattice parameter plot, (d) ND cell volume plot. The lattice parameters and cell volume for x = 0.125 and 0.15 have been omitted as both were of mixed phase.*

Measuring the bond lengths between the *B*-site and oxygen can be used as a guide to the magnitude of the displacement (if present). Whilst, this does not confirm the presence of polar behaviour it can be used as an indication with large bond length differences perhaps indicative of polar character whilst more regular BO_6 octahedra are more suggestive of centrosymmetry. In *figure 5.30* are plots that show the bond length variance between the apical or equatorial oxygen and the *B*-site. Plotting both allows us to see the differences in the displacement behaviour arising as a result of the structural differences between the *P*4*mm* and *P*2_1*ma* space groups. For example, the origin of the displacement in the *P*4*mm* structure is from the two apical oxygen bond lengths which lie in the lattice *c*-direction. In contrast in the *P*2_1*ma* structure the origin of the displacement is found in the equatorial oxygen bond lengths lying in the crystallographic *a*-*c* plane. It can be seen that, for the most part, the *B*-site displacement reduces as *x* increases which could be due to phase competition between the *P*2_1*ma* and *Pbcm* phases due to the polymorphic behaviour. Whist we cannot definitively conclude that these materials are polar, these displacements are significant enough to suggest that polar materials are obtained throughout the phase diagram.

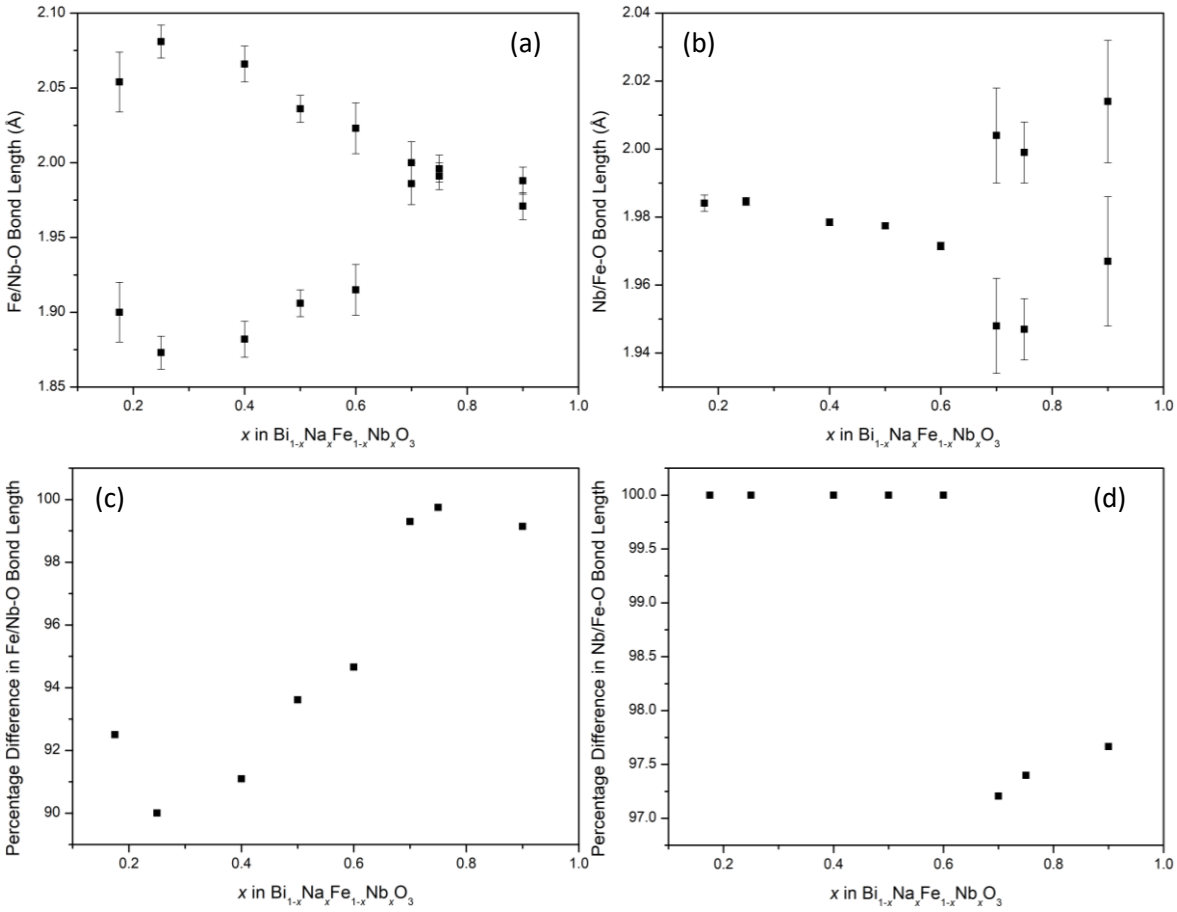

Figure 5.30: *Room temperature PND bond lengths plotted as a function of x in $Bi_{1-x}Na_xFe_{1-x}Nb_xO_3$ where (a) Apical Fe/Nb-O bond lengths, (b) Equatorial Fe/Nb-O bond lengths, (c) percentage difference in apical Fe/Nb-O bond lengths, (d) percentage difference in equatorial Fe/Nb-O bond lengths.*

5.3 Low Temperature Structural Characterisation

Low temperature diffraction measurements were performed on an Empyrean XRD equipped with a Phenix cryostat. This allowed PXRD measurements down to 12 K.

For the *R*3*c* region no changes in symmetry are seen down to 12 K across the three samples synthesised x = 0.05, 0.075, 0.10. Shown below in *figure 5.31* are a selection of patterns from 12 K to 298 K for the x = 0.05 sample. It can be seen that apart from the shifting of peaks as the temperature changes no structural changes occur. This would suggest that the symmetry does not change as a function of temperature down to 12 K.

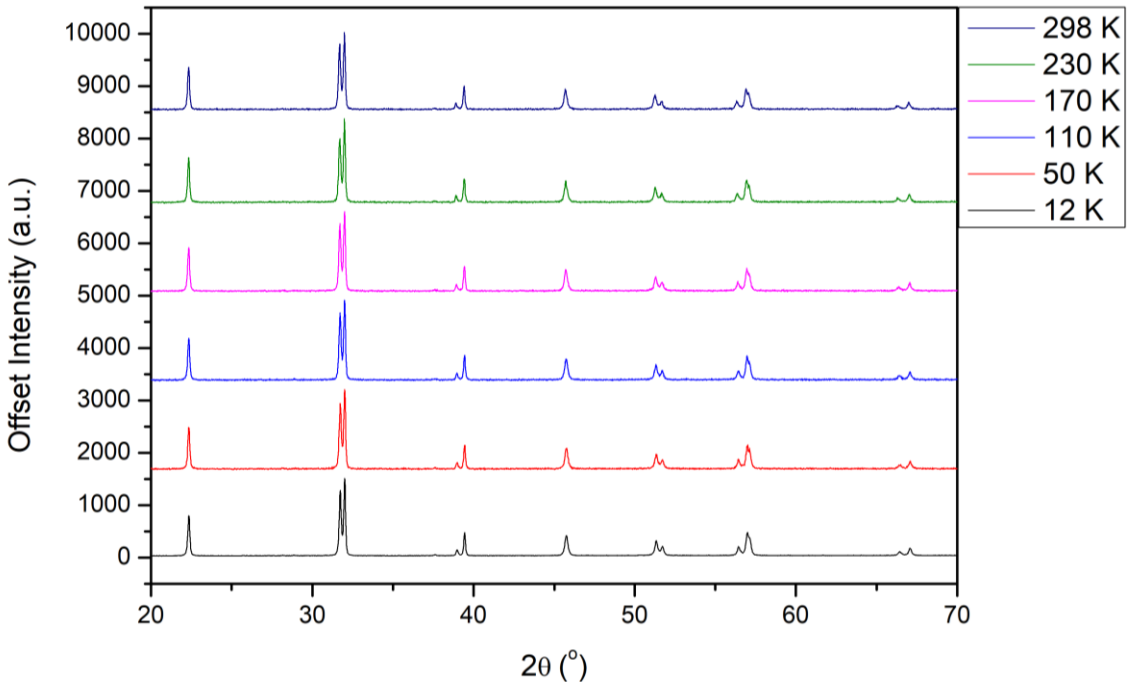

Figure 5.31: *Selection of XRD patterns collected for $Bi_{0.95}Na_{0.05}Fe_{0.95}Nb_{0.05}O_3$ as a function of temperature. Note: the 12K pattern intensity has been scaled down to match the intensities of the other temperature points that were taken with shorter scan times. Patterns have also been shifted for clarity.*

The Rietveld refinement of the x = 0.05 data at 12 K is shown in *figure 5.32* reinforces this assumption as the *R*3*c* model shows a good fit to the data. Full refinement parameters and fits for the temperature range 30 K to 298 K can be found in appendix *table A3.3* and *figure A3.19*. The lattice parameter and cell volume fits are shown in appendix *figure A3.18* which show the lattice parameters and cell volume decreasing as the temperature decreases.

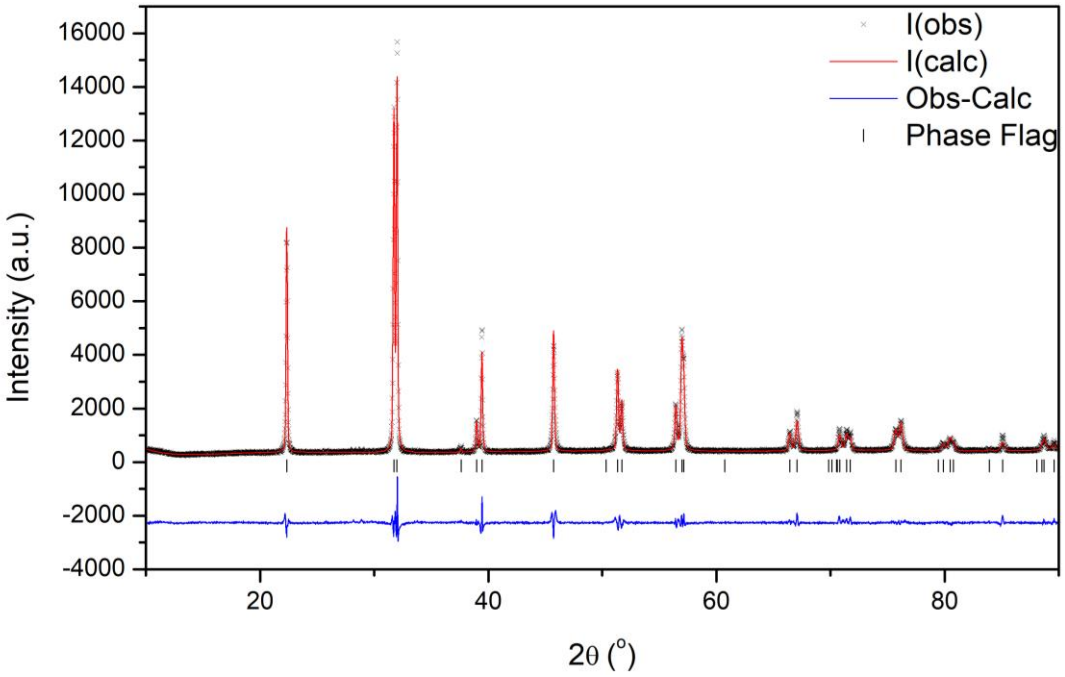

Figure 5.32: *Rietveld refinement of the 12 K PXRD data collected for $Bi_{0.95}Na_{0.05}Fe_{0.95}Nb_{0.05}O_3$; $\chi^2 = 3.277$, $R_{wp} = 7.5\%$ and $R_p = 5.54$; the black crosses represent the observed intensity, the red line represents the calculated intensity from the model, the blue line represents the difference between the observed pattern and calculated pattern and the black tick marker represents the R3c model.*

The mixed phase region, $0.1 < x < 0.175$, represented by the $x = 0.15$ sample does not crystallise into a single phase at low temperature as suggested by the Rietveld refinement shown in *figure 5.34*. This refinement shows the $x = 0.15$ at 12 K fit to an *R*3*c* and *P*4*mm* model similar to those performed for the room temperature data in *figure 5.14*. This is supported by the fact that the XRD patterns do not change between 12 K and 298 K as seen in *figure 5.33*. There does, however, seem to be a change in the phase ratio between the room temperature refinement and the 12 K refinement. It was found in the 12 K refinement that the ratio between the *R*3*c* and *P*4*mm* models was 0.31(3):0.69(3) but in the room temperature refinement, in *figure 5.14*, it was found to be 0.284(2):0.716(2). This seems to imply that lowering the temperature leads to an increase in the amount of the *R*3*c* phase. It was not possible to follow this change as the temperature increased as the ratio between the two phases was fixed from 30 K to 298 K as this data was of lower resolution compared to the 12 K data obtained on the Phenix cryostat sample chamber. The ratio between the two phases presented at 298 K was obtained from a refinement on the diffraction data obtained at ambient conditions on the reflection/transmission sample spinner stage. Full refinement parameters and fits for the temperature range 30 K to 298 K can be found in appendix *table A3.4* and *figure A3.21*.

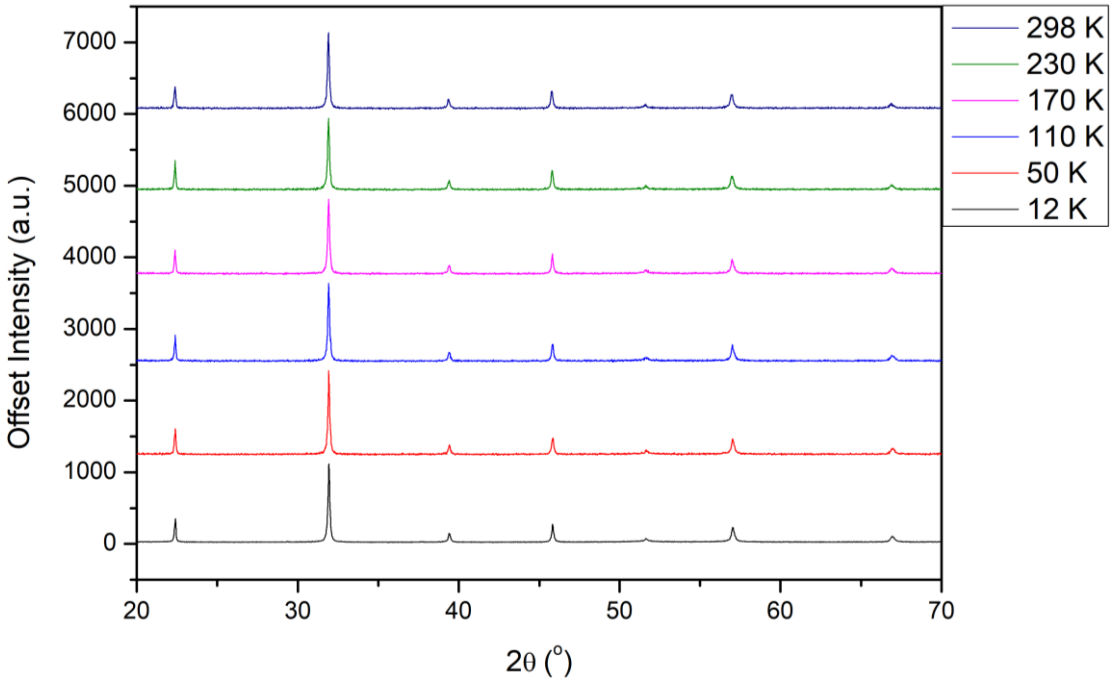

Figure 5.33: *Selection of PXRD patterns collected for $Bi_{0.85}Na_{0.15}Fe_{0.85}Nb_{0.15}O_3$ as a function of temperature 12K pattern intensity has been scaled down to match the intensities of the other temperature points that were taken with shorter scan times. All patterns are shifted for clarity.*

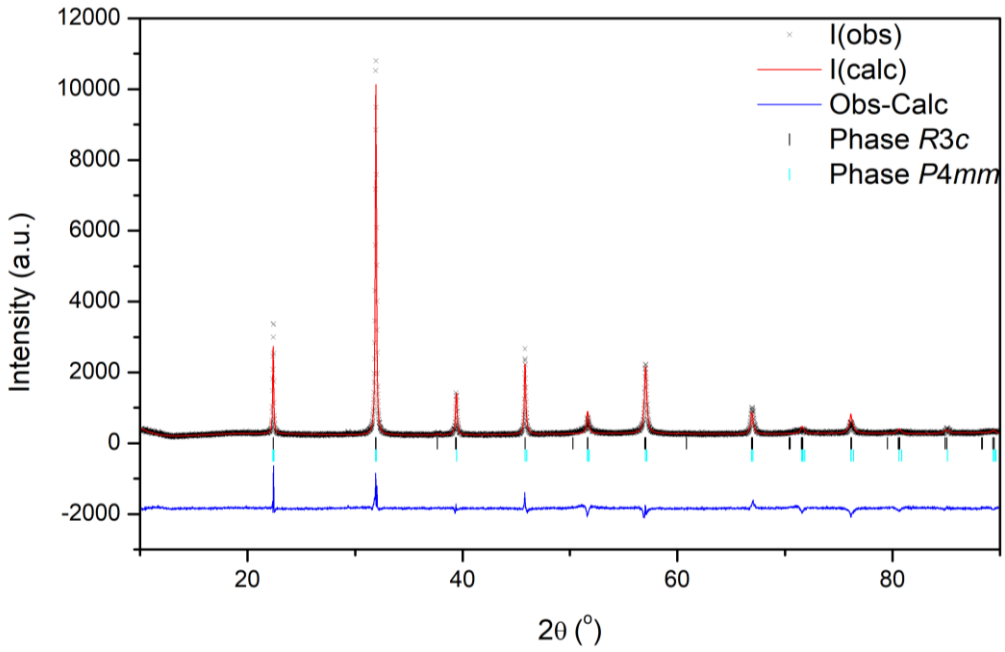

Figure 5.34: *Rietveld refinement of the 12 K PXRD data collected for $Bi_{0.85}Na_{0.15}Fe_{0.85}Nb_{0.15}O_3$; χ^2 = 2.959, R_{wp} = 9.48% and R_p = 7.23; the black crosses represent the observed intensity, the red line represents the calculated intensity from the model, the blue line represents the difference between the observed pattern and calculated pattern, the black tick marker represents the R3c model and the cyan tick marker represents the P4mm model.*

Furthermore, this the lack of structural phase transitions on lowering the temperature is also seen in the *P4mm* region. Across *figures 5.35* to *5.40* a similar result can be seen with the *x* = 0.25, 0.4 and 0.6 samples all showing patterns that look identical at 12 K and 298 K. Full refinement parameters, lattice parameter plots and Rietveld fits for the temperature range 30 K to 298 K for

samples $0.2 \leq x \leq 0.65$ can be found in appendix *tables A3.5-A3.11* and *figures A3.24-A3.50*. The lattice parameters and cell volume decrease as the temperature decreases. The main difference between these data sets is that for the $x = 0.6$ sample was run on the Phenix after an upgrade was made to the equipment which has resulted in higher quality data and thus an improvement in the *R* value. On the whole a good fit to the *P*4*mm* model is seen across all refinements across all temperatures. The lattice parameter and cell volume fits shown in the appendix decrease as the temperature decreases. A transition back to *R*3*c* was originally expected as it is known to be the low temperature structure of NNO as well as the room temperature structure of BFO[19]. However, this transition was not observed, though this does not rule out the possibility of more subtle phase changes.

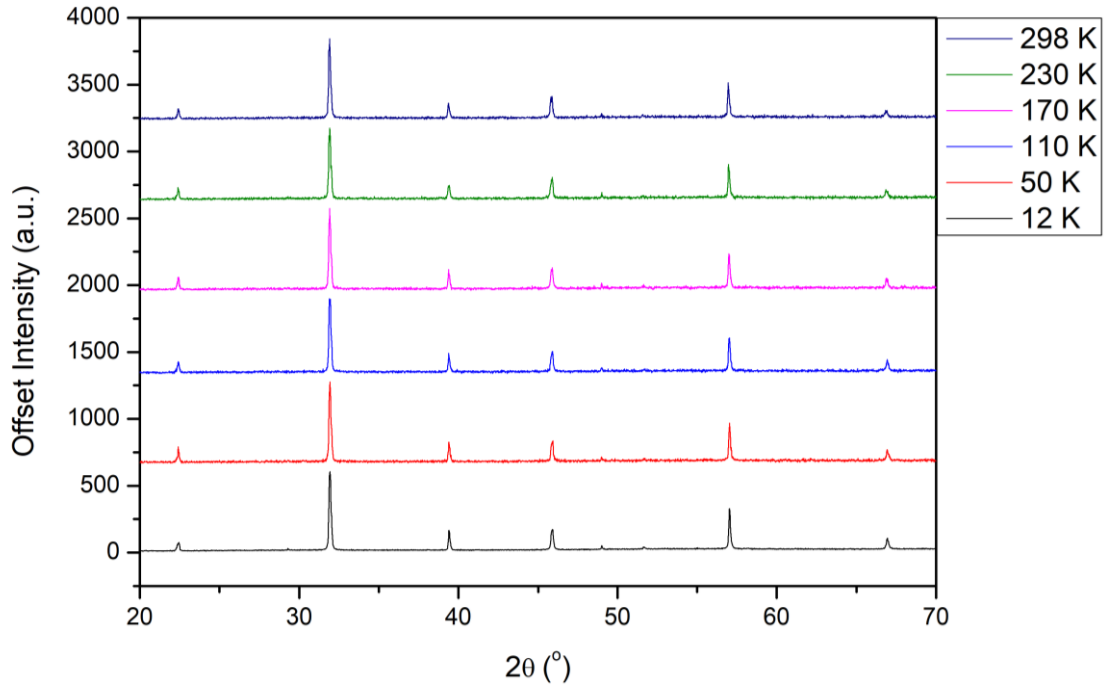

***Figure 5.35**: Selection of PXRD patterns collected for $Bi_{0.75}Na_{0.25}Fe_{0.75}Nb_{0.25}O_3$ as a function of temperature 12K pattern intensity has been scaled down to match the intensities of the other temperature points that were taken with shorter scan times. All patterns are shifted for clarity.*

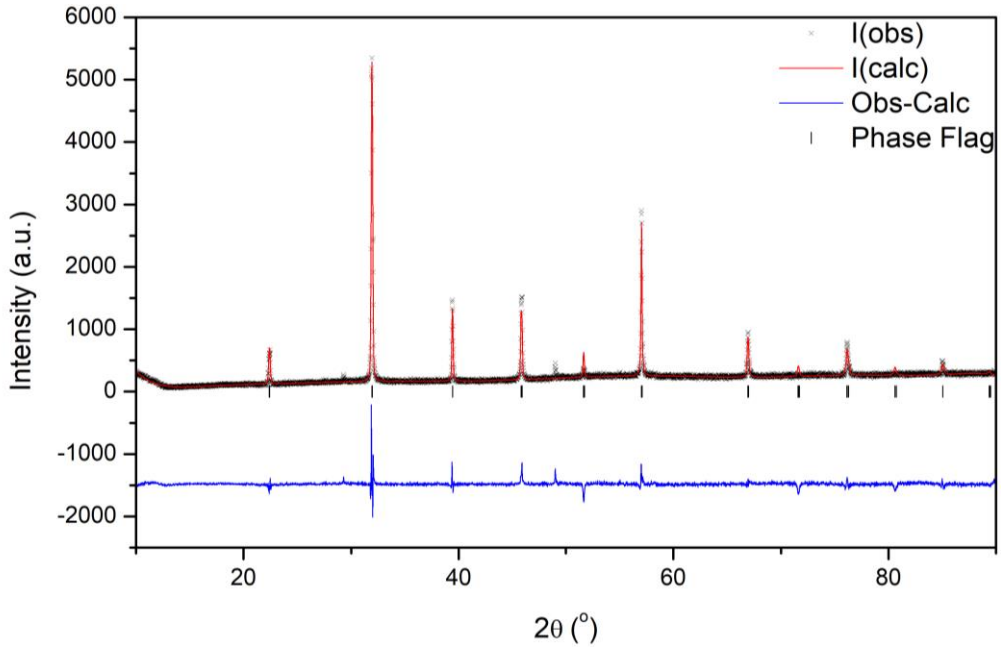

Figure 5.36: *Rietveld refinement of 12 K PXRD data collected for $Bi_{0.75}Na_{0.25}Fe_{0.75}Nb_{0.25}O_3$; $\chi^2 = 2.485$, $R_{wp} = 10.23\%$ and $R_p = 7.64$; the black crosses represent the observed intensity, the red line represents the calculated intensity from the model, the blue line represents the difference between the observed pattern and calculated pattern and the black tick marker represents the P4mm model.*

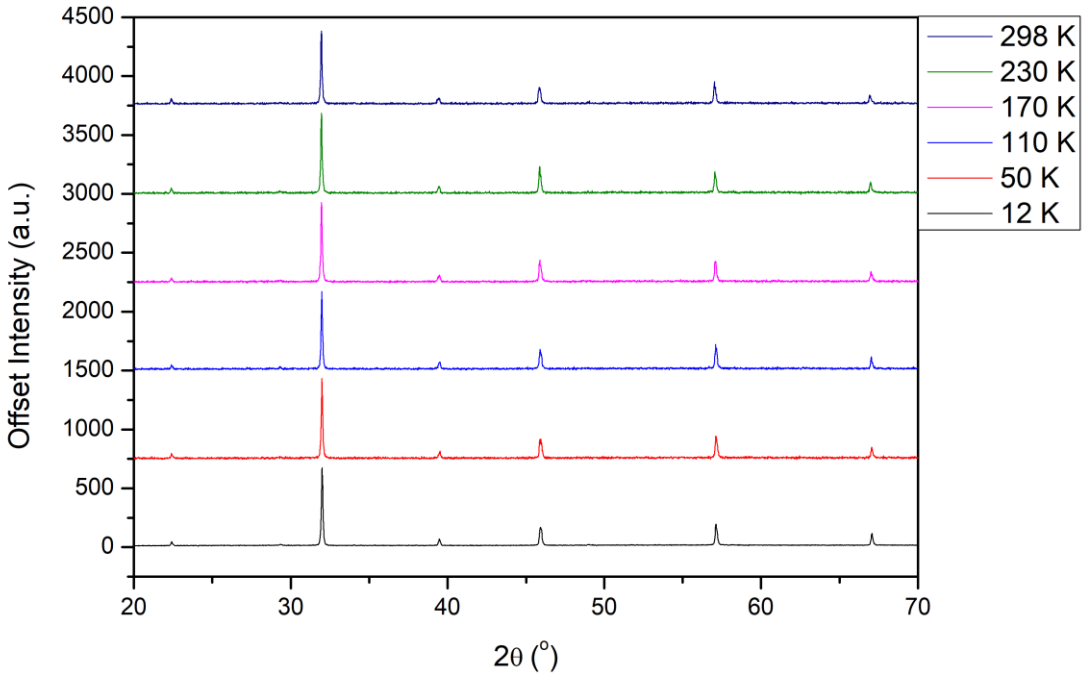

Figure 5.37: *Selection of PXRD patterns collected as a function of temperature for $Bi_{0.6}Na_{0.4}Fe_{0.6}Nb_{0.4}O_3$. 12K pattern intensity has been scaled down to match the intensities of the other temperature points that were taken with shorter scan times. All patterns shifted for clarity.*

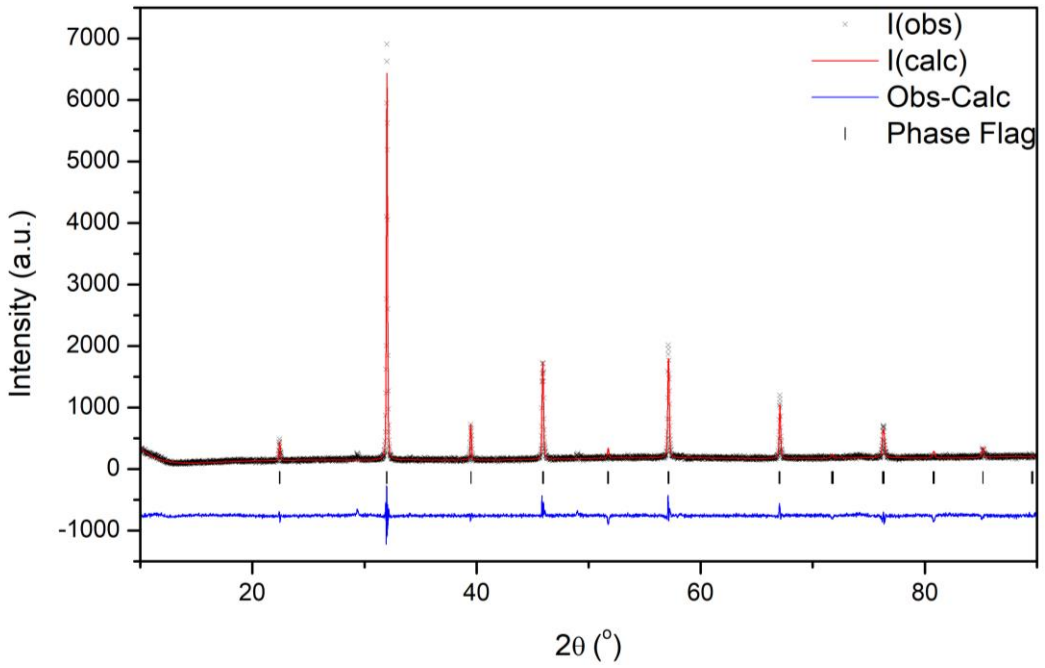

Figure 5.38: *Rietveld refinement of 12 K PXRD data collected for $Bi_{0.6}Na_{0.4}Fe_{0.6}Nb_{0.4}O_3$; $\chi^2 = 1.738$, $R_{wp} = 9.42\%$ and $R_p = 7.42$; the black crosses represent the observed intensity, the red line represents the calculated intensity from the model, the blue line represents the difference between the observed pattern and calculated pattern and the black tick marker represents the P4mm model.*

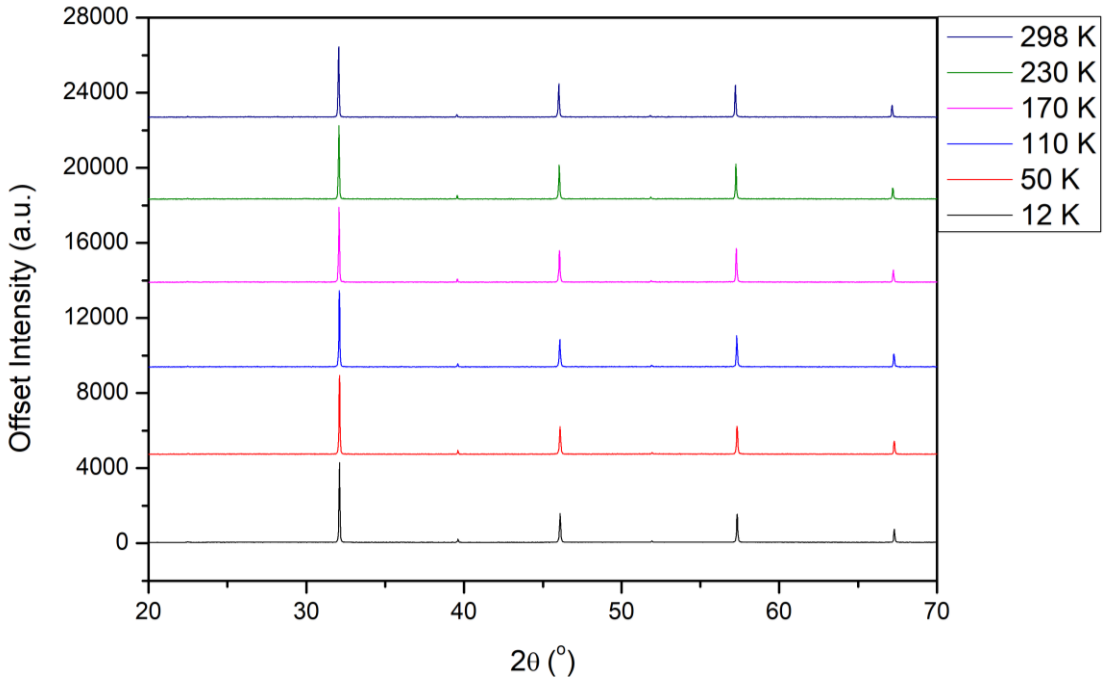

Figure 5.39: *Selection of PXRD patterns collected as a function of temperature for $Bi_{0.4}Na_{0.6}Fe_{0.4}Nb_{0.6}O_3$. 12K pattern intensity has been scaled down to match the intensities of the other temperature points that were taken with shorter scan times. All patterns are shifted for clarity.*

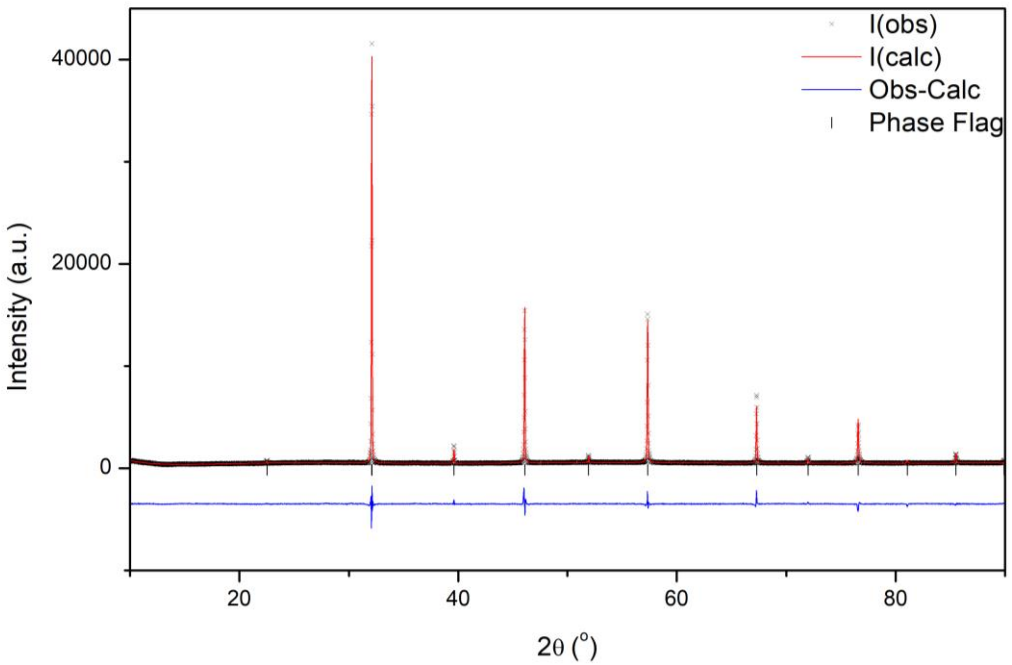

Figure 5.40: *Rietveld refinement of 12 K PXRD data collected for $Bi_{0.4}Na_{0.6}Fe_{0.4}Nb_{0.6}O_3$ at; χ^2 = 3.244, R_{wp} = 7.19% and R_p = 5.09; the black crosses represent the observed intensity, the red line represents the calculated intensity from the model, the blue line represents the difference between the observed pattern and calculated pattern and the black tick marker represents the P4mm model.*

The same results can be seen in the $P2_1ma$ region with no obvious changes seen to the patterns as the temperature is decreased down to 12 K. The Rietveld refinement shown in *figure 5.42* for the x = 0.75 sample at 12 K confirms that the model fits the pattern at 12 K and thus a low temperature phase transition does not occur. This is supported by the fact that the XRD patterns do not change between 12 K and 298 K as seen in *figure 5.41*. Full refinement parameters, lattice parameter plots and Rietveld fits for the temperature range 30 K to 298 K for samples $0.7 \leq x \leq 0.8$ can be found in appendix *tables A3.12-A3.14* and *figures A3.53-A3.63*. The lattice parameters and cell volume decrease as the temperature decreases.

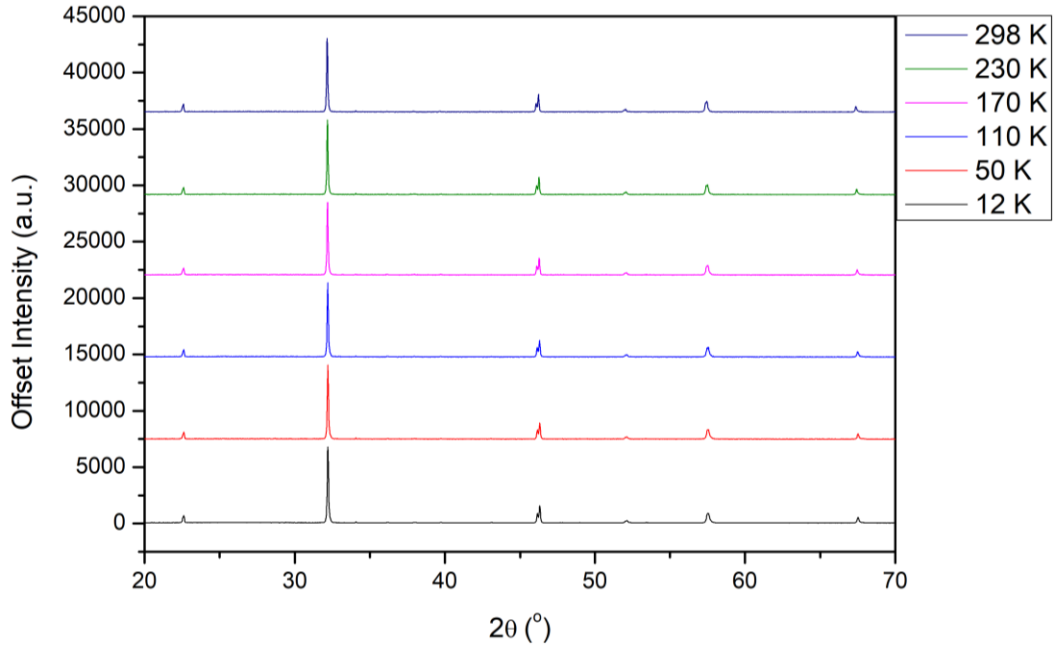

Figure 5.41: *Selection of PXRD patterns collected as a function of temperature for $Bi_{0.25}Na_{0.75}Fe_{0.25}Nb_{0.75}O_3$. 12K pattern intensity has been scaled down to match the intensities of the other temperature points that were taken with shorter scan times. All patterns are shifted for clarity.*

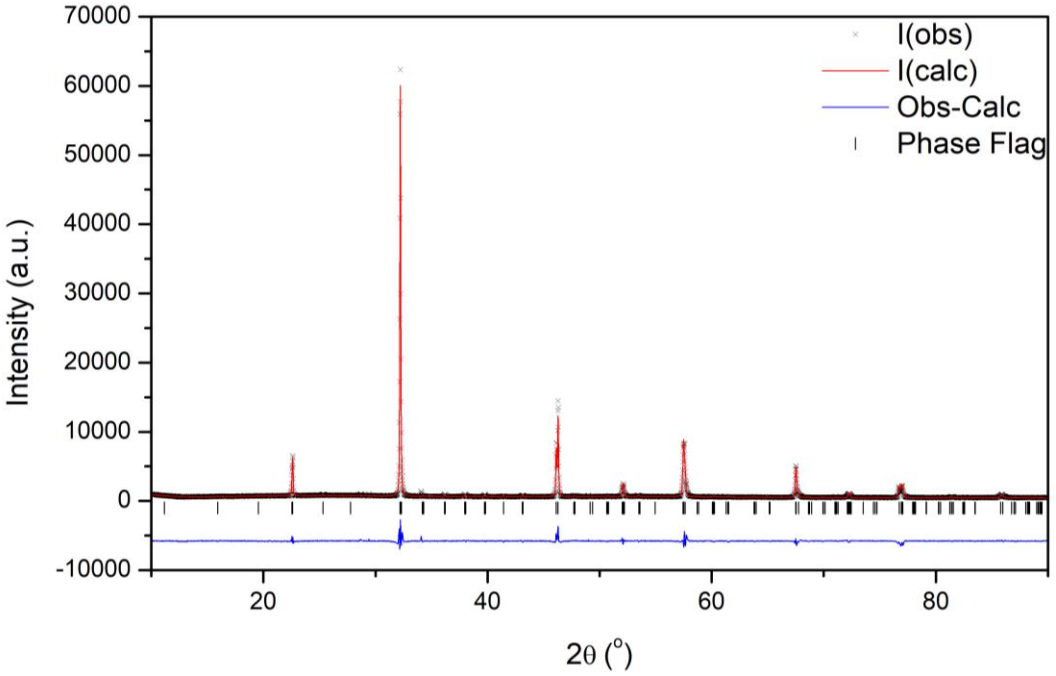

Figure 5.42: *Rietveld refinement of 12 K PXRD data collected for $Bi_{0.25}Na_{0.75}Fe_{0.25}Nb_{0.75}O_3$; χ^2 = 5.867, R_{wp} = 8.54% and R_p = 5.78; the black crosses represent the observed intensity, the red line represents the calculated intensity from the model, the blue line represents the difference between the observed pattern and calculated pattern and the black tick marker represents the $P2_1ma$ model.*

The *x* = 0.9 sample also does not show a low temperature transition as shown in figure 5.43. However, the Rietveld refinement shown in *figure* 5.44 was refined to just $P2_1ma$ as it was found to be difficult to add the *Pbcm* phase. It is likely that contributions from the other phase are still present, however, it may be possible that reducing the temperature leads to a higher main phase

contribution or the reduction in intensity and resolution from the Phenix equipment has made this phase indistinguishable from the main phase. Full refinement parameters, lattice parameter plots and Rietveld fits for the temperature range 30 K to 298 K for $x = 0.9$ can be found in appendix *table A3.15* and *figures A3.65 and A3.66*. The lattice parameters and cell volume decrease as the temperature decreases.

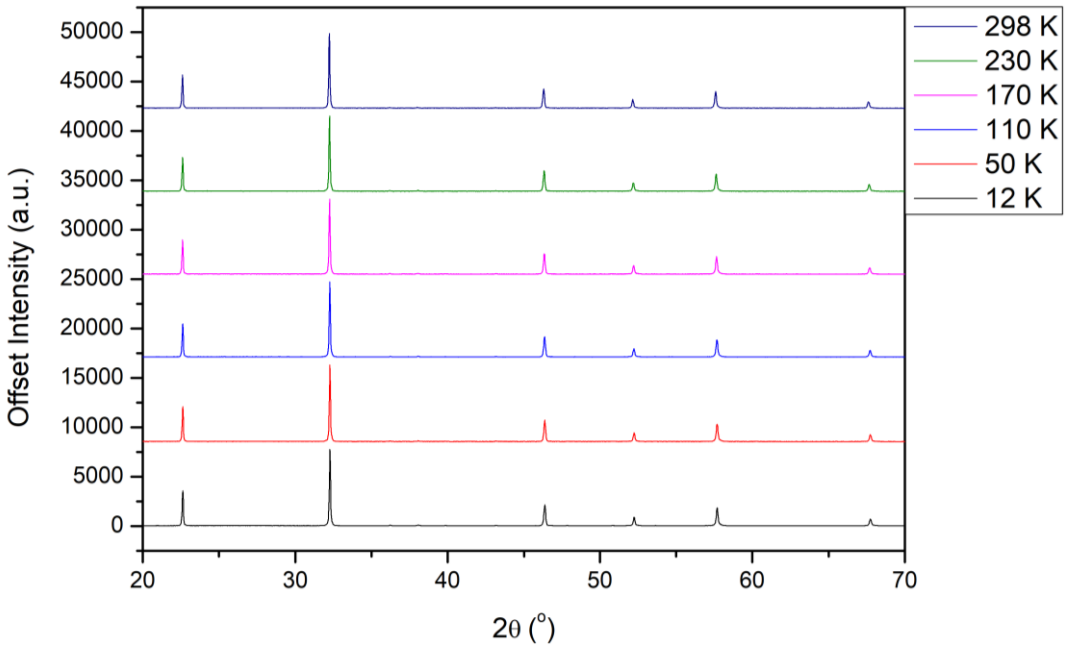

Figure 5.43: *Selection of PXRD patterns collected as a function of temperature for $Bi_{0.1}Na_{0.9}Fe_{0.1}Nb_{0.9}O_3$. 12K pattern intensity has been scaled down to match the intensities of the other temperature points that were taken with shorter scan times. All patterns are shifted for clarity.*

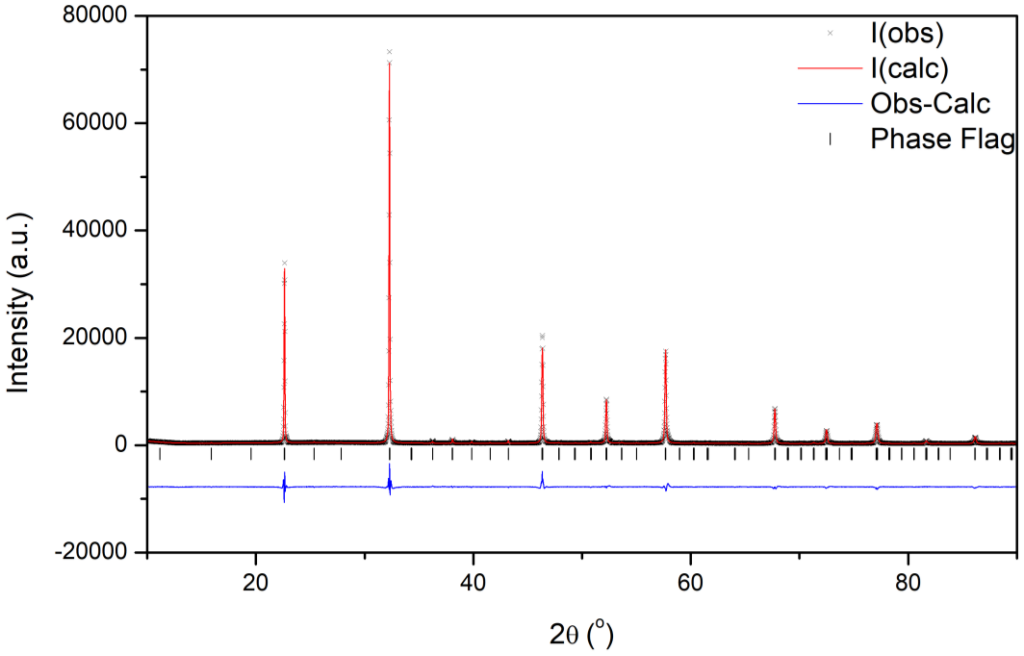

Figure 5.44: *Rietveld refinement of 12 K PXRD data collected for $Bi_{0.1}Na_{0.9}Fe_{0.1}Nb_{0.9}O_3$; $\chi^2 = 5.428$, $R_{wp} = 8.91\%$ and $R_p = 6.57$; the black crosses represent the observed intensity, the red line represents the calculated intensity from the model, the blue line represents the difference between the observed pattern and calculated pattern and the black tick marker represents the $P2_1ma$ model.*

Low temperature neutron diffraction was performed on the HRPD beamline at ISIS. Two samples, *x* = 0.25 and 0.75, were examined at 10 K. Refinement of the *x* = 0.25 pattern shown in *figure 5.45* seems to have a similar degree of fit to the P4mm model to that observed at room temperature as shown in *figure 5.10*. The main difference between the two patterns seems to be the increase in intensity of the suspected magnetic Bragg peaks, which adds weight to their identification. There does not seem to be any other major change bar the expected contraction of the unit cell due to the reduction in temperature. In addition, the diffuse scattering does not seem to change though it does also show a shift in *d*-spacing as would be expected. The *x* = 0.75 pattern shown in *figure 5.46* does not seem to show any major differences either when compared with the room temperature pattern shown in *figure 5.23* other than the expected shift in lattice parameters. These data confirm the observations of the PXRD study discussed above. Full refinement parameters for both *x* = 0.25 and 0.75 can be found in appendix *table A3.16*.

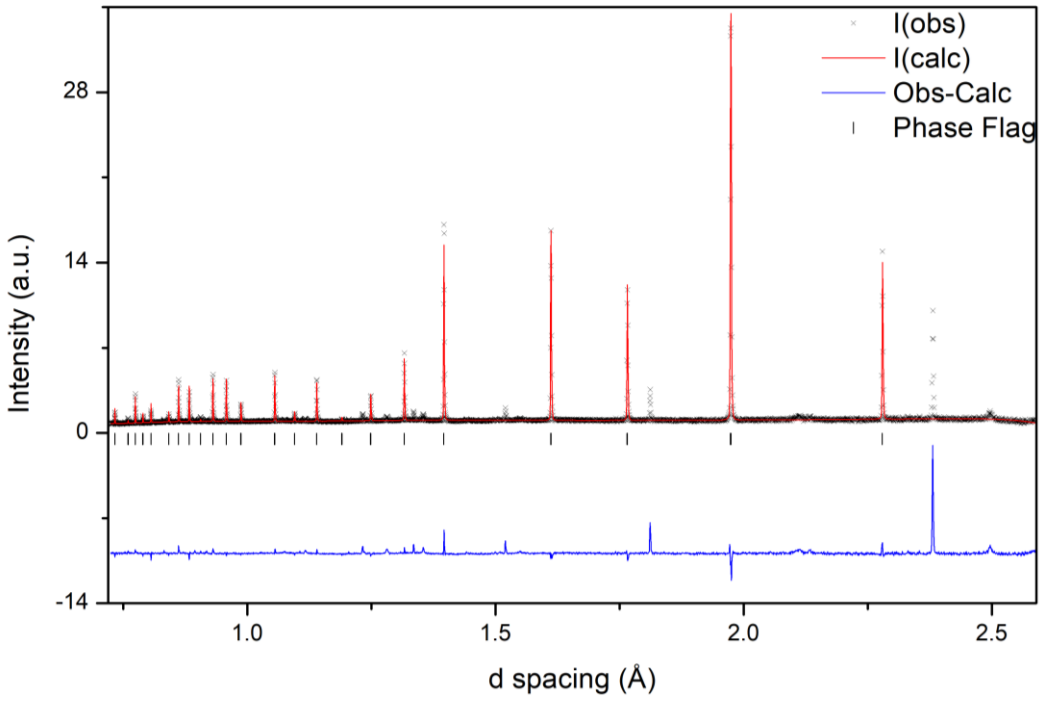

Figure 5.45: *Rietveld refinement of 10 K PND data collected for $Bi_{0.75}Na_{0.25}Fe_{0.75}Nb_{0.25}O_3$; χ^2 = 5.74, R_{wp} = 8.24% and R_p = 6.51; the black crosses represent the observed intensity, the red line represents the calculated intensity from the model, the blue line represents the difference between the observed pattern and calculated pattern and the black tick marker represents the P4mm model.*

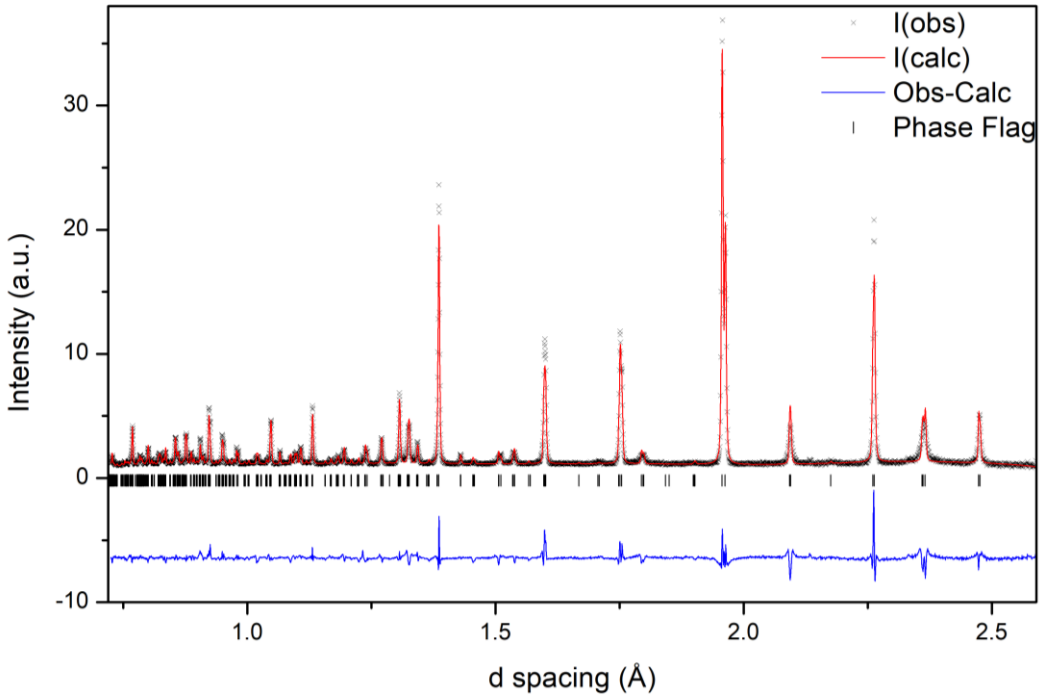

Figure 5.46: *Rietveld refinement of 10 K PND data collected for $Bi_{0.25}Na_{0.75}Fe_{0.25}Nb_{0.75}O_3$; χ^2 = 8.816, R_{wp} = 8.33% and R_p = 7.16; the black crosses represent the observed intensity, the red line represents the calculated intensity from the model, the blue line represents the difference between the observed pattern and calculated pattern and the black tick marker represents the $P2_1ma$ model.*

5.4 High Temperature Characterisation

Thermal analysis via combined thermal gravimetric analysis (TGA) and differential scanning calorimetry (DSC) was used in an attempt determine the ferroelectric Curie temperature, phase transition temperatures and decomposition points of the studied materials. Samples were heated up to 1270 K under nitrogen gas. The resulting DSC plot was then also plotted as a derivative to pick out any small changes in the data that may be suggestive of changes to the sample.

The TGA data for x = 0.05, shown in *figure 5.47*, indicates that the mass does not change as the temperature increases. This would suggest that the sample is thermally stable up to 1270 K. The DSC and derivative DSC data suggests that there is a possible change between 1040 K and 1050 K due to a small change in the DSC, a second larger DSC change is seen between 1250 K and 1260 K and finally a big decrease is seen from 1260 K onwards. The first small change is close to the ferroelectric to paraelectric transition, Curie temperature, for pure BFO around 1100 K[20]. This seems likely to be the Curie temperature for this material considering that the XRD data suggests it crystallises with *R*3*c* symmetry and contains only a small amount of NNO. The next DSC change is likely the decomposition of the material as pure BFO is found to decompose into $Bi_2Fe_4O_9$ and Fe_2O_3 at around 1220 K[21]. The last change in the DSC can likely be attributed to the decomposition

$Bi_2Fe_4O_9$ into bismuth oxide (Bi_2O_3) and Fe_2O_3[21]. Results for x = 0.075 can be found in appendix *figure A3.67*.

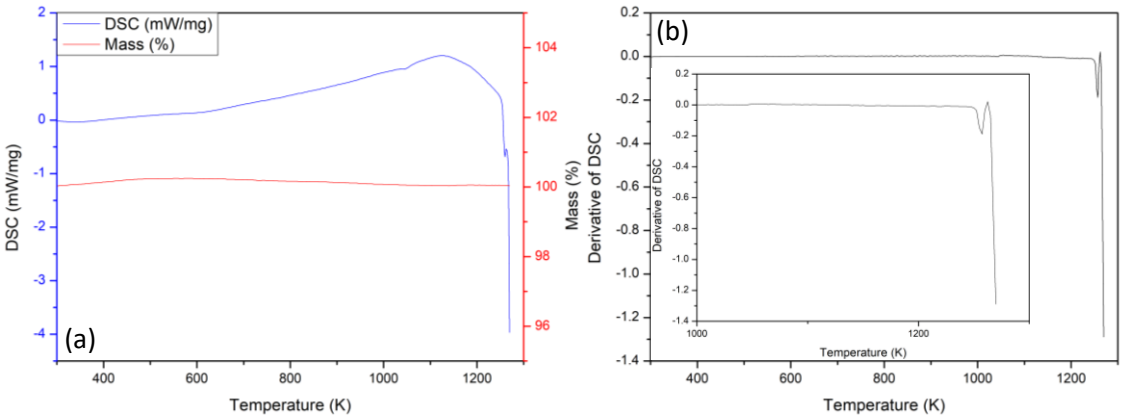

Figure 5.47: *TGA/DSC data collected for $Bi_{0.95}Na_{0.05}Fe_{0.95}Nb_{0.05}O_3$ (a) Full TGA/DSC plot from 298 K to 1270 K, (b) Derivative of DSC against temperature from 298 K to 1270 K.*

The *P*4*mm* region does not seem to show many differences from the *R*3*c* region. The results for x = 0.25, 0.40 and 0.60 are shown in *figures 5.48-5.50* and indicate a small decrease in mass, close to 1%, as the temperature is increased. Results for x = 0.2, 0.3, 0.35 and 0.65 can be found in appendix *figures A3.69-A3.72*. This loss of mass could be linked to loss of excess volatiles. The reason for this is the DSC data does not indicate any intrinsic structural change is occurring around the period of mass loss and so it is likely an external change. The DSC and derivative DSC data for this region seems to be harder to interpret as the derivative DSC data seems to be considerably noisier than the data collected for the x = 0.05 material. This has made it difficult to identify a possible Curie temperature on the assumption that the room temperature structure is polar. This is not unusual and is often seen in doped $BiFeO_3$ materials and may arise as a result of the lack of a sharp phase transition. One apparent trend seems to be that the big decrease seen towards the end of the x = 0.25 DSC data indicative of the decomposition point seems to not be present in the x = 0.4 and 0.6 data. This seems to indicate that the increase of NNO has led to an increase in the decomposition point.

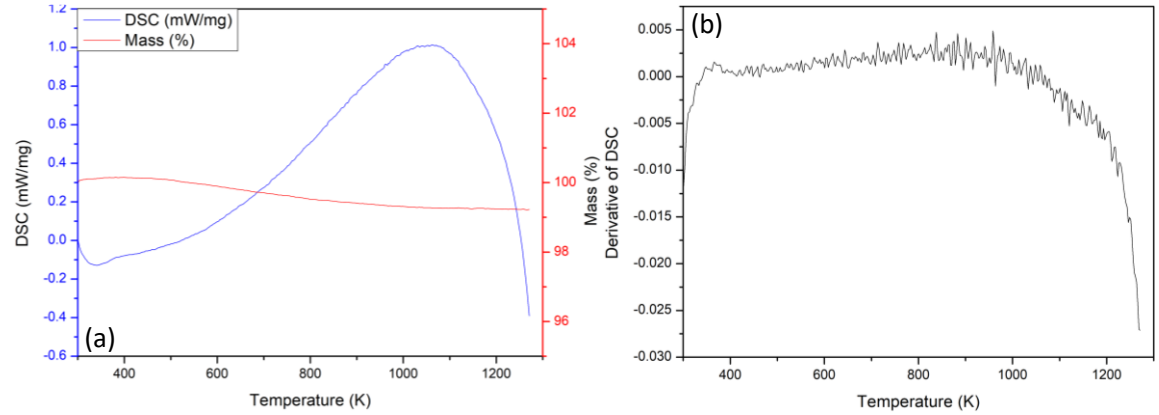

Figure 5.48: *TGA/DSC data collected for $Bi_{0.75}Na_{0.25}Fe_{0.75}Nb_{0.25}O_3$ (a) Full TGA/DSC plot from 298 K to 1270 K, (b) Derivative of DSC against temperature from 298 K to 1270 K.*

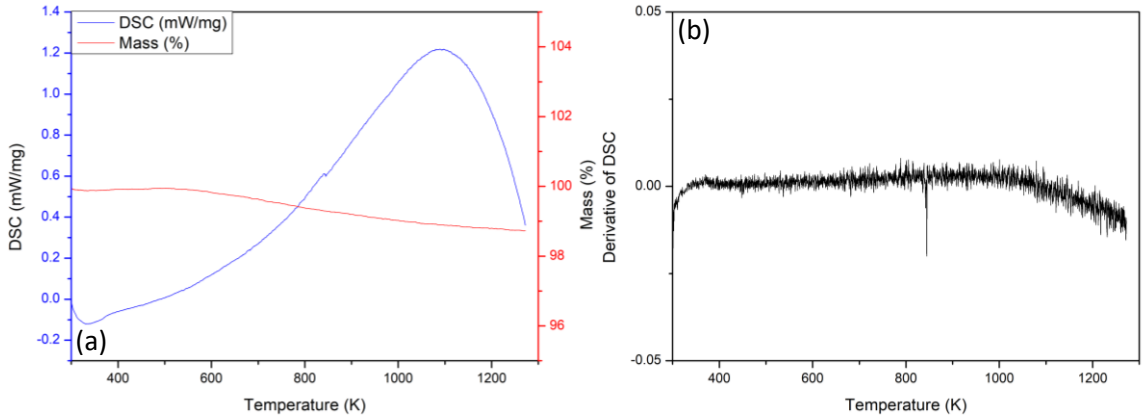

Figure 5.49: *TGA/DSC data collected for $Bi_{0.6}Na_{0.4}Fe_{0.6}Nb_{0.4}O_3$ (a) Full TGA/DSC plot from 298 K to 1270 K, (b) Derivative of DSC against temperature from 298 K to 1270 K.*

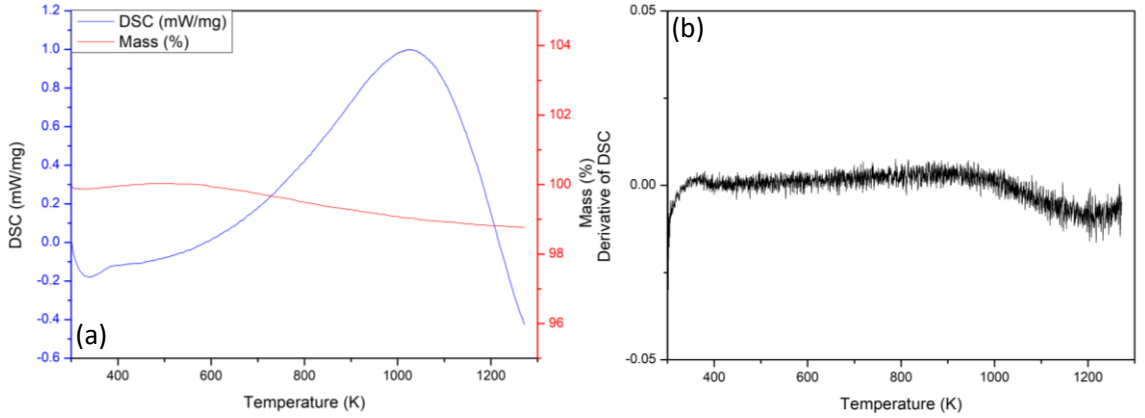

Figure 5.50: *TGA/DSC data collected for $Bi_{0.4}Na_{0.6}Fe_{0.4}Nb_{0.6}O_3$ (a) Full TGA/DSC plot from 298 K to 1270 K, (b) Derivative of DSC against temperature from 298 K to 1270 K.*

The mixed phase region, $0.1 < x < 0.175$, are represented by the $x = 0.15$ material in *figure 5.51* and $x = 0.125$ in appendix *figure A3.68*. The TGA/DSC data for $x = 0.15$ seems to show similar behaviour to the $x = 0.25$ in *figure 5.48* which may indicate that the sample is mostly *P*4*mm* as it thermally behaves closer to that sample than the known *R*3*c* materials. This can then be contrasted by the *x*

= 0.125 material which thermally behaves more similarly to the *x* = 0.075 found in appendix *figure A3.67* indicating it is mostly *R*3*c*.

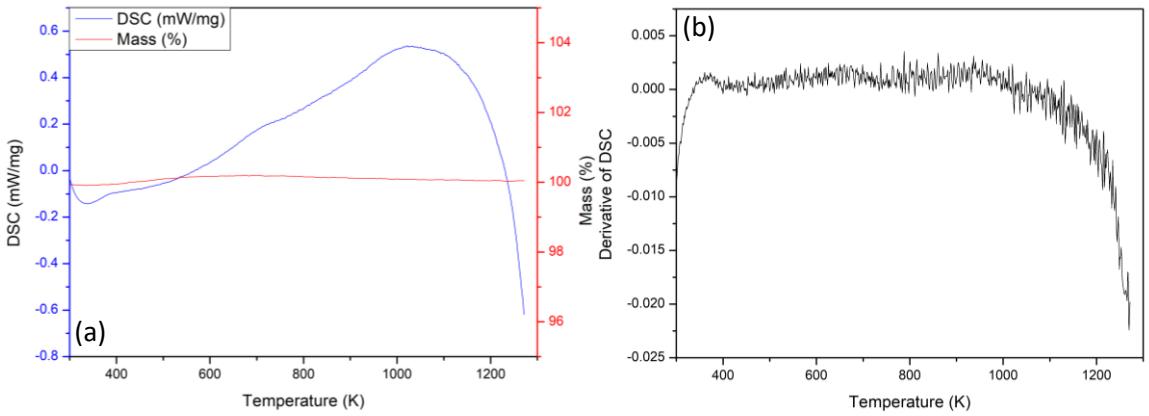

Figure 5.51: *TGA/DSC data collected for $Bi_{0.85}Na_{0.15}Fe_{0.85}Nb_{0.15}O_3$ (a) Full TGA/DSC plot from 298 K to 1270 K, (b) Derivative of DSC against temperature from 298 K to 1270 K.*

The *P*2$_1$*ma* region appears to have differences from previous data. The results for *x* = 0.75 and 0.9 samples can be seen in *figures 5.52 and 5.53*. Results for *x* = 0.675, 0.7, 0.8, 0.85 and 0.95 can be found in appendix *figures A3.73-A3.77*. In the TGA data for both there is an increase in the mass as the temperature increases, which does not seem to correlate with the DSC data so may be an external factor and not related to the sample or may be instrument related. The derivative DSC data for the *x* = 0.75 sample is hard to interpret due to the noise but there may be a small change around 1100 K that could be a phase transition. There does seem to be a large drop at the end of this data compared to the that seen in the *P*4*mm* region where the decomposition point seemed to increase, however, it could be leading to the drop seen at around 950 K in the *x* = 0.9 DSC data. The *x* = 0.9 derivative DSC data does show a clear change around 950 K, which is especially interesting as pure NNO has a phase transition to the cubic structure, $Pm\bar{3}m$ around this temperature[22]. However, this transition does not seem to be the ferroelectric to paraelectric transition in NNO so it is possible that other transitions may be present that the DSC data is unable to show. On the whole no conclusive data can be inferred from these analyses. In order to fully characterise the phase transitions in these materials high temperature neutron or X-ray diffraction data is required.

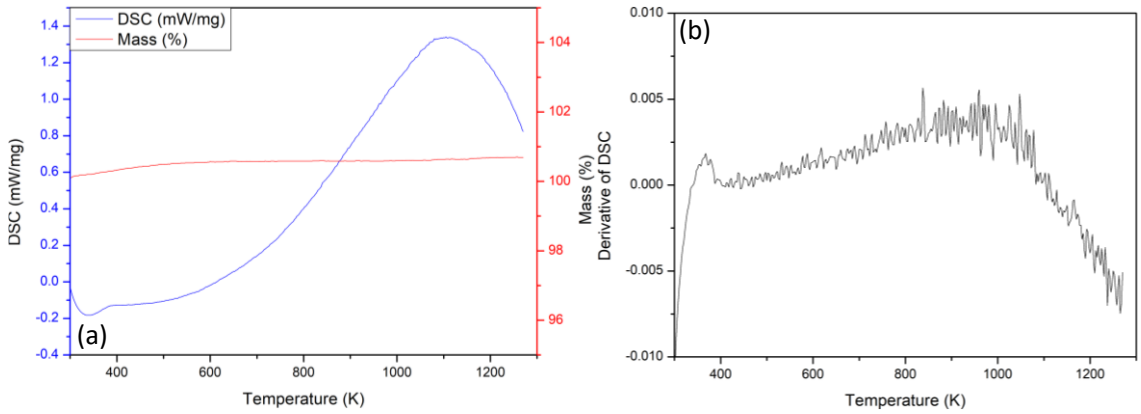

Figure 5.52: *TGA/DSC data collected for $Bi_{0.25}Na_{0.75}Fe_{0.25}Nb_{0.75}O_3$ (a) Full TGA/DSC plot from 298 K to 1270 K, (b) Derivative of DSC against temperature from 298 K to 1270 K.*

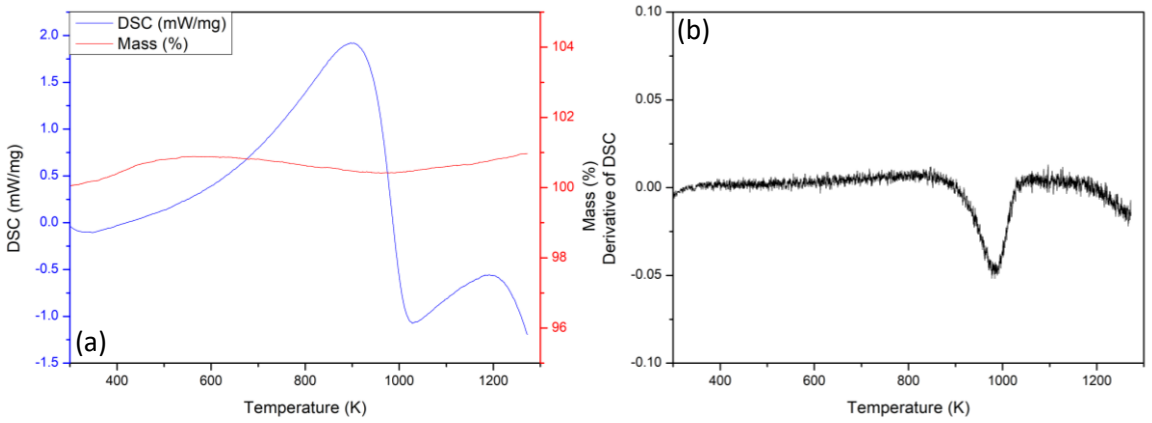

Figure 5.53: *TGA/DSC data collected for $Bi_{0.1}Na_{0.9}Fe_{0.1}Nb_{0.9}O_3$ (a) Full TGA/DSC plot from 298 K to 1270 K, (b) Derivative of DSC against temperature from 298 K to 1270 K.*

5.5 Magnetic Characterisation

A SQUID magnetometer was used to determine the presence of magnetic hysteresis and susceptibility behaviour in these materials from 2 K to 300 K. The temperature was increased to 380 K in some materials in an attempt to determine the Néel temperature (T_N). SQUID data not included in the main thesis body can be found in appendix *figures A3.78-A3.86*. This includes data for x = 0.2, 0.3 and 0.35 in appendix *figures A.3.80, A3.82 and A3.83*.

Similar to the x = 0.10 sample discussed in chapter 3, the x = 0.05 sample showed weak magnetic hysteresis with a small coercive field as shown in *figure 5.54 (a)*. This indicates that even a small amount of dopant is able to cause a change in the magnetic structure. Based on conclusion reached in Chapter 3 it is suggested that the spin cycloid has an intermittent length between that observed in pure $BiFeO_3$ and the $Bi_{0.9}Na_{0.1}Fe_{0.9}Nb_{0.1}O_3$ materials. The zero field cooled (ZFC), field cooled (FC) data are likely incorrect as it suggests that the T_N is around 375 K. However, this value is below the

T_N found for the x = 0.10 material (discussed in chapter 3) which occurs at approximately 580 K. Since it would be expected that T_N decreases with increasing NNO content it should be expected that T_N would lie between 640 K (BFO) and 580 K (x = 0.10). However, it is apparent that these data are quite noisy and in fact the ZFC and FC data do not really diverge but rather cross. This suggests that the sample may be shifting during the measurement.

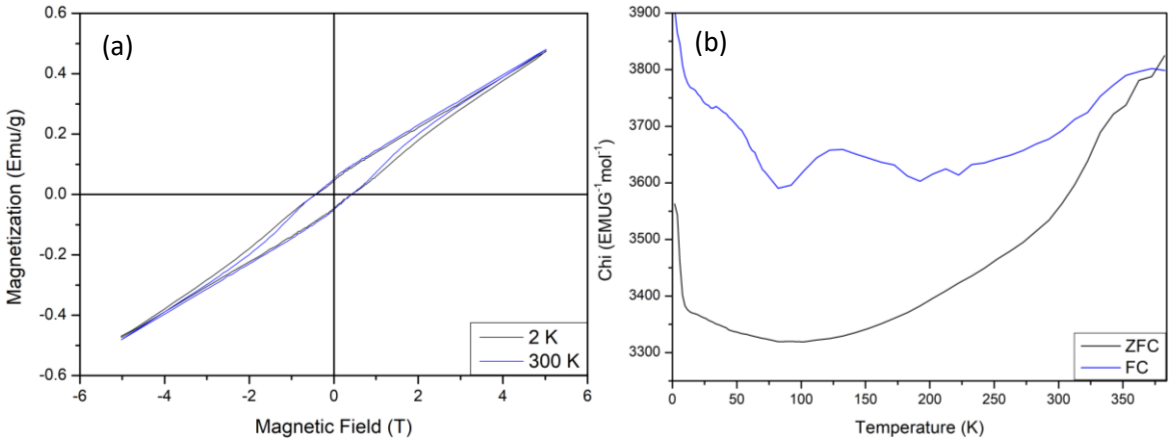

Figure 5.54: *Magnetic data collected using SQUID magnetometry for $Bi_{0.95}Na_{0.05}Fe_{0.95}Nb_{0.05}O_3$, (a) Hysteresis loops from 2 K to 300 K at fields from -5 T to 5 T, (b) Variable temperature Zero field cooled and Field cooled data at 0.1 T.*

The SQUID magnetometer data for the mixed phase region, the x = 0.15 material, suggests that it displays room temperature antiferromagnetic order from *figure 5.55*. The ZFC, FC data in *figure 5.55 (b)* suggests that the Néel transition is closer to room temperature, likely around 400 K, when compared to the NNO10% material in chapter 3.

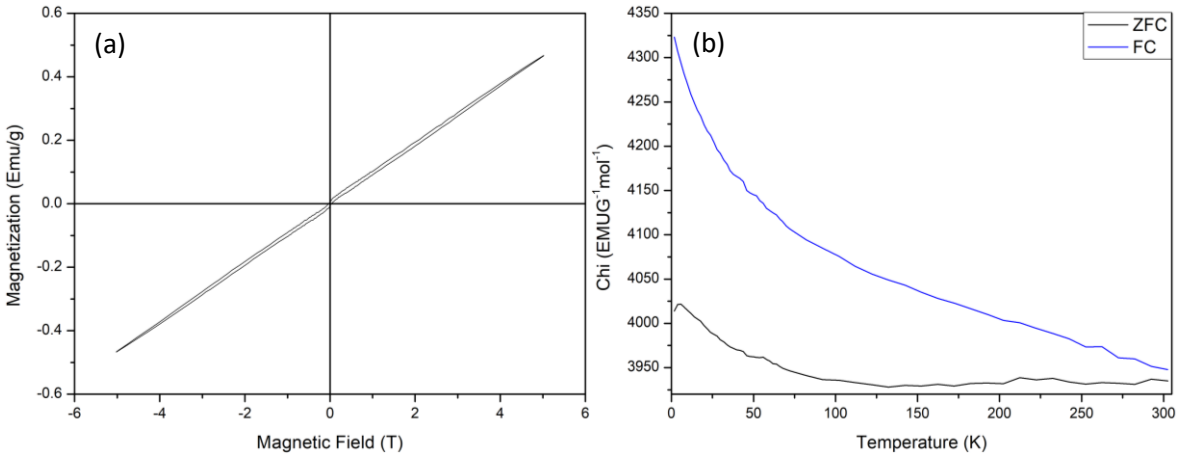

Figure 5.55: *Magnetic data collected using SQUID magnetometry for $Bi_{0.85}Na_{0.15}Fe_{0.85}Nb_{0.15}O_3$, (a) Hysteresis loops at 300 K at fields from -5 T to 5 T, (b) Variable temperature Zero field cooled and Field cooled data at 0.1 T.*

The SQUID magnetometer data for the *P*4*mm* region suggests that these materials are magnetically ordered at room temperature consistent with the observation of magnetic Bragg peaks in the neutron diffraction data. The data for the x = 0.25 and 0.4 samples, plotted in *figures 5.56 and 5.57,* show no real hysteresis at either 2 K or 300 K consistent with antiferromagnetic ordering. The ZFC

and FC data indicates that T_N is above room temperature. In the x = 0.25 sample data there is a divergence between the ZFC and FC data at 100 K in *figure 5.56 (b)*. This may indicate a secondary magnetic transition; it is also found in the x = 0.2 data found in *appendix figure A5.77*. However, there is no obvious change in the magnetic Bragg peaks in the PND data collected at room temperature and 10 K. Additionally, whilst there is some divergence between ZFC and FC data (typical of site disorder) it is not present in the other materials in this region, x = 0.3, 0.35, 0.4 and 0.5. It is possible that this transition arises as a result of NNO and BFO rich and mixed areas as indicated by the diffuse scattering in the PND data or alternatively the presence of a magnetic impurity.

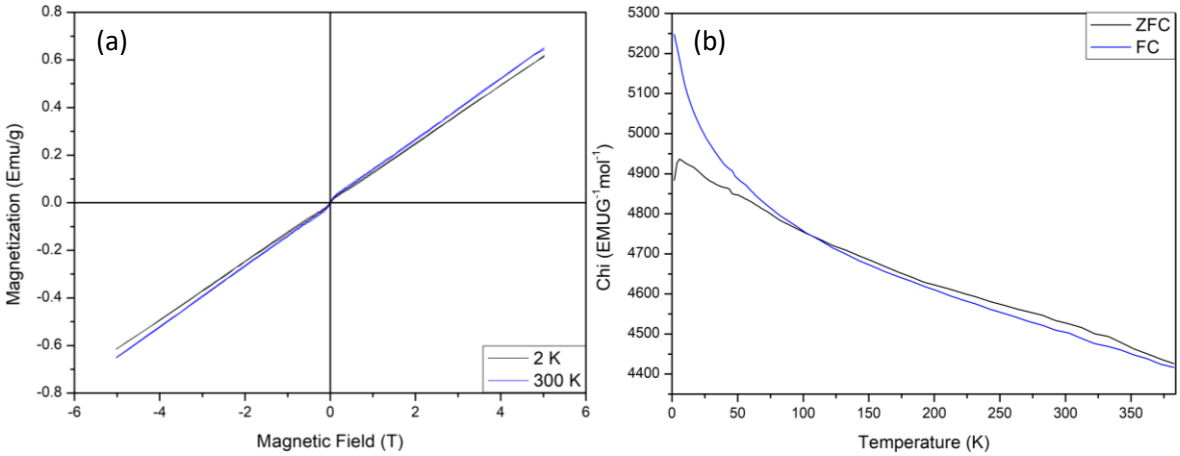

Figure 5.56: *Magnetic data collected using SQUID magnetometry for $Bi_{0.75}Na_{0.25}Fe_{0.75}Nb_{0.25}O_3$, (a) Hysteresis loops from 2 K to 300 K at fields from -5 T to 5 T, (b) Variable temperature Zero field cooled and Field cooled data at 0.1 T.*

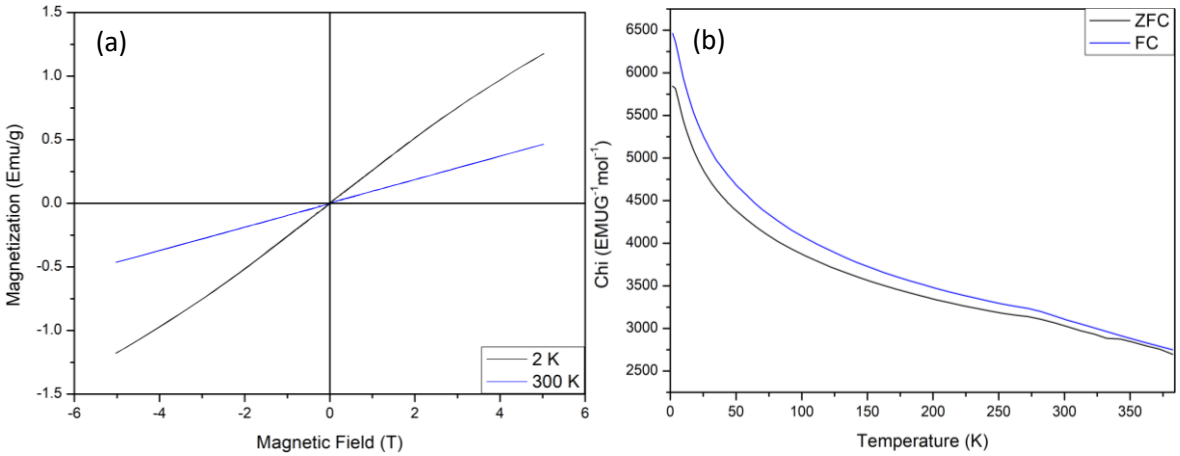

Figure 5.57: *Magnetic data collected using SQUID magnetometry for $Bi_{0.6}Na_{0.4}Fe_{0.6}Nb_{0.4}O_3$, (a) Hysteresis loops from 2 K to 300 K at fields from -5 T to 5 T, (b) Variable temperature Zero field cooled and Field cooled data at 0.1 T.*

As the iron within the samples are replaced with niobium it is expected that the magnetic behaviour will weaken and this is shown in the $P2_1ma$ region. Magnetic measurements of x = 0.7 and 0.8 can be seen in *figures 5.58 and 5.59*. At 2 K both materials display weak hysteresis typical of site disordered materials such as spin glass systems. Magnetic transitions occur around 10 K and 3 K

for the *x* = 0.7 and 0.8 samples, respectively. At room temperature both are found as paramagnets, which agrees with the room temperature and low temperature neutron data collected for the *x* = 0.75. It is clear from the SQUID magnetometry data collected for these materials that, as expected, as the NNO content increases the magnetic transition temperature decreases.

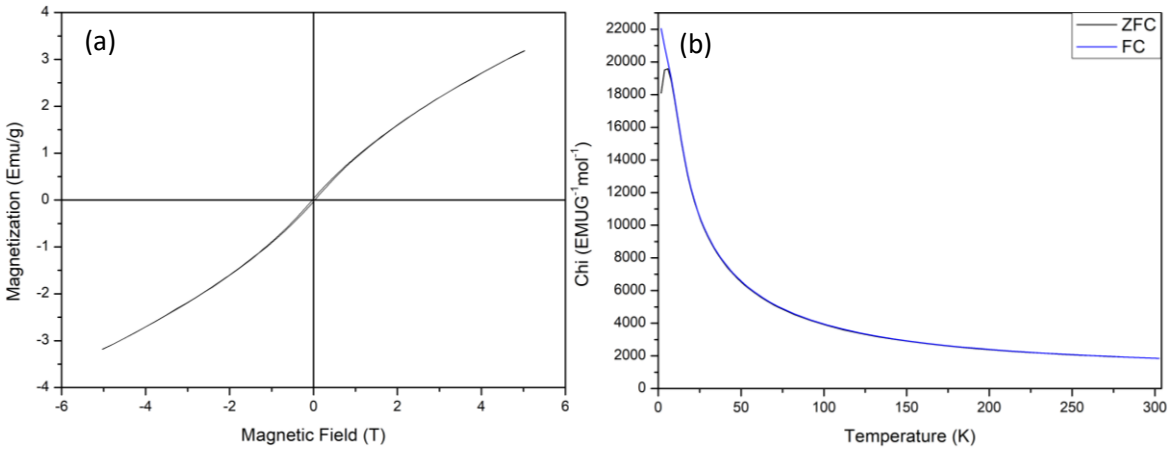

Figure 5.58: *Magnetic data collected using SQUID magnetometry for $Bi_{0.3}Na_{0.7}Fe_{0.3}Nb_{0.7}O_3$, (a) Hysteresis loops at 2 K at fields from -5 T to 5 T, (b) Variable temperature Zero field cooled and Field cooled data at 0.1 T.*

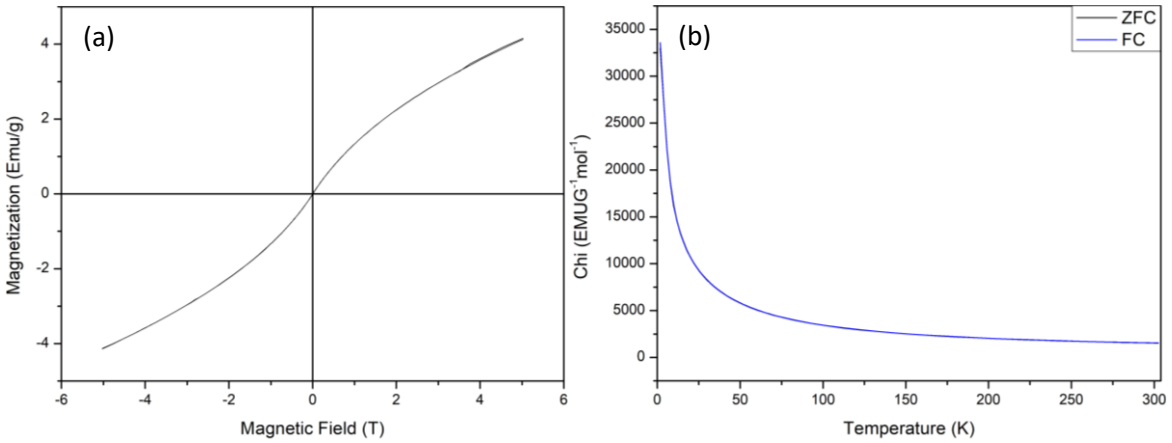

Figure 5.59: *Magnetic data collected using SQUID magnetometry for $Bi_{0.2}Na_{0.8}Fe_{0.2}Nb_{0.8}O_3$, (a) Hysteresis loops at 2 K at fields from -5 T to 5 T, (b) Variable temperature Zero field cooled and Field cooled data at 0.1 T.*

5.6 Solid State NMR

Two samples, *x* = 0.9 and 0.95, were analysed using a Bruker Avance III spectrometer solid state NMR at the University of Durham by Dr Karen Johnston. ^{23}Na and ^{93}Nb MAS NMR was used to identify the possible sodium and niobium environments. Shown in *figure 5.60* are the results for the ^{23}Na MAS NMR. The first spectra shows the *x* = 0.9 result with the second spectra showing the result for the *x* = 0.95 material. For both samples a resonance at δ = -7.8 ppm can be observed which can be attributed to paramagnetism likely arising from the iron present in the sample. Additionally, the *x* = 0.95 sample shows an additional resonance at δ = 3.9 ppm which may be

related to a sodium-based impurity due to its small size. The ^{93}Nb MAS NMR is shown in *figure 5.61*. For both samples a resonance is seen at δ = -1096.4 ppm that again can be attributed to the presence of paramagnetism due to the iron content. This suggests that a small unknown second phase is present in the x = 0.95, which is consistent with the XRD data. Unfortunately, it is difficult to interpret this data and compare it to previous solid state NMR in the literature by Johnston *et al*[14,15] due to the paramagnetic signal produced by the iron which masks the data.

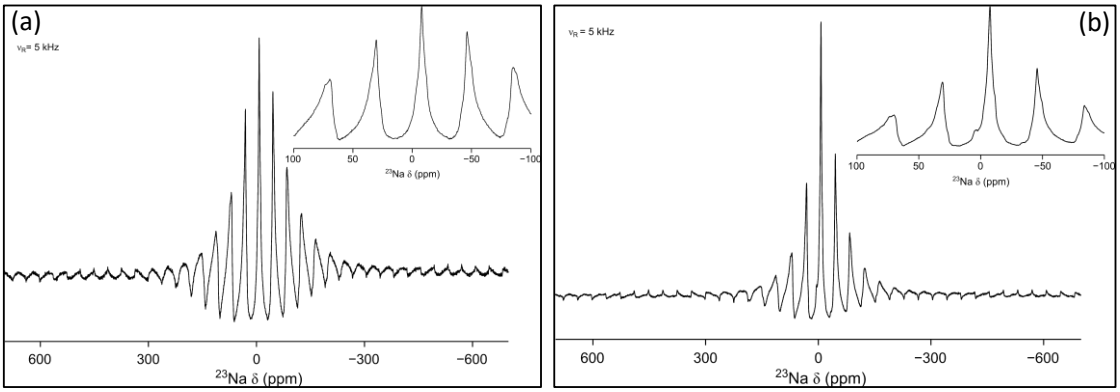

Figure 5.60: *^{23}Na MAS NMR collected for (a) $Bi_{0.1}Na_{0.9}Fe_{0.1}Nb_{0.9}O_3$ and (b) $Bi_{0.05}Na_{0.95}Fe_{0.05}Nb_{0.95}O_3$.*

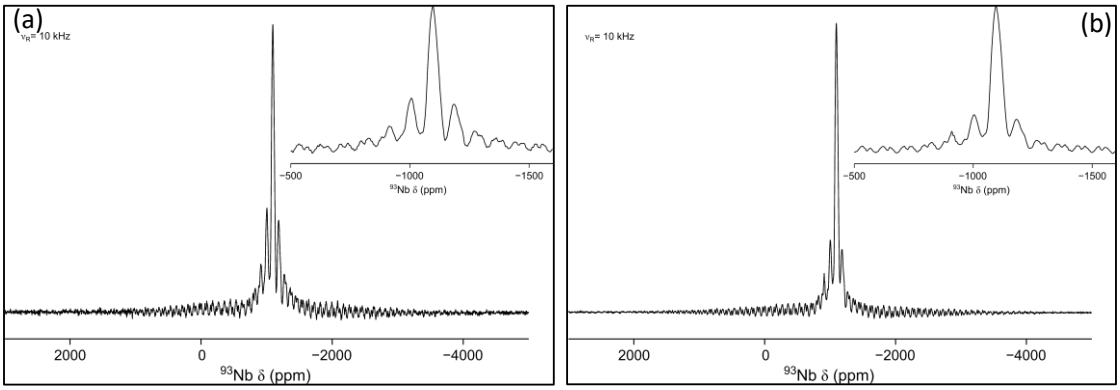

Figure 5.61: *^{93}Nb MAS NMR collected for (a) $Bi_{0.1}Na_{0.9}Fe_{0.1}Nb_{0.9}O_3$ and (b) $Bi_{0.05}Na_{0.95}Fe_{0.05}Nb_{0.95}O_3$.*

5.7 Conclusions

The $Bi_{1-x}Na_xFe_{1-x}Nb_xO_3$ solid solution phase diagram is complicated. Room temperature PXRD showed that there were three distinct crystallographic regions present and the structures were identified as *R*3*c*, *P*4*mm* and *P*2$_1$*ma*. Room temperature PND data confirms the phase assignments made using XRD. However, the sensitivity of PND to oxygen demonstrated additional complexities. Between x = 0.2 and 0.6 diffuse scattering is clearly observed. These diffuse peaks occur at locations where peaks would be expected in the *P*2$_1$*ma* symmetry. It is suggested that whilst on average

these materials exhibit *P*4*mm* symmetry the local environment may be closer to $P2_1ma$ as a result of $NaNbO_3$ and $BiFeO_3$ rich regions. These peaks, whilst sharper in materials, with $x > 0.65$ retain some broadening suggesting that domain formation is still present in these materials. However, these materials are now better described on average using the $P2_1ma$ symmetry consistent with the PXRD analyses. The possibility of morphotropic phase boundaries where a potential PZT-like sample could be found was also explored. The preferential boundary would be at the *R*3*c* and *P*4*mm* phase transition (the same transition is seen PZT) since this region also exhibits room temperature magnetic ordering giving rise to a multiferroic with enhanced electrical properties. Unfortunately, there is no sharp phase boundary in this region with instead a mixture of the *R*3*c* and *P*4*mm* phases has been found instead despite attempts to synthesise a single-phase sample. Within the phase diagram there is also a phase boundary between *P*4*mm* and $P2_1ma$. However, whilst this phase boundary appears sharp in symmetry terms this is a diffuse phase transition which occurs over a large composition range as NNO content increases as described above.

Close inspection of the octahedral bond arrangement suggests that there are still significant *B*-site displacements in these materials indicating polar behaviour and thus these materials are likely to be ferroelectric. However, electrical measurements proved difficult to accomplish due to insufficient density of pellets, a problem seen consistently in the literature involving alkaline niobates[23-25].

The outline of a variable temperature phase diagram can be built using low temperature XRD. Despite the low quality of some of the patterns there was enough information to determine there does not seem to be any low temperature structural changes in these materials. In the absence of high temperature diffraction data, TGA was used in an attempt to discern high temperature structural changes. However, these measurements did not prove to be sensitive enough. This could possibly be due to only subtle changes occurring such as a transition from tetragonal *P*4*mm* to cubic $Pm\bar{3}m$ or *P*4/*mmm* or possibly due to diffuse ferroelectric-paraelectric phase transitions which are typical of doped $BiFeO_3$ materials. Alternatively, of course, these materials could be paraelectric at room temperature and this cannot be ruled out.

However, room temperature magnetic Bragg peaks are observed in $x < 0.4$ materials. SQUID magnetometry suggests these materials are antiferromagnetic and become systematically more glassy-like with increasing NNO content. The magnetic transition temperature is seen to decrease with increasing NNO content. Overall this phase diagram shows some exciting potential for interesting multiferroic materials and further investigations are necessary to explore these in more detail.

5.8 References

1 I. P. Raevski, S. P. Kubrin, J. -. Dellis, S. I. Raevskaya, D. A. Sarychev, V. G. Smotrakov, V. V. Eremkin and M. A. Seredkina, *Ferroelectrics,* 2008, **371**, 113-118 (DOI:10.1080/00150190802397767).

2 Y. Ma and X. Chen, *J. Appl. Phys.,* 2009, **105**, 054107 (DOI:10.1063/1.3081648).

3 S. Dash, R. Padhee, P. Das and R. Choudhary, *J Mater Sci: Mater Electron,* 2013, **24**, 3315-3323 (DOI:10.1007/s10854-013-1249-4).

4 P. Teslenko, A. Razumnaya, V. Ponomarenko, A. Rudskaya, A. Nazarenko, A. Anokhin, M. Avramenko, D. Levshov, M. Kupriyanov and Y. Yuzyuk, *Phys. Solid State,* 2014, **56**, 1866-1871 (DOI:10.1134/S1063783414090285).

5 S. Dash, R. Choudhary and M. Goswami, *J Polym Res,* 2015, **22**, 1-7 (DOI:10.1007/s10965-015-0696-4).

6 M. De and H. S. Tewari, *Ferroelectrics,* 2017, **519**, 43-48 (DOI:10.1080/00150193.2017.1362284).

7 M. De, S. P. Patel and H. S. Tewari, *J. Mater. Sci. : Mater. Electron.,* 2017, **28**, 6928-6935 (DOI:10.1007/s10854-017-6393-9).

8 Y. Saad, I. Álvarez-Serrano, M. L. López and M. Hidouri, *Ceram. Int.,* 2018, **44**, 18560-18570 (DOI:https://doi.org/10.1016/j.ceramint.2018.07.078).

9 M. De, S. Hajra, R. Tiwari, S. Sahoo, R. N. P. Choudhary and H. S. Tewari, *Ceram. Int.,* 2018, **44**, 11792-11797 (DOI:https://doi.org/10.1016/j.ceramint.2018.03.263).

10 R. C. Lennox, D. D. Taylor, L. J. Vera Stimpson, G. B. G. Stenning, M. Jura, M. C. Price, E. E. Rodriguez and D. C. Arnold, *Dalton Trans.,* 2015, **44**, 10608-10613 (DOI:10.1039/c5dt00140d).

11 M. W. Lufaso, T. A. Vanderah, I. M. Pazos, I. Levin, R. S. Roth, J. C. Nino, V. Provenzano and P. K. Schenck, *Phase formation, crystal chemistry, and properties in the system Bi2O3–Fe2O3–Nb2O5*, 2006.

12 R. Radha, Y. Ravi Kumar, M. Sakar, K. Rohith Vinod and S. Balakumar, *Understanding the lattice composition directed in situ structural disorder for enhanced visible light photocatalytic activity in Bismuth iron niobate pyrochlore*, 2018.

13 G. King and P. M. Woodward, *J. Mater. Chem.,* 2010, **20**, 5785-5796 (DOI:10.1039/B926757C).

14 K. E. Johnston, C. C. Tang, J. E. Parker, K. S. Knight, P. Lightfoot and S. E. Ashbrook, *J. Am. Chem. Soc.,* 2010, **132**, 8732-8746 (DOI:10.1021/ja101860r).

15 K. E. Johnston, J. M. Griffin, R. I. Walton, D. M. Dawson, P. Lightfoot and S. E. Ashbrook, *Phys. Chem. Chem. Phys.,* 2011, **13**, 7565-7576 (DOI:10.1039/C1CP20258H).

16 D. W. Baker, P. A. Thomas, N. Zhang and A. M. Glazer, *Appl. Phys. Lett.,* 2009, **95**, 091903 (DOI:10.1063/1.3212861).

17 R. P. Ummer, P. Sreekanth, B. Raneesh, R. Philip, D. Rouxel, S. Thomas and N. Kalarikkal, *RSC Adv.,* 2015, **5**, 67157-67164 (DOI:10.1039/c5ra10422j).

18 S. Dash and R. N. P. Choudhary, *IEEE Trans. Dielectr. Electr. Insul.,* 2016, **23**, 3652-3658 (DOI:10.1109/TDEI.2016.005755).

19 S. K. Mishra, N. Choudhury, S. L. Chaplot, P. S. R. Krishna and R. Mittal, *Phys. Rev. B,* 2007, **76**, 024110 (DOI:10.1103/PhysRevB.76.024110).

20 D. C. Arnold, K. S. Knight, F. Morrison and P. Lightfoot, *Phys. Rev. Lett.,* 2009, **102**, 027602 (DOI:10.1103/PhysRevLett.102.027602).

21 D. C. Arnold, K. S. Knight, G. Catalan, S. Redfern, J. Scott, P. Lightfoot and F. Morrison, *Adv. Funct. Mater.,* 2010, **20**, 2116-2123 (DOI:10.1002/adfm.201000118).

22 S. K. Mishra, R. Mittal, V. Y. Pomjakushin and S. L. Chaplot, *Phys. Rev. B,* 2011, **83**, 134105 (DOI:10.1103/PhysRevB.83.134105).

23 J. Koruza and B. Malič, *J. Eur. Ceram,* 2014, **34**, 1971-1979 (DOI:https://doi.org/10.1016/j.jeurceramsoc.2014.01.035).

24 B. Malic, J. Koruza, J. Hrescak, J. Bernard, K. Wang, J. G. Fisher and A. Bencan, *Materials,* 2015, **8**, 8117-8146 (DOI:10.3390/ma8125449).

25 J. Acker, H. Kungl and M. J. Hoffmann, *J Am Ceram Soc,* 2010, **93**, 1270-1281 (DOI:10.1111/j.1551-2916.2010.03578.x).

Chapter Six: Conclusions and Future Work

The room temperature multiferroic $BiFeO_3$ (BFO) and ferroelectric $NaNbO_3$ (NNO) are incredibly interesting and complex materials in their own right. This led to the theory that putting the two materials together could lead to improved room temperature multiferroic behaviour. In lead zirconate titanate (PZT) at the morphotropic phase boundary composition, $PbZr_{0.52}Ti_{0.48}O_3$, competition between the polar phases, *R*3*m* and *P*4*mm*, leads to improved dielectric constant and piezoelectric properties[1,2]. BFO and NNO seemed good candidates to replicate this behaviour.

To avoid problems such as inhomogeneity associated with the BFO-$KNbO_3$ (KNO) phase diagram a modified synthesis procedure inspired by Levin *et al*[3] was used[4]. This involved much longer heating of the materials during synthesis. Powder X-ray powder diffraction (PXRD) patterns were found to possess sharp peaks with flat backgrounds suggesting the success of this procedure with highly crystalline materials produced. Analysis of the PXRD patterns of the $Bi_{1-x}Na_xFe_{1-x}Nb_xO_3$ solid solution with Rietveld refinement led to a series of phase transitions, from the BFO parent structure *R*3*c* ($0.05 \leq x \leq 0.1$) to the tetragonal *P*4*mm* structure ($0.175 \leq x \leq 0.65$) to the polar NNO structure $P2_1ma$ ($0.675 \leq x \leq 0.95$). It was found as the $P2_1ma$ region reached $x = 0.85$ and above this composition another phase was found to grow in the PXRD patterns which was identified as the anti-polar NNO structure *Pbcm*. The observed phase diagram led to two morphotropic phase boundaries between *R*3*c* - *P*4*mm* and *P*4*mm* - $P2_1ma$. The *R*3*c* - *P4mm* phase boundary ($0.1 < x < 0.175$) was found to produce materials that were mixed phase in nature. The two samples synthesised in this region $x = 0.125$ and 0.15 were found to be mostly *P4mm* and did not show evidence of a monoclinic phase as is seen in PZT[5]. The *P*4*mm* - $P2_1ma$ phase boundary was found to be different in nature in that a sharp phase transition with no noticeable area of phase co-existence was present promising for probing MPB behaviour.

Room temperature powder neutron diffraction (PND) found that the structures were much more complicated than the PXRD alluded to. The *P*4*mm* region was plagued with diffuse scattering not seen in the PXRD data and the $P2_1ma$ region possessed peaks, in a similar position to the diffuse peaks in the *P*4*mm* region, that were broader than expected. This was likely to be oxygen tilt related as these features were missing in the PXRD patterns and likely short range in nature due to the diffuse nature of the peaks. Two possible theories on the origin of the variation of oxygen tilts were proposed. The first was the possibility of short range order on the *A*-site which was restricted as there was not enough of a size difference on the *B*-site. The second was proposed due to the similarity observed earlier between the diffuse peaks in the *P*4*mm* region and the broad peaks in

the $P2_1ma$ region and whether this was related. This would imply that there is short range order of NNO rich regions with a local tilt environment and the local structure may be $P2_1ma$. If the diffuse scattering is related to the $P2_1ma$ structure then the phase transition may be a continuous phase transition which could explain the sharp phase transition seen at the $P4mm$ - $P2_1ma$ phase boundary. Future work is required for a conclusive answer. The use of selected area electron diffraction could be used to analyse the structure at greater length by looking at the atomic scale. To investigate the possibility of the local structure and the possibility of short range order, X-ray absorption fine structure (XAFS) and (X-ray and neutron) atomic pair distribution function (PDF) could be employed.

Low temperature PND and PXRD were used to determine whether any low temperature transitions occurred. All materials seem to remain at the same structure found at room temperature down to around 12 K. High temperature PND of the x = 0.1 and 0.5 materials were performed to determine high temperature phase transitions. The x = 0.1 material is present in the $R3c$ structure until 973 K where a high temperature transition occurs. Unfortunately, the new phase has yet to be identified, with a deviation from the high temperature β-phase of BFO, $Pbnm$[6]. The disappearance of magnetic Bragg peaks identified the Néel temperature (T_N) as being between 573 K and 598 K. The high temperature analysis of the x = 0.5 material found that a subtle phase transition occurs at 973 K to $Pm\bar{3}m$ (or $P4/mmm$) which from the B-O bond lengths may be the Curie temperature (ferroelectric to paraelectric phase transition).

Materials from $0.05 \leq x \leq 0.4$ were found to possess room temperature magnetism. The T_N was found to decrease as x increases in $Bi_{1-x}Na_xFe_{1-x}Nb_xO_3$. The magnetism was found to be optimal in the x = 0.1 material which was found to possess a coercive field which is not indicative of pure antiferromagnetic order. Attempts to identify the magnetic structure of the x = 0.1 material through room temperature PND was found to be difficult due to the presence of strain in the structure. The presence of strain was supported by the presence of small grains and domains through Raman spectroscopy. Preliminary refinements suggest that the spin cycloid is significantly lengthened when compared with undoped BFO. The cycloid length now exceeds the size of the domains meaning that it is no longer spatially averaged to zero resulting in magnetic hysteresis. However, these refinements could not rule out the possibility of a k = (0,0,0) magnetic structure with hysteresis arising from spin canting. High temperature SQUID of the x = 0.1 material found a T_N in line with the high temperature PND. Further analysis of the data is required to probe the magnetism in greater depth. Despite the x = 0.1 material possessing improved magnetic order over undoped BFO the SQUID hysteresis loop at 2 K and 300 K is unable to saturate at 5 T. This may be linked to the diamagnetic Nb^{5+} sharing the B-site with Fe^{3+}, a possibility to improve the magnetism may be

to replace this with Mo^{5+} or W^{5+} which have one unpaired electron. This would complicate the synthesis procedure as the production of both Mo^{5+} or W^{5+} would require reduction during synthesis but it is possible as shown in the double perovskite Sr_2FeMoO_6[7,8].

Further investigation of the magnetism for the x = 0.5 material found an interesting difference between the Na and K materials which was not identified in the previous BFO-$KNbO_3$ study[4]. $Bi_{0.5}K_{0.5}Fe_{0.5}Nb_{0.5}O_3$ was found to possess weak antiferromagnetic order at room temperature from room temperature PND. This was found due to similarities in the magnetic Bragg peaks identified to those identified in the low temperature PND for the x = 0.5, $Bi_{0.5}Na_{0.5}Fe_{0.5}Nb_{0.5}O_3$, material. Bond angles for $Bi_{0.5}K_{0.5}Fe_{0.5}Nb_{0.5}O_3$ were found to be around 180° and decrease in the $Bi_{0.5}Na_{0.5}Fe_{0.5}Nb_{0.5}O_3$ thus this change in the bond angles leads to a change in the superexchange pathways lowering the transition temperature in the sodium derivative.

Attempts were made to measure the electrical properties of samples to determine the presence of ferroelectric behaviour. However, it was found to be difficult to produce dense pellets for the purpose of these measurements, with multiple attempts on various compositions leading to only a single pellet of the x = 0.1 composition possessing a density over 90%. To produce pellets of the required density a different press such as a cold isostatic press could be employed or spark plasma sintering may be required. With a reliable procedure to produce dense pellets it would be interesting to measure the electric properties of *P*4*mm* samples due to the possibility of phase competition between *P*4*mm* and $P2_1ma$ suggested by PND to explore the likelihood of PZT-like enhanced electrical properties. This then could be further expanded by attempting the procedure used by Mandal *et al*[9,10] where the magnetic properties of materials could be improved by adding additional iron to improve percolation pathways. This could enable room temperature multiferroic behaviour in over a wider composition range.

With the differences seen in the properties between doping with Na and K on the *A*-site it would be interesting to find an *A*-site with 1+ charge that sits in between the two in size. Silver is a potential candidate. However, attempts to synthesise materials in the $Bi_{1-x}Ag_xFe_{1-x}Nb_xO_3$ solid solution failed. Replacing Na and K on the *A*-site with Ag leads to a decrease in the thermal stability of materials during synthesis thus requiring an altered synthesis pathway for this solid solution. To create a size difference in the *B*-site cations doping with Sb^{5+} was seen as a potential solution. Unfortunately, the synthesis pathway using Sb_2O_3 did not seem to work as the Sb^{3+} did not seem to oxidise readily enough to form materials in the $Bi_{1-x}Na_xFe_{1-x}Sb_xO_3$ solid solution and Sb_2O_5 was not available to purchase. Another interesting future experiment would be to determine whether the anti-polar phase seen in small amounts at the NNO end of the phase diagram could be prioritised

over the polar structure. It has been found previously that doping BFO with rare earths leads to the formation of antiferroelectric phases[11]. Replacing Bi in the $P2_1ma$ region ($0.675 \leq x \leq 0.95$) with a rare earth such as lanthanum could lead to the synthesis of materials with the *Pbcm* structure as the major phase.

Overall, this work demonstrates that materials with interesting properties can be realised in the BFO-NNO solid solution. These materials will hopefully provide a starting point for developing multiferroic materials suitable for commercial application.

6.2 References

1 B. Jaffe, W. R. Cook Jr. and H. Jaffe, *Piezoelectric Ceramics*, Academic Press, London, UK, 1971.

2 C. A. Randall, N. Kim, J. Kucera, W. Cao and T. R. Shrout, *J Am Ceram Soc,* 1998, **81**, 677-688 (DOI:10.1111/j.1151-2916.1998.tb02389.x).

3 I. Levin, M. G. Tucker, H. Wu, V. Provenzano, C. L. Dennis, S. Karimi, T. Comyn, T. Stevenson, R. I. Smith and I. M. Reaney, *Chem. Mater.,* 2011, **23**, 2166-2175 (DOI:10.1021/cm1036925).

4 R. C. Lennox, D. D. Taylor, L. J. Vera Stimpson, G. B. G. Stenning, M. Jura, M. C. Price, E. E. Rodriguez and D. C. Arnold, *Dalton Trans.,* 2015, **44**, 10608-10613 (DOI:10.1039/c5dt00140d).

5 B. Noheda, D. E. Cox, G. Shirane, J. A. Gonzalo, L. E. Cross and S. Park, *Appl. Phys. Lett.,* 1999, **74**, 2059-2061 (DOI:10.1063/1.123756).

6 D. C. Arnold, K. S. Knight, F. Morrison and P. Lightfoot, *Phys. Rev. Lett.,* 2009, **102**, 027602 (DOI:10.1103/PhysRevLett.102.027602).

7 Y. Tomioka, T. Okuda, Y. Okimoto, R. Kumai, K. -. Kobayashi and Y. Tokura, *Phys. Rev. B,* 2000, **61**, 422-427 (DOI:10.1103/PhysRevB.61.422).

8 L. Balcells, J. Navarro, M. Bibes, A. Roig, B. Martínez and J. Fontcuberta, *Appl. Phys. Lett.,* 2001, **78**, 781-783 (DOI:10.1063/1.1346624).

9 P. Mandal, M. J. Pitcher, J. Alaria, H. Niu, P. Borisov, P. Stamenov, J. B. Claridge and M. J. Rosseinsky, *Nature,* 2015, **525**, 363-366 (DOI:10.1038/nature14881).

10 P. Mandal, M. J. Pitcher, J. Alaria, H. Niu, M. Zanella, J. B. Claridge and M. J. Rosseinsky, *Adv. Funct. Mater.,* 2016, **26**, 2523-2531 (DOI:10.1002/adfm.201504911).

11 D. C. Arnold, *IEEE Trans. Ultrason. Ferroelectr. Freq. Control,* 2015, **62**, 62-82 (DOI:10.1109/TUFFC.2014.006668).

Appendix 1 for Chapter Three: Investigation of $Bi_{0.9}Na_{0.1}Fe_{0.9}Nb_{0.1}O_3$ material

Table A1.1: *Rietveld refinement parameters for RT XRD of $Bi_{0.9}Na_{0.1}Fe_{0.9}Nb_{0.1}O_3$, $Bi_{0.9}K_{0.1}Fe_{0.9}Nb_{0.1}O_3$, $Bi_{0.9}Na_{0.1}Fe_{0.9}Ta_{0.1}O_3$, $Bi_{0.9}K_{0.1}Fe_{0.9}Ta_{0.1}O_3$ and $Bi_{0.925}K_{0.075}Fe_{0.925}Nb_{0.075}O_3$.*

Parameter		$Bi_{0.9}A_{0.1}Fe_{0.9}B_{0.1}O_3$					0.075
A, B		Na, Nb	K, Nb		Na, Ta	K, Ta	K, Nb
Space Group		*R* 3*c*	*R* 3*c* + *P* 4*mm*		*R* 3*c*	*R* 3*c*	*R* 3*c*
χ^2		8.179	11.95		10.66	10.60	7.739
wRp (%)		4.59	7.82		6.97	8.59	4.48
Rp (%)		2.98	5.43		4.57	4.91	9.97
a (Å)		5.58341(12)	5.6027(4)	3.97213(19)	5.58133(18)	5.59854(22)	5.59519(16)
b (Å)		5.58341(12)	5.6027(4)	3.97213(19)	5.58133(18)	5.59854(22)	5.59519(16)
c (Å)		13.8171(4)	13.8317(16)	3.96772(33)	13.8070(5)	13.8433(6)	13.8577(5)
α (°)		90	90	90	90	90	90
β (°)		90	90	90	90	90	90
γ (°)		120	120	90	120	120	120
Cell vol. (Å3)		373.033(22)	376.02(6)	62.602(7)	372.482(21)	375.768(27)	375.709(20)
Bi/Na 1	x	0.000	0.000	0.000	0.000	0.000	0.000
	y	0.000	0.000	0.000	0.000	0.000	0.000
	z	0.000	0.000	0.000	0.000	0.000	0.000
	UISO*100	5.26(19)	1.00*	1.00*	2.37(5)	2.26(11)	1.71(9)
Fe/Nb 1	x	0.000	0.000	0.500	0.000	0.000	0.000
	y	0.000	0.000	0.500	0.000	0.000	0.000
	z	0.22591(23)	0.2256(14)	0.508(12)	0.2295(4)	0.2321(6)	0.2284(4)
	UISO*100	0.96(12)	1.00*	1.00*	0.93(12)	1.49(15)	1.00*
O1	x	0.4403(25)	0.451(11)	0.500	0.452(4)	0.455(5)	0.4436(35)
	y	0.0068(24)	0.010(10)	0.500	0.001(4)	-0.004(5)	0.0058(33)
	z	0.9632(9)	0.966(4)	-0.022(32)	0.9666(15)	0.9670(19)	0.9651(13)
	UISO*100	1.00*	1.00*	1.00*	1.00*	1.00*	1.00*
O2	x	N/A	N/A	0.500	N/A	N/A	N/A
	y	N/A	N/A	0.000	N/A	N/A	N/A
	z	N/A	N/A	0.584(5)	N/A	N/A	N/A
	UISO*100	1.00*	1.00*	1.00*	1.00*	1.00*	1.00*
Phase Ratio 1 to 2		N/A	0.092	0.907	N/A	N/A	N/A
Nb/Fe – O bond length (Å)		2.092(15)	2.02195(11)	2.10(11)	2.102(23)	2.144(29)	2.103(20)
		2.092(15)	2.02195(11)	1.86(11)	2.102(23)	2.144(29)	2.103(20)
		2.092(15)	2.02195(11)	2.009(7)	2.102(23)	2.144(29)	2.103(20)
		1.945(14)	2.01303(11)	2.009(7)	1.905(22)	1.869(27)	1.937(18)
		1.945(14)	2.01303(11)	2.009(7)	1.905(22)	1.869(27)	1.937(18)
		1.945(14)	2.01303(11)	2.009(7)	1.905(22)	1.869(27)	1.937(18)
Nb/Fe – O – Nb/Fe bond angle (o)		157.8(4)	159.208(1)	180.000(0) 162.8(26)	162.3(7)	163.4(9)	158.8(7)

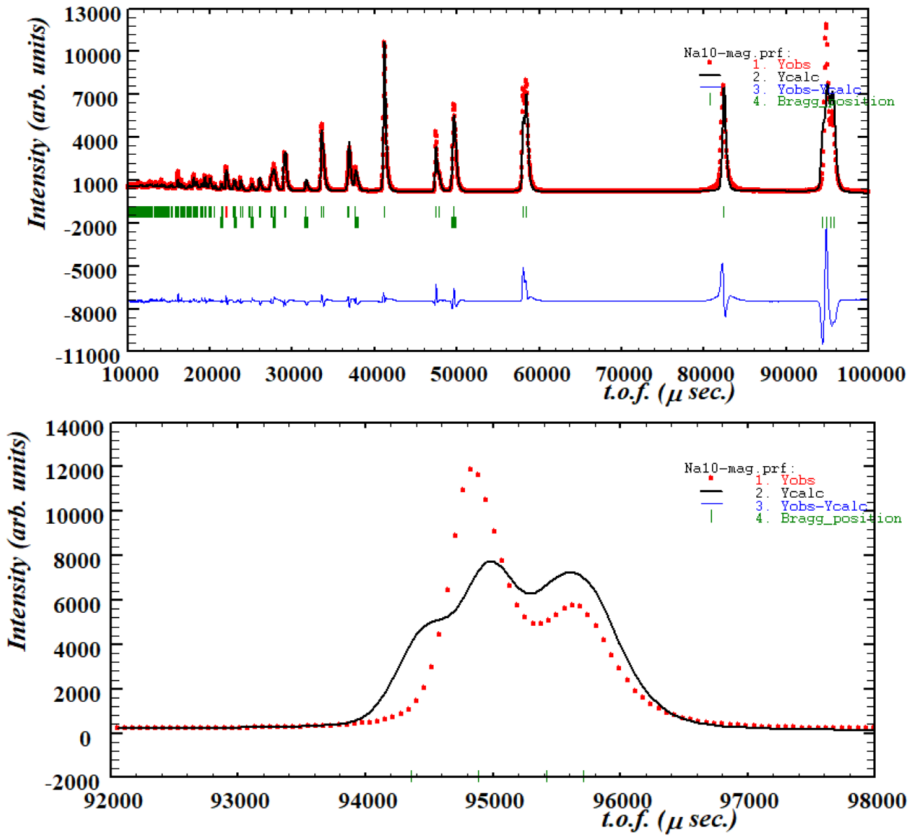

Figure A1.1: *Rietveld refinement obtained from PND of $Bi_{0.9}Na_{0.1}Fe_{0.9}Nb_{0.1}O_3$. R3c and unrefined spin cycloid model.*

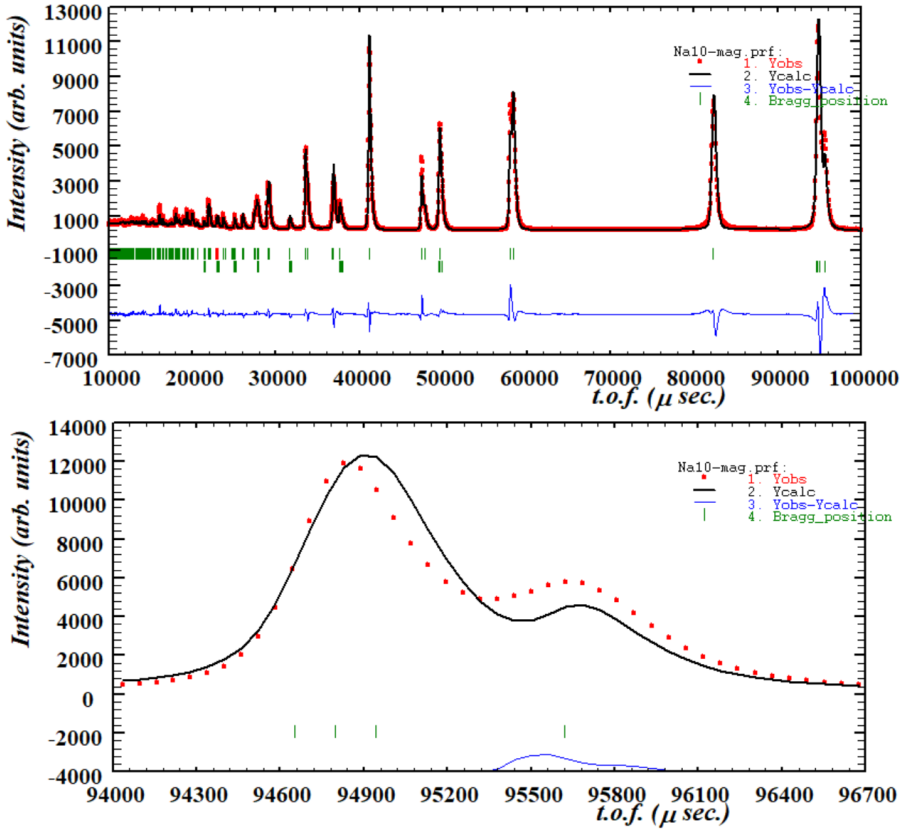

Figure A1.2: *Rietveld refinement obtained from PND of $Bi_{0.9}Na_{0.1}Fe_{0.9}Nb_{0.1}O_3$. R3c and refined spin cycloid model.*

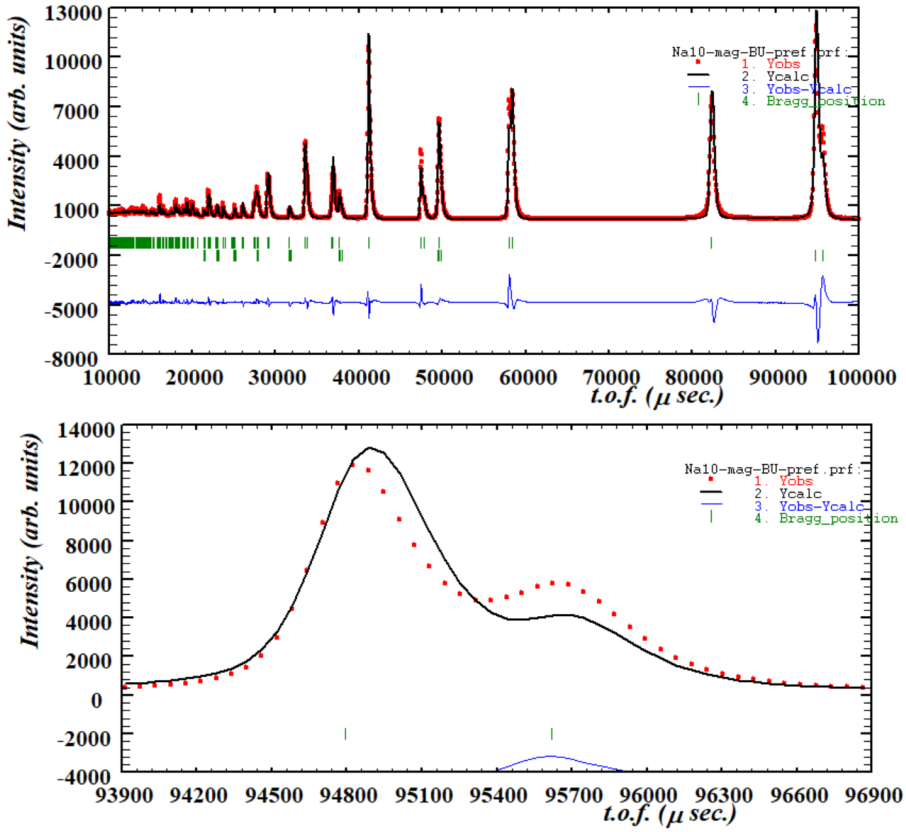

Figure A1.3: *Rietveld refinement obtained from PND of $Bi_{0.9}Na_{0.1}Fe_{0.9}Nb_{0.1}O_3$. R3c and k vector = 0,0,0 model.*

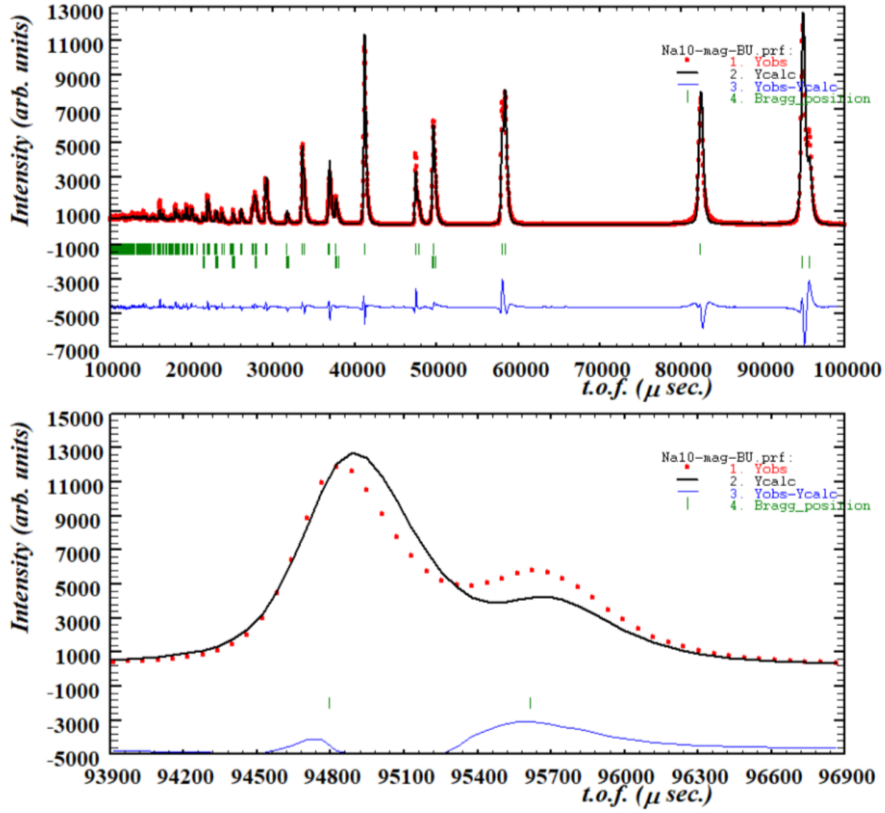

Figure A1.4: *Rietveld refinement obtained from PND of $Bi_{0.9}Na_{0.1}Fe_{0.9}Nb_{0.1}O_3$. R3c and k vector = 0,0,0 with spin canting model.*

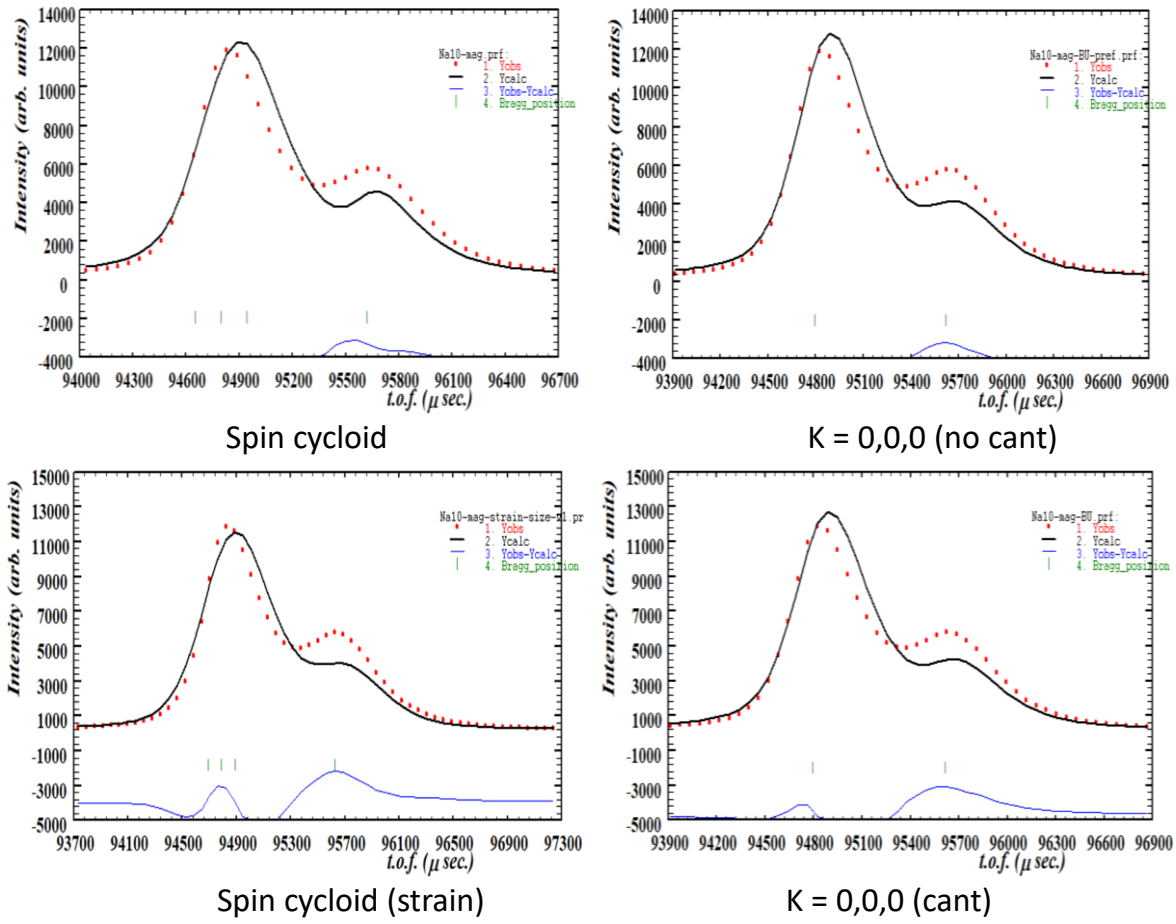

Figure A1.5: *Comparison of Rietveld refinement fits to $Bi_{0.9}Na_{0.1}Fe_{0.9}Nb_{0.1}O_3$ peak at 4.6 Å.*

Table A1.2: *Rietveld refinement parameters for RT WISH ND of $Bi_{0.9}Na_{0.1}Fe_{0.9}Nb_{0.1}O_3$. The standard deviations reported are very high as the magnetic and nuclear phases were refined simultaneously with a poor fit to the magnetic phase.*

Parameter		$Bi_{0.9}Na_{0.1}Fe_{0.9}Nb_{0.1}O_3$		
Space Group		*R* 3*c*	*R* 3*c*	*R* 3*c*
Magnetism		Spin Cycloid (No strain)	K = (0,0,0) (No strain)	Spin Cycloid (and strain)
K vector (δ,δ,0)		0.0011(18)	0	0.00079(27)
wRp (%)		13.9	14.0	11.7
Rp (%)		15.2	15.1	13.6
Nuclear R factor		4.04	4.01	2.92
Magnetic R factor		9.00	9.29	8.60
Magnetic Moment		3.438(29)	1.751(24)	3.274(24)
a (Å)		5.60(13)	5.602(74)	5.63078(0)
b (Å)		5.60(13)	5.602(74)	5.63078(0)
c (Å)		13.86(33)	13.86(18)	13.92889(0)
α (°)		90	90	90
β (°)		90	90	90
γ (°)		120	120	120
Cell vol. (Å3)		376(16)	377(9)	382.459(0)
Bi/Na 1	x	0.000	0.000	0.000
	y	0.000	0.000	0.000
	z	0.000	0.000	0.000
	Biso	2.37(10)	2.35(10)	2.087(82)
Fe/Nb 1	x	0.000	0.000	0.000
	y	0.000	0.000	0.000
	z	0.22639(25)	0.23(25)	0.22576(22)
	Biso	1.180(61)	1.163(61)	1.227(52)
O1	x	0.44835(57)	0.44824(57)	0.44491(48)
	y	0.0160(6)	0.01593(60)	0.01263(51)
	z	0.96102(34)	0.96104(34)	0.96083(29)
	Biso	1.772(66)	1.752(66)	1.661(54)

Table A1.3: *Rietveld refinement parameters for LT XRD of $Bi_{0.9}Na_{0.1}Fe_{0.9}Nb_{0.1}O_3$.*

Parameter		$Bi_{0.9}Na_{0.1}Fe_{0.9}Nb_{0.1}O_3$															
Temperature (K)		12	30	50	70	90	110	130	150	170	190	210	230	250	270	290	298
Space Group		*R* 3*c*	*R* 3*c*	*R* 3*c*	*R* 3*c*	*R* 3*c*	*R* 3*c*	*R* 3*c*	*R* 3*c*	*R* 3*c*	*R* 3*c*	*R* 3*c*	*R* 3*c*	*R* 3*c*	*R* 3*c*	*R* 3*c*	*R* 3*c*
χ^2		3.459	1.462	1.4	1.47	1.404	1.426	1.401	1.416	1.415	1.371	1.424	1.391	1.37	1.353	1.323	1.356
wRp (%)		8.280	15.92	15.6	16.01	15.69	15.85	15.65	15.77	15.78	15.54	15.86	15.69	15.52	15.44	15.32	15.49
Rp (%)		6.160	12.15	11.94	12.32	12.09	12.08	11.84	12.23	12.01	11.92	12.17	11.87	11.95	11.91	11.84	11.98
a (Å)		5.56912(18)	5.56957(13)	5.5697(4)	5.5697(4)	5.5707(4)	5.57144(13)	5.5710(4)	5.5720(4)	5.5721(4)	5.5727(4)	5.5732(4)	5.5745(4)	5.5751(4)	5.5765(4)	5.5772(4)	5.5773(4)
b (Å)		5.56912(18)	5.56957(13)	5.5697(4)	5.5697(4)	5.5707(4)	5.57144(13)	5.5710(4)	5.5720(4)	5.5721(4)	5.5727(4)	5.5732(4)	5.5745(4)	5.5751(4)	5.5765(4)	5.5772(4)	5.5773(4)
c (Å)		13.7760(6)	13.7760(7)	13.7778(11)	13.7786(12)	13.7817(11)	13.7841(7)	13.7846(11)	13.7848(12)	13.7872(11)	13.7882(11)	13.7899(12)	13.7926(12)	13.7950(11)	13.8001(11)	13.8019(11)	13.8037(12)
α (°)		90.000	90.000	90.000	90.000	90.000	90.000	90.000	90.000	90.000	90.000	90.000	90.000	90.000	90.000	90.000	90.000
β (°)		90.000	90.000	90.000	90.000	90.000	90.000	90.000	90.000	90.000	90.000	90.000	90.000	90.000	90.000	90.000	90.000
γ (°)		120.000	120.000	120.000	120.000	120.000	120.000	120.000	120.000	120.000	120.000	120.000	120.000	120.000	120.000	120.000	120.000
Cell vol. (Å3)		370.020(23)	370.081(22)	370.15(5)	370.17(5)	370.38(5)	370.548(22)	370.51(5)	370.65(5)	370.71(5)	370.82(5)	370.94(5)	371.18(5)	371.33(5)	371.65(5)	371.79(5)	371.86(5)
Bi/Na 1	x	0.000	0.000	0.000	0.000	0.000	0.000	0.000	0.000	0.000	0.000	0.000	0.000	0.000	0.000	0.000	0.000
	y	0.000	0.000	0.000	0.000	0.000	0.000	0.000	0.000	0.000	0.000	0.000	0.000	0.000	0.000	0.000	0.000
	z	0.000	0.000	0.000	0.000	0.000	0.000	0.000	0.000	0.000	0.000	0.000	0.000	0.000	0.000	0.000	0.000
Fe/Nb 1	x	0.000	0.000	0.000	0.000	0.000	0.000	0.000	0.000	0.000	0.000	0.000	0.000	0.000	0.000	0.000	0.000
	y	0.000	0.000	0.000	0.000	0.000	0.000	0.000	0.000	0.000	0.000	0.000	0.000	0.000	0.000	0.000	0.000
	z	0.2298(4)	0.2298(4)	0.2298(4)	0.2298(4)	0.2298(4)	0.2298(4)	0.2298(4)	0.2298(4)	0.2298(4)	0.2298(4)	0.2298(4)	0.2298(4)	0.2298(4)	0.2298(4)	0.2298(4)	0.2298(4)
O1	x	0.4310(30)	0.4310(30)	0.4310(30)	0.4310(30)	0.4310(30)	0.4310(30)	0.4310(30)	0.4310(30)	0.4310(30)	0.4310(30)	0.4310(30)	0.4310(30)	0.4310(30)	0.4310(30)	0.4310(30)	0.4310(30)
	y	0.003(4)	0.003(4)	0.003(4)	0.003(4)	0.003(4)	0.003(4)	0.003(4)	0.003(4)	0.003(4)	0.003(4)	0.003(4)	0.003(4)	0.003(4)	0.003(4)	0.003(4)	0.003(4)
	z	0.9662(10)	0.9662(10)	0.9662(10)	0.9662(10)	0.9662(10)	0.9662(10)	0.9662(10)	0.9662(10)	0.9662(10)	0.9662(10)	0.9662(10)	0.9662(10)	0.9662(10)	0.9662(10)	0.9662(10)	0.9662(10)
Nb/Fe – O bond length (Å)		2.114(16)	2.11393(5)	2.11407(11)	2.11412(11)	2.11453(11)	2.11485(5)	2.11479(11)	2.11503(11)	2.11518(11)	2.11538(11)	2.11561(11)	2.11607(11)	2.11635(11)	2.11699(11)	2.11725(11)	2.11740(11)
		2.114(16)	2.11393(5)	2.11407(11)	2.11412(11)	2.11453(11)	2.11485(5)	2.11479(11)	2.11503(11)	2.11518(11)	2.11538(11)	2.11561(11)	2.11607(11)	2.11635(11)	2.11699(11)	2.11725(11)	2.11740(11)
		2.114(16)	2.11393(5)	2.11407(11)	2.11412(11)	2.11453(11)	2.11485(5)	2.11479(11)	2.11503(11)	2.11518(11)	2.11538(11)	2.11561(11)	2.11607(11)	2.11635(11)	2.11699(11)	2.11725(11)	2.11740(11)
		1.928(16)	1.92789(4)	1.92800(10)	1.92802(11)	1.92838(10)	1.92866(4)	1.92857(10)	1.92884(11)	1.92893(11)	1.92913(11)	1.92933(11)	1.92975(11)	1.93000(11)	1.93054(11)	1.93077(11)	1.93088(11)
		1.928(16)	1.92789(4)	1.92800(10)	1.92802(11)	1.92838(10)	1.92866(4)	1.92857(10)	1.92884(11)	1.92893(11)	1.92913(11)	1.92933(11)	1.92975(11)	1.92999(11)	1.93054(11)	1.93077(11)	1.93088(11)
		1.928(16)	1.92789(4)	1.92800(10)	1.92802(11)	1.92838(10)	1.92866(4)	1.92857(10)	1.92884(11)	1.92893(11)	1.92913(11)	1.92933(11)	1.92975(11)	1.93000(11)	1.93054(11)	1.93077(11)	1.93088(11)
Nb/Fe – O – Nb/Fe bond angle (o)		155.7(5)	155.657(0)	155.657(1)	155.658(1)	155.658(1)	155.658(0)	155.659(1)	155.658(1)	155.659(1)	155.659(1)	155.659(1)	155.659(1)	155.659(1)	155.660(1)	155.660(1)	155.660(1)

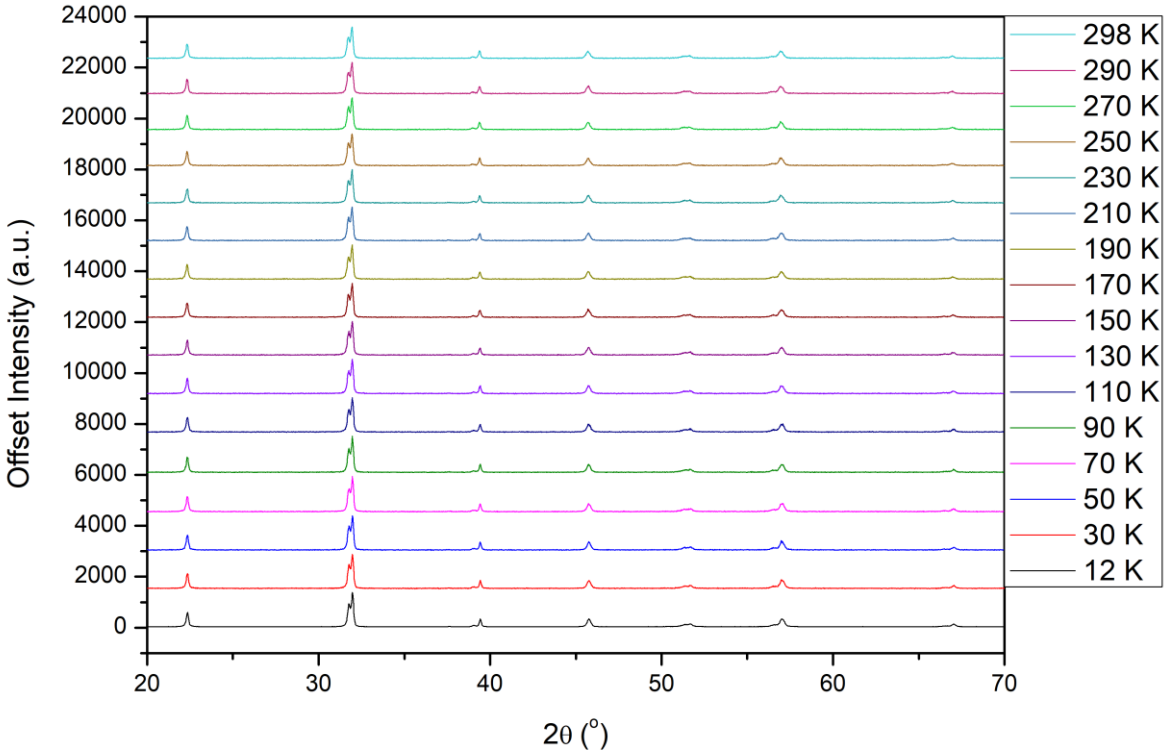

Figure A1.6: *All patterns for the LT PXRD of $Bi_{0.9}Na_{0.1}Fe_{0.9}Nb_{0.1}O_3$. 12K pattern intensity has been scaled down to match the intensities of the other temperature points that were taken with shorter scan times.*

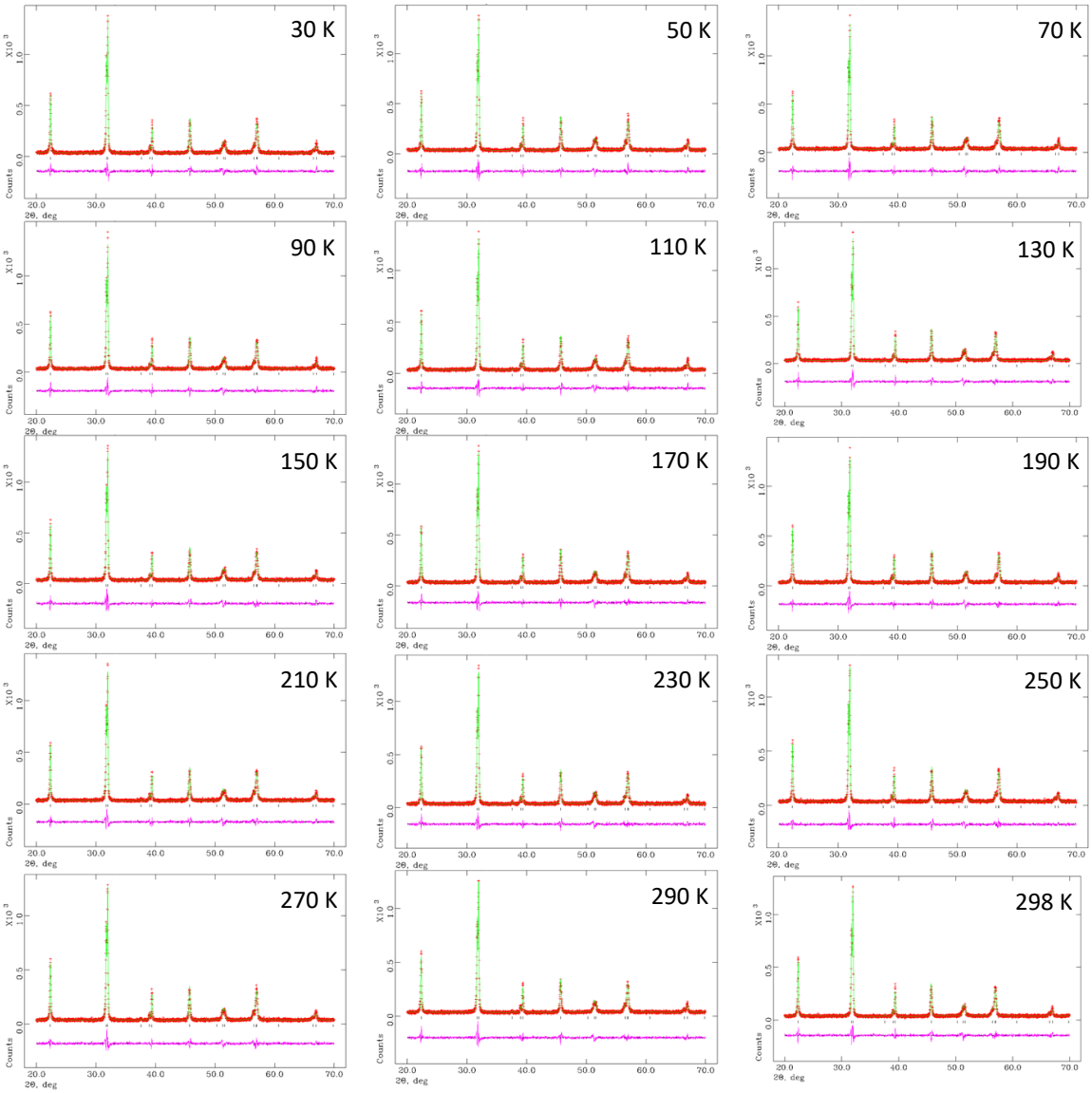

Figure A1.7: *Rietveld refinements obtained from LT PXRD of $Bi_{0.9}Na_{0.1}Fe_{0.9}Nb_{0.1}O_3$ in the temperature range 30 K to 298 K.*

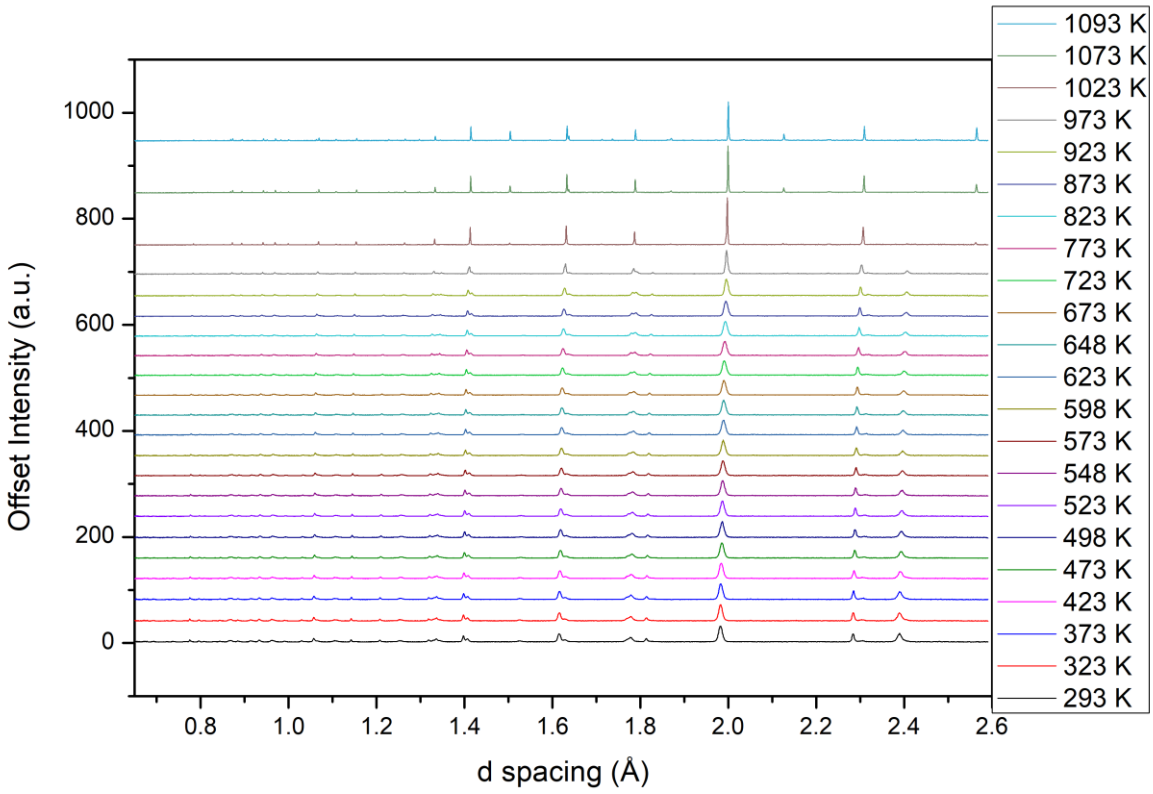

Figure A1.8: *All patterns for the HT PND of $Bi_{0.9}Na_{0.1}Fe_{0.9}Nb_{0.1}O_3$ on bank 1 HRPD.*

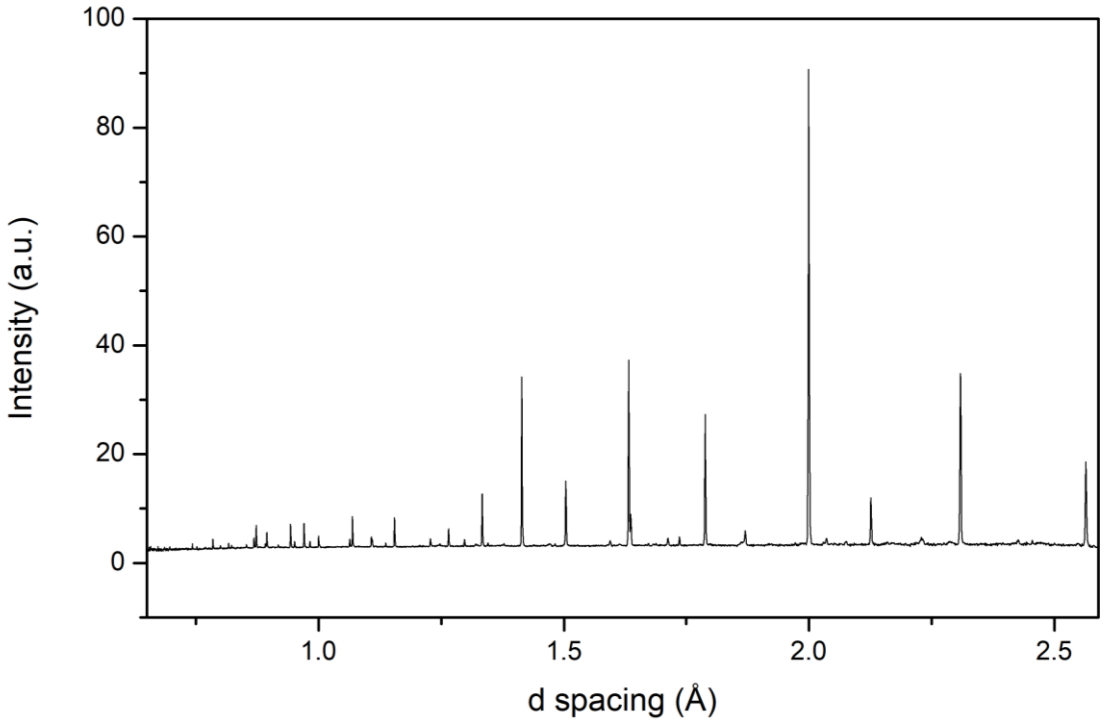

Figure A1.9: *HRPD Bank 1 PND of $Bi_{0.9}Na_{0.1}Fe_{0.9}Nb_{0.1}O_3$ at 1073 K.*

Figure A1.10: *Rietveld refinements to R3c model obtained from HT PND of $Bi_{0.9}Na_{0.1}Fe_{0.9}Nb_{0.1}O_3$ in the temperature range 293 K to 1093 K.*

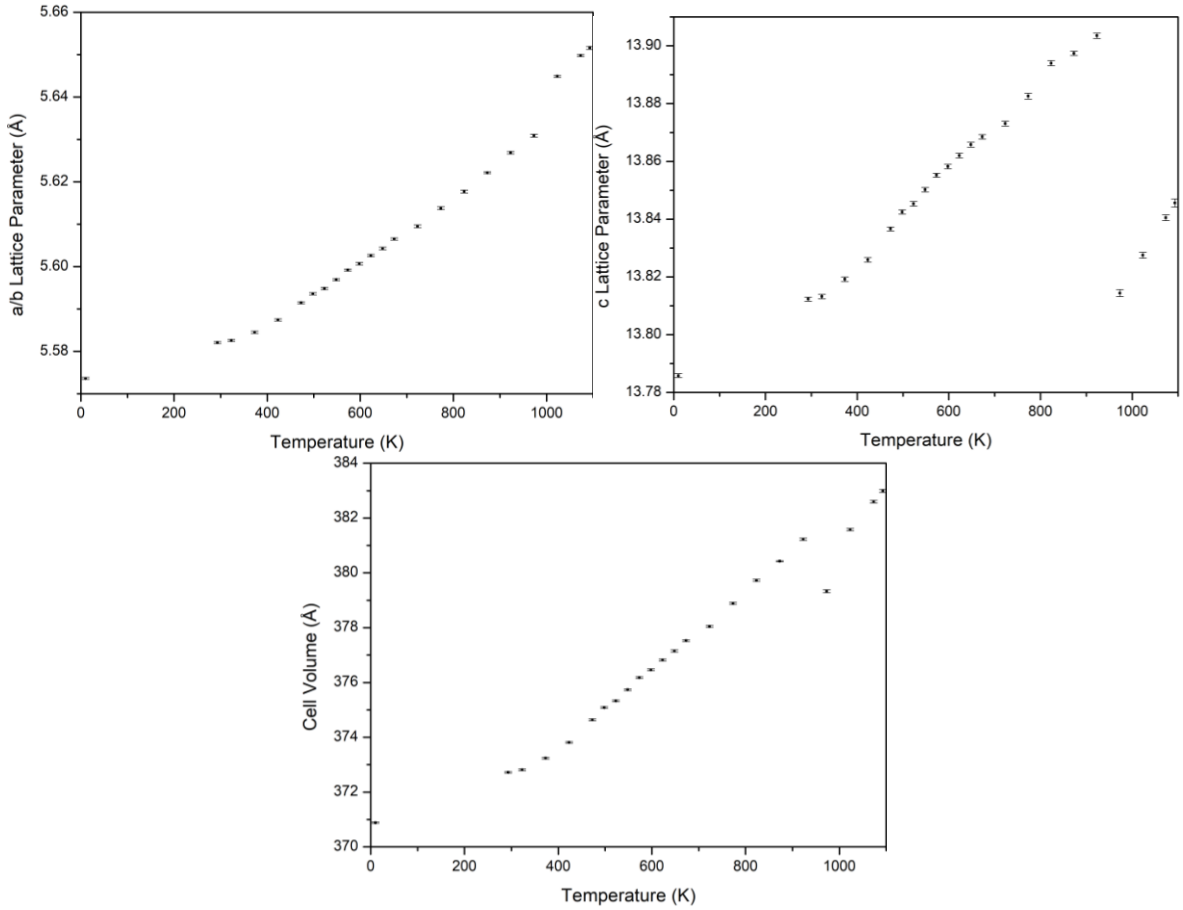

Figure A1.11: *Lattice Parameter and Cell Volume plots for $Bi_{0.9}Na_{0.1}Fe_{0.9}Nb_{0.1}O_3$ (a) a/b Lattice parameter plot for temperatures between 10 K and 1073 K from ND data, (b) c Lattice parameter plot for temperatures between 10 K and 1073 K from ND data, (c) Cell volume plot for temperatures between 10 K and 1073 K from ND data.*

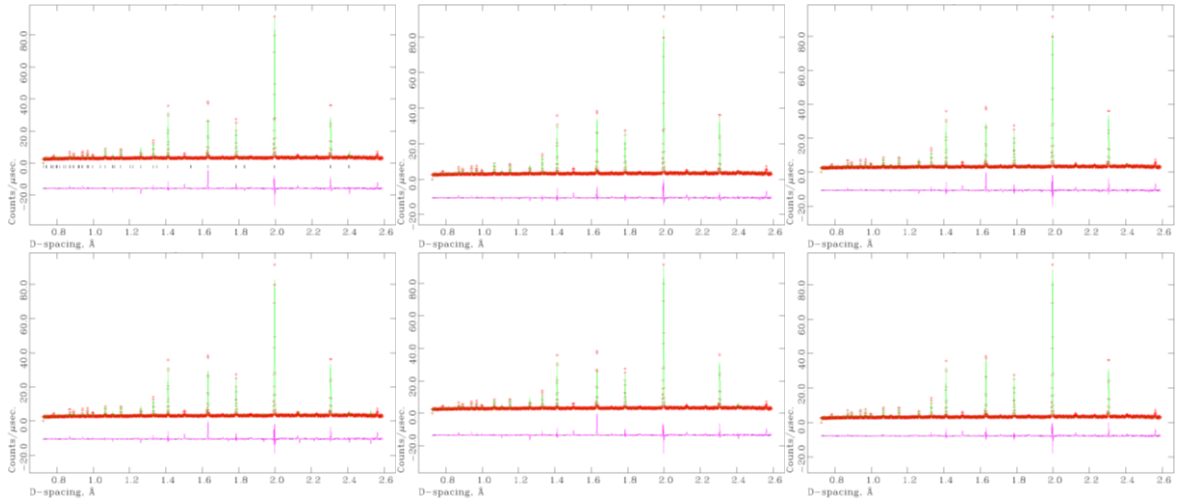

Figure A1.12: *Rietveld refinements to (a) Imma, (b) $P2_1ma$, (c) Pbam, (d) Pbnm, (e) $R\bar{3}c$ and (f) P4/mbm models obtained from HT PND of $Bi_{0.9}Na_{0.1}Fe_{0.9}Nb_{0.1}O_3$ at the temperature 1023 K.*

Table A1.4: *Rietveld refinement parameters for VT ND of $Bi_{0.9}Na_{0.1}Fe_{0.9}Nb_{0.1}O_3$.*

Parameter		$Bi_{0.9}Na_{0.1}Fe_{0.9}Nb_{0.1}O_3$																					
Temperature		10 K	293 K	323 K	373 K	423 K	473 K	498 K	523 K	548 K	573 K	598 K	623 K	648 K	673 K	723 K	773 K	823 K	873 K	923 K	973 K	1023 K	1073 K	1093 K
Space Group		*R* 3*c*	*R* 3*c*	*R* 3*c*	*R* 3*c*	*R* 3*c*	*R* 3*c*	*R* 3*c*	*R* 3*c*	*R* 3*c*	*R* 3*c*	*R* 3*c*	*R* 3*c*	*R* 3*c*	*R* 3*c*	*R* 3*c*	*R* 3*c*	*R* 3*c*	*R* 3*c*	*R* 3*c*	*R* 3*c*	*R* 3*c*	*R* 3*c*	*R* 3*c*
χ^2		19.83	3.812	3.821	3.598	3.380	10.200	3.134	3.067	3.000	9.252	2.989	2.964	3.115	10.070	3.306	3.407	3.164	4.154	3.074	4.201	3.160	18.38	7.62
wRp (%)		10.27	8.04	8.14	7.89	7.65	6.66	7.35	7.27	7.18	6.33	7.16	7.13	7.30	6.56	7.49	7.61	7.28	4.19	7.17	8.38	7.26	8.77	11.26
Rp (%)		9.91	7.99	7.95	7.85	7.52	5.95	7.05	6.97	6.70	5.32	6.52	6.63	6.73	5.32	6.84	6.95	6.60	3.76	6.48	7.24	6.14	5.49	7.77
a (Å)		5.57362(21)	5.58206(25)	5.58259(25)	5.58452(25)	5.58745(25)	5.59146(23)	5.59361(26)	5.59484(26)	5.59692(26)	5.59919(24)	5.60069(27)	5.60261(28)	5.60428(29)	5.60653(27)	5.60950(31)	5.61378(33)	5.61771(32)	5.62215(17)	5.62686(30)	5.63089(34)	5.64489(22)	5.64980(23)	5.65160(31)
b (Å)		5.57362(21)	5.58206(25)	5.58259(25)	5.58452(25)	5.58745(25)	5.59146(23)	5.59361(26)	5.59484(26)	5.59692(26)	5.59919(24)	5.60069(27)	5.60261(28)	5.60428(29)	5.60653(27)	5.60950(31)	5.61378(33)	5.61771(32)	5.62215(17)	5.62686(30)	5.63089(34)	5.64489(22)	5.64980(23)	5.65160(31)
c (Å)		13.7858(7)	13.8123(7)	13.8132(8)	13.8192(8)	13.8259(8)	13.8366(7)	13.8425(8)	13.8453(8)	13.8502(8)	13.8552(7)	13.8582(8)	13.8620(8)	13.8658(9)	13.8685(8)	13.8731(9)	13.8826(10)	13.8940(9)	13.8974(7)	13.9035(9)	13.8144(12)	13.8275(10)	13.8405(10)	13.8456(14)
α (°)		90	90	90	90	90	90	90	90	90	90	90	90	90	90	90	90	90	90	90	90	90	90	90
β (°)		90	90	90	90	90	90	90	90	90	90	90	90	90	90	90	90	90	90	90	90	90	90	90
γ (°)		120	120	120	120	120	120	120	120	120	120	120	120	120	120	120	120	120	120	120	120	120	120	120
Cell vol. (Å^3)		370.883(27)	372.722(31)	372.817(31)	373.239(31)	373.811(31)	374.638(29)	375.086(32)	375.327(33)	375.739(33)	376.179(30)	376.462(34)	376.823(35)	377.15(4)	377.526(33)	378.05(4)	378.89(4)	379.73(4)	380.425(25)	381.23(4)	379.33(5)	381.58(4)	382.60(4)	382.99(5)
Bi/Na 1	x	0.000	0.000	0.000	0.000	0.000	0.000	0.000	0.000	0.000	0.000	0.000	0.000	0.000	0.000	0.000	0.000	0.000	0.000	0.000	0.000	0.000	0.000	0.000
	y	0.000	0.000	0.000	0.000	0.000	0.000	0.000	0.000	0.000	0.000	0.000	0.000	0.000	0.000	0.000	0.000	0.000	0.000	0.000	0.000	0.000	0.000	0.000
	z	0.000	0.000	0.000	0.000	0.000	0.000	0.000	0.000	0.000	0.000	0.000	0.000	0.000	0.000	0.000	0.000	0.000	0.000	0.000	0.000	0.000	0.000	0.000
	U_{iso} *100	1.50(7)	2.24(9)	2.15(9)	2.39(9)	2.45(9)	2.83(9)	2.93(10)	2.96(10)	3.15(10)	3.28(9)	3.41(11)	3.54(11)	3.71(12)	4.01(11)	4.33(13)	4.73(14)	4.86(14)	5.05(8)	5.92(15)	6.3(4)	9.0(5)	9.1(7)	9.1(10)
Fe/Nb 1	x	0.000	0.000	0.000	0.000	0.000	0.000	0.000	0.000	0.000	0.000	0.000	0.000	0.000	0.000	0.000	0.000	0.000	0.000	0.000	0.000	0.000	0.000	0.000
	y	0.000	0.000	0.000	0.000	0.000	0.000	0.000	0.000	0.000	0.000	0.000	0.000	0.000	0.000	0.000	0.000	0.000	0.000	0.000	0.000	0.000	0.000	0.000
	z	0.22444(17)	0.22504(19)	0.22506(19)	0.22523(19)	0.22529(19)	0.22565(18)	0.22557(20)	0.22598(20)	0.22600(20)	0.22610(19)	0.22643(22)	0.22662(22)	0.22683(23)	0.22704(22)	0.22763(26)	0.22808(28)	0.22816(27)	0.22811(19)	0.22955(31)	0.2340(10)	0.2409(32)	0.240(4)	0.239(5)
	U_{iso} *100	0.37(5)	0.62(5)	0.68(5)	0.69(5)	0.80(5)	0.85(5)	0.83(5)	0.91(5)	0.90(5)	0.95(4)	0.97(5)	1.03(5)	1.04(5)	1.16(5)	1.22(5)	1.31(6)	1.47(6)	1.532(32)	1.56(5)	2.07(8)	2.45(6)	2.67(8)	2.74(12)
O1	x	0.4429(5)	0.4443(5)	0.4446(5)	0.4452(5)	0.4465(5)	0.4476(5)	0.4478(5)	0.4492(5)	0.4499(6)	0.4513(5)	0.4514(6)	0.4527(6)	0.4531(6)	0.4540(6)	0.4546(7)	0.4565(7)	0.4575(7)	0.4576(4)	0.4622(7)	0.4726(12)	0.5029(21)	0.5100(29)	0.512(4)
	y	0.0159(6)	0.0151(7)	0.0147(7)	0.0155(7)	0.0156(7)	0.0158(6)	0.0154(7)	0.0163(7)	0.0167(7)	0.0171(6)	0.0165(8)	0.0177(8)	0.0176(8)	0.0183(7)	0.0180(9)	0.0191(9)	0.0191(9)	0.0171(6)	0.0218(9)	0.0266(18)	0.037(4)	0.038(4)	0.039(6)
	z	0.95876(25)	0.95966(28)	0.95960(28)	0.95944(28)	0.96000(28)	0.96026(25)	0.96009(28)	0.96065(29)	0.96043(29)	0.96055(26)	0.96088(30)	0.96102(31)	0.96104(32)	0.96117(30)	0.9620(4)	0.9624(4)	0.9623(4)	0.96415(27)	0.9637(4)	0.9695(12)	0.975(4)	0.974(5)	0.974(6)
	U_{iso} *100	0.73(4)	1.16(4)	1.14(5)	1.26(5)	1.44(5)	1.68(4)	1.80(5)	1.84(5)	1.99(5)	2.11(5)	2.19(6)	2.30(6)	2.40(6)	2.59(6)	2.79(7)	3.03(8)	3.30(8)	3.49(5)	3.86(10)	4.38(15)	5.42(15)	5.54(19)	5.46(28)
Bi/Na – O bond length (Å)		2.4912(20)	2.5021(22)	2.5051(22)	2.5075(22)	2.5141(22)	2.5204(20)	2.5243(22)	2.5280(22)	2.5327(23)	2.5403(21)	2.5417(24)	2.5462(24)	2.5497(25)	2.5534(23)	2.5559(27)	2.5644(29)	2.5717(28)	2.5747(16)	2.5913(30)	2.623(5)	2.935(7)	2.903(12)	2.896(20)
		2.4912(20)	2.5021(22)	2.5051(22)	2.5075(22)	2.5141(22)	2.5204(20)	2.5243(22)	2.5280(22)	2.5327(23)	2.5403(21)	2.5417(24)	2.5462(24)	2.5497(25)	2.5534(23)	2.5559(27)	2.5644(29)	2.5717(28)	2.5747(16)	2.5913(30)	2.623(5)	2.763(7)	2.804(12)	2.814(20)
		2.4912(20)	2.5021(22)	2.5051(22)	2.5075(22)	2.5141(22)	2.5204(20)	2.5243(22)	2.5280(22)	2.5327(23)	2.5403(21)	2.5417(24)	2.5462(24)	2.5497(25)	2.5534(23)	2.5559(27)	2.5644(29)	2.5717(28)	2.5747(16)	2.5913(30)	2.623(5)	2.935(7)	2.903(12)	2.896(20)
		N/A	N/A	N/A	N/A	N/A	N/A	N/A	N/A	N/A	N/A	N/A	N/A	N/A	N/A	N/A	N/A	N/A	N/A	N/A	N/A	2.763(7)	2.804(12)	2.814(20)
		N/A	N/A	N/A	N/A	N/A	N/A	N/A	N/A	N/A	N/A	N/A	N/A	N/A	N/A	N/A	N/A	N/A	N/A	N/A	N/A	2.763(7)	2.804(12)	2.814(20)
		N/A	N/A	N/A	N/A	N/A	N/A	N/A	N/A	N/A	N/A	N/A	N/A	N/A	N/A	N/A	N/A	N/A	N/A	N/A	N/A	2.935(7)	2.903(12)	2.896(20)
		2.3386(33)	2.353(4)	2.353(4)	2.350(4)	2.355(4)	2.3584(33)	2.359(4)	2.361(4)	2.358(4)	2.3582(34)	2.364(4)	2.362(4)	2.363(4)	2.362(4)	2.372(4)	2.373(5)	2.374(5)	2.3994(31)	2.380(5)	2.414(10)	2.440(33)	2.43(4)	2.42(5)
		2.3386(33)	2.353(4)	2.353(4)	2.350(4)	2.355(4)	2.3584(33)	2.359(4)	2.361(4)	2.358(4)	2.3582(34)	2.364(4)	2.362(4)	2.363(4)	2.362(4)	2.372(4)	2.373(5)	2.374(5)	2.3994(31)	2.380(5)	2.414(10)	2.440(33)	2.43(4)	2.42(5)
		2.3386(33)	2.353(4)	2.353(4)	2.350(4)	2.355(4)	2.3584(33)	2.359(4)	2.361(4)	2.358(4)	2.3582(34)	2.364(4)	2.362(4)	2.363(4)	2.362(4)	2.372(4)	2.373(5)	2.374(5)	2.3994(31)	2.380(5)	2.414(10)	2.440(33)	2.43(4)	2.42(5)
Fe/Nb – O bond length (Å)		2.0839(28)	2.0859(32)	2.0875(33)	2.0882(32)	2.0834(33)	2.0841(31)	2.0871(35)	2.0818(35)	2.083(4)	2.0812(32)	2.084(4)	2.080(4)	2.082(4)	2.080(4)	2.080(4)	2.077(5)	2.078(5)	2.0690(33)	2.069(5)	2.029(11)	1.998(21)	1.994(24)	1.990(33)
		2.0839(28)	2.0859(32)	2.0875(33)	2.0882(32)	2.0834(33)	2.0841(31)	2.0871(35)	2.0818(35)	2.083(4)	2.0812(32)	2.084(4)	2.080(4)	2.082(4)	2.080(4)	2.080(4)	2.077(5)	2.078(5)	2.0690(33)	2.069(5)	2.029(11)	1.998(21)	1.994(24)	1.990(33)
		2.0839(28)	2.0859(32)	2.0875(33)	2.0882(32)	2.0834(33)	2.0841(31)	2.0871(35)	2.0818(35)	2.083(4)	2.0812(32)	2.084(4)	2.080(4)	2.082(4)	2.080(4)	2.080(4)	2.077(5)	2.078(5)	2.0690(33)	2.069(5)	2.029(11)	1.998(21)	1.994(24)	1.990(33)
		1.9602(28)	1.9601(32)	1.9578(33)	1.9596(32)	1.9629(33)	1.9637(30)	1.9615(34)	1.9662(34)	1.9662(35)	1.9676(32)	1.965(4)	1.970(4)	1.968(4)	1.971(4)	1.972(4)	1.976(5)	1.976(5)	1.9807(32)	1.987(5)	2.009(11)	2.037(21)	2.043(25)	2.048(33)
		1.9602(28)	1.9601(32)	1.9578(33)	1.9596(32)	1.9629(33)	1.9637(30)	1.9615(34)	1.9662(34)	1.9662(35)	1.9676(32)	1.965(4)	1.970(4)	1.968(4)	1.971(4)	1.972(4)	1.976(5)	1.976(5)	1.9807(32)	1.987(5)	2.009(11)	2.037(21)	2.043(25)	2.048(33)
		1.9602(28)	1.9601(32)	1.9578(33)	1.9596(32)	1.9629(33)	1.9637(30)	1.9615(34)	1.9662(34)	1.9662(35)	1.9676(32)	1.965(4)	1.970(4)	1.968(4)	1.971(4)	1.972(4)	1.976(5)	1.976(5)	1.9807(32)	1.987(5)	2.009(11)	2.037(21)	2.043(25)	2.048(33)
Fe/Nb – O – Fe/Nb bond angle (°)		155.75(10)	156.40(10)	156.53(11)	156.40(11)	156.90(11)	157.10(10)	157.22(11)	157.41(11)	157.45(11)	157.74(10)	157.88(12)	157.94(12)	158.01(12)	158.05(11)	158.31(13)	158.53(14)	158.73(14)	159.91(9)	159.26(15)	161.14(26)	163.18(26)	163.6(4)	163.5(5)

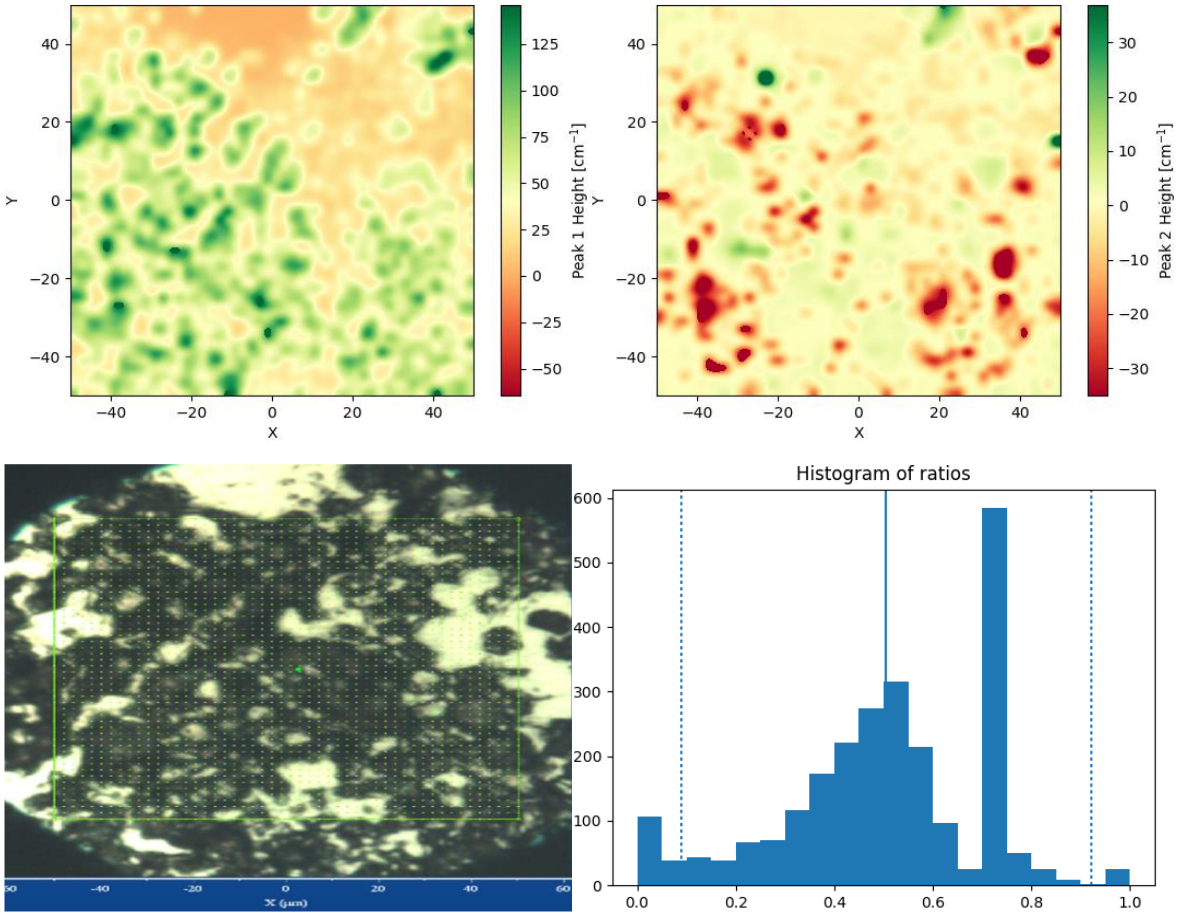

Figure A1.13: *Raman maps of $Bi_{0.9}Na_{0.1}Fe_{0.9}Nb_{0.1}O_3$.*

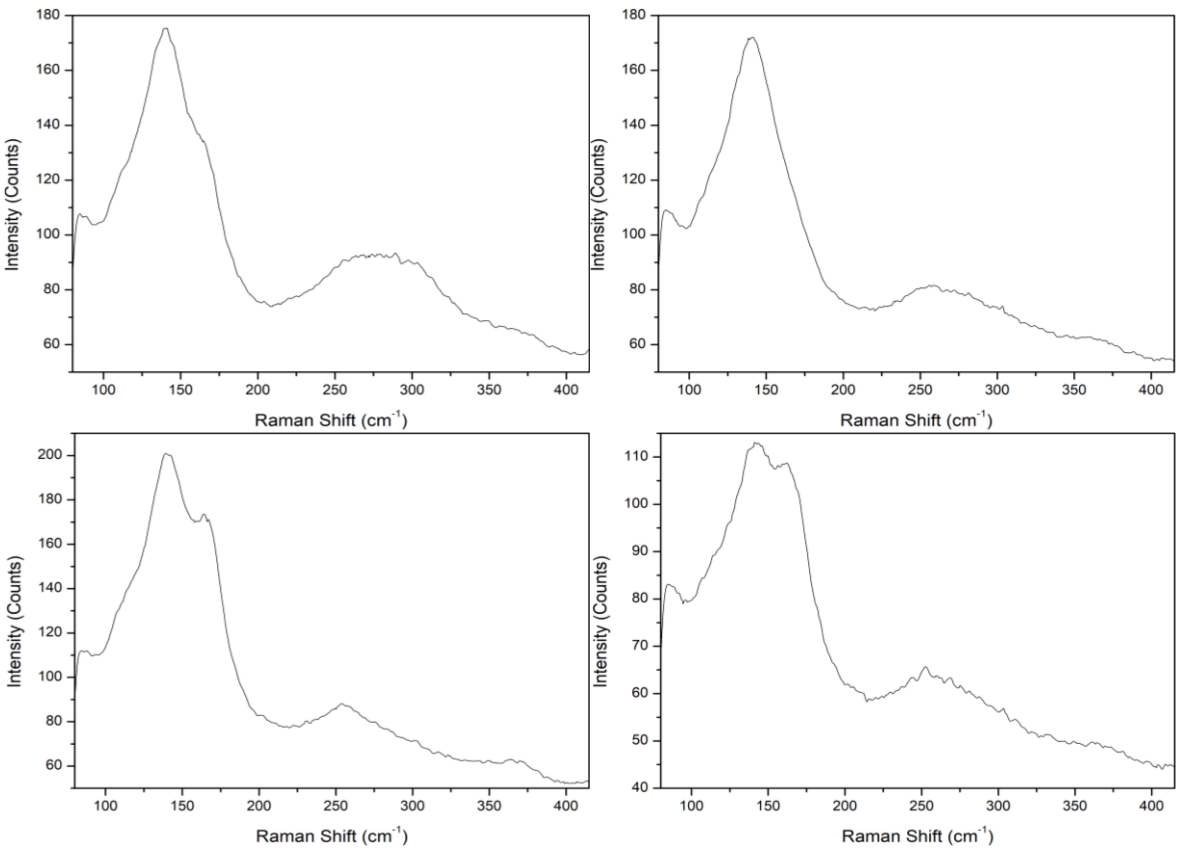

Figure A1.14: *Selection of spectra taken from Raman map.*

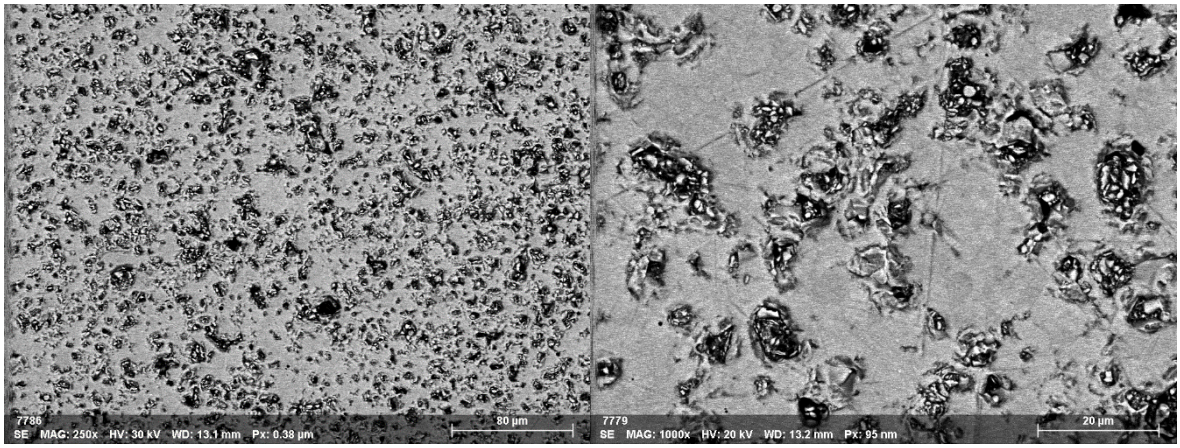

Figure A1.15: *Scanning Electron microscopy back scattered electron images of $Bi_{0.9}Na_{0.1}Fe_{0.9}Nb_{0.1}O_3$ pellet.*

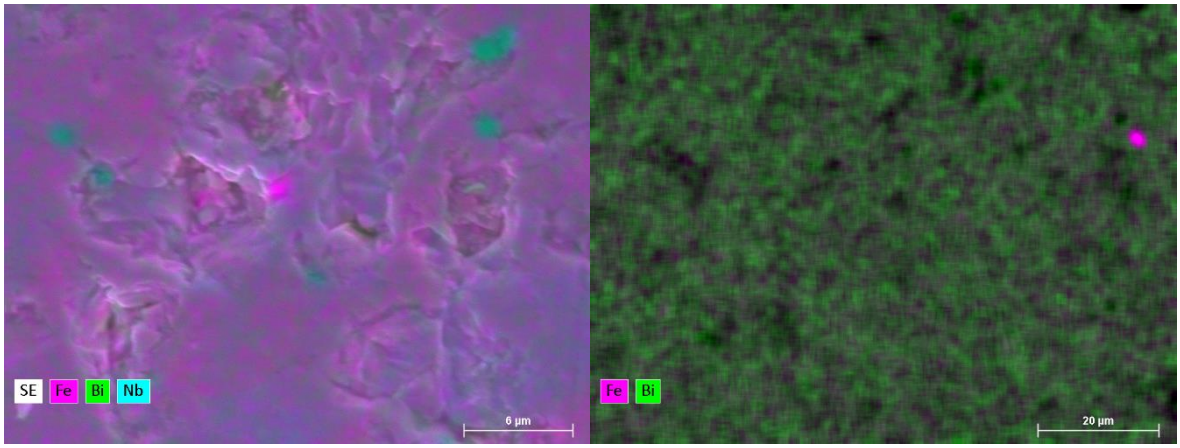

Figure A1.16: *Scanning Electron microscopy images of $Bi_{0.9}Na_{0.1}Fe_{0.9}Nb_{0.1}O_3$ pellet. Electron Dispersive X-Ray Analysis map.*

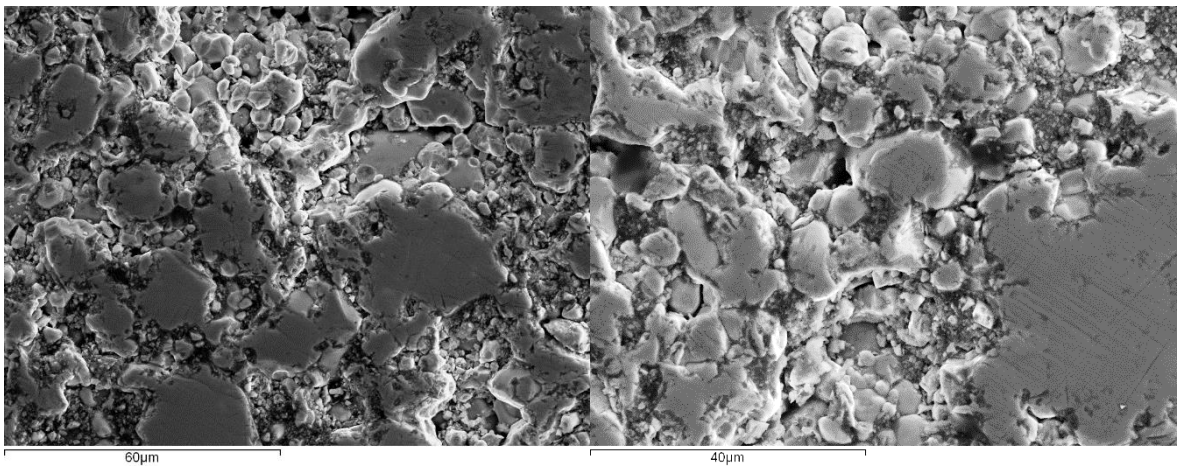

Figure A1.17: *Scanning Electron microscopy Secondary electron images of $Bi_{0.9}Na_{0.1}Fe_{0.9}Nb_{0.1}O_3$ pellet*

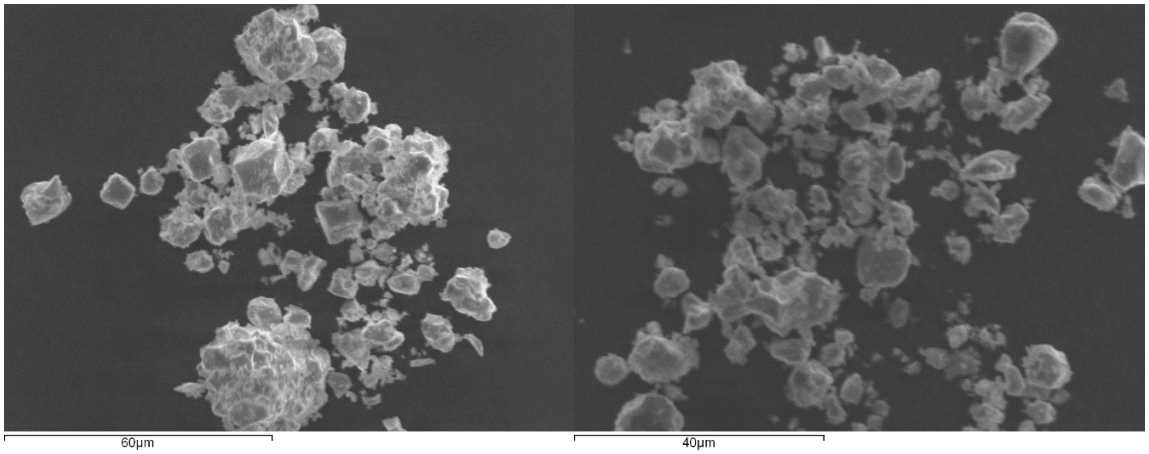

Figure A1.18: *Scanning Electron Secondary electron microscopy images of $Bi_{0.9}Na_{0.1}Fe_{0.9}Nb_{0.1}O_3$ powder.*

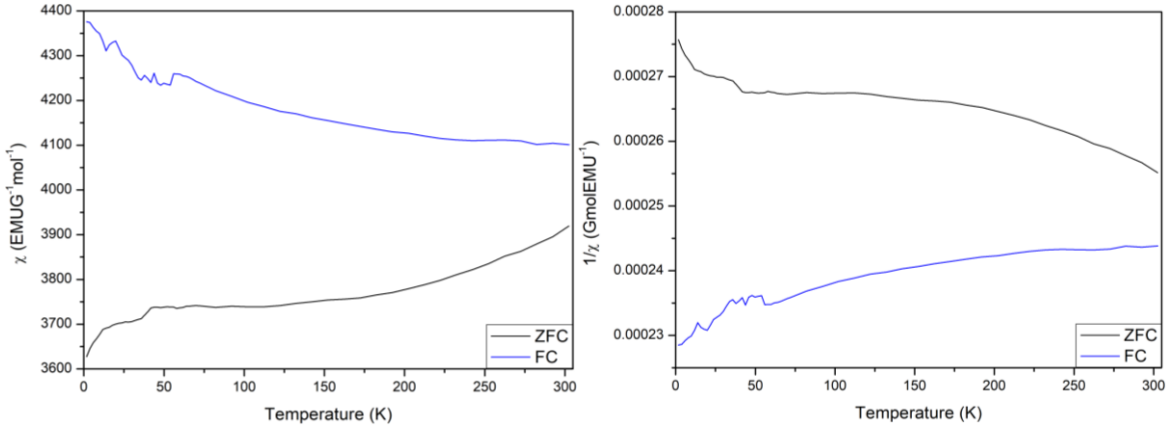

Figure A1.19: *χ and 1/χ SQUID data for $Bi_{0.9}Na_{0.1}Fe_{0.9}Nb_{0.1}O_3$.*

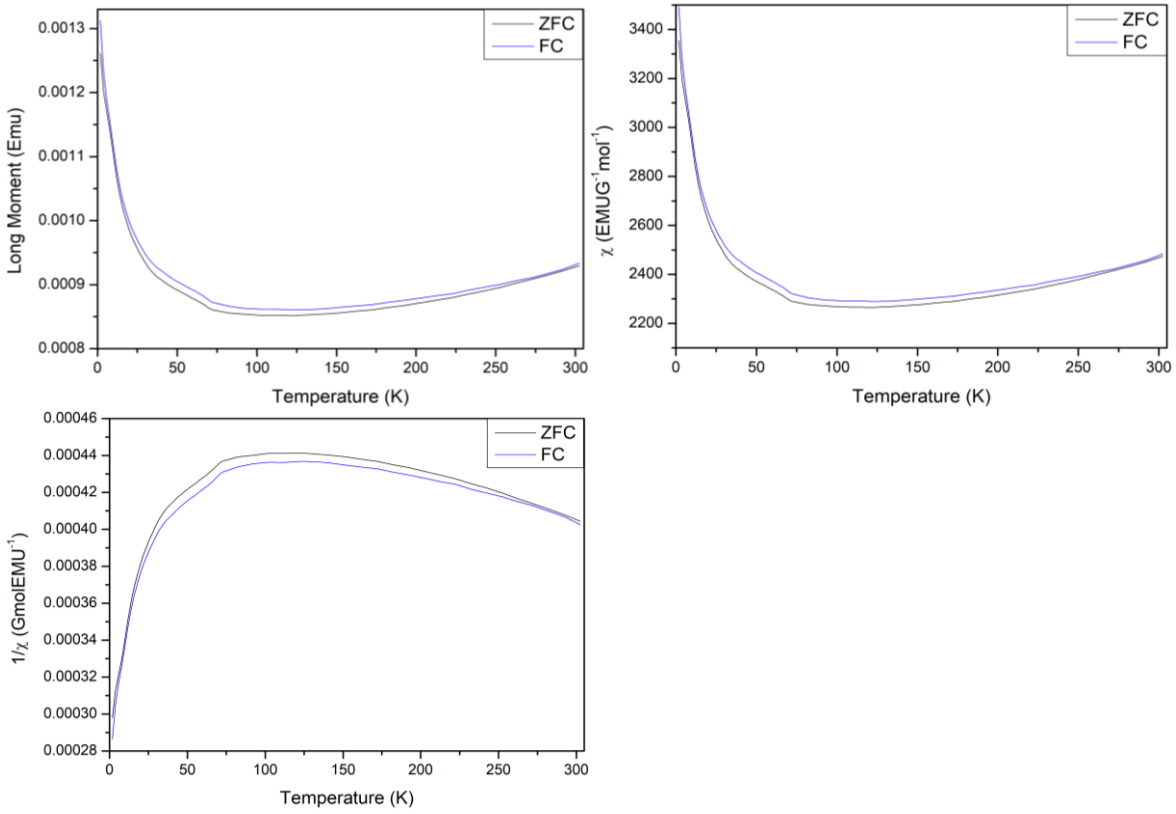

Figure A1.20: *Magnetic data from SQUID for $Bi_{0.9}K_{0.1}Fe_{0.9}Ta_{0.1}O_3$, (a) Variable temperature Zero field cooled and Field cooled data at 0.1 T, (b) χ SQUID data, (c) 1/χ SQUID data.*

Appendix 2 for Chapter Four: Investigation of Bi*A*FeNbO$_6$ (A = Na, K) materials

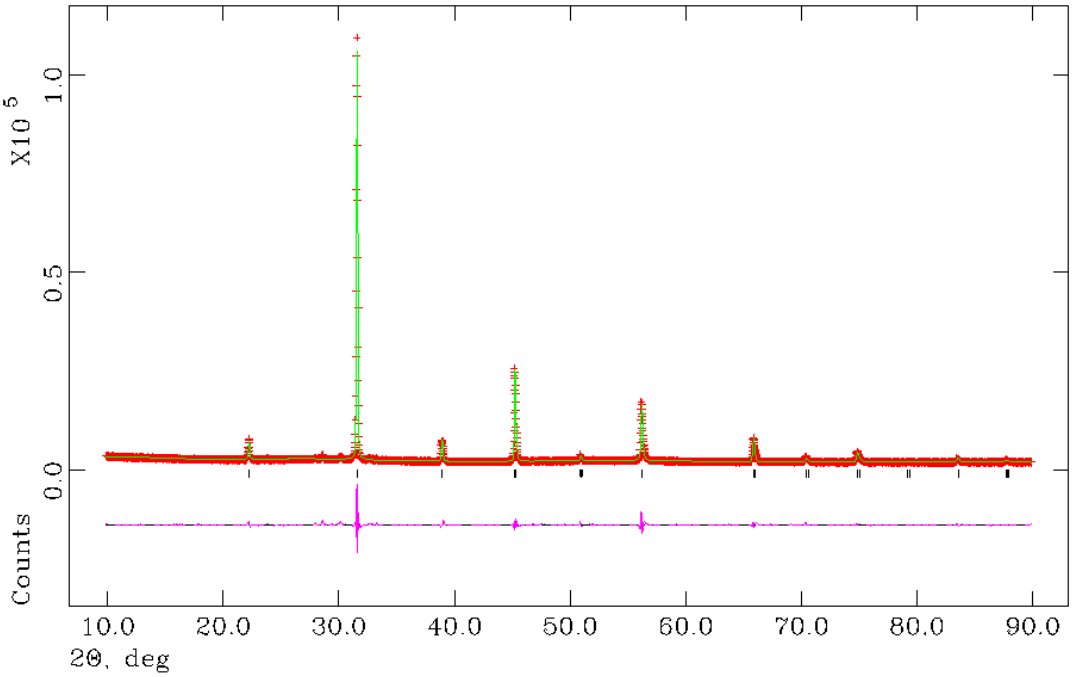

Figure A2.1: *Rietveld refinement obtained from PXRD of previous $Bi_{0.5}K_{0.5}Fe_{0.5}Nb_{0.5}O_3$; χ^2 = 7.33, R_{wp} = 5.20% and R_p = 3.54; the black crosses represent the observed intensity, the red line represents the calculated intensity from the model, the blue line represents the difference between the observed pattern and calculated pattern and the black tick marker represents the P4mm model.*

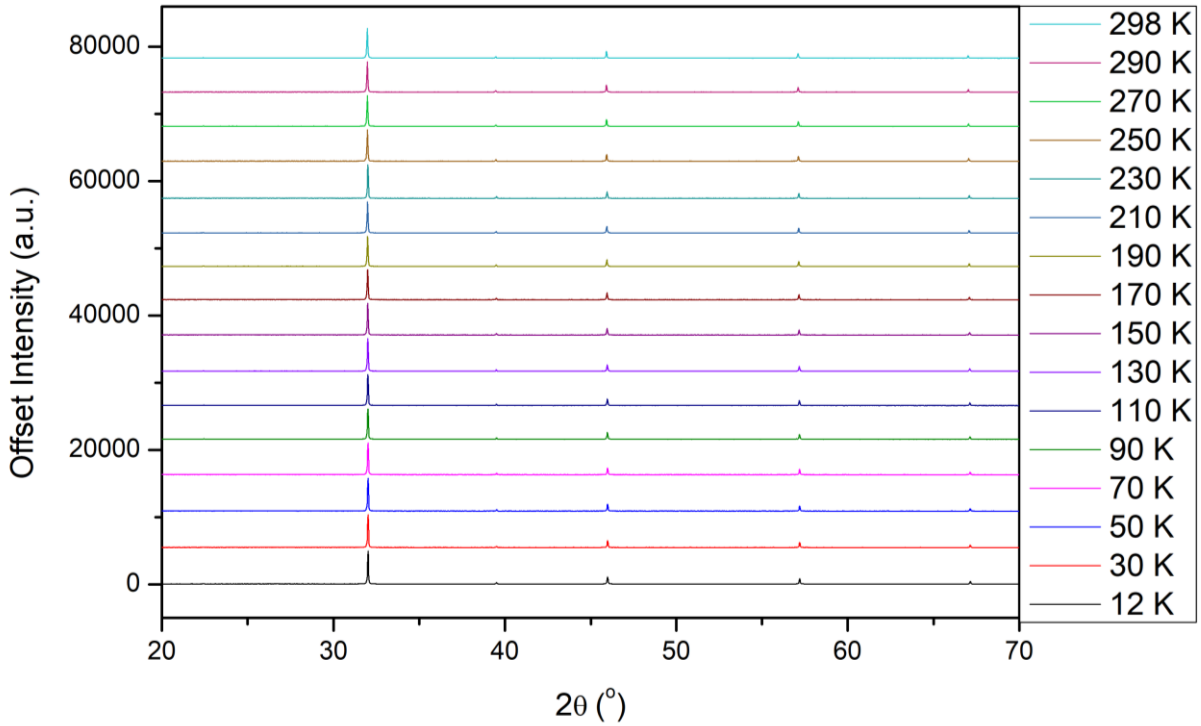

Figure A2.2: *All patterns for the LT PXRD of $Bi_{0.5}Na_{0.5}Fe_{0.5}Nb_{0.5}O_3$. 12 K pattern intensity has been scaled down to match the intensities of the other temperature points that were taken with shorter scan times.*

Table A2.1: *Rietveld refinement parameters for RT XRD of $Bi_{0.5}Na_{0.5}Fe_{0.5}Nb_{0.5}O_3$, $Bi_{0.5}K_{0.5}Fe_{0.5}Nb_{0.5}O_3$ and $Bi_{0.5}Na_{0.25}K_{0.25}Fe_{0.5}Nb_{0.5}O_3$.*

Parameter		$Bi_{0.5}A_{0.5}Fe_{0.5}B_{0.5}O_3$		
A, B		Na, Nb	Na, K, Nb	K, Nb
Space Group		*P* 4*mm*	*P* 4*mm*	*P* 4*mm*
χ^2		3.415	3.580	7.334
wRp (%)		4.14	4.27	5.37
Rp (%)		2.69	2.91	3.47
a (Å)		3.941397(31)	3.98050(6)	4.00560(6)
b (Å)		3.941397(31)	3.98050(6)	4.00560(6)
c (Å)		3.94221(8)	3.98190(9)	4.00029(12)
Tetragonality		1.00021	1.00035	0.99867
α (^{o})		90.000	90.000	90.000
β (^{o})		90.000	90.000	90.000
γ (^{o})		90.000	90.000	90.000
Cell vol. (Å^3)		61.2407(15)	63.0908(19)	64.1840(23)
Bi/A 1	x	0	0	0
	y	0	0	0
	z	0	0	0
	UISO*100	5.26(19)	10.74(4)	8.92(6)
Fe/B 1	x	0.5	0.5	0.5
	y	0.5	0.5	0.5
	z	0.5421(16)	0.4901(27)	0.5735(21)
	UISO*100	0.96(12)	1.761(30)	1.52(6)
O1	x	0.5	0.5	0.5
	y	0.5	0.5	0.5
	z	0.054(20)	0.000(16)	0.086(9)
	UISO*100	1.00*	1.00*	1.00*
O2	x	0.5	0.5	0.5
	y	0	0	0
	z	0.553(10)	0.482(7)	0.564(4)
	UISO*100	1.00*	1.00*	1.00*
Fe/B – O bond length (Å)		1.93(8)	1.95(6)	1.948(32)
		2.02(8)	2.03(6)	2.052(32)
		1.9712(8)	1.9905(5)	2.0032(4)
		1.9712(8)	1.9905(5)	2.0032(4)
		1.9712(8)	1.9905(5)	2.0032(4)
		1.9712(8)	1.9905(5)	2.0032(4)
Fe/B – O – Fe/B bond angle (^{o})		180.000(0)	180.000(0)	180.000(0)
		177.5(21)	178.2(18)	177.8(11)

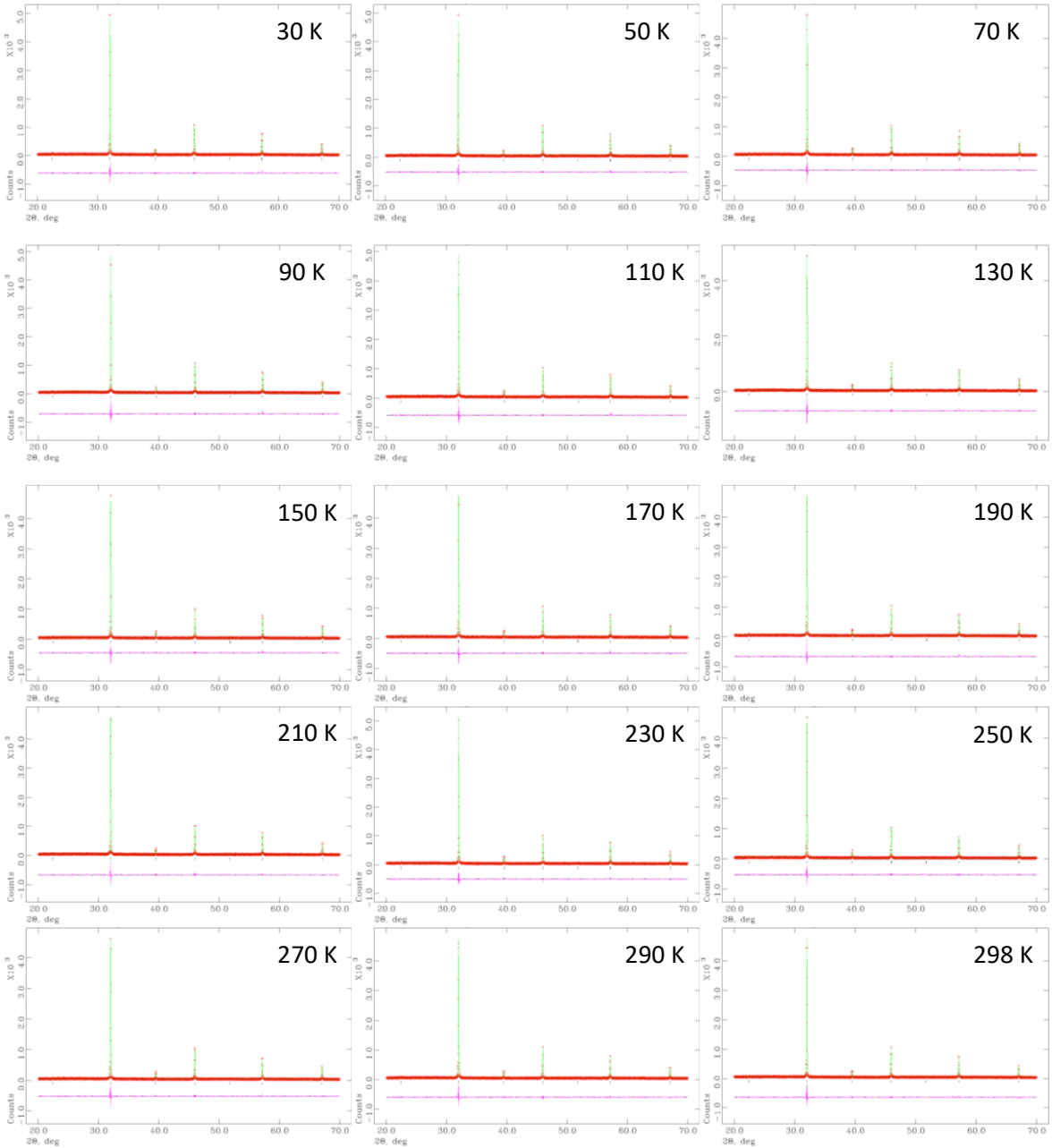

Figure A2.3: *Rietveld refinements obtained from LT PXRD of $Bi_{0.5}Na_{0.5}Fe_{0.5}Nb_{0.5}O_3$ in the temperature range 30 K to 298 K.*

Table A2.2: *Rietveld refinement parameters for LT XRD of $Bi_{0.5}Na_{0.5}Fe_{0.5}Nb_{0.5}O_3$.*

Parameter		$Bi_{0.5}Na_{0.5}Fe_{0.5}Nb_{0.5}O_3$															
Temperature (K)		12	30	50	70	90	110	130	150	170	190	210	230	250	270	290	298
Space Group		*P 4mm*	*P 4mm*	*P 4mm*	*P 4mm*	*P 4mm*	*P 4mm*	*P 4mm*	*P 4mm*	*P 4mm*	*P 4mm*	*P 4mm*	*P 4mm*	*P 4mm*	*P 4mm*	*P 4mm*	*P 4mm*
χ^2		1.996	1.222	1.242	1.205	1.251	1.206	1.248	1.165	1.199	1.243	1.190	1.191	1.180	1.268	1.191	1.176
wRp (%)		6.44	14.69	14.84	14.58	14.87	14.60	14.79	14.29	14.48	14.76	14.40	14.37	14.36	14.84	14.35	14.32
Rp (%)		4.84	11.34	11.58	11.37	11.58	11.35	11.48	11.03	11.19	11.50	11.15	10.94	11.14	11.36	11.14	11.06
a (Å)		3.93206(4)	3.93215(10)	3.93234(10)	3.93261(10)	3.93309(12)	3.93347(11)	3.93386(11)	3.93434(10)	3.93479(9)	3.93532(10)	3.93613(9)	3.93727(8)	3.93777(12)	3.93847(12)	3.93934(11)	3.94002(10)
b (Å)		3.93206(4)	3.93215(10)	3.93234(10)	3.93261(10)	3.93309(12)	3.93347(11)	3.93386(11)	3.93434(10)	3.93479(9)	3.93532(10)	3.93613(9)	3.93727(8)	3.93777(12)	3.93847(12)	3.93934(11)	3.94002(10)
c (Å)		3.93302(14)	3.93345(34)	3.9333(4)	3.9337(4)	3.9335(5)	3.9341(4)	3.9347(4)	3.93554(35)	3.93609(33)	3.9363(4)	3.93738(34)	3.93925(23)	3.9375(5)	3.9384(5)	3.9399(4)	3.9389(4)
Tetragonality		1.00024	1.00033	1.00024	1.00028	1.00010	1.00016	1.00021	1.00031	1.00033	1.00025	1.00032	1.00050	0.99993	0.99998	1.00014	0.99972
α (°)		90	90	90	90	90	90	90	90	90	90	90	90	90	90	90	90
β (°)		90	90	90	90	90	90	90	90	90	90	90	90	90	90	90	90
γ (°)		90	90	90	90	90	90	90	90	90	90	90	90	90	90	90	90
Cell vol. (Å3)		60.8089(24)	60.818(6)	60.822(6)	60.837(6)	60.849(8)	60.869(7)	60.890(7)	60.919(6)	60.941(6)	60.961(6)	61.002(6)	61.067(4)	61.055(8)	61.090(8)	61.141(7)	61.147(6)
Bi/Na 1	x	0	0	0	0	0	0	0	0	0	0	0	0	0	0	0	0
	y	0	0	0	0	0	0	0	0	0	0	0	0	0	0	0	0
	z	0	0	0	0	0	0	0	0	0	0	0	0	0	0	0	0
Fe/Nb 1	x	0.5	0.5	0.5	0.5	0.5	0.5	0.5	0.5	0.5	0.5	0.5	0.5	0.5	0.5	0.5	0.5
	y	0.5	0.5	0.5	0.5	0.5	0.5	0.5	0.5	0.5	0.5	0.5	0.5	0.5	0.5	0.5	0.5
	z	0.5415(20)	0.5415(20)	0.5415(20)	0.5415(20)	0.5415(20)	0.5415(20)	0.5415(20)	0.5415(20)	0.5415(20)	0.5415(20)	0.5415(20)	0.5415(20)	0.5415(20)	0.5415(20)	0.5415(20)	0.5415(20)
O1	x	0.5	0.5	0.5	0.5	0.5	0.5	0.5	0.5	0.5	0.5	0.5	0.5	0.5	0.5	0.5	0.5
	y	0.5	0.0	0.0	0.0	0.0	0.0	0.0	0.0	0.0	0.0	0.0	0.0	0.0	0.0	0.0	0.0
	z	0.057(6)	0.057(6)	0.057(6)	0.057(6)	0.057(6)	0.057(6)	0.057(6)	0.057(6)	0.057(6)	0.057(6)	0.057(6)	0.057(6)	0.057(6)	0.057(6)	0.057(6)	0.057(6)
O2	x	0.5	0.5	0.5	0.5	0.5	0.5	0.5	0.5	0.5	0.5	0.5	0.5	0.5	0.5	0.5	0.5
	y	0.0	0.0	0.0	0.0	0.0	0.0	0.0	0.0	0.0	0.0	0.0	0.0	0.0	0.0	0.0	0.0
	z	0.514(6)	0.514(6)	0.514(6)	0.514(6)	0.514(6)	0.514(6)	0.514(6)	0.514(6)	0.514(6)	0.514(6)	0.514(6)	0.514(6)	0.514(6)	0.514(6)	0.514(6)	0.514(6)
Nb/Fe – O bond length (Å)		1.903(8)	1.903(8)	1.903(8)	1.903(8)	1.903(8)	1.903(8)	1.903(8)	1.903(8)	1.903(8)	1.903(8)	1.903(8)	1.903(8)	1.903(8)	1.903(8)	1.903(8)	1.903(8)
		2.030(8)	2.030(8)	2.030(8)	2.030(8)	2.030(8)	2.030(8)	2.030(8)	2.030(8)	2.030(8)	2.030(8)	2.030(8)	2.030(8)	2.030(8)	2.030(8)	2.030(8)	2.030(8)
		1.9691(16)	1.9691(16)	1.9691(16)	1.9691(16)	1.9691(16)	1.9691(16)	1.9691(16)	1.9691(16)	1.9691(16)	1.9691(16)	1.9691(16)	1.9691(16)	1.9691(16)	1.9691(16)	1.9691(16)	1.9691(16)
		1.9691(16)	1.9691(16)	1.9691(16)	1.9691(16)	1.9691(16)	1.9691(16)	1.9691(16)	1.9691(16)	1.9691(16)	1.9691(16)	1.9691(16)	1.9691(16)	1.9691(16)	1.9691(16)	1.9691(16)	1.9691(16)
		1.9691(16)	1.9691(16)	1.9691(16)	1.9691(16)	1.9691(16)	1.9691(16)	1.9691(16)	1.9691(16)	1.9691(16)	1.9691(16)	1.9691(16)	1.9691(16)	1.9691(16)	1.9691(16)	1.9691(16)	1.9691(16)
		1.9691(16)	1.9691(16)	1.9691(16)	1.9691(16)	1.9691(16)	1.9691(16)	1.9691(16)	1.9691(16)	1.9691(16)	1.9691(16)	1.9691(16)	1.9691(16)	1.9691(16)	1.9691(16)	1.9691(16)	1.9691(16)
Nb/Fe – O – Nb/Fe bond angle (o)		180.000	180.000	180.000	180.000	180.000	180.000	180.000	180.000	180.000	180.000	180.000	180.000	180.000	180.000	180.000	180.000
		173.6(16)	173.6(16)	173.6(16)	173.6(16)	173.6(16)	173.6(16)	173.6(16)	173.6(16)	173.6(16)	173.6(16)	173.6(16)	173.6(16)	173.6(16)	173.6(16)	173.6(16)	173.6(16)

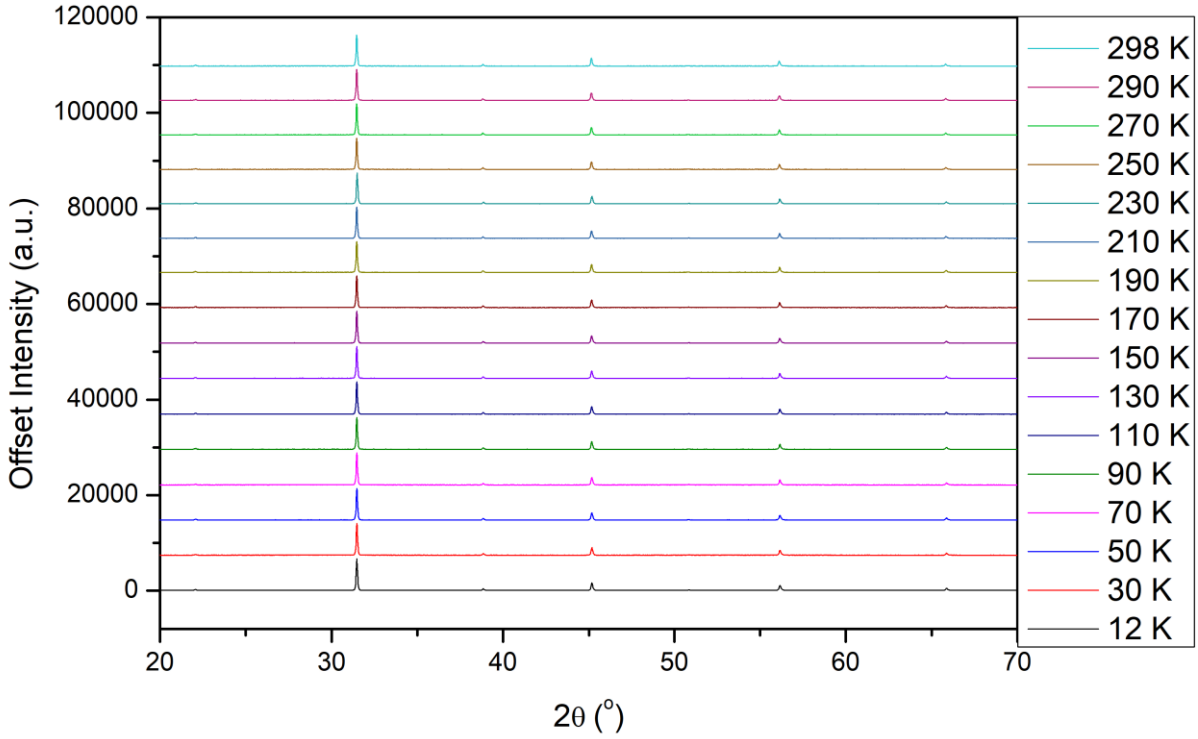

Figure A2.4: *All patterns for the LT PXRD of $Bi_{0.5}K_{0.5}Fe_{0.5}Nb_{0.5}O_3$. 12 K pattern intensity has been scaled down to match the intensities of the other temperature points that were taken with shorter scan times.*

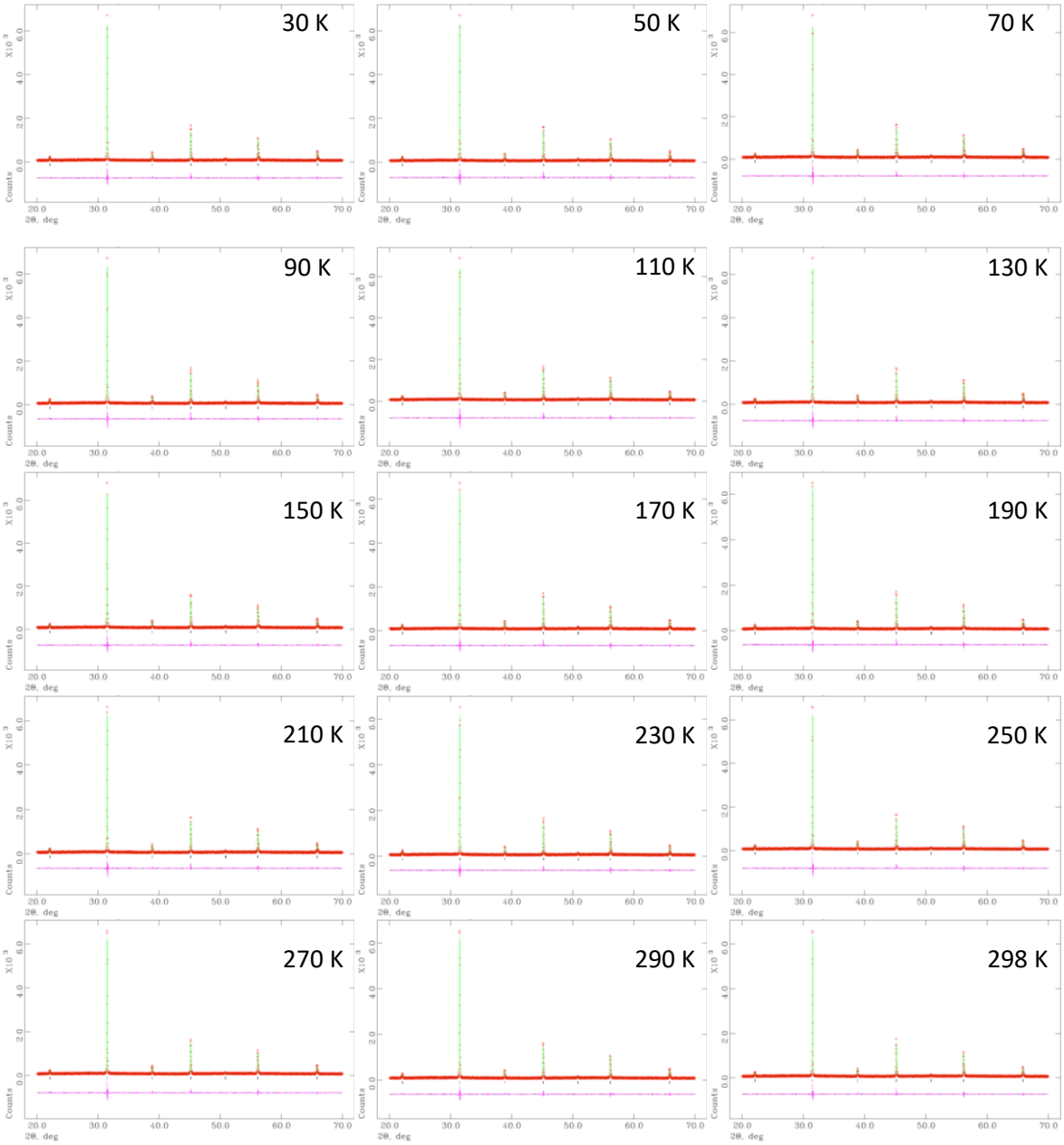

Figure A2.5: *Rietveld refinements obtained from LT PXRD of $Bi_{0.5}K_{0.5}Fe_{0.5}Nb_{0.5}O_3$ in the temperature range 30 K to 298 K*

Table A2.3: *Rietveld refinement parameters for LT XRD of $Bi_{0.5}K_{0.5}Fe_{0.5}Nb_{0.5}O_3$.*

Parameter		$Bi_{0.5}K_{0.5}Fe_{0.5}Nb_{0.5}O_3$															
Temperature (K)		12	30	50	70	90	110	130	150	170	190	210	230	250	270	290	298
Space Group		*P 4mm*	*P 4mm*	*P 4mm*	*P 4mm*	*P 4mm*	*P 4mm*	*P 4mm*	*P 4mm*	*P 4mm*	*P 4mm*	*P 4mm*	*P 4mm*	*P 4mm*	*P 4mm*	*P 4mm*	*P 4mm*
χ^2		3.828	1.441	1.447	1.457	1.479	1.415	1.453	1.471	1.464	1.430	1.475	1.473	1.443	1.459	1.333	1.343
wRp (%)		6.40	11.41	11.44	11.51	11.57	11.32	11.48	11.52	11.49	11.36	11.55	11.46	11.43	11.52	11.00	11.03
Rp (%)		4.66	9.07	9.04	9.11	9.22	8.93	9.10	9.09	9.05	8.91	8.90	8.95	9.02	9.12	8.64	8.60
a (Å)		3.99995(7)	4.00011(13)	4.00009(15)	4.00030(14)	4.00075(14)	4.00111(13)	4.00099(15)	4.00140(14)	4.00164(15)	4.00205(14)	4.00267(13)	4.00385(14)	4.00351(14)	4.00397(14)	4.00447(13)	4.00479(13)
b (Å)		3.99995(7)	4.00011(13)	4.00009(15)	4.00030(14)	4.00075(14)	4.00111(13)	4.00099(15)	4.00140(14)	4.00164(15)	4.00205(14)	4.00267(13)	4.00385(14)	4.00351(14)	4.00397(14)	4.00447(13)	4.00479(13)
c (Å)		3.99618(14)	3.99542(23)	3.99611(29)	3.99607(26)	3.99645(25)	3.99660(23)	3.99722(29)	3.99731(28)	3.99791(29)	3.99802(26)	3.99804(23)	3.99968(26)	3.99951(26)	3.99993(25)	4.00023(23)	4.00093(25)
Tetragonality		0.99906	0.99883	0.99901	0.99894	0.99893	0.99887	0.99906	0.99898	0.99907	0.99899	0.99884	0.99896	0.99900	0.99899	0.99894	0.99904
α (°)		90	90	90	90	90	90	90	90	90	90	90	90	90	90	90	90
β (°)		90	90	90	90	90	90	90	90	90	90	90	90	90	90	90	90
γ (°)		90	90	90	90	90	90	90	90	90	90	90	90	90	90	90	90
Cell vol. (Å3)		63.9374(28)	63.930(5)	63.941(6)	63.947(5)	63.967(5)	63.981(5)	63.987(6)	64.002(6)	64.019(6)	64.034(5)	64.054(5)	64.118(5)	64.104(5)	64.126(5)	64.147(5)	64.168(5)
Bi/K 1	x	0	0	0	0	0	0	0	0	0	0	0	0	0	0	0	0
	y	0	0	0	0	0	0	0	0	0	0	0	0	0	0	0	0
	z	0	0	0	0	0	0	0	0	0	0	0	0	0	0	0	0
Fe/Nb 1	x	0.5	0.5	0.5	0.5	0.5	0.5	0.5	0.5	0.5	0.5	0.5	0.5	0.5	0.5	0.5	0.5
	y	0.5	0.5	0.5	0.5	0.5	0.5	0.5	0.5	0.5	0.5	0.5	0.5	0.5	0.5	0.5	0.5
	z	0.4631(10)	0.4631(10)	0.4631(10)	0.4631(10)	0.4631(10)	0.4631(10)	0.4631(10)	0.4631(10)	0.4631(10)	0.4631(10)	0.4631(10)	0.4631(10)	0.4631(10)	0.4631(10)	0.4631(10)	0.4631(10)
O1	x	0.5	0.5	0.5	0.5	0.5	0.5	0.5	0.5	0.5	0.5	0.5	0.5	0.5	0.5	0.5	0.5
	y	0.5	0.5	0.5	0.5	0.5	0.5	0.5	0.5	0.5	0.5	0.5	0.5	0.5	0.5	0.5	0.5
	z	0.0246(57)	0.0246(57)	0.0246(57)	0.0246(57)	0.0246(57)	0.0246(57)	0.0246(57)	0.0246(57)	0.0246(57)	0.0246(57)	0.0246(57)	0.0246(57)	0.0246(57)	0.0246(57)	0.0246(57)	0.0246(57)
O2	x	0.5	0.5	0.5	0.5	0.5	0.5	0.5	0.5	0.5	0.5	0.5	0.5	0.5	0.5	0.5	0.5
	y	0.0	0.0	0.0	0.0	0.0	0.0	0.0	0.0	0.0	0.0	0.0	0.0	0.0	0.0	0.0	0.0
	z	0.4426(29)	0.4426(29)	0.4426(29)	0.4426(29)	0.4426(29)	0.4426(29)	0.4426(29)	0.4426(29)	0.4426(29)	0.4426(29)	0.4426(29)	0.4426(29)	0.4426(29)	0.4426(29)	0.4426(29)	0.4426(29)
Nb/Fe – O bond length (Å)		1.752(23)	1.752(23)	1.752(23)	1.752(23)	1.752(23)	1.752(23)	1.752(23)	1.752(23)	1.752(23)	1.752(23)	1.752(23)	1.752(23)	1.752(23)	1.752(23)	1.752(23)	1.752(23)
		2.244(23)	2.244(23)	2.244(23)	2.244(23)	2.244(23)	2.244(23)	2.244(23)	2.244(23)	2.244(23)	2.244(23)	2.244(23)	2.244(23)	2.244(23)	2.244(23)	2.244(23)	2.244(23)
		2.0017(6)	2.0017(6)	2.0017(6)	2.0017(6)	2.0017(6)	2.0017(6)	2.0017(6)	2.0017(6)	2.0017(6)	2.0017(6)	2.0017(6)	2.0017(6)	2.0017(6)	2.0017(6)	2.0017(6)	2.0017(6)
		2.0017(6)	2.0017(6)	2.0017(6)	2.0017(6)	2.0017(6)	2.0017(6)	2.0017(6)	2.0017(6)	2.0017(6)	2.0017(6)	2.0017(6)	2.0017(6)	2.0017(6)	2.0017(6)	2.0017(6)	2.0017(6)
		2.0017(6)	2.0017(6)	2.0017(6)	2.0017(6)	2.0017(6)	2.0017(6)	2.0017(6)	2.0017(6)	2.0017(6)	2.0017(6)	2.0017(6)	2.0017(6)	2.0017(6)	2.0017(6)	2.0017(6)	2.0017(6)
		2.0017(6)	2.0017(6)	2.0017(6)	2.0017(6)	2.0017(6)	2.0017(6)	2.0017(6)	2.0017(6)	2.0017(6)	2.0017(6)	2.0017(6)	2.0017(6)	2.0017(6)	2.0017(6)	2.0017(6)	2.0017(6)
Nb/Fe – O – Nb/Fe bond angle (o)		180.000	180.000	180.000	180.000	180.000	180.000	180.000	180.000	180.000	180.000	180.000	180.000	180.000	180.000	180.000	180.000
		175.3(8)	175.3(8)	175.3(8)	175.3(8)	175.3(8)	175.3(8)	175.3(8)	175.3(8)	175.3(8)	175.3(8)	175.3(8)	175.3(8)	175.3(8)	175.3(8)	175.3(8)	175.3(8)

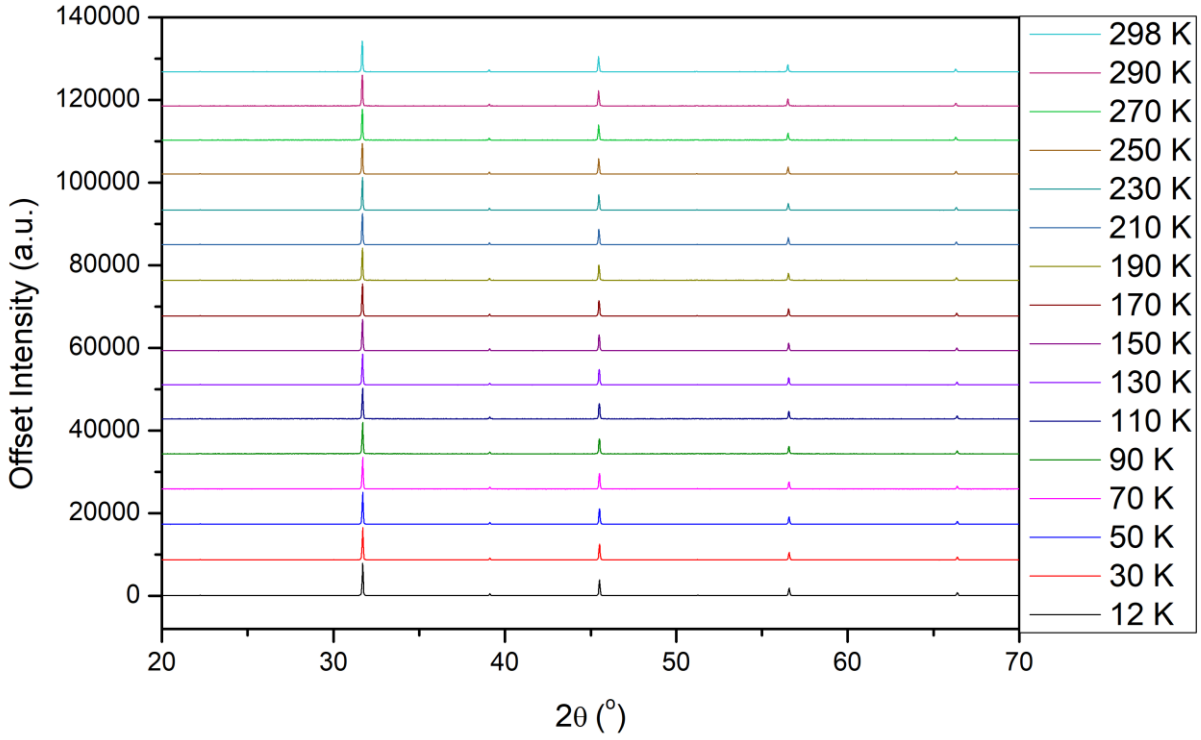

Figure A2.6: *All patterns for the LT PXRD of $Bi_{0.5}Na_{0.25}K_{0.25}Fe_{0.5}Nb_{0.5}O_3$. 12 K pattern intensity has been scaled down to match the intensities of the other temperature points that were taken with shorter scan times.*

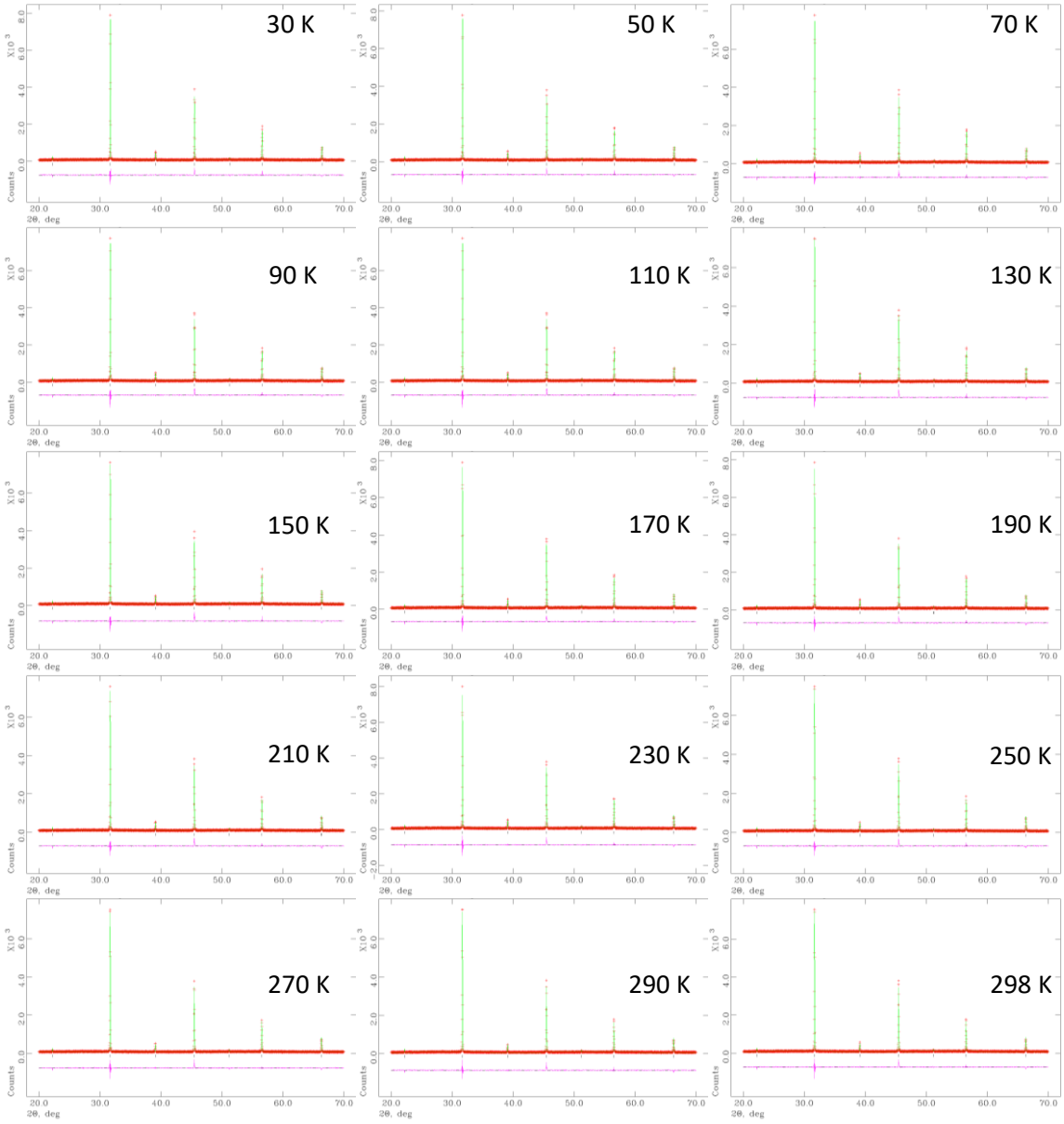

Figure A2.7: *Rietveld refinements obtained from LT PXRD of $Bi_{0.5}Na_{0.25}K_{0.25}Fe_{0.5}Nb_{0.5}O_3$ in the temperature range 30 K to 298 K.*

Table A2.4: *Rietveld refinement parameters for LT XRD of $Bi_{0.5}Na_{0.25}K_{0.25}Fe_{0.5}Nb_{0.5}O_3$.*

Parameter		$Bi_{0.5}Na_{0.25}K_{0.25}Fe_{0.5}Nb_{0.5}O_3$															
Temperature (K)		12	30	50	70	90	110	130	150	170	190	210	230	250	270	290	298
Space Group		*P 4mm*	*P 4mm*	*P 4mm*	*P 4mm*	*P 4mm*	*P 4mm*	*P 4mm*	*P 4mm*	*P 4mm*	*P 4mm*	*P 4mm*	*P 4mm*	*P 4mm*	*P 4mm*	*P 4mm*	*P 4mm*
χ^2		7.686	1.526	1.512	1.545	1.545	1.512	1.496	1.538	1.555	1.559	1.572	1.548	1.479	1.509	1.530	1.556
wRp (%)		8.96	11.61	11.56	11.71	11.68	11.55	11.49	11.67	11.72	11.73	11.78	11.67	11.41	11.53	11.61	11.69
Rp (%)		5.33	8.97	8.92	9.05	9.07	8.97	8.93	9.00	9.03	9.12	9.16	9.14	8.89	8.92	8.92	9.17
a (Å)		3.97305(5)	3.97323(7)	3.97324(7)	3.97348(7)	3.97377(7)	3.97429(7)	3.97473(7)	3.97501(7)	3.97547(7)	3.97610(7)	3.97669(7)	3.97739(7)	3.97789(7)	3.97873(7)	3.97915(7)	3.97962(7)
b (Å)		3.97305(5)	3.97323(7)	3.97324(7)	3.97348(7)	3.97377(7)	3.97429(7)	3.97473(7)	3.97501(7)	3.97547(7)	3.97610(7)	3.97669(7)	3.97739(7)	3.97789(7)	3.97873(7)	3.97915(7)	3.97962(7)
c (Å)		3.97291(14)	3.97285(18)	3.97320(19)	3.97336(18)	3.97384(19)	3.97396(18)	3.97452(18)	3.97481(18)	3.97521(18)	3.97570(19)	3.97647(19)	3.97719(19)	3.97796(18)	3.97849(18)	3.97943(18)	3.97929(18)
Tetragonality		0.99996	0.99990	0.99999	0.99997	1.00002	0.99992	0.99995	0.99995	0.99993	0.99990	0.99994	0.99995	1.00002	0.99994	1.00007	0.99992
α (°)		90	90	90	90	90	90	90	90	90	90	90	90	90	90	90	90
β (°)		90	90	90	90	90	90	90	90	90	90	90	90	90	90	90	90
γ (°)		90	90	90	90	90	90	90	90	90	90	90	90	90	90	90	90
Cell vol. (Å3)		62.7130(24)	62.7175(33)	62.7236(34)	62.7337(33)	62.7504(34)	62.7685(33)	62.7914(33)	62.8050(33)	62.8257(33)	62.8532(34)	62.8842(34)	62.9176(34)	62.9456(33)	62.9807(33)	63.0087(33)	63.0214(33)
Bi/Na/K 1	x	0	0	0	0	0	0	0	0	0	0	0	0	0	0	0	0
	y	0	0	0	0	0	0	0	0	0	0	0	0	0	0	0	0
	z	0	0	0	0	0	0	0	0	0	0	0	0	0	0	0	0
Fe/Nb 1	x	0.5	0.5	0.5	0.5	0.5	0.5	0.5	0.5	0.5	0.5	0.5	0.5	0.5	0.5	0.5	0.5
	y	0.5	0.5	0.5	0.5	0.5	0.5	0.5	0.5	0.5	0.5	0.5	0.5	0.5	0.5	0.5	0.5
	z	0.5232(32)	0.5232(32)	0.5232(32)	0.5232(32)	0.5232(32)	0.5232(32)	0.5232(32)	0.5232(32)	0.5232(32)	0.5232(32)	0.5232(32)	0.5232(32)	0.5232(32)	0.5232(32)	0.5232(32)	0.5232(32)
O1	x	0.5	0.5	0.5	0.5	0.5	0.5	0.5	0.5	0.5	0.5	0.5	0.5	0.5	0.5	0.5	0.5
	y	0.5	0.5	0.5	0.5	0.5	0.5	0.5	0.5	0.5	0.5	0.5	0.5	0.5	0.5	0.5	0.5
	z	0.014(27)	0.014(27)	0.014(27)	0.014(27)	0.014(27)	0.014(27)	0.014(27)	0.014(27)	0.014(27)	0.014(27)	0.014(27)	0.014(27)	0.014(27)	0.014(27)	0.014(27)	0.014(27)
O2	x	0.5	0.5	0.5	0.5	0.5	0.5	0.5	0.5	0.5	0.5	0.5	0.5	0.5	0.5	0.5	0.5
	y	0.0	0.0	0.0	0.0	0.0	0.0	0.0	0.0	0.0	0.0	0.0	0.0	0.0	0.0	0.0	0.0
	z	0.408(9)	0.408(9)	0.408(9)	0.408(9)	0.408(9)	0.408(9)	0.408(9)	0.408(9)	0.408(9)	0.408(9)	0.408(9)	0.408(9)	0.408(9)	0.408(9)	0.408(9)	0.408(9)
Nb/Fe – O bond length (Å)		2.02(10)	2.02(10)	2.02(10)	2.02(10)	2.02(10)	2.02(10)	2.02(10)	2.02(10)	2.02(10)	2.02(10)	2.02(10)	2.02(10)	2.02(10)	2.02(10)	2.02(10)	2.02(10)
		1.95(10)	1.95(10)	1.95(10)	1.95(10)	1.95(10)	1.95(10)	1.95(10)	1.95(10)	1.95(10)	1.95(10)	1.95(10)	1.95(10)	1.95(10)	1.95(10)	1.95(10)	1.95(10)
		2.038(8)	2.038(8)	2.038(8)	2.038(8)	2.038(8)	2.038(8)	2.038(8)	2.038(8)	2.038(8)	2.038(8)	2.038(8)	2.038(8)	2.038(8)	2.038(8)	2.038(8)	2.038(8)
		2.038(8)	2.038(8)	2.038(8)	2.038(8)	2.038(8)	2.038(8)	2.038(8)	2.038(8)	2.038(8)	2.038(8)	2.038(8)	2.038(8)	2.038(8)	2.038(8)	2.038(8)	2.038(8)
		2.038(8)	2.038(8)	2.038(8)	2.038(8)	2.038(8)	2.038(8)	2.038(8)	2.038(8)	2.038(8)	2.038(8)	2.038(8)	2.038(8)	2.038(8)	2.038(8)	2.038(8)	2.038(8)
		2.038(8)	2.038(8)	2.038(8)	2.038(8)	2.038(8)	2.038(8)	2.038(8)	2.038(8)	2.038(8)	2.038(8)	2.038(8)	2.038(8)	2.038(8)	2.038(8)	2.038(8)	2.038(8)
Nb/Fe – O – Nb/Fe bond angle (o)		180.000	180.000	180.000	180.000	180.000	180.000	180.000	180.000	180.000	180.000	180.000	180.000	180.000	180.000	180.000	180.000
		154.1(20)	154.1(20)	154.1(20)	154.1(20)	154.1(20)	154.1(20)	154.1(20)	154.1(20)	154.1(20)	154.1(20)	154.1(20)	154.1(20)	154.1(20)	154.1(20)	154.1(20)	154.1(20)

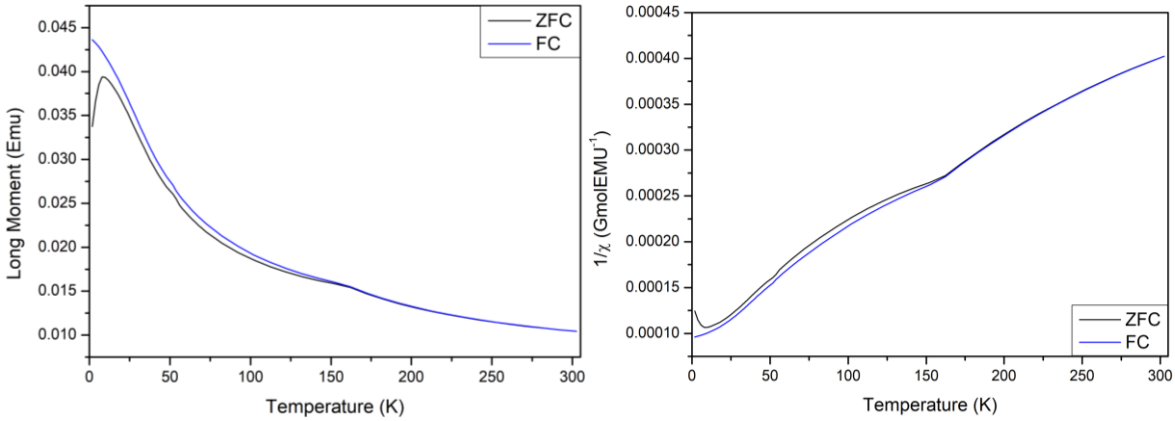

Figure A2.8: *Magnetic data from SQUID for $Bi_{0.5}Na_{0.5}Fe_{0.5}Nb_{0.5}O_3$, (a) Zero field cooled, field cooled SQUID data, (b) 1/χ SQUID data.*

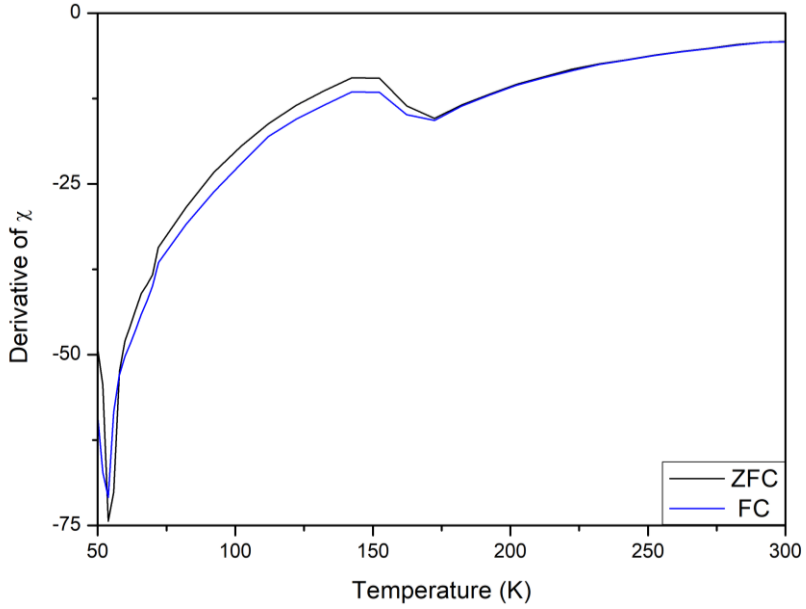

Figure A2.9: *Magnetic data from SQUID for $Bi_{0.5}Na_{0.5}Fe_{0.5}Nb_{0.5}O_3$, derivative of χ SQUID data.*

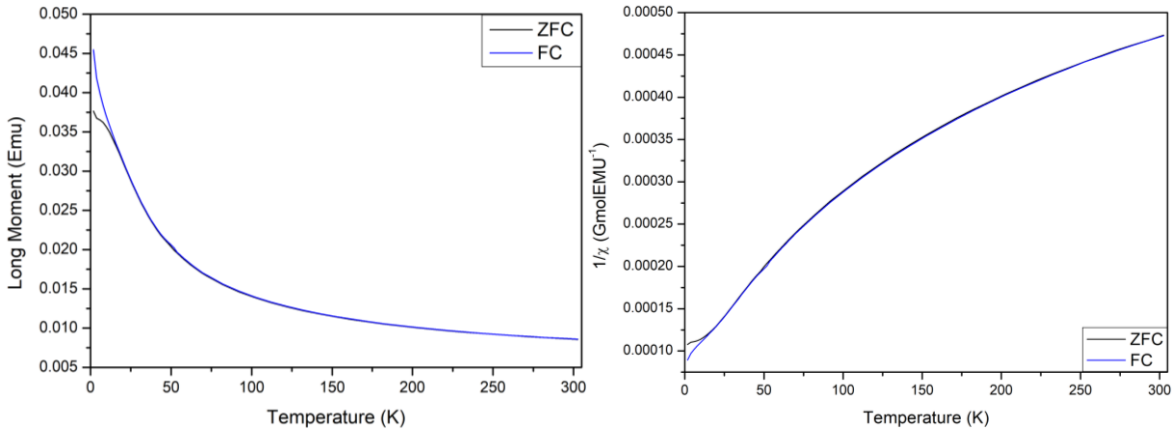

Figure A2.10: *Magnetic data from SQUID for $Bi_{0.5}K_{0.5}Fe_{0.5}Nb_{0.5}O_3$, (a) Zero field cooled, field cooled SQUID data, (b) 1/χ SQUID data.*

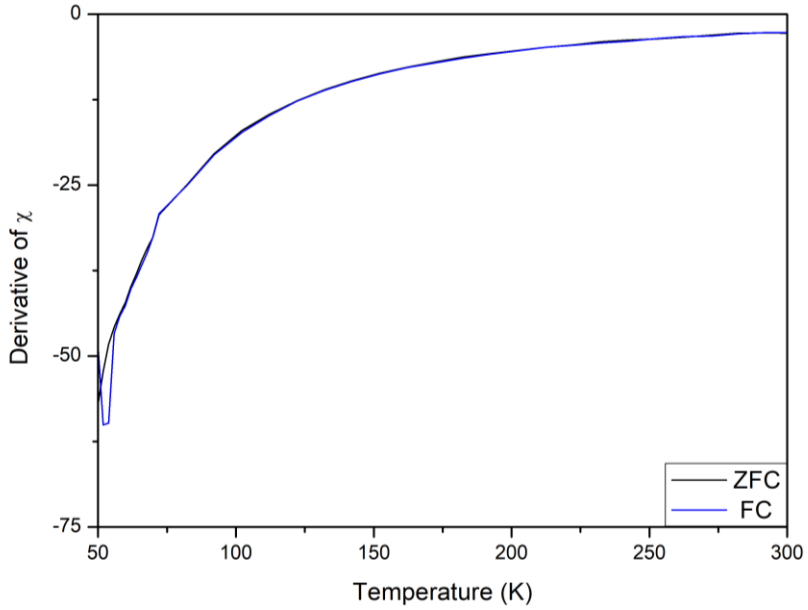

Figure A2.11: *Magnetic data from SQUID for $Bi_{0.5}K_{0.5}Fe_{0.5}Nb_{0.5}O_3$, derivative of χ SQUID data.*

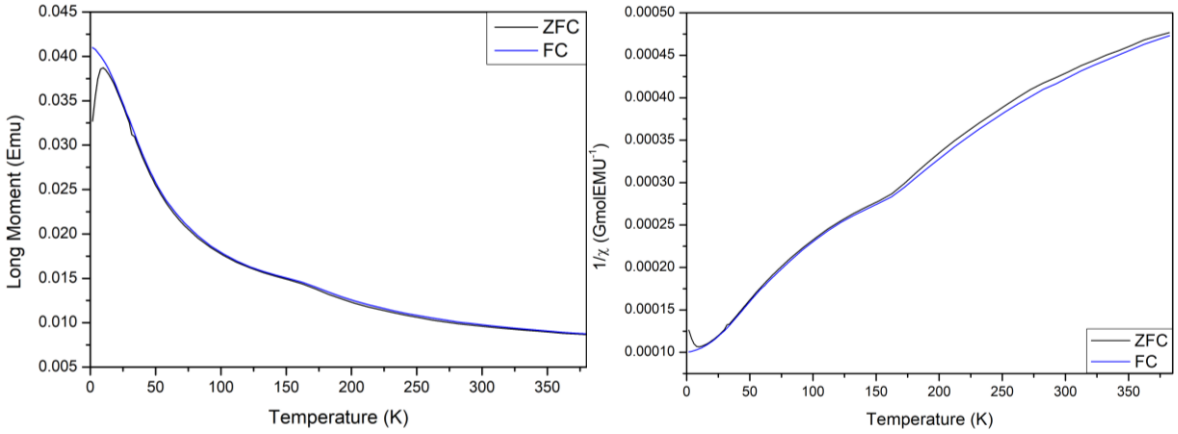

Figure A2.12: *Magnetic data from SQUID for $Bi_{0.5}Na_{0.25}K_{0.25}Fe_{0.5}Nb_{0.5}O_3$, (a) Zero field cooled, field cooled SQUID data, (b) 1/χ SQUID data.*

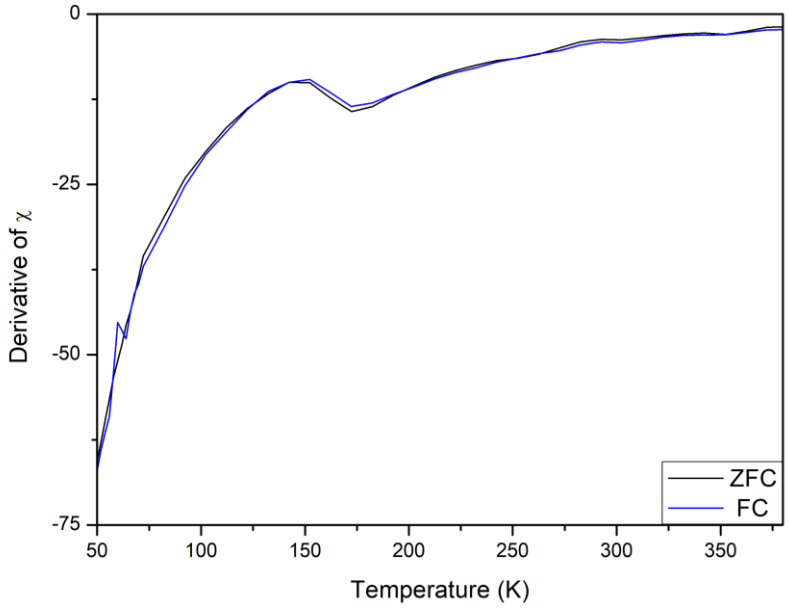

Figure A2.13: *Magnetic data from SQUID for $Bi_{0.5}Na_{0.25}K_{0.25}Fe_{0.5}Nb_{0.5}O_3$, derivative of χ SQUID data.*

Table A2.5: *Rietveld refinement parameters for RT ND of $Bi_{0.5}Na_{0.5}Fe_{0.5}Nb_{0.5}O_3$, $Bi_{0.5}K_{0.5}Fe_{0.5}Nb_{0.5}O_3$ and $Bi_{0.5}Na_{0.25}K_{0.25}Fe_{0.5}Nb_{0.5}O_3$.*

Parameter		$Bi_{0.5}A_{0.5}Fe_{0.5}Nb_{0.5}O_3$		
A		Na	Na, K	K
Space Group		*P* 4*mm*	*P* 4*mm*	*P* 4*mm*
χ^2		13.47	1.875	3.597
wRp (%)		9.67	5.12	7.95
Rp (%)		8.21	4.82	7.78
a (Å)		3.94282(6)	3.982285(30)	4.00736(5)
b (Å)		3.94282(6)	3.982285(30)	4.00736(5)
c (Å)		3.94174(10)	3.98048(6)	4.00371(9)
Tetragonality		0.99973	0.99955	0.99909
Tolerance Factor		0.958	0.980	1.001
α (°)		90	90	90
β (°)		90	90	90
γ (°)		90	90	90
Cell vol. (Å^3)		61.2777(20)	63.1248(11)	64.2953(19)
Bi/A 1	x	0	0	0
	y	0	0	0
	z	0	0	0
	U_{iso} *100	6.62(20)	8.63(7)	8.74(22)
Fe/Nb 1	x	0.5	0.5	0.5
	y	0.5	0.5	0.5
	z	0.524(5)	0.493(12)	0.522(9)
	U_{iso} *100	1.248(30)	1.414(30)	1.404(26)
O1	x	0.5	0.5	0.5
	y	0.5	0.5	0.5
	z	0.041(5)	0.010(11)	0.033(7)
	U_{111} *100	10.0(12)	5.28(28)	2.63(22)
	U_{222} *100	10.00(119)	5.28(28)	2.63(22)
	U_{333} *100	-0.4(4)	0.14(17)	0.82(25)
O2	x	0.5	0.5	0.5
	y	0	0	0
	z	0.563(6)	0.487(7)	0.519(11)
	U_{111} *100	10.4(14)	3.09(21)	1.22(22)
	U_{222} *100	0.89(25)	0.96(9)	0.76(10)
	U_{333} *100	8.6(9)	6.18(31)	6.01(24)
Bi/A – O bond length (Å)		2.7927(12)	2.8162(6)	2.8366(12)
		2.7927(12)	2.8162(6)	2.8366(12)
		2.7927(12)	2.8162(6)	2.8366(12)
		2.7927(12)	2.8162(6)	2.8366(12)
		2.618(16)	2.852(20)	2.778(31)
		2.969(19)	2.779(20)	2.887(33)
		2.618(16)	2.852(20)	2.778(31)
		2.969(19)	2.779(20)	2.887(33)
		2.618(16)	2.852(20)	2.778(31)
		2.969(19)	2.779(20)	2.887(33)
		2.618(16)	2.852(20)	2.778(31)
		2.969(19)	2.779(20)	2.887(33)
Fe/Nb – O bond length (Å)		1.906(9)	1.925(7)	1.959(16)
		2.036(9)	2.056(7)	2.045(16)
		1.9773(8)	1.99131(33)	2.00371(23)
		1.9773(8)	1.99131(33)	2.00371(23)
		1.9773(8)	1.99131(33)	2.00371(23)
		1.9773(8)	1.99131(33)	2.00371(23)
Fe/Nb – O – Fe/Nb bond angle (°)		180.000(0)	180.000(0)	180.000(0)
		171.1(6)	178.5(15)	180.000(26)

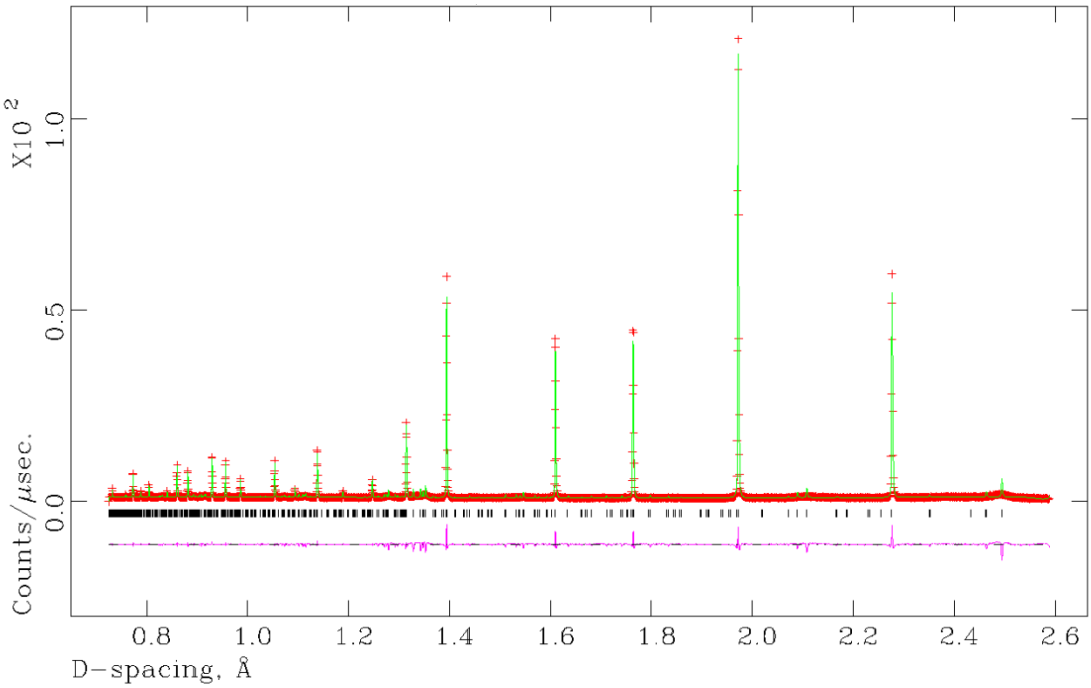

Figure A2.14: *Le Bail refinement of room temperature PND data collected for $Bi_{0.5}Na_{0.5}Fe_{0.5}Nb_{0.5}O_3$. χ^2 = 22.71, R_{wp} = 12.57% and R_p = 8.16; the red crosses represent the observed intensity, the green line represents the calculated intensity from the model, the pink line represents the difference between the observed pattern and calculated pattern and the black tick marker represents the P4mm model.*

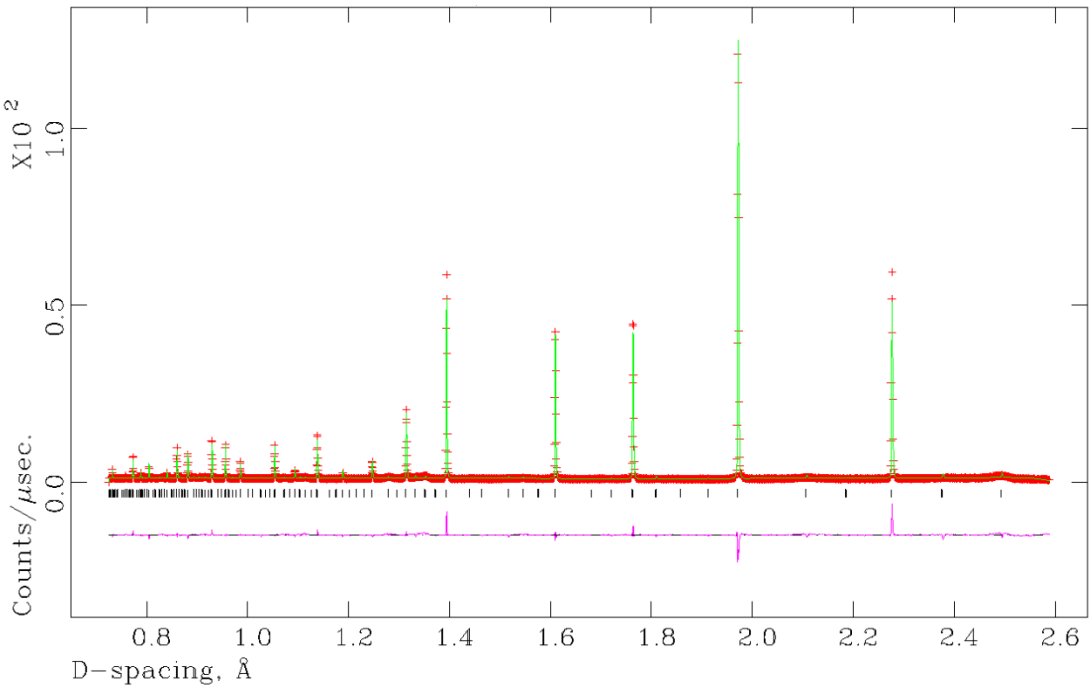

Figure A2.15: *Rietveld refinement of room temperature PND data collected for $Bi_{0.5}Na_{0.5}Fe_{0.5}Nb_{0.5}O_3$. χ^2 = 12.86, R_{wp} = 9.46% and R_p = 7.70; the red crosses represent the observed intensity, the green line represents the calculated intensity from the model, the pink line represents the difference between the observed pattern and calculated pattern and the black tick marker represents the P21 model. .*Unstable refinement and was not able to converge.*

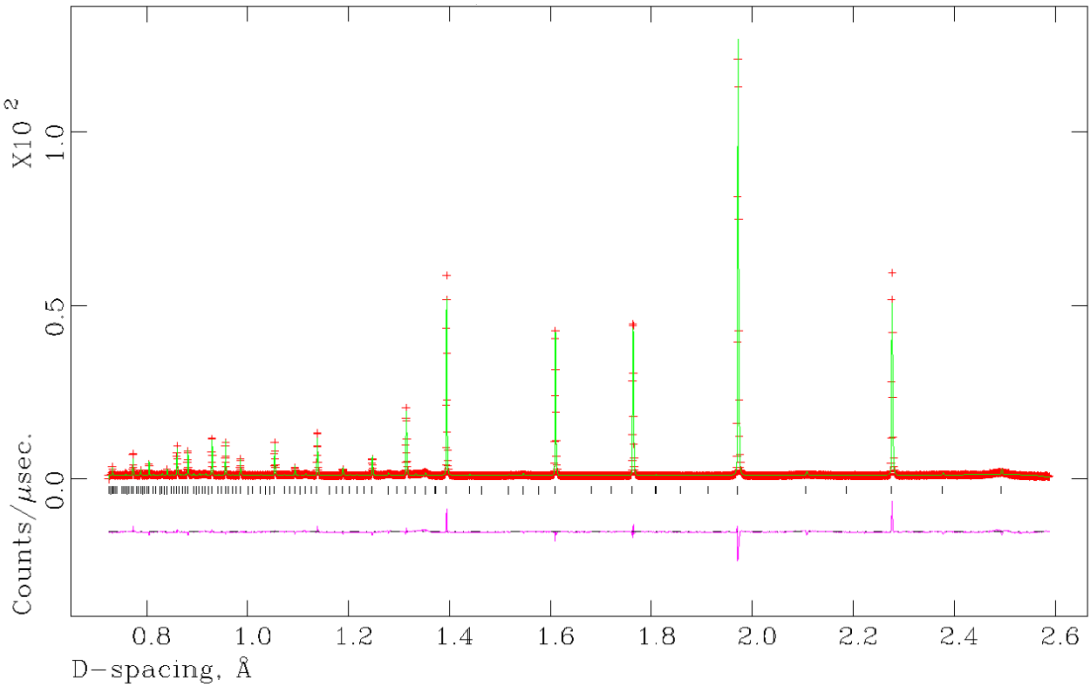

Figure A2.16: *Rietveld refinement of room temperature PND data collected for $Bi_{0.5}Na_{0.5}Fe_{0.5}Nb_{0.5}O_3$. χ^2 = 11.63, R_{wp} = 8.99% and R_p = 7.51; the red crosses represent the observed intensity, the green line represents the calculated intensity from the model, the pink line represents the difference between the observed pattern and calculated pattern and the black tick marker represents the $P2_1ma$ model. .*Unstable refinement and was not able to converge.*

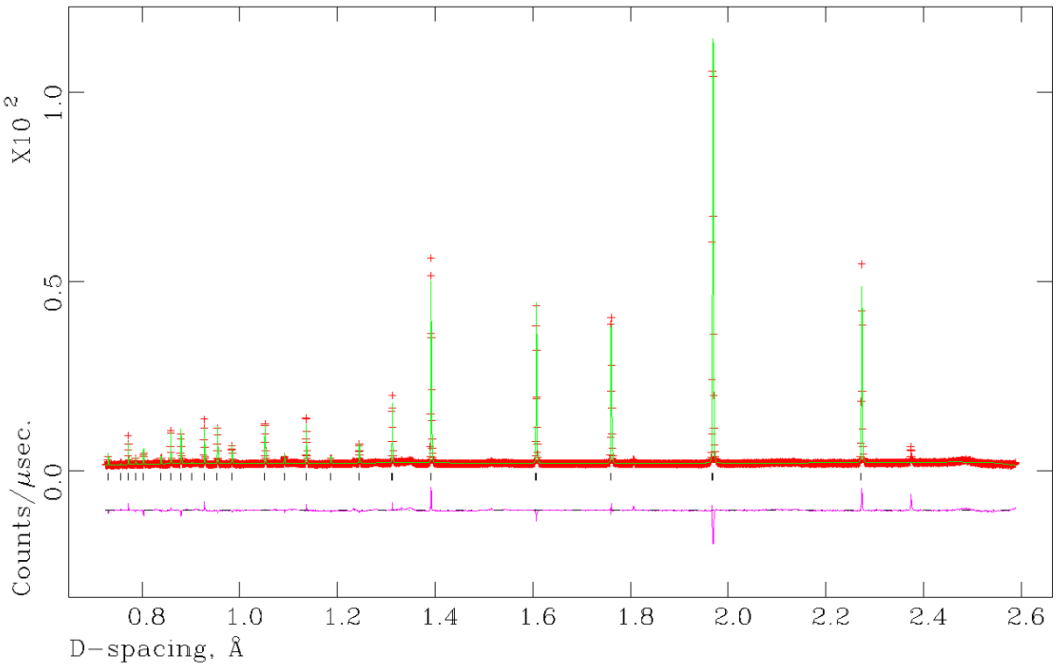

Figure A2.17: *Rietveld refinement obtained from LT PND of $Bi_{0.5}Na_{0.5}Fe_{0.5}Nb_{0.5}O_3$ at 100 K; χ^2 = 10.01, R_{wp} = 7.33% and R_p = 5.87; the red crosses represent the observed intensity, the green line represents the calculated intensity from the model, the pink line represents the difference between the observed pattern and calculated pattern and the black tick marker represents the P4mm model.*

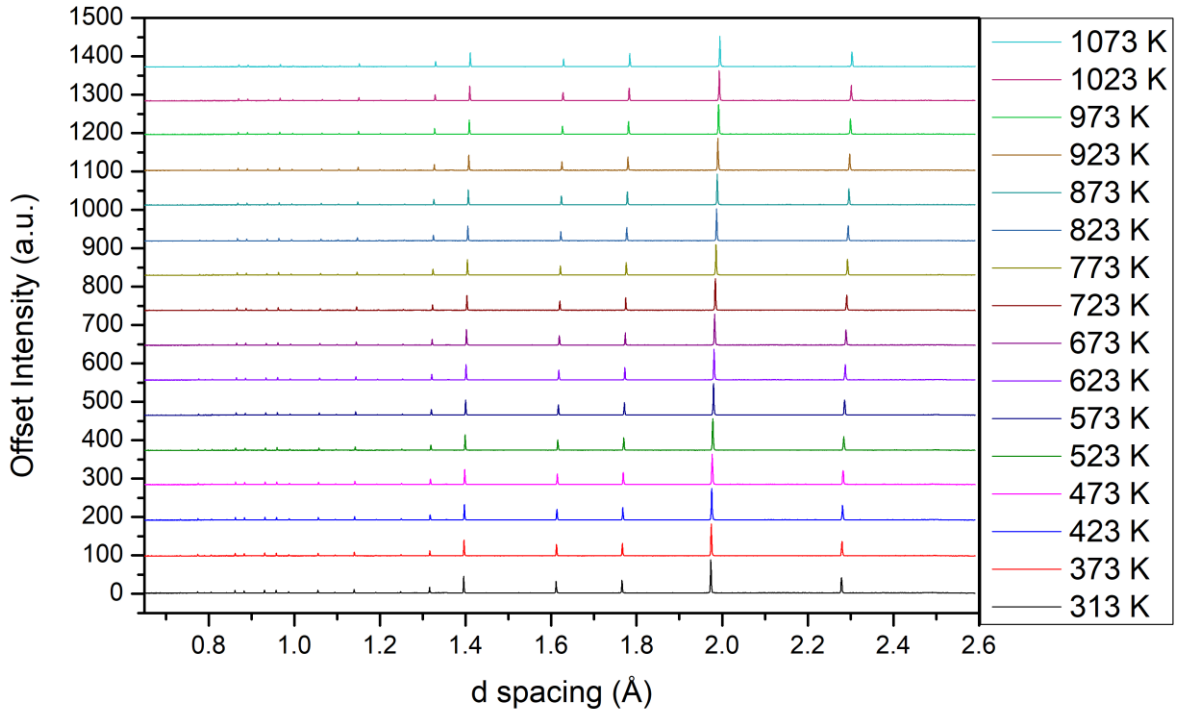

Figure A2.18: *All patterns for the HT PND of $Bi_{0.5}Na_{0.5}Fe_{0.5}Nb_{0.5}O_3$*

Table A2.6: *Rietveld refinement parameters for VT ND of $Bi_{0.5}Na_{0.5}Fe_{0.5}Nb_{0.5}O_3$.*

Parameter		$Bi_{0.5}Na_{0.5}Fe_{0.5}Nb_{0.5}O_3$																	
Temperature		10 K	100 K	323 K	373 K	423 K	473 K	523 K	573 K	623 K	673 K	723 K	773 K	823 K	873 K	923 K	973 K	1023 K	1073 K
Space Group		*P* 4*mm*	*P* 4*mm*	*P* 4*mm*	*P* 4*mm*	*P* 4*mm*	*P* 4*mm*	*P* 4*mm*	*P* 4*mm*	*P* 4*mm*	*P* 4*mm*	*P* 4*mm*	*P* 4*mm*	*P* 4*mm*	*P* 4*mm*	*P* 4*mm*	*Pm*$^-$*3m*	*Pm*$^-$*3m*	*Pm*$^-$*3m*
χ^2		10.23	10.01	1.828	1.804	1.646	1.678	1.547	3.564	1.501	1.410	1.385	2.664	1.293	1.297	1.217	1.305	1.301	1.344
wRp (%)		7.58	7.33	5.89	5.89	5.60	5.65	5.42	4.12	5.33	5.15	5.13	3.54	4.91	4.91	4.75	4.92	4.91	4.77
Rp (%)		6.21	5.87	5.58	5.63	5.36	5.49	5.27	3.72	5.21	5.02	4.98	3.23	4.89	4.90	4.80	4.90	4.95	4.81
a (Å)		3.93582(5)	3.93667(5)	3.94343(6)	3.94556(5)	3.94779(5)	3.94999(6)	3.95275(6)	3.95601(4)	3.95850(6)	3.96133(5)	3.96431(5)	3.96743(4)	3.97035(5)	3.97328(6)	3.97646(5)	3.979097(31)	3.982410(31)	3.985573(31)
b (Å)		3.93582(5)	3.93667(5)	3.94343(6)	3.94556(5)	3.94779(5)	3.94999(6)	3.95275(6)	3.95601(4)	3.95850(6)	3.96133(5)	3.96431(5)	3.96743(4)	3.97035(5)	3.97328(6)	3.97646(5)	3.979097(31)	3.982410(31)	3.985573(31)
c (Å)		3.93466(8)	3.93559(8)	3.94225(9)	3.94426(9)	3.94630(8)	3.94876(10)	3.95145(9)	3.95476(7)	3.95733(9)	3.96010(8)	3.96315(8)	3.96641(6)	3.96924(8)	3.97242(10)	3.97536(7)	3.979097(31)	3.982410(31)	3.985573(31)
Tetragonality		0.99971	0.99973	0.99970	0.99967	0.99962	0.99969	0.99967	0.99968	0.99970	0.99969	0.99971	0.99974	0.99972	0.99978	0.99972	1.00000	1.00000	1.00000
α (°)		90	90	90	90	90	90	90	90	90	90	90	90	90	90	90	90	90	90
β (°)		90	90	90	90	90	90	90	90	90	90	90	90	90	90	90	90	90	90
γ (°)		90	90	90	90	90	90	90	90	90	90	90	90	90	90	90	90	90	90
Cell vol. (Å^3)		60.9506(16)	60.9913(17)	61.3045(18)	61.4022(18)	61.5031(16)	61.6100(20)	61.7385(19)	61.8919(14)	62.0104(19)	62.1424(18)	62.2840(17)	62.4335(13)	62.5697(17)	62.7124(21)	62.8595(16)	63.0019(9)	63.1594(9)	63.3100(9)
Bi/Na 1	x	0	0	0	0	0	0	0	0	0	0	0	0	0	0	0	0	0	0
	y	0	0	0	0	0	0	0	0	0	0	0	0	0	0	0	0	0	0
	z	0	0	0	0	0	0	0	0	0	0	0	0	0	0	0	0	0	0
	U_{iso} *100	4.78(20)	4.98(20)	5.59(25)	5.80(25)	5.89(24)	5.85(28)	6.36(27)	6.45(23)	6.51(31)	6.59(33)	6.42(34)	6.48(27)	6.5(4)	6.9(4)	6.5(4)	9.98(9)	10.23(10)	10.54(10)
Fe/Nb 1	x	0.5	0.5	0.5	0.5	0.5	0.5	0.5	0.5	0.5	0.5	0.5	0.5	0.5	0.5	0.5	0.5	0.5	0.5
	y	0.5	0.5	0.5	0.5	0.5	0.5	0.5	0.5	0.5	0.5	0.5	0.5	0.5	0.5	0.5	0.5	0.5	0.5
	z	0.534(4)	0.534(4)	0.540(4)	0.538(4)	0.541(4)	0.544(4)	0.543(4)	0.5460(34)	0.548(4)	0.554(4)	0.557(4)	0.5610(32)	0.563(4)	0.563(5)	0.571(4)	0.5	0.5	0.5
	U_{iso} *100	0.649(31)	0.714(31)	1.03(4)	0.979(35)	1.102(33)	1.12(4)	1.236(34)	1.331(27)	1.41(4)	1.499(34)	1.56(4)	1.704(27)	1.81(4)	1.88(4)	1.99(4)	1.837(29)	1.845(29)	1.933(29)
O1	x	0.5	0.5	0.5	0.5	0.5	0.5	0.5	0.5	0.5	0.5	0.5	0.5	0.5	0.5	0.5	0.5	0.5	0.5
	y	0.5	0.5	0.5	0.5	0.5	0.5	0.5	0.5	0.5	0.5	0.5	0.5	0.5	0.5	0.5	0.5	0.5	0.5
	z	0.050(4)	0.050(4)	0.055(4)	0.050(5)	0.054(4)	0.057(4)	0.057(4)	0.0549(35)	0.058(5)	0.0613(43)	0.0644(39)	0.0663(30)	0.0677(38)	0.0665(45)	0.0737(34)	0	0	0
	U_{111} *100	9.8(11)	9.7(11)	9.1(10)	8.8(10)	9.0(9)	8.7(10)	8.8(10)	8.5(7)	8.2(10)	8.2(9)	7.8(9)	7.7(6)	8.0(8)	7.7(10)	7.4(8)	8.52(7)	8.27(7)	8.32(7)
	U_{222} *100	9.80(109)	9.65(106)	9.10(102)	8.83(101)	9.00(92)	8.72(102)	8.81(97)	8.46(74)	8.17(96)	8.21(89)	7.85(89)	7.70(64)	7.98(83)	7.66(104)	7.38(78)	8.52(7)	8.27(7)	8.32(7)
	U_{333} *100	-0.6(4)	-0.7(4)	-0.6(4)	-0.5(4)	0.0(4)	-0.4(4)	-0.1(4)	-0.07(32)	-0.2(4)	0.2(4)	-0.3(4)	0.01(32)	-0.1(4)	0.0(5)	0.0(4)	1.08(7)	1.21(7)	1.21(7)
O2	x	0.5	0.5	0.5	0.5	0.5	0.5	0.5	0.5	0.5	0.5	0.5	0.5	0.5	0.5	0.5	N/A	N/A	N/A
	y	0	0	0	0	0	0	0	0	0	0	0	0	0	0	0	N/A	N/A	N/A
	z	0.583(4)	0.584(4)	0.588(4)	0.586(4)	0.583(4)	0.590(4)	0.587(4)	0.5869(29)	0.592(4)	0.5888(34)	0.5956(31)	0.5957(21)	0.5958(28)	0.5984(31)	0.6026(24)	N/A	N/A	N/A
	U_{111} *100	10.5(12)	10.5(12)	9.9(11)	9.6(11)	9.8(10)	9.5(11)	9.2(10)	9.1(8)	9.0(10)	9.2(10)	8.6(9)	9.0(7)	8.8(9)	8.5(10)	8.5(8)	N/A	N/A	N/A
	U_{222} *100	0.25(24)	0.37(25)	0.40(25)	0.49(25)	0.28(21)	0.47(26)	0.58(24)	0.62(19)	0.66(26)	0.65(24)	0.60(24)	0.84(19)	0.88(25)	0.98(30)	1.03(24)	N/A	N/A	N/A
	U_{333} *100	6.7(6)	6.5(6)	6.3(6)	6.2(6)	6.6(5)	6.0(5)	6.5(6)	6.36(43)	6.0(5)	6.3(6)	6.2(6)	6.06(44)	6.0(6)	6.1(7)	5.9(6)	N/A	N/A	N/A
Bi/Na – O bond length (Å)		2.7900(12)	2.7906(12)	2.7968(13)	2.7970(13)	2.7996(13)	2.8020(14)	2.8042(14)	2.8057(11)	2.8084(15)	2.8116(15)	2.8148(14)	2.8177(11)	2.8203(14)	2.8219(17)	2.8270(14)	2.81365(2)	2.81599(2)	2.81823(2)
		2.7900(12)	2.7906(12)	2.7968(13)	2.7970(13)	2.7996(13)	2.8020(14)	2.8042(14)	2.8057(11)	2.8084(15)	2.8116(15)	2.8148(14)	2.8177(11)	2.8203(14)	2.8219(17)	2.8270(14)	2.81365(2)	2.81599(2)	2.81823(2)
		2.7900(12)	2.7906(12)	2.7968(13)	2.7970(13)	2.7996(13)	2.8020(14)	2.8042(14)	2.8057(11)	2.8084(15)	2.8116(15)	2.8148(14)	2.8177(11)	2.8203(14)	2.8219(17)	2.8270(14)	2.81365(2)	2.81599(2)	2.81823(2)
		2.7900(12)	2.7906(12)	2.7968(13)	2.7970(13)	2.7996(13)	2.8020(14)	2.8042(14)	2.8057(11)	2.8084(15)	2.8116(15)	2.8148(14)	2.8177(11)	2.8203(14)	2.8219(17)	2.8270(14)	2.81365(2)	2.81599(2)	2.81823(2)
		2.562(10)	2.560(10)	2.554(10)	2.561(10)	2.569(9)	2.553(10)	2.562(10)	2.565(7)	2.555(9)	2.564(8)	2.549(8)	2.551(5)	2.552(7)	2.548(8)	2.539(6)	2.81365(2)	2.81599(2)	2.81823(2)
		3.023(12)	3.026(12)	3.044(12)	3.038(12)	3.032(11)	3.055(12)	3.048(12)	3.050(9)	3.066(11)	3.059(10)	3.082(9)	3.085(6)	3.088(9)	3.098(10)	3.113(7)	2.81365(2)	2.81599(2)	2.81823(2)
		2.562(10)	2.560(10)	2.554(10)	2.561(10)	2.569(9)	2.553(10)	2.562(10)	2.565(7)	2.555(9)	2.564(8)	2.549(8)	2.551(5)	2.552(7)	2.548(8)	2.539(6)	2.81365(2)	2.81599(2)	2.81823(2)
		3.023(12)	3.026(12)	3.044(12)	3.038(12)	3.032(11)	3.055(12)	3.048(12)	3.050(9)	3.066(11)	3.059(10)	3.082(9)	3.085(6)	3.088(9)	3.098(10)	3.113(7)	2.81365(2)	2.81599(2)	2.81823(2)
		2.562(10)	2.560(10)	2.554(10)	2.561(10)	2.569(9)	2.553(10)	2.562(10)	2.565(7)	2.555(9)	2.564(8)	2.549(8)	2.551(5)	2.552(7)	2.548(8)	2.539(6)	2.81365(2)	2.81599(2)	2.81823(2)
		3.023(12)	3.026(12)	3.044(12)	3.038(12)	3.032(11)	3.055(12)	3.048(12)	3.050(9)	3.066(11)	3.059(10)	3.082(9)	3.085(6)	3.088(9)	3.098(10)	3.113(7)	2.81365(2)	2.81599(2)	2.81823(2)
Fe/Nb – O bond length (Å)		1.904(8)	1.906(8)	1.911(8)	1.923(8)	1.922(9)	1.924(8)	1.920(8)	1.942(7)	1.940(8)	1.949(10)	1.952(10)	1.962(8)	1.965(12)	1.973(13)	1.976(13)	1.98955(2)	1.99120(2)	1.99279(2)
		2.031(8)	2.029(8)	2.031(8)	2.021(8)	2.024(9)	2.025(8)	2.031(8)	2.012(7)	2.017(8)	2.011(10)	2.011(10)	2.004(8)	2.005(12)	2.000(13)	1.999(13)	1.98955(2)	1.99120(2)	1.99279(2)
		1.9773(9)	1.9780(9)	1.9810(9)	1.9818(9)	1.9809(8)	1.9835(9)	1.9840(8)	1.9846(6)	1.9868(8)	1.9856(8)	1.9881(9)	1.9885(7)	1.9895(9)	1.9916(10)	1.9922(10)	1.98955(2)	1.99120(2)	1.99279(2)
		1.9773(9)	1.9780(9)	1.9810(9)	1.9818(9)	1.9809(8)	1.9835(9)	1.9840(8)	1.9846(6)	1.9868(8)	1.9856(8)	1.9881(9)	1.9885(7)	1.9895(9)	1.9916(10)	1.9922(10)	1.98955(2)	1.99120(2)	1.99279(2)
		1.9773(9)	1.9780(9)	1.9810(9)	1.9818(9)	1.9809(8)	1.9835(9)	1.9840(8)	1.9846(6)	1.9868(8)	1.9856(8)	1.9881(9)	1.9885(7)	1.9895(9)	1.9916(10)	1.9922(10)	1.98955(2)	1.99120(2)	1.99279(2)
		1.9773(9)	1.9780(9)	1.9810(9)	1.9818(9)	1.9809(8)	1.9835(9)	1.9840(8)	1.9846(6)	1.9868(8)	1.9856(8)	1.9881(9)	1.9885(7)	1.9895(9)	1.9916(10)	1.9922(10)	1.98955(2)	1.99120(2)	1.99279(2)
Fe/Nb – O – Fe/Nb bond angle (°)		180.000	180.000	180.000	180.000	180.000	180.000	180.000	180.000	180.000	180.000	180.000	180.000	180.000	180.000	180.000	180.000(0)	180.000(0)	180.000(0)
		168.8(5)	168.7(5)	168.9(5)	169.1(5)	170.4(5)	169.4(6)	170.0(5)	170.7(4)	170.0(6)	171.9(7)	171.2(6)	172.1(6)	172.4(8)	171.9(8)	172.7(9)			

Figure A2.19: *Rietveld refinements obtained from HT PND of $Bi_{0.5}Na_{0.5}Fe_{0.5}Nb_{0.5}O_3$ in the temperature range 323 K to 1023 K.*

Table A2.7: *Rietveld refinement parameters for RT XRD of $Bi_{0.5}Na_{0.5}Fe_{0.5}Ta_{0.5}O_3$, $Bi_{0.5}K_{0.5}Fe_{0.5}Ta_{0.5}O_3$.*

Parameter		$Bi_{0.5}A_{0.5}Fe_{0.5}B_{0.5}O_3$	
A, B		Na, Ta	K, Ta
Space Group		*P* 4*mm*	*P* 4*mm*
χ^2		7.956	5.773
wRp (%)		6.33	6.19
Rp (%)		3.94	3.81
a (Å)		3.93839(5)	3.99822(5)
b (Å)		3.93839(5)	3.99822(5)
c (Å)		3.93528(8)	3.99884(11)
Tetragonality		0.99921	1.00016
α (°)		90.000	90.000
β (°)		90.000	90.000
γ (°)		90.000	90.000
Cell vol. (Å^3)		61.0397(16)	63.9246(21)
Bi/A 1	x	0	0
	y	0	0
	z	0	0
	UISO*100	6.74(8)	11.83(21)
Fe/B 1	x	0.5	0.5
	y	0.5	0.5
	z	0.491(6)	0.473(4)
	UISO*100	0.16(6)	1.00*
O1	x	0.5	0.5
	y	0.5	0.5
	z	-0.031(36)	-0.041(22)
	UISO*100	1.00*	1.00*
O2	x	0.5	0.5
	y	0	0
	z	0.593(12)	0.500(9)
	UISO*100	1.00*	1.00*
Fe/B – O bond length (Å)		2.05(12)	2.06(7)
		1.88(12)	1.94(7)
		2.010(5)	2.0021(14)
		2.010(5)	2.0021(14)
		2.010(5)	2.0021(14)
		2.010(5)	2.0021(14)
Fe/B – O – Fe/B bond angle (°)		180.000(0)	180.000(0)
		157.0(15)	173.8(14)

Table A2.8: *Rietveld refinement parameters for LT XRD of $Bi_{0.5}Na_{0.5}Fe_{0.5}Ta_{0.5}O_3$.*

Parameter		$Bi_{0.5}Na_{0.5}Fe_{0.5}Ta_{0.5}O_3$															
Temperature (K)		12	30	50	70	90	110	130	150	170	190	210	230	250	270	290	298
Space Group		*P*4*mm*	*P*4*mm*	*P*4*mm*	*P*4*mm*	*P*4*mm*	*P*4*mm*	*P*4*mm*	*P*4*mm*	*P*4*mm*	*P*4*mm*	*P*4*mm*	*P*4*mm*	*P*4*mm*	*P*4*mm*	*P*4*mm*	*P*4*mm*
χ^2		2.654	1.330	1.314	1.361	1.296	1.334	1.334	1.319	1.295	1.337	1.296	1.324	1.250	1.294	1.457	1.283
wRp (%)		6.02	12.29	12.21	12.46	12.19	12.38	12.37	12.30	12.19	12.41	12.23	12.37	12.00	12.21	12.92	12.17
Rp (%)		4.36	9.20	9.16	9.36	9.09	9.35	9.27	9.22	9.19	9.36	9.20	9.40	8.88	9.13	9.70	9.33
a (Å)		3.927999(30)	3.92821(8)	3.92845(8)	3.92856(8)	3.92891(8)	3.92934(8)	3.92970(8)	3.93045(8)	3.93103(8)	3.93156(8)	3.93234(8)	3.93375(8)	3.93384(7)	3.93449(8)	3.93549(8)	3.93581(8)
b (Å)		3.927999(30)	3.92821(8)	3.92845(8)	3.92856(8)	3.92891(8)	3.92934(8)	3.92970(8)	3.93045(8)	3.93103(8)	3.93156(8)	3.93234(8)	3.93375(8)	3.93384(7)	3.93449(8)	3.93549(8)	3.93581(8)
c (Å)		3.92799(6)	3.92823(14)	3.92836(14)	3.92853(14)	3.92888(14)	3.92941(14)	3.92990(14)	3.93024(14)	3.93086(14)	3.93137(15)	3.93213(14)	3.93327(14)	3.93360(14)	3.93426(14)	3.93549(15)	3.93567(14)
α (°)		90	90	90	90	90	90	90	90	90	90	90	90	90	90	90	90
β (°)		90	90	90	90	90	90	90	90	90	90	90	90	90	90	90	90
γ (°)		90	90	90	90	90	90	90	90	90	90	90	90	90	90	90	90
Cell vol. (Å3)		60.6056(12)	60.6159(28)	60.6252(27)	60.6312(28)	60.6476(27)	60.6690(28)	60.6878(28)	60.7162(28)	60.7437(27)	60.7677(28)	60.8035(28)	60.8651(28)	60.8728(27)	60.9031(28)	60.9533(29)	60.9659(27)
Bi/Na 1	x	0	0	0	0	0	0	0	0	0	0	0	0	0	0	0	0
	y	0	0	0	0	0	0	0	0	0	0	0	0	0	0	0	0
	z	0	0	0	0	0	0	0	0	0	0	0	0	0	0	0	0
Fe/Ta 1	x	0.5	0.5	0.5	0.5	0.5	0.5	0.5	0.5	0.5	0.5	0.5	0.5	0.5	0.5	0.5	0.5
	y	0.5	0.5	0.5	0.5	0.5	0.5	0.5	0.5	0.5	0.5	0.5	0.5	0.5	0.5	0.5	0.5
	z	0.5537(7)	0.5537(7)	0.5537(7)	0.5537(7)	0.5537(7)	0.5537(7)	0.5537(7)	0.5537(7)	0.5537(7)	0.5537(7)	0.5537(7)	0.5537(7)	0.5537(7)	0.5537(7)	0.5537(7)	0.5537(7)
O1	x	0.5	0.5	0.5	0.5	0.5	0.5	0.5	0.5	0.5	0.5	0.5	0.5	0.5	0.5	0.5	0.5
	y	0.5	0.0	0.0	0.0	0.0	0.0	0.0	0.0	0.0	0.0	0.0	0.0	0.0	0.0	0.0	0.0
	z	0.0384(90)	0.0384(90)	0.0384(90)	0.0384(90)	0.0384(90)	0.0384(90)	0.0384(90)	0.0384(90)	0.0384(90)	0.0384(90)	0.0384(90)	0.0384(90)	0.0384(90)	0.0384(90)	0.0384(90)	0.0384(90)
O2	x	0.5	0.5	0.5	0.5	0.5	0.5	0.5	0.5	0.5	0.5	0.5	0.5	0.5	0.5	0.5	0.5
	y	0.0	0.0	0.0	0.0	0.0	0.0	0.0	0.0	0.0	0.0	0.0	0.0	0.0	0.0	0.0	0.0
	z	0.6591(29)	0.6591(29)	0.6591(29)	0.6591(29)	0.6591(29)	0.6591(29)	0.6591(29)	0.6591(29)	0.6591(29)	0.6591(29)	0.6591(29)	0.6591(29)	0.6591(29)	0.6591(29)	0.6591(29)	0.6591(29)
Ta/Fe – O bond length (Å)		2.02(4)	2.02(4)	2.02(4)	2.02(4)	2.02(4)	2.02(4)	2.02(4)	2.02(4)	2.02(4)	2.02(4)	2.02(4)	2.02(4)	2.02(4)	2.02(4)	2.02(4)	2.02(4)
		1.90(4)	1.90(4)	1.90(4)	1.90(4)	1.90(4)	1.90(4)	1.90(4)	1.90(4)	1.90(4)	1.90(4)	1.90(4)	1.90(4)	1.90(4)	1.90(4)	1.90(4)	1.90(4)
		2.0071(22)	2.0071(22)	2.0071(22)	2.0071(22)	2.0071(22)	2.0071(22)	2.0071(22)	2.0071(22)	2.0071(22)	2.0071(22)	2.0071(22)	2.0071(22)	2.0071(22)	2.0071(22)	2.0071(22)	2.0071(22)
		2.0071(22)	2.0071(22)	2.0071(22)	2.0071(22)	2.0071(22)	2.0071(22)	2.0071(22)	2.0071(22)	2.0071(22)	2.0071(22)	2.0071(22)	2.0071(22)	2.0071(22)	2.0071(22)	2.0071(22)	2.0071(22)
		2.0071(22)	2.0071(22)	2.0071(22)	2.0071(22)	2.0071(22)	2.0071(22)	2.0071(22)	2.0071(22)	2.0071(22)	2.0071(22)	2.0071(22)	2.0071(22)	2.0071(22)	2.0071(22)	2.0071(22)	2.0071(22)
		2.0071(22)	2.0071(22)	2.0071(22)	2.0071(22)	2.0071(22)	2.0071(22)	2.0071(22)	2.0071(22)	2.0071(22)	2.0071(22)	2.0071(22)	2.0071(22)	2.0071(22)	2.0071(22)	2.0071(22)	2.0071(22)
Ta/Fe – O – Ta/Fe bond angle (o)		180.000	180.000	180.000	180.000	180.000	180.000	180.000	180.000	180.000	180.000	180.000	180.000	180.000	180.000	180.000	180.000
		156.2(6)	156.2(6)	156.2(6)	156.2(6)	156.2(6)	156.2(6)	156.2(6)	156.2(6)	156.2(6)	156.2(6)	156.2(6)	156.2(6)	156.2(6)	156.2(6)	156.2(6)	156.2(6)

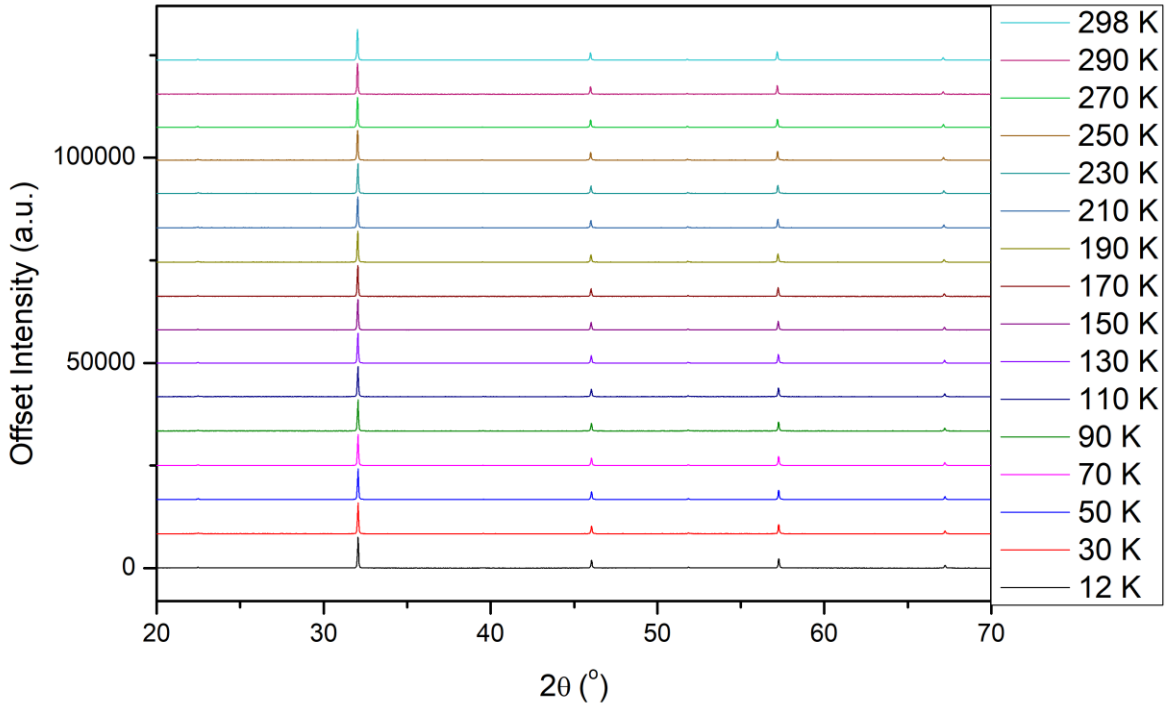

Figure A2.20: *All patterns for the LT PXRD of $Bi_{0.5}Na_{0.5}Fe_{0.5}Ta_{0.5}O_3$. 12 K pattern intensity has been scaled down to match the intensities of the other temperature points that were taken with shorter scan times.*

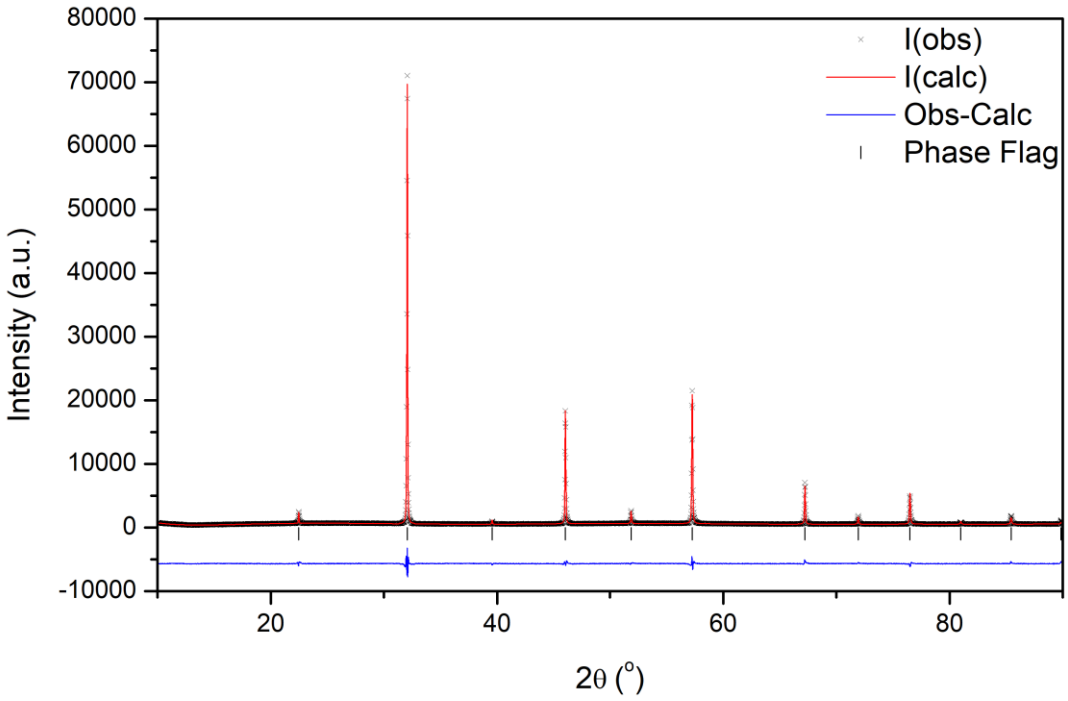

Figure A2.21: *Rietveld refinement obtained from LT PXRD of $Bi_{0.5}Na_{0.5}Fe_{0.5}Ta_{0.5}O_3$ at 12 K; χ^2 = 2.654, R_{wp} = 6.02% and R_p = 4.36; the black crosses represent the observed intensity, the red line represents the calculated intensity from the model, the blue line represents the difference between the observed pattern and calculated pattern and the black tick marker represents the P4mm model.*

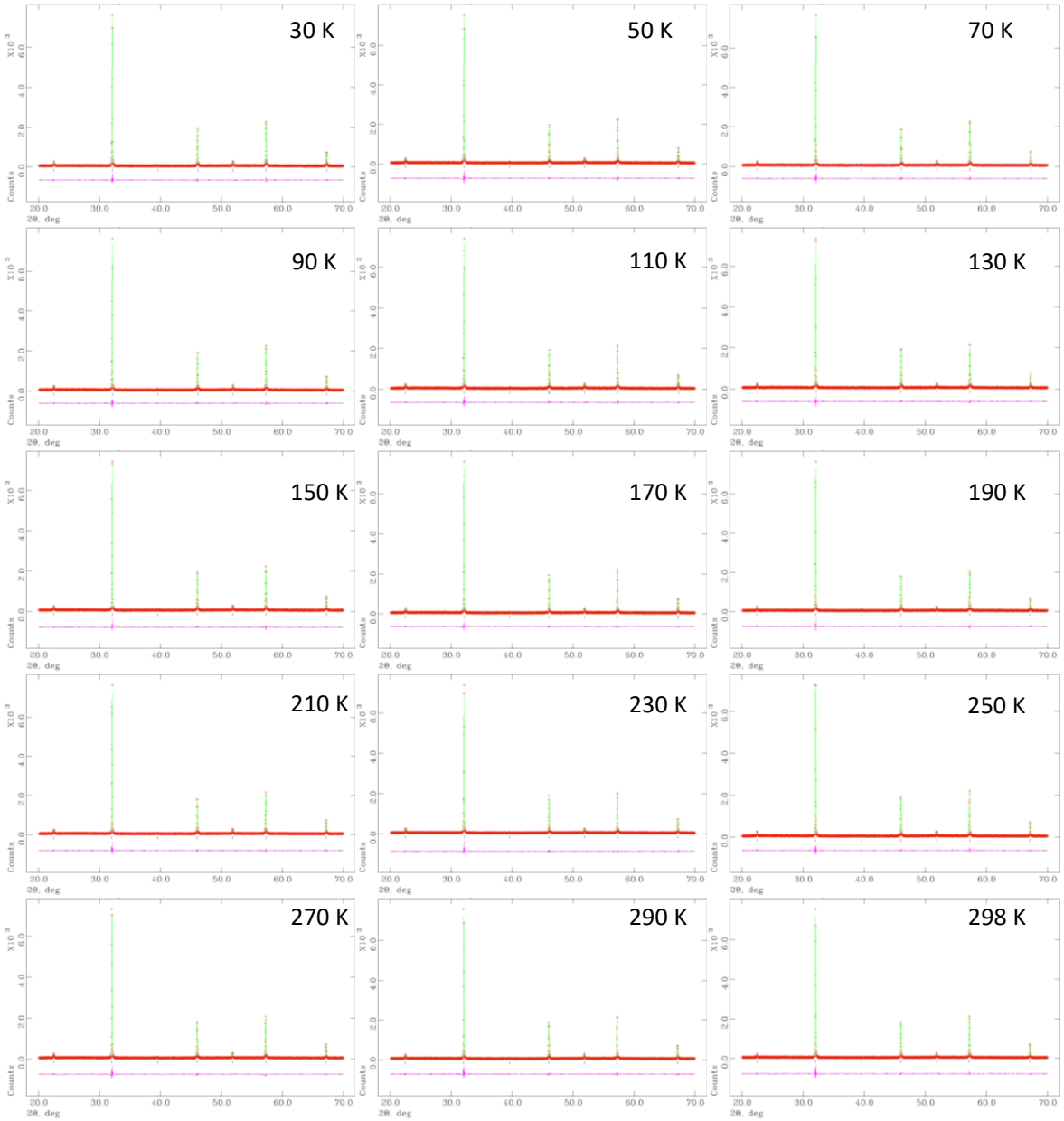

Figure A2.22: *Rietveld refinements obtained from LT PXRD of $Bi_{0.5}Na_{0.5}Fe_{0.5}Ta_{0.5}O_3$ in the temperature range 30 K to 298 K.*

Appendix 3 for Chapter Five: Investigation of the $BiFeO_3$-$NaNbO_3$ Phase Diagram

***Table A3.1**: Rietveld refinement parameters for RT PXRD of all $Bi_{1-x}Na_xFe_{1-x}Nb_xO_3$ samples.*

Parameter		x in $Bi_{1-x}Na_xFe_{1-x}Nb_xO_3$ materials																											
x		0.05	0.075	0.10	0.125		0.15		0.175	0.20	0.25	0.30	0.35	0.40	0.50	0.60	0.65	0.675	0.70	0.75	0.80	0.85		0.90		0.95	
Space Group		*R 3c*	*R 3c*	*R 3c*	*R 3c*	*P 4mm*	*R 3c*	*P 4mm*	*P 4mm*	*P 4mm*	*P 4mm*	*P 4mm*	*P 4mm*	*P 4mm*	*P 4mm*	*P 4mm*	*P 4mm*	*P 2$_1$ma*	*P 2$_1$ma*	*P 2$_1$ma*	*P 2$_1$ma*	*P 2$_1$ma*	*Pbcm*	*P 2$_1$ma*	*Pbcm*	*P 2$_1$ma*	*Pbcm*
χ^2		8.705	9.395	8.179	9.009		13.19		2.726	4.47	2.741	3.916	5.096	7.399	3.415	2.974	3.13	2.776	2.216	3.219	7.168	2.884		4.203		8.418	
wRp (%)		6.69	7.38	4.59	6.68		6.10		4.57	3.48	4.57	3.53	3.83	4.49	4.14	4.93	4.86	5.26	4.53	4.71	5.39	3.34		5.91		6.51	
Rp (%)		4.28	4.68	2.98	4.58		3.74		3.37	2.51	3.21	2.44	2.43	2.67	2.69	3.44	3.35	3.78	3.40	3.36	3.43	2.49		4.28		4.29	
a (Å)		5.57849(10)	5.57882(10)	5.58341(12)	5.57889(21)	3.95407(35)	5.60356(27)	3.95400(34)	3.95291(4)	3.95481(4)	3.95349(4)	3.95139(4)	3.949502(28)	3.94674(4)	3.941397(31)	3.936143(33)	3.93344(4)	5.55087(8)	5.55097(10)	5.54914(10)	5.53526(9)	5.53771(12)	5.51778(21)	5.5285(5)	5.5154(6)	5.52893(15)	5.51614(20)
b (Å)		5.57849(10)	5.57882(10)	5.58341(12)	5.57889(21)	3.95407(35)	5.60356(27)	3.95400(34)	3.95291(4)	3.95481(4)	3.95349(4)	3.95139(4)	3.949502(28)	3.94674(4)	3.941397(31)	3.936143(33)	3.93344(4)	7.87592(9)	7.87110(9)	7.86627(10)	7.85555(9)	7.84588(9)	5.54795(28)	7.82935(10)	5.5472(6)	7.81364(13)	5.55629(15)
c (Å)		13.85166(26)	13.84419(27)	13.8171(4)	13.7890(7)	3.9520(7)	13.6613(16)	3.9534(7)	3.95484(4)	3.95272(7)	3.95514(8)	3.95266(11)	3.94921(5)	3.94833(6)	3.94221(8)	3.93356(5)	3.93021(5)	5.55555(13)	5.54548(10)	5.54049(9)	5.54335(9)	5.53169(13)	15.6762(6)	5.5287(5)	15.5557(8)	5.53427(15)	15.5832(4)
α (°)		90	90	90	90	90	90	90	90	90	90	90	90	90	90	90	90	90	90	90	90	90	90	90	90	90	90	90
β (°)		90	90	90	90	90	90	90	90	90	90	90	90	90	90	90	90	90	90	90	90	90	90	90	90	90	90	90
γ (°)		120	120	120	120	90	120	90	90	90	90	90	90	90	90	90	90	90	90	90	90	90	90	90	90	90	90	90
Cell vol. (Å^3)		373.049(13)	373.150(12)	373.033(15)	371.672(27)	61.789(13)	371.66(5)	61.808(13)	61.7966(11)	61.8226(13)	61.8189(15)	61.7147(19)	61.6020(10)	61.5022(13)	61.2407(15)	60.9435(10)	60.8082(12)	242.879(7)	242.294(7)	241.848(7)	241.039(6)	240.342(8)	479.88(4)	239.307(33)	475.93(8)	239.086(10)	477.615(26)
Phase Ratio a:b		N/A	N/A	N/A	0.275	0.725	0.183	0.817	N/A	N/A	N/A	N/A	N/A	N/A	N/A	N/A	N/A	N/A	N/A	N/A	N/A	0.782	0.218	0.956	0.044	0.743	0.257
Bi/Na 1	x	0	0	0	0	0	0	0	0	0	0	0	0	0	0	0	0	0.2643(16)	0.2717(12)	0.2768(12)	0.2720(14)	0.2700(24)	0.2255(26)	0.2758(17)	0.172(6)	0.2744(23)	0.2524(71)
	y	0	0	0	0	0	0	0	0	0	0	0	0	0	0	0	0	0	0	0	0	0	0.25	0	0.25	0	0.25
	z	0	0	0	0	0	0	0	0	0	0	0	0	0	0	0	0	0.7528(16)	0.7602(12)	0.7653(12)	0.7605(14)	0.7585(24)	0	0.7643(17)	0	0.7629(23)	0
	UISO*100	0.50(8)	0.68(9)	5.26(19)	1.00*	1.00*	1.00*	1.00*	5.27(7)	7.58(9)	6.23(9)	8.02(11)	7.20(7)	7.30(9)	5.26(19)	5.68(4)	5.63(11)	5.4(5)	4.67(34)	4.75(27)	3.19(35)	3.6(6)	3.0(5)	3.25(30)	3.31(30)	1.3(7)	4.0(6)
Bi/Na 2	x	N/A	N/A	N/A	N/A	N/A	N/A	N/A	N/A	N/A	N/A	N/A	N/A	N/A	N/A	N/A	N/A	0.2882(14)	0.2949(12)	0.2953(11)	0.2931(13)	0.2981(16)	0.2696(21)	0.2958(19)	0.263(6)	0.2950(22)	0.2465(25)
	y	N/A	N/A	N/A	N/A	N/A	N/A	N/A	N/A	N/A	N/A	N/A	N/A	N/A	N/A	N/A	N/A	0.5	0.5	0.5	0.5	0.5	0.2643(21)	0.5	0.257(6)	0.5	0.2412(25)
	z	N/A	N/A	N/A	N/A	N/A	N/A	N/A	N/A	N/A	N/A	N/A	N/A	N/A	N/A	N/A	N/A	0.7294(14)	0.7361(12)	0.7365(11)	0.7343(13)	0.7393(16)	0.25	0.7370(19)	0.25	0.7362(22)	0.25
	UISO*100	N/A	N/A	N/A	N/A	N/A	N/A	N/A	N/A	N/A	N/A	N/A	N/A	N/A	N/A	N/A	N/A	4.9(5)	4.54(36)	4.36(32)	4.76(44)	3.2(7)	6.3(7)	3.69(35)	3.30(30)	0.6(7)	5.0(7)
Fe/Nb 1	x	0	0	0	0	0.5	0	0.5	0.5	0.5	0.5	0.5	0.5	0.5	0.5	0.5	0.5	0.2638(9)	0.2650(6)	0.2637(5)	0.2644(7)	0.2636(8)	0.2531(4)	0.2642(5)	0.2548(10)	0.2632(9)	0.25454(22)
	y	0	0	0	0	0.5	0	0.5	0.5	0.5	0.5	0.5	0.5	0.5	0.5	0.5	0.5	0.2513(9)	0.2525(6)	0.2512(5)	0.2519(7)	0.2511(8)	0.7322(4)	0.2517(5)	0.7339(10)	0.2507(9)	0.73364(22)
	z	0.22168(33)	0.2233(4)	0.22591(23)	0.2328(6)	0.4898	0.2322(8)	0.4898	0.5112(28)	0.5115(25)	0.5108(34)	0.491(6)	0.5034(34)	0.5069(15)	0.5421(16)	0.4858(14)	0.4767(18)	0.2479(9)	0.2491(6)	0.2478(5)	0.2485(7)	0.2477(8)	0.1256(4)	0.2483(5)	0.1273(10)	0.2473(9)	0.12704(22)
	UISO*100	0.01(16)	0.03(17)	0.96(12)	1.00*	1.00*	1.00*	1.00*	0.52(9)	1.04(8)	0.86(8)	0.81(10)	0.88(6)	1.58(7)	0.96(12)	0.086(30)	0.71(6)	1.491(33)	0.70(5)	0.96(5)	0.44(5)	0.91(5)	0.90(5)	1.829(23)	1.00*	1.173(29)	0.070(35)
O1	x	0.440(4)	0.432(4)	0.4403(25)	0.442(5)	0.5	0.442	0.5	0.5	0.5	0.5	0.5	0.5	0.5	0.5	0.5	0.5	0.211(6)	0.366(6)	0.3563(62)	0.323(5)	0.247(6)	0.612(8)	0.325(5)	0.663(19)	0.298(10)	0.688(8)
	y	0.0136(34)	-0.002(4)	0.0068(24)	0.041(6)	0.5	0.041	0.5	0.5	0.5	0.5	0.5	0.5	0.5	0.5	0.5	0.5	0	0	0	0	0	0.25	0	0.25	0	0.25
	z	0.9553(12)	0.9625(12)	0.9632(9)	0.9689(23)	0.0216	0.9689	0.0216	0.0579(43)	0.0346(91)	0.057(12)	0.014(25)	0.0345(144)	-0.0264(69)	0.054(20)	-0.0175(70)	-0.0234(107)	0.224(11)	0.289(6)	0.283(5)	0.276(9)	0.225(9)	0	0.259(9)	0	0.244(11)	0
	UISO*100	1.00*	1.00*	1.00*	1.00*	1.00*	1.00*	1.00*	1.00*	1.00*	1.00*	1.00*	1.00*	1.00*	1.00*	1.00*	1.00*	1.00*	1.00*	1.00*	1.00*	1.00*	1.00*	1.00*	1.00*	1.00*	1.00*
O2	x	N/A	N/A	N/A	N/A	0.5	N/A	0.5	0.5	0.5	0.5	0.5	0.5	0.5	0.5	0.5	0.5	0.223(6)	0.370(6)	0.4280(57)	0.300(5)	0.218(6)	0.232(9)	0.309(6)	0.146(21)	0.291(10)	0.237(11)
	y	N/A	N/A	N/A	N/A	0	N/A	0	0	0	0	0	0	0	0	0	0	0.5	0.5	0.5	0.5	0.5	0.677(9)	0.5	0.768(24)	0.5	0.7067(40)
	z	N/A	N/A	N/A	N/A	0.5132	N/A	0.5132	0.5735(24)	0.6189(24)	0.591(4)	0.646(7)	0.6091(27)	0.6008(17)	0.553(10)	0.5742(28)	0.5908(35)	0.217(11)	0.297(5)	0.363(5)	0.272(8)	0.297(8)	0.25	0.261(9)	0.25	0.288(9)	0.25
	UISO*100	N/A	N/A	N/A	N/A	1.00*	N/A	1.00*	1.00*	1.00*	1.00*	1.00*	1.00*	1.00*	1.00*	1.00*	1.00*	1.00*	1.00*	1.00*	1.00*	1.00*	1.00*	1.00*	1.00*	1.00*	1.00*
O3	x	N/A	N/A	N/A	N/A	N/A	N/A	N/A	N/A	N/A	N/A	N/A	N/A	N/A	N/A	N/A	N/A	0.073(4)	0.020(5)	0.0134(43)	-0.049(4)	-0.008(5)	0.452(5)	0.018(5)	0.4743	-0.060(7)	0.497(4)
	y	N/A	N/A	N/A	N/A	N/A	N/A	N/A	N/A	N/A	N/A	N/A	N/A	N/A	N/A	N/A	N/A	0.2413(41)	0.2331(32)	0.2283(25)	0.2290(26)	0.220(4)	0.414(6)	0.2147(16)	0.4653	0.232(4)	0.4531(27)
	z	N/A	N/A	N/A	N/A	N/A	N/A	N/A	N/A	N/A	N/A	N/A	N/A	N/A	N/A	N/A	N/A	0.564(5)	0.501(7)	0.502(8)	0.434(6)	0.475(6)	0.1320(27)	0.510(9)	0.1279(55)	0.446(5)	0.1479(17)
	UISO*100	N/A	N/A	N/A	N/A	N/A	N/A	N/A	N/A	N/A	N/A	N/A	N/A	N/A	N/A	N/A	N/A	1.00*	1.00*	1.00*	1.00*	1.00*	1.00*	1.00*	1.00*	1.00*	1.00*
O4	x	N/A	N/A	N/A	N/A	N/A	N/A	N/A	N/A	N/A	N/A	N/A	N/A	N/A	N/A	N/A	N/A	0.025(5)	-0.028(4)	-0.0195(28)	0.021(4)	0.059(5)	-0.007(10)	-0.045(8)	0.039(15)	0.022(6)	0.042(4)
	y	N/A	N/A	N/A	N/A	N/A	N/A	N/A	N/A	N/A	N/A	N/A	N/A	N/A	N/A	N/A	N/A	0.2660(31)	0.2547(35)	0.2584(26)	0.2737(32)	0.272(4)	-0.021(7)	0.2622(25)	0.033(14)	0.273(4)	0.0059(37)
	z	N/A	N/A	N/A	N/A	N/A	N/A	N/A	N/A	N/A	N/A	N/A	N/A	N/A	N/A	N/A	N/A	-0.024(10)	0.043(5)	0.029(7)	-0.008(6)	-0.055(7)	0.1203(28)	0.054(7)	0.1058(35)	0.036	0.1063(18)
	UISO*100	N/A	N/A	N/A	N/A	N/A	N/A	N/A	N/A	N/A	N/A	N/A	N/A	N/A	N/A	N/A	N/A	1.00*	1.00*	1.00*	1.00*	1.00*	1.00*	1.00*	1.00*	1.00*	1.00*
Nb/Fe – O bond length (Å)		2.106(21)	2.114(20)	2.092(15)	2.093(35)	1.85035(31)	2.100(5)	1.85098(31)	1.793(23)	1.885(33)	1.79(4)	1.89(8)	1.85(5)	1.843(25)	1.93(8)	1.980(24)	1.97(4)	2.00458(2)	2.077(11)	2.051(10)	2.011(7)	1.976(7)	2.107(15)	2.000(7)	2.033(27)	1.968(8)	2.007(7)
		2.106(21)	2.114(20)	2.092(15)	2.093(35)	2.1017(4)	2.100(5)	2.1024(4)	2.162(23)	2.068(33)	2.16(4)	2.07(8)	2.10(5)	2.106(25)	2.02(8)	1.954(24)	1.96(4)	1.97921(2)	2.051(11)	2.250(14)	1.963(6)	1.988(9)	1.977(10)	1.961(6)	2.01(4)	1.967(9)	1.924(5)
		2.106(21)	2.114(20)	2.092(15)	2.093(35)	1.97920(17)	2.100(5)	1.97916(17)	1.9917(20)	2.0224(28)	2.0022(35)	2.069(8)	2.018(4)	2.0079(16)	1.9712(8)	1.9986(19)	2.0172(25)	2.05062(3)	1.96(4)	1.985(35)	2.026(28)	1.976(31)	2.080(32)	2.01(5)	1.9200(11)	2.10(4)	2.080(18)
		1.952(19)	1.924(19)	1.945(14)	1.995(35)	1.97920(17)	1.987(7)	1.97916(17)	1.9917(20)	2.0224(28)	2.0022(35)	2.069(8)	2.018(4)	2.0079(16)	1.9712(8)	1.9986(19)	2.0172(25)	2.01219(2)	1.987(33)	1.969(34)	2.047(33)	2.002(31)	1.919(30)	1.96(5)	1.970(8)	1.964(34)	1.863(20)
		1.952(19)	1.924(19)	1.945(14)	1.995(35)	1.97920(17)	1.987(7)	1.97916(17)	1.9917(20)	2.0224(28)	2.0022(35)	2.069(8)	2.018(4)	2.0079(16)	1.9712(8)	1.9986(19)	2.0172(25)	2.01414(3)	1.989(29)	1.987(29)	1.97(4)	2.03(4)	1.99(5)	2.02(5)	2.0753(13)	1.782(25)	1.941(22)
		1.952(19)	1.924(19)	1.945(14)	1.995(35)	1.97920(17)	1.987(7)	1.97916(17)	1.9917(20)	2.0224(28)	2.0022(35)	2.069(8)	2.018(4)	2.0079(16)	1.9712(8)	1.9986(19)	2.0172(25)	1.91225(2)	1.984(30)	1.949(33)	1.956(35)	1.961(33)	1.95(5)	1.98(5)	1.994(10)	2.129(23)	2.093(23)
Nb/Fe – O – Nb/Fe bond angle (o)		155.1(7)	157.8(8)	157.8(4)	150.8(8)	180.000(0) 174.644(1)	150.91(24)	180.000(0) 174.642(1)	180.000(0) 165.8(9)	180.000(0) 155.8(7)	180.000(0) 161.7(12)	180.000(0) 145.5(15)	180.000(0) 156.1(11)	180.000(0) 158.7(5)	180.000(0) 177.5(21)	180.000(0) 160.0(6)	180.000(0) 154.3(6)	161.617(0) 163.660(0) 152.174(0) 169.479(0)	146.2(18) 143.6(18) 171.0(15) 160.5(10)	148.9(16) 120.8(12) 169.5(11) 165.5(15)	159.4(16) 166.4(20) 149.4(14) 169.4(17)	171.0(27) 158.3(21) 162.5(21) 155.4(19)	138.6(22) 161.0(31) 153.0(16) 174.6(27)	160.4(17) 164.9(20) 162.9(8) 153.9(12)	154.(6) 143.(6) 169.6(4) 152.0(4)	168.6(31) 164.1(29) 150.5(17) 168.0(17)	161.8(25) 169.3(24) 159.5(16) 156.5(15)

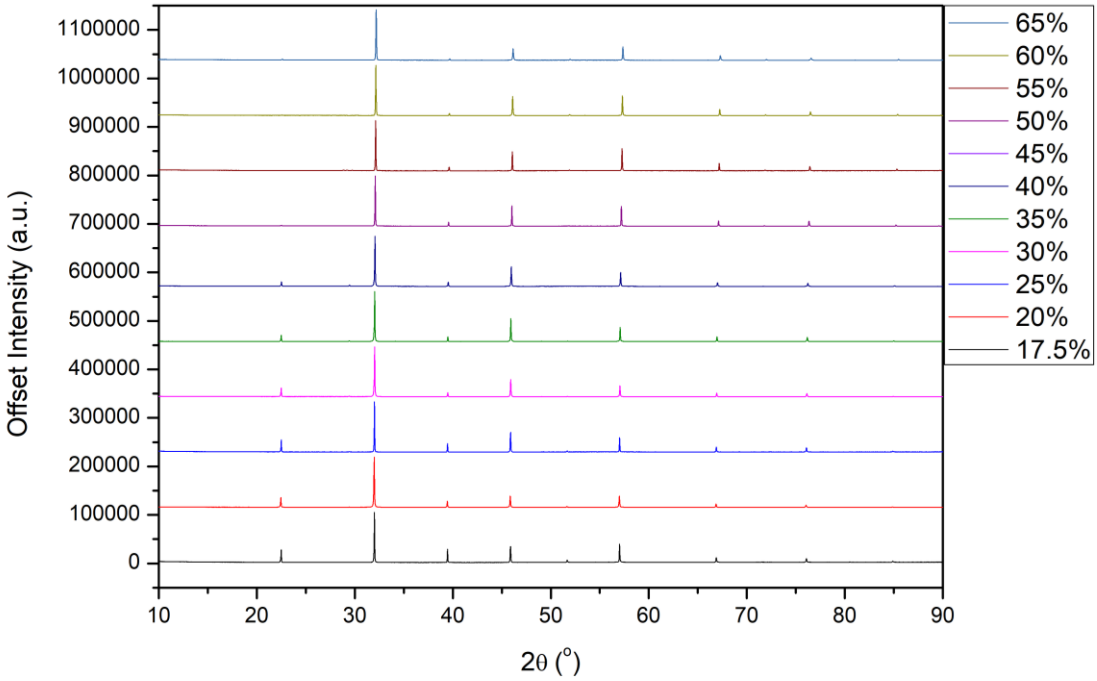

Figure A3.1: *All room temperature PXD patterns from $Bi_{0.825}Na_{0.175}Fe_{0.825}Nb_{0.175}O_3$ to $Bi_{0.35}Na_{0.65}Fe_{0.35}Nb_{0.65}O_3$. Patterns were scaled to match intensity and offset for clarity.*

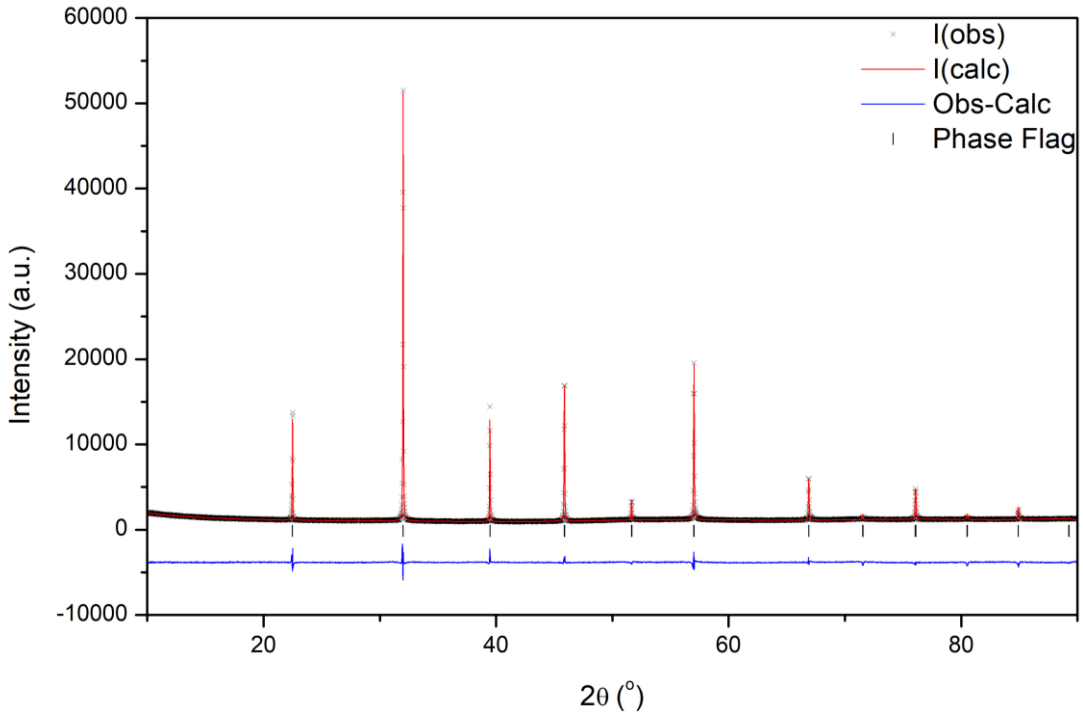

Figure A3.2: *Rietveld refinement of room temperature PXRD data collected for $Bi_{0.825}Na_{0.175}Fe_{0.825}Nb_{0.175}O_3$; χ^2 = 2.726, Rwp = 4.57% and Rp = 3.37; the black crosses represent the observed intensity, the red line represents the calculated intensity from the model, the blue line represents the difference between the observed pattern and calculated pattern and the black tick marker represents the P4mm model.*

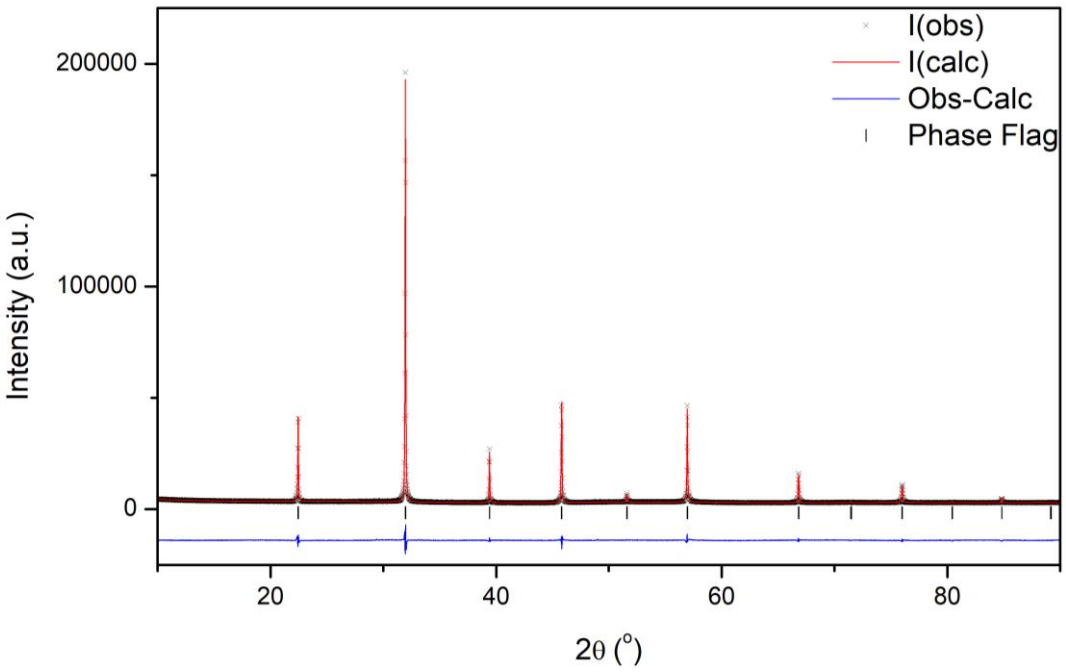

Figure A3.3: *Rietveld refinement of room temperature PXRD data collected for $Bi_{0.8}Na_{0.2}Fe_{0.8}Nb_{0.2}O_3$; χ^2 = 4.47, Rwp = 3.48% and Rp = 2.51; the black crosses represent the observed intensity, the red line represents the calculated intensity from the model, the blue line represents the difference between the observed pattern and calculated pattern and the black tick marker represents the P4mm model.*

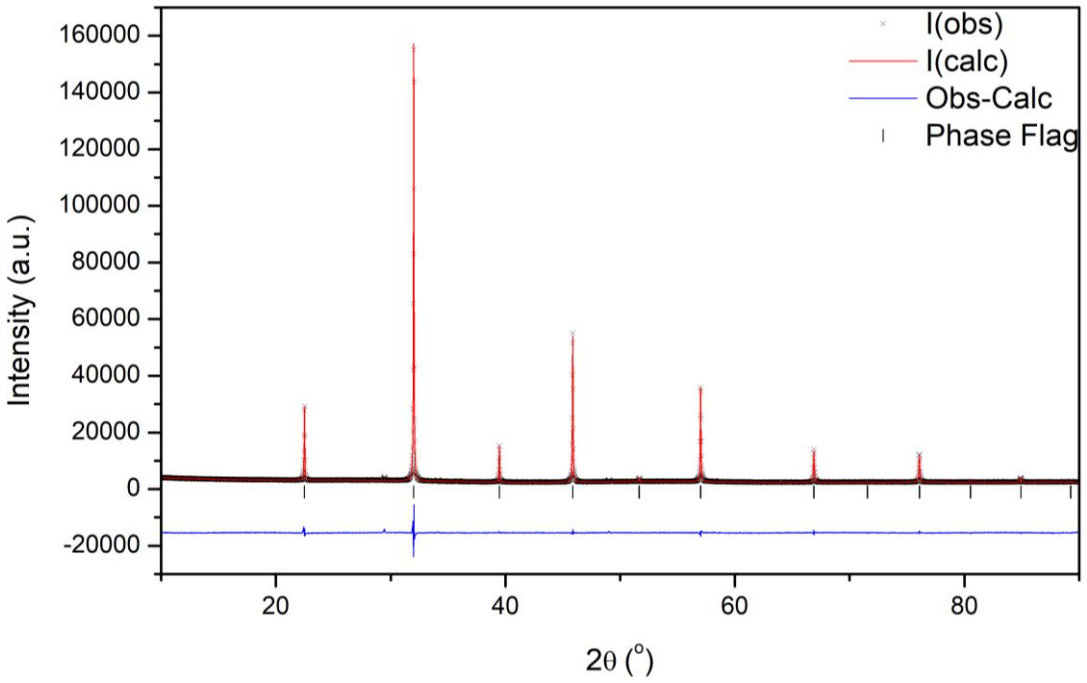

Figure A3.4: *Rietveld refinement of room temperature PXRD data collected for $Bi_{0.7}Na_{0.3}Fe_{0.7}Nb_{0.3}O_3$; χ^2 = 3.916, Rwp = 3.53% and Rp = 2.44; the black crosses represent the observed intensity, the red line represents the calculated intensity from the model, the blue line represents the difference between the observed pattern and calculated pattern and the black tick marker represents the P4mm model.*

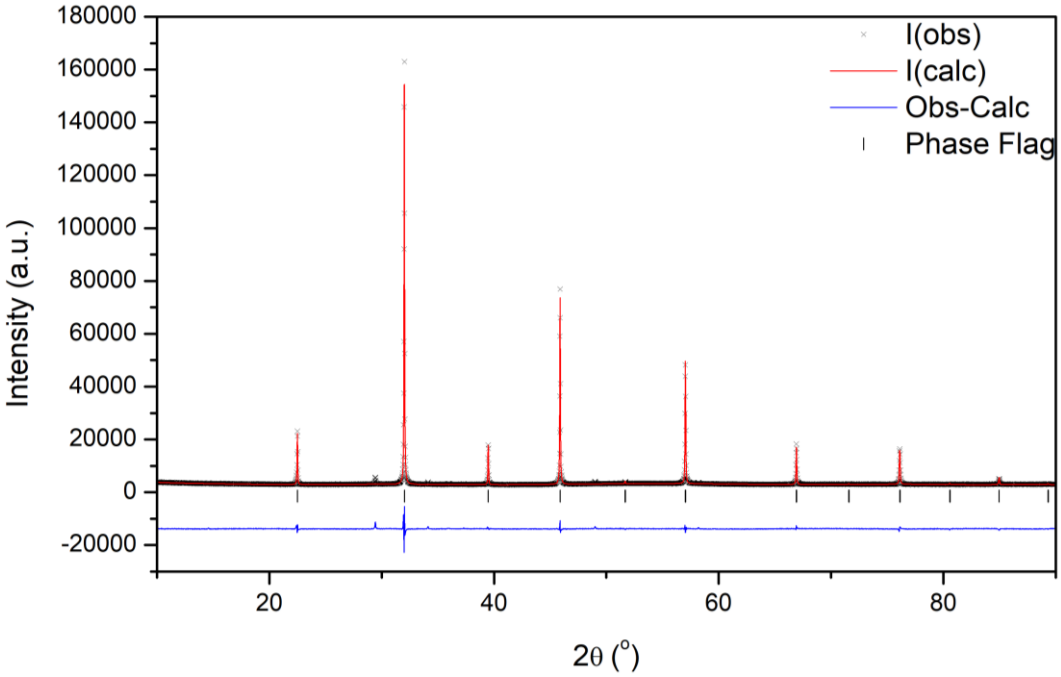

Figure A3.5: *Rietveld refinement of room temperature PXRD data collected for $Bi_{0.65}Na_{0.35}Fe_{0.65}Nb_{0.35}O_3$; $\chi^2 = 5.096$, $R_{wp} = 3.83\%$ and $R_p = 2.43$; the black crosses represent the observed intensity, the red line represents the calculated intensity from the model, the blue line represents the difference between the observed pattern and calculated pattern and the black tick marker represents the P4mm model.*

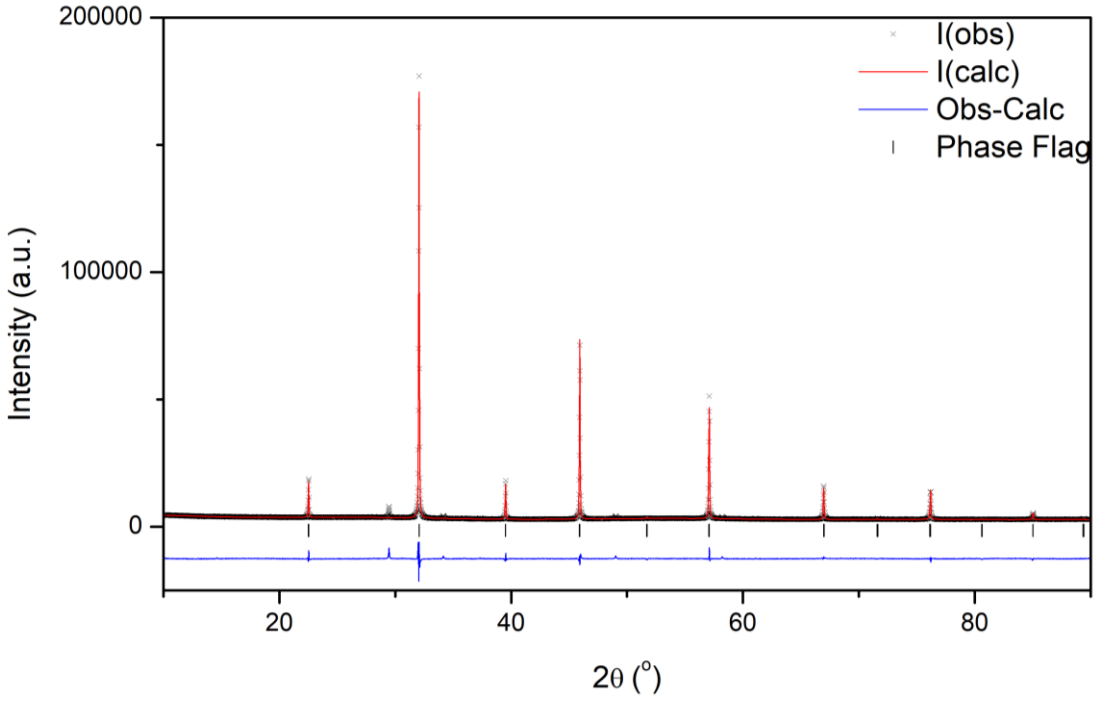

Figure A3.6: *Rietveld refinement of room temperature PXRD data collected for $Bi_{0.6}Na_{0.4}Fe_{0.6}Nb_{0.4}O_3$; $\chi^2 = 7.399$, Rwp = 4.49% and Rp = 2.67; the black crosses represent the observed intensity, the red line represents the calculated intensity from the model, the blue line represents the difference between the observed pattern and calculated pattern and the black tick marker represents the P4mm model.*

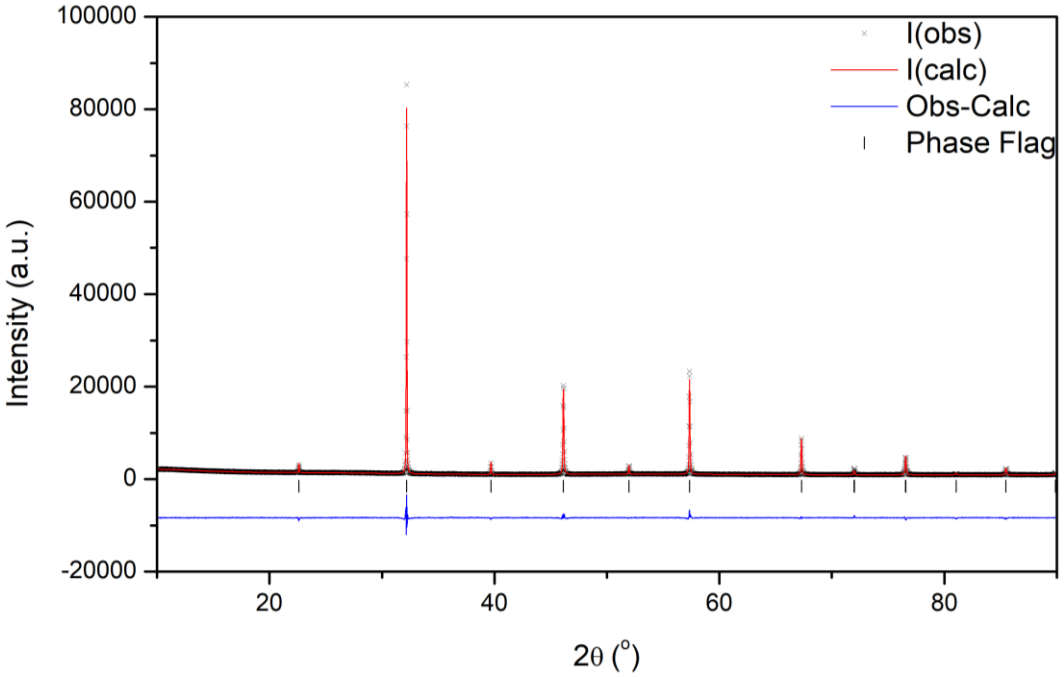

Figure A3.7: *Rietveld refinement of room temperature PXRD data collected for $Bi_{0.35}Na_{0.65}Fe_{0.35}Nb_{0.65}O_3$; $\chi^2 = 3.13$, Rwp = 4.86% and Rp = 3.35; the black crosses represent the observed intensity, the red line represents the calculated intensity from the model, the blue line represents the difference between the observed pattern and calculated pattern and the black tick marker represents the P4mm model.*

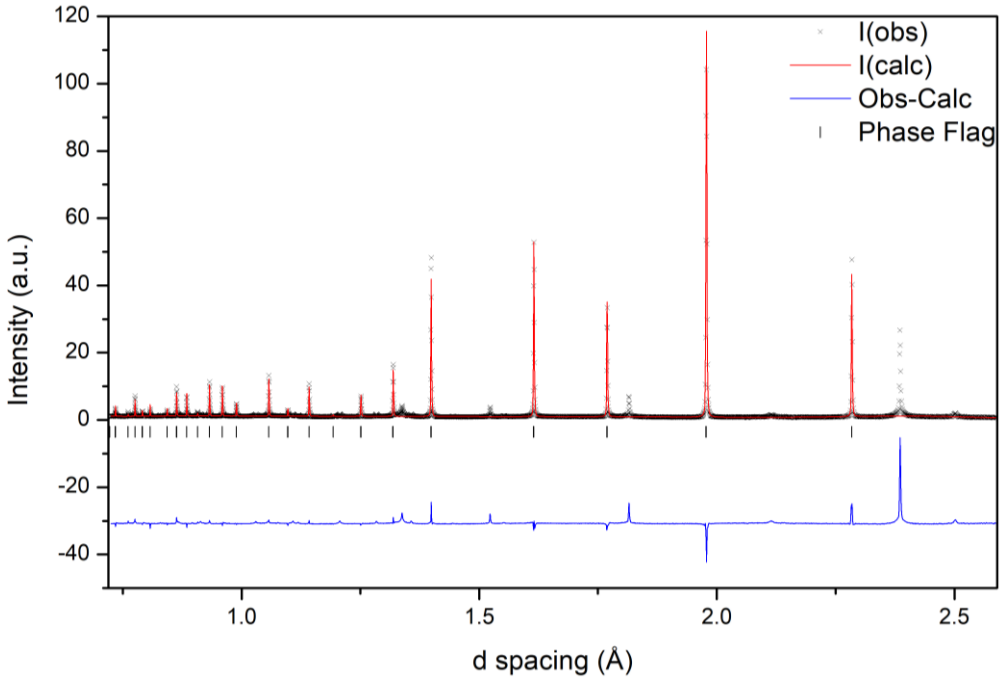

Figure A3.8: *Rietveld refinement of room temperature PND data collected for $Bi_{0.825}Na_{0.175}Fe_{0.825}Nb_{0.175}O_3$; $\chi^2 = 43.13$, Rwp = 15.46% and Rp = 13.19; the black crosses represent the observed intensity, the red line represents the calculated intensity from the model, the blue line represents the difference between the observed pattern and calculated pattern and the black tick marker represents the P4mm model.*

Table A3.2: *Rietveld refinement parameters for RT PND of $Bi_{1-x}Na_xFe_{1-x}Nb_xO_3$ samples.*

Parameter		x in $Bi_{1-x}Na_xFe_{1-x}Nb_xO_3$ materials											
x		0.075	0.175	0.25	0.40	0.50	0.60	0.70	0.75	0.85		0.90	
Space Group		*R 3c*	*P 4mm*	*P 4mm*	*P 4mm*	*P 4mm*	*P 4mm*	*P 2_1ma*	*P 2_1ma*	*P 2_1ma*	*Pbcm*	*P 2_1ma*	*Pbcm*
χ^2		21.92	43.13	24.64	10.82	13.47	17.41	20.56	14.18	15.96		12.49	
wRp (%)		12.36	15.46	12.72	9.78	9.67	11.56	12.17	10.37	10.14		10.38	
Rp (%)		13.48	13.19	10.80	8.14	8.21	9.24	10.42	8.76	9.10		8.60	
a (Å)		5.58142(14)	3.95586(7)	3.95540(6)	3.94971(7)	3.94282(6)	3.93768(6)	5.55178(11)	5.55079(14)	5.53953(14)	5.53603(23)	5.53163(16)	5.5161(9)
b (Å)		5.58142(14)	3.95586(7)	3.95540(6)	3.94971(7)	3.94282(6)	3.93768(6)	7.87235(9)	7.86896(18)	7.84475(19)	5.53578(29)	7.83193(23)	5.5633(8)
c (Å)		13.8489(4)	3.95406(11)	3.95383(10)	3.94825(10)	3.94174(10)	3.93551(7)	5.54563(12)	5.54234(16)	5.52825(16)	15.6677(4)	5.53124(24)	15.5579(18)
Tetragonality		N/A	0.99954	0.99960	0.99963	0.99973	0.99945	0.99889	0.99848	N/A	N/A	N/A	N/A
α (°)		90	90	90	90	90	90	90	90	90	90	90	90
β (°)		90	90	90	90	90	90	90	90	90	90	90	90
γ (°)		120	90	90	90	90	90	90	90	90	90	90	90
Cell vol. (Å^3)		373.624(17)	61.8765(23)	61.8584(20)	61.5937(23)	61.2777(20)	61.0214(16)	242.375(8)	242.084(11)	240.237(11)	480.156(35)	239.632(14)	477.44(12)
Phase Ratio a:b		N/A	N/A	N/A	N/A	N/A	N/A	N/A	N/A	0.928	0.072	0.957	0.043
Bi/Na 1	x	0	0	0	0	0	0	0.240(5)	0.2639(23)	0.233(5)	0.26(4)	0.2726(29)	0.270(10)
	y	0	0	0	0	0	0	0	0	0	0.25	0	0.25
	z	0	0	0	0	0	0	0.756(7)	0.7524(23)	0.747(4)	0	0.7611(29)	0
	U_{iso} *100	1.45(6)	7.50(28)	7.37(26)	6.79(14)	6.62(20)	5.67(11)	5.1(10)	3.38(29)	3.4(8)	7.9(28)	1.81(27)	2.1(11)
Bi/Na 2	x	N/A	N/A	N/A	N/A	N/A	N/A	0.233(5)	0.2814(29)	0.252(5)	0.23(4)	0.2777(39)	0.243(6)
	y	N/A	N/A	N/A	N/A	N/A	N/A	0.5	0.5	0.5	0.257(14)	0.5	0.237(6)
	z	N/A	N/A	N/A	N/A	N/A	N/A	0.755(6)	0.7226(29)	0.730(4)	0.25	0.7190(39)	0.25
	U_{iso} *100	N/A	N/A	N/A	N/A	N/A	N/A	4.5(10)	5.06(44)	2.5(7)	4.2(19)	3.86(41)	10.0(29)
Fe/Nb 1	x	0	0.5	0.5	0.5	0.5	0.5	0.2395(23)	0.2631(11)	0.2391(28)	0.247(7)	0.2641(17)	0.2630(9)
	y	0	0.5	0.5	0.5	0.5	0.5	0.2497(18)	0.2506(11)	0.2495(21)	0.739(4)	0.2516(17)	0.7421(9)
	z	0.22225(14)	0.520(8)	0.529(5)	0.524(5)	0.524(5)	0.519(5)	0.2464(26)	0.2472(11)	0.2509(18)	0.1255(29)	0.2482(17)	0.1355(9)
	U_{iso} *100	0.35(4)	0.96(4)	0.954(35)	1.13(5)	1.248(30)	1.28(4)	1.06(4)	0.993(31)	0.65(4)	3.1(5)	1.034(29)	1.57(29)
O1	x	0.4445(4)	0.5	0.5	0.5	0.5	0.5	0.2780(32)	0.3003(19)	0.2229(29)	0.748(20)	0.2977(29)	0.670(6)
	y	0.0158(5)	0.5	0.5	0.5	0.5	0.5	0	0	0	0.25	0	0.25
	z	0.95505(20)	0.039(8)	0.047(6)	0.048(5)	0.041(5)	0.041(5)	0.2119(29)	0.2050(19)	0.3066(26)	0	0.1940(26)	0
	U_{111} *100	0.891(34)	12.6(19)	11.0(13)	10.0(11)	10.0(12)	9.8(9)	2.04(30)	1.82(24)	0.82(32)	5.8(25)	3.61(36)	0.1(4)
	U_{222} *100	N/A	12.59(191)	10.97(127)	9.97(109)	10.00(119)	9.78(88)	N/A	N/A	N/A	N/A	N/A	N/A
	U_{333} *100	N/A	0.1(6)	-0.7(4)	-2.04(18)	-0.4(4)	-1.53(19)	N/A	N/A	N/A	N/A	N/A	N/A
O2	x	N/A	0.5	0.5	0.5	0.5	0.5	0.2859(33)	0.3029(25)	0.2098(31)	0.202(24)	0.2986(27)	0.179(6)
	y	N/A	0	0	0	0	0	0.5	0.5	0.5	0.728(17)	0.5	0.750(13)
	z	N/A	0.559(14)	0.571(8)	0.495(6)	0.563(6)	0.492(5)	0.2869(30)	0.2925(20)	0.1996(28)	0.25	0.3050(21)	0.25
	U_{111} *100	N/A	12.5(22)	11.5(16)	10.3(16)	10.4(14)	9.9(11)	2.38(30)	2.44(26)	1.45(35)	6.9(38)	2.52(28)	3.8(9)
	U_{222} *100	N/A	0.87(32)	1.02(27)	1.37(30)	0.89(25)	1.00(18)	N/A	N/A	N/A	N/A	N/A	N/A
	U_{333} *100	N/A	11.3(18)	9.2(11)	9.22(96)	8.6(9)	8.65(62)	N/A	N/A	N/A	N/A	N/A	N/A
O3	x	N/A	N/A	N/A	N/A	N/A	N/A	0.0254(14)	0.0463(20)	0.020499	0.463(10)	0.0491(25)	0.469(5)
	y	N/A	N/A	N/A	N/A	N/A	N/A	0.2246(13)	0.2226(10)	0.2739(17)	0.461(11)	0.2226(16)	0.489(9)
	z	N/A	N/A	N/A	N/A	N/A	N/A	0.5360(23)	0.5335(16)	0.5379(22)	0.1254(34)	0.5366(23)	0.1494(16)
	U_{iso} *100	N/A	N/A	N/A	N/A	N/A	N/A	2.15(19)	1.97(17)	1.34(30)	3.8(10)	1.58(17)	0.1(4)
O4	x	N/A	N/A	N/A	N/A	N/A	N/A	-0.040075	-0.0187(21)	-0.0535(11)	-0.010(11)	-0.0162(27)	0.016(6)
	y	N/A	N/A	N/A	N/A	N/A	N/A	0.2679(14)	0.2694(10)	0.2214(16)	0.002(15)	0.2725(17)	0.011(8)
	z	N/A	N/A	N/A	N/A	N/A	N/A	0.0358(24)	0.0398(16)	0.0398(21)	0.1189(133)	0.0394(27)	0.1071(14)
	U_{iso} *100	N/A	N/A	N/A	N/A	N/A	N/A	2.21(20)	1.65(14)	0.94(27)	7.0(26)	1.74(18)	0.1(4)
Bi/Na – O bond length (Å)		2.5161(16)	2.8015(18)	2.8031(15)	2.7992(12)	2.7927(12)	2.7891(10)	3.02(4)	3.041(15)	2.424(27)	2.72(21)	3.139(21)	2.19(8)
		2.5161(16)	2.8015(18)	2.8031(15)	2.7992(12)	2.7927(12)	2.7891(10)	2.54(4)	2.516(17)	3.106(27)	2.82(21)	2.399(23)	2.797(9)
		2.5161(16)	2.8015(18)	2.8031(15)	2.7992(12)	2.7927(12)	2.7891(10)	2.574(23)	2.585(17)	2.843(29)	2.771(13)	2.637(22)	2.797(9)
		2.3070(25)	2.8015(18)	2.8031(15)	2.7992(12)	2.7927(12)	2.7891(10)	2.990(24)	2.986(19)	2.729(28)	2.771(13)	2.917(23)	2.88(5)
		2.3070(25)	2.64(4)	2.605(20)	2.807(16)	2.618(16)	2.807(15)	2.61(4)	2.387(18)	2.711(21)	2.52(10)	2.473(18)	3.08(5)
		2.3070(25)	2.97(4)	3.002(23)	2.778(16)	2.969(19)	2.760(15)	2.96(4)	3.161(19)	3.101(20)	2.95(12)	2.842(13)	3.08(5)
		N/A	2.64(4)	2.605(20)	2.807(16)	2.618(16)	2.807(15)	2.493(25)	2.657(23)	2.711(21)	2.95(12)	2.473(18)	2.88(5)
		N/A	2.97(4)	3.002(23)	2.778(16)	2.969(19)	2.760(15)	3.078(25)	2.896(22)	3.101(20)	2.52(10)	2.842(13)	2.55(6)
		N/A	2.64(4)	2.605(20)	2.807(16)	2.618(16)	2.807(15)	2.740(24)	2.750(17)	2.860(21)	2.82(11)	3.080(13)	2.74(6)
		N/A	2.97(4)	3.002(23)	2.778(16)	2.969(19)	2.760(15)	3.154(21)	2.990(9)	2.405(23)	2.71(10)	2.671(20)	2.74(6)
		N/A	2.64(4)	2.605(20)	2.807(16)	2.618(16)	2.807(15)	2.740(24)	2.750(17)	2.860(21)	2.71(10)	3.080(13)	2.55(6)
		N/A	2.97(4)	3.002(23)	2.778(16)	2.969(19)	2.760(15)	3.154(21)	2.990(9)	2.405(23)	2.82(11)	2.671(20)	2.73(10)
		N/A	N/A	N/A	N/A	N/A	N/A	2.456(29)	2.450(15)	2.942(26)	2.89(13)	2.293(21)	2.89(9)
		N/A	N/A	N/A	N/A	N/A	N/A	2.871(22)	2.835(9)	2.606(27)	2.65(13)	2.650(26)	2.34(7)
		N/A	N/A	N/A	N/A	N/A	N/A	2.456(29)	2.450(15)	3.030(28)	2.55(20)	2.888(25)	3.18(8)
		N/A	N/A	N/A	N/A	N/A	N/A	2.871(22)	2.835(9)	2.566(28)	2.99(20)	2.710(24)	2.42(8)
		N/A	N/A	N/A	N/A	N/A	N/A	3.048(23)	3.081(9)	2.433(22)	2.61(11)	2.993(12)	2.63(4)
		N/A	N/A	N/A	N/A	N/A	N/A	2.697(25)	2.697(15)	2.745(20)	3.07(11)	2.710(24)	2.63(4)
		N/A	N/A	N/A	N/A	N/A	N/A	3.048(23)	3.081(9)	2.433(22)	3.07(11)	2.993(12)	2.42(8)
		N/A	N/A	N/A	N/A	N/A	N/A	2.697(25)	2.697(15)	2.745(20)	2.61(11)	2.996(13)	2.86(7)
		N/A	N/A	N/A	N/A	N/A	N/A	2.838(22)	3.026(9)	2.749(19)	2.82(10)	2.500(23)	3.06(4)
		N/A	N/A	N/A	N/A	N/A	N/A	2.503(27)	2.502(18)	2.749(19)	2.69(10)	2.996(13)	3.06(4)
		N/A	N/A	N/A	N/A	N/A	N/A	2.838(22)	3.026(9)		2.69(10)	2.500(23)	2.86(7)
		N/A	N/A	N/A	N/A	N/A	N/A	2.503(27)	2.502(18)		2.82(10)		
Nb/Fe – O bond length (Å)		2.1022(22)	1.900(20)	1.906(12)	1.882(12)	1.906(9)	1.879(10)	1.986(14)	1.996(9)	1.986(20)	1.97(5)	2.004(14)	2.141(15)
		2.1022(22)	2.054(20)	2.048(12)	2.066(12)	2.036(9)	2.056(10)	2.000(14)	1.991(9)	1.991(20)	1.95(6)	1.978(14)	1.844(16)
		2.1022(22)	1.9840(24)	1.9846(13)	1.9783(10)	1.9773(8)	1.9717(9)	2.008(15)	2.004(10)	2.002(15)	1.95(6)	1.999(14)	1.83(5)
		1.9525(22)	1.9840(24)	1.9846(13)	1.9783(10)	1.9773(8)	1.9717(9)	2.004(14)	1.999(9)	1.959(14)	2.03(7)	1.989(10)	2.02(5)
		1.9525(22)	1.9840(24)	1.9846(13)	1.9783(10)	1.9773(8)	1.9717(9)	1.948(14)	1.947(9)	2.011(14)	2.04(8)	1.939(11)	2.07(5)
		1.9525(22)	1.9840(24)	1.9846(13)	1.9783(10)	1.9773(8)	1.9717(9)	1.991(17)	2.005(11)	1.989(14)	1.85(8)	2.013(17)	2.06(5)
Nb/Fe – O – Nb/Fe bond angle (o)		155.67(8)	180.000(0)	180.000(0)	180.000(0)	180.000(0)	180.000(0)	163.4(10)	162.0(6)	161.1(11)	176.(6)	159.7(8)	160.4(23)
								160.3(11)	160.7(6)	161.1(11)	173.(6)	158.7(6)	149.9(28)
			171.0(18)	170.4(9)	173.2(10)	171.1(6)	173.8(9)	160.2(9)	160.3(6)	160.6(12)	164.8(22)	159.3(7)	165.0(21)
								162.8(9)	161.5(6)	157.3(12)	177.(5)	161.3(7)	153.7(18)

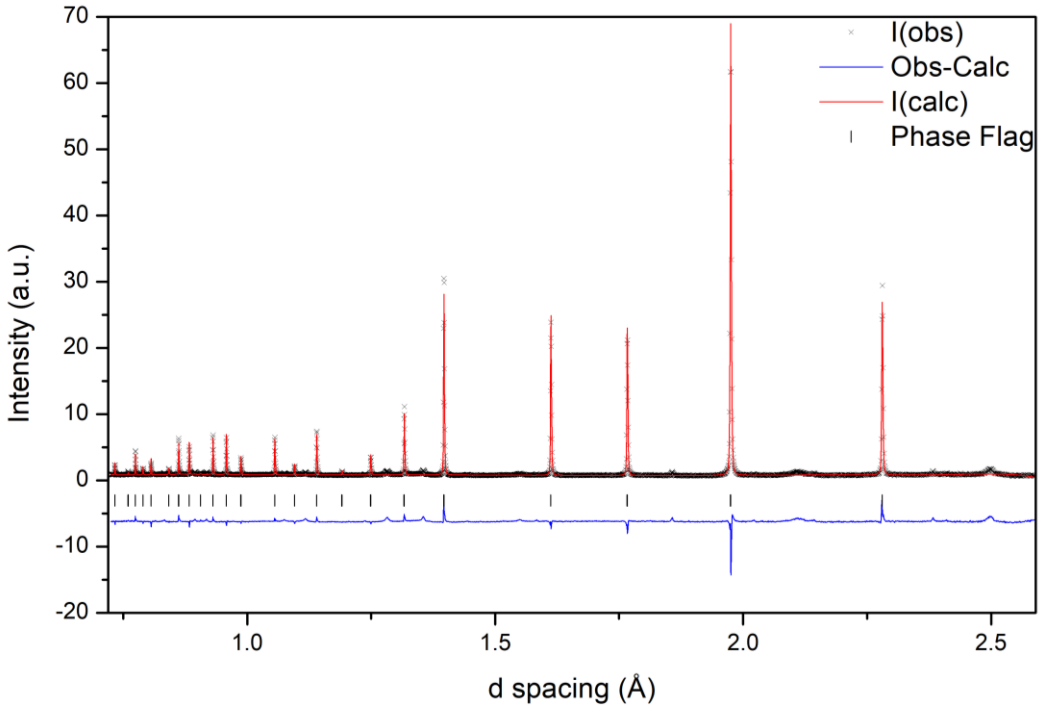

Figure A3.9: *Rietveld refinement of room temperature PND data collected for $Bi_{0.6}Na_{0.4}Fe_{0.6}Nb_{0.4}O_3$; χ^2 = 10.82, Rwp = 9.78% and Rp = 8.14; the black crosses represent the observed intensity, the red line represents the calculated intensity from the model, the blue line represents the difference between the observed pattern and calculated pattern and the black tick marker represents the P4mm model.*

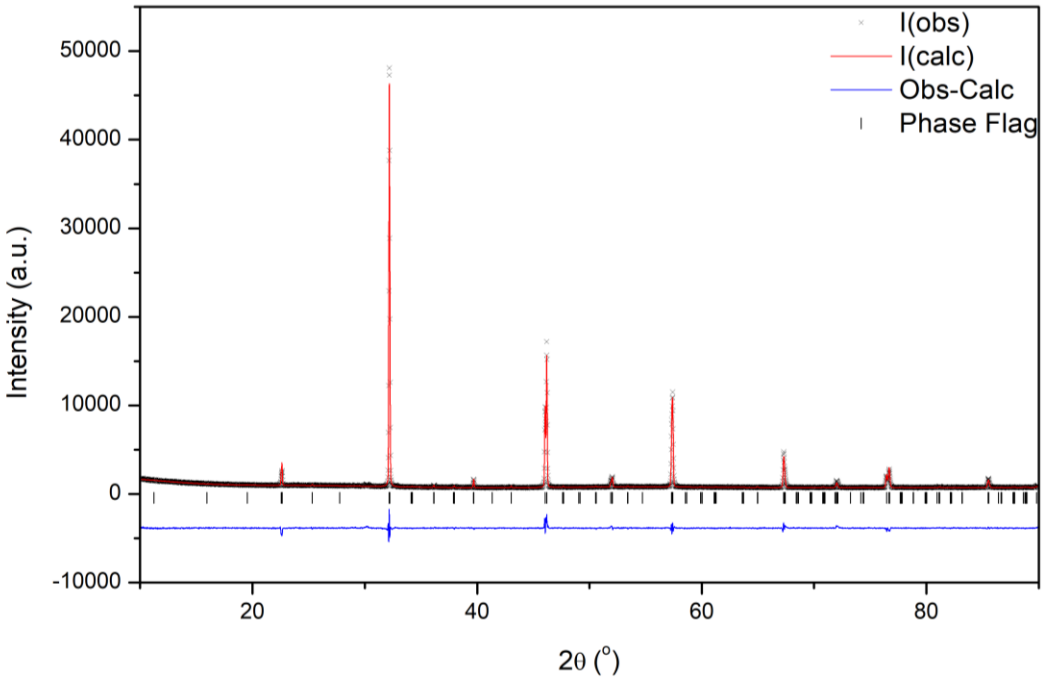

Figure A3.10: *Rietveld refinement of room temperature PXRD data collected for $Bi_{0.325}Na_{0.675}Fe_{0.325}Nb_{0.675}O_3$; χ^2 = 2.776, Rwp = 5.26% and Rp = 3.78; the black crosses represent the observed intensity, the red line represents the calculated intensity from the model, the blue line represents the difference between the observed pattern and calculated pattern and the black tick marker represents the $P2_1ma$ model.*

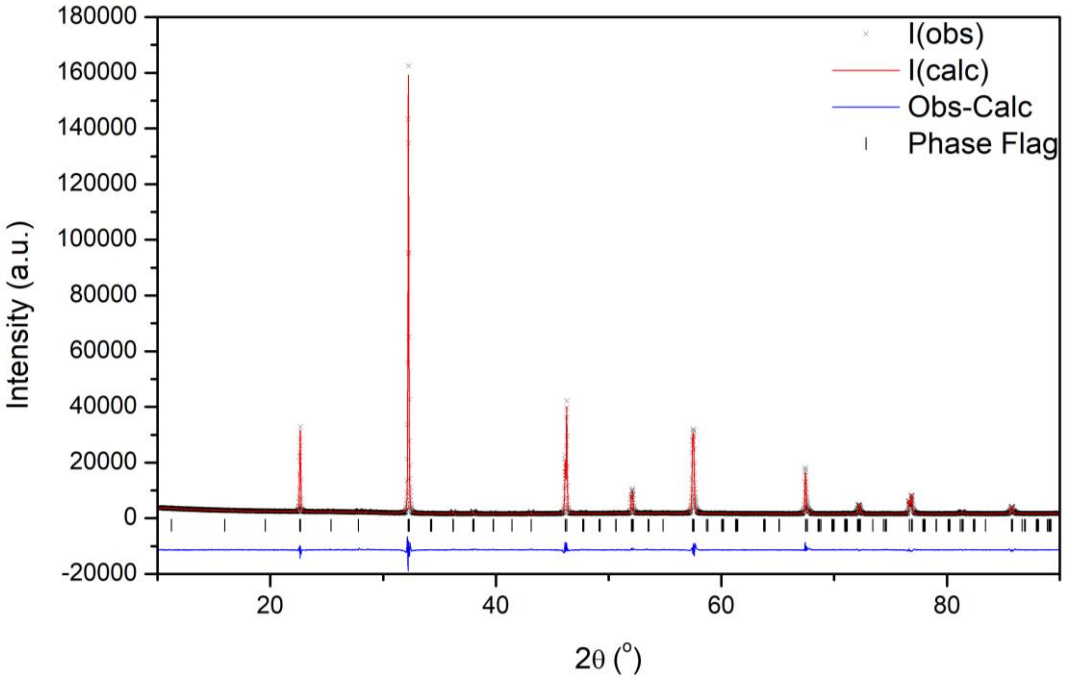

Figure A3.11: *Rietveld refinement of room temperature PXRD data collected for $Bi_{0.2}Na_{0.8}Fe_{0.2}Nb_{0.8}O_3$; χ^2 = 7.168, Rwp = 5.39% and Rp = 3.43; the black crosses represent the observed intensity, the red line represents the calculated intensity from the model, the blue line represents the difference between the observed pattern and calculated pattern and the black tick marker represents the $P2_1ma$ model.*

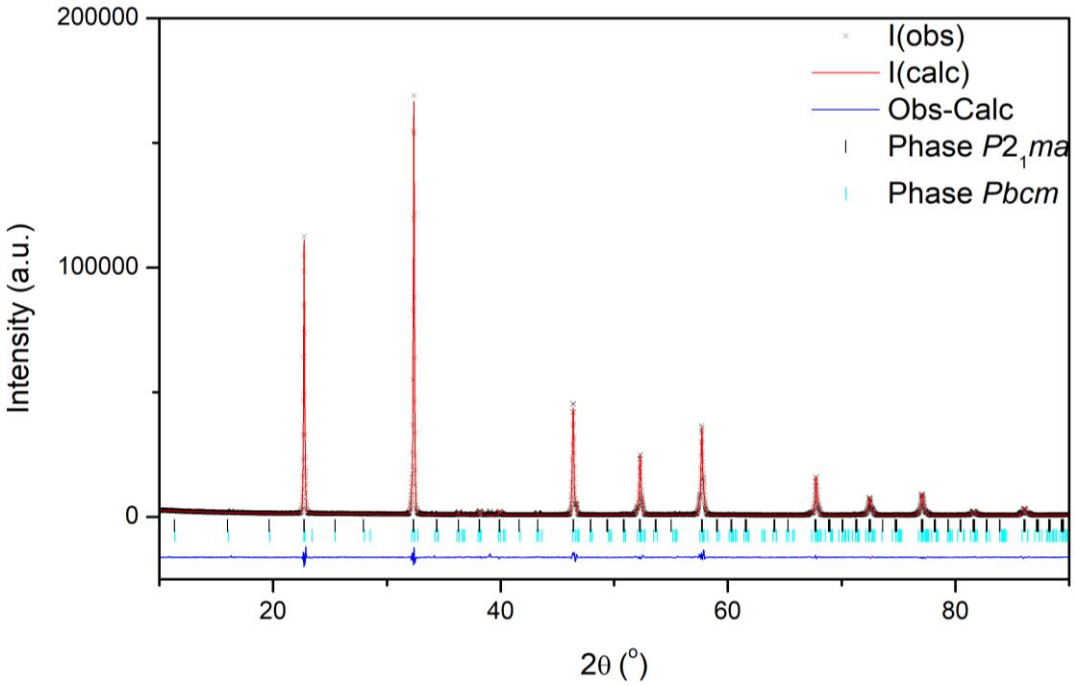

Figure A3.12: *Rietveld refinement of room temperature PXRD data collected for $Bi_{0.05}Na_{0.95}Fe_{0.05}Nb_{0.95}O_3$; χ^2 = 8.418, R_{wp} = 6.51% and R_p = 4.29; the black crosses represent the observed intensity, the red line represents the calculated intensity from the model, the blue line represents the difference between the observed pattern and calculated pattern, the black tick marker represents the $P2_1ma$ model and the cyan tick marker represents the Pbcm model.*

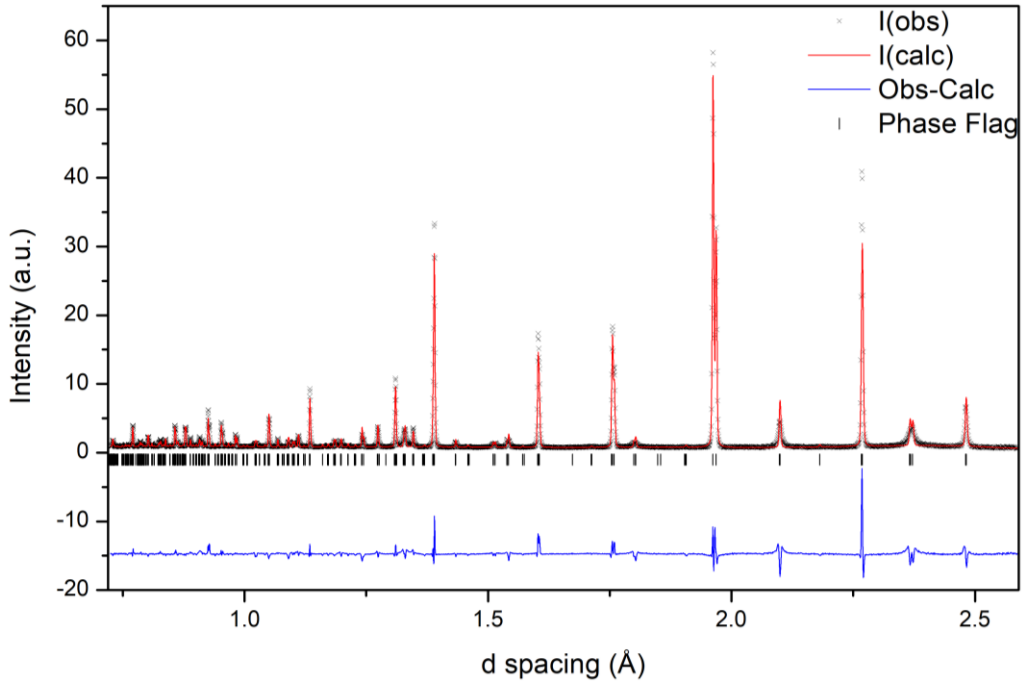

Figure A3.13: *Rietveld refinement of room temperature PND data collected for $Bi_{0.3}Na_{0.7}Fe_{0.3}Nb_{0.7}O_3$; χ^2 = 20.56, R_{wp} = 12.17% and R_p = 10.42; the black crosses represent the observed intensity, the red line represents the calculated intensity from the model, the blue line represents the difference between the observed pattern and calculated pattern and the black tick marker represents the $P2_1ma$ model.*

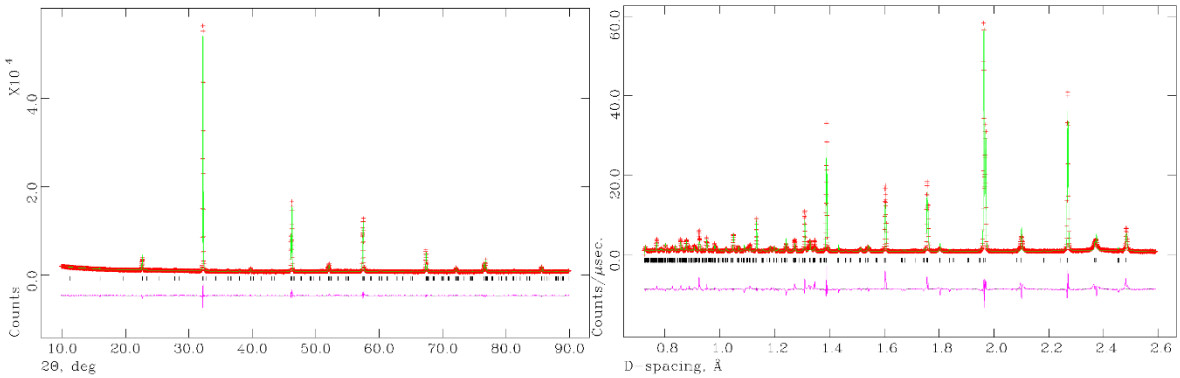

Figure A3.14: *Rietveld refinement of room temperature (a) PXRD and (b) PND data collected for $Bi_{0.3}Na_{0.7}Fe_{0.3}Nb_{0.7}O_3$ against the Pbcm model.*

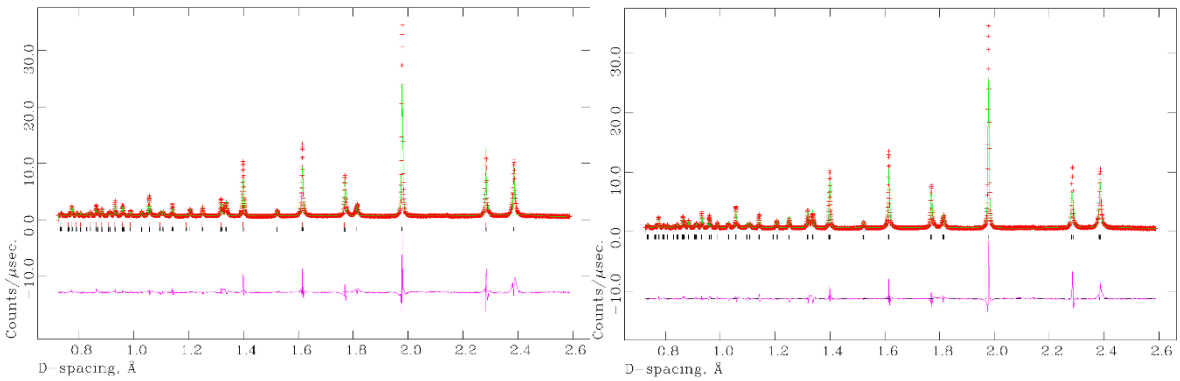

Figure A3.15: *Rietveld refinement of room temperature PND data collected for $Bi_{0.85}Na_{0.15}Fe_{0.85}Nb_{0.15}O_3$ against the (a) R3c and P4mm (b) Cc models.*

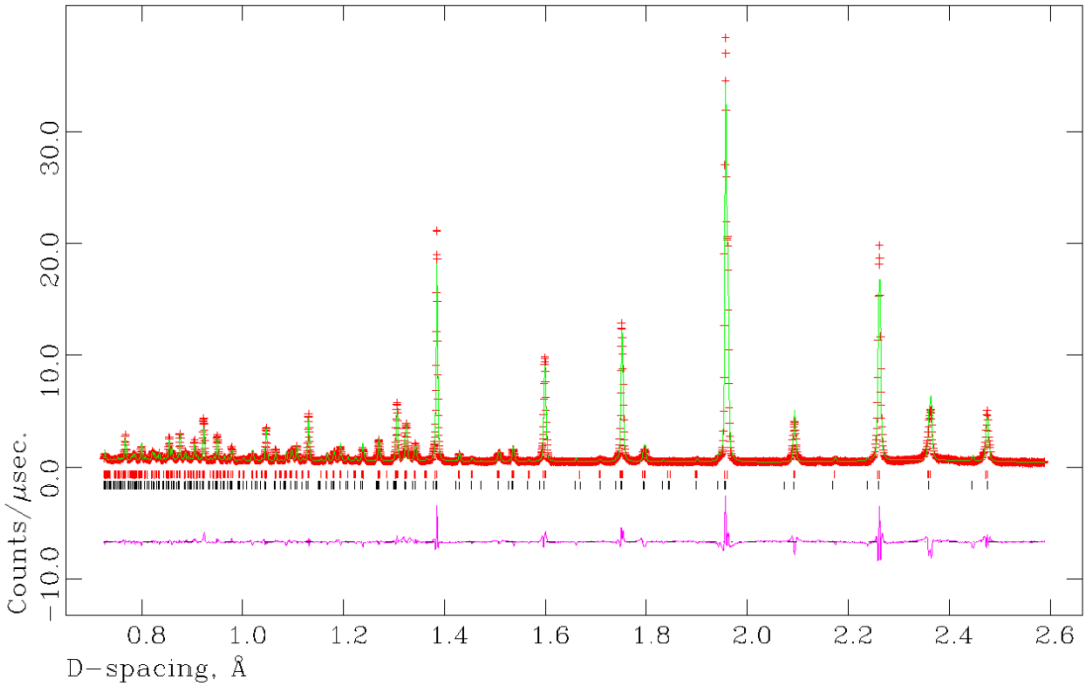

Figure A3.16: *Rietveld refinement of room temperature PND data collected for $Bi_{0.15}Na_{0.85}Fe_{0.15}Nb_{0.85}O_3$; $\chi^2 = 15.96$, $R_{wp} = 10.14\%$ and $R_p = 9.1$; the black crosses represent the observed intensity, the red line represents the calculated intensity from the model, the blue line represents the difference between the observed pattern and calculated pattern, the red tick marker represents the $P2_1ma$ model and the black tick marker represents the Pbcm model.*

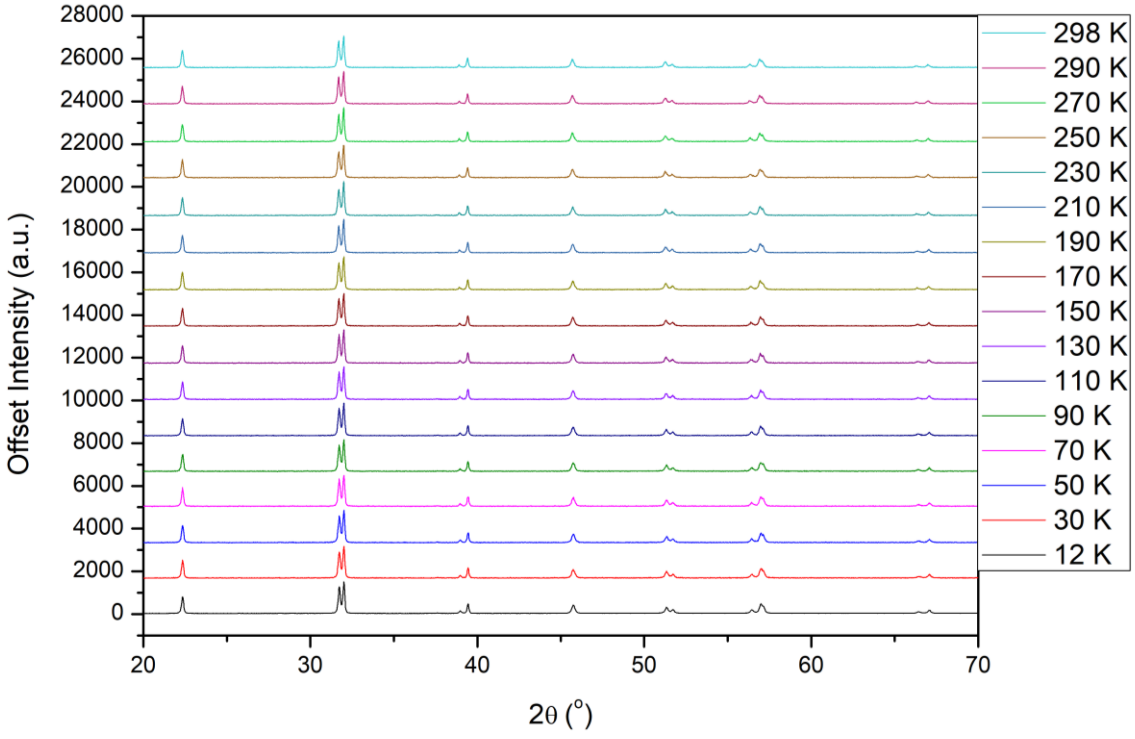

Figure A3.17: *All patterns for the LT PXRD of $Bi_{0.95}Na_{0.05}Fe_{0.95}Nb_{0.05}O_3$. 12K pattern intensity has been scaled down to match the intensities of the other temperature points that were taken with shorter scan times.*

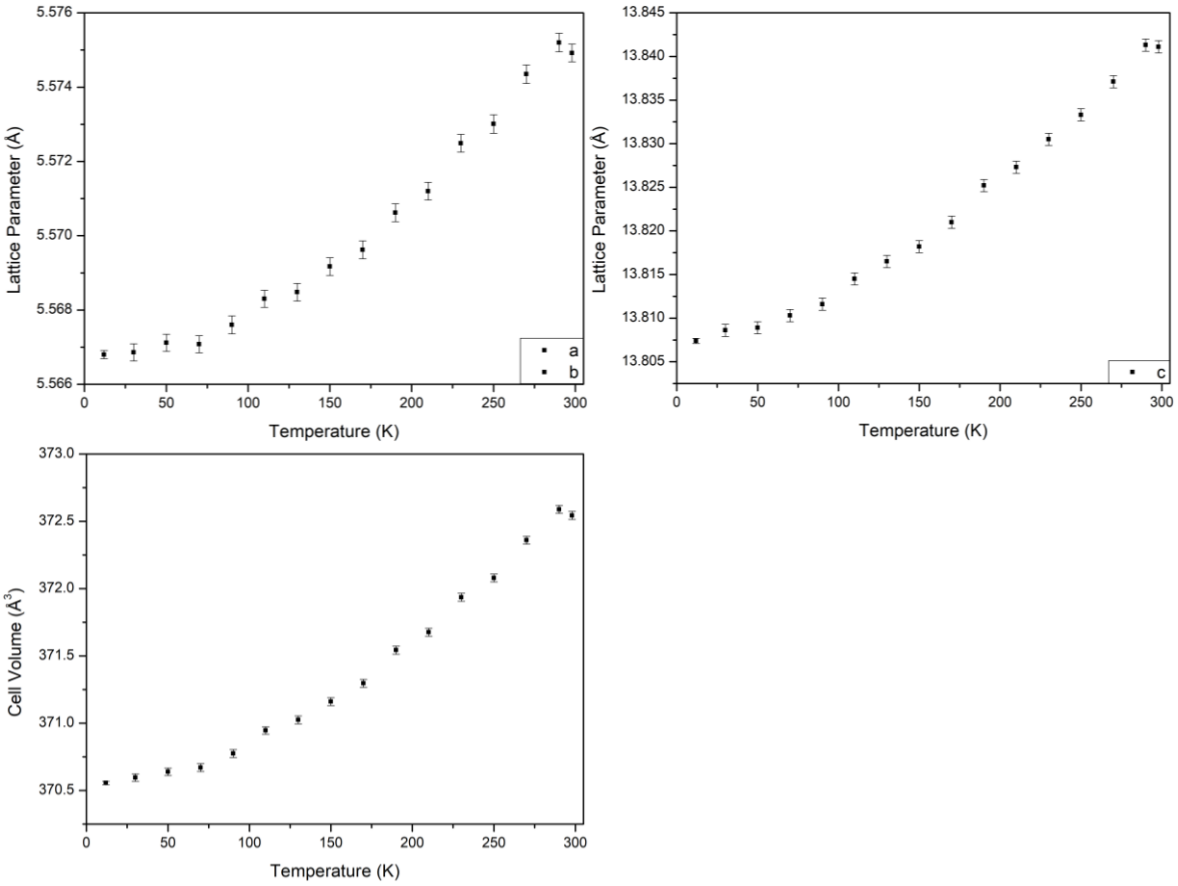

Figure A3.18: *LT PXRD of $Bi_{0.95}Na_{0.05}Fe_{0.95}Nb_{0.05}O_3$: (a) + (b) Lattice Parameter against temperature plot, (c) Cell Volume against temperature plot.*

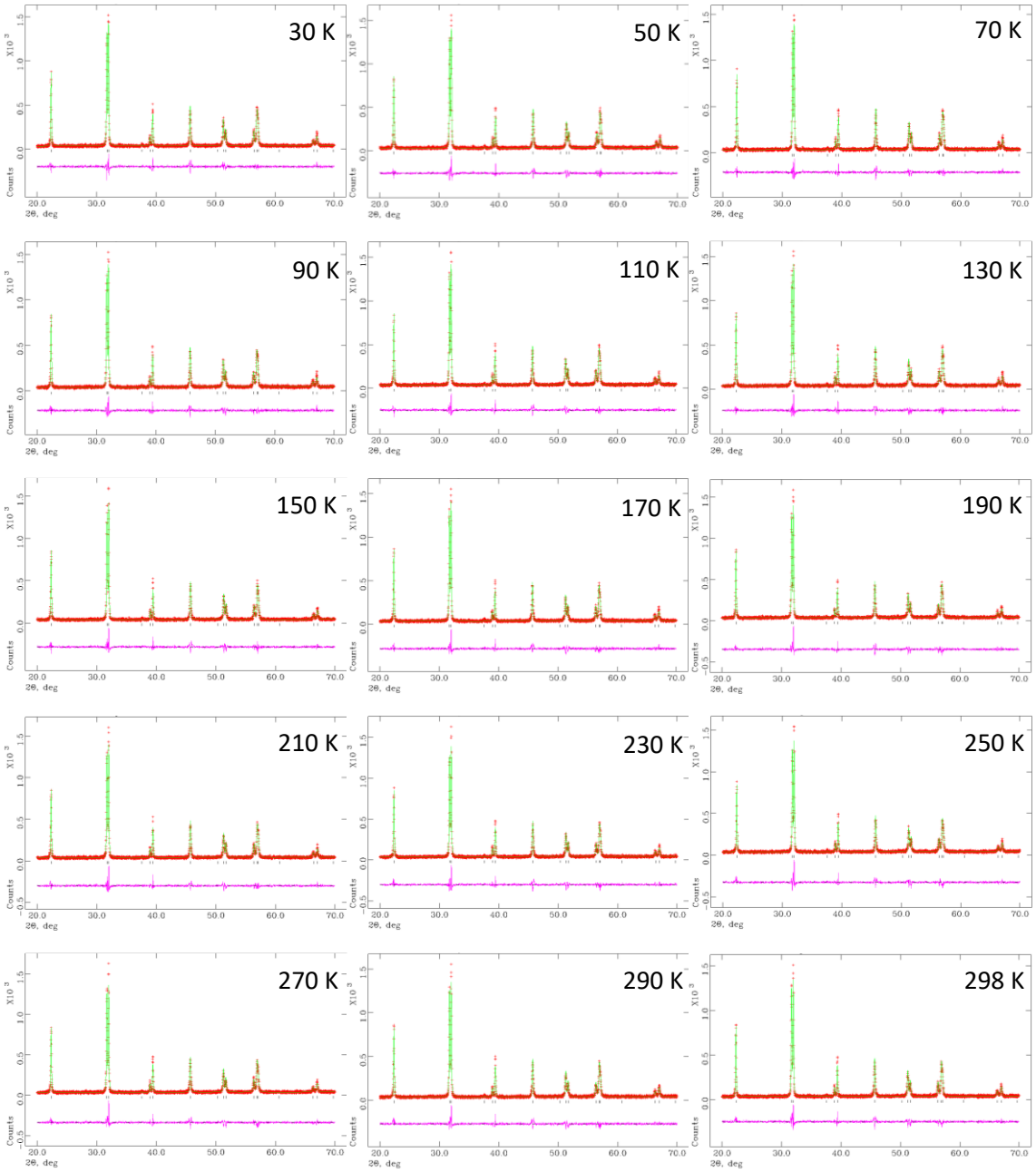

Figure A3.19: *Rietveld refinements obtained from LT PXRD of $Bi_{0.95}Na_{0.05}Fe_{0.95}Nb_{0.05}O_3$ in the temperature ranges 30 K to 298 K.*

Table A3.3: *Rietveld refinement parameters for LT XRD of $Bi_{0.95}Na_{0.05}Fe_{0.05}Nb_{0.05}O_3$.*

Parameter		$Bi_{0.95}Na_{0.05}Fe_{0.95}Nb_{0.05}O_3$															
Temperature (K)		12	30	50	70	90	110	130	150	170	190	210	230	250	270	290	298
Space Group		*R* 3*c*	*R* 3*c*	*R* 3*c*	*R* 3*c*	*R* 3*c*	*R* 3*c*	*R* 3*c*	*R* 3*c*	*R* 3*c*	*R* 3*c*	*R* 3*c*	*R* 3*c*	*R* 3*c*	*R* 3*c*	*R* 3*c*	*R* 3*c*
χ^2		3.277	1.362	1.382	1.382	1.412	1.324	1.391	1.417	1.435	1.469	1.427	1.459	1.452	1.491	1.444	1.405
wRp (%)		7.500	14.57	14.8	14.84	14.95	14.32	14.68	14.78	14.93	15.08	14.84	15.02	15.01	15.23	14.98	14.81
Rp (%)		5.540	10.94	11.19	11.09	11.17	10.86	11.15	11.32	11.47	11.37	11.49	11.54	11.56	11.81	11.61	11.36
a (Å)		5.56680(11)	5.56686(23)	5.56712(23)	5.56708(23)	5.56760(24)	5.56830(23)	5.56848(24)	5.56917(24)	5.56962(24)	5.57062(24)	5.57120(24)	5.57249(24)	5.57301(25)	5.57435(25)	5.57520(25)	5.57492(24)
b (Å)		5.56680(11)	5.56686(23)	5.56712(23)	5.56708(23)	5.56760(24)	5.56830(23)	5.56848(24)	5.56917(24)	5.56962(24)	5.57062(24)	5.57120(24)	5.57249(24)	5.57301(25)	5.57435(25)	5.57520(25)	5.57492(24)
c (Å)		13.80739(30)	13.8086(7)	13.8089(7)	13.8103(7)	13.8116(7)	13.8145(7)	13.8165(7)	13.8182(7)	13.8210(7)	13.8252(7)	13.8273(7)	13.8305(7)	13.8333(7)	13.8371(7)	13.8413(7)	13.8411(7)
α (°)		90.000	90.000	90.000	90.000	90.000	90.000	90.000	90.000	90.000	90.000	90.000	90.000	90.000	90.000	90.000	90.000
β (°)		90.000	90.000	90.000	90.000	90.000	90.000	90.000	90.000	90.000	90.000	90.000	90.000	90.000	90.000	90.000	90.000
γ (°)		120.000	120.000	120.000	120.000	120.000	120.000	120.000	120.000	120.000	120.000	120.000	120.000	120.000	120.000	120.000	120.000
Cell vol. (Å3)		370.556(13)	370.596(28)	370.639(28)	370.670(29)	370.775(29)	370.946(28)	371.025(29)	371.161(29)	371.297(29)	371.543(30)	371.676(29)	371.936(30)	372.079(30)	372.360(30)	372.589(30)	372.544(30)
Bi/Na 1	x	0.000	0.000	0.000	0.000	0.000	0.000	0.000	0.000	0.000	0.000	0.000	0.000	0.000	0.000	0.000	0.000
	y	0.000	0.000	0.000	0.000	0.000	0.000	0.000	0.000	0.000	0.000	0.000	0.000	0.000	0.000	0.000	0.000
	z	0.000	0.000	0.000	0.000	0.000	0.000	0.000	0.000	0.000	0.000	0.000	0.000	0.000	0.000	0.000	0.000
Fe/Nb 1	x	0.000	0.000	0.000	0.000	0.000	0.000	0.000	0.000	0.000	0.000	0.000	0.000	0.000	0.000	0.000	0.000
	y	0.000	0.000	0.000	0.000	0.000	0.000	0.000	0.000	0.000	0.000	0.000	0.000	0.000	0.000	0.000	0.000
	z	0.22242(26)	0.22242(26)	0.22242(26)	0.22242(26)	0.22242(26)	0.22242(26)	0.22242(26)	0.22242(26)	0.22242(26)	0.22242(26)	0.22242(26)	0.22242(26)	0.22242(26)	0.22242(26)	0.22242(26)	0.22242(26)
O1	x	0.4560(29)	0.4560(29)	0.4560(29)	0.4560(29)	0.4560(29)	0.4560(29)	0.4560(29)	0.4560(29)	0.4560(29)	0.4560(29)	0.4560(29)	0.4560(29)	0.4560(29)	0.4560(29)	0.4560(29)	0.4560(29)
	y	0.0154(27)	0.0154(27)	0.0154(27)	0.0154(27)	0.0154(27)	0.0154(27)	0.0154(27)	0.0154(27)	0.0154(27)	0.0154(27)	0.0154(27)	0.0154(27)	0.0154(27)	0.0154(27)	0.0154(27)	0.0154(27)
	z	0.9597(9)	0.9597(9)	0.9597(9)	0.9597(9)	0.9597(9)	0.9597(9)	0.9597(9)	0.9597(9)	0.9597(9)	0.9597(9)	0.9597(9)	0.9597(9)	0.9597(9)	0.9597(9)	0.9597(9)	0.9597(9)
Nb/Fe – O bond length (Å)		2.047(16)	2.04741(6)	2.04748(6)	2.04756(7)	2.04775(7)	2.04808(6)	2.04825(7)	2.04850(7)	2.04877(7)	2.04924(7)	2.04950(7)	2.04998(7)	2.05026(7)	2.05078(7)	2.05123(7)	2.05115(7)
		2.047(16)	2.04741(6)	2.04748(6)	2.04756(7)	2.04775(7)	2.04808(6)	2.04825(7)	2.04850(7)	2.04877(7)	2.04924(7)	2.04950(7)	2.04998(7)	2.05026(7)	2.05078(7)	2.05123(7)	2.05115(7)
		2.047(16)	2.04741(6)	2.04748(6)	2.04756(7)	2.04775(7)	2.04808(6)	2.04825(7)	2.04850(7)	2.04877(7)	2.04924(7)	2.04950(7)	2.04998(7)	2.05026(7)	2.05078(7)	2.05123(7)	2.05115(7)
		1.965(15)	1.96459(7)	1.96467(7)	1.96471(7)	1.96490(7)	1.96518(7)	1.96530(7)	1.96554(7)	1.96576(7)	1.96617(7)	1.96640(7)	1.96686(7)	1.96709(7)	1.96758(7)	1.96796(7)	1.96788(7)
		1.965(15)	1.96459(7)	1.96467(7)	1.96471(7)	1.96490(7)	1.96518(7)	1.96530(7)	1.96554(7)	1.96576(7)	1.96617(7)	1.96640(7)	1.96686(7)	1.96709(7)	1.96758(7)	1.96796(7)	1.96788(7)
		1.965(15)	1.96459(7)	1.96467(7)	1.96471(7)	1.96490(7)	1.96518(7)	1.96530(7)	1.96554(7)	1.96576(7)	1.96618(7)	1.96640(7)	1.96686(7)	1.96709(7)	1.96758(7)	1.96796(7)	1.96788(7)
Nb/Fe – O – Nb/Fe bond angle (o)		160.3(6)	160.327(0)	160.326(0)	160.327(0)	160.327(0)	160.327(0)	160.327(0)	160.327(0)	160.328(0)	160.328(0)	160.328(0)	160.328(0)	160.328(0)	160.328(0)	160.329(0)	160.329(0)

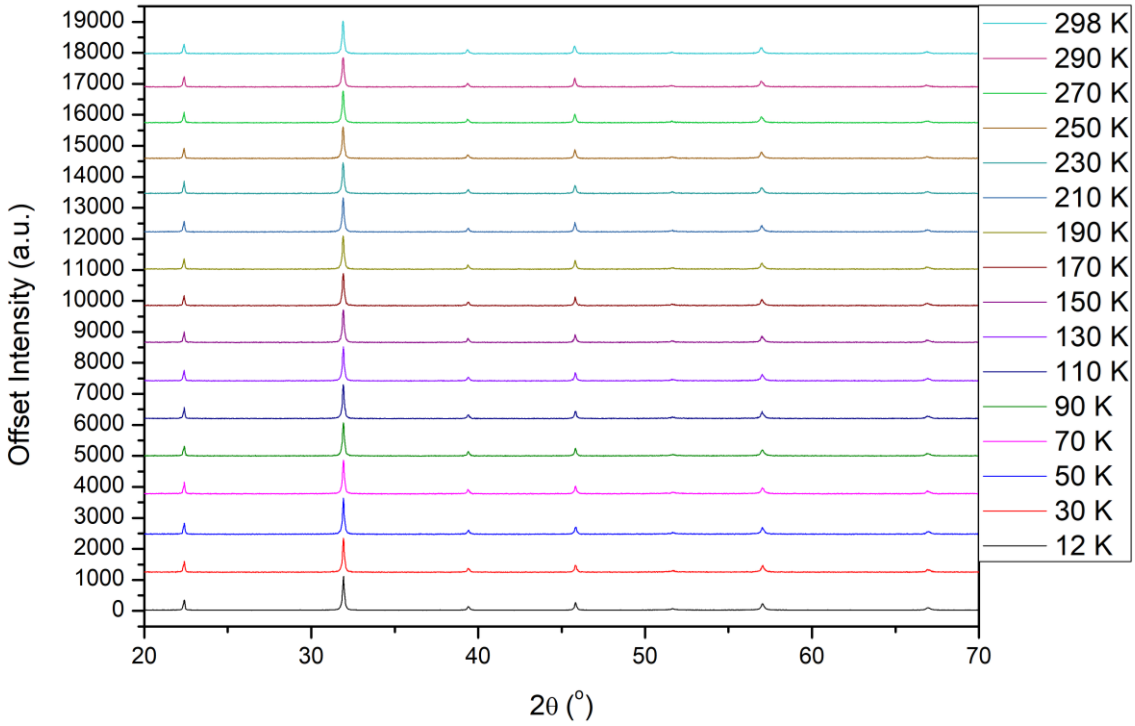

Figure A3.20: *All patterns for the LT PXRD of $Bi_{0.85}Na_{0.15}Fe_{0.85}Nb_{0.15}O_3$. 12K pattern intensity has been scaled down to match the intensities of the other temperature points that were taken with shorter scan times.*

Figure A3.21: *Rietveld refinements obtained from LT PXRD of $Bi_{0.85}Na_{0.15}Fe_{0.85}Nb_{0.15}O_3$ in the temperature ranges 30 K to 298 K.*

Table A3.4: *Rietveld refinement parameters for LT XRD of $Bi_{0.85}Na_{0.15}Fe_{0.85}Nb_{0.15}O_3$.*

Parameter		$Bi_{0.85}Na_{0.15}Fe_{0.85}Nb_{0.15}O_3$																															
Temperature (K)		12	12	30	30	50	50	70	70	90	90	110	110	130	130	150	150	170	170	190	190	210	210	230	230	250	250	270	270	290	290	298	298
Space Group		*R 3c*	*P 4mm*	*R 3c*	*P 4mm*	*R 3c*	*P 4mm*	*R 3c*	*P 4mm*	*R 3c*	*P 4mm*	*R 3c*	*P 4mm*	*R 3c*	*P 4mm*	*R 3c*	*P 4mm*	*R 3c*	*P 4mm*	*R 3c*	*P 4mm*	*R 3c*	*P 4mm*	*R 3c*	*P 4mm*	*R 3c*	*P 4mm*	*R 3c*	*P 4mm*	*R 3c*	*P 4mm*	*R 3c*	*P 4mm*	*R 3c*	*P 4mm*
χ^2		2.959		1.325		1.369		1.344		1.346		1.297		1.255		1.312		1.289		1.402		1.376		1.365		1.343		1.328		1.392		1.273	
wRp (%)		9.480		19.12		19.46		19.22		19.25		18.87		18.58		19.04		18.86		19.63		19.46		19.43		19.24		19.19		19.66		18.71	
Rp (%)		7.230		14.61		14.94		15.03		14.93		14.65		14.34		14.87		14.68		15.40		15.17		15.13		15.17		14.94		15.26		14.51	
a (Å)		5.57330(30)	3.94450(20)	5.5726(6)	3.9442(5)	5.5736(6)	3.9443(5)	5.5736(6)	3.9455(5)	5.5739(7)	3.9455(5)	5.5749(7)	3.9453(5)	5.5742(6)	3.9455(4)	5.5754(6)	3.9469(5)	5.5765(6)	3.9471(5)	5.5771(6)	3.9468(5)	5.5775(6)	3.9479(5)	5.5772(7)	3.9478(5)	5.5786(7)	3.9481(5)	5.5805(7)	3.9497(5)	5.5801(7)	3.9500(5)	5.5812(6)	3.9510(5)
b (Å)		5.57330(30)	3.94450(20)	5.5726(6)	3.9442(5)	5.5736(6)	3.9443(5)	5.5736(6)	3.9455(5)	5.5739(7)	3.9455(5)	5.5749(7)	3.9453(5)	5.5742(6)	3.9455(4)	5.5754(6)	3.9469(5)	5.5765(6)	3.9471(5)	5.5771(6)	3.9468(5)	5.5775(6)	3.9479(5)	5.5772(7)	3.9478(5)	5.5786(7)	3.9481(5)	5.5805(7)	3.9497(5)	5.5801(7)	3.9500(5)	5.5812(6)	3.9510(5)
c (Å)		13.6752(20)	3.9313(17)	13.672(4)	3.9334(25)	13.6739(34)	3.9334(23)	13.674(4)	3.9351(27)	13.682(4)	3.9363(28)	13.675(4)	3.9351(27)	13.6828(29)	3.9336(21)	13.679(4)	3.9342(24)	13.6849(34)	3.9351(23)	13.6856(34)	3.9353(23)	13.6913(30)	3.9354(21)	13.689(4)	3.943(4)	13.693(4)	3.9410(33)	13.7016(31)	3.9403(26)	13.7035(32)	3.9398(28)	13.699(4)	3.9421(29)
α (°)		90.000	90.000	90.000	90.000	90.000	90.000	90.000	90.000	90.000	90.000	90.000	90.000	90.000	90.000	90.000	90.000	90.000	90.000	90.000	90.000	90.000	90.000	90.000	90.000	90.000	90.000	90.000	90.000	90.000	90.000	90.000	90.000
β (°)		90.000	90.000	90.000	90.000	90.000	90.000	90.000	90.000	90.000	90.000	90.000	90.000	90.000	90.000	90.000	90.000	90.000	90.000	90.000	90.000	90.000	90.000	90.000	90.000	90.000	90.000	90.000	90.000	90.000	90.000	90.000	90.000
γ (°)		120.000	90.000	120.000	90.000	120.000	90.000	120.000	90.000	120.000	90.000	120.000	90.000	120.000	90.000	120.000	90.000	120.000	90.000	120.000	90.000	120.000	90.000	120.000	90.000	120.000	90.000	120.000	90.000	120.000	90.000	120.000	90.000
Cell vol. (Å3)		367.87(6)	61.167(27)	367.68(11)	61.19(4)	367.88(11)	61.19(4)	367.88(12)	61.26(4)	368.12(11)	61.28(5)	368.07(12)	61.25(4)	368.18(9)	61.235(34)	368.26(11)	61.29(4)	368.55(11)	61.31(4)	368.65(11)	61.30(4)	368.86(10)	61.337(35)	368.75(14)	61.45(6)	369.03(12)	61.43(5)	369.53(10)	61.47(4)	369.53(11)	61.47(4)	369.56(11)	61.54(5)
Phase Ratio a:b		0.315	0.685	0.315	0.685	0.315	0.685	0.315	0.685	0.315	0.685	0.315	0.685	0.315	0.685	0.315	0.685	0.315	0.685	0.315	0.685	0.315	0.685	0.315	0.685	0.315	0.685	0.315	0.685	0.315	0.685	0.315	0.685
Bi/Na 1	x	0.000	0.000	0.000	0.000	0.000	0.000	0.000	0.000	0.000	0.000	0.000	0.000	0.000	0.000	0.000	0.000	0.000	0.000	0.000	0.000	0.000	0.000	0.000	0.000	0.000	0.000	0.000	0.000	0.000	0.000	0.000	0.000
	y	0.000	0.000	0.000	0.000	0.000	0.000	0.000	0.000	0.000	0.000	0.000	0.000	0.000	0.000	0.000	0.000	0.000	0.000	0.000	0.000	0.000	0.000	0.000	0.000	0.000	0.000	0.000	0.000	0.000	0.000	0.000	0.000
	z	0.000	0.175(28)	0.000	0.175(28)	0.000	0.175(28)	0.000	0.175(28)	0.000	0.175(28)	0.000	0.175(28)	0.000	0.175(28)	0.000	0.175(28)	0.000	0.175(28)	0.000	0.175(28)	0.000	0.175(28)	0.000	0.175(28)	0.000	0.175(28)	0.000	0.175(28)	0.000	0.175(28)	0.000	0.175(28)
Fe/Nb 1	x	0.000	0.500	0.000	0.500	0.000	0.500	0.000	0.500	0.000	0.500	0.000	0.500	0.000	0.500	0.000	0.500	0.000	0.500	0.000	0.500	0.000	0.500	0.000	0.500	0.000	0.500	0.000	0.500	0.000	0.500	0.000	0.500
	y	0.000	0.500	0.000	0.500	0.000	0.500	0.000	0.500	0.000	0.500	0.000	0.500	0.000	0.500	0.000	0.500	0.000	0.500	0.000	0.500	0.000	0.500	0.000	0.500	0.000	0.500	0.000	0.500	0.000	0.500	0.000	0.500
	z	0.2465(24)	0.662(9)	0.2465(24)	0.662(9)	0.2465(24)	0.662(9)	0.2465(24)	0.662(9)	0.2465(24)	0.662(9)	0.2465(24)	0.662(9)	0.2465(24)	0.662(9)	0.2465(24)	0.662(9)	0.2465(24)	0.662(9)	0.2465(24)	0.662(9)	0.2465(24)	0.662(9)	0.2465(24)	0.662(9)	0.2465(24)	0.662(9)	0.2465(24)	0.662(9)	0.2465(24)	0.662(9)	0.2465(24)	0.662(9)
O1	x	0.453(11)	0.500	0.453(11)	0.500	0.453(11)	0.500	0.453(11)	0.500	0.453(11)	0.500	0.453(11)	0.500	0.453(11)	0.500	0.453(11)	0.500	0.453(11)	0.500	0.453(11)	0.500	0.453(11)	0.500	0.453(11)	0.500	0.453(11)	0.500	0.453(11)	0.500	0.453(11)	0.500	0.453(11)	0.500
	y	0.029(16)	0.500	0.029(16)	0.500	0.029(16)	0.500	0.029(16)	0.500	0.029(16)	0.500	0.029(16)	0.500	0.029(16)	0.500	0.029(16)	0.500	0.029(16)	0.500	0.029(16)	0.500	0.029(16)	0.500	0.029(16)	0.500	0.029(16)	0.500	0.029(16)	0.500	0.029(16)	0.500	0.029(16)	0.500
	z	0.9846(34)	0.005(29)	0.9846(34)	0.005(29)	0.9846(34)	0.005(29)	0.9846(34)	0.005(29)	0.9846(34)	0.005(29)	0.9846(34)	0.005(29)	0.9846(34)	0.005(29)	0.9846(34)	0.005(29)	0.9846(34)	0.005(29)	0.9846(34)	0.005(29)	0.9846(34)	0.005(29)	0.9846(34)	0.005(29)	0.9846(34)	0.005(29)	0.9846(34)	0.005(29)	0.9846(34)	0.005(29)	0.9846(34)	0.005(29)
O2	x	N/A	0.500	N/A	0.500	N/A	0.500	N/A	0.500	N/A	0.500	N/A	0.500	N/A	0.500	N/A	0.500	N/A	0.500	N/A	0.500	N/A	0.500	N/A	0.500	N/A	0.500	N/A	0.500	N/A	0.500	N/A	0.500
	y	N/A	0.000	N/A	0.000	N/A	0.000	N/A	0.000	N/A	0.000	N/A	0.000	N/A	0.000	N/A	0.000	N/A	0.000	N/A	0.000	N/A	0.000	N/A	0.000	N/A	0.000	N/A	0.000	N/A	0.000	N/A	0.000
	z	N/A	0.510(23)	N/A	0.510(23)	N/A	0.510(23)	N/A	0.510(23)	N/A	0.510(23)	N/A	0.510(23)	N/A	0.510(23)	N/A	0.510(23)	N/A	0.510(23)	N/A	0.510(23)	N/A	0.510(23)	N/A	0.510(23)	N/A	0.510(23)	N/A	0.510(23)	N/A	0.510(23)	N/A	0.510(23)
Nb/Fe – O bond length (Å)		1.99262(13)	1.3496(6)	1.99226(26)	1.3504(8)	1.99262(25)	1.3504(8)	1.99263(27)	1.3510(9)	1.99315(26)	1.3514(10)	1.99295(28)	1.3510(9)	1.99328(21)	1.3505(7)	1.99332(25)	1.3507(8)	1.99389(24)	1.3510(8)	1.99406(25)	1.3511(8)	1.99449(22)	1.3511(7)	1.99429(31)	1.3536(13)	1.99479(28)	1.3530(11)	1.99575(24)	1.3528(9)	1.99578(24)	1.3526(10)	1.99575(26)	1.3534(10)
		1.99262(13)	2.5814(12)	1.99227(26)	2.5830(16)	1.99262(25)	2.5830(15)	1.99263(27)	2.5841(18)	1.99315(26)	2.5849(19)	1.99295(28)	2.5841(17)	1.99328(21)	2.5831(14)	1.99332(25)	2.5835(15)	1.99389(24)	2.5841(15)	1.99406(25)	2.5842(15)	1.99449(22)	2.5843(14)	1.99429(31)	2.5891(26)	1.99479(28)	2.5880(22)	1.99575(24)	2.5875(17)	1.99578(24)	2.5872(18)	1.99575(26)	2.5887(19)
		1.99262(13)	2.06069(12)	1.99227(26)	2.06065(25)	1.99262(25)	2.06070(25)	1.99263(27)	2.06132(25)	1.99315(26)	2.06140(25)	1.99295(28)	2.06123(25)	1.99328(21)	2.06128(23)	1.99332(25)	2.06197(24)	1.99389(24)	2.06212(24)	1.99406(25)	2.06195(25)	1.99449(22)	2.06250(24)	1.99429(31)	2.06276(29)	1.99479(28)	2.06286(27)	1.99575(24)	2.06355(25)	1.99578(24)	2.06372(26)	1.99575(26)	2.06429(25)
		2.03197(11)	2.06069(12)	2.03165(21)	2.06065(25)	2.03202(20)	2.06070(25)	2.03202(22)	2.06132(25)	2.03237(22)	2.06140(25)	2.03242(23)	2.06123(25)	2.03247(19)	2.06128(23)	2.03271(21)	2.06197(24)	2.03320(20)	2.06212(24)	2.03340(21)	2.06195(25)	2.03370(19)	2.06250(24)	2.03354(25)	2.06276(29)	2.03405(24)	2.06286(27)	2.03490(21)	2.06355(25)	2.03485(22)	2.06372(26)	2.03502(21)	2.06429(25)
		2.03197(11)	2.06069(12)	2.03165(21)	2.06065(25)	2.03202(20)	2.06070(25)	2.03202(22)	2.06132(25)	2.03237(22)	2.06140(25)	2.03242(23)	2.06123(25)	2.03247(19)	2.06128(23)	2.03271(21)	2.06197(24)	2.03320(20)	2.06212(24)	2.03340(21)	2.06195(25)	2.03370(19)	2.06250(24)	2.03354(25)	2.06276(29)	2.03405(24)	2.06286(27)	2.03490(21)	2.06355(25)	2.03485(22)	2.06372(26)	2.03502(21)	2.06429(25)
		2.03197(11)	2.06069(12)	2.03165(21)	2.06065(25)	2.03202(20)	2.06070(25)	2.03202(22)	2.06132(25)	2.03237(22)	2.06140(25)	2.03242(23)	2.06123(25)	2.03247(19)	2.06128(23)	2.03271(21)	2.06197(24)	2.03320(20)	2.06212(24)	2.03340(21)	2.06195(25)	2.03370(19)	2.06250(24)	2.03354(25)	2.06276(29)	2.03405(24)	2.06286(27)	2.03490(21)	2.06355(25)	2.03485(22)	2.06372(26)	2.03502(21)	2.06429(25)
Nb/Fe – O – Nb/Fe bond angle (o)		156.909(1)	146.309(14)	156.909(1)	146.287(20)	156.909(1)	146.288(19)	156.909(1)	146.284(23)	156.911(1)	146.274(23)	156.908(1)	146.282(22)	156.911(1)	146.296(17)	156.909(1)	146.302(19)	156.910(1)	146.297(19)	156.910(1)	146.293(19)	156.911(1)	146.301(18)	156.910(1)	146.240(32)	156.911(1)	146.257(27)	156.912(1)	146.276(22)	156.912(1)	146.282(23)	156.911(1)	146.271(24)

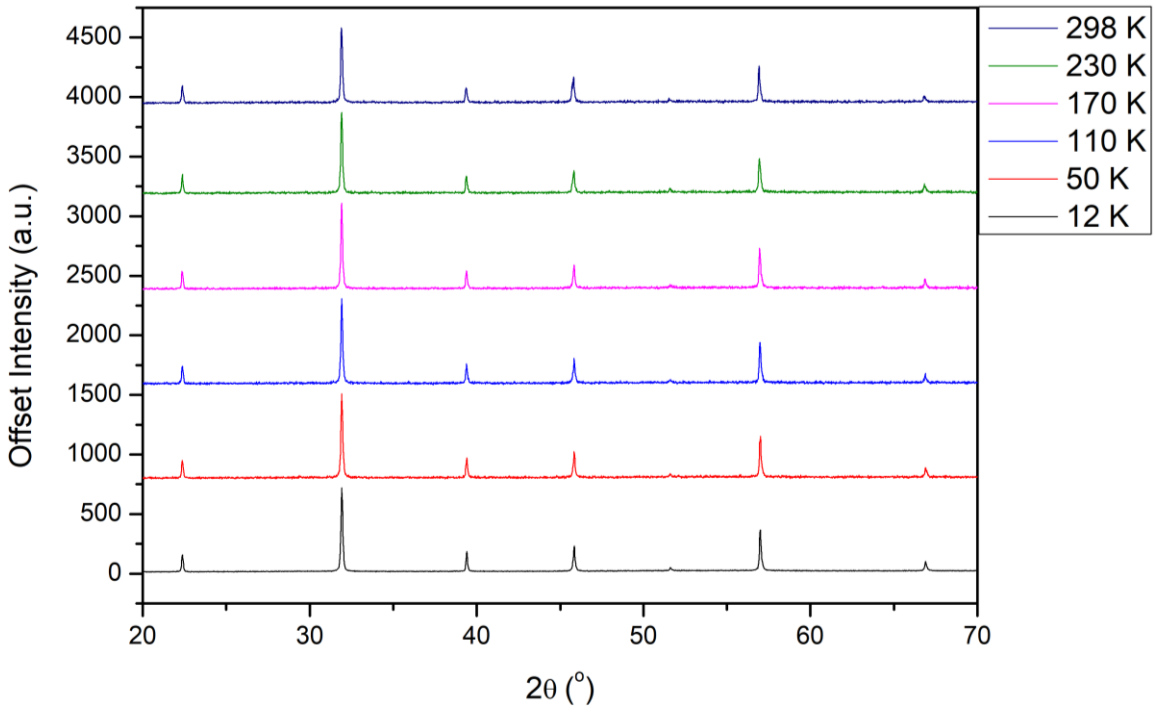

Figure A3.22: *Selection of patterns for the LT PXRD of $Bi_{0.8}Na_{0.2}Fe_{0.8}Nb_{0.2}O_3$. 12K pattern intensity has been scaled down to match the intensities of the other temperature points that were taken with shorter scan times.*

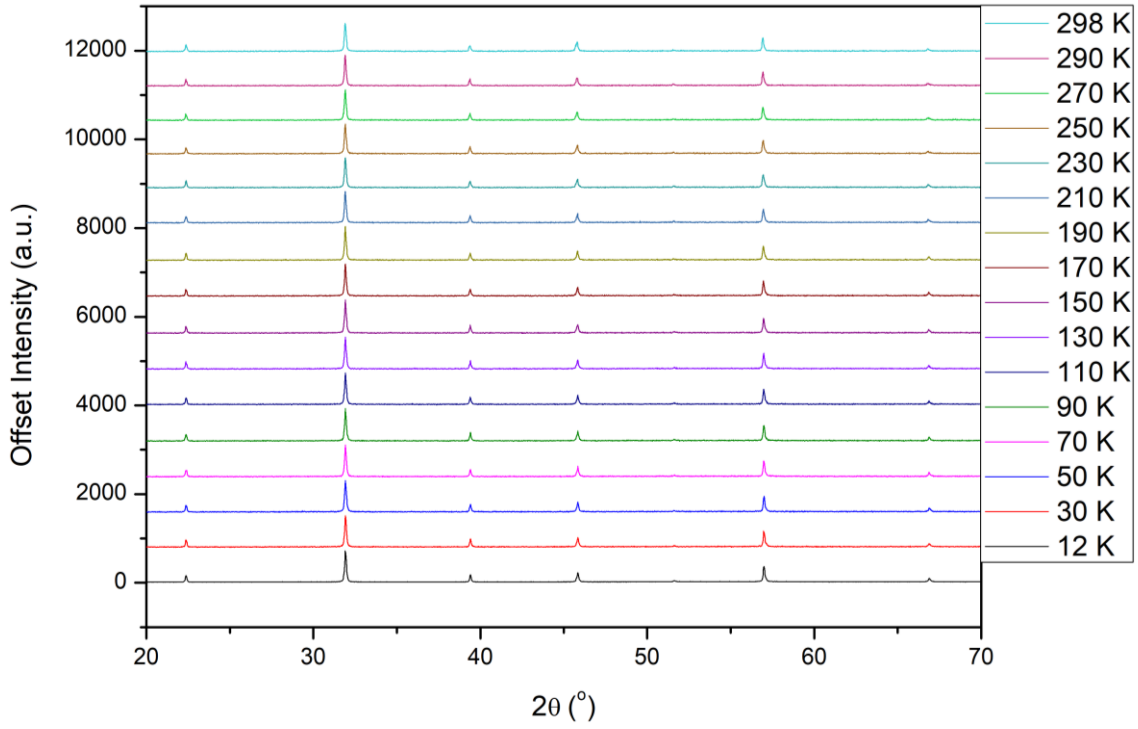

Figure A3.23: *All patterns for the LT PXRD of $Bi_{0.8}Na_{0.2}Fe_{0.8}Nb_{0.2}O_3$. 12K pattern intensity has been scaled down to match the intensities of the other temperature points that were taken with shorter scan times.*

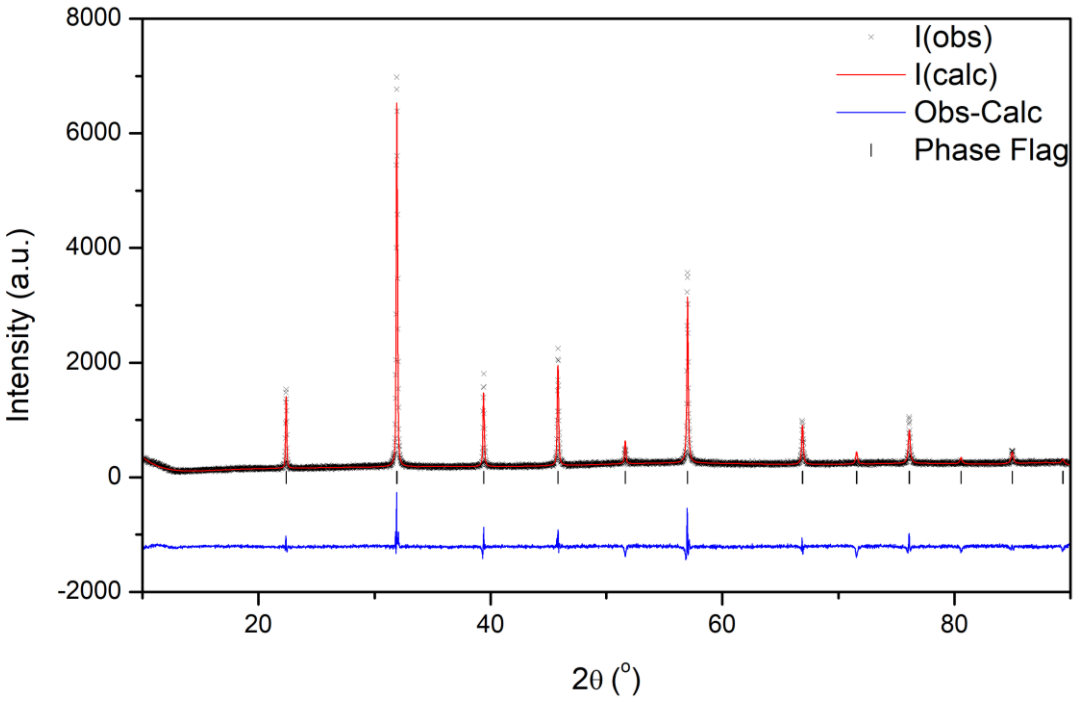

Figure A3.24: *Rietveld refinement of 12 K PXRD data collected for $Bi_{0.8}Na_{0.2}Fe_{0.8}Nb_{0.2}O_3$; χ^2 = 1.742, R_{wp} = 8.38% and R_p = 6.48; the black crosses represent the observed intensity, the red line represents the calculated intensity from the model, the blue line represents the difference between the observed pattern and calculated pattern, the black tick marker represents the P4mm model.*

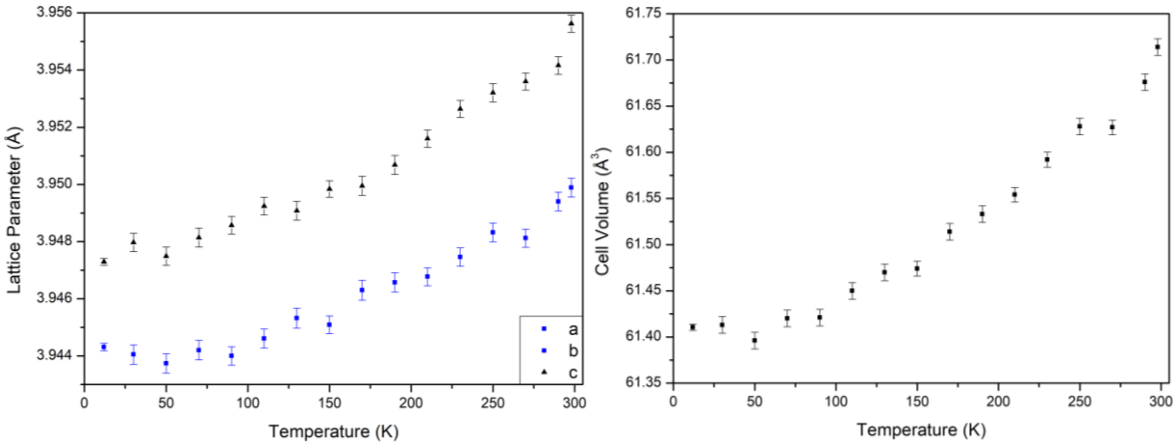

Figure A3.25: *LT PXRD of $Bi_{0.8}Na_{0.2}Fe_{0.8}Nb_{0.2}O_3$: (a) Lattice Parameter against temperature plot, (b) Cell Volume against temperature plot.*

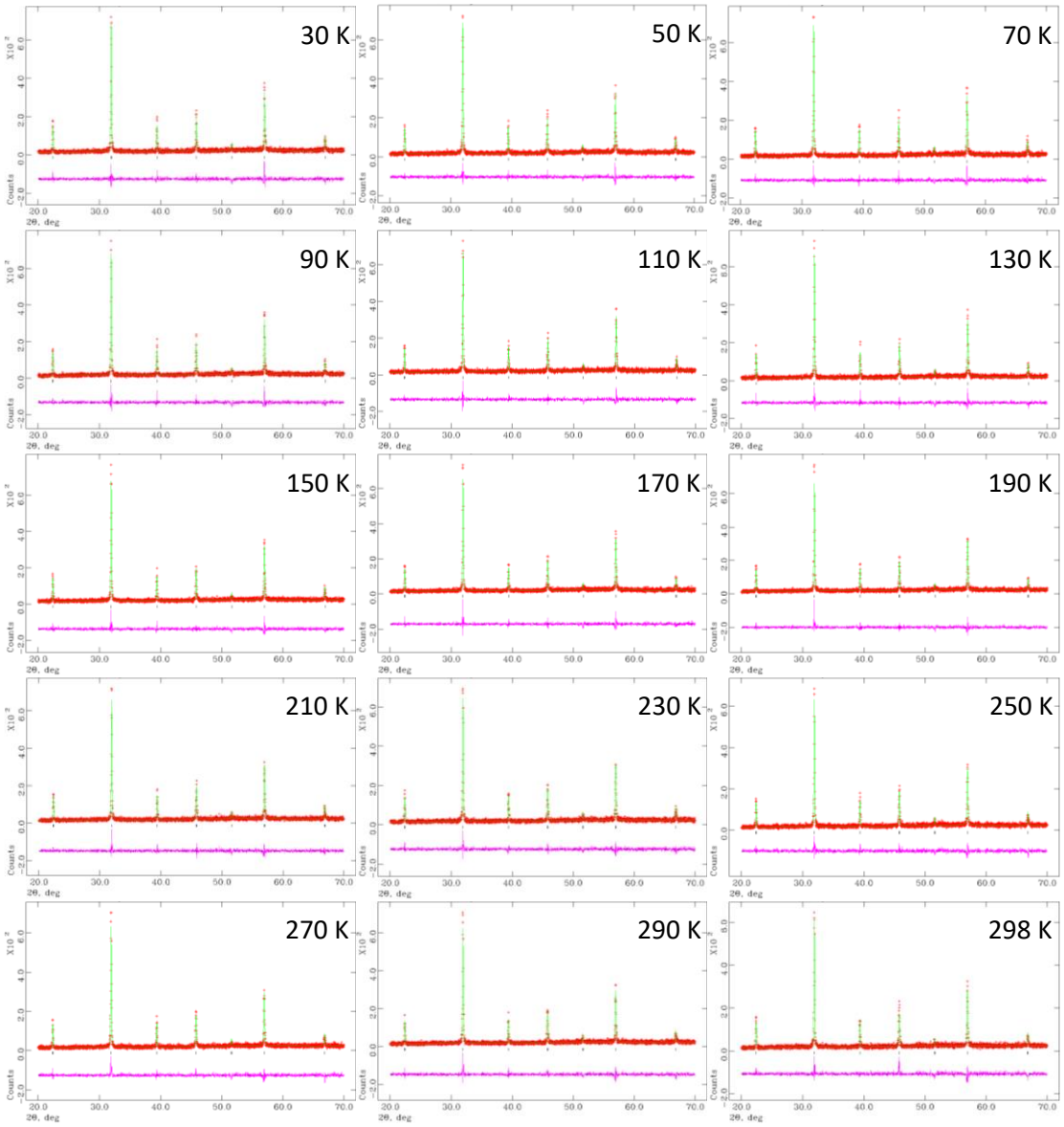

Figure A3.26: *Rietveld refinements obtained from LT PXRD of $Bi_{0.8}Na_{0.2}Fe_{0.8}Nb_{0.2}O_3$ in the temperature ranges 30 K to 298 K.*

Table A3.5: *Rietveld refinement parameters for LT XRD of $Bi_{0.8}Na_{0.2}Fe_{0.8}Nb_{0.2}O_3$.*

Parameter		$Bi_{0.8}Na_{0.2}Fe_{0.8}Nb_{0.2}O_3$															
Temperature (K)		12	30	50	70	90	110	130	150	170	190	210	230	250	270	290	298
Space Group		*P 4mm*	*P 4mm*	*P 4mm*	*P 4mm*	*P 4mm*	*P 4mm*	*P 4mm*	*P 4mm*	*P 4mm*	*P 4mm*	*P 4mm*	*P 4mm*	*P 4mm*	*P 4mm*	*P 4mm*	*P 4mm*
χ^2		1.742	1.261	1.227	1.288	1.253	1.290	1.232	1.201	1.234	1.296	1.198	1.225	1.288	1.230	1.203	1.244
wRp (%)		8.38	21.61	21.44	21.90	21.68	22.03	21.55	21.22	21.58	21.93	21.15	21.34	22.02	21.48	21.26	21.60
Rp (%)		6.48	16.54	16.42	16.70	16.40	16.91	16.46	16.37	16.70	16.73	16.14	16.23	16.86	16.45	16.15	16.61
a (Å)		3.94431(13)	3.94405(34)	3.94374(34)	3.94420(34)	3.94400(32)	3.94461(33)	3.94532(35)	3.94509(31)	3.94630(35)	3.94657(34)	3.94677(32)	3.94746(32)	3.94832(33)	3.94812(32)	3.94940(33)	3.94989(33)
b (Å)		3.94431(13)	3.94405(34)	3.94374(34)	3.94420(34)	3.94400(32)	3.94461(33)	3.94532(35)	3.94509(31)	3.94630(35)	3.94657(34)	3.94677(32)	3.94746(32)	3.94832(33)	3.94812(32)	3.94940(33)	3.94989(33)
c (Å)		3.94729(12)	3.94797(32)	3.94749(32)	3.94814(33)	3.94857(31)	3.94924(31)	3.94908(33)	3.94984(29)	3.94995(33)	3.95068(33)	3.95160(30)	3.95264(30)	3.95321(32)	3.95360(30)	3.95416(31)	3.95562(30)
α (°)		90.000	90.000	90.000	90.000	90.000	90.000	90.000	90.000	90.000	90.000	90.000	90.000	90.000	90.000	90.000	90.000
β (°)		90.000	90.000	90.000	90.000	90.000	90.000	90.000	90.000	90.000	90.000	90.000	90.000	90.000	90.000	90.000	90.000
γ (°)		90.000	90.000	90.000	90.000	90.000	90.000	90.000	90.000	90.000	90.000	90.000	90.000	90.000	90.000	90.000	90.000
Cell vol. (Å3)		61.4104(34)	61.413(9)	61.396(9)	61.420(9)	61.421(9)	61.450(9)	61.470(9)	61.474(8)	61.514(9)	61.533(9)	61.554(8)	61.592(8)	61.628(9)	61.627(8)	61.676(9)	61.714(9)
Bi/Na 1	x	0.000	0.000	0.000	0.000	0.000	0.000	0.000	0.000	0.000	0.000	0.000	0.000	0.000	0.000	0.000	0.000
	y	0.000	0.000	0.000	0.000	0.000	0.000	0.000	0.000	0.000	0.000	0.000	0.000	0.000	0.000	0.000	0.000
	z	0.000	0.000	0.000	0.000	0.000	0.000	0.000	0.000	0.000	0.000	0.000	0.000	0.000	0.000	0.000	0.000
Fe/Nb 1	x	0.500	0.500	0.500	0.500	0.500	0.500	0.500	0.500	0.500	0.500	0.500	0.500	0.500	0.500	0.500	0.500
	y	0.500	0.500	0.500	0.500	0.500	0.500	0.500	0.500	0.500	0.500	0.500	0.500	0.500	0.500	0.500	0.500
	z	0.497(4)	0.497(4)	0.497(4)	0.497(4)	0.497(4)	0.497(4)	0.497(4)	0.497(4)	0.497(4)	0.497(4)	0.497(4)	0.497(4)	0.497(4)	0.497(4)	0.497(4)	0.497(4)
O1	x	0.500	0.500	0.500	0.500	0.500	0.500	0.500	0.500	0.500	0.500	0.500	0.500	0.500	0.500	0.500	0.500
	y	0.500	0.500	0.500	0.500	0.500	0.500	0.500	0.500	0.500	0.500	0.500	0.500	0.500	0.500	0.500	0.500
	z	0.0407(81)	0.0407(81)	0.0407(81)	0.0407(81)	0.0407(81)	0.0407(81)	0.0407(81)	0.0407(81)	0.0407(81)	0.0407(81)	0.0407(81)	0.0407(81)	0.0407(81)	0.0407(81)	0.0407(81)	0.0407(81)
O2	x	0.500	0.500	0.500	0.500	0.500	0.500	0.500	0.500	0.500	0.500	0.500	0.500	0.500	0.500	0.500	0.500
	y	0.000	0.000	0.000	0.000	0.000	0.000	0.000	0.000	0.000	0.000	0.000	0.000	0.000	0.000	0.000	0.000
	z	0.6276(27)	0.6276(27)	0.6276(27)	0.6276(27)	0.6276(27)	0.6276(27)	0.6276(27)	0.6276(27)	0.6276(27)	0.6276(27)	0.6276(27)	0.6276(27)	0.6276(27)	0.6276(27)	0.6276(27)	0.6276(27)
Nb/Fe – O bond length (Å)		1.80(4)	1.80(4)	1.80(4)	1.80(4)	1.80(4)	1.80(4)	1.80(4)	1.80(4)	1.80(4)	1.80(4)	1.80(4)	1.80(4)	1.80(4)	1.80(4)	1.80(4)	1.80(4)
		2.15(4)	2.15(4)	2.15(4)	2.15(4)	2.15(4)	2.15(4)	2.15(4)	2.15(4)	2.15(4)	2.15(4)	2.15(4)	2.15(4)	2.15(4)	2.15(4)	2.15(4)	2.15(4)
		2.039(6)	2.039(6)	2.039(6)	2.039(6)	2.039(6)	2.039(6)	2.039(6)	2.039(6)	2.039(6)	2.039(6)	2.039(6)	2.039(6)	2.039(6)	2.039(6)	2.039(6)	2.039(6)
		2.039(6)	2.039(6)	2.039(6)	2.039(6)	2.039(6)	2.039(6)	2.039(6)	2.039(6)	2.039(6)	2.039(6)	2.039(6)	2.039(6)	2.039(6)	2.039(6)	2.039(6)	2.039(6)
		2.039(6)	2.039(6)	2.039(6)	2.039(6)	2.039(6)	2.039(6)	2.039(6)	2.039(6)	2.039(6)	2.039(6)	2.039(6)	2.039(6)	2.039(6)	2.039(6)	2.039(6)	2.039(6)
		2.039(6)	2.039(6)	2.039(6)	2.039(6)	2.039(6)	2.039(6)	2.039(6)	2.039(6)	2.039(6)	2.039(6)	2.039(6)	2.039(6)	2.039(6)	2.039(6)	2.039(6)	2.039(6)
Nb/Fe – O – Nb/Fe bond angle (o)		180.000(0)	180.000(0)	180.000(0)	180.000(0)	180.000(0)	180.000(0)	180.000(0)	180.000(0)	180.000(0)	180.000(0)	180.000(0)	180.000(0)	180.000(0)	180.000(0)	180.000(0)	180.000(0)
		150.6(12)	150.6(12)	150.6(12)	150.6(12)	150.6(12)	150.6(12)	150.6(12)	150.6(12)	150.6(12)	150.6(12)	150.6(12)	150.6(12)	150.6(12)	150.6(12)	150.6(12)	150.6(12)

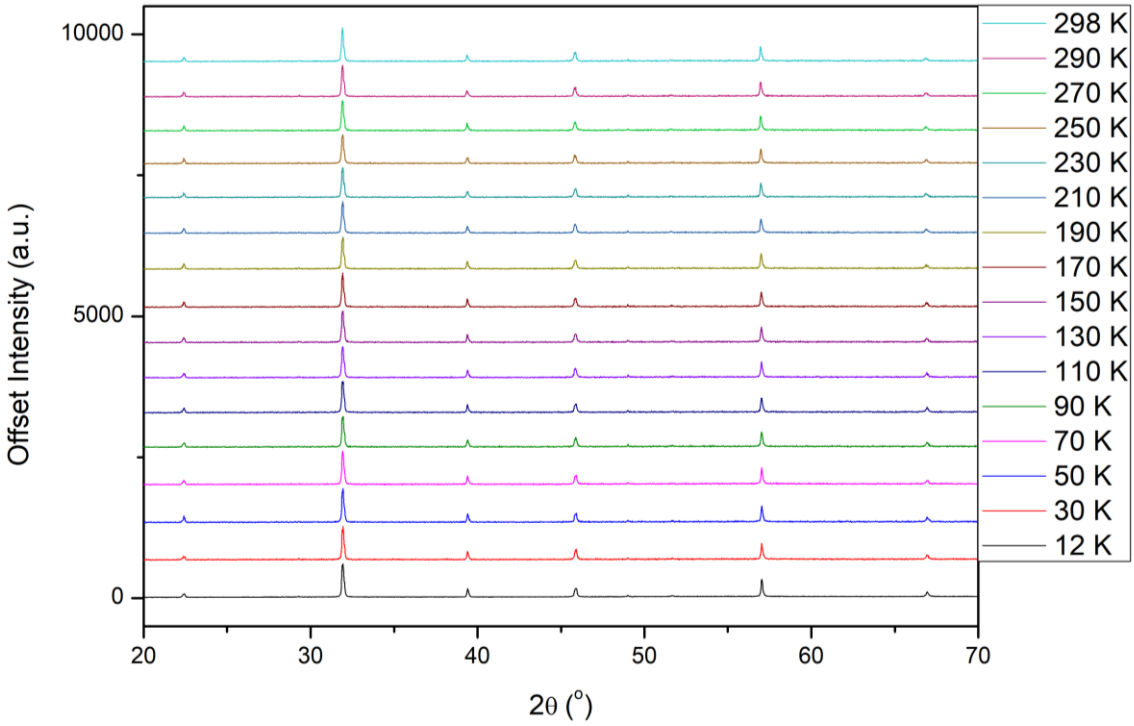

Figure A3.27: *All patterns for the LT PXRD of $Bi_{0.75}Na_{0.25}Fe_{0.75}Nb_{0.25}O_3$. 12K pattern intensity has been scaled down to match the intensities of the other temperature points that were taken with shorter scan times.*

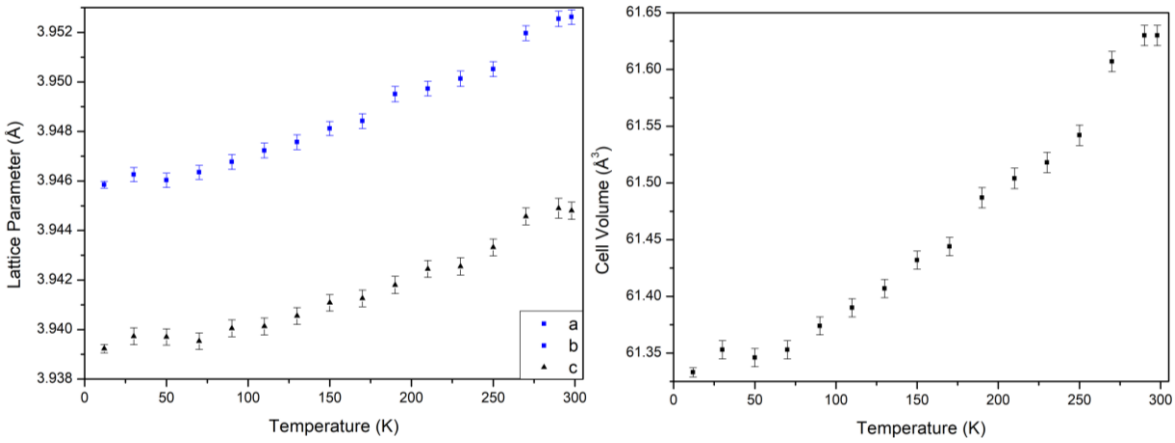

Figure A3.28: *LT PXRD of $Bi_{0.75}Na_{0.25}Fe_{0.75}Nb_{0.25}O_3$: (a) Lattice Parameter against temperature plot, (b) Cell Volume against temperature plot.*

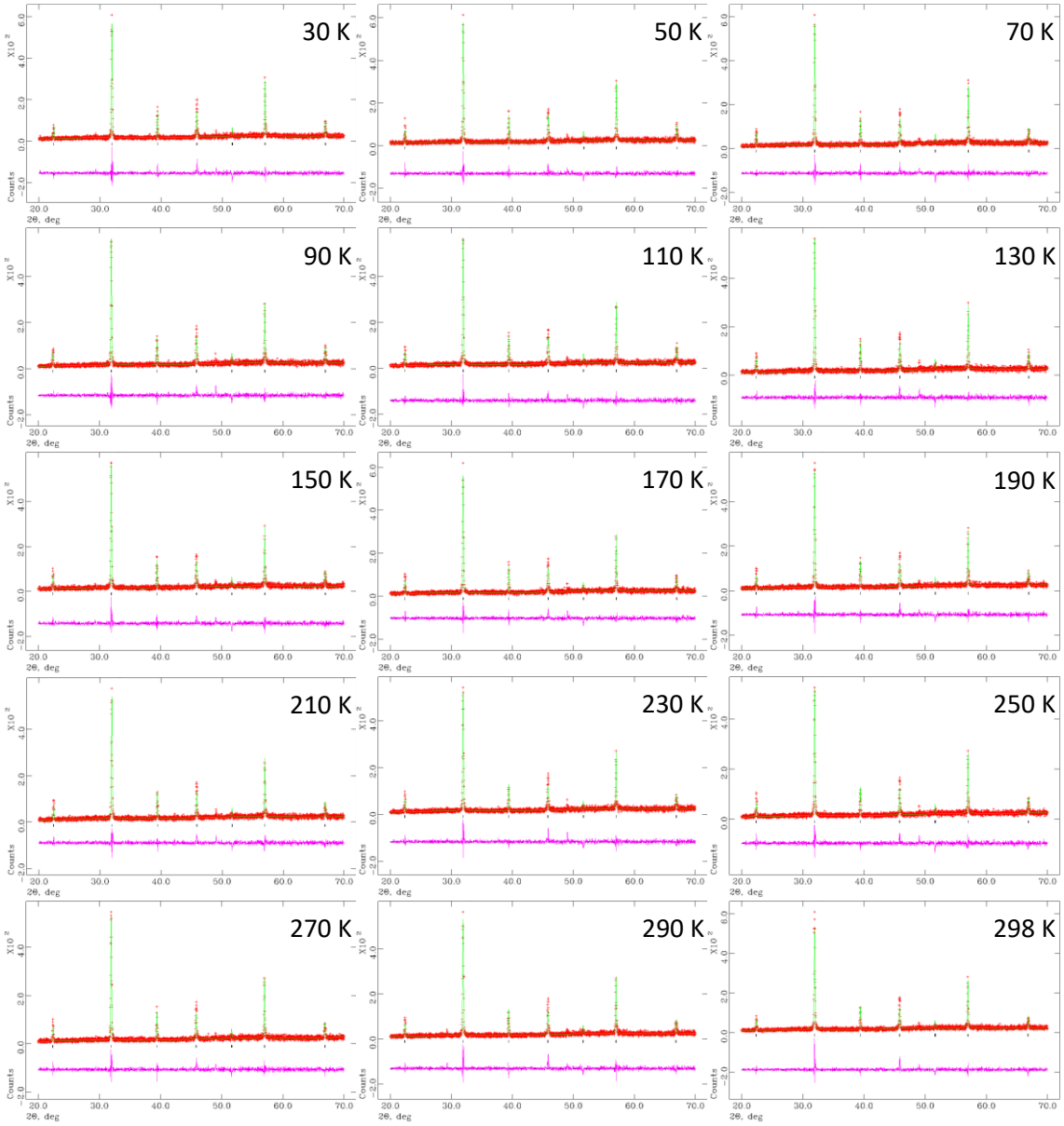

Figure A3.29: *Rietveld refinements obtained from LT PXRD of $Bi_{0.75}Na_{0.25}Fe_{0.75}Nb_{0.25}O_3$ in the temperature ranges 30 K to 298 K.*

Table A3.6: *Rietveld refinement parameters for LT XRD of $Bi_{0.75}Na_{0.25}Fe_{0.75}Nb_{0.25}O_3$.*

Parameter		$Bi_{0.75}Na_{0.25}Fe_{0.75}Nb_{0.25}O_3$															
Temperature (K)		12	30	50	70	90	110	130	150	170	190	210	230	250	270	290	298
Space Group		*P 4mm*	*P 4mm*	*P 4mm*	*P 4mm*	*P 4mm*	*P 4mm*	*P 4mm*	*P 4mm*	*P 4mm*	*P 4mm*	*P 4mm*	*P 4mm*	*P 4mm*	*P 4mm*	*P 4mm*	*P 4mm*
χ^2		2.485	1.350	1.318	1.300	1.354	1.401	1.369	1.363	1.352	1.374	1.361	1.340	1.299	1.296	1.361	1.355
wRp (%)		10.23	23.29	22.90	22.79	23.29	23.49	23.38	23.34	23.23	23.56	23.51	23.56	23.09	23.08	23.72	23.62
Rp (%)		7.64	18.18	18.15	17.88	18.28	18.25	18.36	18.34	18.10	18.23	18.29	18.52	17.92	18.11	18.73	18.45
a (Å)		3.94585(14)	3.94626(29)	3.94603(29)	3.94635(28)	3.94677(30)	3.94723(30)	3.94757(30)	3.94812(29)	3.94842(30)	3.94951(31)	3.94973(30)	3.95013(31)	3.95052(30)	3.95197(30)	3.95255(31)	3.95262(30)
b (Å)		3.94585(14)	3.94626(29)	3.94603(29)	3.94635(28)	3.94677(30)	3.94723(30)	3.94757(30)	3.94812(29)	3.94842(30)	3.94951(31)	3.94973(30)	3.95013(31)	3.95052(30)	3.95197(30)	3.95255(31)	3.95262(30)
c (Å)		3.93923(17)	3.93973(34)	3.93970(33)	3.93953(33)	3.94005(34)	3.94013(34)	3.94055(34)	3.94108(33)	3.94126(34)	3.94180(35)	3.94245(34)	3.94255(35)	3.94332(34)	3.94457(34)	3.9449(4)	3.94480(35)
α (°)		90.000	90.000	90.000	90.000	90.000	90.000	90.000	90.000	90.000	90.000	90.000	90.000	90.000	90.000	90.000	90.000
β (°)		90.000	90.000	90.000	90.000	90.000	90.000	90.000	90.000	90.000	90.000	90.000	90.000	90.000	90.000	90.000	90.000
γ (°)		90.000	90.000	90.000	90.000	90.000	90.000	90.000	90.000	90.000	90.000	90.000	90.000	90.000	90.000	90.000	90.000
Cell vol. (Å3)		61.333(4)	61.353(8)	61.346(8)	61.353(8)	61.374(8)	61.390(8)	61.407(8)	61.432(8)	61.444(8)	61.487(9)	61.504(9)	61.518(9)	61.542(9)	61.607(9)	61.630(9)	61.630(9)
Bi/Na 1	x	0.000	0.000	0.000	0.000	0.000	0.000	0.000	0.000	0.000	0.000	0.000	0.000	0.000	0.000	0.000	0.000
	y	0.000	0.000	0.000	0.000	0.000	0.000	0.000	0.000	0.000	0.000	0.000	0.000	0.000	0.000	0.000	0.000
	z	0.000	0.000	0.000	0.000	0.000	0.000	0.000	0.000	0.000	0.000	0.000	0.000	0.000	0.000	0.000	0.000
Fe/Nb 1	x	0.500	0.500	0.500	0.500	0.500	0.500	0.500	0.500	0.500	0.500	0.500	0.500	0.500	0.500	0.500	0.500
	y	0.500	0.500	0.500	0.500	0.500	0.500	0.500	0.500	0.500	0.500	0.500	0.500	0.500	0.500	0.500	0.500
	z	0.519(4)	0.519(4)	0.519(4)	0.519(4)	0.519(4)	0.519(4)	0.519(4)	0.519(4)	0.519(4)	0.519(4)	0.519(4)	0.519(4)	0.519(4)	0.519(4)	0.519(4)	0.519(4)
O1	x	0.500	0.500	0.500	0.500	0.500	0.500	0.500	0.500	0.500	0.500	0.500	0.500	0.500	0.500	0.500	0.500
	y	0.500	0.500	0.500	0.500	0.500	0.500	0.500	0.500	0.500	0.500	0.500	0.500	0.500	0.500	0.500	0.500
	z	-0.003(33)	-0.003(33)	-0.003(33)	-0.003(33)	-0.003(33)	-0.003(33)	-0.003(33)	-0.003(33)	-0.003(33)	-0.003(33)	-0.003(33)	-0.003(33)	-0.003(33)	-0.003(33)	-0.003(33)	-0.003(33)
O2	x	0.500	0.500	0.500	0.500	0.500	0.500	0.500	0.500	0.500	0.500	0.500	0.500	0.500	0.500	0.500	0.500
	y	0.000	0.000	0.000	0.000	0.000	0.000	0.000	0.000	0.000	0.000	0.000	0.000	0.000	0.000	0.000	0.000
	z	0.435(6)	0.435(6)	0.435(6)	0.435(6)	0.435(6)	0.435(6)	0.435(6)	0.435(6)	0.435(6)	0.435(6)	0.435(6)	0.435(6)	0.435(6)	0.435(6)	0.435(6)	0.435(6)
Nb/Fe – O bond length (Å)		1.88(13)	1.88(13)	1.88(13)	1.88(13)	1.88(13)	1.88(13)	1.88(13)	1.88(13)	1.88(13)	1.88(13)	1.88(13)	1.88(13)	1.88(13)	1.88(13)	1.88(13)	1.88(13)
		2.06(13)	2.06(13)	2.06(13)	2.06(13)	2.06(13)	2.06(13)	2.06(13)	2.06(13)	2.06(13)	2.06(13)	2.06(13)	2.06(13)	2.06(13)	2.06(13)	2.06(13)	2.06(13)
		2.000(5)	2.000(5)	2.000(5)	2.000(5)	2.000(5)	2.000(5)	2.000(5)	2.000(5)	2.000(5)	2.000(5)	2.000(5)	2.000(5)	2.000(5)	2.000(5)	2.000(5)	2.000(5)
		2.000(5)	2.000(5)	2.000(5)	2.000(5)	2.000(5)	2.000(5)	2.000(5)	2.000(5)	2.000(5)	2.000(5)	2.000(5)	2.000(5)	2.000(5)	2.000(5)	2.000(5)	2.000(5)
		2.000(5)	2.000(5)	2.000(5)	2.000(5)	2.000(5)	2.000(5)	2.000(5)	2.000(5)	2.000(5)	2.000(5)	2.000(5)	2.000(5)	2.000(5)	2.000(5)	2.000(5)	2.000(5)
		2.000(5)	2.000(5)	2.000(5)	2.000(5)	2.000(5)	2.000(5)	2.000(5)	2.000(5)	2.000(5)	2.000(5)	2.000(5)	2.000(5)	2.000(5)	2.000(5)	2.000(5)	2.000(5)
Nb/Fe – O – Nb/Fe bond angle (o)		180.000(0)	180.000(0)	180.000(0)	180.000(0)	180.000(0)	180.000(0)	180.000(0)	180.000(0)	180.000(0)	180.000(0)	180.000(0)	180.000(0)	180.000(0)	180.000(0)	180.000(0)	180.000(0)
		161.0(16)	161.0(16)	161.0(16)	161.0(16)	161.0(16)	161.0(16)	161.0(16)	161.0(16)	161.0(16)	161.0(16)	161.0(16)	161.0(16)	161.0(16)	161.0(16)	161.0(16)	161.0(16)

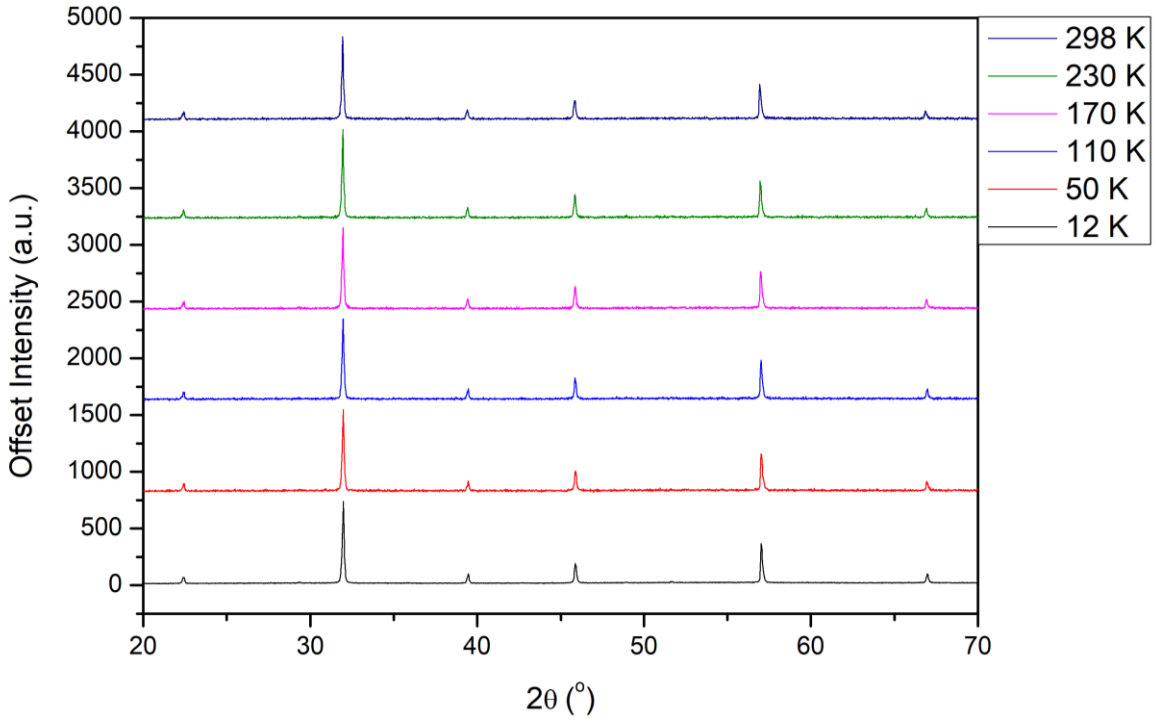

Figure A3.30: *Selection of patterns for the LT PXRD of $Bi_{0.7}Na_{0.3}Fe_{0.7}Nb_{0.3}O_3$. 12K pattern intensity has been scaled down to match the intensities of the other temperature points that were taken with shorter scan times.*

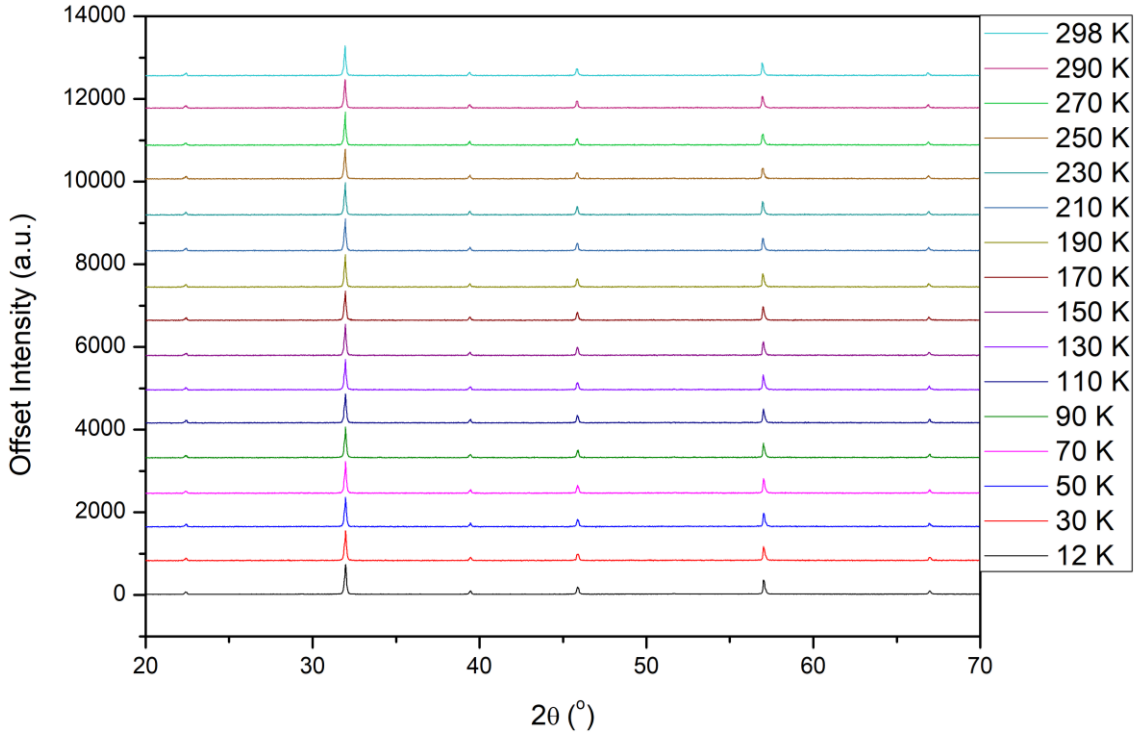

Figure A3.31: *All patterns for the LT PXRD of $Bi_{0.7}Na_{0.3}Fe_{0.7}Nb_{0.3}O_3$. 12K pattern intensity has been scaled down to match the intensities of the other temperature points that were taken with shorter scan times.*

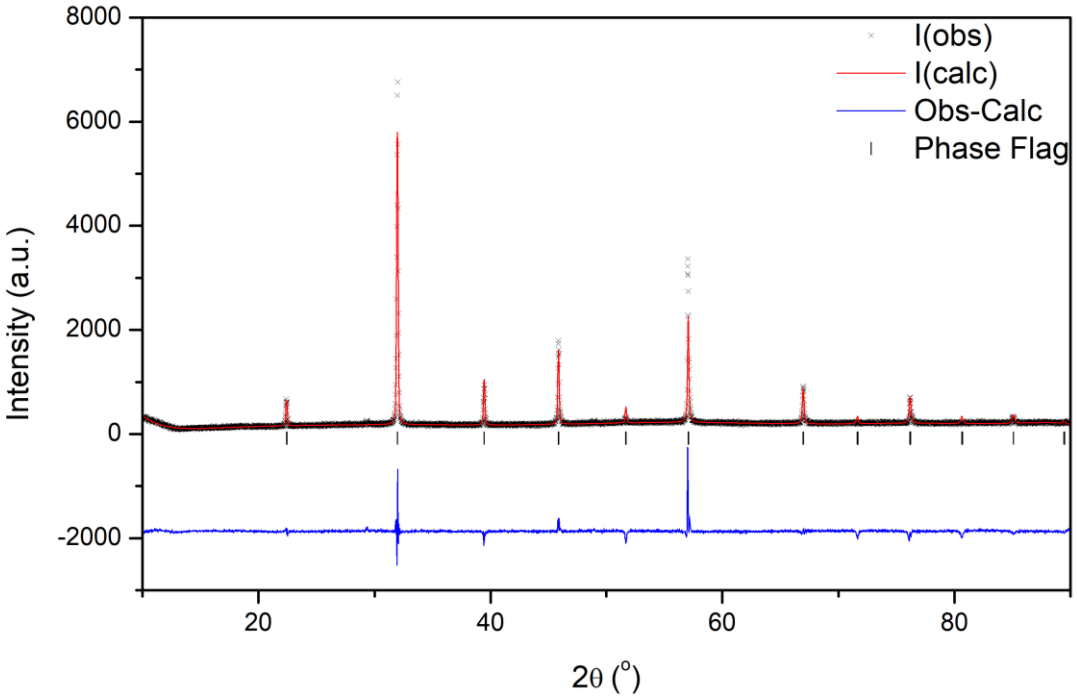

Figure A3.32: *Rietveld refinement of 12 K PXRD data collected for $Bi_{0.7}Na_{0.3}Fe_{0.7}Nb_{0.3}O_3$; χ^2 = 1.873, R_{wp} = 9.15% and R_p = 7.11; the black crosses represent the observed intensity, the red line represents the calculated intensity from the model, the blue line represents the difference between the observed pattern and calculated pattern, the black tick marker represents the P4mm model.*

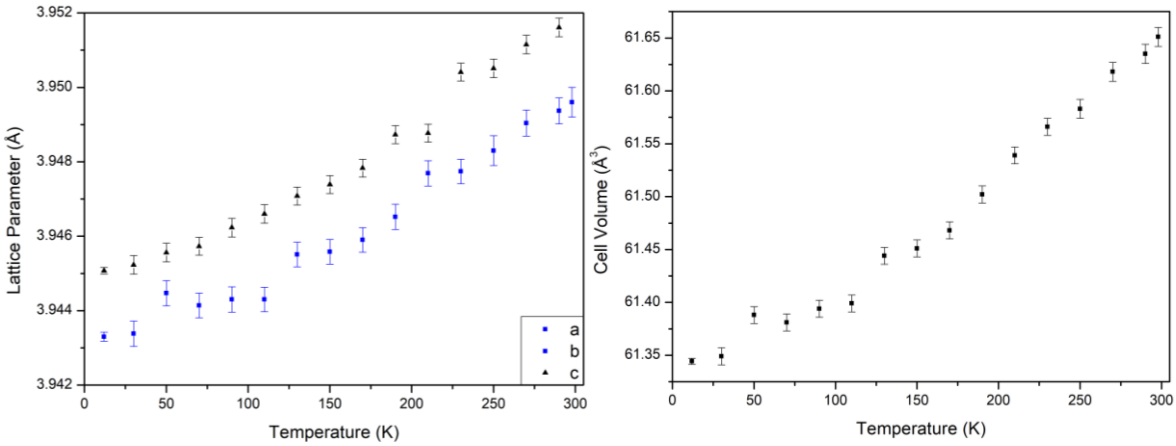

Figure A3.33: *LT PXRD of $Bi_{0.7}Na_{0.3}Fe_{0.7}Nb_{0.3}O_3$: (a) Lattice Parameter against temperature plot, (b) Cell Volume against temperature plot.*

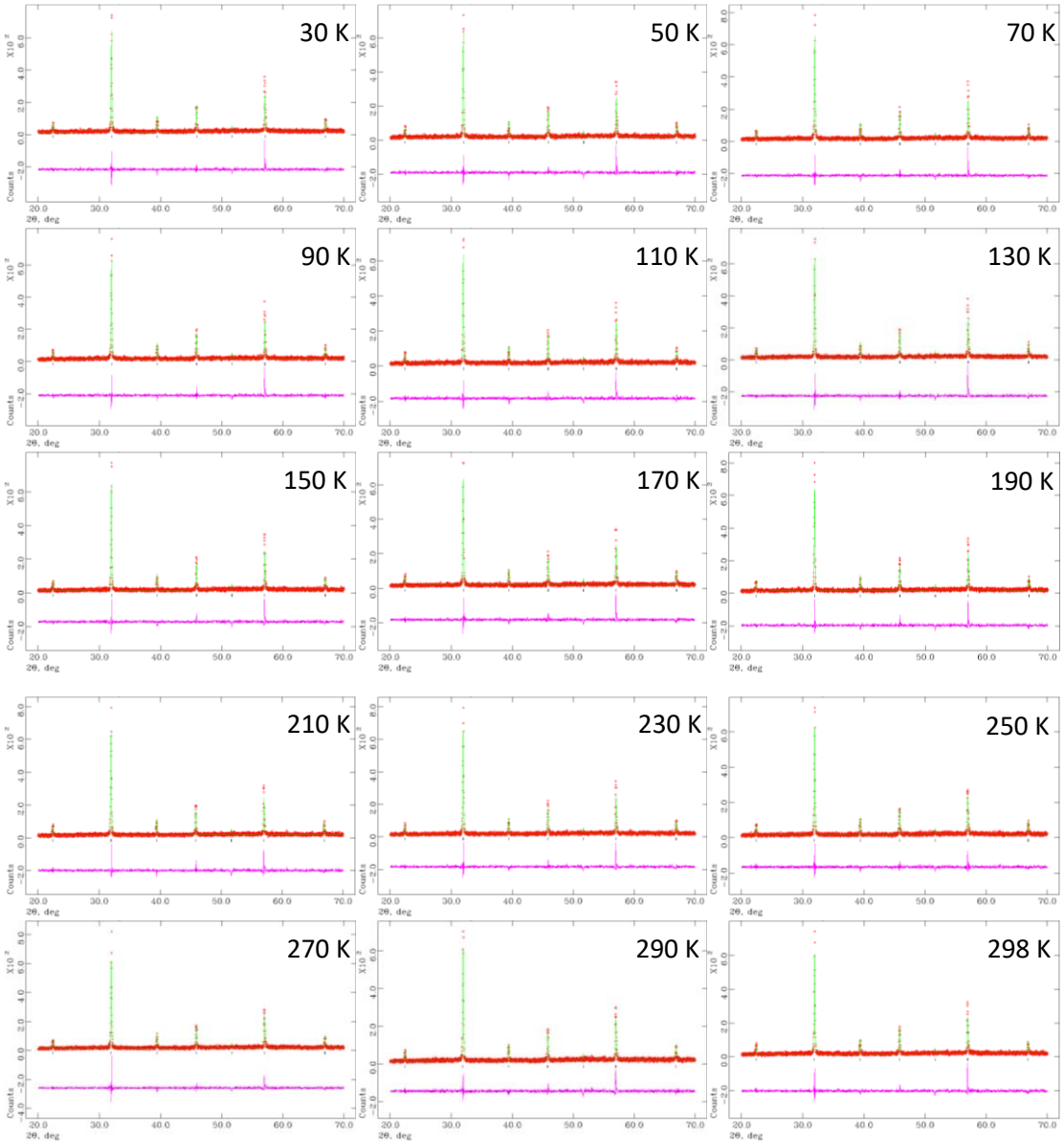

Figure A3.34: *Rietveld refinements obtained from LT PXRD of $Bi_{0.7}Na_{0.3}Fe_{0.7}Nb_{0.3}O_3$ in the temperature ranges 30 K to 298 K.*

Table A3.7: *Rietveld refinement parameters for LT XRD of $Bi_{0.7}Na_{0.3}Fe_{0.7}Nb_{0.3}O_3$.*

Parameter		$Bi_{0.7}Na_{0.3}Fe_{0.7}Nb_{0.3}O_3$															
Temperature (K)		12	30	50	70	90	110	130	150	170	190	210	230	250	270	290	298
Space Group		*P 4mm*	*P 4mm*	*P 4mm*	*P 4mm*	*P 4mm*	*P 4mm*	*P 4mm*	*P 4mm*	*P 4mm*	*P 4mm*	*P 4mm*	*P 4mm*	*P 4mm*	*P 4mm*	*P 4mm*	*P 4mm*
χ^2		1.873	1.305	1.333	1.282	1.310	1.322	1.252	1.302	1.282	1.282	1.294	1.295	1.315	1.298	1.311	1.328
wRp (%)		9.15	22.93	23.16	22.61	22.88	22.94	22.33	22.83	22.61	22.48	22.70	22.70	22.97	22.82	22.91	23.17
Rp (%)		7.11	18.04	17.85	17.59	17.55	17.65	17.48	17.79	17.53	17.55	17.37	17.46	17.79	17.50	17.67	17.69
a (Å)		3.94330(12)	3.94338(34)	3.94447(34)	3.94414(33)	3.94430(34)	3.94430(33)	3.94551(33)	3.94558(33)	3.94590(33)	3.94652(34)	3.94769(34)	3.94774(33)	3.9483(4)	3.94904(35)	3.94937(35)	3.9496(4)
b (Å)		3.94330(12)	3.94338(34)	3.94447(34)	3.94414(33)	3.94430(34)	3.94430(33)	3.94551(33)	3.94558(33)	3.94590(33)	3.94652(34)	3.94769(34)	3.94774(33)	3.9483(4)	3.94904(35)	3.94937(35)	3.9496(4)
c (Å)		3.94507(9)	3.94523(25)	3.94556(25)	3.94573(24)	3.94623(25)	3.94660(25)	3.94708(24)	3.94739(24)	3.94783(24)	3.94873(24)	3.94877(24)	3.95041(24)	3.95051(25)	3.95115(25)	3.95161(25)	3.95220(25)
α (°)		90.000	90.000	90.000	90.000	90.000	90.000	90.000	90.000	90.000	90.000	90.000	90.000	90.000	90.000	90.000	90.000
β (°)		90.000	90.000	90.000	90.000	90.000	90.000	90.000	90.000	90.000	90.000	90.000	90.000	90.000	90.000	90.000	90.000
γ (°)		90.000	90.000	90.000	90.000	90.000	90.000	90.000	90.000	90.000	90.000	90.000	90.000	90.000	90.000	90.000	90.000
Cell vol. (Å3)		61.3443(30)	61.349(8)	61.388(8)	61.381(8)	61.394(8)	61.399(8)	61.444(8)	61.451(8)	61.468(8)	61.502(8)	61.539(8)	61.566(8)	61.583(9)	61.618(9)	61.635(9)	61.651(9)
Bi/Na 1	x	0.000	0.000	0.000	0.000	0.000	0.000	0.000	0.000	0.000	0.000	0.000	0.000	0.000	0.000	0.000	0.000
	y	0.000	0.000	0.000	0.000	0.000	0.000	0.000	0.000	0.000	0.000	0.000	0.000	0.000	0.000	0.000	0.000
	z	0.000	0.000	0.000	0.000	0.000	0.000	0.000	0.000	0.000	0.000	0.000	0.000	0.000	0.000	0.000	0.000
Fe/Nb 1	x	0.500	0.500	0.500	0.500	0.500	0.500	0.500	0.500	0.500	0.500	0.500	0.500	0.500	0.500	0.500	0.500
	y	0.500	0.500	0.500	0.500	0.500	0.500	0.500	0.500	0.500	0.500	0.500	0.500	0.500	0.500	0.500	0.500
	z	0.488(4)	0.488(4)	0.488(4)	0.488(4)	0.488(4)	0.488(4)	0.488(4)	0.488(4)	0.488(4)	0.488(4)	0.488(4)	0.488(4)	0.488(4)	0.488(4)	0.488(4)	0.488(4)
O1	x	0.500	0.500	0.500	0.500	0.500	0.500	0.500	0.500	0.500	0.500	0.500	0.500	0.500	0.500	0.500	0.500
	y	0.500	0.500	0.500	0.500	0.500	0.500	0.500	0.500	0.500	0.500	0.500	0.500	0.500	0.500	0.500	0.500
	z	-0.009(22)	-0.009(22)	-0.009(22)	-0.009(22)	-0.009(22)	-0.009(22)	-0.009(22)	-0.009(22)	-0.009(22)	-0.009(22)	-0.009(22)	-0.009(22)	-0.009(22)	-0.009(22)	-0.009(22)	-0.009(22)
O2	x	0.500	0.500	0.500	0.500	0.500	0.500	0.500	0.500	0.500	0.500	0.500	0.500	0.500	0.500	0.500	0.500
	y	0.000	0.000	0.000	0.000	0.000	0.000	0.000	0.000	0.000	0.000	0.000	0.000	0.000	0.000	0.000	0.000
	z	0.692(6)	0.692(6)	0.692(6)	0.692(6)	0.692(6)	0.692(6)	0.692(6)	0.692(6)	0.692(6)	0.692(6)	0.692(6)	0.692(6)	0.692(6)	0.692(6)	0.692(6)	0.692(6)
Nb/Fe – O bond length (Å)		1.96(9)	1.96(9)	1.96(9)	1.96(9)	1.96(9)	1.96(9)	1.96(9)	1.96(9)	1.96(9)	1.96(9)	1.96(9)	1.96(9)	1.96(9)	1.96(9)	1.96(9)	1.96(9)
		1.99(9)	1.99(9)	1.99(9)	1.99(9)	1.99(9)	1.99(9)	1.99(9)	1.99(9)	1.99(9)	1.99(9)	1.99(9)	1.99(9)	1.99(9)	1.99(9)	1.99(9)	1.99(9)
		2.131(14)	2.131(14)	2.131(14)	2.131(14)	2.131(14)	2.131(14)	2.131(14)	2.131(14)	2.131(14)	2.131(14)	2.131(14)	2.131(14)	2.131(14)	2.131(14)	2.131(14)	2.131(14)
		2.131(14)	2.131(14)	2.131(14)	2.131(14)	2.131(14)	2.131(14)	2.131(14)	2.131(14)	2.131(14)	2.131(14)	2.131(14)	2.131(14)	2.131(14)	2.131(14)	2.131(14)	2.131(14)
		2.131(14)	2.131(14)	2.131(14)	2.131(14)	2.131(14)	2.131(14)	2.131(14)	2.131(14)	2.131(14)	2.131(14)	2.131(14)	2.131(14)	2.131(14)	2.131(14)	2.131(14)	2.131(14)
		2.131(14)	2.131(14)	2.131(14)	2.131(14)	2.131(14)	2.131(14)	2.131(14)	2.131(14)	2.131(14)	2.131(14)	2.131(14)	2.131(14)	2.131(14)	2.131(14)	2.131(14)	2.131(14)
Nb/Fe – O – Nb/Fe bond angle (o)		180.000(0)	180.000(0)	180.000(0)	180.000(0)	180.000(0)	180.000(0)	180.000(0)	180.000(0)	180.000(0)	180.000(0)	180.000(0)	180.000(0)	180.000(0)	180.000(0)	180.000(0)	180.000(0)
		135.4(18)	135.4(18)	135.4(18)	135.4(18)	135.4(18)	135.4(18)	135.4(18)	135.4(18)	135.4(18)	135.4(18)	135.4(18)	135.4(18)	135.4(18)	135.4(18)	135.4(18)	135.4(18)

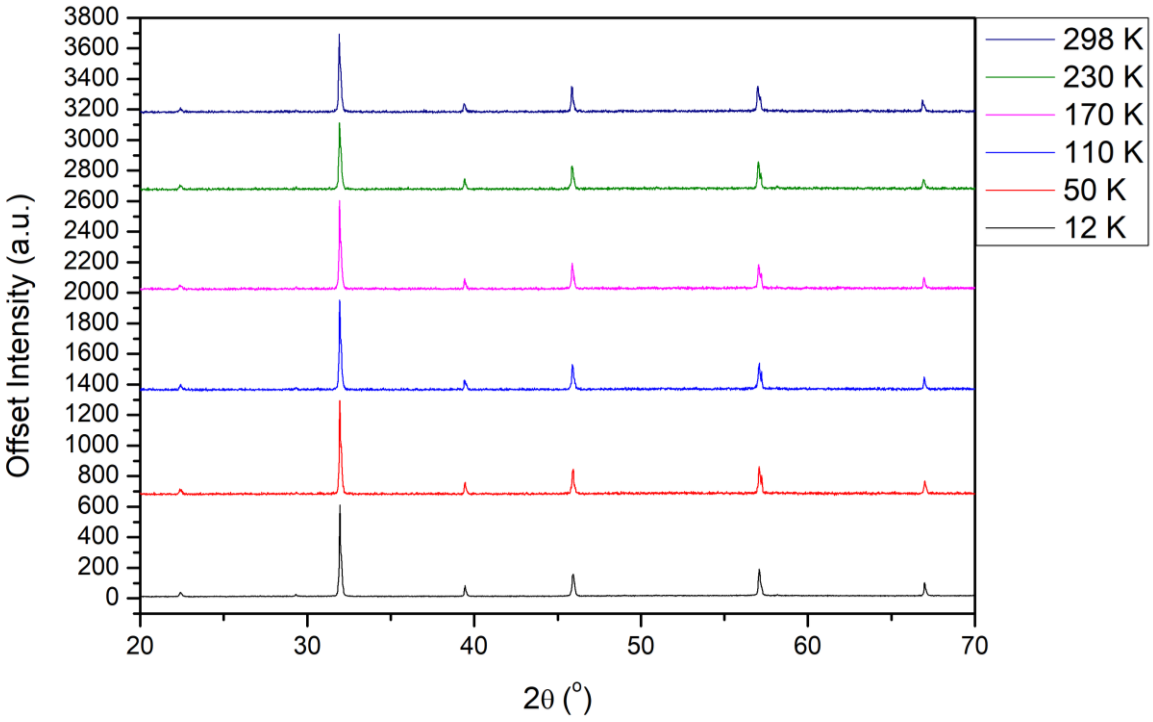

Figure A3.35: *Selection of patterns for the LT PXRD of $Bi_{0.65}Na_{0.35}Fe_{0.65}Nb_{0.35}O_3$. 12K pattern intensity has been scaled down to match the intensities of the other temperature points that were taken with shorter scan times.*

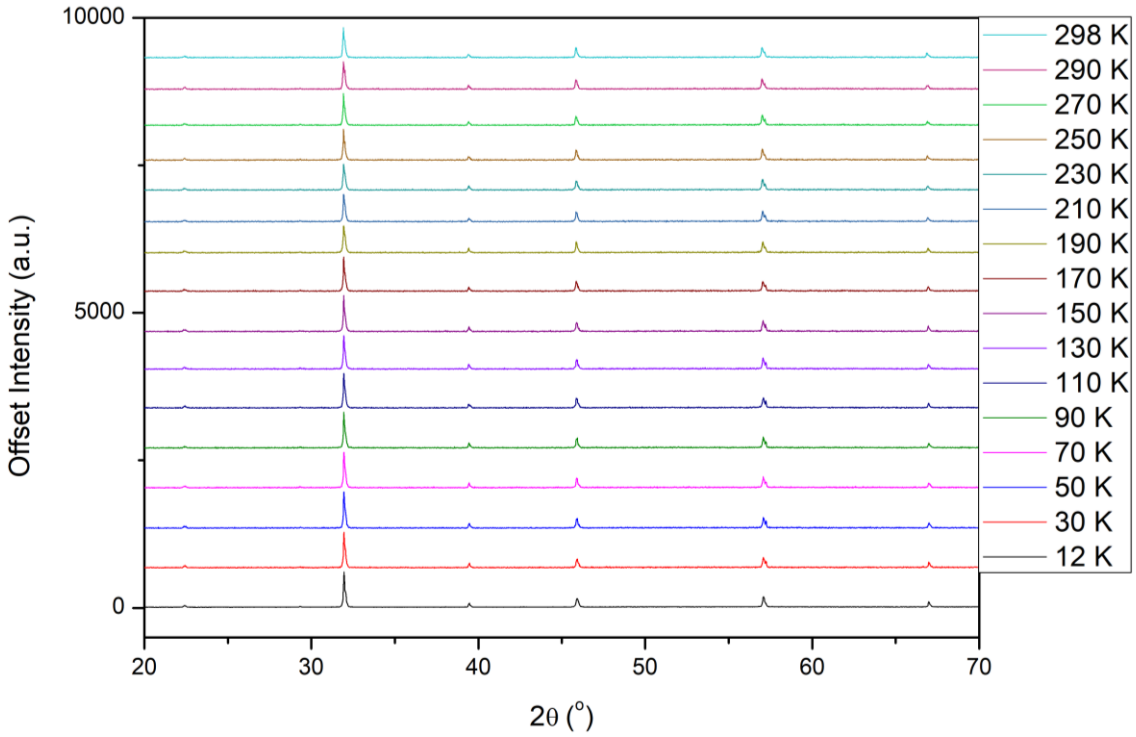

Figure A3.36: *All patterns for the LT PXRD of $Bi_{0.65}Na_{0.35}Fe_{0.65}Nb_{0.35}O_3$. 12K pattern intensity has been scaled down to match the intensities of the other temperature points that were taken with shorter scan times.*

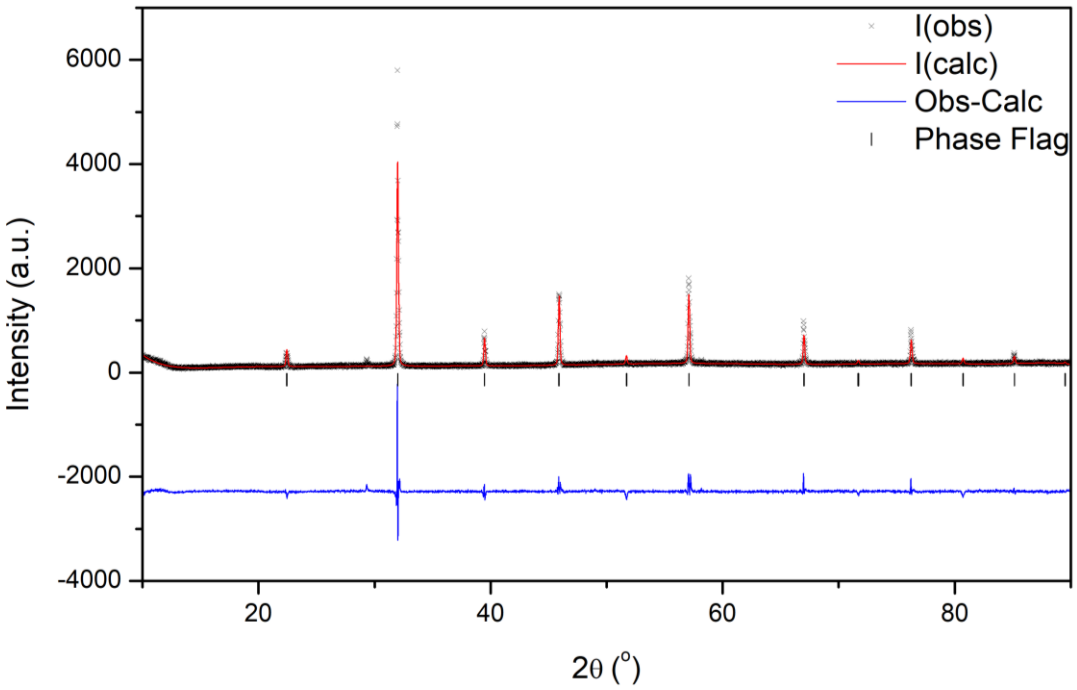

Figure A3.37: *Rietveld refinement of 12 K PXRD data collected for $Bi_{0.65}Na_{0.35}Fe_{0.65}Nb_{0.35}O_3$; χ^2 = 2.421, Rwp = 11.80% and Rp = 8.84; the black crosses represent the observed intensity, the red line represents the calculated intensity from the model, the blue line represents the difference between the observed pattern and calculated pattern, the black tick marker represents the P4mm model.*

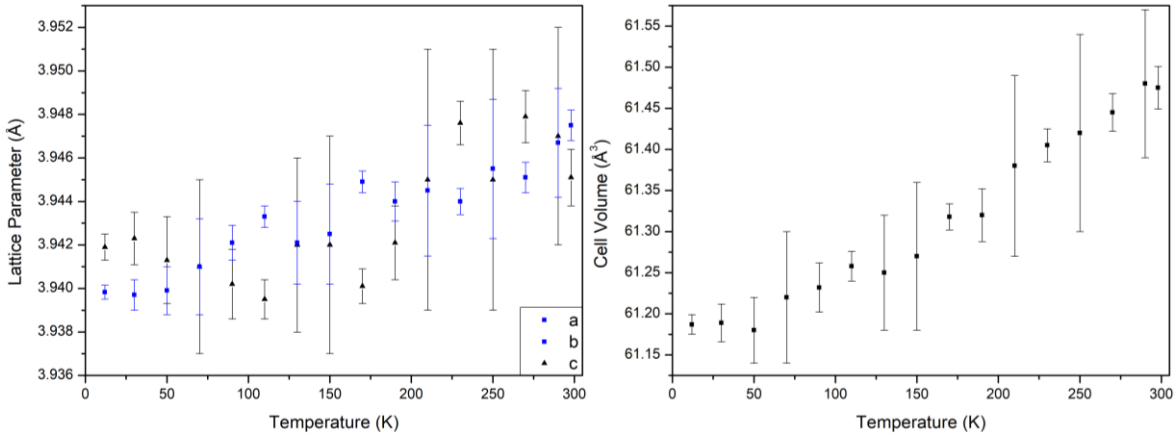

Figure A3.38: *LT PXRD of $Bi_{0.65}Na_{0.35}Fe_{0.65}Nb_{0.35}O_3$: (a) Lattice Parameter against temperature plot, (b) Cell Volume against temperature plot.*

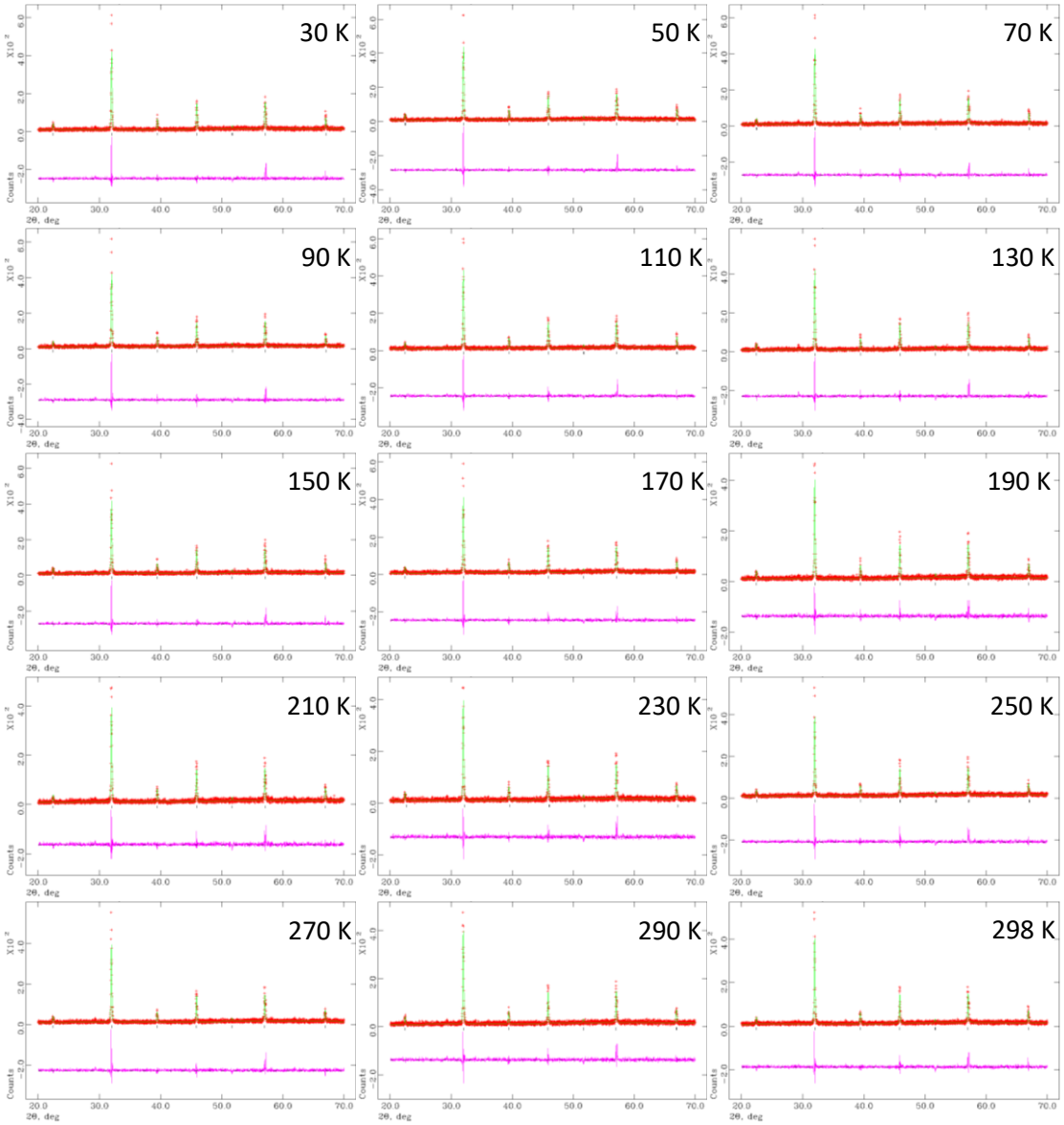

Figure A3.39: *Rietveld refinements obtained from LT PXRD of $Bi_{0.65}Na_{0.35}Fe_{0.65}Nb_{0.35}O_3$ in the temperature ranges 30 K to 298 K.*

Table A3.8: *Rietveld refinement parameters for LT XRD of $Bi_{0.65}Na_{0.35}Fe_{0.65}Nb_{0.35}O_3$.*

Parameter		$Bi_{0.65}Na_{0.35}Fe_{0.65}Nb_{0.35}O_3$															
Temperature (K)		12	30	50	70	90	110	130	150	170	190	210	230	250	270	290	298
Space Group		*P 4mm*	*P 4mm*	*P 4mm*	*P 4mm*	*P 4mm*	*P 4mm*	*P 4mm*	*P 4mm*	*P 4mm*	*P 4mm*	*P 4mm*	*P 4mm*	*P 4mm*	*P 4mm*	*P 4mm*	*P 4mm*
χ^2		2.421	1.402	1.395	1.389	1.440	1.431	1.442	1.439	1.488	1.431	1.463	1.433	1.416	1.428	1.418	1.448
wRp (%)		11.80	27.85	27.61	27.64	28.22	28.00	28.10	28.11	28.56	28.02	28.20	28.03	27.97	27.92	27.73	28.07
Rp (%)		8.84	22.01	21.86	22.11	22.38	22.16	22.25	22.37	22.68	22.28	22.60	22.22	22.53	22.33	21.88	22.45
a (Å)		3.93983(32)	3.9397(7)	3.9399(11)	3.9410(22)	3.9421(8)	3.9433(5)	3.9421(19)	3.9425(23)	3.9449(5)	3.9440(9)	3.9445(30)	3.9440(6)	3.9455(32)	3.9451(7)	3.9467(25)	3.9475(7)
b (Å)		3.93983(32)	3.9397(7)	3.9399(11)	3.9410(22)	3.9421(8)	3.9433(5)	3.9421(19)	3.9425(23)	3.9449(5)	3.9440(9)	3.9445(30)	3.9440(6)	3.9455(32)	3.9451(7)	3.9467(25)	3.9475(7)
c (Å)		3.9419(6)	3.9423(12)	3.9413(20)	3.941(4)	3.9402(16)	3.9395(9)	3.942(4)	3.942(5)	3.9401(8)	3.9421(17)	3.945(6)	3.9476(10)	3.945(6)	3.9479(12)	3.947(5)	3.9451(13)
α (°)		90.000	90.000	90.000	90.000	90.000	90.000	90.000	90.000	90.000	90.000	90.000	90.000	90.000	90.000	90.000	90.000
β (°)		90.000	90.000	90.000	90.000	90.000	90.000	90.000	90.000	90.000	90.000	90.000	90.000	90.000	90.000	90.000	90.000
γ (°)		90.000	90.000	90.000	90.000	90.000	90.000	90.000	90.000	90.000	90.000	90.000	90.000	90.000	90.000	90.000	90.000
Cell vol. (Å3)		61.187(12)	61.189(23)	61.18(4)	61.22(8)	61.232(30)	61.258(18)	61.25(7)	61.27(9)	61.318(16)	61.320(32)	61.38(11)	61.405(20)	61.42(12)	61.445(23)	61.48(9)	61.475(26)
Bi/Na 1	x	0.000	0.000	0.000	0.000	0.000	0.000	0.000	0.000	0.000	0.000	0.000	0.000	0.000	0.000	0.000	0.000
	y	0.000	0.000	0.000	0.000	0.000	0.000	0.000	0.000	0.000	0.000	0.000	0.000	0.000	0.000	0.000	0.000
	z	0.000	0.000	0.000	0.000	0.000	0.000	0.000	0.000	0.000	0.000	0.000	0.000	0.000	0.000	0.000	0.000
Fe/Nb 1	x	0.500	0.500	0.500	0.500	0.500	0.500	0.500	0.500	0.500	0.500	0.500	0.500	0.500	0.500	0.500	0.500
	y	0.500	0.500	0.500	0.500	0.500	0.500	0.500	0.500	0.500	0.500	0.500	0.500	0.500	0.500	0.500	0.500
	z	0.499(10)	0.499(10)	0.499(10)	0.499(10)	0.499(10)	0.499(10)	0.499(10)	0.499(10)	0.499(10)	0.499(10)	0.499(10)	0.499(10)	0.499(10)	0.499(10)	0.499(10)	0.499(10)
O1	x	0.500	0.500	0.500	0.500	0.500	0.500	0.500	0.500	0.500	0.500	0.500	0.500	0.500	0.500	0.500	0.500
	y	0.500	0.500	0.500	0.500	0.500	0.500	0.500	0.500	0.500	0.500	0.500	0.500	0.500	0.500	0.500	0.500
	z	0.00(4)	0.00(4)	0.00(4)	0.00(4)	0.00(4)	0.00(4)	0.00(4)	0.00(4)	0.00(4)	0.00(4)	0.00(4)	0.00(4)	0.00(4)	0.00(4)	0.00(4)	0.00(4)
O2	x	0.500	0.500	0.500	0.500	0.500	0.500	0.500	0.500	0.500	0.500	0.500	0.500	0.500	0.500	0.500	0.500
	y	0.000	0.000	0.000	0.000	0.000	0.000	0.000	0.000	0.000	0.000	0.000	0.000	0.000	0.000	0.000	0.000
	z	0.567(7)	0.567(7)	0.567(7)	0.567(7)	0.567(7)	0.567(7)	0.567(7)	0.567(7)	0.567(7)	0.567(7)	0.567(7)	0.567(7)	0.567(7)	0.567(7)	0.567(7)	0.567(7)
Nb/Fe – O bond length (Å)		1.95(4)	1.95(4)	1.95(4)	1.95(4)	1.95(4)	1.95(4)	1.95(4)	1.95(4)	1.95(4)	1.95(4)	1.95(4)	1.95(4)	1.95(4)	1.95(4)	1.95(4)	1.95(4)
		1.99(4)	1.99(4)	1.99(4)	1.99(4)	1.99(4)	1.99(4)	1.99(4)	1.99(4)	1.99(4)	1.99(4)	1.99(4)	1.99(4)	1.99(4)	1.99(4)	1.99(4)	1.99(4)
		1.988(7)	1.988(7)	1.988(7)	1.988(7)	1.988(7)	1.988(7)	1.988(7)	1.988(7)	1.988(7)	1.988(7)	1.988(7)	1.988(7)	1.988(7)	1.988(7)	1.988(7)	1.988(7)
		1.988(7)	1.988(7)	1.988(7)	1.988(7)	1.988(7)	1.988(7)	1.988(7)	1.988(7)	1.988(7)	1.988(7)	1.988(7)	1.988(7)	1.988(7)	1.988(7)	1.988(7)	1.988(7)
		1.988(7)	1.988(7)	1.988(7)	1.988(7)	1.988(7)	1.988(7)	1.988(7)	1.988(7)	1.988(7)	1.988(7)	1.988(7)	1.988(7)	1.988(7)	1.988(7)	1.988(7)	1.988(7)
		1.988(7)	1.988(7)	1.988(7)	1.988(7)	1.988(7)	1.988(7)	1.988(7)	1.988(7)	1.988(7)	1.988(7)	1.988(7)	1.988(7)	1.988(7)	1.988(7)	1.988(7)	1.988(7)
Nb/Fe – O – Nb/Fe bond angle (o)		180.000(0)	180.000(0)	180.000(0)	180.000(0)	180.000(0)	180.000(0)	180.000(0)	180.000(0)	180.000(0)	180.000(0)	180.000(0)	180.000(0)	180.000(0)	180.000(0)	180.000(0)	180.000(0)
		164.6(31)	164.6(31)	164.6(31)	164.6(31)	164.6(31)	164.6(31)	164.6(31)	164.6(31)	164.6(31)	164.6(31)	164.6(31)	164.6(31)	164.6(31)	164.6(31)	164.6(31)	164.6(31)

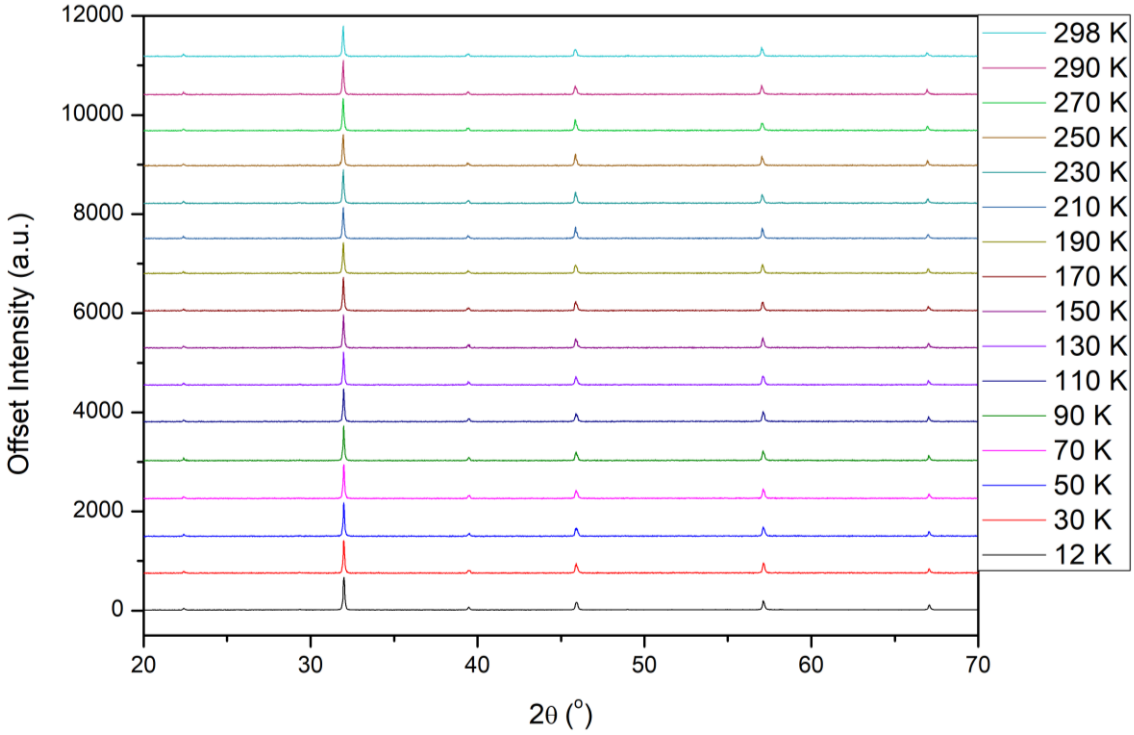

Figure A3.40: *All patterns for the LT PXRD of $Bi_{0.6}Na_{0.4}Fe_{0.6}Nb_{0.4}O_3$. 12K pattern intensity has been scaled down to match the intensities of the other temperature points that were taken with shorter scan times.*

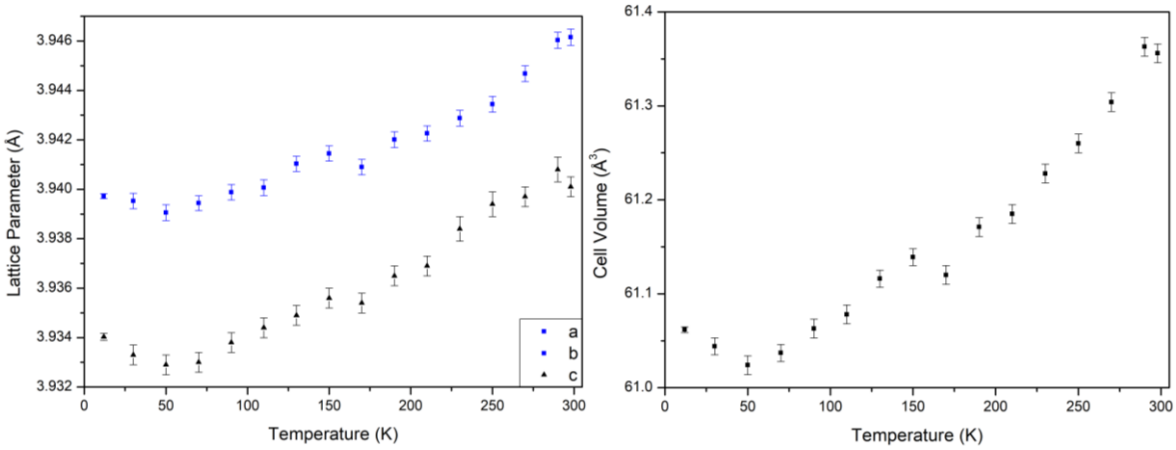

Figure A3.41: *LT PXRD of $Bi_{0.6}Na_{0.4}Fe_{0.6}Nb_{0.4}O_3$: (a) Lattice Parameter against temperature plot, (b) Cell Volume against temperature plot.*

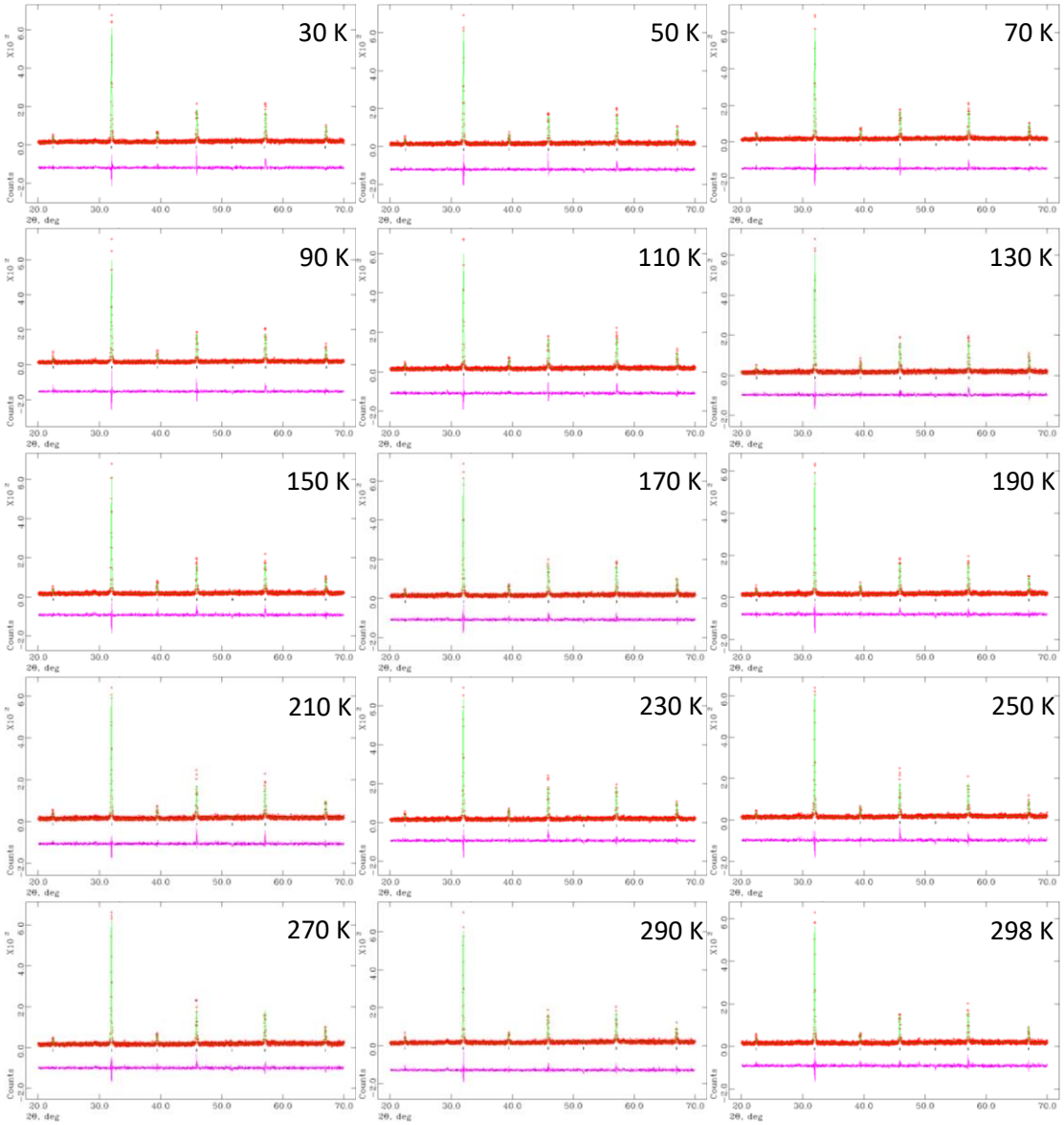

Figure A3.42: *Rietveld refinements obtained from LT PXRD of $Bi_{0.6}Na_{0.4}Fe_{0.6}Nb_{0.4}O_3$ in the temperature ranges 30 K to 298 K.*

Table A3.9: *Rietveld refinement parameters for LT XRD of $Bi_{0.6}Na_{0.4}Fe_{0.6}Nb_{0.4}O_3$.*

Parameter		$Bi_{0.6}Na_{0.4}Fe_{0.6}Nb_{0.4}O_3$															
Temperature (K)		12	30	50	70	90	110	130	150	170	190	210	230	250	270	290	298
Space Group		*P 4mm*	*P 4mm*	*P 4mm*	*P 4mm*	*P 4mm*	*P 4mm*	*P 4mm*	*P 4mm*	*P 4mm*	*P 4mm*	*P 4mm*	*P 4mm*	*P 4mm*	*P 4mm*	*P 4mm*	*P 4mm*
χ^2		1.738	1.351	1.411	1.344	1.361	1.386	1.346	1.369	1.380	1.349	1.329	1.367	1.310	1.377	1.380	1.368
wRp (%)		9.42	25.30	26.00	25.29	25.37	25.69	25.24	25.46	25.58	25.51	25.19	25.33	24.90	25.54	25.45	25.64
Rp (%)		7.42	20.03	20.70	20.00	20.21	20.09	20.05	19.81	19.93	20.03	19.95	19.73	19.44	19.85	19.93	20.20
a (Å)		3.93972(10)	3.93953(31)	3.93906(32)	3.93944(30)	3.93988(31)	3.94007(32)	3.94103(31)	3.94145(31)	3.94090(31)	3.94201(32)	3.94226(31)	3.94288(32)	3.94344(32)	3.94468(32)	3.94603(32)	3.94615(33)
b (Å)		3.93972(10)	3.93953(31)	3.93906(32)	3.93944(30)	3.93988(31)	3.94007(32)	3.94103(31)	3.94145(31)	3.94090(31)	3.94201(32)	3.94226(31)	3.94288(32)	3.94344(32)	3.94468(32)	3.94603(32)	3.94615(33)
c (Å)		3.93403(14)	3.9333(4)	3.9329(4)	3.9330(4)	3.9338(4)	3.9344(4)	3.9349(4)	3.9356(4)	3.9354(4)	3.9365(4)	3.9369(4)	3.9384(5)	3.9394(5)	3.9397(4)	3.9408(5)	3.9401(4)
α (°)		90.000	90.000	90.000	90.000	90.000	90.000	90.000	90.000	90.000	90.000	90.000	90.000	90.000	90.000	90.000	90.000
β (°)		90.000	90.000	90.000	90.000	90.000	90.000	90.000	90.000	90.000	90.000	90.000	90.000	90.000	90.000	90.000	90.000
γ (°)		90.000	90.000	90.000	90.000	90.000	90.000	90.000	90.000	90.000	90.000	90.000	90.000	90.000	90.000	90.000	90.000
Cell vol. (Å3)		61.0617(30)	61.044(9)	61.024(10)	61.037(9)	61.063(10)	61.078(10)	61.116(9)	61.139(9)	61.120(10)	61.171(10)	61.185(10)	61.228(10)	61.260(10)	61.304(10)	61.363(10)	61.356(10)
Bi/Na 1	x	0.000	0.000	0.000	0.000	0.000	0.000	0.000	0.000	0.000	0.000	0.000	0.000	0.000	0.000	0.000	0.000
	y	0.000	0.000	0.000	0.000	0.000	0.000	0.000	0.000	0.000	0.000	0.000	0.000	0.000	0.000	0.000	0.000
	z	0.000	0.000	0.000	0.000	0.000	0.000	0.000	0.000	0.000	0.000	0.000	0.000	0.000	0.000	0.000	0.000
Fe/Nb 1	x	0.500	0.500	0.500	0.500	0.500	0.500	0.500	0.500	0.500	0.500	0.500	0.500	0.500	0.500	0.500	0.500
	y	0.500	0.500	0.500	0.500	0.500	0.500	0.500	0.500	0.500	0.500	0.500	0.500	0.500	0.500	0.500	0.500
	z	0.501(7)	0.501(7)	0.501(7)	0.501(7)	0.501(7)	0.501(7)	0.501(7)	0.501(7)	0.501(7)	0.501(7)	0.501(7)	0.501(7)	0.501(7)	0.501(7)	0.501(7)	0.501(7)
O1	x	0.500	0.500	0.500	0.500	0.500	0.500	0.500	0.500	0.500	0.500	0.500	0.500	0.500	0.500	0.500	0.500
	y	0.500	0.500	0.500	0.500	0.500	0.500	0.500	0.500	0.500	0.500	0.500	0.500	0.500	0.500	0.500	0.500
	z	0.001(29)	0.001(29)	0.001(29)	0.001(29)	0.001(29)	0.001(29)	0.001(29)	0.001(29)	0.001(29)	0.001(29)	0.001(29)	0.001(29)	0.001(29)	0.001(29)	0.001(29)	0.001(29)
O2	x	0.500	0.500	0.500	0.500	0.500	0.500	0.500	0.500	0.500	0.500	0.500	0.500	0.500	0.500	0.500	0.500
	y	0.000	0.000	0.000	0.000	0.000	0.000	0.000	0.000	0.000	0.000	0.000	0.000	0.000	0.000	0.000	0.000
	z	0.540(6)	0.540(6)	0.540(6)	0.540(6)	0.540(6)	0.540(6)	0.540(6)	0.540(6)	0.540(6)	0.540(6)	0.540(6)	0.540(6)	0.540(6)	0.540(6)	0.540(6)	0.540(6)
Nb/Fe – O bond length (Å)		1.964(29)	1.964(29)	1.964(29)	1.964(29)	1.964(29)	1.964(29)	1.964(29)	1.964(29)	1.964(29)	1.964(29)	1.964(29)	1.964(29)	1.964(29)	1.964(29)	1.964(29)	1.964(29)
		1.970(29)	1.970(29)	1.970(29)	1.970(29)	1.970(29)	1.970(29)	1.970(29)	1.970(29)	1.970(29)	1.970(29)	1.970(29)	1.970(29)	1.970(29)	1.970(29)	1.970(29)	1.970(29)
		1.9760(32)	1.9760(32)	1.9760(32)	1.9760(32)	1.9760(32)	1.9760(32)	1.9760(32)	1.9760(32)	1.9760(32)	1.9760(32)	1.9760(32)	1.9760(32)	1.9760(32)	1.9760(32)	1.9760(32)	1.9760(32)
		1.9760(32)	1.9760(32)	1.9760(32)	1.9760(32)	1.9760(32)	1.9760(32)	1.9760(32)	1.9760(32)	1.9760(32)	1.9760(32)	1.9760(32)	1.9760(32)	1.9760(32)	1.9760(32)	1.9760(32)	1.9760(32)
		1.9760(32)	1.9760(32)	1.9760(32)	1.9760(32)	1.9760(32)	1.9760(32)	1.9760(32)	1.9760(32)	1.9760(32)	1.9760(32)	1.9760(32)	1.9760(32)	1.9760(32)	1.9760(32)	1.9760(32)	1.9760(32)
		1.9760(32)	1.9760(32)	1.9760(32)	1.9760(32)	1.9760(32)	1.9760(32)	1.9760(32)	1.9760(32)	1.9760(32)	1.9760(32)	1.9760(32)	1.9760(32)	1.9760(32)	1.9760(32)	1.9760(32)	1.9760(32)
Nb/Fe – O – Nb/Fe bond angle (o)		180.000(0)	180.000(0)	180.000(0)	180.000(0)	180.000(0)	180.000(0)	180.000(0)	180.000(0)	180.000(0)	180.000(0)	180.000(0)	180.000(0)	180.000(0)	180.000(0)	180.000(0)	180.000(0)
		171.0(23)	171.0(23)	171.0(23)	171.0(23)	171.0(23)	171.0(23)	171.0(23)	171.0(23)	171.0(23)	171.0(23)	171.0(23)	171.0(23)	171.0(23)	171.0(23)	171.0(23)	171.0(23)

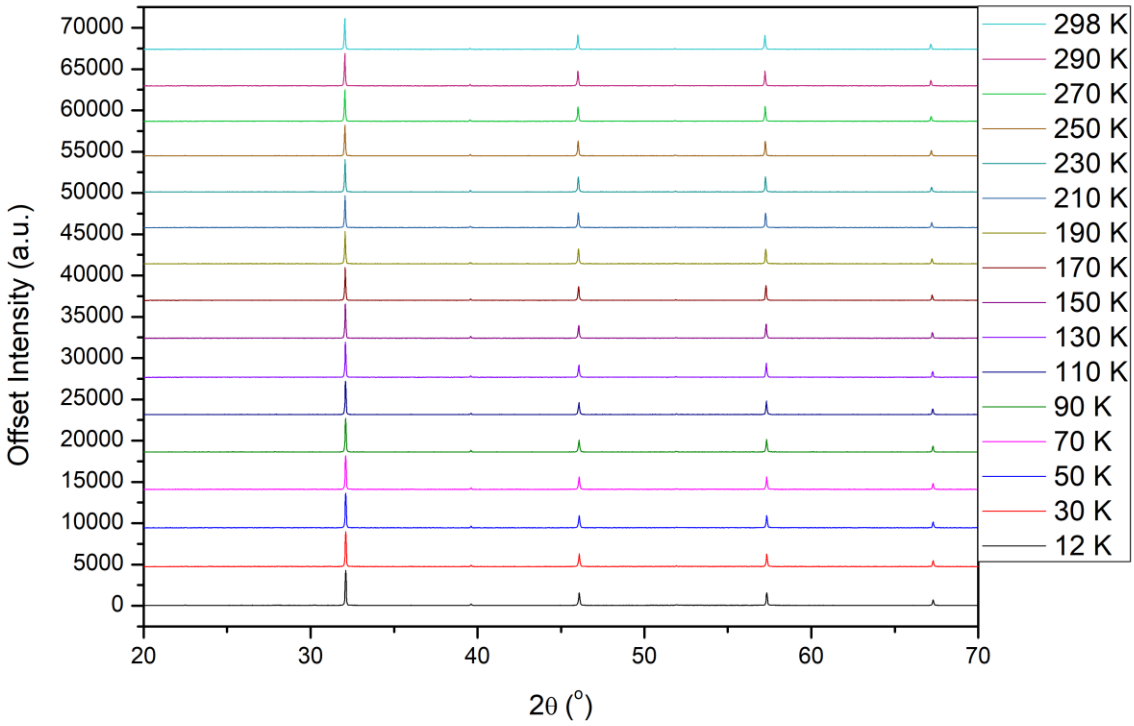

Figure A3.43: *All patterns for the LT PXRD of $Bi_{0.4}Na_{0.6}Fe_{0.4}Nb_{0.6}O_3$. 12K pattern intensity has been scaled down to match the intensities of the other temperature points that were taken with shorter scan times.*

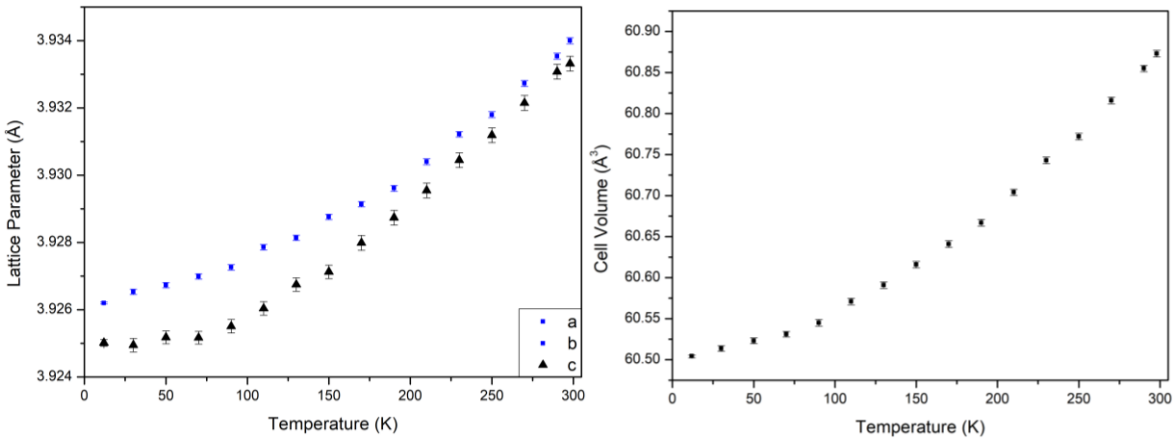

Figure A3.44: *LT PXRD of $Bi_{0.4}Na_{0.6}Fe_{0.4}Nb_{0.6}O_3$: (a) Lattice Parameter against temperature plot, (b) Cell Volume against temperature plot.*

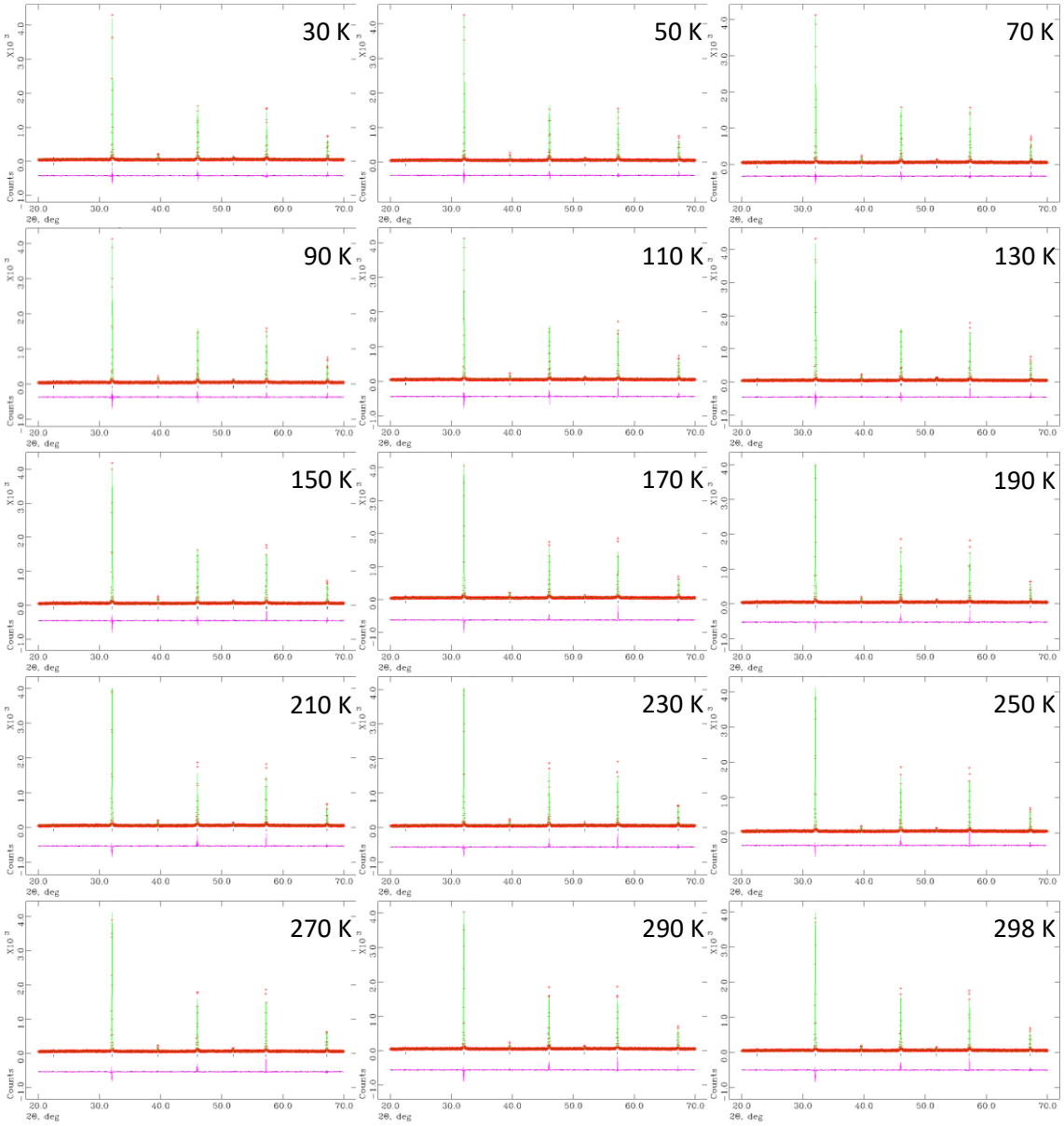

Figure A3.45: *Rietveld refinements obtained from LT PXRD of $Bi_{0.4}Na_{0.6}Fe_{0.4}Nb_{0.6}O_3$ in the temperature ranges 30 K to 298 K.*

Table A3.10: *Rietveld refinement parameters for LT XRD of $Bi_{0.4}Na_{0.6}Fe_{0.4}Nb_{0.6}O_3$.*

Parameter		$Bi_{0.4}Na_{0.6}Fe_{0.4}Nb_{0.6}O_3$															
Temperature (K)		12	30	50	70	90	110	130	150	170	190	210	230	250	270	290	298
Space Group		*P 4mm*	*P 4mm*	*P 4mm*	*P 4mm*	*P 4mm*	*P 4mm*	*P 4mm*	*P 4mm*	*P 4mm*	*P 4mm*	*P 4mm*	*P 4mm*	*P 4mm*	*P 4mm*	*P 4mm*	*P 4mm*
χ^2		3.244	1.370	1.348	1.359	1.454	1.429	1.390	1.450	1.508	1.503	1.529	1.491	1.513	1.516	1.520	1.478
wRp (%)		7.19	13.80	13.75	13.80	14.29	14.17	13.91	14.20	14.51	14.47	14.61	14.36	14.52	14.51	14.52	14.31
Rp (%)		5.09	10.84	10.85	10.70	11.36	11.21	11.00	11.26	11.64	11.69	11.67	11.47	11.75	11.63	11.67	11.58
a (Å)		3.926198(31)	3.92653(8)	3.92673(8)	3.92699(8)	3.92726(8)	3.92786(8)	3.92814(8)	3.92876(8)	3.92914(8)	3.92961(9)	3.93040(9)	3.93122(8)	3.93180(9)	3.93273(9)	3.93354(9)	3.93400(9)
b (Å)		3.926198(31)	3.92653(8)	3.92673(8)	3.92699(8)	3.92726(8)	3.92786(8)	3.92814(8)	3.92876(8)	3.92914(8)	3.92961(9)	3.93040(9)	3.93122(8)	3.93180(9)	3.93273(9)	3.93354(9)	3.93400(9)
c (Å)		3.92502(10)	3.92495(20)	3.92518(19)	3.92517(19)	3.92551(20)	3.92604(20)	3.92675(20)	3.92713(20)	3.92799(22)	3.92874(22)	3.92955(22)	3.93045(22)	3.93119(22)	3.93215(22)	3.93308(22)	3.93332(22)
α (°)		90.000	90.000	90.000	90.000	90.000	90.000	90.000	90.000	90.000	90.000	90.000	90.000	90.000	90.000	90.000	90.000
β (°)		90.000	90.000	90.000	90.000	90.000	90.000	90.000	90.000	90.000	90.000	90.000	90.000	90.000	90.000	90.000	90.000
γ (°)		90.000	90.000	90.000	90.000	90.000	90.000	90.000	90.000	90.000	90.000	90.000	90.000	90.000	90.000	90.000	90.000
Cell vol. (Å3)		60.5043(16)	60.5136(35)	60.5231(35)	60.5310(35)	60.545(4)	60.571(4)	60.591(4)	60.616(4)	60.641(4)	60.667(4)	60.704(4)	60.743(4)	60.772(4)	60.816(4)	60.855(4)	60.873(4)
Bi/Na 1	x	0.000	0.000	0.000	0.000	0.000	0.000	0.000	0.000	0.000	0.000	0.000	0.000	0.000	0.000	0.000	0.000
	y	0.000	0.000	0.000	0.000	0.000	0.000	0.000	0.000	0.000	0.000	0.000	0.000	0.000	0.000	0.000	0.000
	z	0.000	0.000	0.000	0.000	0.000	0.000	0.000	0.000	0.000	0.000	0.000	0.000	0.000	0.000	0.000	0.000
Fe/Nb 1	x	0.500	0.500	0.500	0.500	0.500	0.500	0.500	0.500	0.500	0.500	0.500	0.500	0.500	0.500	0.500	0.500
	y	0.500	0.500	0.500	0.500	0.500	0.500	0.500	0.500	0.500	0.500	0.500	0.500	0.500	0.500	0.500	0.500
	z	0.5429(14)	0.5429(14)	0.5429(14)	0.5429(14)	0.5429(14)	0.5429(14)	0.5429(14)	0.5429(14)	0.5429(14)	0.5429(14)	0.5429(14)	0.5429(14)	0.5429(14)	0.5429(14)	0.5429(14)	0.5429(14)
O1	x	0.500	0.500	0.500	0.500	0.500	0.500	0.500	0.500	0.500	0.500	0.500	0.500	0.500	0.500	0.500	0.500
	y	0.500	0.500	0.500	0.500	0.500	0.500	0.500	0.500	0.500	0.500	0.500	0.500	0.500	0.500	0.500	0.500
	z	0.040(18)	0.040(18)	0.040(18)	0.040(18)	0.040(18)	0.040(18)	0.040(18)	0.040(18)	0.040(18)	0.040(18)	0.040(18)	0.040(18)	0.040(18)	0.040(18)	0.040(18)	0.040(18)
O2	x	0.500	0.500	0.500	0.500	0.500	0.500	0.500	0.500	0.500	0.500	0.500	0.500	0.500	0.500	0.500	0.500
	y	0.000	0.000	0.000	0.000	0.000	0.000	0.000	0.000	0.000	0.000	0.000	0.000	0.000	0.000	0.000	0.000
	z	0.650(4)	0.650(4)	0.650(4)	0.650(4)	0.650(4)	0.650(4)	0.650(4)	0.650(4)	0.650(4)	0.650(4)	0.650(4)	0.650(4)	0.650(4)	0.650(4)	0.650(4)	0.650(4)
Nb/Fe – O bond length (Å)		1.95(7)	1.95(7)	1.95(7)	1.95(7)	1.95(7)	1.95(7)	1.95(7)	1.95(7)	1.95(7)	1.95(7)	1.95(7)	1.95(7)	1.95(7)	1.95(7)	1.95(7)	1.95(7)
		1.98(7)	1.98(7)	1.98(7)	1.98(7)	1.98(7)	1.98(7)	1.98(7)	1.98(7)	1.98(7)	1.98(7)	1.98(7)	1.98(7)	1.98(7)	1.98(7)	1.98(7)	1.98(7)
		2.0074(34)	2.0074(34)	2.0074(34)	2.0074(34)	2.0074(34)	2.0074(34)	2.0074(34)	2.0074(34)	2.0074(34)	2.0074(34)	2.0074(34)	2.0074(34)	2.0074(34)	2.0074(34)	2.0074(34)	2.0074(34)
		2.0074(34)	2.0074(34)	2.0074(34)	2.0074(34)	2.0074(34)	2.0074(34)	2.0074(34)	2.0074(34)	2.0074(34)	2.0074(34)	2.0074(34)	2.0074(34)	2.0074(34)	2.0074(34)	2.0074(34)	2.0074(34)
		2.0074(34)	2.0074(34)	2.0074(34)	2.0074(34)	2.0074(34)	2.0074(34)	2.0074(34)	2.0074(34)	2.0074(34)	2.0074(34)	2.0074(34)	2.0074(34)	2.0074(34)	2.0074(34)	2.0074(34)	2.0074(34)
		2.0074(34)	2.0074(34)	2.0074(34)	2.0074(34)	2.0074(34)	2.0074(34)	2.0074(34)	2.0074(34)	2.0074(34)	2.0074(34)	2.0074(34)	2.0074(34)	2.0074(34)	2.0074(34)	2.0074(34)	2.0074(34)
Nb/Fe – O – Nb/Fe bond angle (o)		180.000(0) 155.9(9)	180.000(0) 155.9(9)	180.000(0) 155.9(9)	180.000(0) 155.9(9)	180.000(0) 155.9(9)	180.000(0) 155.9(9)	180.000(0) 155.9(9)	180.000(0) 155.9(9)	180.000(0) 155.9(9)	180.000(0) 155.9(9)	180.000(0) 155.9(9)	180.000(0) 155.9(9)	180.000(0) 155.9(9)	180.000(0) 155.9(9)	180.000(0) 155.9(9)	180.000(0) 155.9(9)

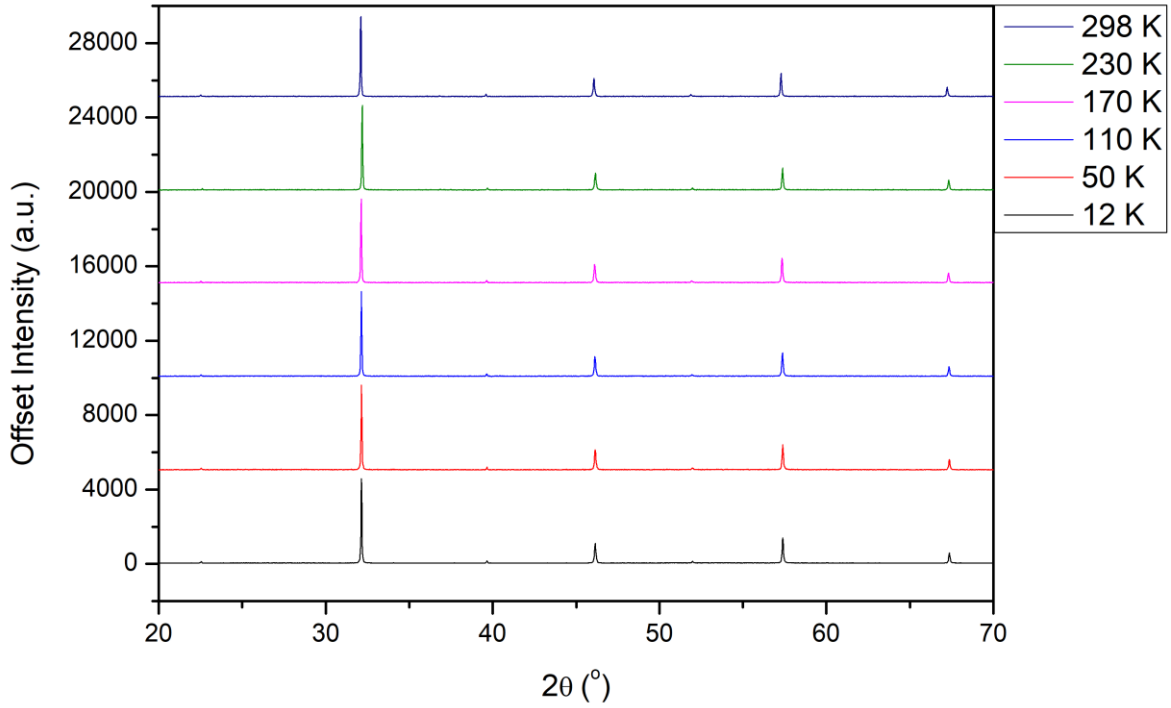

Figure A3.46: *Selection of patterns for the LT PXRD of $Bi_{0.35}Na_{0.65}Fe_{0.35}Nb_{0.65}O_3$. 12K pattern intensity has been scaled down to match the intensities of the other temperature points that were taken with shorter scan times.*

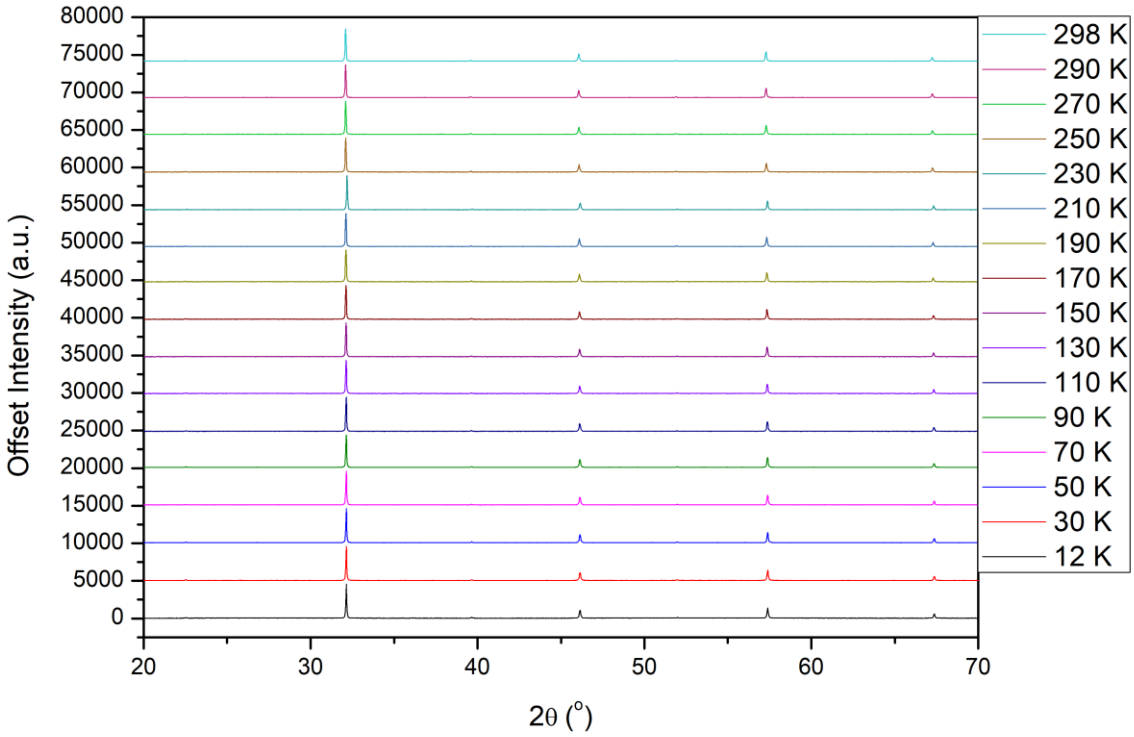

Figure A3.47: *All patterns for the LT PXRD of $Bi_{0.35}Na_{0.65}Fe_{0.35}Nb_{0.65}O_3$. 12K pattern intensity has been scaled down to match the intensities of the other temperature points that were taken with shorter scan times.*

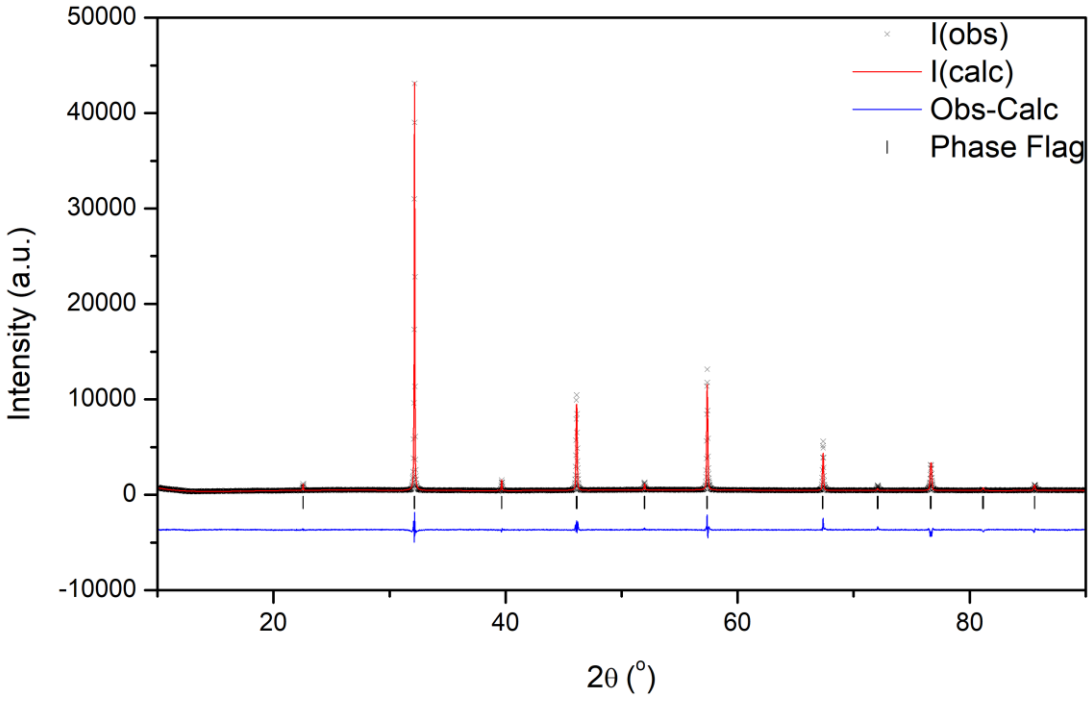

Figure A3.48: *Rietveld refinement of 12 K PXRD data collected for $Bi_{0.35}Na_{0.65}Fe_{0.35}Nb_{0.65}O_3$; χ^2 = 3.203, R_{wp} = 7.57% and R_p = 5.37; the black crosses represent the observed intensity, the red line represents the calculated intensity from the model, the blue line represents the difference between the observed pattern and calculated pattern, the black tick marker represents the P4mm model.*

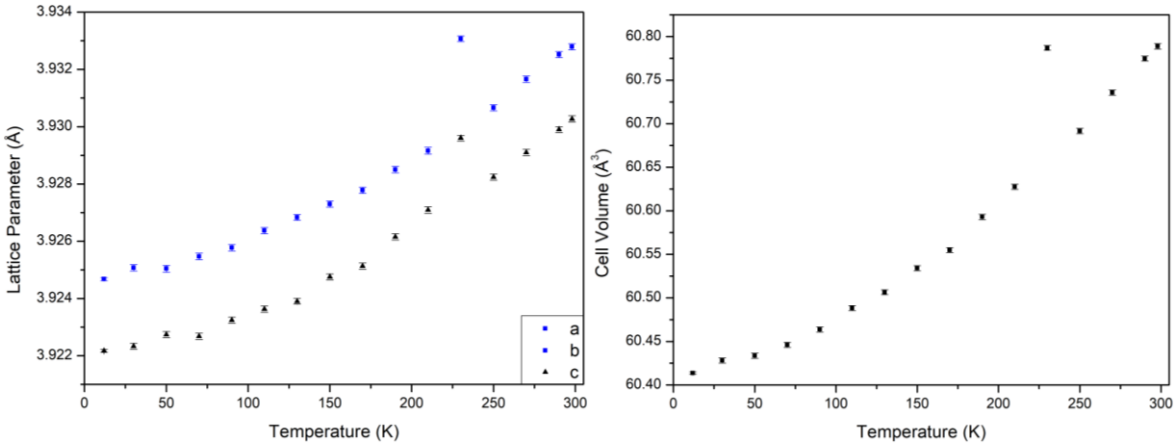

Figure A3.49: *LT PXRD of $Bi_{0.35}Na_{0.65}Fe_{0.35}Nb_{0.65}O_3$: (a) Lattice Parameter against temperature plot, (b) Cell Volume against temperature plot.*

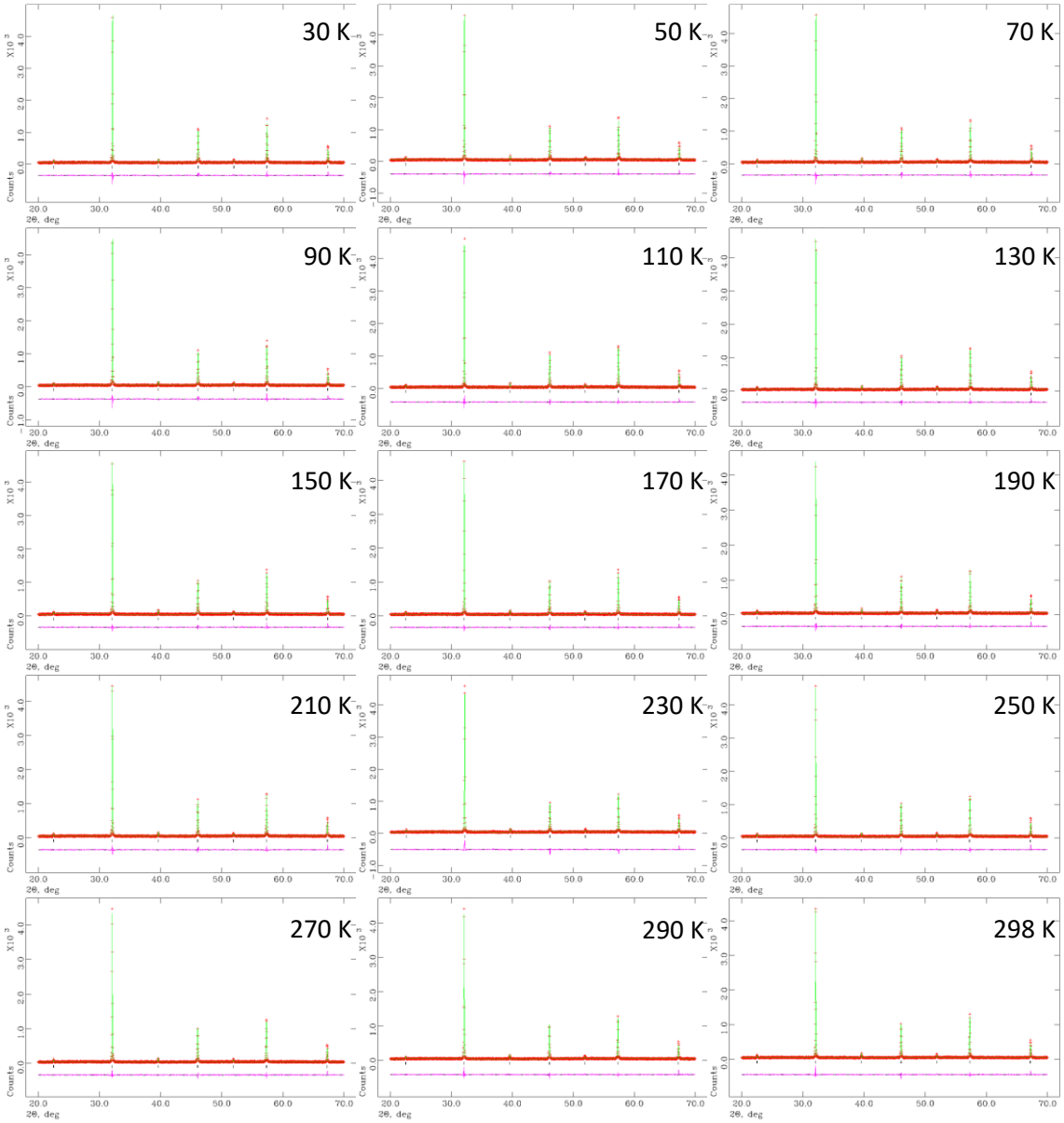

Figure A3.50: *Rietveld refinements obtained from LT PXRD of $Bi_{0.35}Na_{0.65}Fe_{0.35}Nb_{0.65}O_3$ in the temperature ranges 30 K to 298 K.*

Table A3.11: *Rietveld refinement parameters for LT XRD of $Bi_{0.35}Na_{0.65}Fe_{0.35}Nb_{0.65}O_3$.*

Parameter		$Bi_{0.35}Na_{0.65}Fe_{0.35}Nb_{0.65}O_3$															
Temperature (K)		12	30	50	70	90	110	130	150	170	190	210	230	250	270	290	298
Space Group		*P 4mm*	*P 4mm*	*P 4mm*	*P 4mm*	*P 4mm*	*P 4mm*	*P 4mm*	*P 4mm*	*P 4mm*	*P 4mm*	*P 4mm*	*P 4mm*	*P 4mm*	*P 4mm*	*P 4mm*	*P 4mm*
χ^2		3.203	1.350	1.347	1.322	1.327	1.345	1.218	1.316	1.329	1.343	1.298	1.349	1.283	1.333	1.269	1.316
wRp (%)		7.57	14.46	14.48	14.40	14.42	14.49	13.80	14.36	14.40	14.46	14.19	14.48	14.19	14.45	14.12	14.39
Rp (%)		5.37	11.35	11.27	11.15	11.24	11.30	10.65	10.98	10.93	11.11	10.84	11.47	10.89	11.14	10.90	11.19
a (Å)		3.92468(5)	3.92507(11)	3.92504(12)	3.92547(11)	3.92577(11)	3.92637(11)	3.92683(10)	3.92730(11)	3.92778(11)	3.92850(11)	3.92916(12)	3.93307(10)	3.93066(11)	3.93166(11)	3.93252(11)	3.93279(11)
b (Å)		3.92468(5)	3.92507(11)	3.92504(12)	3.92547(11)	3.92577(11)	3.92637(11)	3.92683(10)	3.92730(11)	3.92778(11)	3.92850(11)	3.92916(12)	3.93307(10)	3.93066(11)	3.93166(11)	3.93252(11)	3.93279(11)
c (Å)		3.92217(5)	3.92233(11)	3.92274(11)	3.92268(11)	3.92324(11)	3.92363(11)	3.92390(10)	3.92475(11)	3.92513(11)	3.92615(11)	3.92709(11)	3.92960(10)	3.92824(11)	3.92910(11)	3.92990(10)	3.93027(11)
α (°)		90.000	90.000	90.000	90.000	90.000	90.000	90.000	90.000	90.000	90.000	90.000	90.000	90.000	90.000	90.000	90.000
β (°)		90.000	90.000	90.000	90.000	90.000	90.000	90.000	90.000	90.000	90.000	90.000	90.000	90.000	90.000	90.000	90.000
γ (°)		90.000	90.000	90.000	90.000	90.000	90.000	90.000	90.000	90.000	90.000	90.000	90.000	90.000	90.000	90.000	90.000
Cell vol. (Å3)		60.4137(14)	60.4281(29)	60.4336(30)	60.4460(29)	60.4637(30)	60.4882(29)	60.5065(27)	60.5341(29)	60.5548(29)	60.5929(30)	60.6275(30)	60.7870(28)	60.6916(29)	60.7357(30)	60.7748(29)	60.7888(30)
Bi/Na 1	x	0.000	0.000	0.000	0.000	0.000	0.000	0.000	0.000	0.000	0.000	0.000	0.000	0.000	0.000	0.000	0.000
	y	0.000	0.000	0.000	0.000	0.000	0.000	0.000	0.000	0.000	0.000	0.000	0.000	0.000	0.000	0.000	0.000
	z	0.000	0.000	0.000	0.000	0.000	0.000	0.000	0.000	0.000	0.000	0.000	0.000	0.000	0.000	0.000	0.000
Fe/Nb 1	x	0.500	0.500	0.500	0.500	0.500	0.500	0.500	0.500	0.500	0.500	0.500	0.500	0.500	0.500	0.500	0.500
	y	0.500	0.500	0.500	0.500	0.500	0.500	0.500	0.500	0.500	0.500	0.500	0.500	0.500	0.500	0.500	0.500
	z	0.5241(6)	0.5241(6)	0.5241(6)	0.5241(6)	0.5241(6)	0.5241(6)	0.5241(6)	0.5241(6)	0.5241(6)	0.5241(6)	0.5241(6)	0.5241(6)	0.5241(6)	0.5241(6)	0.5241(6)	0.5241(6)
O1	x	0.500	0.500	0.500	0.500	0.500	0.500	0.500	0.500	0.500	0.500	0.500	0.500	0.500	0.500	0.500	0.500
	y	0.500	0.500	0.500	0.500	0.500	0.500	0.500	0.500	0.500	0.500	0.500	0.500	0.500	0.500	0.500	0.500
	z	0.0474(36)	0.0474(36)	0.0474(36)	0.0474(36)	0.0474(36)	0.0474(36)	0.0474(36)	0.0474(36)	0.0474(36)	0.0474(36)	0.0474(36)	0.0474(36)	0.0474(36)	0.0474(36)	0.0474(36)	0.0474(36)
O2	x	0.500	0.500	0.500	0.500	0.500	0.500	0.500	0.500	0.500	0.500	0.500	0.500	0.500	0.500	0.500	0.500
	y	0.000	0.000	0.000	0.000	0.000	0.000	0.000	0.000	0.000	0.000	0.000	0.000	0.000	0.000	0.000	0.000
	z	0.5983(17)	0.5983(17)	0.5983(17)	0.5983(17)	0.5983(17)	0.5983(17)	0.5983(17)	0.5983(17)	0.5983(17)	0.5983(17)	0.5983(17)	0.5983(17)	0.5983(17)	0.5983(17)	0.5983(17)	0.5983(17)
Nb/Fe – O bond length (Å)		1.870(15)	1.870(15)	1.870(15)	1.870(15)	1.870(15)	1.870(15)	1.870(15)	1.870(15)	1.870(15)	1.870(15)	1.870(15)	1.870(15)	1.870(15)	1.870(15)	1.870(15)	1.870(15)
		2.052(15)	2.052(15)	2.052(15)	2.052(15)	2.052(15)	2.052(15)	2.052(15)	2.052(15)	2.052(15)	2.052(15)	2.052(15)	2.052(15)	2.052(15)	2.052(15)	2.052(15)	2.052(15)
		1.9838(11)	1.9838(11)	1.9838(11)	1.9838(11)	1.9838(11)	1.9838(11)	1.9838(11)	1.9838(11)	1.9838(11)	1.9838(11)	1.9838(11)	1.9838(11)	1.9838(11)	1.9838(11)	1.9838(11)	1.9838(11)
		1.9838(11)	1.9838(11)	1.9838(11)	1.9838(11)	1.9838(11)	1.9838(11)	1.9838(11)	1.9838(11)	1.9838(11)	1.9838(11)	1.9838(11)	1.9838(11)	1.9838(11)	1.9838(11)	1.9838(11)	1.9838(11)
		1.9838(11)	1.9838(11)	1.9838(11)	1.9838(11)	1.9838(11)	1.9838(11)	1.9838(11)	1.9838(11)	1.9838(11)	1.9838(11)	1.9838(11)	1.9838(11)	1.9838(11)	1.9838(11)	1.9838(11)	1.9838(11)
		1.9838(11)	1.9838(11)	1.9838(11)	1.9838(11)	1.9838(11)	1.9838(11)	1.9838(11)	1.9838(11)	1.9838(11)	1.9838(11)	1.9838(11)	1.9838(11)	1.9838(11)	1.9838(11)	1.9838(11)	1.9838(11)
Nb/Fe – O – Nb/Fe bond angle (o)		180.000(0)	180.000(0)	180.000(0)	180.000(0)	180.000(0)	180.000(0)	180.000(0)	180.000(0)	180.000(0)	180.000(0)	180.000(0)	180.000(0)	180.000(0)	180.000(0)	180.000(0)	180.000(0)
		163.1(4)	163.1(4)	163.1(4)	163.1(4)	163.1(4)	163.1(4)	163.1(4)	163.1(4)	163.1(4)	163.1(4)	163.1(4)	163.1(4)	163.1(4)	163.1(4)	163.1(4)	163.1(4)

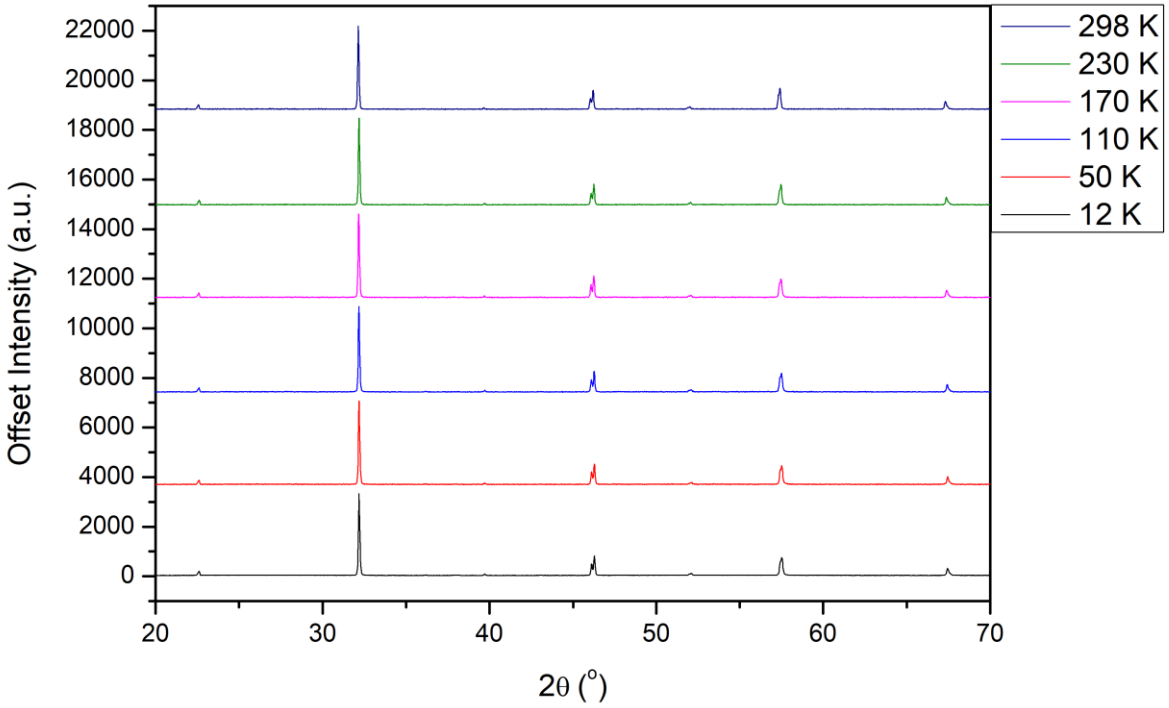

Figure A3.51: *Selection of patterns for the LT PXRD of $Bi_{0.3}Na_{0.7}Fe_{0.3}Nb_{0.7}O_3$. 12K pattern intensity has been scaled down to match the intensities of the other temperature points that were taken with shorter scan times.*

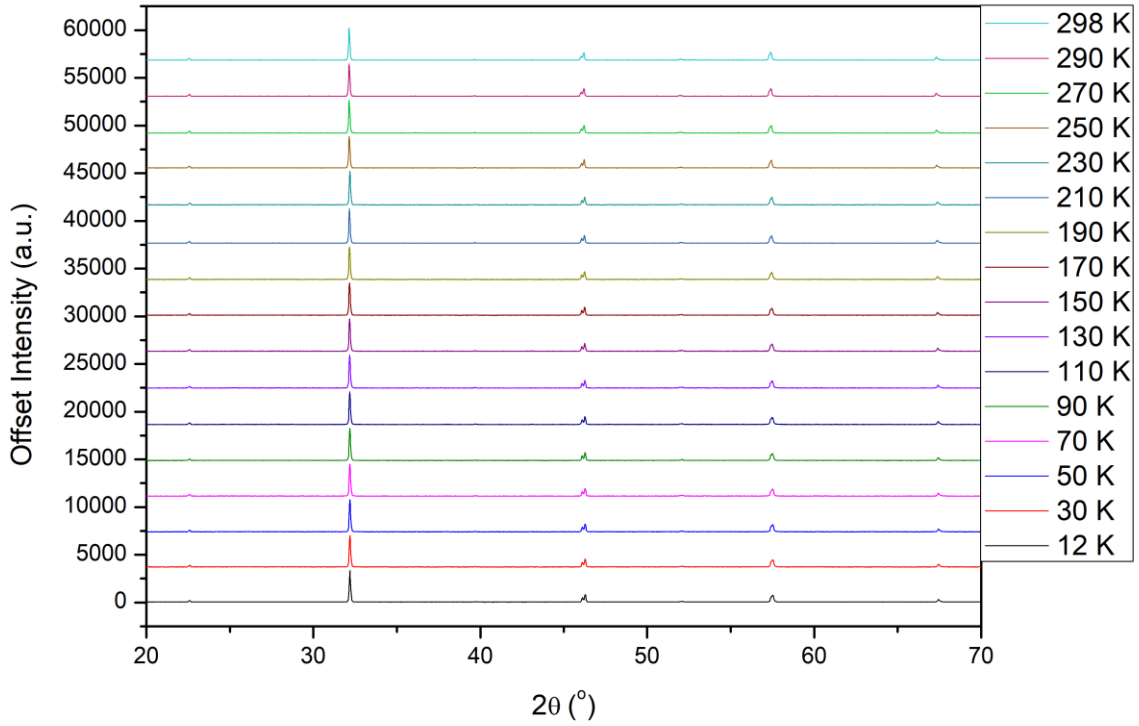

Figure A3.52: *All patterns for the LT PXRD of $Bi_{0.3}Na_{0.7}Fe_{0.3}Nb_{0.7}O_3$. 12K pattern intensity has been scaled down to match the intensities of the other temperature points that were taken with shorter scan times.*

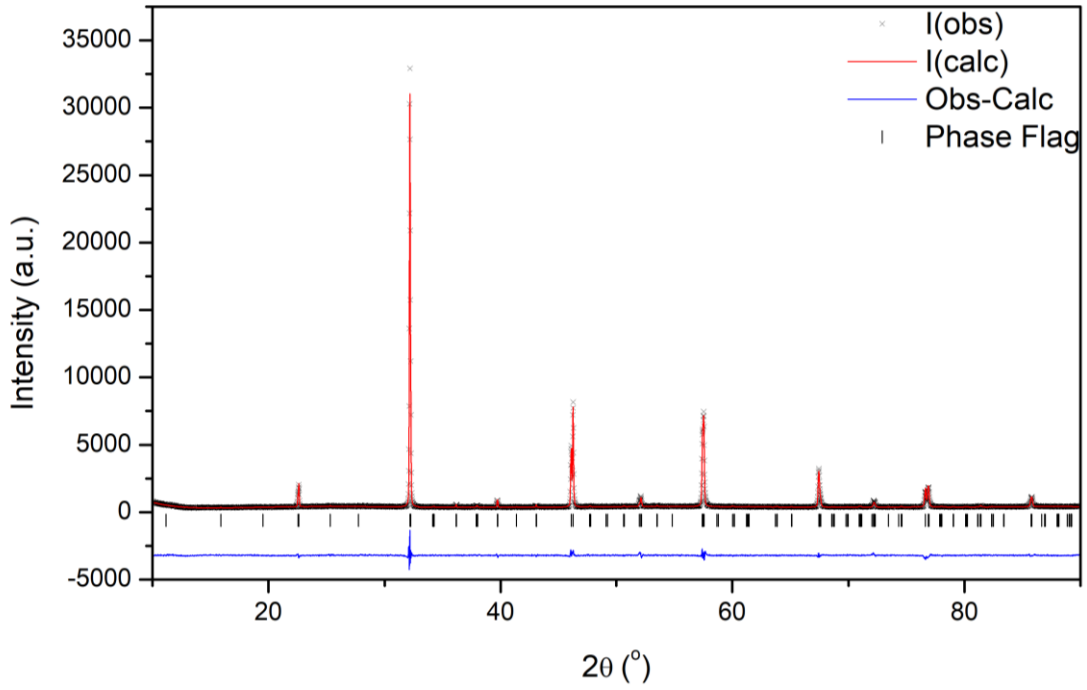

Figure A3.53: *Rietveld refinement of 12 K PXRD data collected for $Bi_{0.3}Na_{0.7}Fe_{0.3}Nb_{0.7}O_3$; $\chi^2 = 2.213$, $R_{wp} = 6.63\%$ and $R_p = 5.07$; the black crosses represent the observed intensity, the red line represents the calculated intensity from the model, the blue line represents the difference between the observed pattern and calculated pattern and the black tick marker represents the $P2_1ma$ model.*

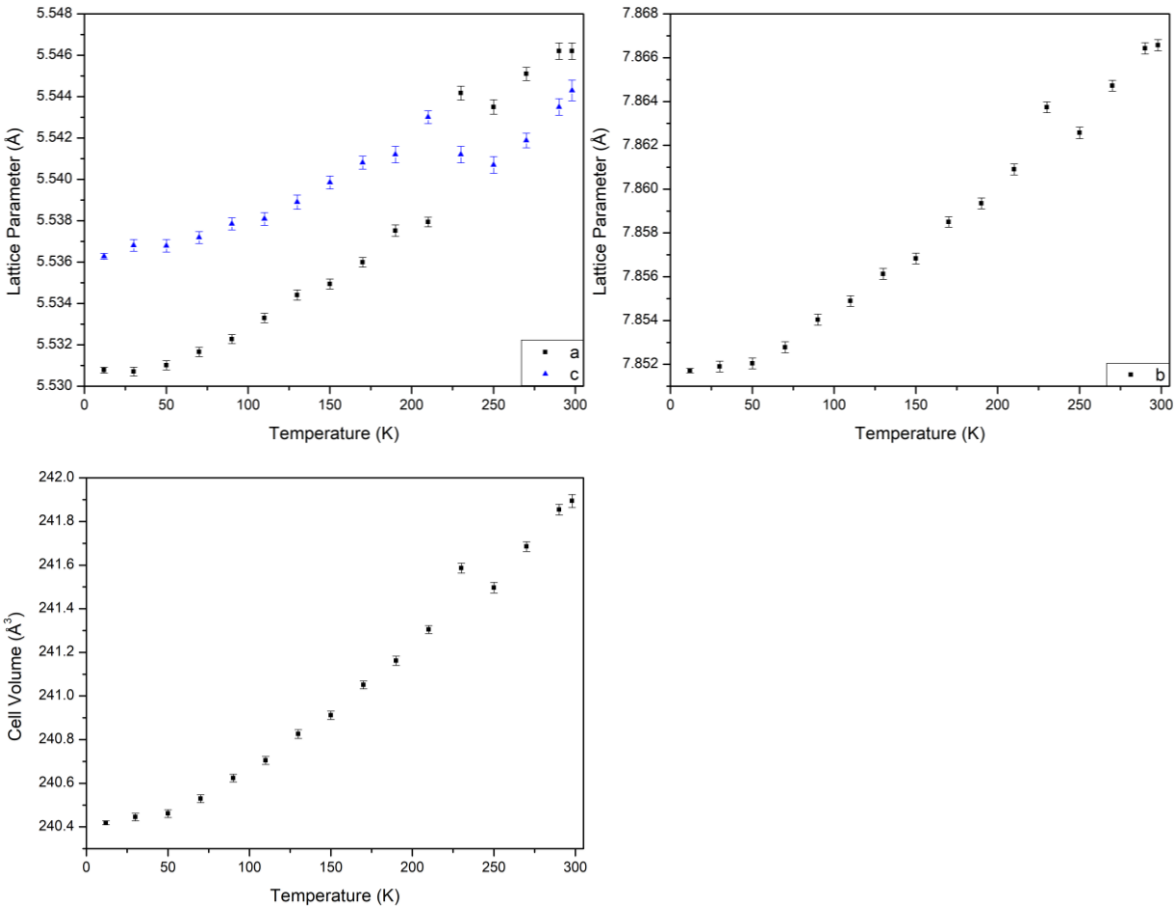

Figure A3.54: *LT PXRD of $Bi_{0.3}Na_{0.7}Fe_{0.3}Nb_{0.7}O_3$: (a) + (b) Lattice Parameter against temperature plot, (c) Cell Volume against temperature plot.*

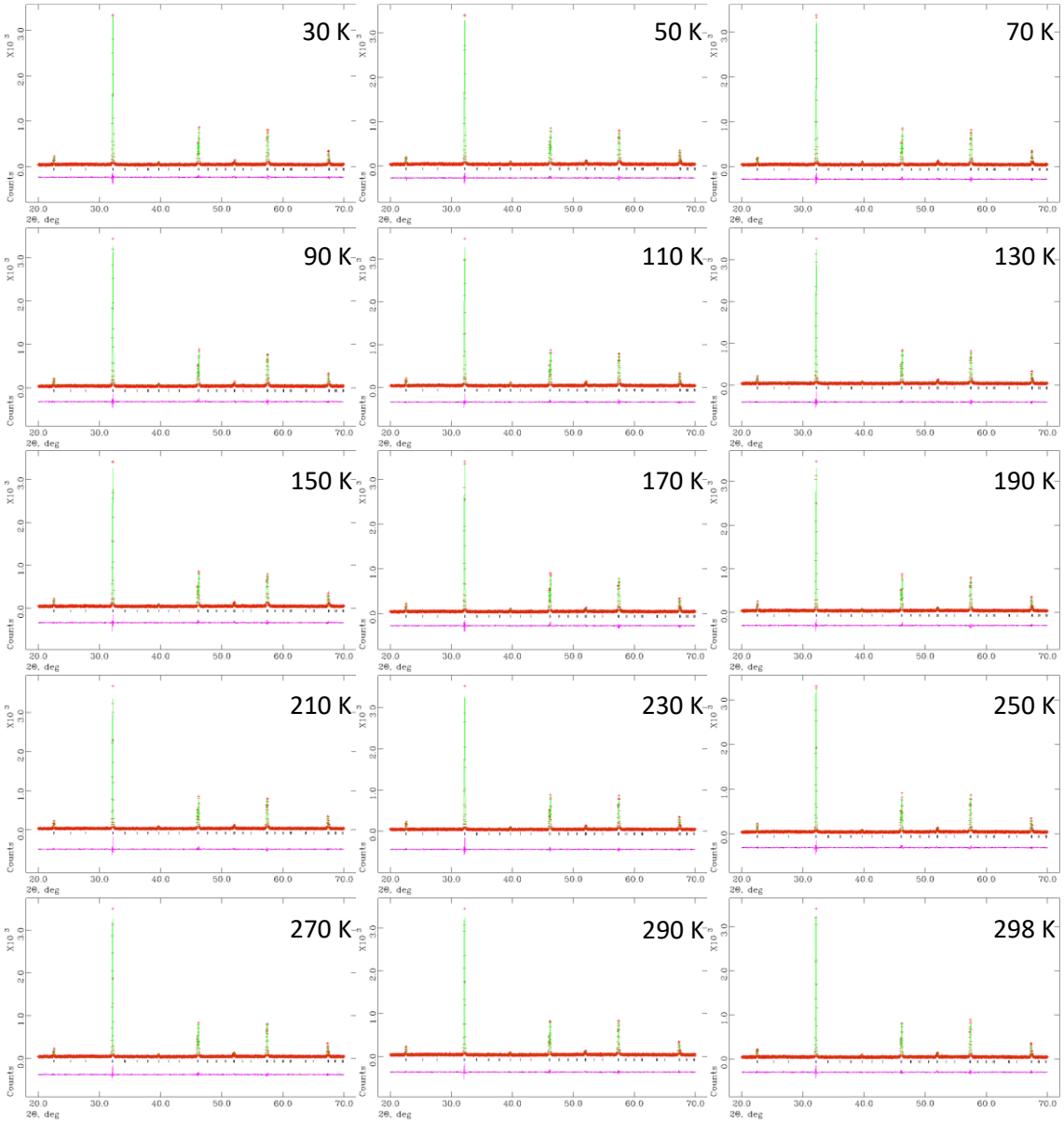

Figure A3.55: *Rietveld refinements obtained from LT PXRD of $Bi_{0.3}Na_{0.7}Fe_{0.3}Nb_{0.7}O_3$ in the temperature ranges 30 K to 298 K.*

Table A3.12: *Rietveld refinement parameters for LT XRD of $Bi_{0.3}Na_{0.7}Fe_{0.3}Nb_{0.7}O_3$.*

Parameter		$Bi_{0.3}Na_{0.7}Fe_{0.3}Nb_{0.7}O_3$															
Temperature (K)		12	30	50	70	90	110	130	150	170	190	210	230	250	270	290	298
Space Group		*P* 2_1ma	*P* 2_1ma	*P* 2_1ma	*P* 2_1ma	*P* 2_1ma	*P* 2_1ma	*P* 2_1ma	*P* 2_1ma	*P* 2_1ma	*P* 2_1ma	*P* 2_1ma	*P* 2_1ma	*P* 2_1ma	*P* 2_1ma	*P* 2_1ma	*P* 2_1ma
χ^2		2.213	1.220	1.299	1.209	1.216	1.154	1.294	1.214	1.210	1.236	1.211	1.204	1.236	1.201	1.232	1.208
wRp (%)		6.63	14.55	14.96	14.48	14.58	14.15	15.02	14.52	14.42	14.62	14.46	14.36	14.62	14.40	14.64	14.46
Rp (%)		5.07	10.78	11.16	10.93	10.87	10.50	11.19	10.92	10.91	10.96	10.96	10.99	10.83	10.59	10.92	11.00
a (Å)		5.53078(14)	5.53071(21)	5.53101(22)	5.53166(22)	5.53228(22)	5.53330(23)	5.53441(25)	5.53494(24)	5.53599(23)	5.53752(28)	5.53794(23)	5.54417(34)	5.54350(35)	5.54510(32)	5.5462(4)	5.5462(4)
b (Å)		7.85171(10)	7.85190(25)	7.85204(25)	7.85278(25)	7.85404(25)	7.85489(24)	7.85613(25)	7.85683(25)	7.85850(24)	7.85935(25)	7.86090(25)	7.86374(25)	7.86257(26)	7.86472(25)	7.86643(26)	7.86657(26)
c (Å)		5.53628(14)	5.53681(28)	5.53679(30)	5.53719(29)	5.53785(29)	5.53809(31)	5.53890(34)	5.53985(31)	5.54081(31)	5.5412(4)	5.54301(31)	5.5412(4)	5.5407(4)	5.54188(35)	5.5435(4)	5.5443(5)
α (°)		90.000	90.000	90.000	90.000	90.000	90.000	90.000	90.000	90.000	90.000	90.000	90.000	90.000	90.000	90.000	90.000
β (°)		90.000	90.000	90.000	90.000	90.000	90.000	90.000	90.000	90.000	90.000	90.000	90.000	90.000	90.000	90.000	90.000
γ (°)		90.000	90.000	90.000	90.000	90.000	90.000	90.000	90.000	90.000	90.000	90.000	90.000	90.000	90.000	90.000	90.000
Cell vol. ($Å^3$)		240.419(9)	240.445(17)	240.461(18)	240.529(18)	240.624(18)	240.705(18)	240.826(20)	240.912(19)	241.051(18)	241.162(21)	241.305(18)	241.586(23)	241.497(24)	241.685(22)	241.854(25)	241.894(30)
Bi/Na 1	x	0.2815(9)	0.2815(9)	0.2815(9)	0.2815(9)	0.2815(9)	0.2815(9)	0.2815(9)	0.2815(9)	0.2815(9)	0.2815(9)	0.2815(9)	0.2815(9)	0.2815(9)	0.2815(9)	0.2815(9)	0.2815(9)
	y	0.000	1.000	2.000	3.000	4.000	5.000	6.000	7.000	8.000	9.000	10.000	11.000	12.000	13.000	14.000	15.000
	z	0.7700(9)	0.7700(9)	0.7700(9)	0.7700(9)	0.7700(9)	0.7700(9)	0.7700(9)	0.7700(9)	0.7700(9)	0.7700(9)	0.7700(9)	0.7700(9)	0.7700(9)	0.7700(9)	0.7700(9)	0.7700(9)
Bi/Na 2	x	0.3065(7)	0.3065(7)	0.3065(7)	0.3065(7)	0.3065(7)	0.3065(7)	0.3065(7)	0.3065(7)	0.3065(7)	0.3065(7)	0.3065(7)	0.3065(7)	0.3065(7)	0.3065(7)	0.3065(7)	0.3065(7)
	y	0.500	1.500	2.500	3.500	4.500	5.500	6.500	7.500	8.500	9.500	10.500	11.500	12.500	13.500	14.500	15.500
	z	0.7477(7)	0.7477(7)	0.7477(7)	0.7477(7)	0.7477(7)	0.7477(7)	0.7477(7)	0.7477(7)	0.7477(7)	0.7477(7)	0.7477(7)	0.7477(7)	0.7477(7)	0.7477(7)	0.7477(7)	0.7477(7)
Fe/Nb 1	x	0.2652(7)	0.2652(7)	0.2652(7)	0.2652(7)	0.2652(7)	0.2652(7)	0.2652(7)	0.2652(7)	0.2652(7)	0.2652(7)	0.2652(7)	0.2652(7)	0.2652(7)	0.2652(7)	0.2652(7)	0.2652(7)
	y	0.2527(7)	0.2527(7)	0.2527(7)	0.2527(7)	0.2527(7)	0.2527(7)	0.2527(7)	0.2527(7)	0.2527(7)	0.2527(7)	0.2527(7)	0.2527(7)	0.2527(7)	0.2527(7)	0.2527(7)	0.2527(7)
	z	0.2493(7)	0.2493(7)	0.2493(7)	0.2493(7)	0.2493(7)	0.2493(7)	0.2493(7)	0.2493(7)	0.2493(7)	0.2493(7)	0.2493(7)	0.2493(7)	0.2493(7)	0.2493(7)	0.2493(7)	0.2493(7)
O1	x	0.172(8)	0.172(8)	0.172(8)	0.172(8)	0.172(8)	0.172(8)	0.172(8)	0.172(8)	0.172(8)	0.172(8)	0.172(8)	0.172(8)	0.172(8)	0.172(8)	0.172(8)	0.172(8)
	y	0.000	1.000	2.000	3.000	4.000	5.000	6.000	7.000	8.000	9.000	10.000	11.000	12.000	13.000	14.000	15.000
	z	0.330(8)	0.330(8)	0.330(8)	0.330(8)	0.330(8)	0.330(8)	0.330(8)	0.330(8)	0.330(8)	0.330(8)	0.330(8)	0.330(8)	0.330(8)	0.330(8)	0.330(8)	0.330(8)
O2	x	0.176(8)	0.176(8)	0.176(8)	0.176(8)	0.176(8)	0.176(8)	0.176(8)	0.176(8)	0.176(8)	0.176(8)	0.176(8)	0.176(8)	0.176(8)	0.176(8)	0.176(8)	0.176(8)
	y	0.500	1.500	2.500	3.500	4.500	5.500	6.500	7.500	8.500	9.500	10.500	11.500	12.500	13.500	14.500	15.500
	z	0.337(8)	0.337(8)	0.337(8)	0.337(8)	0.337(8)	0.337(8)	0.337(8)	0.337(8)	0.337(8)	0.337(8)	0.337(8)	0.337(8)	0.337(8)	0.337(8)	0.337(8)	0.337(8)
O3	x	0.019(6)	0.019(6)	0.019(6)	0.019(6)	0.019(6)	0.019(6)	0.019(6)	0.019(6)	0.019(6)	0.019(6)	0.019(6)	0.019(6)	0.019(6)	0.019(6)	0.019(6)	0.019(6)
	y	0.2334(33)	0.2334(33)	0.2334(33)	0.2334(33)	0.2334(33)	0.2334(33)	0.2334(33)	0.2334(33)	0.2334(33)	0.2334(33)	0.2334(33)	0.2334(33)	0.2334(33)	0.2334(33)	0.2334(33)	0.2334(33)
	z	0.523(8)	0.523(8)	0.523(8)	0.523(8)	0.523(8)	0.523(8)	0.523(8)	0.523(8)	0.523(8)	0.523(8)	0.523(8)	0.523(8)	0.523(8)	0.523(8)	0.523(8)	0.523(8)
O4	x	0.011(7)	0.011(7)	0.011(7)	0.011(7)	0.011(7)	0.011(7)	0.011(7)	0.011(7)	0.011(7)	0.011(7)	0.011(7)	0.011(7)	0.011(7)	0.011(7)	0.011(7)	0.011(7)
	y	0.2708(34)	0.2708(34)	0.2708(34)	0.2708(34)	0.2708(34)	0.2708(34)	0.2708(34)	0.2708(34)	0.2708(34)	0.2708(34)	0.2708(34)	0.2708(34)	0.2708(34)	0.2708(34)	0.2708(34)	0.2708(34)
	z	-0.028(8)	-0.028(8)	-0.028(8)	-0.028(8)	-0.028(8)	-0.028(8)	-0.028(8)	-0.028(8)	-0.028(8)	-0.028(8)	-0.028(8)	-0.028(8)	-0.028(8)	-0.028(8)	-0.028(8)	-0.028(8)
Nb/Fe – O bond length (Å)		2.098(14)	2.09835(6)	2.09839(6)	2.09858(6)	2.09891(6)	2.09914(6)	2.09948(6)	2.09967(6)	2.10011(6)	2.10036(6)	2.10077(6)	2.10156(6)	2.10126(6)	2.10183(6)	2.10229(6)	2.10233(6)
		2.061(15)	2.06087(6)	2.06090(6)	2.06110(6)	2.06142(6)	2.06164(6)	2.06197(6)	2.06217(6)	2.06260(6)	2.06284(6)	2.06324(6)	2.06400(6)	2.06370(6)	2.06426(6)	2.06472(6)	2.06477(6)
		2.043(29)	2.04302(7)	2.04307(7)	2.04326(7)	2.04350(7)	2.04371(7)	2.04406(8)	2.04434(7)	2.04471(7)	2.04505(9)	2.04548(7)	2.04615(9)	2.04593(10)	2.04643(9)	2.04693(10)	2.04710(12)
		1.893(31)	1.89283(6)	1.89288(6)	1.89307(6)	1.89329(6)	1.89352(6)	1.89385(7)	1.89410(6)	1.89444(6)	1.89480(8)	1.89515(6)	1.89606(8)	1.89584(9)	1.89633(8)	1.89678(9)	1.89690(11)
		2.086(27)	2.08580(7)	2.08585(7)	2.08605(7)	2.08629(7)	2.08651(7)	2.08687(8)	2.08715(7)	2.08753(7)	2.08788(9)	2.08832(7)	2.08903(9)	2.08880(10)	2.08932(9)	2.08983(10)	2.09000(13)
		1.836(28)	1.83629(6)	1.83634(6)	1.83652(6)	1.83673(6)	1.83696(6)	1.83728(7)	1.83752(6)	1.83785(6)	1.83819(7)	1.83854(6)	1.83941(8)	1.83921(9)	1.83968(8)	1.84011(9)	1.84023(11)
Nb/Fe – O – Nb/Fe bond angle (o)		142.0(20)	142.015(2)	142.014(2)	142.014(2)	142.016(2)	142.015(2)	142.015(2)	142.013(2)	142.014(2)	142.011(2)	142.012(2)	142.007(2)	142.005(2)	142.006(2)	142.005(2)	142.004(2)
		140.9(20)	140.864(2)	140.864(2)	140.863(2)	140.865(2)	140.865(2)	140.864(2)	140.863(2)	140.864(2)	140.861(2)	140.861(2)	140.859(2)	140.858(2)	140.859(2)	140.858(2)	140.856(2)
		169.2(22)	169.230(0)	169.230(0)	169.230(0)	169.230(0)	169.230(0)	169.230(0)	169.230(0)	169.230(0)	169.231(0)	169.231(0)	169.231(0)	169.231(0)	169.231(0)	169.231(0)	169.232(0)
		170.1(23)	170.063(0)	170.063(0)	170.063(0)	170.062(0)	170.062(0)	170.062(0)	170.063(0)	170.063(0)	170.063(0)	170.063(0)	170.063(0)	170.064(0)	170.064(0)	170.064(0)	170.064(0)

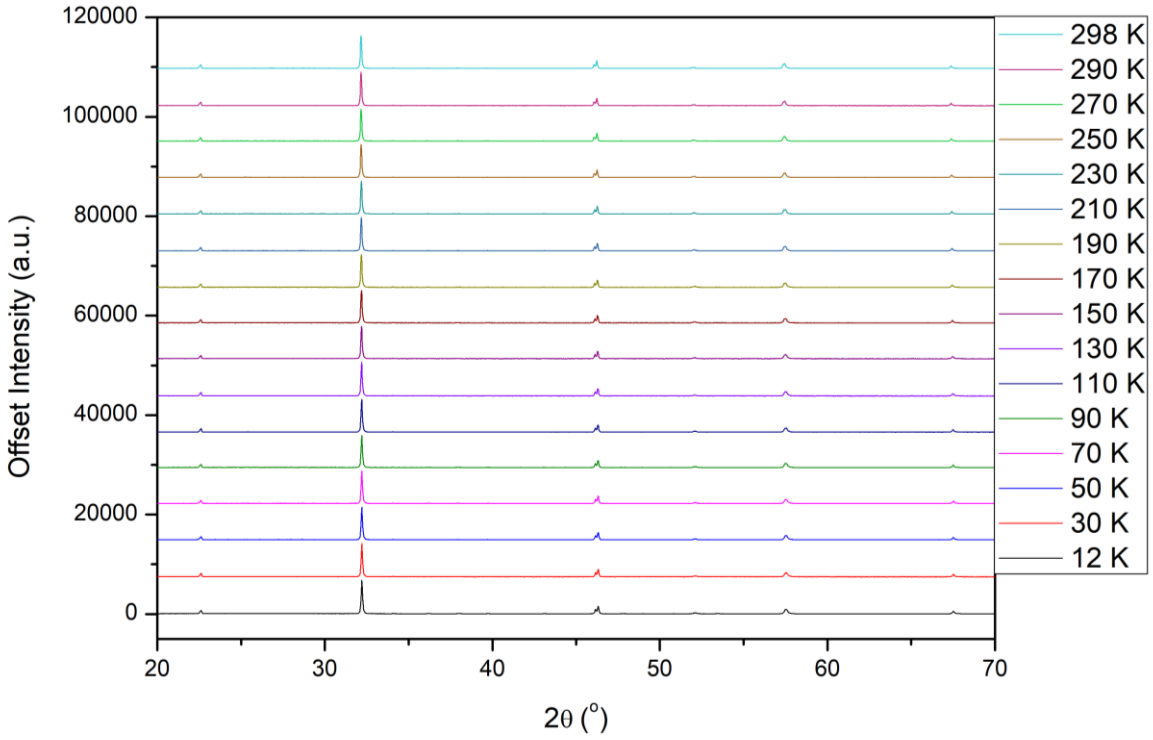

Figure A3.56: *All patterns for the LT PXRD of $Bi_{0.25}Na_{0.75}Fe_{0.25}Nb_{0.75}O_3$. 12K pattern intensity has been scaled down to match the intensities of the other temperature points that were taken with shorter scan times.*

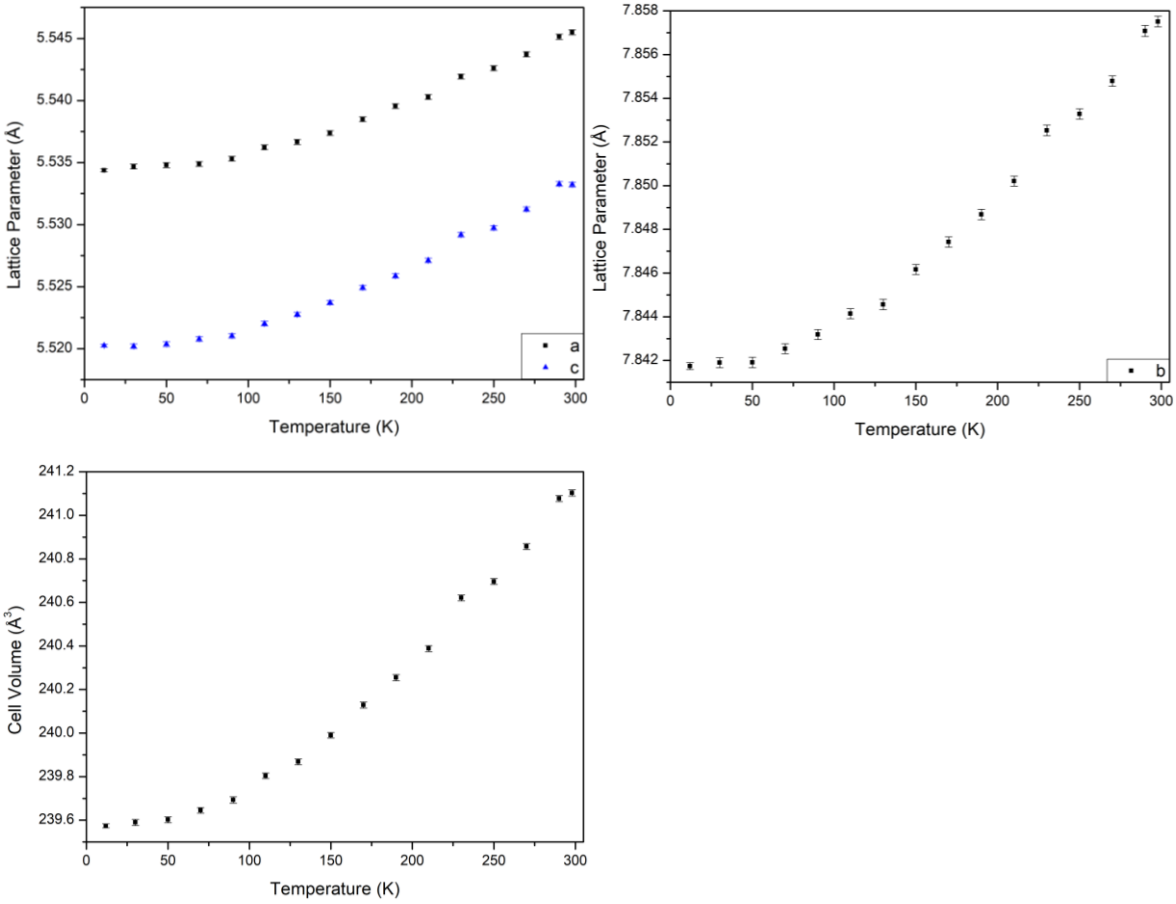

Figure A3.57: *LT PXRD of $Bi_{0.25}Na_{0.75}Fe_{0.25}Nb_{0.75}O_3$: (a) + (b) Lattice Parameter against temperature plot, (c) Cell Volume against temperature plot.*

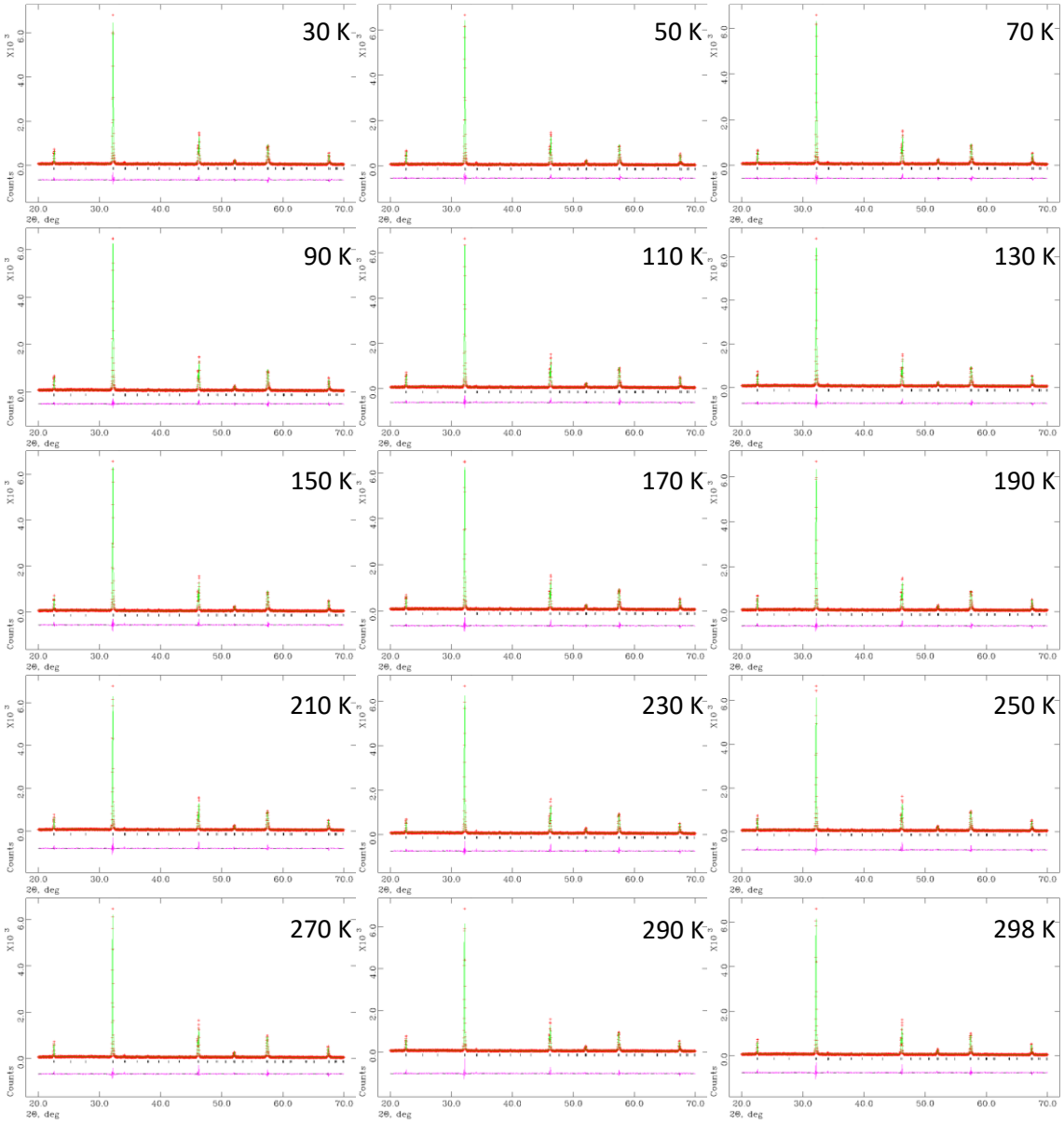

Figure A3.58: *Rietveld refinements obtained from LT PXRD of $Bi_{0.25}Na_{0.75}Fe_{0.25}Nb_{0.75}O_3$ in the temperature ranges 30 K to 298 K.*

Table A3.13: *Rietveld refinement parameters for LT XRD of $Bi_{0.25}Na_{0.75}Fe_{0.25}Nb_{0.75}O_3$.*

Parameter		$Bi_{0.25}Na_{0.75}Fe_{0.25}Nb_{0.75}O_3$															
Temperature (K)		12	30	50	70	90	110	130	150	170	190	210	230	250	270	290	298
Space Group		*P* 2_1ma	*P* 2_1ma	*P* 2_1ma	*P* 2_1ma	*P* 2_1ma	*P* 2_1ma	*P* 2_1ma	*P* 2_1ma	*P* 2_1ma	*P* 2_1ma	*P* 2_1ma	*P* 2_1ma	*P* 2_1ma	*P* 2_1ma	*P* 2_1ma	*P* 2_1ma
χ^2		5.867	1.637	1.725	1.574	1.631	1.592	1.629	1.574	1.682	1.633	1.576	1.681	1.659	1.639	1.714	1.703
wRp (%)		8.54	12.95	13.29	12.72	12.93	12.77	12.90	12.69	13.10	12.90	12.69	13.12	13.05	12.95	13.26	13.20
Rp (%)		5.78	9.95	9.89	9.70	9.82	9.79	9.83	9.68	10.08	9.90	9.98	10.02	10.16	9.96	10.27	10.33
a (Å)		5.53438(13)	5.53468(19)	5.53479(20)	5.53489(19)	5.53531(19)	5.53623(19)	5.53666(20)	5.53738(19)	5.53849(20)	5.53955(20)	5.54029(19)	5.54194(20)	5.54260(20)	5.54372(20)	5.54514(21)	5.54550(21)
b (Å)		7.84174(16)	7.84190(23)	7.84191(24)	7.84254(23)	7.84319(23)	7.84414(23)	7.84456(24)	7.84616(23)	7.84742(24)	7.84868(24)	7.85021(23)	7.85253(24)	7.85328(24)	7.85479(24)	7.85708(25)	7.85751(24)
c (Å)		5.52025(12)	5.52020(18)	5.52036(19)	5.52079(18)	5.52104(18)	5.52202(18)	5.52276(18)	5.52371(18)	5.52493(19)	5.52587(18)	5.52712(18)	5.52919(19)	5.52974(19)	5.53124(19)	5.53328(19)	5.53322(19)
α (°)		90.000	90.000	90.000	90.000	90.000	90.000	90.000	90.000	90.000	90.000	90.000	90.000	90.000	90.000	90.000	90.000
β (°)		90.000	90.000	90.000	90.000	90.000	90.000	90.000	90.000	90.000	90.000	90.000	90.000	90.000	90.000	90.000	90.000
γ (°)		90.000	90.000	90.000	90.000	90.000	90.000	90.000	90.000	90.000	90.000	90.000	90.000	90.000	90.000	90.000	90.000
Cell vol. ($Å^3$)		239.574(9)	239.590(14)	239.602(14)	239.645(13)	239.693(14)	239.804(13)	239.868(14)	239.990(13)	240.129(14)	240.255(14)	240.388(14)	240.621(14)	240.696(14)	240.857(14)	241.077(14)	241.103(14)
Bi/Na 1	x	0.2844(8)	0.2844(8)	0.2844(8)	0.2844(8)	0.2844(8)	0.2844(8)	0.2844(8)	0.2844(8)	0.2844(8)	0.2844(8)	0.2844(8)	0.2844(8)	0.2844(8)	0.2844(8)	0.2844(8)	0.2844(8)
	y	0.000	1.000	2.000	3.000	4.000	5.000	6.000	7.000	8.000	9.000	10.000	11.000	12.000	13.000	14.000	15.000
	z	0.7729(8)	0.7729(8)	0.7729(8)	0.7729(8)	0.7729(8)	0.7729(8)	0.7729(8)	0.7729(8)	0.7729(8)	0.7729(8)	0.7729(8)	0.7729(8)	0.7729(8)	0.7729(8)	0.7729(8)	0.7729(8)
Bi/Na 2	x	0.2962(8)	0.2962(8)	0.2962(8)	0.2962(8)	0.2962(8)	0.2962(8)	0.2962(8)	0.2962(8)	0.2962(8)	0.2962(8)	0.2962(8)	0.2962(8)	0.2962(8)	0.2962(8)	0.2962(8)	0.2962(8)
	y	0.500	1.500	2.500	3.500	4.500	5.500	6.500	7.500	8.500	9.500	10.500	11.500	12.500	13.500	14.500	15.500
	z	0.7374(8)	0.7374(8)	0.7374(8)	0.7374(8)	0.7374(8)	0.7374(8)	0.7374(8)	0.7374(8)	0.7374(8)	0.7374(8)	0.7374(8)	0.7374(8)	0.7374(8)	0.7374(8)	0.7374(8)	0.7374(8)
Fe/Nb 1	x	0.2550(4)	0.2550(4)	0.2550(4)	0.2550(4)	0.2550(4)	0.2550(4)	0.2550(4)	0.2550(4)	0.2550(4)	0.2550(4)	0.2550(4)	0.2550(4)	0.2550(4)	0.2550(4)	0.2550(4)	0.2550(4)
	y	0.2425(4)	0.2425(4)	0.2425(4)	0.2425(4)	0.2425(4)	0.2425(4)	0.2425(4)	0.2425(4)	0.2425(4)	0.2425(4)	0.2425(4)	0.2425(4)	0.2425(4)	0.2425(4)	0.2425(4)	0.2425(4)
	z	0.2391(4)	0.2391(4)	0.2391(4)	0.2391(4)	0.2391(4)	0.2391(4)	0.2391(4)	0.2391(4)	0.2391(4)	0.2391(4)	0.2391(4)	0.2391(4)	0.2391(4)	0.2391(4)	0.2391(4)	0.2391(4)
O1	x	0.338(8)	0.338(8)	0.338(8)	0.338(8)	0.338(8)	0.338(8)	0.338(8)	0.338(8)	0.338(8)	0.338(8)	0.338(8)	0.338(8)	0.338(8)	0.338(8)	0.338(8)	0.338(8)
	y	0.000	1.000	2.000	3.000	4.000	5.000	6.000	7.000	8.000	9.000	10.000	11.000	12.000	13.000	14.000	15.000
	z	0.253(6)	0.253(6)	0.253(6)	0.253(6)	0.253(6)	0.253(6)	0.253(6)	0.253(6)	0.253(6)	0.253(6)	0.253(6)	0.253(6)	0.253(6)	0.253(6)	0.253(6)	0.253(6)
O2	x	0.217(7)	0.217(7)	0.217(7)	0.217(7)	0.217(7)	0.217(7)	0.217(7)	0.217(7)	0.217(7)	0.217(7)	0.217(7)	0.217(7)	0.217(7)	0.217(7)	0.217(7)	0.217(7)
	y	0.500	1.500	2.500	3.500	4.500	5.500	6.500	7.500	8.500	9.500	10.500	11.500	12.500	13.500	14.500	15.500
	z	0.266(6)	0.266(6)	0.266(6)	0.266(6)	0.266(6)	0.266(6)	0.266(6)	0.266(6)	0.266(6)	0.266(6)	0.266(6)	0.266(6)	0.266(6)	0.266(6)	0.266(6)	0.266(6)
O3	x	-0.070(4)	-0.070(4)	-0.070(4)	-0.070(4)	-0.070(4)	-0.070(4)	-0.070(4)	-0.070(4)	-0.070(4)	-0.070(4)	-0.070(4)	-0.070(4)	-0.070(4)	-0.070(4)	-0.070(4)	-0.070(4)
	y	0.2446(37)	0.2446(37)	0.2446(37)	0.2446(37)	0.2446(37)	0.2446(37)	0.2446(37)	0.2446(37)	0.2446(37)	0.2446(37)	0.2446(37)	0.2446(37)	0.2446(37)	0.2446(37)	0.2446(37)	0.2446(37)
	z	0.445(6)	0.445(6)	0.445(6)	0.445(6)	0.445(6)	0.445(6)	0.445(6)	0.445(6)	0.445(6)	0.445(6)	0.445(6)	0.445(6)	0.445(6)	0.445(6)	0.445(6)	0.445(6)
O4	x	0.013(4)	0.013(4)	0.013(4)	0.013(4)	0.013(4)	0.013(4)	0.013(4)	0.013(4)	0.013(4)	0.013(4)	0.013(4)	0.013(4)	0.013(4)	0.013(4)	0.013(4)	0.013(4)
	y	0.2729(34)	0.2729(34)	0.2729(34)	0.2729(34)	0.2729(34)	0.2729(34)	0.2729(34)	0.2729(34)	0.2729(34)	0.2729(34)	0.2729(34)	0.2729(34)	0.2729(34)	0.2729(34)	0.2729(34)	0.2729(34)
	z	0.013(6)	0.013(6)	0.013(6)	0.013(6)	0.013(6)	0.013(6)	0.013(6)	0.013(6)	0.013(6)	0.013(6)	0.013(6)	0.013(6)	0.013(6)	0.013(6)	0.013(6)	0.013(6)
Nb/Fe – O bond length (Å)		1.958(11)	1.95828(6)	1.95829(6)	1.95844(5)	1.95860(6)	1.95884(6)	1.95895(6)	1.95934(5)	1.95966(6)	1.95998(6)	1.96035(5)	1.96093(6)	1.96112(6)	1.96150(6)	1.96207(6)	1.96218(6)
		2.036(6)	2.03561(6)	2.03562(6)	2.03578(6)	2.03595(6)	2.03619(6)	2.03630(6)	2.03672(6)	2.03705(6)	2.03738(6)	2.03777(6)	2.03837(6)	2.03857(6)	2.03896(6)	2.03956(6)	2.03967(6)
		2.129(28)	2.12944(6)	2.12949(6)	2.12957(6)	2.12971(6)	2.13007(6)	2.13027(6)	2.13057(6)	2.13101(6)	2.13141(6)	2.13175(6)	2.13243(6)	2.13267(6)	2.13315(6)	2.13376(6)	2.13385(6)
		1.993(33)	1.99283(5)	1.99288(5)	1.99301(5)	1.99312(5)	1.99346(5)	1.99371(5)	1.99403(5)	1.99446(5)	1.99481(5)	1.99522(5)	1.99593(5)	1.99613(5)	1.99665(5)	1.99733(6)	1.99734(6)
		1.848(28)	1.84837(4)	1.84841(4)	1.84850(4)	1.84861(4)	1.84893(4)	1.84912(4)	1.84940(4)	1.84978(5)	1.85012(4)	1.85045(4)	1.85106(5)	1.85126(5)	1.85170(5)	1.85227(5)	1.85232(5)
		2.006(28)	2.00596(5)	2.00601(5)	2.00611(5)	2.00623(5)	2.00657(5)	2.00678(5)	2.00708(5)	2.00751(5)	2.00787(5)	2.00823(5)	2.00890(5)	2.00912(5)	2.00959(5)	2.01022(5)	2.01027(5)
Nb/Fe – O – Nb/Fe bond angle (o)		152.4(26)	152.408(1)	152.407(1)	152.409(1)	152.409(1)	152.408(1)	152.407(1)	152.409(1)	152.408(1)	152.407(1)	152.409(1)	152.409(1)	152.408(1)	152.408(1)	152.409(1)	152.408(1)
		165.4(23)	165.423(1)	165.422(1)	165.423(1)	165.423(1)	165.422(1)	165.422(1)	165.423(1)	165.422(1)	165.422(1)	165.422(1)	165.422(1)	165.421(1)	165.421(1)	165.421(1)	165.421(1)
		151.4(12)	151.351(0)	151.351(0)	151.351(0)	151.351(0)	151.351(0)	151.351(0)	151.351(0)	151.351(0)	151.351(0)	151.351(0)	151.351(0)	151.351(0)	151.351(0)	151.352(0)	151.352(0)
		165.7(16)	165.742(1)	165.742(1)	165.742(1)	165.742(1)	165.742(1)	165.743(1)	165.742(1)	165.743(1)	165.743(1)	165.743(1)	165.744(1)	165.744(1)	165.744(1)	165.745(1)	165.744(1)

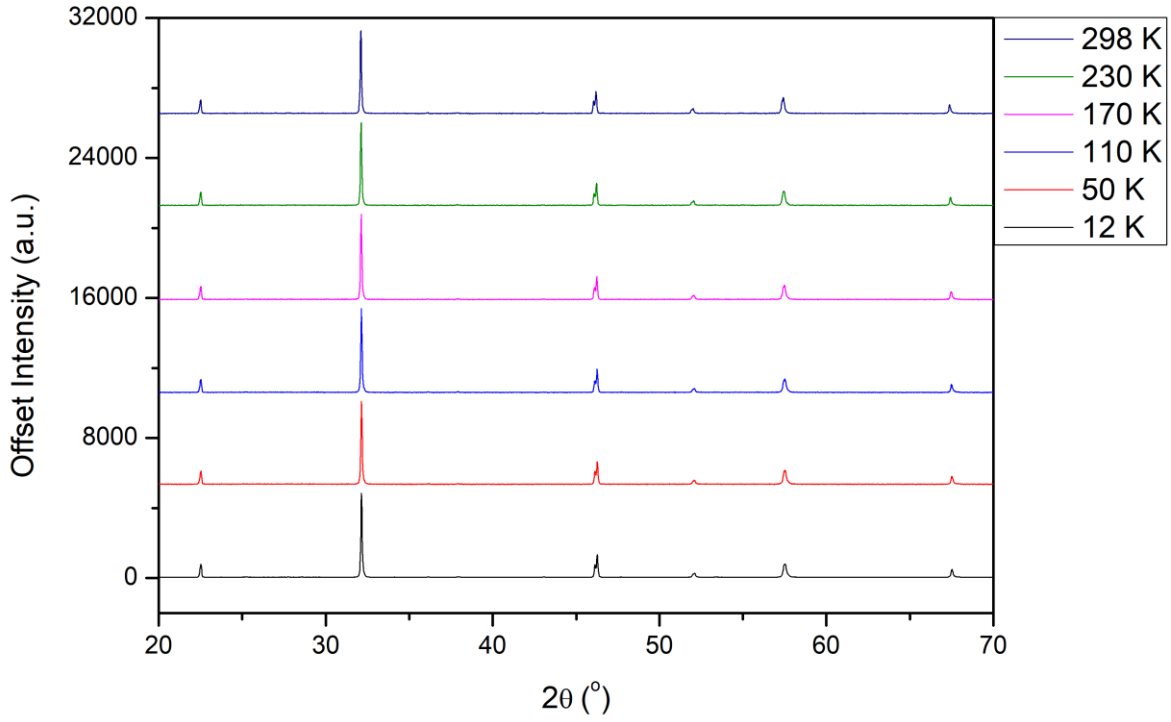

Figure A3.59: *Selection of patterns for the LT PXRD of $Bi_{0.2}Na_{0.8}Fe_{0.2}Nb_{0.8}O_3$. 12K pattern intensity has been scaled down to match the intensities of the other temperature points that were taken with shorter scan times.*

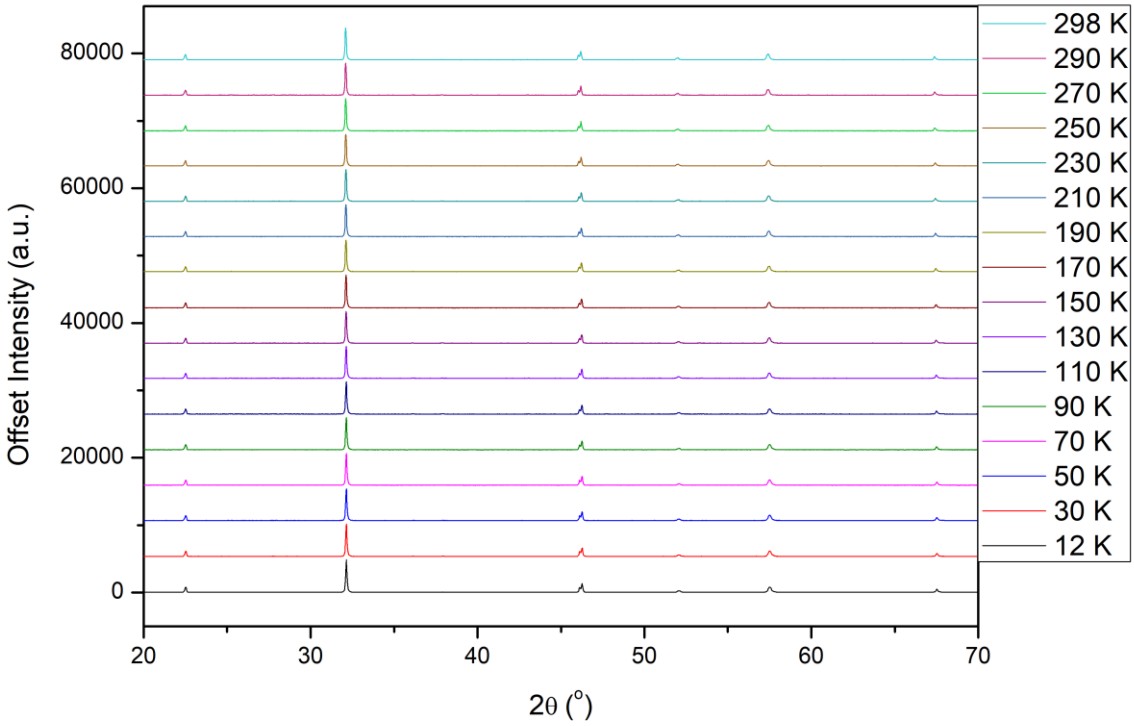

Figure A3.60: *All patterns for the LT PXRD of $Bi_{0.2}Na_{0.8}Fe_{0.2}Nb_{0.8}O_3$. 12K pattern intensity has been scaled down to match the intensities of the other temperature points that were taken with shorter scan times.*

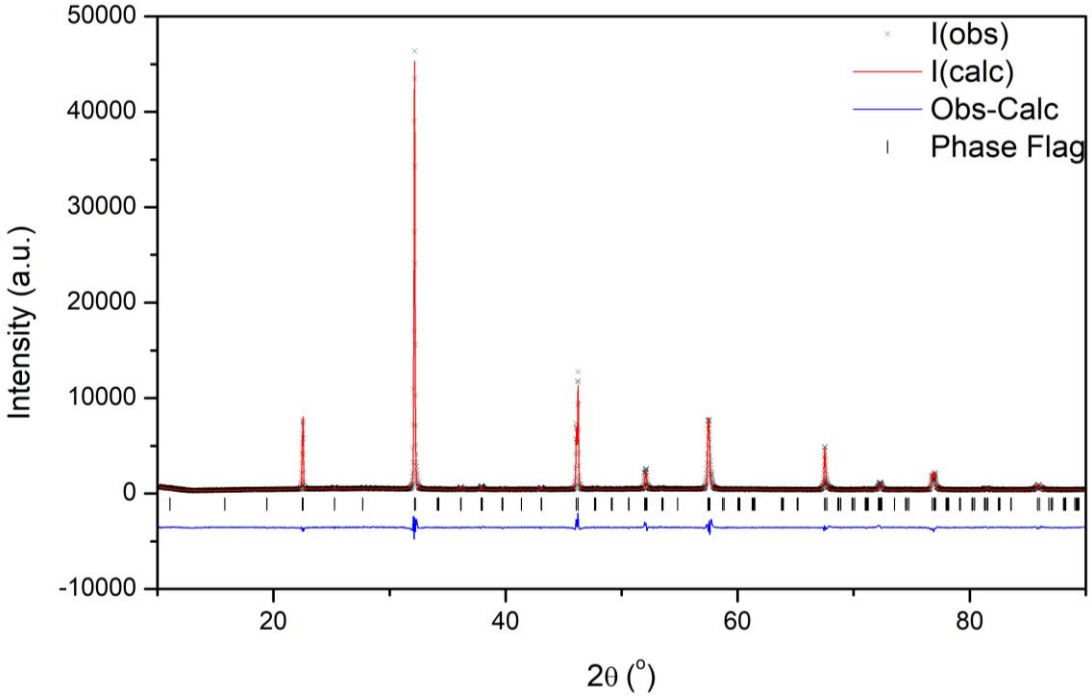

Figure A3.61: *Rietveld refinement of 12 K PXRD data collected for $Bi_{0.2}Na_{0.8}Fe_{0.2}Nb_{0.8}O_3$; $\chi^2 = 4.642$, $R_{wp} = 8.78\%$ and $R_p = 6.31$; the black crosses represent the observed intensity, the red line represents the calculated intensity from the model, the blue line represents the difference between the observed pattern and calculated pattern and the black tick marker represents the $P2_1ma$ model.*

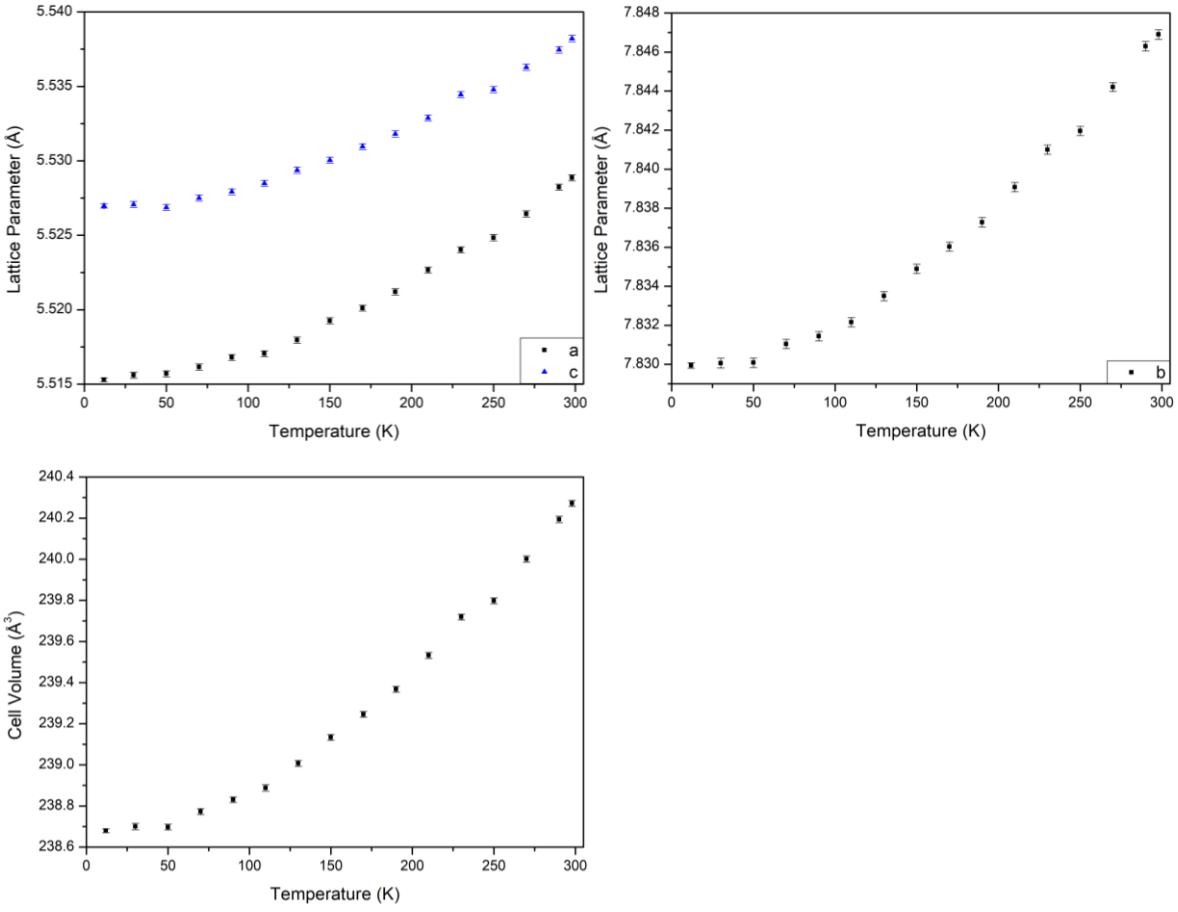

Figure A3.62: *LT PXRD of $Bi_{0.2}Na_{0.8}Fe_{0.2}Nb_{0.8}O_3$: (a) + (b) Lattice Parameter against temperature plot, (c) Cell Volume against temperature plot.*

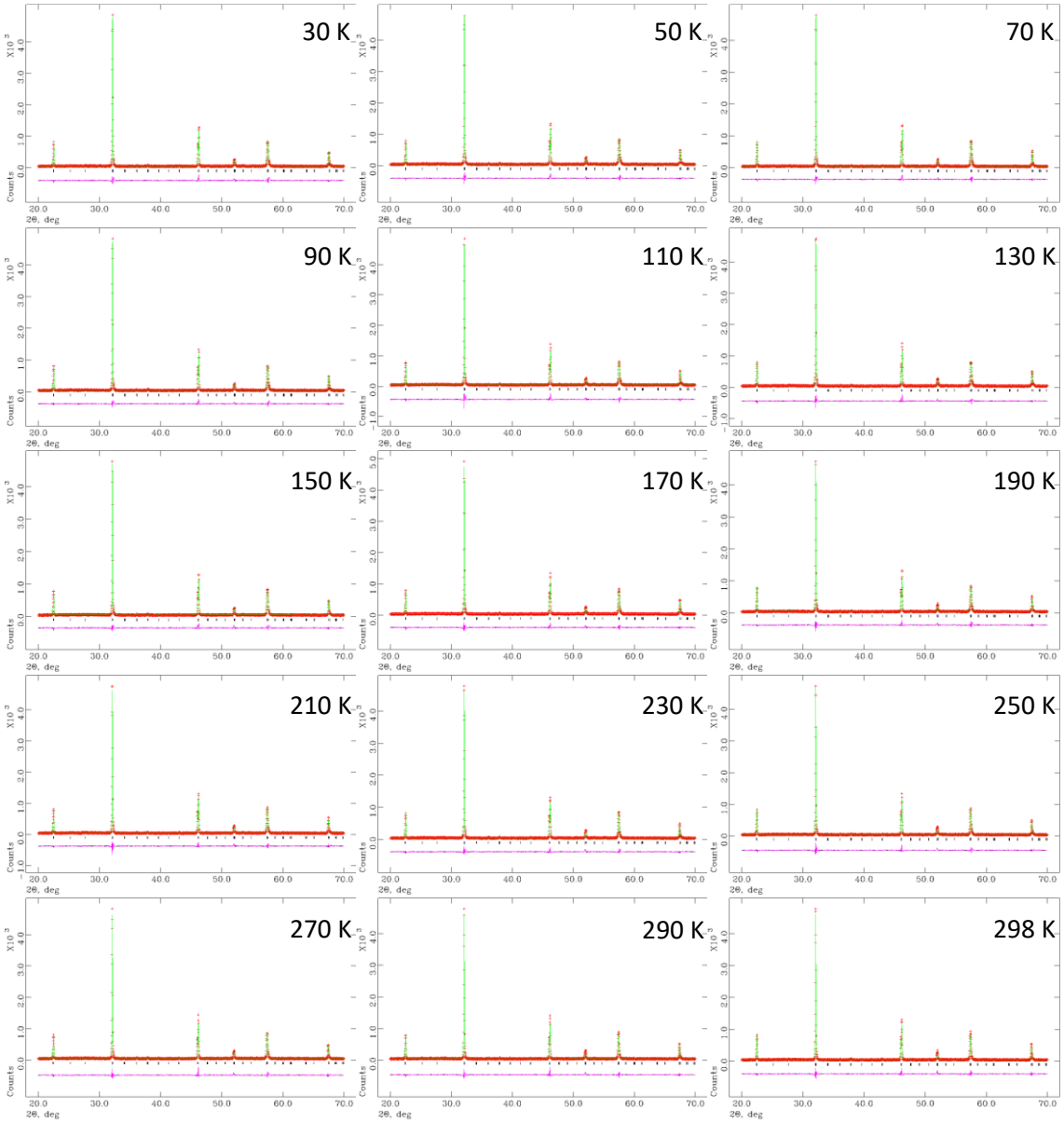

Figure A3.63: *Rietveld refinements obtained from LT PXRD of $Bi_{0.2}Na_{0.8}Fe_{0.2}Nb_{0.8}O_3$ in the temperature ranges 30 K to 298 K.*

Table A3.14: *Rietveld refinement parameters for LT XRD of $Bi_{0.2}Na_{0.8}Fe_{0.2}Nb_{0.8}O_3$.*

Parameter		$Bi_{0.2}Na_{0.8}Fe_{0.2}Nb_{0.8}O_3$															
Temperature (K)		12	30	50	70	90	110	130	150	170	190	210	230	250	270	290	298
Space Group		*P* 2_1ma	*P* 2_1ma	*P* 2_1ma	*P* 2_1ma	*P* 2_1ma	*P* 2_1ma	*P* 2_1ma	*P* 2_1ma	*P* 2_1ma	*P* 2_1ma	*P* 2_1ma	*P* 2_1ma	*P* 2_1ma	*P* 2_1ma	*P* 2_1ma	*P* 2_1ma
χ^2		4.642	1.596	1.511	1.559	1.503	1.518	1.553	1.497	1.445	1.521	1.533	1.487	1.473	1.459	1.534	1.533
wRp (%)		8.78	14.88	14.49	14.76	14.47	14.59	14.75	14.46	14.21	14.57	14.60	14.41	14.31	14.25	14.57	14.57
Rp (%)		6.31	10.99	10.90	10.90	10.63	10.90	10.98	10.56	10.72	10.86	10.94	10.69	10.68	10.76	10.91	10.89
a (Å)		5.51530(13)	5.51560(21)	5.51570(20)	5.51615(21)	5.51680(20)	5.51705(20)	5.51796(21)	5.51926(20)	5.52011(20)	5.52121(21)	5.52267(21)	5.52403(21)	5.52484(21)	5.52644(21)	5.52824(21)	5.52886(21)
b (Å)		7.82994(14)	7.83006(25)	7.83009(24)	7.83104(24)	7.83144(24)	7.83216(24)	7.83350(24)	7.83489(24)	7.83603(23)	7.83728(24)	7.83908(24)	7.84100(24)	7.84196(23)	7.84421(23)	7.84630(24)	7.84690(24)
c (Å)		5.52697(14)	5.52707(21)	5.52687(21)	5.52750(21)	5.52792(20)	5.52848(21)	5.52937(21)	5.53004(21)	5.53095(20)	5.53181(21)	5.53288(21)	5.53445(21)	5.53478(21)	5.53629(21)	5.53746(22)	5.53821(22)
α (°)		90.000	90.000	90.000	90.000	90.000	90.000	90.000	90.000	90.000	90.000	90.000	90.000	90.000	90.000	90.000	90.000
β (°)		90.000	90.000	90.000	90.000	90.000	90.000	90.000	90.000	90.000	90.000	90.000	90.000	90.000	90.000	90.000	90.000
γ (°)		90.000	90.000	90.000	90.000	90.000	90.000	90.000	90.000	90.000	90.000	90.000	90.000	90.000	90.000	90.000	90.000
Cell vol. ($Å^3$)		238.680(9)	238.700(15)	238.697(14)	238.773(15)	238.831(14)	238.888(15)	239.007(15)	239.134(15)	239.246(14)	239.368(15)	239.533(15)	239.719(15)	239.798(15)	240.001(15)	240.194(15)	240.272(15)
Bi/Na 1	x	0.2887(9)	0.2887(9)	0.2887(9)	0.2887(9)	0.2887(9)	0.2887(9)	0.2887(9)	0.2887(9)	0.2887(9)	0.2887(9)	0.2887(9)	0.2887(9)	0.2887(9)	0.2887(9)	0.2887(9)	0.2887(9)
	y	0.000	1.000	2.000	3.000	4.000	5.000	6.000	7.000	8.000	9.000	10.000	11.000	12.000	13.000	14.000	15.000
	z	0.7772(9)	0.7772(9)	0.7772(9)	0.7772(9)	0.7772(9)	0.7772(9)	0.7772(9)	0.7772(9)	0.7772(9)	0.7772(9)	0.7772(9)	0.7772(9)	0.7772(9)	0.7772(9)	0.7772(9)	0.7772(9)
Bi/Na 2	x	0.3095(9)	0.3095(9)	0.3095(9)	0.3095(9)	0.3095(9)	0.3095(9)	0.3095(9)	0.3095(9)	0.3095(9)	0.3095(9)	0.3095(9)	0.3095(9)	0.3095(9)	0.3095(9)	0.3095(9)	0.3095(9)
	y	0.500	1.500	2.500	3.500	4.500	5.500	6.500	7.500	8.500	9.500	10.500	11.500	12.500	13.500	14.500	15.500
	z	0.7507(9)	0.7507(9)	0.7507(9)	0.7507(9)	0.7507(9)	0.7507(9)	0.7507(9)	0.7507(9)	0.7507(9)	0.7507(9)	0.7507(9)	0.7507(9)	0.7507(9)	0.7507(9)	0.7507(9)	0.7507(9)
Fe/Nb 1	x	0.2631(5)	0.2631(5)	0.2631(5)	0.2631(5)	0.2631(5)	0.2631(5)	0.2631(5)	0.2631(5)	0.2631(5)	0.2631(5)	0.2631(5)	0.2631(5)	0.2631(5)	0.2631(5)	0.2631(5)	0.2631(5)
	y	0.2506(5)	0.2506(5)	0.2506(5)	0.2506(5)	0.2506(5)	0.2506(5)	0.2506(5)	0.2506(5)	0.2506(5)	0.2506(5)	0.2506(5)	0.2506(5)	0.2506(5)	0.2506(5)	0.2506(5)	0.2506(5)
	z	0.2472(5)	0.2472(5)	0.2472(5)	0.2472(5)	0.2472(5)	0.2472(5)	0.2472(5)	0.2472(5)	0.2472(5)	0.2472(5)	0.2472(5)	0.2472(5)	0.2472(5)	0.2472(5)	0.2472(5)	0.2472(5)
O1	x	0.246(8)	0.246(8)	0.246(8)	0.246(8)	0.246(8)	0.246(8)	0.246(8)	0.246(8)	0.246(8)	0.246(8)	0.246(8)	0.246(8)	0.246(8)	0.246(8)	0.246(8)	0.246(8)
	y	0.000	1.000	2.000	3.000	4.000	5.000	6.000	7.000	8.000	9.000	10.000	11.000	12.000	13.000	14.000	15.000
	z	0.291(5)	0.291(5)	0.291(5)	0.291(5)	0.291(5)	0.291(5)	0.291(5)	0.291(5)	0.291(5)	0.291(5)	0.291(5)	0.291(5)	0.291(5)	0.291(5)	0.291(5)	0.291(5)
O2	x	0.152(9)	0.152(9)	0.152(9)	0.152(9)	0.152(9)	0.152(9)	0.152(9)	0.152(9)	0.152(9)	0.152(9)	0.152(9)	0.152(9)	0.152(9)	0.152(9)	0.152(9)	0.152(9)
	y	0.500	1.500	2.500	3.500	4.500	5.500	6.500	7.500	8.500	9.500	10.500	11.500	12.500	13.500	14.500	15.500
	z	0.375(6)	0.375(6)	0.375(6)	0.375(6)	0.375(6)	0.375(6)	0.375(6)	0.375(6)	0.375(6)	0.375(6)	0.375(6)	0.375(6)	0.375(6)	0.375(6)	0.375(6)	0.375(6)
O3	x	0.024(7)	0.024(7)	0.024(7)	0.024(7)	0.024(7)	0.024(7)	0.024(7)	0.024(7)	0.024(7)	0.024(7)	0.024(7)	0.024(7)	0.024(7)	0.024(7)	0.024(7)	0.024(7)
	y	0.2176(23)	0.2176(23)	0.2176(23)	0.2176(23)	0.2176(23)	0.2176(23)	0.2176(23)	0.2176(23)	0.2176(23)	0.2176(23)	0.2176(23)	0.2176(23)	0.2176(23)	0.2176(23)	0.2176(23)	0.2176(23)
	z	0.523(9)	0.523(9)	0.523(9)	0.523(9)	0.523(9)	0.523(9)	0.523(9)	0.523(9)	0.523(9)	0.523(9)	0.523(9)	0.523(9)	0.523(9)	0.523(9)	0.523(9)	0.523(9)
O4	x	0.020(7)	0.020(7)	0.020(7)	0.020(7)	0.020(7)	0.020(7)	0.020(7)	0.020(7)	0.020(7)	0.020(7)	0.020(7)	0.020(7)	0.020(7)	0.020(7)	0.020(7)	0.020(7)
	y	0.2539(23)	0.2539(23)	0.2539(23)	0.2539(23)	0.2539(23)	0.2539(23)	0.2539(23)	0.2539(23)	0.2539(23)	0.2539(23)	0.2539(23)	0.2539(23)	0.2539(23)	0.2539(23)	0.2539(23)	0.2539(23)
	z	-0.023(9)	-0.023(9)	-0.023(9)	-0.023(9)	-0.023(9)	-0.023(9)	-0.023(9)	-0.023(9)	-0.023(9)	-0.023(9)	-0.023(9)	-0.023(9)	-0.023(9)	-0.023(9)	-0.023(9)	-0.023(9)
Nb/Fe – O bond length (Å)		1.979(5)	1.97895(6)	1.97895(6)	1.97919(6)	1.97929(6)	1.97948(6)	1.97981(6)	1.98016(6)	1.98045(6)	1.98077(6)	1.98122(6)	1.98171(6)	1.98195(6)	1.98252(6)	1.98305(6)	1.98320(6)
		2.165(18)	2.16535(6)	2.16535(5)	2.16560(6)	2.16573(5)	2.16593(6)	2.16629(6)	2.16667(5)	2.16699(5)	2.16735(6)	2.16784(5)	2.16838(5)	2.16864(5)	2.16926(5)	2.16983(6)	2.17002(6)
		2.03(4)	2.03357(5)	2.03355(5)	2.03375(5)	2.03394(5)	2.03410(5)	2.03443(5)	2.03478(5)	2.03510(5)	2.03546(5)	2.03591(5)	2.03646(5)	2.03666(5)	2.03723(5)	2.03776(6)	2.03801(6)
		1.94(4)	1.93517(5)	1.93516(5)	1.93534(5)	1.93553(5)	1.93567(5)	1.93599(5)	1.93635(5)	1.93665(5)	1.93700(5)	1.93745(5)	1.93796(5)	1.93817(5)	1.93872(5)	1.93925(5)	1.93949(5)
		2.01(4)	2.00536(5)	2.00534(5)	2.00554(5)	2.00573(5)	2.00588(5)	2.00621(5)	2.00655(5)	2.00687(5)	2.00722(5)	2.00768(5)	2.00821(5)	2.00841(5)	2.00897(5)	2.00950(6)	2.00975(6)
		1.88(4)	1.88403(5)	1.88402(5)	1.88420(5)	1.88438(5)	1.88452(5)	1.88482(5)	1.88517(5)	1.88547(5)	1.88581(5)	1.88625(5)	1.88675(5)	1.88695(5)	1.88749(5)	1.88801(5)	1.88824(5)
Nb/Fe – O – Nb/Fe bond angle (o)		165.0(16)	165.039(1)	165.040(1)	165.040(1)	165.040(1)	165.040(1)	165.040(1)	165.040(1)	165.040(1)	165.040(1)	165.040(1)	165.040(1)	165.041(1)	165.041(1)	165.041(1)	165.041(1)
		128.8(18)	128.818(2)	128.818(2)	128.819(2)	128.818(2)	128.818(2)	128.818(2)	128.819(2)	128.818(2)	128.818(2)	128.818(2)	128.817(2)	128.818(2)	128.818(2)	128.819(2)	128.816(2)
		163.2(17)	163.212(1)	163.212(1)	163.212(1)	163.212(1)	163.212(1)	163.212(1)	163.212(1)	163.212(1)	163.212(1)	163.212(1)	163.213(1)	163.212(1)	163.212(1)	163.212(1)	163.213(1)
		173.0(30)	173.039(0)	173.039(0)	173.039(0)	173.039(0)	173.039(0)	173.039(0)	173.039(0)	173.039(0)	173.039(0)	173.039(0)	173.039(0)	173.039(0)	173.039(0)	173.039(0)	173.039(0)

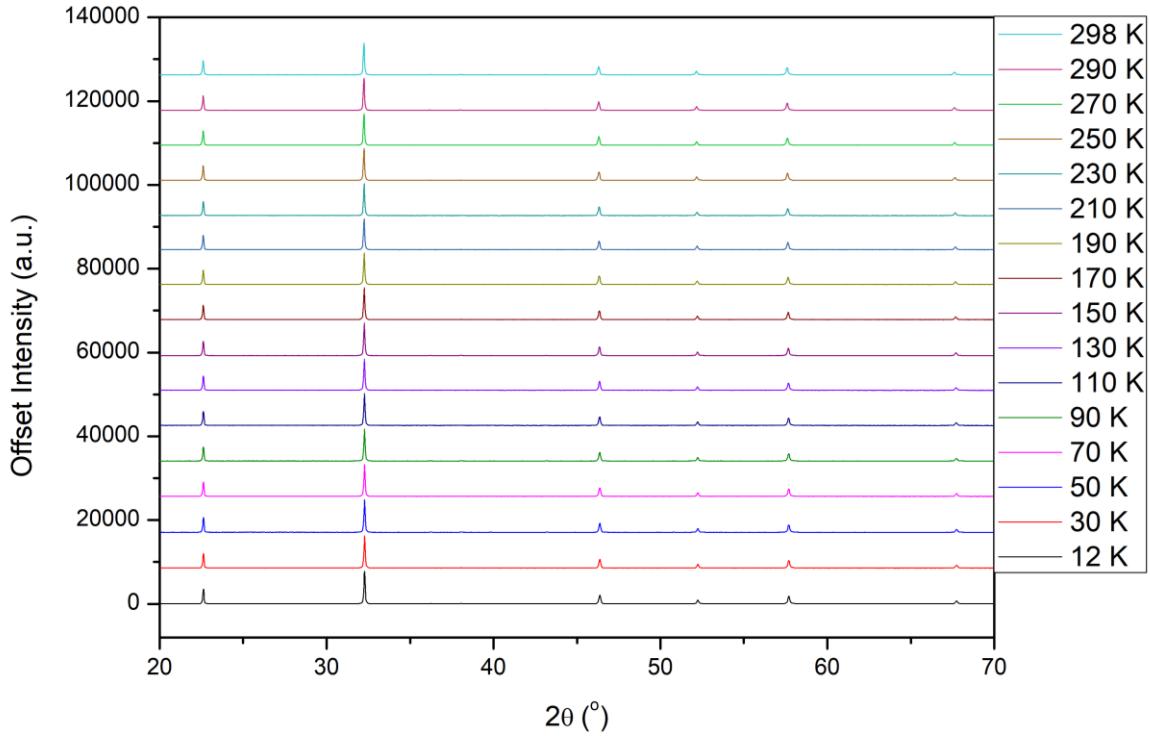

Figure A3.64: *All patterns for the LT PXRD of $Bi_{0.1}Na_{0.9}Fe_{0.1}Nb_{0.9}O_3$. 12K pattern intensity has been scaled down to match the intensities of the other temperature points that were taken with shorter scan times.*

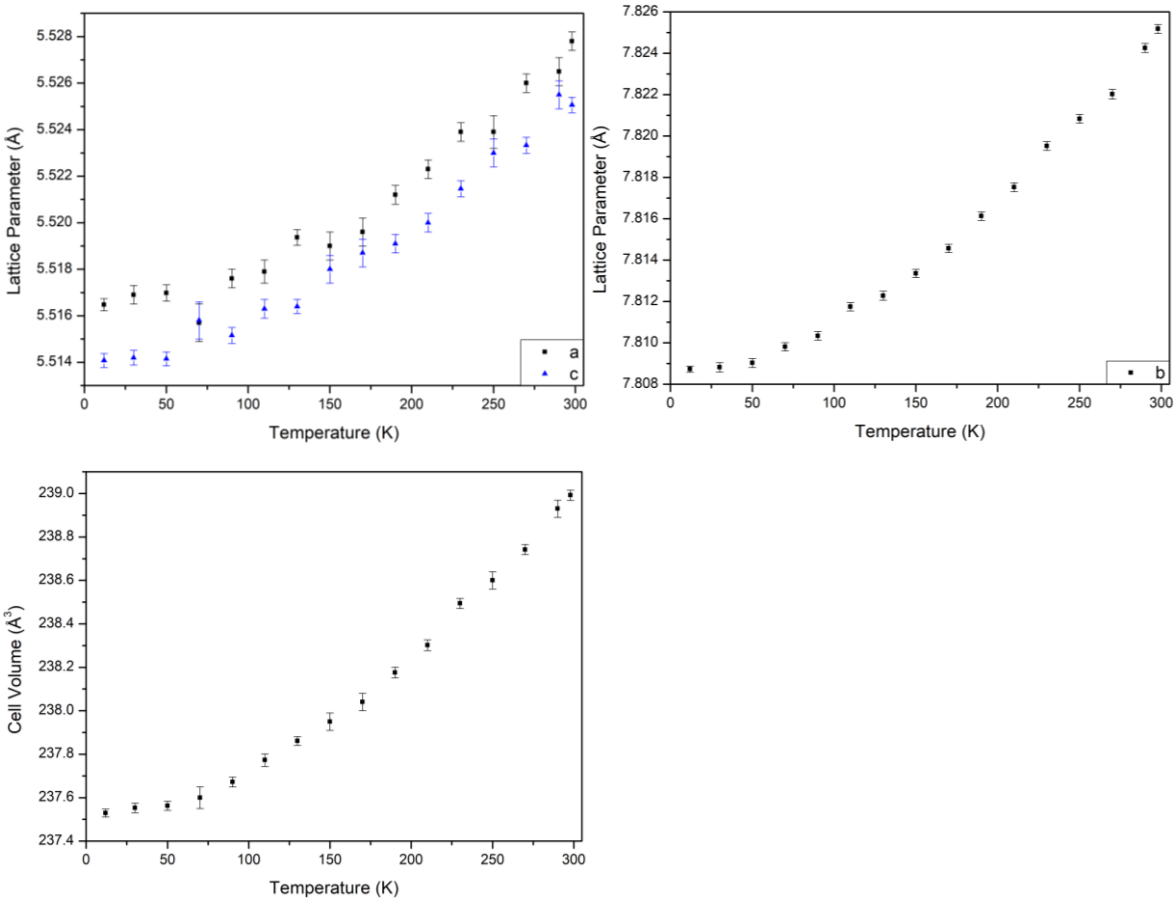

Figure A3.65: *LT PXRD of $Bi_{0.1}Na_{0.9}Fe_{0.1}Nb_{0.9}O_3$: (a) + (b) Lattice Parameter against temperature plot, (c) Cell Volume against temperature plot.*

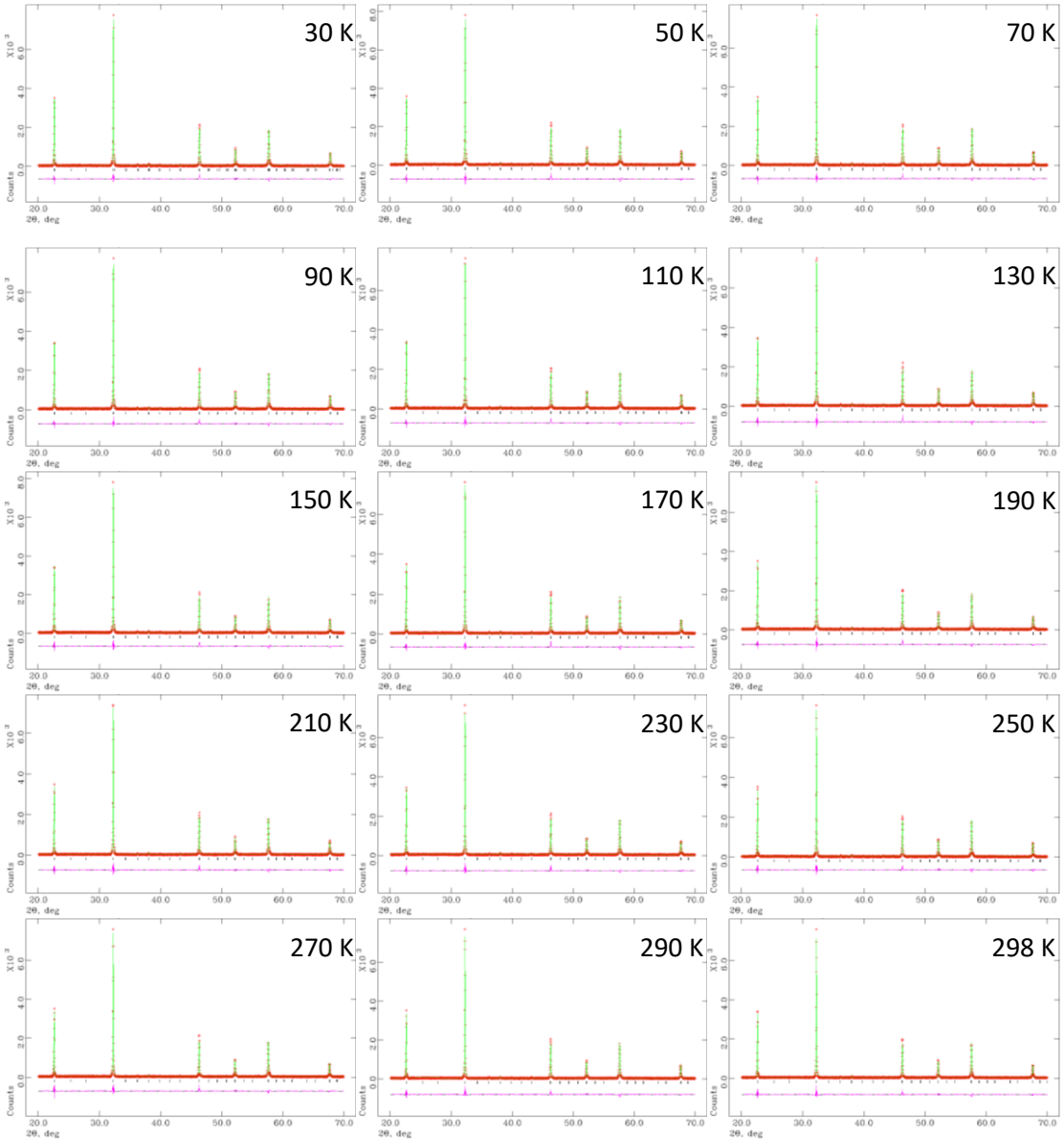

Figure A3.66: *Rietveld refinements obtained from LT PXRD of $Bi_{0.1}Na_{0.9}Fe_{0.1}Nb_{0.9}O_3$ in the temperature ranges 30 K to 298 K.*

Table A3.15: *Rietveld refinement parameters for LT XRD of $Bi_{0.1}Na_{0.9}Fe_{0.1}Nb_{0.9}O_3$.*

Parameter		$Bi_{0.1}Na_{0.9}Fe_{0.1}Nb_{0.9}O_3$															
Temperature (K)		12	30	50	70	90	110	130	150	170	190	210	230	250	270	290	298
Space Group		*P* 2_1ma	*P* 2_1ma	*P* 2_1ma	*P* 2_1ma	*P* 2_1ma	*P* 2_1ma	*P* 2_1ma	*P* 2_1ma	*P* 2_1ma	*P* 2_1ma	*P* 2_1ma	*P* 2_1ma	*P* 2_1ma	*P* 2_1ma	*P* 2_1ma	*P* 2_1ma
χ^2		5.428	1.700	1.702	1.643	1.655	1.592	1.664	1.619	1.708	1.665	1.699	1.638	1.757	1.846	1.886	1.801
wRp (%)		8.91	14.09	14.05	13.86	13.93	13.62	13.95	13.72	14.08	13.93	14.08	13.81	14.30	14.68	14.84	14.56
Rp (%)		6.57	10.42	10.39	10.22	10.16	10.02	10.33	9.97	10.36	10.26	10.38	10.04	10.46	10.61	10.75	10.54
a (Å)		5.51648(26)	5.5169(4)	5.51698(35)	5.5157(8)	5.5176(4)	5.5179(5)	5.51937(34)	5.5190(6)	5.5196(6)	5.5212(4)	5.5223(4)	5.5239(4)	5.5239(7)	5.5260(4)	5.5265(6)	5.5278(4)
b (Å)		7.80873(15)	7.80882(22)	7.80903(22)	7.80981(20)	7.81034(21)	7.81175(20)	7.81228(22)	7.81336(20)	7.81457(20)	7.81613(21)	7.81753(21)	7.81952(21)	7.82083(21)	7.82202(23)	7.82426(22)	7.82518(22)
c (Å)		5.51408(30)	5.51420(32)	5.51415(30)	5.5158(8)	5.51516(34)	5.5163(4)	5.51640(30)	5.5180(6)	5.5187(6)	5.5191(4)	5.5200(4)	5.52146(34)	5.5230(6)	5.52333(34)	5.5255(6)	5.52506(33)
α (°)		90.000	90.000	90.000	90.000	90.000	90.000	90.000	90.000	90.000	90.000	90.000	90.000	90.000	90.000	90.000	90.000
β (°)		90.000	90.000	90.000	90.000	90.000	90.000	90.000	90.000	90.000	90.000	90.000	90.000	90.000	90.000	90.000	90.000
γ (°)		90.000	90.000	90.000	90.000	90.000	90.000	90.000	90.000	90.000	90.000	90.000	90.000	90.000	90.000	90.000	90.000
Cell vol. ($Å^3$)		237.529(18)	237.553(22)	237.562(21)	237.60(5)	237.672(23)	237.773(29)	237.861(20)	237.95(4)	238.04(4)	238.176(25)	238.302(25)	238.494(23)	238.60(4)	238.742(23)	238.93(4)	238.992(23)
Bi/Na 1	x	0.2894(14)	0.2894(14)	0.2894(14)	0.2894(14)	0.2894(14)	0.2894(14)	0.2894(14)	0.2894(14)	0.2894(14)	0.2894(14)	0.2894(14)	0.2894(14)	0.2894(14)	0.2894(14)	0.2894(14)	0.2894(14)
	y	0.000	1.000	2.000	3.000	4.000	5.000	6.000	7.000	8.000	9.000	10.000	11.000	12.000	13.000	14.000	15.000
	z	0.7779(14)	0.7779(14)	0.7779(14)	0.7779(14)	0.7779(14)	0.7779(14)	0.7779(14)	0.7779(14)	0.7779(14)	0.7779(14)	0.7779(14)	0.7779(14)	0.7779(14)	0.7779(14)	0.7779(14)	0.7779(14)
Bi/Na 2	x	0.3122(15)	0.3122(15)	0.3122(15)	0.3122(15)	0.3122(15)	0.3122(15)	0.3122(15)	0.3122(15)	0.3122(15)	0.3122(15)	0.3122(15)	0.3122(15)	0.3122(15)	0.3122(15)	0.3122(15)	0.3122(15)
	y	0.500	1.500	2.500	3.500	4.500	5.500	6.500	7.500	8.500	9.500	10.500	11.500	12.500	13.500	14.500	15.500
	z	0.7534(15)	0.7534(15)	0.7534(15)	0.7534(15)	0.7534(15)	0.7534(15)	0.7534(15)	0.7534(15)	0.7534(15)	0.7534(15)	0.7534(15)	0.7534(15)	0.7534(15)	0.7534(15)	0.7534(15)	0.7534(15)
Fe/Nb 1	x	0.2652(4)	0.2652(4)	0.2652(4)	0.2652(4)	0.2652(4)	0.2652(4)	0.2652(4)	0.2652(4)	0.2652(4)	0.2652(4)	0.2652(4)	0.2652(4)	0.2652(4)	0.2652(4)	0.2652(4)	0.2652(4)
	y	0.2527(4)	0.2527(4)	0.2527(4)	0.2527(4)	0.2527(4)	0.2527(4)	0.2527(4)	0.2527(4)	0.2527(4)	0.2527(4)	0.2527(4)	0.2527(4)	0.2527(4)	0.2527(4)	0.2527(4)	0.2527(4)
	z	0.2493(4)	0.2493(4)	0.2493(4)	0.2493(4)	0.2493(4)	0.2493(4)	0.2493(4)	0.2493(4)	0.2493(4)	0.2493(4)	0.2493(4)	0.2493(4)	0.2493(4)	0.2493(4)	0.2493(4)	0.2493(4)
O1	x	0.282(8)	0.282(8)	0.282(8)	0.282(8)	0.282(8)	0.282(8)	0.282(8)	0.282(8)	0.282(8)	0.282(8)	0.282(8)	0.282(8)	0.282(8)	0.282(8)	0.282(8)	0.282(8)
	y	0.000	1.000	2.000	3.000	4.000	5.000	6.000	7.000	8.000	9.000	10.000	11.000	12.000	13.000	14.000	15.000
	z	0.313(6)	0.313(6)	0.313(6)	0.313(6)	0.313(6)	0.313(6)	0.313(6)	0.313(6)	0.313(6)	0.313(6)	0.313(6)	0.313(6)	0.313(6)	0.313(6)	0.313(6)	0.313(6)
O2	x	0.237(10)	0.237(10)	0.237(10)	0.237(10)	0.237(10)	0.237(10)	0.237(10)	0.237(10)	0.237(10)	0.237(10)	0.237(10)	0.237(10)	0.237(10)	0.237(10)	0.237(10)	0.237(10)
	y	0.500	1.500	2.500	3.500	4.500	5.500	6.500	7.500	8.500	9.500	10.500	11.500	12.500	13.500	14.500	15.500
	z	0.196(6)	0.196(6)	0.196(6)	0.196(6)	0.196(6)	0.196(6)	0.196(6)	0.196(6)	0.196(6)	0.196(6)	0.196(6)	0.196(6)	0.196(6)	0.196(6)	0.196(6)	0.196(6)
O3	x	-0.050(4)	-0.050(4)	-0.050(4)	-0.050(4)	-0.050(4)	-0.050(4)	-0.050(4)	-0.050(4)	-0.050(4)	-0.050(4)	-0.050(4)	-0.050(4)	-0.050(4)	-0.050(4)	-0.050(4)	-0.050(4)
	y	0.2542(34)	0.2542(34)	0.2542(34)	0.2542(34)	0.2542(34)	0.2542(34)	0.2542(34)	0.2542(34)	0.2542(34)	0.2542(34)	0.2542(34)	0.2542(34)	0.2542(34)	0.2542(34)	0.2542(34)	0.2542(34)
	z	0.474(4)	0.474(4)	0.474(4)	0.474(4)	0.474(4)	0.474(4)	0.474(4)	0.474(4)	0.474(4)	0.474(4)	0.474(4)	0.474(4)	0.474(4)	0.474(4)	0.474(4)	0.474(4)
O4	x	0.025(4)	0.025(4)	0.025(4)	0.025(4)	0.025(4)	0.025(4)	0.025(4)	0.025(4)	0.025(4)	0.025(4)	0.025(4)	0.025(4)	0.025(4)	0.025(4)	0.025(4)	0.025(4)
	y	0.2212(29)	0.2212(29)	0.2212(29)	0.2212(29)	0.2212(29)	0.2212(29)	0.2212(29)	0.2212(29)	0.2212(29)	0.2212(29)	0.2212(29)	0.2212(29)	0.2212(29)	0.2212(29)	0.2212(29)	0.2212(29)
	z	0.033(5)	0.033(5)	0.033(5)	0.033(5)	0.033(5)	0.033(5)	0.033(5)	0.033(5)	0.033(5)	0.033(5)	0.033(5)	0.033(5)	0.033(5)	0.033(5)	0.033(5)	0.033(5)
Nb/Fe – O bond length (Å)		2.006(6)	2.00605(5)	2.00610(5)	2.00631(5)	2.00643(5)	2.00680(5)	2.00693(5)	2.00722(5)	2.00753(5)	2.00792(5)	2.00828(5)	2.00879(5)	2.00913(5)	2.00943(6)	2.01002(5)	2.01024(5)
		1.960(7)	1.95978(5)	1.95983(5)	1.96003(5)	1.96016(5)	1.96051(5)	1.96065(5)	1.96092(5)	1.96122(5)	1.96161(5)	1.96196(5)	1.96246(5)	1.96279(5)	1.96309(6)	1.96366(5)	1.96388(5)
		2.133(28)	2.13358(10)	2.13360(10)	2.13347(22)	2.13389(11)	2.13410(14)	2.13451(10)	2.13462(17)	2.13486(18)	2.13534(12)	2.13572(12)	2.13632(11)	2.13652(19)	2.13710(11)	2.13752(18)	2.13780(11)
		1.836(28)	1.83613(8)	1.83614(8)	1.83637(19)	1.83643(9)	1.83671(11)	1.83690(8)	1.83722(14)	1.83744(15)	1.83772(10)	1.83803(9)	1.83853(9)	1.83888(16)	1.83917(9)	1.83972(15)	1.83976(9)
		1.800(24)	1.80033(8)	1.80035(8)	1.80035(18)	1.80060(8)	1.80081(11)	1.80111(7)	1.80127(13)	1.80148(14)	1.80184(9)	1.80216(9)	1.80266(8)	1.80288(15)	1.80331(8)	1.80372(14)	1.80390(8)
		2.130(25)	2.12969(9)	2.12971(9)	2.12981(21)	2.13003(10)	2.13030(12)	2.13060(8)	2.13086(16)	2.13111(17)	2.13150(11)	2.13187(10)	2.13246(10)	2.13278(17)	2.13322(10)	2.13376(17)	2.13391(9)
Nb/Fe – O – Nb/Fe bond angle (o)		159.3(17)	159.251(1)	159.252(1)	159.249(3)	159.252(1)	159.251(2)	159.252(1)	159.249(2)	159.250(2)	159.252(1)	159.252(1)	159.252(1)	159.250(2)	159.252(1)	159.250(2)	159.254(1)
		160.4(19)	160.392(1)	160.393(1)	160.391(2)	160.393(1)	160.393(1)	160.393(1)	160.391(2)	160.392(2)	160.393(1)	160.393(1)	160.393(1)	160.392(2)	160.393(1)	160.392(2)	160.394(1)
		159.3(10)	159.314(0)	159.314(0)	159.314(0)	159.314(0)	159.314(0)	159.314(0)	159.314(0)	159.314(0)	159.314(0)	159.314(0)	159.314(0)	159.314(0)	159.314(0)	159.314(0)	159.314(0)
		164.5(13)	164.543(1)	164.542(1)	164.541(1)	164.542(1)	164.541(1)	164.542(1)	164.542(1)	164.541(1)	164.541(1)	164.541(1)	164.542(1)	164.541(1)	164.542(1)	164.541(1)	164.541(1)

Table A3.16: *Rietveld refinement parameters for LT ND of $Bi_{0.75}Na_{0.25}Fe_{0.75}Nb_{0.25}O_3$, and $Bi_{0.25}Na_{0.75}Fe_{0.25}Nb_{0.75}O_3$.*

Parameter		x in $Bi_{1-x}Na_xFe_{1-x}Nb_xO_3$ materials	
x		0.25	0.75
Temperature		10 K	10 K
Space Group		*P* 4*mm*	*P* 2_1ma
χ^2		5.666	8.816
wRp (%)		8.18	8.33
Rp (%)		6.43	7.16
a (Å)		3.94883(6)	5.53932(15)
b (Å)		3.94883(6)	7.85149(21)
c (Å)		3.94725(8)	5.52847(18)
Tetragonality		0.99960	0.99804
α (°)		90	90
β (°)		90	90
γ (°)		90	90
Cell vol. (Å^3)		61.5506(18)	240.444(12)
Bi/Na 1	x	0	0.2671(20)
	y	0	0
	z	0	0.7556(20)
	U_{iso} *100	5.90(27)	1.60(18)
Bi/Na 2	x	N/A	0.2886(28)
	y	N/A	0.5
	z	N/A	0.7298(28)
	U_{iso} *100	N/A	4.01(40)
Fe/Nb 1	x	0.5	0.2628(9)
	y	0.5	0.2503(9)
	z	0.536(4)	0.2469(9)
	U_{iso} *100	0.48(4)	0.226(34)
O1	x	0.5	0.2947(23)
	y	0.5	0
	z	0.058(5)	0.2020(18)
	U_{111} *100	10.4(12)	1.19(20)
	U_{222} *100	10.36(121)	N/A
	U_{333} *100	-1.68(33)	N/A
O2	x	0.5	0.2886(21)
	y	0	0.5
	z	0.581(6)	0.3057(17)
	U_{111} *100	12.1(16)	0.75(20)
	U_{222} *100	0.46(29)	N/A
	U_{333} *100	7.87(101)	N/A
O3	x	N/A	0.0437(26)
	y	N/A	0.2194(11)
	z	N/A	0.5314(16)
	U_{iso} *100	N/A	1.62(19)
O4	x	N/A	-0.0291(25)
	y	N/A	0.2739(9)
	z	N/A	0.0474(16)
	U_{iso} *100	N/A	0.43(12)
Bi/Na – O bond length (Å)		2.8017(15)	3.065(13)
		2.8017(15)	2.472(14)
		2.8017(15)	2.628(17)
		2.8017(15)	2.932(18)
		2.577(16)	2.457(16)
		3.025(19)	2.799(10)
		2.577(16)	2.457(16)
		3.025(19)	2.799(10)
		2.577(16)	3.150(10)
		3.025(19)	2.662(14)
		2.577(16)	3.150(10)
		3.025(19)	2.662(14)
		N/A	2.345(17)
		N/A	3.184(17)
		N/A	2.776(22)
		N/A	2.777(20)
		N/A	2.810(19)
		N/A	2.989(10)
		N/A	2.810(19)
		N/A	2.989(10)
		N/A	3.054(11)
		N/A	2.385(19)
		N/A	3.054(11)
		N/A	2.385(19)
Fe/Nb – O bond length (Å)		1.884(11)	1.989(8)
		2.063(11)	1.992(8)
		1.9824(14)	2.001(11)
		1.9824(14)	1.995(12)
		1.9824(14)	1.966(11)
		1.9824(14)	2.003(10)
Fe/Nb – O – Fe/Nb bond angle (°)		180.000	162.4(6)
			159.5(6)
		169.7(9)	160.2(6)
			157.0(7)

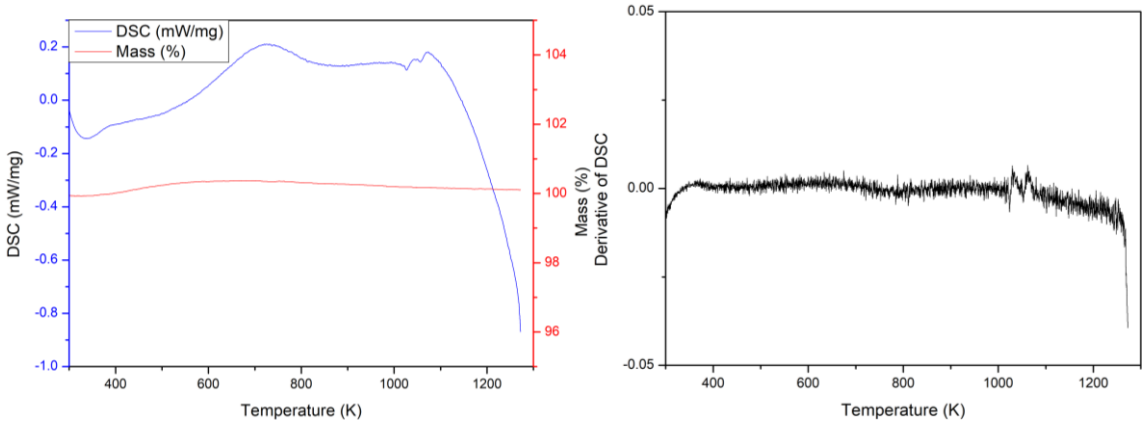

Figure A3.67: *TGA/DSC results for $Bi_{0.925}Na_{0.075}Fe_{0.925}Nb_{0.075}O_3$ (a) Full TGA/DSC plot from 298 K to 1270 K, (b) Derivative of DSC against temperature from 298 K to 1270 K.*

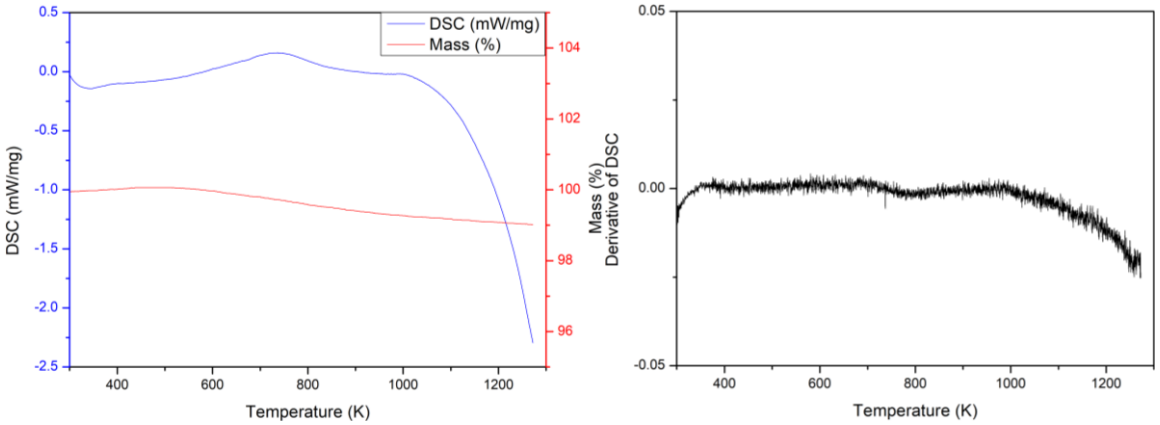

Figure A3.68: *TGA/DSC results for $Bi_{0.875}Na_{0.125}Fe_{0.875}Nb_{0.125}O_3$ (a) Full TGA/DSC plot from 298 K to 1270 K, (b) Derivative of DSC against temperature from 298 K to 1270 K.*

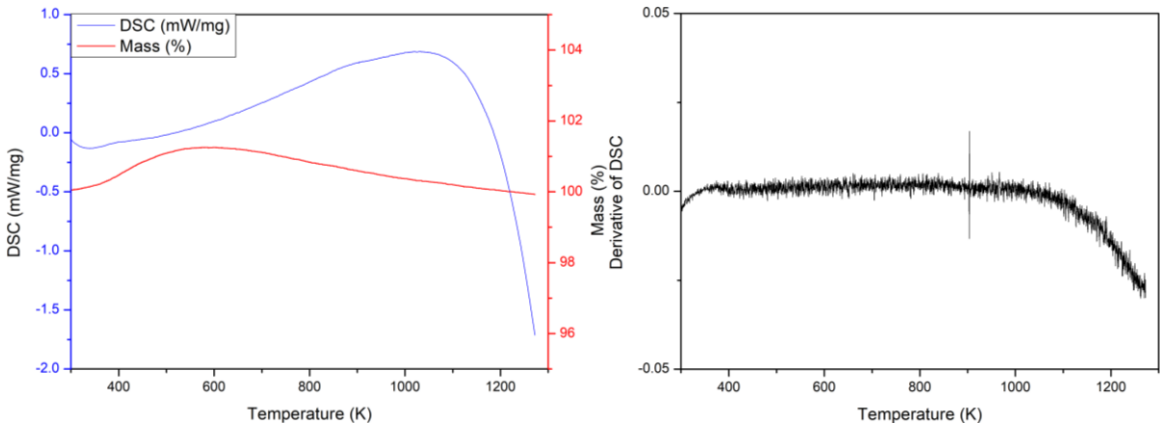

Figure A3.69: *TGA/DSC results for $Bi_{0.8}Na_{0.2}Fe_{0.8}Nb_{0.2}O_3$ (a) Full TGA/DSC plot from 298 K to 1270 K, (b) Derivative of DSC against temperature from 298 K to 1270 K.*

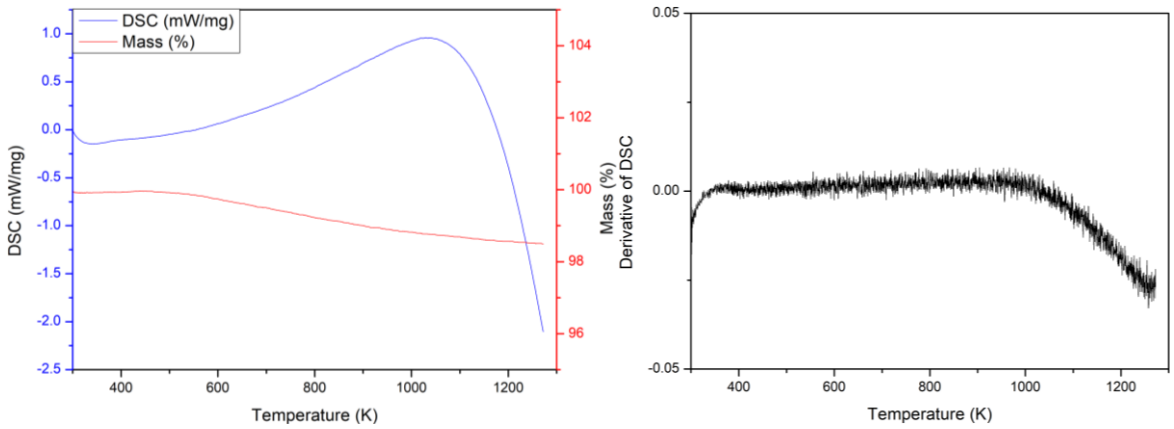

Figure A3.70: *TGA/DSC results for $Bi_{0.7}Na_{0.3}Fe_{0.7}Nb_{0.3}O_3$ (a) Full TGA/DSC plot from 298 K to 1270 K, (b) Derivative of DSC against temperature from 298 K to 1270 K.*

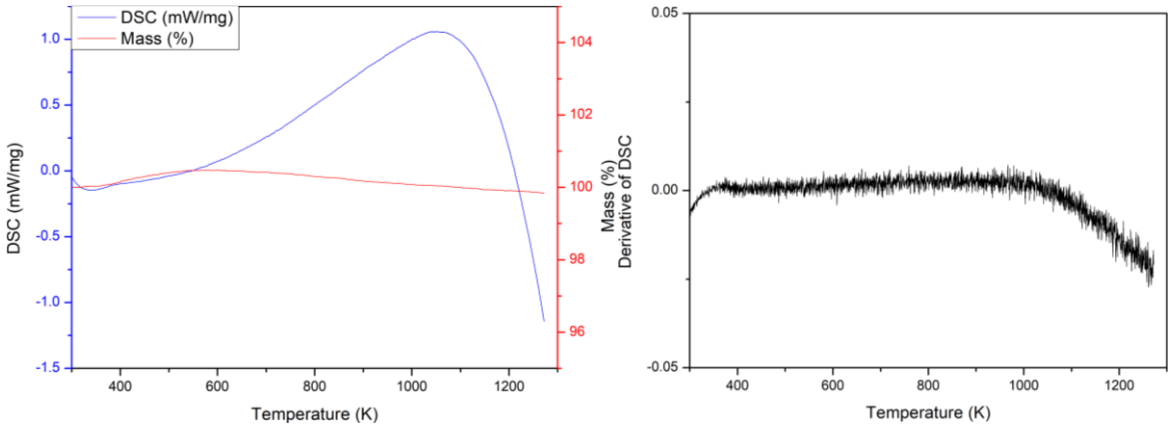

Figure A3.71: *TGA/DSC results for $Bi_{0.65}Na_{0.35}Fe_{0.65}Nb_{0.35}O_3$ (a) Full TGA/DSC plot from 298 K to 1270 K, (b) Derivative of DSC against temperature from 298 K to 1270 K.*

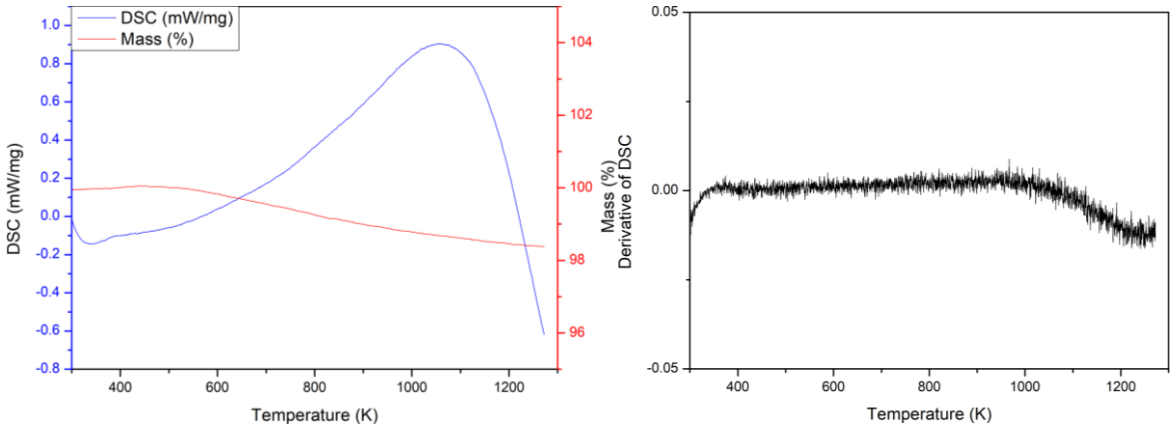

Figure A3.72: *TGA/DSC results for $Bi_{0.35}Na_{0.65}Fe_{0.35}Nb_{0.65}O_3$ (a) Full TGA/DSC plot from 298 K to 1270 K, (b) Derivative of DSC against temperature from 298 K to 1270 K.*

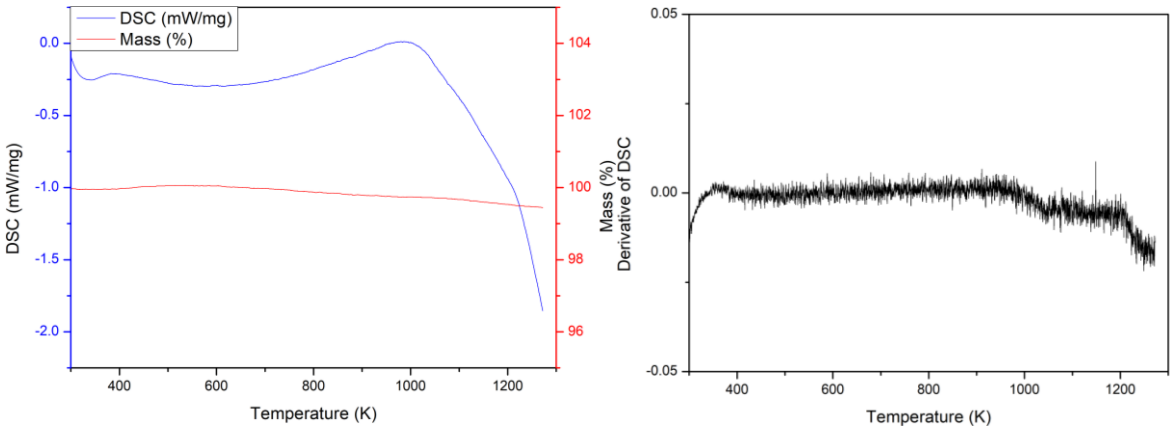

Figure A3.73: *TGA/DSC results for $Bi_{0.325}Na_{0.675}Fe_{0.325}Nb_{0.675}O_3$ (a) Full TGA/DSC plot from 298 K to 1270 K, (b) Derivative of DSC against temperature from 298 K to 1270 K.*

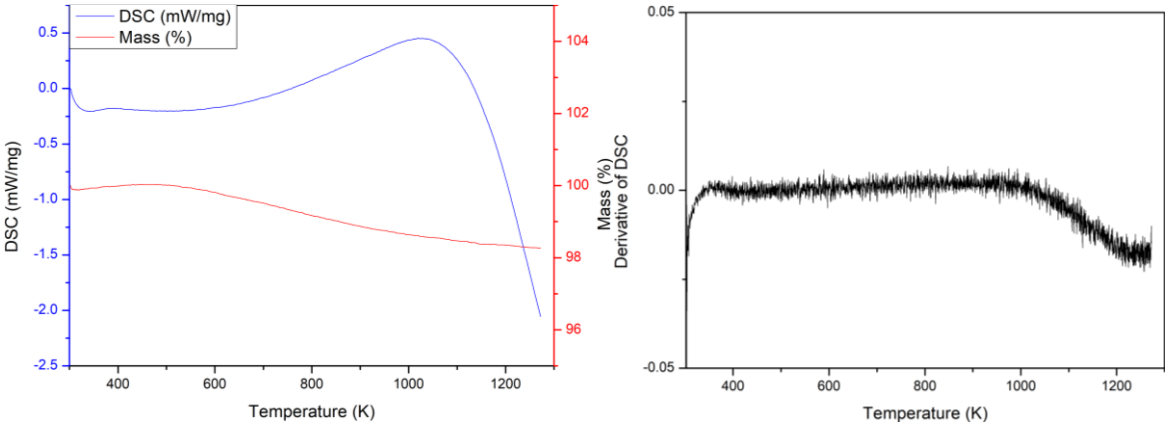

Figure A3.74: *TGA/DSC results $Bi_{0.3}Na_{0.7}Fe_{0.3}Nb_{0.7}O_3$ (a) Full TGA/DSC plot from 298 K to 1270 K, (b) Derivative of DSC against temperature from 298 K to 1270 K.*

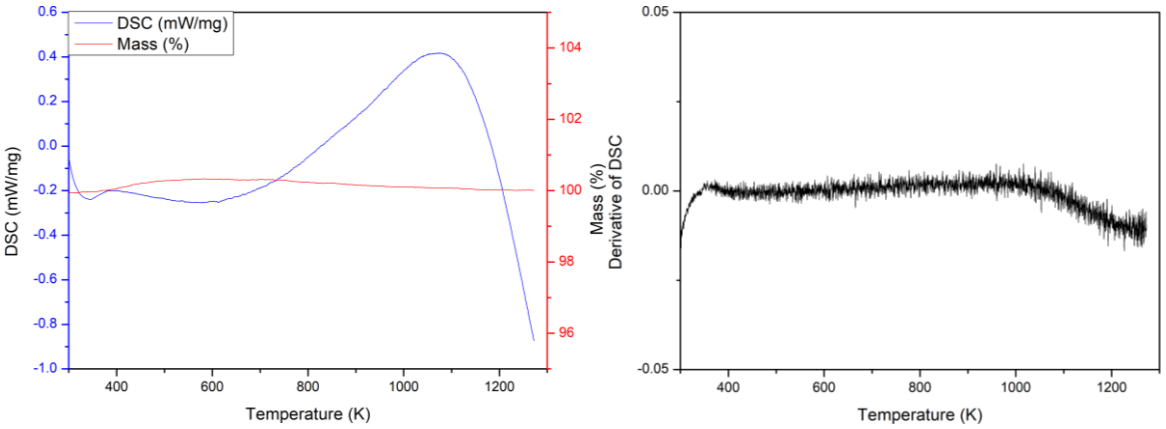

Figure A3.75: *TGA/DSC results $Bi_{0.2}Na_{0.8}Fe_{0.2}Nb_{0.8}O_3$ (a) Full TGA/DSC plot from 298 K to 1270 K, (b) Derivative of DSC against temperature from 298 K to 1270 K.*

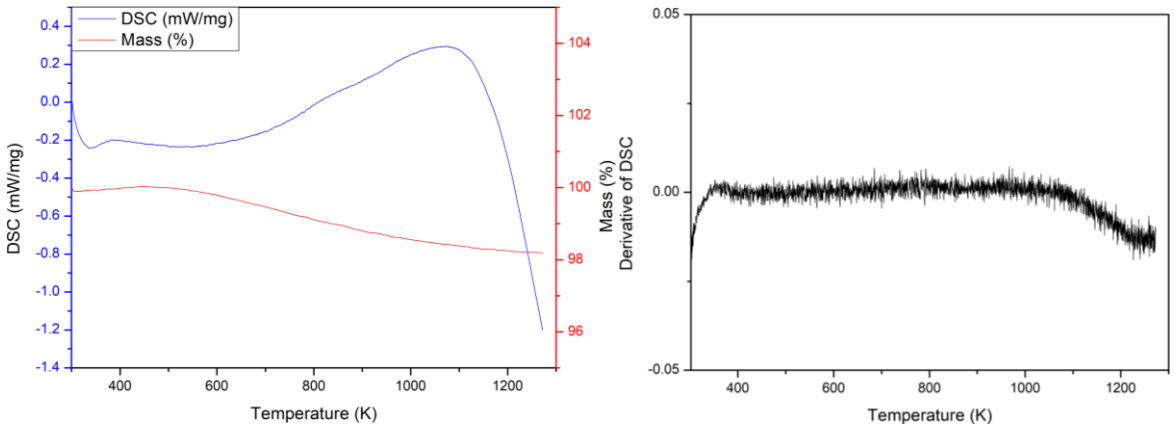

Figure A3.76: *TGA/DSC results $Bi_{0.15}Na_{0.85}Fe_{0.15}Nb_{0.85}O_3$ (a) Full TGA/DSC plot from 298 K to 1270 K, (b) Derivative of DSC against temperature from 298 K to 1270 K.*

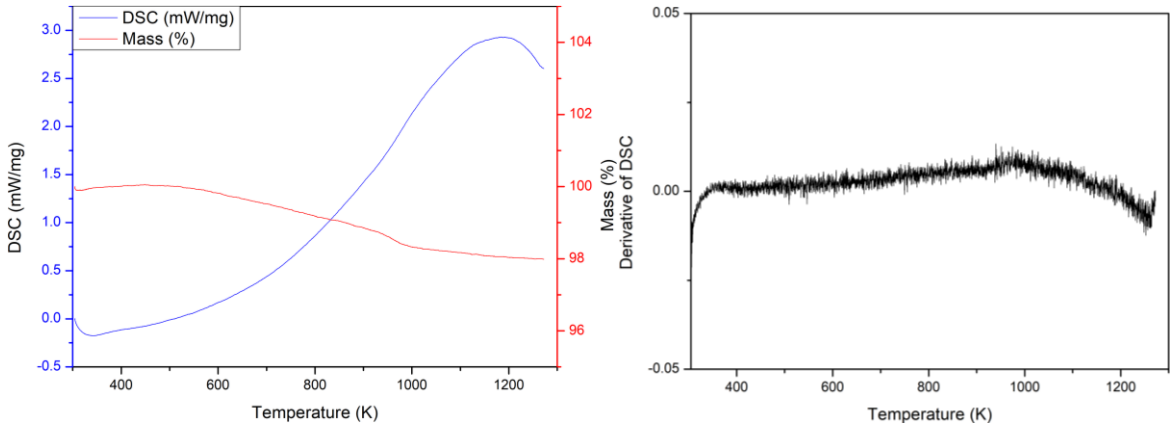

Figure A3.77: *TGA/DSC results $Bi_{0.05}Na_{0.95}Fe_{0.05}Nb_{0.95}O_3$ (a) Full TGA/DSC plot from 298 K to 1270 K, (b) Derivative of DSC against temperature from 298 K to 1270 K.*

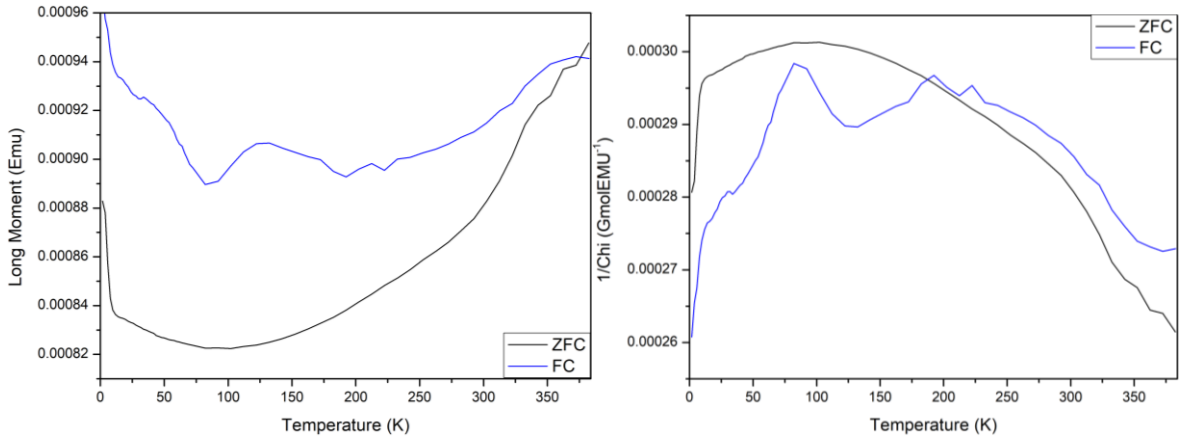

Figure A3.78: *Magnetic data from SQUID for $Bi_{0.95}Na_{0.05}Fe_{0.95}Nb_{0.05}O_3$, (a) Zero field cooled and Field cooled data at 0.1 T, (b) 1/χ SQUID data.*

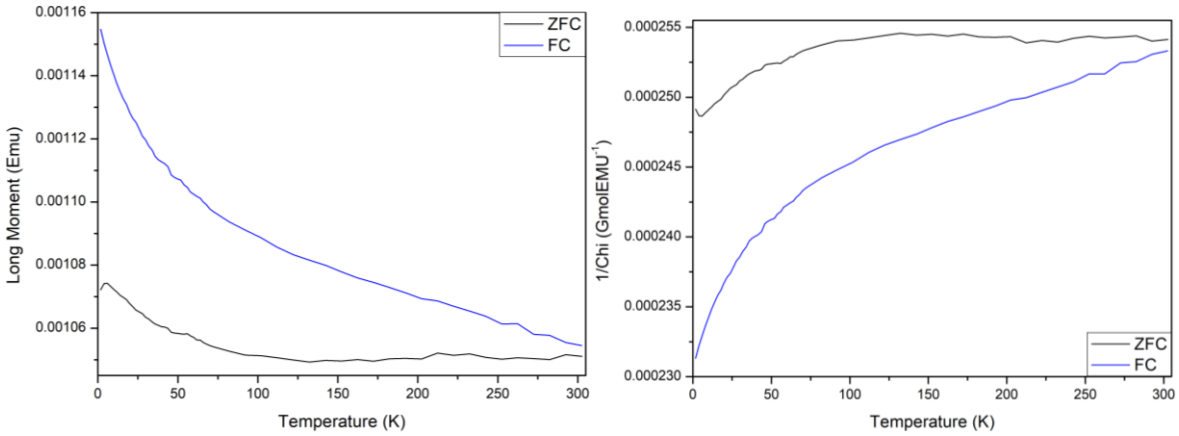

Figure A3.79: *Magnetic data from SQUID for $Bi_{0.85}Na_{0.15}Fe_{0.85}Nb_{0.15}O_3$, (a) Zero field cooled and Field cooled data at 0.1 T, (b) 1/χ SQUID data.*

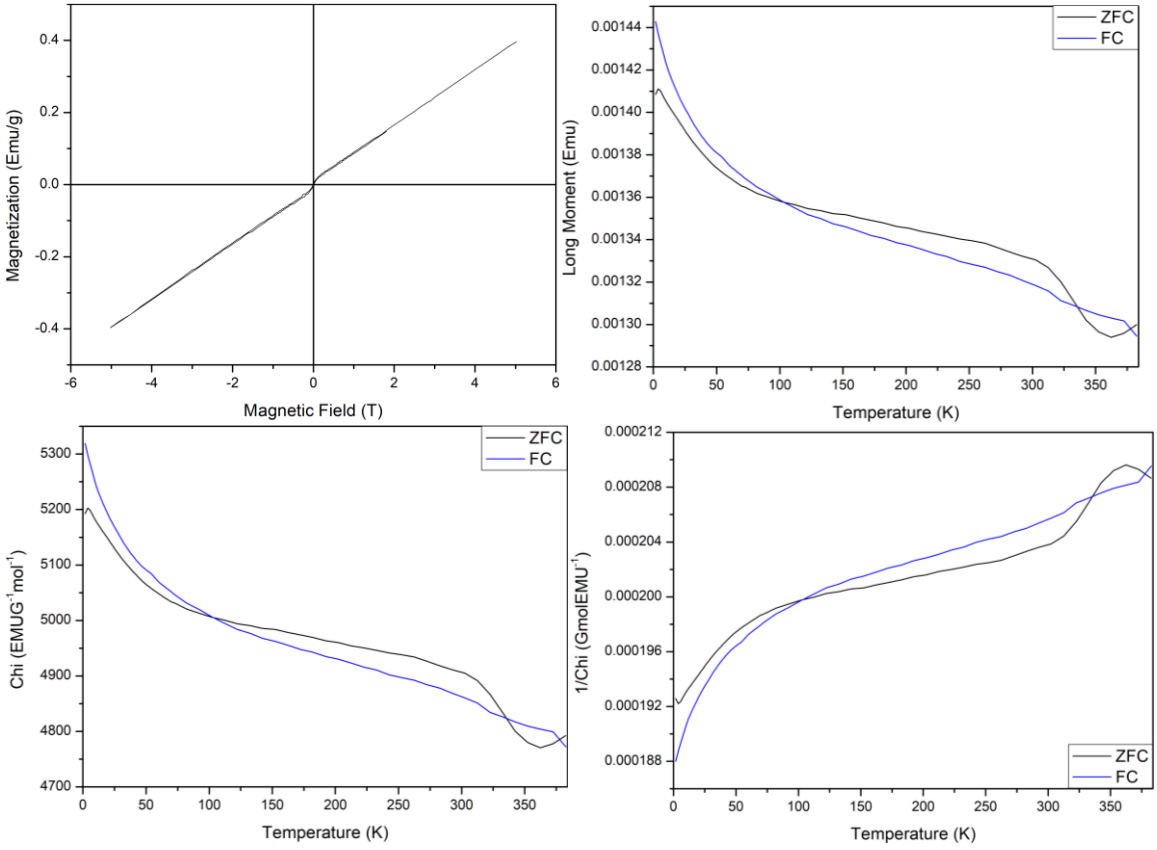

Figure A3.80: *Magnetic data from SQUID for $Bi_{0.8}Na_{0.2}Fe_{0.8}Nb_{0.2}O_3$, (a) Hysteresis loops from 2 K to 300 K at fields from -5 T to 5 T, (b) Variable temperature Zero field cooled and Field cooled data at 0.1, (c) χ SQUID data, (d) 1/χ SQUID data.*

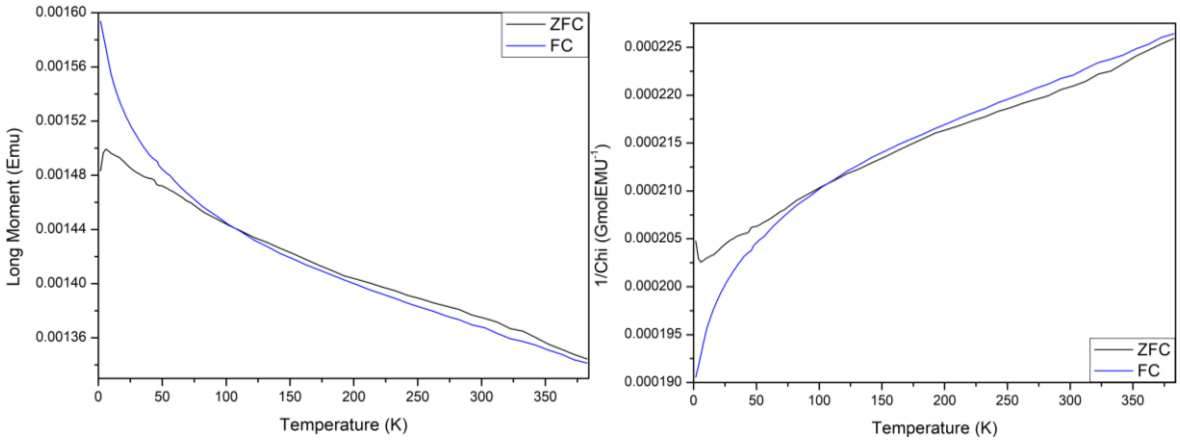

Figure A3.81: *Magnetic data from SQUID for $Bi_{0.75}Na_{0.25}Fe_{0.75}Nb_{0.25}O_3$, (a) Zero field cooled and Field cooled data at 0.1 T, (b) 1/χ SQUID data.*

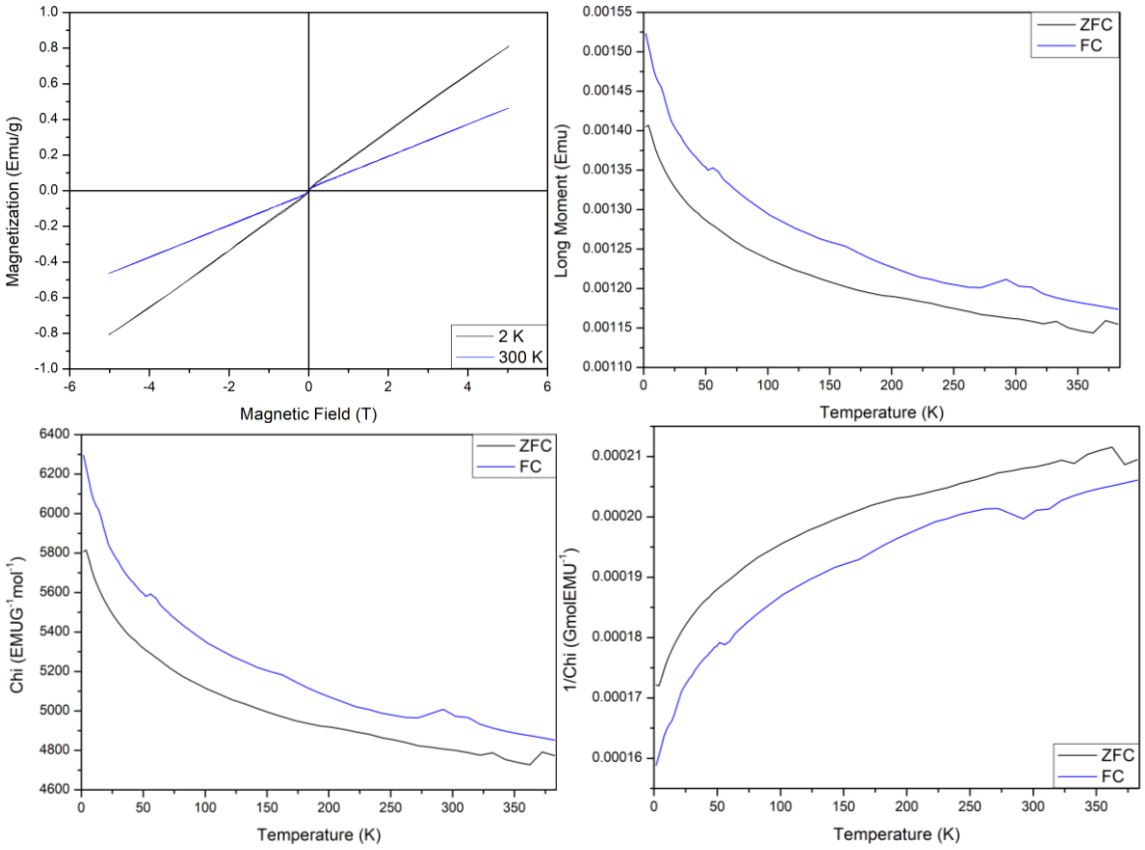

Figure A3.82: *Magnetic data from SQUID for $Bi_{0.7}Na_{0.3}Fe_{0.7}Nb_{0.3}O_3$, (a) Hysteresis loops from 2 K to 300 K at fields from -5 T to 5 T, (b) Variable temperature Zero field cooled and Field cooled data at 0.1, (c) χ SQUID data, (d) 1/χ SQUID data.*

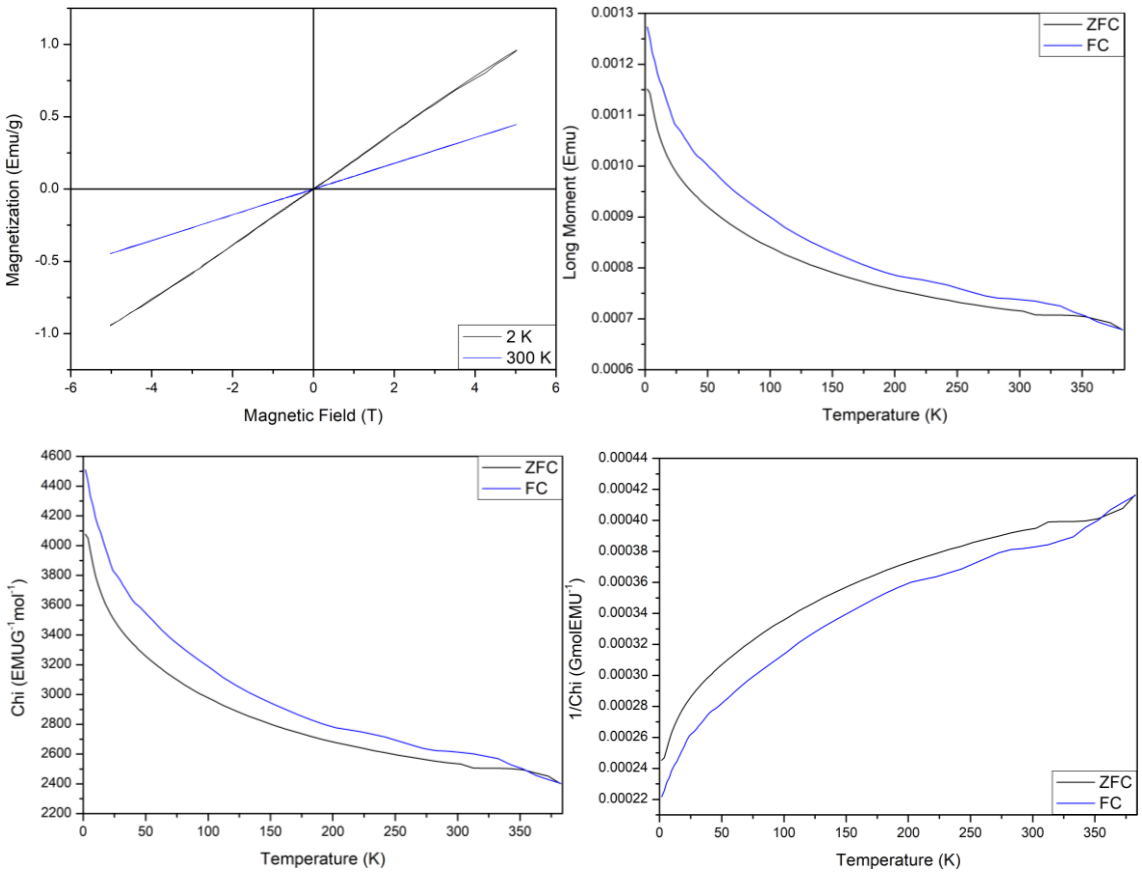

Figure A3.83: *Magnetic data from SQUID for $Bi_{0.65}Na_{0.35}Fe_{0.65}Nb_{0.35}O_3$, (a) Hysteresis loops from 2 K to 300 K at fields from -5 T to 5 T, (b) Variable temperature Zero field cooled and Field cooled data at 0.1, (c) χ SQUID data, (d) 1/χ SQUID data.*

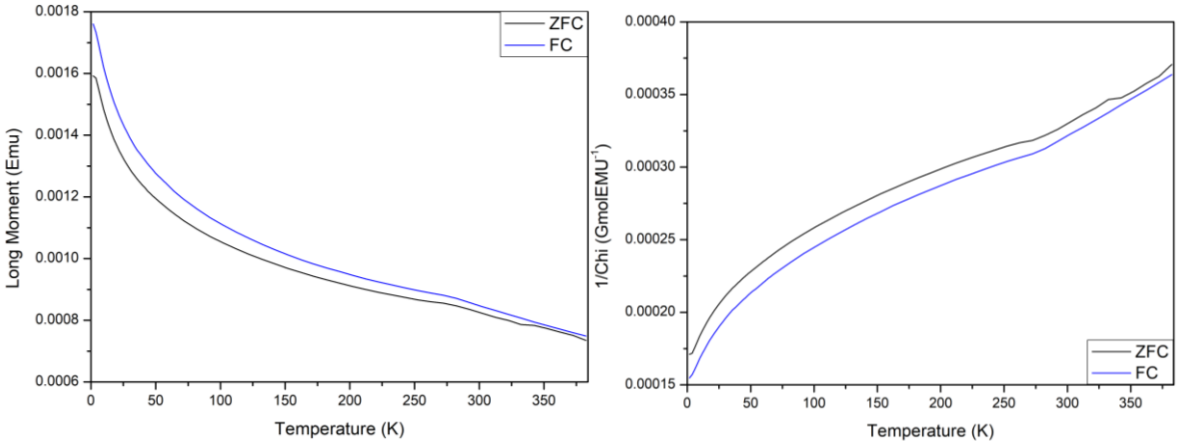

Figure A3.84: *Magnetic data from SQUID for $Bi_{0.6}Na_{0.4}Fe_{0.6}Nb_{0.4}O_3$, (a) Zero field cooled and Field cooled data at 0.1 T, (b) 1/χ SQUID data.*

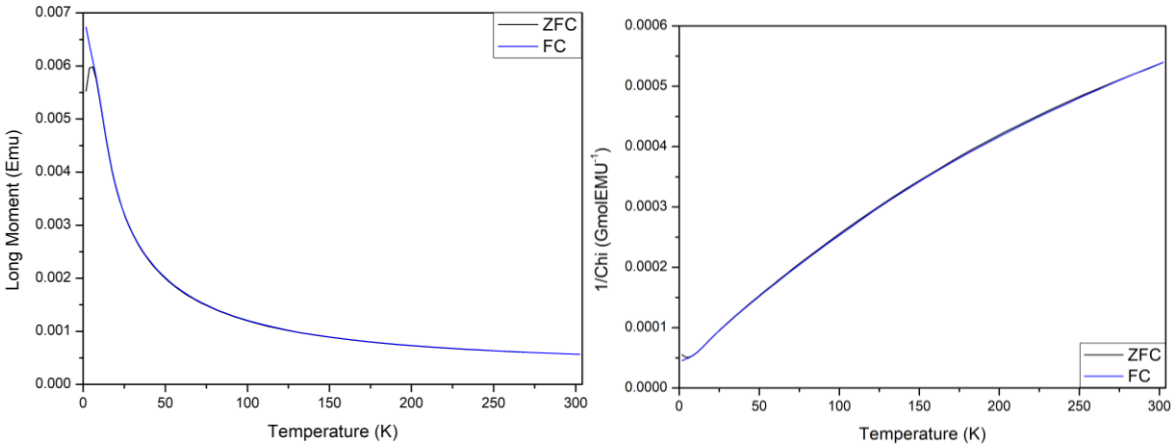

Figure A3.85: *Magnetic data from SQUID for $Bi_{0.3}Na_{0.7}Fe_{0.3}Nb_{0.7}O_3$, (a) Zero field cooled and Field cooled data at 0.1 T, (b) 1/χ SQUID data.*

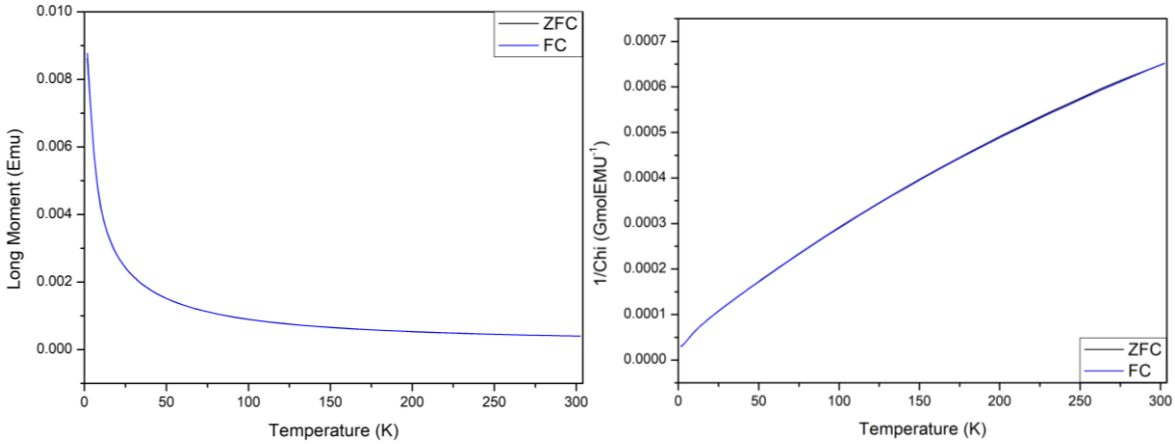

Figure A3.86: *Magnetic data from SQUID for $Bi_{0.2}Na_{0.8}Fe_{0.2}Nb_{0.8}O_3$, (a) Zero field cooled and Field cooled data at 0.1 T, (b) 1/χ SQUID data.*